Witteveen + Bos



DESIGN OF A BRIDGE WITH FLAX FIBRE

Structural feasibility of flax fibre composites in the Seasaw

Tanja Waiboer
5351707
tanjawaiboer@gmail.com

TU Delft

Design of a bridge with flax fibre

MSc Thesis

To obtain the degree of

Master of Science in Civil Engineering

at the Delft University of Technology

Author

Tanja Waiboer

5351707

tanjawaiboer@gmail.com

Supervisors

dr.ir. P.C.J. Hoogenboom

Dr. Y. Mosleh

ir. M.S. van der Wateren

ir. W. Claassen

Company

Witteveen + Bos

August 2026

Cover image: Conceptual design of Seasaw, derived from an internal company presentation by MVRDV, 12 November 2020. The figure is changed with Gemini to look like Flax fibre.

TU Delft Witteveen + Bos

Preface

This thesis was conducted as part of the Master's degree in Civil Engineering at Delft University of Technology. The research was commissioned by Witteveen+Bos. At the time of this research, the Seasaw project was not actively developed due to a lack of funding. This thesis aims to contribute to its potential further development.

Structural engineers working on the Seasaw can find information on the structural analyses in Chapters 9 and 10 and on the finite element model in Chapter 8. Engineers interested in using flax fibre composites for structural applications can find information on the material in Chapter 6.

I would like to thank my supervisors at Witteveen+Bos, ir. W. Claassen and ir. M.S. van der Wateren, and my supervisors at Delft University of Technology, dr.ir. P.C.J. Hoogenboom and Dr. Y. Mosleh, for their guidance and support throughout this thesis. I would also like to thank the employees of Witteveen+Bos, Sanne de Koning and Mark Aarsen, and my fellow student Pauline van Adrichem, for their support throughout the project.

Amsterdam, August 2026
Tanja Waiboer

ChatGPT was used during the writing of this report to assist with sentence structuring and grammar refinement. It also supported the development of code used to generate plots of the deck cross-sections. Additionally, GitHub Copilot was used as a code completion tool during programming.

Summary

The reinforcement of the dike in Den Helder has reduced the visual connection between the city and the sea. To restore this connection, the Seasaw was conceived as a bridge-like pedestrian lookout structure that moves with the tide, by rotating about a central support as the water level changes. It reconnects the city and the sea while functioning as both a landmark and a public space, while demonstrating the potential of sustainable construction materials. This thesis investigates the structural feasibility of designing the Seasaw made of flax fibre composite, a bio-based alternative to conventional fibre-reinforced composites. The main challenges are related to the complex geometry of the structure, the harsh coastal environment, and the variable mechanical properties of flax fibre composites. The objective of this research is therefore to determine whether the Seasaw can satisfy the relevant structural requirements while preserving its original architectural concept.

To evaluate this feasibility, the applicable design loads and verification criteria were established using the relevant Eurocodes for bridges. A literature study was performed to determine the mechanical properties, creep behaviour, and durability aspects of flax fibre composites. Python scripts were developed to calculate the equivalent material and cross-sectional properties required for finite element modelling using RFEM. These properties were validated using simplified beam models and analytical calculations. Two finite element models were developed: a beam model and a plate model. The comparison showed that the beam model overestimated the structural stiffness and underestimated deformations, making it unsuitable for detailed structural verification. The validated plate model was therefore used for the subsequent analyses.

The Seasaw was verified for serviceability limit state, ultimate limit state, stability including buckling, and dynamic behaviour. The analysis demonstrates that the Seasaw can be build using flax fibre composite while satisfying structural requirements. The ultimate limit state requirements were met, and the predicted serviceability deflections were generally acceptable. Local buckling was observed near the supports, indicating that additional local reinforcement is required in these regions. Furthermore, the modal analysis showed that the first natural frequencies fall within the range where pedestrian-induced vibrations may occur, meaning that vibration mitigation measures such as tuned mass dampers are required in the final design.

An equivalent glass fibre composite design was made and analysed to evaluate the influence of material selection. The glass fibre design achieved lower plate thicknesses, lower deflections, and higher natural frequencies while also reducing the total self-weight. However, the reduced plate thicknesses resulted in lower local buckling resistance making buckling the governing criterion for the glass fibre composite design, whereas deflection is governing for the flax fibre composite design. The comparison demonstrates the higher structural efficiency of glass fibre composites.

Finally, wind simulations were performed in RWIND to assess the applicability of Eurocode-based wind loads for the unique geometry of the Seasaw. The results showed that the unconventional geometry causes non-uniform pressure distributions that vary from Eurocode predictions. Nevertheless, the Eurocode provides a conservative basis for overall safety, and the simulations confirm that wind loading does not govern the material strength of the preliminary design.

The results demonstrate that the Seasaw design of flax fibre composite is structurally feasible.

Table of content

Preface 2

Summary 4

1. Project motivation 10

2. Problem analysis 11

2.1 Inventory of the current state of technology 11

2.2 Problem statement 13

3. Societal impact 14

4. System analysis 16

4.1 Area analysis 16

4.2 Stakeholder inventory 16

4.2.1 Public service providers 16

4.2.2 Private service provider 17

4.2.3 Core stakeholders 17

4.2.4 Periphery stakeholders 17

4.3 Process analysis 17

4.3.1 Use processes 17

4.3.2 System processes 18

4.3.3 Natural processes 18

4.4 function analysis 18

5. Requirements, restrictions, and evaluation criteria 19

5.1 Functional requirements 19

5.1.1 Safety of user 19

5.1.2 Usability and comfort 19

5.1.3 Maintainability 19

5.2 Structural requirements 19

5.2.1 Robustness, durability, and sustainability 19

5.2.2 Serviceability requirements 20

5.2.3 Loads on the structure 21

5.2.4 Fire safety 30

5.2.5 Deformation 30

5.3 Evaluation criteria 32

6. Materials 33

6.1 Flax fibre 34

6.1.1 Structure 34

6.1.2 Processing of Flax 36

6.1.3 Flax fibre mats 36

6.1.4 Material properties 37
6.2 Resin 38
6.2.1 Polyester resin 39
6.2.2 Epoxy resin 39
6.3 Flax fibre composite 39
6.3.1 Manufacturing 39
6.3.2 Material properties of a lamella 40
6.4 Design capacity 41
6.4.1 Characteristic value of the stress limit 41
6.4.2 Partial material factor 43
6.4.3 Conversion factor 44
6.5 Strength verification composites 47
6.6 Creep coefficient for deflection 48
6.7 Core material 49
6.8 Bonding paste 49
6.9 Classical Laminate Theory (CLT) 50
6.10 Durability 50
6.10.1 Fatigue 50
6.10.2 Moisture absorption 51
6.11 Coating 52
6.12 Hybrid Composites 53
7. Preliminary design 54
7.1 Thickness C-shaped girders 55
7.2 Thickness bottom plate, bottom face, and top face 57
7.3 Number of girders 59
7.3.1 Loads on top plate 60
7.3.2 Stiffness top plate 60
7.3.3 Deflection top plate 61
7.4 Connection upper and lower deck (De Oksel) 62
7.5 Stiffener plates 65
8. FEM model 66
8.1 Beam model 67
8.2 Plate model 67
8.2.1 Boundary conditions 69
8.2.2 Loads 69
8.2.3 Mesh 74
8.2.4 Validation of the plate model 75

8.3 Comparison plate and beam model 76
8.3.1 Deflection comparison 76
8.3.2 Conclusion 81
9. Static analysis 82
9.1 Preliminary model 82
9.1.1 Ultimate limit state 82
9.1.2 Serviceability limit state 83
9.1.3 Changes to design 87
9.2 Revised design 92
9.2.1 Ultimate limit state 92
9.2.2 Serviceability limit state 101
10. Modal analysis 105
11. Validation 108
11.1 Service life 108
11.2 User safety 108
11.3 Usability and comfort 108
11.4 Structural safety (ULS) 109
11.5 Stability 109
11.6 Serviceability performance (SLS) 109
11.7 Robustness 110
11.8 Durability 110
11.9 Sustainability 110
11.10 Design of the Seasaw 110
12. Comparison of flax and glass fibre composites 111
12.1 Design in glass fibre composite 111
12.1.1 Thickness structure different components 111
12.2 Static analysis 113
12.2.1 Ultimate limit state 113
12.2.2 Serviceability limit state 115
12.3 Modal analysis 119
12.4 Comparison 120
12.4.1 Thickness of the plates 120
12.4.2 Self-weight 121
12.4.3 Stability 121
12.4.4 Deflections 122
12.4.5 Eigenfrequencies and modal shapes 123
13. Eurocode wind loads against RWIND wind loads 124

13.1 Testing of RWIND with simple structure 125
13.2 RWIND simulation Seasaw without modelled dike in x-direction 126
13.2.1 Results of the wind simulations 126
13.2.2 Comparison with Eurocode loads 128
13.3 RWIND simulation Seasaw without modelled dike in y-direction 133
13.3.1 Results of the wind simulations 133
13.3.2 Comparison with Eurocode loads 135
13.4 RWIND simulation Seasaw with modelled dike in x-direction 139
13.4.1 Results of the wind simulations 139
13.4.2 Comparison with Eurocode loads 141
13.5 Comparison RWIND simulations in x-direction with and without dike modelled 146
13.6 Overall assessment of the Eurocode wind-load provisions 149
14. Discussion 150
14.1 Finite element model reliability 150
14.2 Finite element model mesh error 151
14.3 Material properties uncertainty 152
14.4 Applicability to different environmental conditions 152
14.5 Structural optimization and design efficiency 153
14.6 Practical implementation of the Seasaw 154
14.7 Wind simulation reliability 154
15. Conclusion 156
15.1 Finite element model development and validation 156
15.2 Validation of the design 156
15.3 Comparison of flax and glass fibre composite 157
15.4 Wind simulation 157
15.5 Recommendations for further development 157
References 159
Appendix A : Strength verification composites 163
Appendix B : Material properties of different fibre composites 166
Appendix C : Classical Laminate Theory (CLT) 170
Appendix D : Python code for the Classical Laminate Theory (CLT) 182
Appendix E : Explanation and validation of the CLT python code 193
Appendix F : Python code for the stiffness of the cross-section 199
Appendix G : Explanation and validation of the stiffness of the cross-section code 212
Appendix H : Python code for the input for a beam model in RFEM 226
Appendix I : Explanation and validation of the input for a beam model in RFEM code 227
Appendix J : Python code for the input for a plate model in RFEM 237

Appendix K : Explanation and validation of the input for a plate model in RFEM code 243
Appendix L : Design loads preliminary design 256
Appendix M : Cross-sections preliminary design and RFEM input 262
Appendix N : x-coordinates support and stiffener plates preliminary design 276
Appendix O : Load combinations RFEM 277
Appendix P : Description of the beam model 282
Appendix Q : Mesh sensitivity study 288
Appendix R : Load comparison plate and beam model 290
Appendix S : Overview figures components and singularities 295
Appendix T : Unity checks of the preliminary design 311
Appendix U : Deformation plots preliminary design 317
Appendix V : x-coordinates support and stiffener plates revised design 319
Appendix W : Thickness structures and input RFEM plates revised design 321
Appendix X : Stability analysis 327
Appendix Y : Modal shapes 331
Appendix Z : Thickness structures and input RFEM plates glass fibre design 335
Appendix AA : Unity checks and flange design of the glass fibre design 341
Appendix BB : Stability analysis glass fibre design 349
Appendix CC : Creep glass fibre composite 352
Appendix DD : Modal analysis glass fibre design 354
Appendix EE : Testing of RWIND with simple structure 358
Appendix FF : RWIND settings for the wind analysis of the Seasaw 365
Appendix GG : Determining of orography factor 370
Appendix HH : Eurocode wind loads for comparison with RWIND simulations 371

1. Project motivation

In Den Helder, the sea view has traditionally played an important role, offering a clear sense of the tidal movements. Following the dike reinforcement, however, this connection to the sea has been largely lost. The strengthened dike now functions as a visual barrier, making a view of the sea uncommon during an everyday walk. [1]



Figure 1: Illustration of the seasaw[1]

To reconnect the sea and the land, the Seasaw has been proposed, as shown in Figure 1. The Seasaw is a bridge-like structure that rotates about a central support, allowing it to move with the changing tidal water level. As the tide rises and falls, the bridge tilts accordingly, creating a dynamic connection between the city and the sea while enabling visitors to experience the tidal movement. The movement of the Seasaw is illustrated in Figure 2. The Seasaw will be placed on a dike and will be made of sustainable materials.[1]

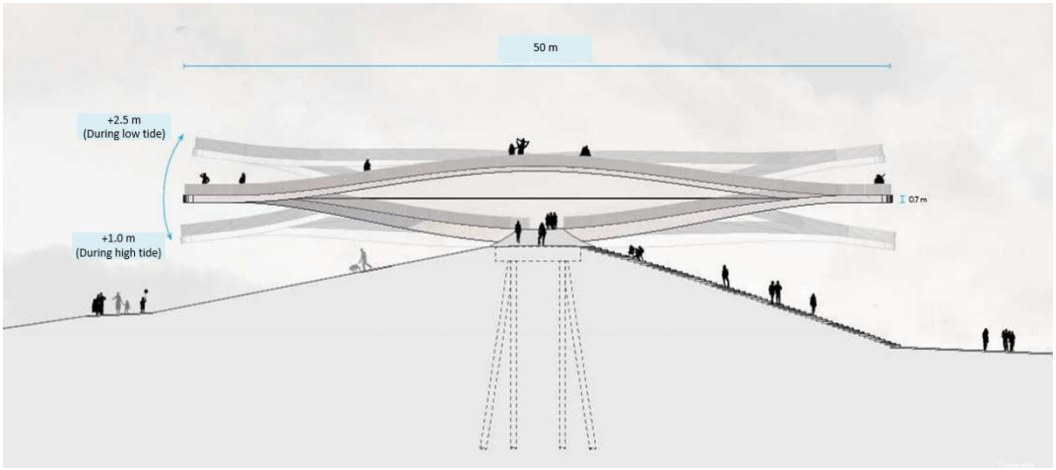

Figure 2: Illustration of the movement with the tide of the seasaw[1]

The planned location lies in an area designated for renewal and expansion, see Figure 3. The main goal is to emphasize the transition between the city and the sea, while creating a striking landmark that will put Den Helder back on the map, not only for its residents but also for visitors from across the Netherlands and beyond.[1] By utilizing sustainable materials and construction methods, the bridge could demonstrate low-impact infrastructure design while supporting societal goals in creating meaningful public spaces, protecting the environment, and strengthening the city's cultural identity.

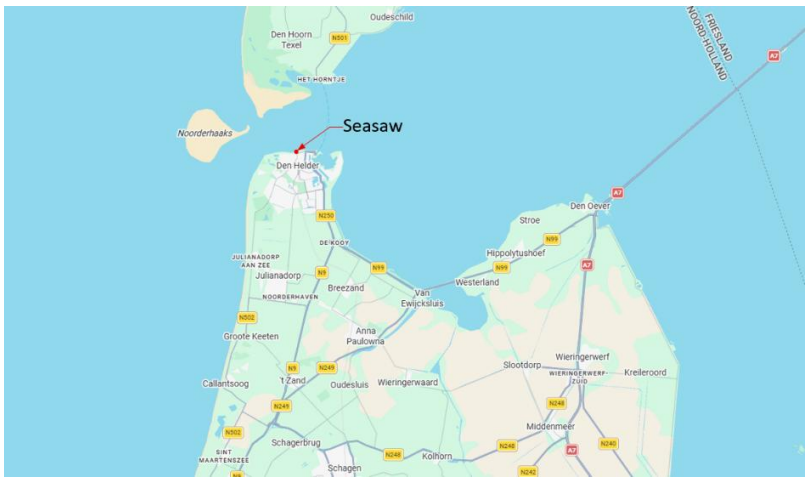

Figure 3: Location of the Seasaw (Maps, 2026)

[1] Company presentation by MVRDV, "Presentatie Haalbaarheidsonderzoek Seasaw", 12 November 2020.

2. Problem analysis

The bridge design will be located in Den Helder on a dike. The location is characterized by strong winds, saltwater exposure, and fluctuating humidity. The bridge must be highly durable due to the presence of harsh coastal elements. The bridge, the Seasaw, will be made out of sustainable materials. For this project, the bridge will be designed out of flax fibre composite. Using flax fibre as primary material introduces uncertainties. Flax fibre composites are bio-based, and while sustainable, they have variable mechanical performance compared with traditional composites. Flax fibre is also sensitive to moisture absorption, which can reduce stiffness and long-term durability. There is still limited long-term performance data in maritime and salt-rich environments. The Seasaw has a complex geometry. Due to the Seasaw's complex geometry, evaluating its internal stress behaviour becomes considerably more challenging. The problems arise throughout the entire project lifecycle: during the design phase, where predicting the behaviour of the flax fibre structure and modelling the bridge are difficult; during construction, when manufacturing challenges and quality control issues may appear; and during operation, as long-term performance and durability under dynamic loads and coastal conditions remain uncertain. (Flax Fibre Reinforcement in Composites, sd) (Pavlovic, Valzania, & Minak, 2025)

2.1 Inventory of the current state of technology

The use of natural fibres as construction material is not a recent invention. It has actually been around since the seventies. For example, they were used in Bangladesh to construct primary schools with jute-fibre-reinforced polyester in 1972–73. Burgueno et al. demonstrated that bio-composites can function as load-bearing elements when their cellular structures are configured to enhance structural efficiency. For their laboratory-scale periodic cellular beams and plates, they produced the materials by impregnating hemp and flax fibres with an unsaturated polyester resin. Uddin et al. developed Natural fibre-reinforced polymeric structural insulated panels (NSIPs) to use in panelized construction. The panel is made from outside layers of laminated polypropylene reinforced with jute, and a core of expanded polystyrene (EPS). Tests showed that it could be used for structural elements, for example in floor and wall construction. Natural fibre composites have been used to develop various structural components, including beams, roof structures, multi-purpose panels, and pedestrian bridges. An example of a beam with natural fibre composites, is a sandwich beam constructed with soybean-oil-based resin, natural fibres (such as flax, recycled paper, and chicken feathers), E-glass fibre, and closed cell structural foam. The beam consists of a top and bottom horizontal face sheet, with two vertical webs connecting them, see Figure 4. (Shahmirzaloo, 2025)

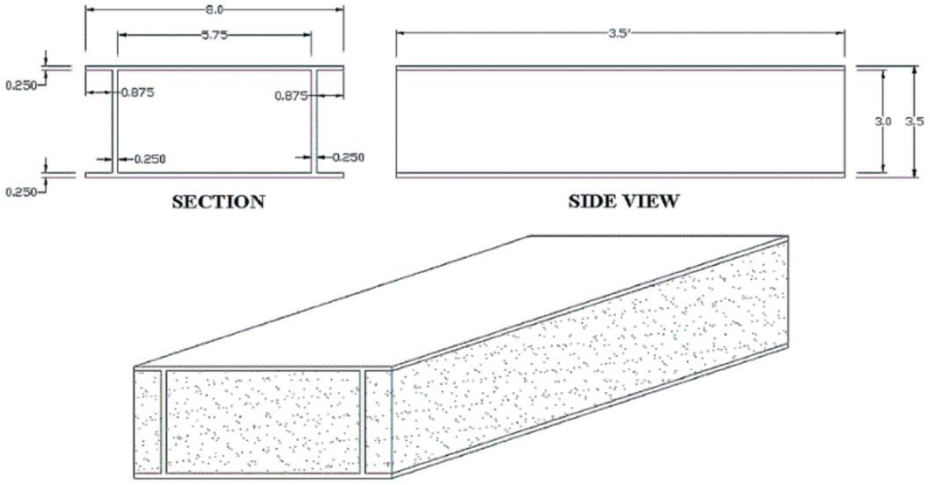

Figure 4: A schematic diagram showing an example of the sandwich beam (Shahmirzaloo, 2025)

Flax fibre has already been incorporated into several bridge projects, including the Ritsumasyl Bridge, the Floriade Footbridge in Almere, a vehicle bridge in Ulm, and the Rijkswaterstaat bridge. These projects demonstrate different approaches to the structural application of bio-based fibre-reinforced composites. The Ritsumasyl Bridge, the vehicle bridge in Ulm, and the Rijkswaterstaat bridge were developed using the construction approach of Delft Infra Composites, in which C-shaped girders are combined with deck plates. The Floriade Footbridge in Almere, developed by Fibercore, uses a different sandwich construction in which the core extends over the full height of the deck. An overview of these four bridge projects is presented in Figure 5.[2]



Figure 5: Overview of four bio-based fibre-reinforced composite bridges[2]

The construction approach used for the vehicle bridge in Ulm is shown in Figure 6. The deck consists of a bottom plate, C-shaped girders, and a top plate. The top plate itself is a sandwich structure composed of a bottom face sheet, webs and core material, and a top face sheet. The combination of the sandwich top plate with C-shaped girders and a bottom plate creates a structural system consisting of separate components. This allows the individual components to be manufactured independently, so that if a defect occurs during production, only the affected component needs to be replaced rather than the entire deck. Another advantage of this approach is the reduced structural weight. The sandwich construction of the top plate provides the required thickness and stiffness while efficiently transferring the applied loads to the other structural components. This design principle was developed by Delft Infra Composites.[2]

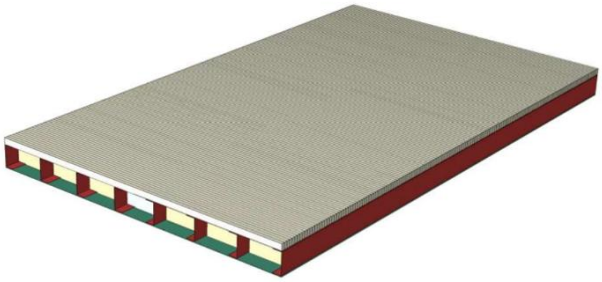

Figure 6: Schematic deck of the bridge in Ulm[2]

[2] Company presentation by W.Claassen and F.Moonen, “OOV-Building with flax fibre”, 26 February 2026.

2.2 Problem statement

The Seasaw combines an unconventional geometry with a sustainable material in a demanding coastal environment. Designing such a structure requires verification that it can safely withstand the relevant actions while satisfying the ultimate limit state (ULS), serviceability limit state (SLS), stability, durability, and user comfort requirements. The use of flax fibre composite introduces additional uncertainty because its mechanical properties, long-term creep behaviour, and durability are less well established than those of conventional structural materials.

The main problem of this thesis is therefore:

Is it structurally feasible to construct the Seasaw in Den Helder using flax fibre composite, while satisfying the applicable structural design requirements and preserving the original architectural concept?

To answer this question, the following aspects are investigated:

- Determination of the applicable design loads and verification criteria.
- Determination of material properties.
- Development and validation of finite element models suitable for analysing the Seasaw.
- Structural verification of the flax fibre design for ULS, SLS, stability, and dynamic behaviour.
- Comparison of the flax fibre design with an equivalent glass fibre composite design.
- Verification of the applicability of the Eurocode wind loads using RWIND simulations.

3. Societal impact

This MSc thesis contributes to the design and feasibility assessment of the Seasaw: a tidal-responsive bridge-like pedestrian lookout structure placed on the dike in Den Helder and constructed from flax fibre composites. While the scope of this thesis focuses on the structural feasibility of flax fibre in a complex coastal bridge design, the outcome of this project can inspire the use of flax fibre in more sustainable infrastructure. First order impacts of the project are:

- The project contributes to more sustainable construction practices by using flax fibre composites.
- The Seasaw enhances public space in Den Helder by restoring the visual and experiential connection between the land and the sea.

The second order impacts are:

- The Seasaw can strengthen Den Helder's cultural identity and international visibility as a city associated with innovation and sustainability.
- Increased tourism and visitor activity may stimulate long-term economic benefits for local businesses and services.

All designs can potentially be misused or have adverse effects. Below are the three most relevant types of adverse societal consequences of this project listed.

- Structural or durability failure of bio-based materials
    - Likelihood: Medium
      Given the limited long-term performance data of flax fibre composites in salt-rich, high-humidity environments, uncertainties remain.
    - Effect: High
      Premature degradation or failure could compromise safety, lead to costly repairs, and undermine public trust in sustainable materials.
    - Mitigation actions:
      During the MSc thesis, conservative design assumptions are applied, sensitivity analyses can be performed, and protective measures are evaluated.
- Increased maintenance burden on public authorities
    - Likelihood: Medium
      Bio-based materials may require more frequent inspection and maintenance than conventional materials, particularly in harsh coastal conditions.
    - Effect: Medium
      Higher long-term operational costs may strain municipal or water authority budgets and reduce willingness to adopt innovative sustainable materials in future projects.
    - Mitigation actions:
      Compare maintenance requirements with conventional alternatives and identify design or material choices that minimize inspection frequency and maintenance intensity.
- Disruption of dike inspection and maintenance operations
    - Likelihood: Low
      The bridge might interfere with routine inspection, reinforcement, or emergency access along the dike.
    - Effect: High
      Reduced accessibility could delay flood defence maintenance or emergency response, indirectly increasing flood risk.

- Mitigation actions:
  Identify spatial and functional constraints of dike management and emphasize coordination with water authorities in design and planning recommendations.

4. System analysis

In the system analysis, a comprehensive understanding of the project is developed by exploring the physical area, mapping the involved stakeholders, and analysing both the processes and the functions that shape the Seasaw's performance within its environment.

4.1 Area analysis

The bridge will be in Den Helder on a dike. The dike geometry is shown in Figure 7. Den Helder is located at the northern tip of Noord-Holland and facing the North Sea, Wadden sea and Marsdiep. The area is heavenly influenced by coastal winds, saltwater exposure, and high groundwater levels. The high wind loads can cause oscillations and vibrations in the bridge and have to be considered when designing the structure of the bridge. The saltwater exposure and salt in the air can damage the flax fibre. Dikes in Den Helder are part of the primary flood defence system, managed mainly by Hollands Noorderkwartier. Dikes in Den Helder typically consist of sand cores with clay layers and a grass cover. The loads of the bridge might affect the local stability of the dike toe, crest pressure distribution, and differential settlement.

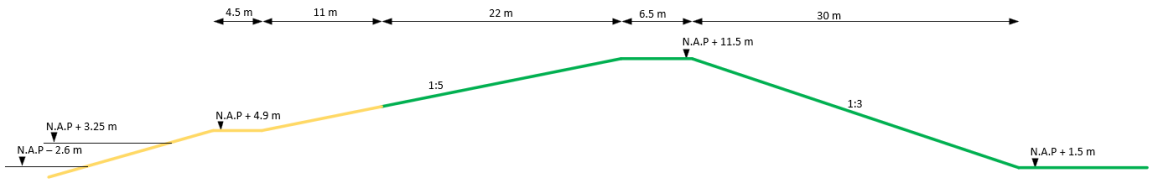

Figure 7: Estimation of the dike geometry

4.2 Stakeholder inventory

The stakeholders will be divided in public service provider, private service provider, core stakeholders, and periphery stakeholders.

4.2.1 Public service providers

The public service provider relevant to the project are:

- **Municipality of Den Helder**
  Initiator of the coastline redevelopment and cultural landmark projects
- **Province of Noord-Holland**
  Involved in spatial planning, economic development, and tourism strategy.
- **Rijkswaterstaat**
  Responsible for coastal defence and national water management, critical for a structure placed on or near the dike.
- **Hoogheemraadschap Hollands Noorderkwartier**
  Guardian of regional flood protection; must approve any intervention near water defences.
- **Public permitting Authorities**
  Oversee environmental impact assessments and construction permits.

4.2.2 Private service provider

The private service provider relevant to the project are:

- **MVRDV (designer of The Seasaw)**
  Provides the artistic concept and technical design.
- **Engineering firms / Consultancies**
  Hydraulics, structural engineering, geotechnical experts.
- **Construction contractors & subcontractors**
  Build the installation (civil works, mechanical systems, foundations).
- **Investors / Private sponsors**
  Depending on funding model, may co-finance or even partially own the installation.
- **Suppliers**
  Lighting systems, materials, fabrication partners.

4.2.3 Core stakeholders

The core stakeholders relevant to the project are:

- **Local residents of Den Helder**
  Interested in noise, sightlines, tourism effects, and public-space changes.
- **Local user groups**
  Walkers, cyclists, beach visitors, neighbourhood associations.
- **Environmental organizations**
  For example: Natuur- en Milieufederatie Noord-Holland, Greenpeace, and Milieudefensie.
- **Tourists and day visitors**
  Will use the Seasaw once completed.

4.2.4 Periphery stakeholders

The periphery stakeholders relevant to the project are:

- **Local businesses who are not directly involved**
  Shops, restaurants, hotels that may benefit indirectly.
- **Cultural & educational institutions**
  Schools, museums, tourism bureaus that might use the structure occasionally.
- **Social organizations & civic groups**
  Neighbourhood clubs, local associations affected indirectly.
- **General public of Den Helder**
  Citizens who are impacted by the area transformation but not directly involved.

4.3 Process analysis

In the process analysis, the various processes that affect the Seasaw are explored, including the activities of users, the operational and maintenance processes of the system, and the natural environmental processes acting on the structure.

4.3.1 Use processes

The Seasaw is expected to be used by a broad range of visitors, including both tourists and local residents. Users will typically approach the installation via the pedestrian and cycling paths that provide access to the site. Upon arrival, they will interact with the structure through activities such as observing the installation, taking photographs, and walking across or around it.

4.3.2 System processes

During operation, the Seasaw requires continuous management and maintenance to ensure safe and reliable performance. Routine system processes include periodic cleaning to remove accumulated sand, salt, and marine deposits that may affect mechanical components or surface finishes. Preventive maintenance must be conducted on all structural, mechanical, and electrical subsystems, accompanied by scheduled inspections to verify structural integrity, mechanical functionality, and electrical safety in a coastal environment.

If the Seasaw incorporates a tidal-responsive or mechanically actuated movement system, this mechanism must be continuously monitored and controlled to ensure proper operation within design limits. Control systems may include sensors, actuators, and software that regulate motion, detect anomalies, and initiate safety shutdowns when necessary. In addition, system processes may involve operational monitoring, logging of performance data, and periodic calibration of moving components to mitigate wear caused by environmental exposure.

4.3.3 Natural processes

The Seasaw is continuously exposed to a range of natural environmental processes characteristic of the coastal zone. Wind loading, particularly during storm events, imposes significant aerodynamic forces on the structure and must be accounted for in its structural design. The marine environment also subjects the installation to saltwater exposure and sea-spray deposition, both of which demand the use of durable, corrosion resistant material or extra protection to the material.

Sand transport driven by coastal winds and beach morphology can lead to abrasion of surfaces and potential accumulation around mechanical components or foundations. Temperature fluctuations induce thermal stresses in structural and mechanical elements, while high humidity and rainfall increase the risk of water ingress into electrical and control systems. Solar radiation contributes to the long-term degradation of coatings and polymer materials through UV exposure. Together, these natural processes define the environmental load spectrum to which the Seasaw must be designed and maintained.

4.4 function analysis

The functional analysis distinguishes between the principal function of the system, the preserving functions required to prevent interference with surrounding systems, and the additional functions that arise as beneficial side effects of the intervention.

- Principle function:
  - Provide a coastal landmark that creates a unique interactive experience for visitors.
- Preserving functions:
  - Maintain structural integrity of the dike and coastline.
  - Avoid negatively influencing flood protection.
  - Preserve natural sand transport.
  - Preserve local ecology.
  - Maintain access routes along the coastline.
  - Avoid obstructing coastal pathways.
- Additional functions:
  - Stimulate local tourism and economic activity.
  - Strengthen local identity and cultural branding.
  - Restore connection to the sea by tidal movement of the Seasaw.
  - Offer aesthetic enhancement of Den Helder’s coastline.

5. Requirements, restrictions, and evaluation criteria

The Seasaw is assumed to function as a footbridge. To determine the requirements and evaluation criteria, the Eurocodes for footbridges are adopted as the governing design framework. The structure is classified in Consequence Class CC2 in accordance with NEN-EN 1990, implying normal consequences of failure and standard requirements for reliability and safety. This chapter first presents the functional requirements governing the intended use of the structure. Subsequently, the structural requirements are defined, including the actions and loads that the Seasaw must resist. Finally, the requirements are summarised in a set of evaluation criteria, which provide a concise checklist for assessing the adequacy of the final structural design.

5.1 Functional requirements

The design service life of the Seasaw is 50 years, in accordance with NEN-EN 1990+A1+A1/C2/NB:2019, Table NB.11-2.1, with a consequence class of CC2. The functional requirements are defined to ensure that the structure performs its intended function safely, comfortably, and reliably throughout this period.

5.1.1 Safety of user

The Seasaw shall provide a safe environment for all intended users under normal operating conditions. The design shall minimise risks related to falling, slipping, loss of balance and other foreseeable hazards during pedestrian use.

5.1.2 Usability and comfort

The Seasaw shall be suitable for its intended function as a pedestrian footbridge and shall provide a level of comfort that encourages normal use. Movements, geometry, and overall behaviour of the structure shall not cause discomfort, fear, or uncertainty for users during regular pedestrian traffic.

5.1.3 Maintainability

The Seasaw shall be designed such that inspection, maintenance and minor repair activities can be conducted safely and efficiently throughout the design working life. The structural concept, detailing and material choices shall support a maintenance strategy that ensures long-term functionality and safety without excessive intervention.

5.2 Structural requirements

The structural requirements define the performance criteria that the Seasaw must satisfy to ensure adequate structural behaviour throughout its design working life. These requirements address the ability of the structure to safely resist actions, maintain stability, provide acceptable serviceability performance, and achieve the intended level of durability, robustness, and sustainability. Compliance with these requirements ensures that the structure performs reliably under all relevant design situations.

5.2.1 Robustness, durability, and sustainability

The requirements are obtained from NEN-EN 1990

Robustness

The structure should be designed to have an adequate level of robustness so that during its design service life it will not be damaged by unforeseen adverse events to an extent disproportionate to the original cause.

Durability

The structure shall be designed such that any deterioration over its design service life does not impair its intended performance, having due regard to its exposure to the environment and its anticipated level of maintenance.

Sustainability

The structure should be designed to limit its adverse impact on non-renewable environmental resources, on society, and on economy during its entire life cycle.

5.2.2 Serviceability requirements

The requirements are obtained from NEN-EN 1990

General requirements

- Specified clearance gauges should be maintained without encroachment by any part of the structure for deformations under the characteristic load combination.
- Wind-induced vibrations of structures and structural elements shall be verified in accordance with EN 1991-1-4.

Approach for the assessment of vibrations due to pedestrian movement

- Human-induced vibration shall be assessed to ensure that vibrations due to pedestrian movement are acceptable.
- Vibrations due to pedestrian movement should be assessed if any relevant natural frequency of the bridge is situated within the critical natural frequency limits.

Critical ranges of natural frequency

- The comfort criteria for pedestrian excitation should be verified for vertical and longitudinal vibrations if the corresponding natural frequencies of the bridge are situated within given critical natural frequency limits. The critical natural frequency limits lie within 1.25 Hz to 2.3 Hz.
- If the bridge is especially sensitive to excitation, the comfort criteria should be verified for vertical and longitudinal vibrations also if the fundamental natural frequency is lower than 4.6 Hz, as specified by the relevant authority or, where not specified, agreed for a specific project by the relevant parties. The comfort criteria for vertical and longitudinal vibrations are also verified for the second natural frequency, as specified in CUR 96.
- The comfort criteria for pedestrian excitation should be verified for lateral or torsional vibrations if the corresponding natural frequencies of the bridge are situated within given critical natural frequency limits. The critical natural frequency limits lie within 0.5 Hz to 1.2 Hz.
- The comfort criteria for jogger excitation should be verified for vertical vibrations if the corresponding natural frequencies of the bridge are situated within given critical natural frequency limits. The critical natural frequency limits lie within 1.9 Hz to 3.5 Hz.
- The ultimate limit state verification for intentional excitation should be verified for vertical vibrations if the corresponding natural frequencies of the bridge are between 1.7 Hz and 3.0 Hz, unless otherwise specified by the relevant authority or, where not specified, agreed for a specific project by the relevant parties depending on the usage of the bridge.

The different frequency ranges are illustrated in Figure 8.

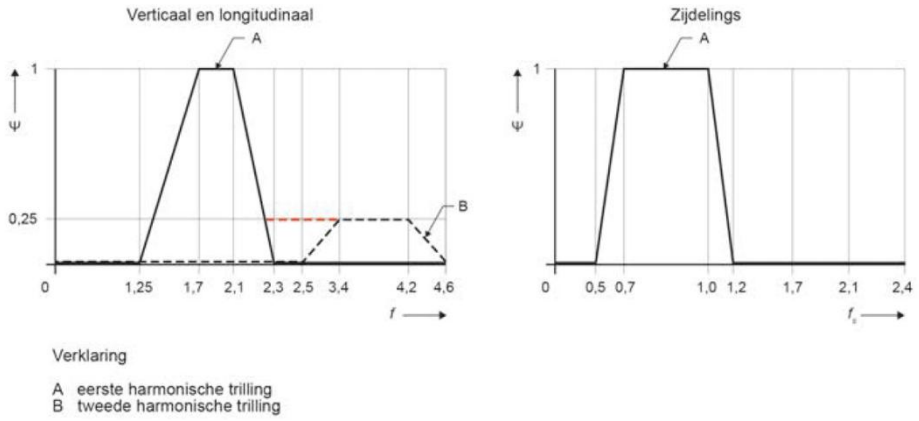

Figure 8: Critical ranges natural frequencies

5.2.3 Loads on the structure

There are multiple loads acting on the structure, including self-weight, permanent loads, traffic loads, wind forces, and snow loads. Table 1 presents the different combination factors for footbridges, obtained from NEN-EN 1990 annex A.2.7.5. Execution and construction will not be considered. Consequently, snow loads can be excluded from the loading considerations, as all the combination factors of snow loads are zero except for execution. From Chapter 7, the width of the bridge deck is approximately 1800 mm, and the bridge height is approximately 5.5 m. The height of the bridge deck varies along the span, reaching a maximum of 1000 mm at the lowest point of the bridge. The cross-section of the bridge deck is given in Figure 9.

Action	Symbol	ψ_0	ψ_1	ψ_2
Traffic loads	gr1	0.40	0.80	0.40
	gr2	0.40	0.80	0
	gr3	0.0	0.80	0
Wind forces	F_{Wk}	0.3	0.6	0
Thermal actions	T_k	0.3	0.8	0.3
Snow loads	$Q_{Sn,k}$ Persistent design situations	0	0	0

Table 1: Combination factors for footbridges, obtained from NEN-EN 1990 NB13

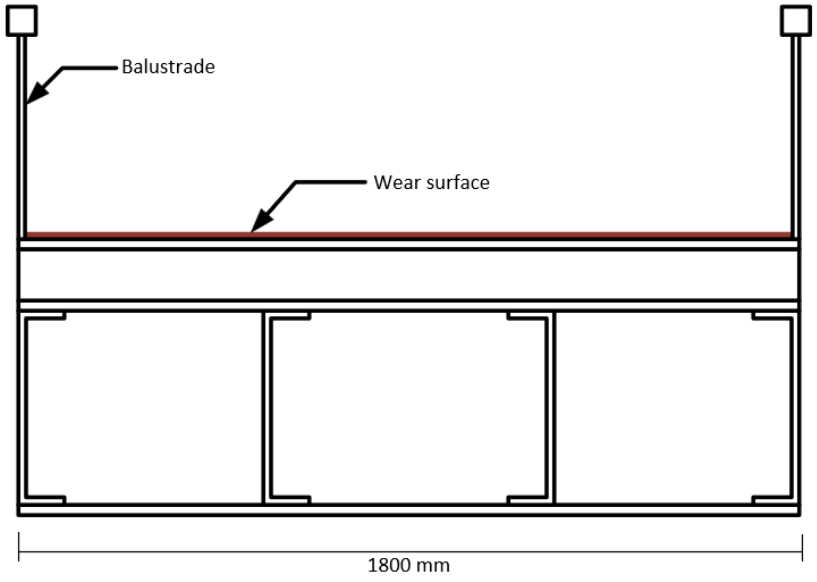

Figure 9: Cross-section bridge deck

Self-weight

The self-weight of the structure is based on the density of the materials. The density should be multiplied by the cross-sectional area to obtain the weight of the structure per unit length. The density of the materials is given in Chapter 6 of this report.

Permanent loads[3]

The permanent loads on the structure are: the balustrade, the wear surface, the coating, the bonding paste, and the resin absorption of the core material.

Balustrade

The design of the balustrade is not part of this report, but the weight of the balustrade on the deck should be considered. The load is determined based on the visualization, where is shown that every 10 cm a solid rod with a diameter of 30 mm. The balustrade will be made from stainless steel with an assumed density of 8000 kg/m^3, 80 kN/m^3. (Stainless steel, 2015) For the weight of the balustrade, a unit load is assumed. The attachment of the railing is not included. The allowed height of the balustrade is 1.2 meters. This height is based on Besluit Bouwerken Leefomgeving. The connection to the side of the deck should also be considered. This result in a hight of 1.4 m. The unit load can be calculated with:

$$q_{balustrade} = 1.4 * \frac{1}{4} * \pi * 0.030^2 * 80 * \frac{1000}{100} = 0.8\ kN/m$$

Wear surface

On the deck a wear surface is applied. The load due to the deck surface is based on an estimation of the thickness of this layer. A grit in epoxy or MMA of approximately 5 mm is assumed. Including a future overlay, a weight of the wearing surface of 20 kg/m^2 is taken into account, $p_{wearing} = 0.20\ kN/m^2$.

Coating

On the structural elements of the bio-composite a coating must be applied, more about this is given in Chapter 6.11. The coating will have a weight of 0.6 kg/m^2, $p_{coating} = 0.006\ kN/m^2$

Bonding paste

The structural elements are connected with bonding paste, more about this is given in Chapter 6.8. For the bonding paste between structural elements a weight of 5 kg/m^2 is considered, $p_{paste} = 0.05\ kN/m^2$

Resin absorption of the core material

The core material can absorb some of the resin, more about the core material is given in Chapter 6.7. The weight of the core material should be increased with 0.5 kg/m^2 for the contact surfaces of the core material, $p_{resin} = 0.005\ kN/m^2$.

[3] The permanent loads are obtained from: Basis of Design by Witteveen+Bos, “Seasaw bio-composite”, 26-5-2025

Traffic loads

The traffic loads are obtained through NEN-EN 1991-2 chapter 7. The following models, mutually exclusive, should be taken into account as relevant:

- a uniformly distributed load: q_{fk}
- a concentrated load: Q_{fwk}
- a concentrated loads representing service vehicles: Q_{serv}

The concentrated loads representing service vehicles will not be considered, since it will not be possible for service vehicles to access the Seasaw.

Uniformly distributed load

The uniformly distributed load can be calculated with the following formula:

$$q_{fk} = 2.0 + \frac{120}{L + 30} \left[\frac{kN}{m^2}\right]$$

$$\text{with } q_{fk} \geq 2.5\ [kN/m^2]\ and\ \ q_{fk} \leq 5.0\ [kN/m^2]$$

Where

L is the length of the unfavourable part of influence surface in [m]

The length of the Seasaw is 50 m so the uniformly distributed load is:

$$q_{fk} = 2.0 + \frac{120}{50 + 30} = 3.5 \left[\frac{kN}{m^2}\right]$$

This formula is obtained from NEN-EN 1991-2. The uniformly distributed load shall be applied only in the unfavourable parts of the influence surface of the footbridge.

Concentrated load

The concentrated load Q_{fwk} is equal to 7 kN acting on a square surface of sides 0.10 m. Where, in a verification, global and local effects can be distinguished, the concentrated load should be considered only for local effects and it is not combined with any other variable load.

Static model for horizontal forces

A horizontal force Q_{flk} should be taken into account, acting along the bridge deck axis at the pavement level. The characteristic value of the horizontal force is 10% of the total load corresponding to the uniformly distributed load. The horizontal force shall be considered as acting simultaneously with the corresponding vertical load.

Groups of traffic loads

The vertical and horizontal forces due to traffic should be taken into account by considering groups of loads defined in Table 2. Each of these groups defining a single variable characteristic action for combination with non-traffic loads.

Load type Load system		Vertical forces			Horizontal forces
		Uniformly distributed load	Service vehicle	Concentrated load	
Groups of loads	gr1	q_{fk}	-	-	Q_{flk}
	gr2	-	Q_{serv}	-	Q_{flk}
	gr3	-	-	Q_{fwk}	-

Table 2: Definition of groups of loads, obtained from NEN-EN 1991-2

Actions on pedestrian balustrades

For structural design, forces that are transferred to the bridge deck by pedestrian balustrades should be considered as variable loads. The line force applied horizontally or vertically on the top of the pedestrian balustrade should be a minimum force of 1.0 kN/m for footbridges. Since the pedestrian balustrade in not considered as adequately protected against vehicle collisions, the structure supporting the pedestrian balustrade should be designed to sustain an accidental load effect corresponding to at least 1.25 times the characteristic resistance of the balustrade and should not be combined with any variable load.

Wind loads

For wind loads, the Seasaw can be loaded in three directions. Parallel to the dike, downward and wind perpendicular to the dike, Figure 10 shows the load direction in comparison to the bridge. The wind loads on the bridge are obtained from NEN-EN 1991-1-4 chapter 8. The wind load parallel to the dike is equal to the force in x-direction from the Eurocode, the wind load downward is equal to forces on the bridge in z-direction from the Eurocode and wind load perpendicular to the bridge is equal to the force in y-direction from the Eurocode.

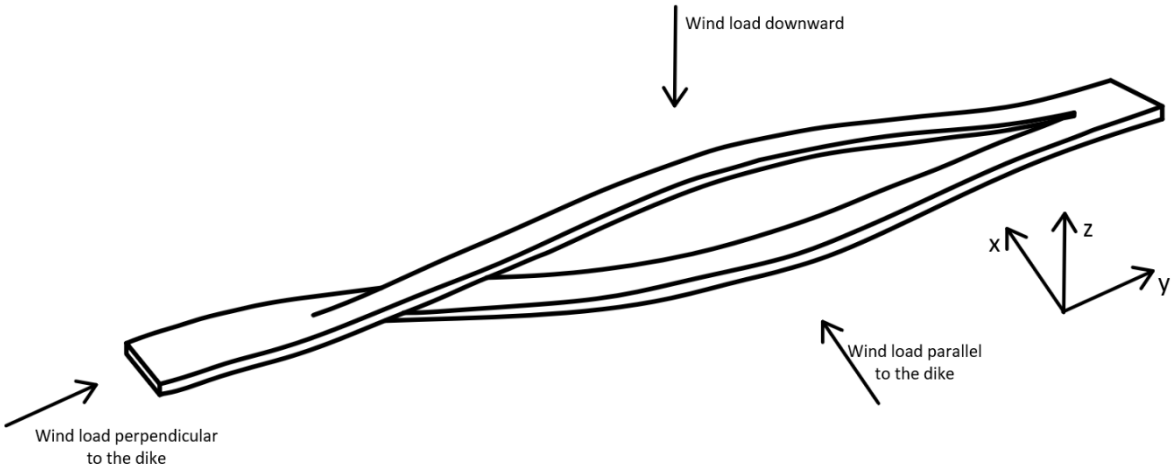

Figure 10: Schematic representation wind directions

Wind load parallel to the dike

The wind load parallel to the dike can be calculated with:

$$F_w = \frac{1}{2} * \rho * v_b^2 * C * A_{ref,x}$$

Where:

v_b	is the basic wind speed
C	is the wind load factor
$A_{ref,x}$	is the reference area
ρ	is the density of air

De basic wind speed has to be calculated with:

$$v_b = C_{dir} * C_{season} * v_{b,0}$$

Where:

$v_{b,0}$ is the fundamental value of the basic wind velocity

C_{dir} is the directional factor

C_{season} is the season factor

The wind area for Den Helder is wind area I. The fundamental value of the basic wind velocity is for wind area I 29.5 m/s. C_{dir} and C_{season} are 1, so $v_b = v_{b,0} = 29.5\ m/s$.

The wind load factor can be calculated with:

$$C = c_e * c_{f,x}$$

Where:

c_e is the exposure factor

$c_{f,x}$ is the force coefficient

The exposure factor can be determined with Figure 11. The exposure factor is 2.4.

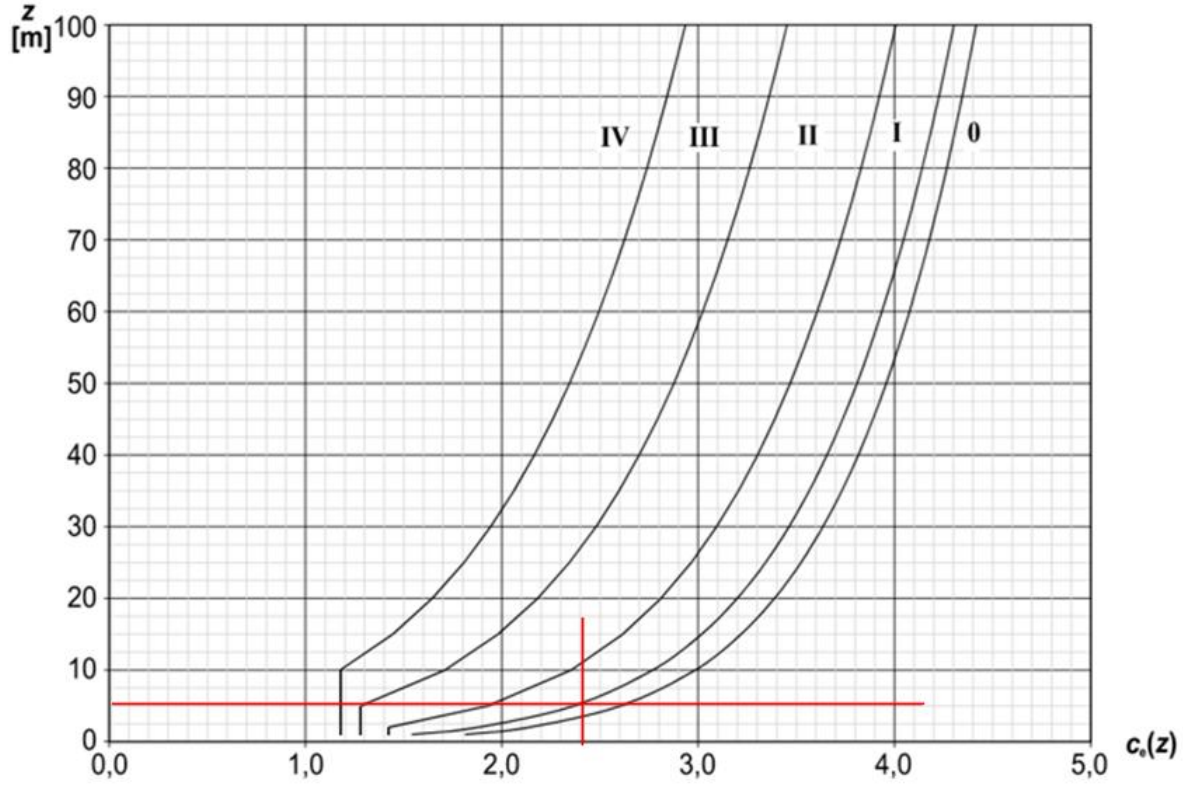

Figure 11: The exposure factor $c_e\ (z)$ for $c_0 = 1.0$ and $k_l = 1.0$, obtained from NEN-EN 1991-1-4 chapter 8

The force coefficient is given by:

$$c_{f,x} = c_{fx,0}$$

Where:

$c_{fx,0}$ is the force coefficient without free-end flow

The force coefficient without free-end flow is determined using Figure 12. The bridge deck has a width of 1800 mm and a height of 1000 mm at the bottom of the structure (see Chapter 7). In accordance with the Eurocode provisions, the total depth of the bridge is taken as

$$d_{tot} = d + 0.6 = 1 + 0.6 = 1.6\,\text{m}$$

Where the additional 0.6 m accounts for the bridge railings on both sides. The width-to-depth ratio used to determine the force coefficient is:

$$\frac{b}{d_{tot}} = \frac{1.8}{1.6} = 1.25$$

Based on Figure 12, the corresponding force coefficient is 2.2. The resulting wind load factor is:

$$C = c_e * c_{f,x} = 2.4 * 2.2 = 5.28$$

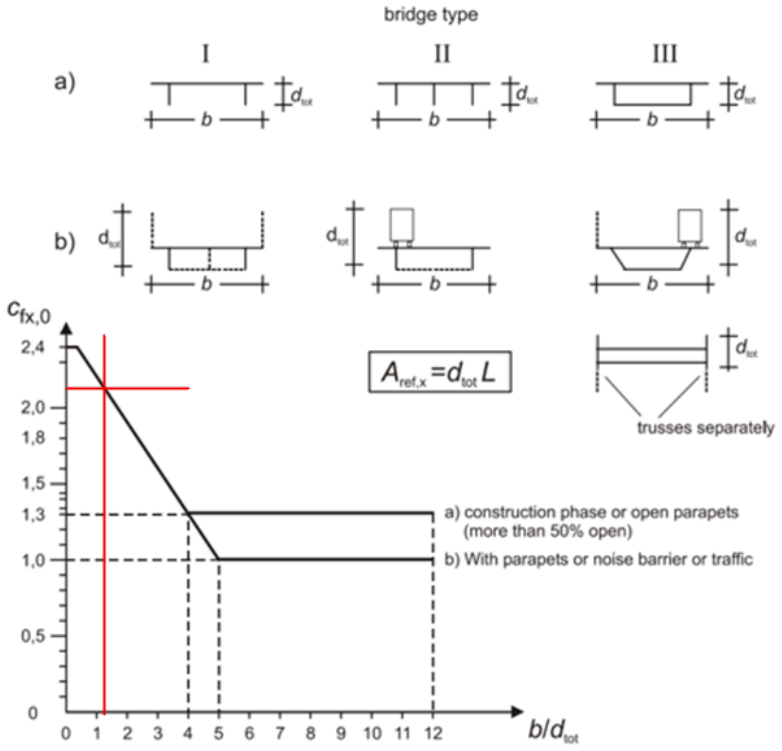

Figure 12: Force coefficient for bridges, $c_{fx,0}$, obtained from NEN-EN 1991-1-4 chapter 8

The reference area can be calculated with:

$$A_{ref,x} = d_{tot} * L$$

Where:

L is the length of the bridge

d_{tot} is $d_{tot} = d + 0.6$ for a bridge railing on both sides

The maximum d_{tot} for the bridge is $d_{tot} = d + 0.6 = 1 + 0.6 = 1.6\,\mathrm{m}$

The density of air is equal to 1.25 kg/m^3. The wind load parallel to the dike is:

$$F_{w,x} = \frac{1}{2} * \rho * v_b^2 * C * A_{ref,x} = \frac{1}{2} * 1.25 * 29.5^2 * 5.28 * d_{tot} * L$$

The distributed wind load on the bridge deck will be:

$$q_{w,x} = \frac{1}{2} * 1.25 * 29.5^2 * 5.25 * d_{tot} = 2855.5 * d_{tot}\ [N/m]$$

Wind load downward

The downward wind load is calculated in almost the same way as the wind load acting parallel to the dike. The main differences the wind load factor and the reference area used in the calculation. The wind load factor is defined as:

$$C = c_{f,z}$$

Where:

$c_{f,z}$ is the force coefficient and is equal to 0.9

So $C = c_{f,z} = 0.9$

The reference area can be calculated with:

$$A_{ref,x} = b * L$$

Where:

L is the length of the bridge

b is the width of the bridge

The wind load downward is:

$$F_{w,z} = \frac{1}{2} * \rho * v_b^2 * C * A_{ref,x} = \frac{1}{2} * 1.25 * 29.5^2 * 0.9 * b * L$$

The distributed wind load on the bridge deck will be:

$$q_{w,z} = \frac{1}{2} * 1.25 * 29.5^2 * 0.9 * b = 489.5 * b = 489.5 * 1.8 = 881.1\ [N/m]$$

The load downward has to be applied with an eccentricity in the x-direction. The eccentricity is $e = \frac{b}{4} = \frac{1800}{4} = 450\ [mm]$.

The wind force in the z-direction must be taken into account simultaneously with the wind force in the x-direction, wind load parallel to the dike, if the effect of the wind force in the z-direction is unfavourable.

Wind load perpendicular to the dike

The wind load perpendicular to the dike is equal to 40% of the wind load parallel to the dike. The load is:

$$F_{w,y} = 0.4 * F_{w,x}$$

$$q_{w,y} = 0.4 * q_{w,x} = 0.4 * 2855.5 * d_{tot} = 1142.2 * d_{tot}\ [N/m]$$

The wind force in the y-direction occurs simultaneously with an equally large wind force in the x-direction.

Thermal actions

Thermal effects are excluded from the scope of this study. Although temperature variations can cause deformations and small local stresses in the structure, a detailed assessment of thermal effects is not considered within the scope of this research.

Ultimate Limit State (ULS)

According to NEN EN 1990, the load on the structure for ULS can be determined with the equation:

$$\sum F_d = \sum_i \gamma_{G,i} G_{k,i} + \gamma_{Q,1} Q_{k,1} + \sum_{j>1} \gamma_{Q,j} \psi_{0,j} Q_{k,j}$$

Where:

- $G_{k,i}$ is the characteristic value of permanent action i
- $\gamma_{G,i}$ is the partial factor for permanent action i
- $Q_{k,1}$ is the characteristic value of the leading variable action 1
- $\gamma_{Q,1}$ is the partial factor for the leading variable action 1
- $Q_{k,j}$ is the characteristic value of an accompanying variable action j
- $\gamma_{Q,j}$ is the partial factor for the variable action j
- $\psi_{0,\mathrm{j}}$ is the combination factor for the variable action j

The combination factors are shown in Table 1 and the partial factors are shown in Table 3. When variations in the magnitude or spatial variation of permanent actions from the same source are significant, ultimate limit states that involve loss of static equilibrium should be verified using partial factors for verification cases VC2(a) and VC2(b) using whichever gives the less favourable design outcome. Verification of verification case VC2(b) may be omitted when it is obvious that verification using verification case VC2(a) governs the design outcome.

Action or effect				Partial factors γ_F and γ_E for verification cases		
Type	Group	Symbol	Resulting effect	Structural resistance	Combined structural resistance and static equilibrium / uplift	
Verification case				VC1	VC2(a)	VC2(b)
Permanent action (G_k)	All	γ_G	unfavourable/ destabilizing	1.35	1.35	1.0
Variable action (Q_k)	Road/ pedestrian traffic		unfavourable	1.35	1.35	1.35
	Other	γ_Q	unfavourable	1.5	1.5	1.5
	All	$\gamma_{Q,fav}$	favourable	0		

Table 3: Partial factors, obtained from NEN-EN 1990

Serviceability limit state (SLS)

For the serviceability limit state there are three different combinations the characteristic, frequent and quasi-permanent combination, according to NEN EN 1990. The characteristic combination is used for irreversible limit state, the frequent combination is used for reversible limit state and the quasi-permanent combination is used for long-term effects and for the appearance of the structure.

The load on the structure for the characteristic combination can be determined with the equation:

$$\sum F_d = \sum_i G_{k,i} + Q_{k,1} + \sum_{j>1} \psi_{0,j} Q_{k,j}$$

Where:

$G_{k,i}$ is the characteristic value of permanent action i

$Q_{k,1}$ is the characteristic value of the leading variable action 1

$Q_{k,j}$ is the characteristic value of an accompanying variable action j

$\psi_{0,\mathrm{j}}$ is the combination factor for the variable action j

The load on the structure for the frequent combination can be determined with the equation:

$$\sum F_d = \sum_i G_{k,i} + \psi_{1,1} Q_{k,1} + \sum_{j>1} \psi_{2,j} Q_{k,j}$$

Where:

$G_{k,i}$ is the characteristic value of permanent action i

$Q_{k,1}$ is the characteristic value of the leading variable action 1

$\psi_{1,1}$ is the combination factor for the variable action 1

$Q_{k,j}$ is the characteristic value of an accompanying variable action j

$\psi_{2,j}$ is the combination factor for the variable action j

The load on the structure for the quasi-permanent combination can be determined with the equation:

$$\sum F_d = \sum_i G_{k,i} + \sum_j \psi_{2,j} Q_{k,j}$$

Where:

$G_{k,i}$ is the characteristic value of permanent action i

$Q_{k,j}$ is the characteristic value of an accompanying variable action j

$\psi_{2,j}$ is the combination factor for the variable action j

5.2.4 Fire safety[4]

A fire safety assessment is deemed unnecessary for this type of structure due to the availability of adequate evacuation routes. In addition, practical fire tests, conducted outside of standard protocols, have demonstrated that the material is not flammable in a typical fire and that the fire does not spread further once the source is removed.

5.2.5 Deformation

The vertical deflections should be calculated using the parameters shown in the figure below.

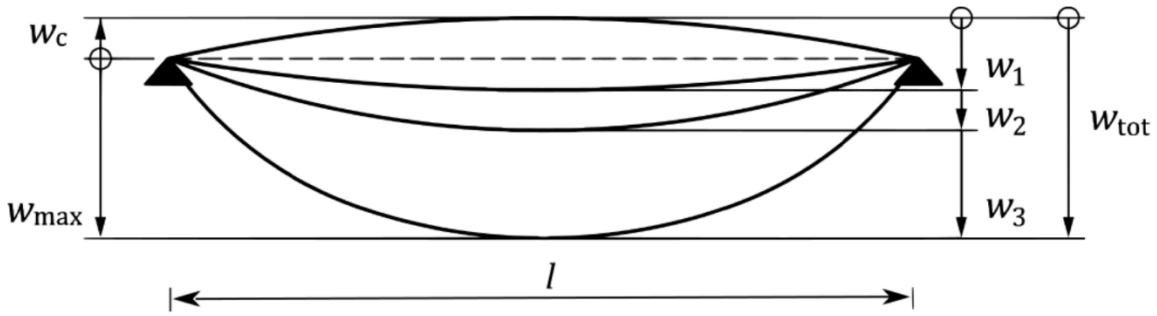

Figure 13: Vertical deflection, obtained from NEN-EN 1990

The parameters are:

w_c	pre-camber in the unloaded structural member
w_1	initial part of the deflection under permanent loads of the relevant combination of actions
w_2	long-term part of the deflection under permanent loads including the quasi-permanent part of variable actions
w_3	instantaneous deflection due to variable actions excluding their quasi-permanent parts
w_{tot}	total deflection as the sum of w_1, w_2, w_3
w_{max}	remaining total deflection taking into account the pre-camber
l	span

The deflections can be calculated using formulas based on CEN/TS 19101:2022.

Deflections for characteristic combination of actions:

$$w_2 = \left(w_{G_k} + \sum_j \psi_{2,j} * w_{Q_{k,j}}\right) * \left(\frac{1}{\eta_{cv}} - 1\right)$$

$$w_3 = w_{Q_{k,1}} + \sum_{j>1} \psi_{0,j} * w_{Q_{k,j}}$$

Deflections for frequent combination of actions:

$$w_2 = \left(w_{G_k} + \sum_j \psi_{2,j} * w_{Q_{k,j}}\right) * \left(\frac{1}{\eta_{cv}} - 1\right)$$

$$w_3 = \psi_{1,1} * w_{Q_{k,1}}$$

[4] Fire safety information obtained from: Basis of Design by Witteveen+Bos, “Seasaw bio-composite”, 26-5-2025

Deflections for quasi-permanent combination of actions:

$$w_1 = w_{G_k}$$

$$w_2 = \left(w_{G_k} + \sum_j \psi_{2,j} * w_{Q\,k,j}\right) * \left(\frac{1}{\eta_{cv}} - 1\right)$$

Where:

w_{G_k}	is the initial part of the deflection under permanent loads
$w_{Q\,k,1}$	is the instantaneous deflection due to the leading variable action
$w_{Q\,k,j}$	is the instantaneous deflection due to accompanying variable actions
$\left(\frac{1}{\eta_{cv}} - 1\right)$	is the creep coefficient
ψ	are the combination factors applied to variable actions to determine their combination value

The quasi-permanent component of the formula for w_2 due to traffic loads may be neglected. Creep deformations due to traffic loads in bridges normally recover during unloaded periods. The maximum deflections are determined based on the conditions for floor and roof systems in buildings.[5] This is because the Eurocodes and the CUR96 do not impose any requirement on the maximum deflection of a composite bridge, comfort is governing If these recommended limits are not fully satisfied but the bridge still provides an acceptable level of comfort for its users, this is not considered a significant issue.

The maximum deflections based on NEN-EN 1990+A1+A1/C2:2019/NB are:

$w_2 + w_3 \leq \frac{l_{span}}{150}$	(comfort, characteristic combination)
$w_2 + w_3 \leq \frac{2*l_{cantiliver}}{150}$	(comfort, characteristic combination)
$w_{max} \leq \frac{l_{span}}{250}$	(aesthetics, quasi-permanent combination)
$w_{max} \leq \frac{2*l_{cantiliver}}{250}$	(aesthetics, quasi-permanent combination)
$w_3 \leq \frac{l_{deckplate}}{750}$	(frequent combination)

The last condition is inspired by table NB.1 of NEN-EN 1995-2/NB and is assumed for the maximum deformation of the deck plate between the webs/girders. In Figure 14 are the lengths shown. The deflection of the bottom-half cantilever, yellow square, is measured at a point 16 m, green point from the centre of the Seasaw, yellow point. The deflection of the side cantilever, blue square, is defined as the difference between the deflections measured at 16 m, green point, and 25 m, blue point, from the centre of the Seasaw, yellow point. The deflection of the top half, red square, is defined as the difference between the deflection at 12.5 m in the top half, red point, and the deflection at the centre of the top half, orange point.

[5] Maximum deflections obtained from: Basis of Design by Witteveen+Bos, “Seasaw bio-composite”, 26-5-2025

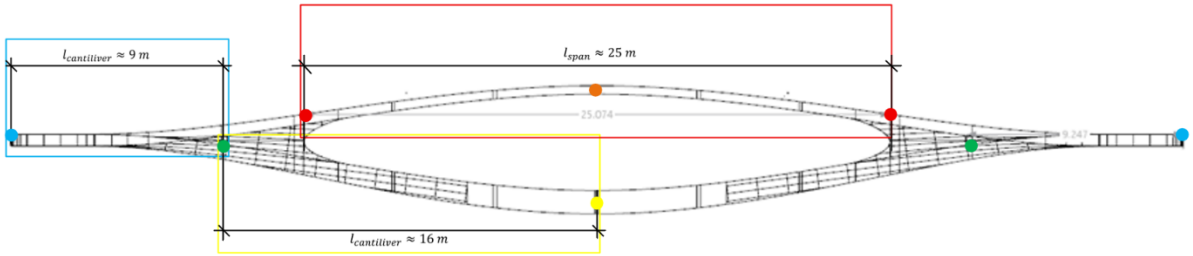

Figure 14: Side view bridge

5.3 Evaluation criteria

The final design of the Seasaw shall be evaluated against the following criteria, derived from the functional and structural requirements and the applicable Eurocodes for footbridges. Compliance with these criteria demonstrates that the structure satisfies the intended performance, safety, and reliability objectives for a CC2 pedestrian bridge. In Table 4 are the evaluation criteria listed.

Service life	The structure achieves a design service life of 50 years
User safety	The design provides a safe environment for pedestrians under normal use, minimising risks related to falling, slipping and loss of balance.
Usability and comfort (SLS)	The structural behaviour, geometry, and movements of the Seasaw do not cause discomfort, fear, or uncertainty for users during pedestrian traffic.
Structural safety (ULS)	The structure safely resists all relevant design actions and load combinations without collapse or loss of structural integrity.
Stability (ULS)	The structure remains stable under all relevant design situations, including unfavourable loading and environmental actions.
Serviceability performance (SLS)	Deformations and vibrations remain within acceptable limits under characteristic load combinations, ensuring adequate comfort and usability.
Robustness	Localised damage or unforeseen events do not lead to disproportionate or progressive collapse of the structure.
Durability	Material degradation over the design working life does not impair structural performance, considering environmental exposure and maintenance.
Sustainability	The design limits adverse environmental, societal, and economic impacts over the full life cycle of the structure.
Appearance of the Seasaw	The design of the Seasaw should retain the overall layout and appearance of the original concept, with only minor changes to its visual appearance.

Table 4: Evaluation criteria

6. Materials

The Seasaw will be made from a flax fibre composite. Flax fibre composite is a material composed of flax fibres and a bio-based resin matrix. Its properties are influenced by the type of resin used, the orientation and layup of the flax fibres, and the manufacturing process. The process from flax cultivation to the production of the flax fibre composite is illustrated in Figure 15. (NEN, 2016)

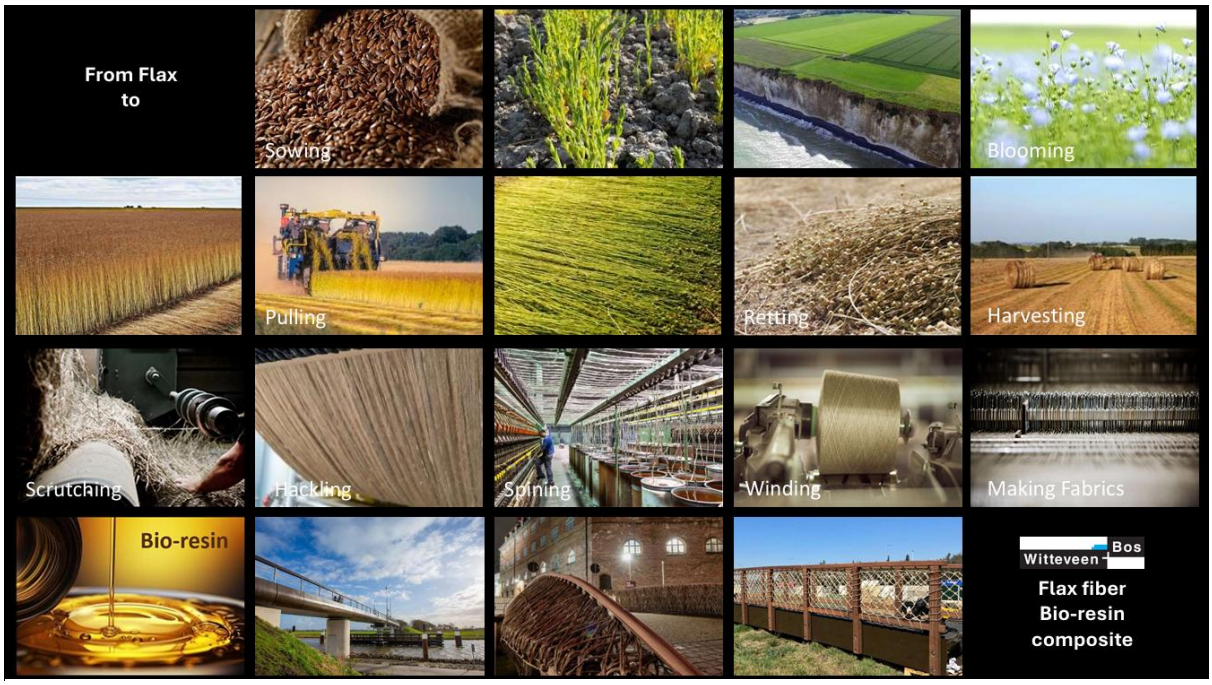

Figure 15: Process of flax fibre composites[2]

For the bridge deck, the same layering approach as used in the Ulm bridge will be adopted, as it results in a lightweight and efficient structure. So, the bridge deck consists of a bottom plate, a C-shaped girder, and a top plate. The top plate itself is composed of multiple layers: a bottom face sheet, webs and core material, and a top face sheet. A schematic representation of these layers is shown in Figure 16. The girders are designed with a C-shaped cross-section to provide a sufficiently large contact area for bonding the components with bonding paste. An I-shaped cross-section was not selected, as it is more challenging to manufacture for composites.

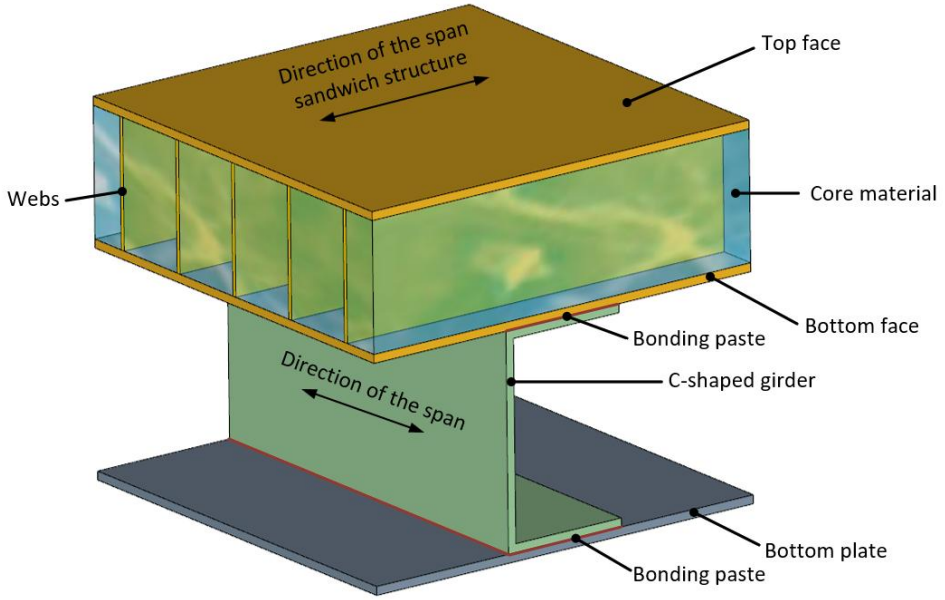

Figure 16: Construction principle

6.1 Flax fibre

Flax fibres are natural fibres obtained from the stem of the flax plant. In a flax fibre composite, the flax fibres form the reinforcing fibres in the composite. The fibres determine the strength and stiffness of the composite. Flax is a natural fibre. In recent years, there has been growing interest in natural fibres such as flax as an alternative to synthetic fibres, relatively low weight, biodegradability, and reduced environmental impact. For this reason, flax is selected for the Seasaw as a sustainable reinforcement material with competitive mechanical properties. (Pavlovic, Valzania, & Minak, 2025)

However, natural fibres also have some disadvantages. A disadvantage of natural fibres is that they are sensitive to moisture absorption and rotting during processing and use. Despite these disadvantages, the strength and stiffness of flax fibres relative to their weight can be of the same order as those of synthetic fibres, making them a promising option for lightweight and more sustainable composite applications. (Nijsen, 2015)

6.1.1 Structure

Flax fibres are natural cellulose-based fibres obtained from the stem of the flax bast plant, see Figure 17. Flax plant ranges in length up to 90 cm. Their structure is hierarchical and organized at multiple scales, from the whole stem down to nanoscale cellulose fibrils. A schematic view of this structure is given in Figure 18. (Yan, Chouw, & Jayaraman, 2013)



Figure 17: Flax plant (Shelton, sd)

At the macroscopic level, the flax stem consists of bark, phloem, xylem, and a central hollow region. At the mesoscopic level, fibre bundles are located in the phloem and contain 10–40 individual fibres bonded together mainly by pectin. Each fibre has an average diameter of 12–16 µm. (Yan, Chouw, & Jayaraman, 2013)

The characteristics of flax fibres can vary depending on their position within the stem. Differences in fibre morphology and chemical composition have been observed between fibres from the upper, middle, and lower parts of the stem. These differences are related to variations in fibre development, secondary-wall formation, and maturation. For example, the number of fibres per bundle and fibre diameter can differ along the stem. Consequently, the position of the fibre within the stem contributes to the variability of flax fibre properties. (Morvan, et al., 2003)

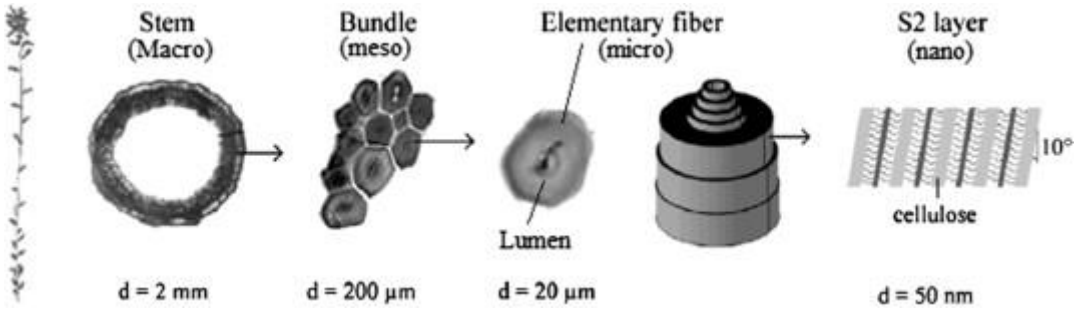

Figure 18: Flax structure from the stem to the cellulosic fibrils (Yan, Chouw, & Jayaraman, 2013)

At the microscopic level, an individual flax fibre is composed of concentric cell walls surrounding a central hollow channel called the lumen, which aids in water absorption. The outermost layer is a thin primary cell wall about 0.2 µm thick, see Figure 19. Beneath it lies the thicker secondary cell wall, which provides most of the fibre's mechanical strength. The dominant layer of the secondary wall, known as S2, makes up most of the fibre's cross-section. (Yan, Chouw, & Jayaraman, 2013)

The cell walls are made of cellulose microfibrils embedded in a matrix of hemicellulose and pectin. In the S2 layer, highly crystalline cellulose microfibrils are oriented at a small angle, about 10°, to the fibre axis, contributing significantly to the fibre's high tensile strength. At the nanoscale, each microfibril consists of crystalline cellulose regions embedded in an amorphous matrix. These microfibrils account for about 70% of the fibre's weight and act as the main reinforcing component. The cellulose and hemicellulose contain hydroxyl groups and contribute to the hydrophilic nature of flax fibres. As a result, flax fibres can absorb significant amounts of moisture, and changes in relative humidity can affect their mechanical properties. (Yan, Chouw, & Jayaraman, 2013)

Overall, the mechanical and moisture-related behaviour of flax fibres is strongly influenced by their hierarchical structure, cellulose content, and the orientation and arrangement of the cellulose microfibrils. The variation in fibre morphology, chemical composition, and porosity along the stem further contributes to the variability of flax fibre properties. (Yan, Chouw, & Jayaraman, 2013)

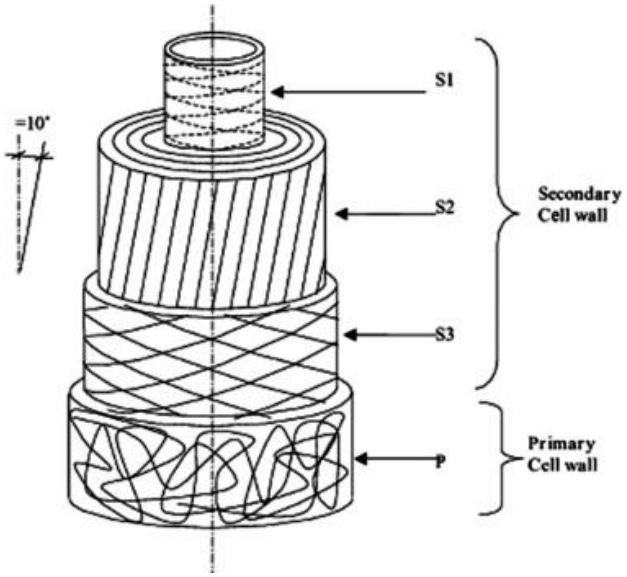

Figure 19: The micro-structure of a flax fibre cell (Yan, Chouw, & Jayaraman, 2013)

6.1.2 Processing of Flax

The fibre is obtained through a three-step process. Initially, the outer layer of the stem, bark is removed in a step known as decortication. Next, the material is mechanically scraped to eliminate most of the remaining outer bark, as well as the parenchyma cells in the bast region and a portion of the gums and pectins. In the final stage, the remaining material is cleaned, dried, and treated to remove residual binding substances, resulting in fibres that are suitable for spinning. (Chand & Fahim, 2021)

6.1.3 Flax fibre mats

From the fibres, textile mats are produced, see Figure 20. The fibres can be bundled into a strand and directly processed into a fibre mat. Such a mat consists of short or long fibres that are bonded together in a random orientation. Alternatively, the fibres can be bundled and twisted into a yarn made up of several fibres. Untwisted strands can be combined into rovings. These bundles can subsequently be processed into woven fabrics (weefsels) or transformed into non-crimp fabrics (legslels). (Nijsen, 2015)

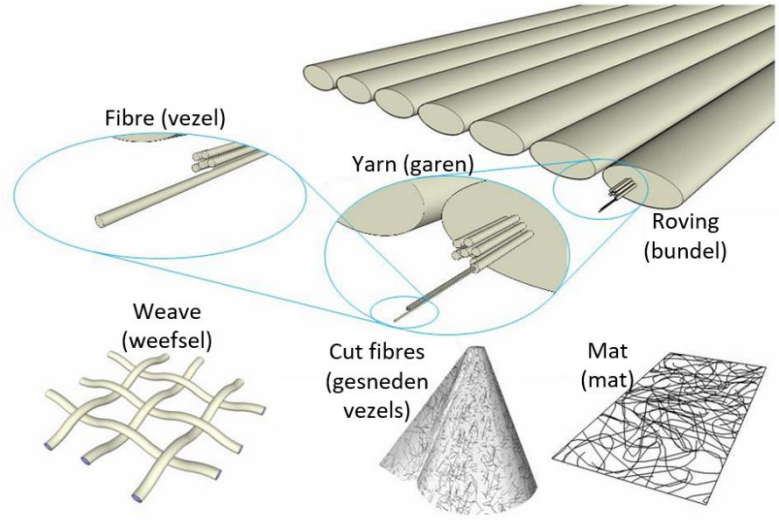

Figure 20: From fibre to textile (Nijsen, 2015)

In a woven fabric, the fibre bundles are interlaced with one another. The crimp, surface texture, and drapeability of the fabric are determined by the weave pattern, the specific way in which the warp and weft alternate and intersect. Crimp does not refer to the extent to which a fabric shrinks but describes the curvature of a fibre within the fabric structure. Figure 21 shows several different weave patterns. The weave has a significant influence on the properties of a lamella. A lamella is a thin layer of impregnated fibre reinforcement. In general, weave structures with a lower degree of interlacing, such as twill and satin, have a better drapeability and increased permeability compared to plain weave. Conversely, plain weave, yields a textile with superior dimensional stability and structural integrity. The stiffness of a composite may vary in different directions as a result of fibre orientation. For this reason, woven fabrics will not be used in the composite for the Seasaw. (Nijsen, 2015)

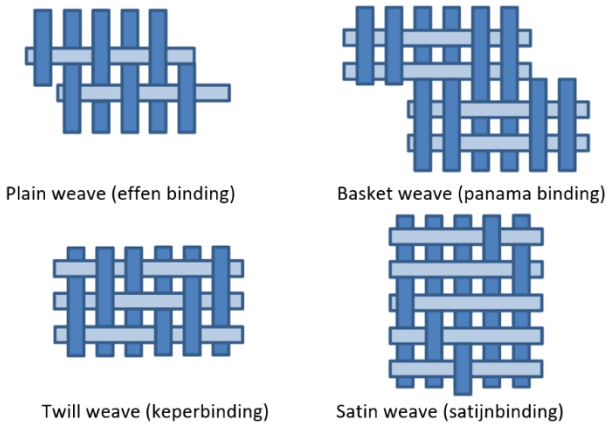

Figure 21: Weave patterns (Nijsen, 2015)

A non-crimp fabric (NCF) contains no inherent crimp, with all fibre bundles aligned in a straight configuration. This is achieved by stitching the bundles together, either directly to each other or to a thin backing layer. The backing may consist of a small amount of fibres oriented transverse to the main textile direction or a thin mat of randomly oriented chopped fibres. Consequently, non-crimp fabrics are often referred to as stitched fabrics. As shown in Figure 22 the fibres can be laid in different direction. These multiple lamellas together create a laminate. Stitched fabrics (legsels) will be used in the composite for the Seasaw. The use of uni-directional fabrics provides greater design flexibility, as the fibre orientations can be tailored to the different load directions within the structure. (Nijsen, 2015)

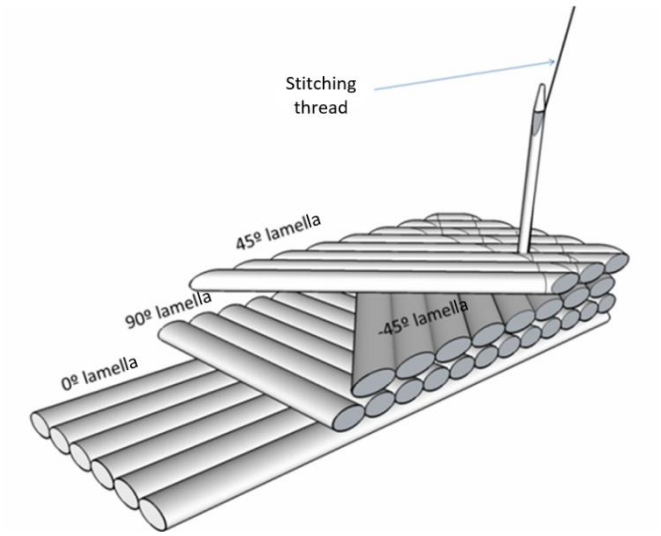

Figure 22: Production of a quasi-isotropic non-crimp fabric by stitching (Nijsen, 2015)

6.1.4 Material properties[6]

For the design of the Seasaw, Bcomp flax fibres will be used. Bcomp flax fibres are used for the Seasaw because they provide a commercially available flax fibre reinforcement with documented material properties. In addition, Bcomp flax fibre composites have already been applied in structural applications, providing a relevant basis for the material selection in this study. A unidirectional (UD) mat and a bi-axial mat with fibres in +45° and -45° will be used. The unidirectional mat is used for fibres aligned with the principal directions 0° and 90°. The biaxial mat is used for fibres oriented in the principal directions +45° and −45°. Using biaxial mats for the ±45° orientations simplifies the manufacturing process, as accurately placing individual fibres at these angles would be difficult and time-consuming. The following Bcomp flax fibres are considered:

- Amplitex™ 300, UD dry
- Amplitex™ 350, bi-axial +/-45° dry

Amplitex consists of twisted yarns, which promote good fibre distribution and homogeneity within a laminate. (Perruchoud, Alderliesten, & Mosleh, Tailoring the fatigue response of flax FRP composites by exploiting Micro-structural re-arrangements and auxiliary loading sequences, 2025)

Fibre volume fraction:

- The minimal fibre volume fraction needs to be 40% and preferably 50% in the top face, bottom face, C-shaped girders, and bottom plate and 25% in the webs of the core material

For fibre-reinforced thermosetting composites, each of the principal directions [0°, 90°, +45°, −45°] shall contain at least 12.5% of the total fibre reinforcement, according to 3.7.3.2 of CUR96.

[6] Material properties obtained from: Basis of Design by Witteveen+Bos, “Seasaw bio-composite”, 26-5-2025

The thickness of a single layer can be calculated based on the properties of the fibre material and the fibre volume fraction. Two types of fibres are used:

- A unidirectional ply with a weight of 280 gram/m^2
- A +/-45° ply with a weight of 350 gram/m^2

The material properties of flax fibres are given in Table 5.

Fibre	ρ_f $[kg/m^3]$	E_{f1} $[N/mm^2]$	$E_{f2,low}$ $[N/mm^2]$	$E_{f2,high}$ $[N/mm^2]$	G_f $[N/mm^2]$	ν_r $[-]$
Bcomp flax fibres	1500	55 000	0	6440	1600	0.380

Table 5: Properties flax fibres

The density of the fibres is around 1400 kg/m^3. For the calculation in this phase a conservative density of 1500 kg/m^3 is considered.

For a specific conservative weight of the fibres of 1500 kg/m^3 and a fibre volume fraction of 40%, the thicknesses are:

- $t_{280} = \frac{280}{1500*0.40} = 0.4667\ mm$
- $t_{350} = \frac{350}{1500*0.40} = 0.5833\ mm$

6.2 Resin

In composites, the fibres are embedded within a resin, known as the matrix. The primary role of the polymer matrix in a composite is to act as a “glue” that holds the fibres together. By surrounding the fibres, the matrix allows them to carry higher compressive loads, as they are supported by the polymer. Another function is that the matrix enables better interaction between fibres, transferring loads from one fibre to another through shear stresses. This ensures that external forces are more evenly distributed across the fibres than in a dry fibre bundle, and if one filament breaks, the load is shared by the remaining filaments. Additional advantages of the polymer matrix include:

- Protection against external factors such as moisture, chemicals, and UV light.
- Influence on the composite’s colour and surface quality.
- Control over light transmission.
- Contribution to fire resistance.

Polymers can be classified into two main categories: thermoplastics and thermosets. Thermoplastics are polymers that melt when heated, become workable, and solidify again upon cooling. Thermosetting polymers do not melt when heated. Instead, they eventually decompose or burn. On a molecular level, most thermosets consist of relatively short chains, which give the uncured material a very low viscosity. Curing occurs through a chemical reaction, in which the short chains form bonds with one another, creating a rigid three-dimensional network. The most commonly used thermosetting polymers are polyesters, vinylesters, and epoxies. Resins considered for the Seasaw are a polyester resin and an epoxy resin. (Nijsen, 2015)

6.2.1 Polyester resin[7]

The material properties of polyester resin according to CUR96 table 3-2 is given in Table 6. UP stands for unsaturated polyester. Polyester requires a catalyst in order to cure properly. An advantage of polyester is that it is relatively inexpensive, making it a popular choice in many applications. A disadvantage of UP resin is its susceptibility to moisture-related degradation, including osmosis when the composite is exposed to water for a prolonged period. Osmosis can occur when moisture penetrates the composite and chemical reactions within the resin lead to the formation of blisters, potentially resulting in local degradation of the material. However, the risk of osmosis can be reduced by applying a suitable moisture-resistant protective coating and by ensuring proper manufacturing and maintenance of the composite. Therefore, although moisture resistance is an important consideration when using UP resin in structures exposed to water, it does not necessarily prevent its application. (OSMOSE, WAT IS HET EN HOE KUNT U HET VOORKOMEN OF BEHANDELEN?, sd)

Resin	$\boldsymbol{\rho_r}$ $[\boldsymbol{kg/m^3}]$	$\boldsymbol{E_r}$ $[\boldsymbol{N/mm^2}]$	$\boldsymbol{G_r}$ $[\boldsymbol{N/mm^2}]$	$\boldsymbol{\nu_r}$ $[-]$
UP-bio resin	1200	3350	1350	0.380

Table 6: Properties polyester resin

6.2.2 Epoxy resin[7]

The material properties of epoxy resin according to CUR96 table 3-2 is given in Table 7. An advantage of epoxy is that it shrinks significantly less during curing than polyester. A disadvantage, however, is that epoxy is more expensive than polyester.

Resin	$\boldsymbol{\rho_r}$ $[\boldsymbol{kg/m^3}]$	$\boldsymbol{E_r}$ $[\boldsymbol{N/mm^2}]$	$\boldsymbol{G_r}$ $[\boldsymbol{N/mm^2}]$	$\boldsymbol{\nu_r}$ $[-]$
Epoxy-bio resin	1250	3100	1500	0.390

Table 7: Properties epoxy resin

6.3 Flax fibre composite

6.3.1 Manufacturing

The flax fibre composite is manufactured using the vacuum-assisted resin infusion process. This method is highly efficient and enables precise production of composite materials. The process involves placing dry fibre mats in a mould and applying a vacuum to the system. Resin is then drawn into the fibre mats by vacuum pressure, ensuring thorough impregnation. (Vacuum Resin Infusion Process Explained, sd)

This technique promotes a uniform distribution of resin, resulting in consistent material quality. The applied vacuum also removes air pockets and compacts the fibres, reducing voids that could otherwise weaken the structure. (Vacuum Resin Infusion Process Explained, sd)

With vacuum-assisted resin infusion, only plates or beam elements may be infused in one injection. Infusion of the total structure at once is not permitted. The separate components must be bonded together. For the infusion process the following is advised:

- Apply vacuum for at least 24 hours at 0 mbar (−1 atm) to improve compaction and help remove moisture from the system.
- Perform resin injection at 40-50 mbar (-0.96 / 0.95 atm)

[7] Material properties obtained from: Basis of Design by Witteveen+Bos, “Seasaw bio-composite”, 26-5-2025

The structure will be manufactured as separate elements and then bonded to achieve the final geometry. Curing shrinkage must be considered during production. [8]

6.3.2 Material properties of a lamella[9]

Two possibilities for the bio-composite material are considered:

- Flax fibre UP-bio composite
- Flax fibre epoxy-bio composite

The difference between the materials is the resin type.

Flax fibre UP-bio composite

Flax fibre UP-bio composite is a combination of Bcomp fibres and polyester. Material properties of Flax fibre UP-bio composite are given in the tables below.

V_f [−]	$E_{1,90\%}$ [GPa]	$E_{2,low}$ [GPa]	$E_{2,high}$ [GPa]	G_f [Gpa]	ν_r [−]
40%	21.1	1.7	5.0	1.1	0.33

Table 8: Properties UD lamella

		CUR 96 Strain limit [%]		Material Stress limit [N/mm^2]
Tension	$\varepsilon_{1t,Rk}$	1.2	σ_{f1t} (test value reference project)	278
	$\varepsilon_{2t,Rk;low}$	1.2	$\sigma_{f2t} = \varepsilon_{2t,Rk;low} * E_{2,low}$	20.7
Compression	$\varepsilon_{1c,Rk}$	1.0	σ_{f1c} (test value reference project)	232
	$\varepsilon_{2c,Rk;low}$	1.2	$\sigma_{f2c} = \varepsilon_{2c,Rk;low} * E_{2,low}$	20.7
Shear	$\gamma_{12,Rk}$	-	τ_{f12} (test value reference project)	23.5

Table 9: Material stress limit for UD lamella

Linear expansion coefficient	UD-Ply fvf, 40%	UD-Ply fvf, 50%
$\alpha_1 - 20℃ \leq T \leq +10℃$	$9.5 * 10^{-6}\ K^{-1}$	$8.3 * 10^{-6}\ K^{-1}$
$\alpha_1 + 10℃ \leq T \leq +40℃$	$0.9 * 10^{-6}\ K^{-1}$	$0.8 * 10^{-6}\ K^{-1}$
$\alpha_1 mean\ value$	$5.2 * 10^{-6}\ K^{-1}$	$4.6 * 10^{-6}\ K^{-1}$
$\alpha_2 - 20℃ \leq T \leq +10℃$	$100 * 10^{-6}\ K^{-1}$	$83.6 * 10^{-6}\ K^{-1}$

Table 10: Thermal expansion coefficient

For the coefficient of thermal expansion, the values for a flax epoxy composite have been applied. However, unsaturated polyester (UP) exhibits a coefficient of thermal expansion approximately twice that of epoxy. The potential impact of this higher thermal expansion in UP must therefore be considered in the calculations.

Flax fibre epoxy-bio composite

Flax fibre epoxy-bio composite is a combination of Bcomp fibres and epoxy. Material properties of Flax fibre epoxy-bio composite are given in the tables below.

V_f [−]	E_1, [GPa]	$E_{2,low}$ [GPa]	$E_{2,high}$ [GPa]	G_f [Gpa]	ν_r [−]
	25	2	5.0	1.4	0.32

Table 11: Properties UD lamella

[8] Information manufacturing obtained from: Basis of Design by Witteveen+Bos, “Seasaw bio-composite”, 26-5-2025

[9] Material properties obtained from: Basis of Design by Witteveen+Bos, “Seasaw bio-composite”, 26-5-2025

		CUR 96 Strain limit [%]		Material Stress limit $[N/mm^2]$
Tension	$\varepsilon_{1t,Rk}$	1.2	$\sigma_{f1t} = \varepsilon_{1t,Rk} * E_{1,90\%}$	300
	$\varepsilon_{2t,Rk;low}$	1.2	$\sigma_{f2t} = \varepsilon_{2t,Rk;low} * E_{2,low}$	24
Compression	$\varepsilon_{1c,Rk}$	1.0	$\sigma_{f1c} = \varepsilon_{1c,Rk} * E_{1,90\%}$	250
	$\varepsilon_{2c,Rk;low}$	1.2	$\sigma_{f2c} = \varepsilon_{2c,Rk;low} * E_{2,low}$	24
Shear	$\gamma_{12,Rk}$	1.6	$\tau_{f12} = \gamma_{12,Rk} * G_f$	22.4

Table 12: Material stress limit for UD lamella

Linear expansion coefficient	UD-Ply fvf, 40%	UD-Ply fvf, 50%
$\alpha_1 - 20℃ \leq T \leq +10℃$	$9.5 * 10^{-6}\ K^{-1}$	$8.3 * 10^{-6}\ K^{-1}$
$\alpha_1 + 10℃ \leq T \leq +40℃$	$0.9 * 10^{-6}\ K^{-1}$	$0.8 * 10^{-6}\ K^{-1}$
$\alpha_1 mean\ value$	$5.2 * 10^{-6}\ K^{-1}$	$4.6 * 10^{-6}\ K^{-1}$
$\alpha_2 - 20℃ \leq T \leq +10℃$	$100 * 10^{-6}\ K^{-1}$	$83.6 * 10^{-6}\ K^{-1}$

Table 13: Thermal expansion coefficient

Average density

The average density of the material can be calculated with:

$$\rho_{com} = V_f \rho_f + (100\% - V_f) * \rho_r$$

Where:

- V_f is the volume of fibres given in percentage
- ρ_f is the density of the fibres which is equal to 1500 kg/m^3 or approximately 15.0 kN/m^3
- ρ_r is the density of the resin which is for polyester equal to 1200 kg/m^3 or approximately 12.0 kN/m^3 and for epoxy 1250 kg/m^3 or approximately 12.5 kN/m^3

6.4 Design capacity[10]

In art 2.4.3 of CUR 96:2019 the design capacity of the material is given with:

$$R_d = \frac{\eta_c * R_k}{\gamma_M}$$

Where:

- R_k is the characteristic value of the specific resistance, determined with the characteristic values of the material
- η_c is the conversion factor
- γ_M is the partial material factor

6.4.1 Characteristic value of the stress limit

In accordance with Article 3.7.3.2 of CUR 96:2019, the simplified strain criterion may be applied for structures composed of glass fibre composites. The simplified criterion provides characteristic strain limits for tension, compression, and shear, which can subsequently be converted into stress limits using the elastic modulus of the material.

[10] Design capacity obtained from: Basis of Design by Witteveen+Bos, “Seasaw bio-composite”, 26-5-2025 and CUR96

However, flax fibre composites are considered instead of glass fibre composites. Since experimental testing of flax fibre composites is outside the scope of this report, the applicability of the simplified strain criterion from CUR 96 to flax fibre composites is evaluated using available literature data. For further structural design of the Seasaw, the characteristic values should subsequently be determined according to NEN-EN 1990 Appendix D7 and compared with the preliminary values adopted in this report.

CUR 96:2019 provides the following characteristic strain limits for glass fibre composites:

- $\varepsilon_{1t,Rk} = 1.2\ [\%]$
- $\varepsilon_{2t,Rk;low} = 1.2\ [\%]$
- $\varepsilon_{1c,Rk} = 1.0\ [\%]$
- $\varepsilon_{2c,Rk;low} = 1.2\ [\%]$
- $\gamma_{12,Rk} = 1.6\ [\%]$

The corresponding characteristic stress limits are derived from the prescribed strain limits assuming linear elastic orthotropic material behaviour:

- $\sigma_{f1t} = \varepsilon_{1t,Rk} * E_{1,90\%}$
- $\sigma_{f2t} = \varepsilon_{2t,Rk;low} * E_{2,low}$
- $\sigma_{f1c} = \varepsilon_{1c,Rk} * E_{1,90\%}$
- $\sigma_{f2c} = \varepsilon_{2c,Rk;low} * E_{2,low}$
- $\tau_{f12} = \gamma_{12,Rk} * G_f$

Where:

$E_{1,90\%}$ is the characteristic longitudinal elastic modulus

$E_{2,low}$ is the characteristic transverse elastic modulus

G_f is the shear modulus

The simplified strain criterion in CUR 96 was originally developed for glass fibre composites, which generally exhibit predominantly linear elastic behaviour up to relatively high strain levels. Flax fibre composites, however, are known to exhibit a more progressive stress-strain response with nonlinear behaviour initiating at relatively low strain levels due to mechanisms such as fibre-matrix debonding, matrix cracking and local fibre rearrangement. Literature on flax/epoxy composites reports bilinear or nonlinear tensile stress-strain behaviour with stiffness degradation occurring before ultimate failure. (Barré, Chotard, & Benzeggagh, 1996) (Pitarresi, Tumino, & Mancuso, 2015)

Despite these differences, several studies indicate that flax fibre composites exhibit deformation and failure mechanisms that are qualitatively comparable to those of conventional fibre reinforced polymer composites. Reported failure mechanisms include fibre fracture, fibre pull-out, matrix cracking, and fibre-matrix debonding. In addition, flax fibre composites exhibit orthotropic mechanical behaviour and stiffness and strength characteristics that are consistent with structural composite action. (Yan, Chouw, & Jayaraman, 2013)

Experimental investigations on flax fibre composites reported tensile moduli up to approximately 15–40 GPa and tensile strengths up to approximately 130–380 MPa depending on fibre architecture, fibre volume fraction, and manufacturing method. Literature further indicates that the tensile strength and stiffness generally increase with increasing fibre volume fraction, while the ultimate strain remains within a relatively limited range. At the same time, significant scatter in mechanical

properties is reported due to the natural variability of flax fibres, fibre waviness, manufacturing effects, and local defects such as kink bands. (Yan, Chouw, & Jayaraman, 2013)

The available literature therefore does not provide sufficient evidence to conclude that the simplified strain criterion from CUR 96:2019 is directly applicable to flax fibre composites in the same manner as for glass fibre composites. Although flax fibre composites may exhibit nonlinear stress–strain behaviour at higher strains, the relatively low strain limits specified in CUR 96:2019 are likely to remain within, or close to, the approximately linear part of the stress–strain response. However, this assumption has not been sufficiently validated for flax fibre composites based on the available literature.

Nevertheless, for a preliminary structural assessment, the simplified strain criterion from CUR 96:2019 may be adopted as a preliminary engineering approximation in the absence of dedicated experimental material characterisation. The criterion provides a consistent methodology for estimating preliminary characteristic stress limits based on the limited available material data and enables an initial structural verification of the Seasaw design. The adopted stress limits should therefore be regarded as provisional values intended for preliminary design only. Final design values remain subject to experimental validation and statistical evaluation in accordance with NEN-EN 1990 Appendix D7.

6.4.2 Partial material factor

The partial material factors are obtained from article 2.4.4.4 of CUR 96:2019 and can be calculated with:

$$\gamma_M = \gamma_{M1} * \gamma_{M2}$$

Where:

γ_{M1} is the partial material factor linked to geometric deviations and model uncertainties in obtaining the correct material properties

γ_{M2} is the partial material factor that allows for uncertainties in the strength properties of the material and is dependent on the variation of material properties

The partial material factors are found in Table 14, with the assumptions:

- For the serviceability limit states, the following applies: $\gamma_M = 1$
- Material properties are determined based on theoretical models, tests, and literature.
- In the preliminary design, it may be assumed that the vacuum injection process achieves a coefficient of variation in the stress level of $V_x \leq 0.10$
- Some parts of the structure can be made with a sandwich structure

Conditions			γ_{M1}	γ_{M2}	γ_M
Serviceability limit states			1.0	1.0	1.0
Ultimate limit state – strength	Post-hardened laminates		1.15	1.2	1.38
	Core material	Shear	1.15	1.5	1.73
		Compression	1.15	1.2	1.38
Ultimate limit state – local stability	Post-hardened laminates		1.15	1.4	1.61
	Core material	Shear	1.15	1.7	1.96
		Compression	1.15	1.4	1.61
Ultimate limit state – global stability	Post-hardened laminates		1.15	1.35	1.55
	Core material	Shear	1.15	1.2	1.38
		Compression	1.15	1.2	1.38

Table 14: Partial material factors according to CUR 96:2019

6.4.3 Conversion factor

The conversion factors are obtained from article 2.4.5 of CUR 96:2019 and can be calculated with:

$$\eta_c = \eta_{ct} * \eta_{cm} * \eta_{cv} * \eta_{cf}$$

Where:

η_{ct} is the conversion factor for temperature effects

η_{cm} is the conversion factor for effects of moisture

η_{cv} is the conversion factor for effect of creep

η_{cf} is the conversion factor for effects of fatigue

In Table 15 is an overview of when which conversion factor should be applied. The conversion factor for the effects of creep only needs to be applied to long-term loads.

Conversion factor	Ultimate limit state			Serviceability limit state			
	Strength	Stability	Fatigue	Deformation long-term load	Deformation short term load	Comfort (vibrations)	Damage
η_{ct}	✓	✓	✓	✓	✓	✓	✓
η_{cm}	✓	✓	✓	✓	✓	✓	✓
η_{cv}	✓	✓		✓			✓
η_{cf}		✓		✓	✓	✓	✓

Table 15: Overview of when which conversion factor should be applied according to CUR 96:2019

Temperature

The conversion factor for temperature accounts for changes of material properties due material temperatures in service conditions relative to the material properties at 20 °C, excluding effect at long-term exposure, in accordance with article 2.4.5.2 of CUR 96:2019.

The instantaneous glass transition temperature of the bio-based resin is:

$$T_g = 112\ °\text{C}\ [11]$$

According to CUR 96:2019, the maximum allowable service temperature is therefore:

$$T_d \leq T_g - 40\ °\text{C} = 112 - 40 = 72\ °\text{C}$$

The conversion factors for temperature effects are:

- 0.9 for ultimate limit state
- 1.0 for serviceability limit state

Long-term exposure to temperature is considered to have a negligible effect because the expected service temperatures remain well below the glass transition temperature of the matrix and within the specified service conditions of the material. In addition, long-term exposure to elevated temperatures below T_g can contribute to post-curing effects, which may slightly improve the mechanical properties of polymeric materials.

[11] Temperature obtained from: Basis of Design by Witteveen+Bos, “Seasaw bio-composite”, 26-5-2025

Additional support for this assumption is provided by experimental research on flax fibre reinforced bio-based thermoset composites by Pisupati et al. (2021). In this study, flax fibre reinforced benzoxazine composites retained their mechanical performance at operating temperatures substantially below the glass transition temperature of the matrix. Significant degradation mainly occurred when the operating temperature approached or exceeded T_g. The study further demonstrated that bio-based thermoset matrices with high glass transition temperatures exhibit good dimensional and mechanical stability under elevated temperature exposure. (Pisupati, Bonnaud, Deléglise-Lagardère, & Hae Park, 2021)

Moisture

The conversion factor for moisture accounts for changes of material properties due to water absorption over time including ageing effect resulting from long-term exposure. According to Article 2.4.5.3 of CUR 96:2019, a conversion factor of 0.9 is applied for structures exposed to alternating environmental conditions, with successive wet and dry periods.

The suitability of this reduction factor is supported by literature on flax fibre composites exposed to humid environments. Research on the environmental durability of flax fibre composites shows that moisture exposure mainly affects the material through water uptake by the fibres, fibre swelling, and degradation of the fibre–matrix interface. These mechanisms can reduce stiffness and strength during long-term exposure to humid conditions. However, the reductions reported in literature remain within the same order of magnitude as the conservative reduction factors prescribed by CUR 96:2019 for moisture effects. (Stamboulis, Baillie, Garkhail, van Melick, & Peijs, 2000)

Suitability of CUR Reduction Factors for Combined Temperature and Moisture Effects

For a flax fibre composite bridge in Ulm, experimental studies were conducted to evaluate the combined influence of temperature and moisture. These effects cannot be treated independently. Therefore, all test specimens were evaluated under hot–wet conditions.

The observed reductions in stiffness and changes in strength remained within the limits prescribed by the CUR reduction factors for combined temperature and moisture effects. (Smart Circular Bridge for a circular built environment, sd)

Creep

The conversion factor for creep accounts for time-dependent deformation under sustained loading, including long-term strain development in fibre-reinforced polymer composites. According to Article 2.4.5.4 of CUR 96:2019, creep effects in FRP materials may be considered through a creep conversion factor that depends on load duration and laminate configuration.

Although CUR 96:2019 provides an analytical formulation to determine the creep conversion factor, this approach is not used in this study. Instead, creep is assessed using a creep constraint line method based on experimentally calibrated long-term laminate behaviour.

To ensure consistency with this approach, the creep conversion factor is taken as:

$$\eta_{cv} = 1.0$$

Creep verification is subsequently performed using the creep constraint diagram shown in Figure 23. This diagram defines a limiting interaction curve between sustained stress level and long-term material utilisation. The design is considered satisfactory when the stresses for certain load cases remains within the boundary of this curve, and the reserve factor is determined graphically.

This method is appropriate for fibre-reinforced polymers because creep behaviour in fibre-reinforced polymers is primarily governed by the polymer matrix, which exhibits viscoelastic time-dependent behaviour, while the fibre reinforcement mainly provides stiffness and restrains deformation in the fibre direction. Consequently, laminates containing off-axis fibre orientations are more sensitive to creep deformation than purely unidirectional laminates.

The creep constraint curve used in this study is based on a quasi-isotropic (QI) laminate configuration as defined in Table 16. This lay-up is representative of a balanced laminate response under multi-directional loading and is commonly used as a reference configuration for long-term behaviour assessment. The stresses in the structure should be translated to the different maximum stress. The total laminate thickness is:

$$4 * 0.467 + 3 * 0.583 = 3.617\ mm$$

(Smart Circular Bridge for a circular built environment, sd)

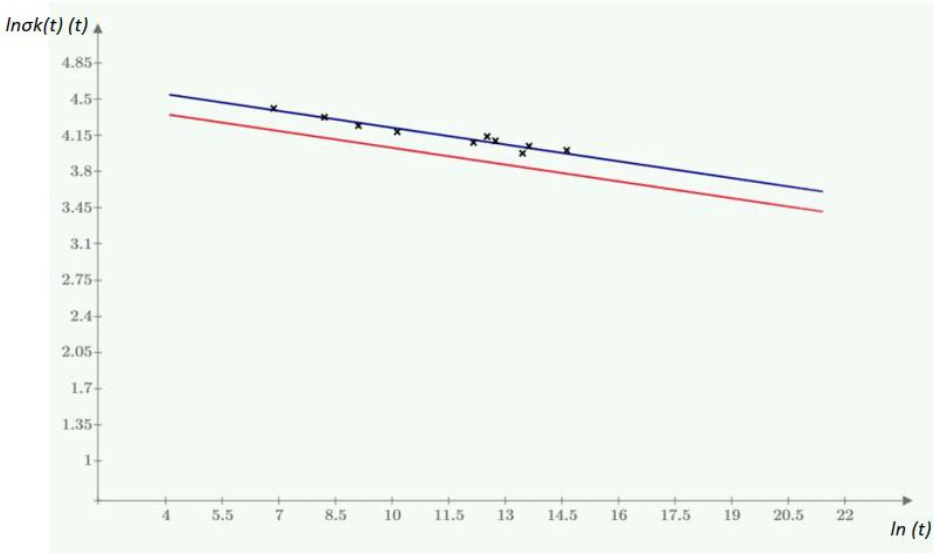

Figure 23: Creep line (blue) and characteristic creep line (red) on log-log scale for a lifetime of 50 years (Smart Circular Bridge for a circular built environment, sd)

Orientation	Flax fibre material	Composite ply thickness
0°	UD Amplitex 5025	0.467 mm
+/-45°	+/-45° Amplitex 5008	0.583 mm
90°	UD Amplitex 5025	0.467 mm
+/-45°	+/-45° Amplitex 5008	0.583 mm
90°	UD Amplitex 5025	0.467 mm
+/-45°	+/-45° Amplitex 5008	0.583 mm
0°	UD Amplitex 5025	0.467 mm

Table 16: Laminate layering of the creep graph (Smart Circular Bridge for a circular built environment, sd)

Fatigue

Fatigue must be considered when structures are subjected to cyclic loading with more than 5000 load cycles or when the cyclic stress exceeds 40% of the ultimate load, as stated in article 2.4.5.5 of CUR 96:2019.

Although wind loading results in a number of load cycles exceeding 5000, the corresponding stress range in the main load-bearing parts of the structure remains low and is expected to stay well below the critical threshold where fatigue damage typically develops. Therefore, fatigue is not expected to govern the design.

This assumption is supported by the findings of Perruchoud, Alderliesten and Mosleh who showed that flax FRP laminates reinforced with twisted yarns do not exhibit the typical progressive stiffness degradation observed in conventional FRPs. Instead, stiffness remained stable or increased during most of the fatigue life due to microstructural re-arrangements such as yarn untwisting and fibre realignment. Any noticeable degradation occurred primarily in the final stage of fatigue life, immediately prior to failure. (Perruchoud, Alderliesten, & Mosleh, Tailoring the fatigue response of flax FRP composites by exploiting Micro-structural re-arrangements and auxiliary loading sequences, 2025)

Given the low expected stress amplitude under wind loading and the favourable fatigue behaviour of twisted-yarn flax FRP, a fatigue conversion factor of 1.0 is adopted.

6.5 Strength verification composites

According to CUR 96:2019, the structural verification of composite materials may be performed at lamina, laminate, and cross-sectional level, depending on the required level of detail and the governing failure mechanism. The corresponding verification procedures are provided in Appendix A. In this study, the structural verification is performed at the laminate level.

In a laminate-level analysis, the failure of the composite laminate is assessed based on a stress or strain criterion applied to the laminate as a whole, rather than to the individual plies. For a uniaxial stress state or pure in-plane shear, the laminate shall satisfy the following strength criteria:

$$\frac{\sigma_{i,Ed}}{f_{i,Rd}} \leq 1.0 \text{ and } \frac{\tau_{kl,Ed}}{\tau_{kl,Rd}} \leq 1.0$$

Where:

$\sigma_{i,Ed}$	is the applied normal stress in the considered loading direction
$\tau_{kl,Ed}$	is the applied shear stress in the considered plane
$f_{i,Rd}$	is the design strength of the laminate in the considered loading direction
$\tau_{kl,Rd}$	is the design shear strength of the laminate in the considered plane
i, k, l	are coordinate axes corresponding to the considered directions

The laminate strength should be determined experimentally which will not be done in this report.

6.6 Creep coefficient for deflection

The creep coefficient associated with the deflection w_2 due to creep is given by:

$$\frac{1}{\eta_{ck}} - 1$$

To remain conservative, the creep of the entire structure is assumed to correspond to a quasi-isotropic laminate. In reality, most of the structure will consist of unidirectional lamella, which exhibit negligible creep. This assumption therefore leads to a conservative estimate of the long-term deflection. The parameter η_{ck} is determined from the degradation curve shown in Figure 23. The decrease of the failure capacity of the laminate over time is equal to the value for η_{ck}. The line in the graph has an equation of:

$$y(t) = failure\ capacity\ laminate * t^{-0.054}$$

For a design life of 50 years, η_{ck}becomes:

$$\eta_{ck} = t^{-0.054} = (50\ years)^{-0.054} = 0.31714$$

The corresponding creep coefficient for the deflection w_2 is then:

$$\frac{1}{0.31714} - 1 = 2.153$$

Flax fibre composite structures typically exhibit a relatively high initial creep rate directly after loading. As time progresses under sustained load, the creep rate gradually decreases, resulting in a progressively flattening creep curve, see creep curve in Figure 24. This behaviour suggests that pre-creep conditioning can be beneficial.

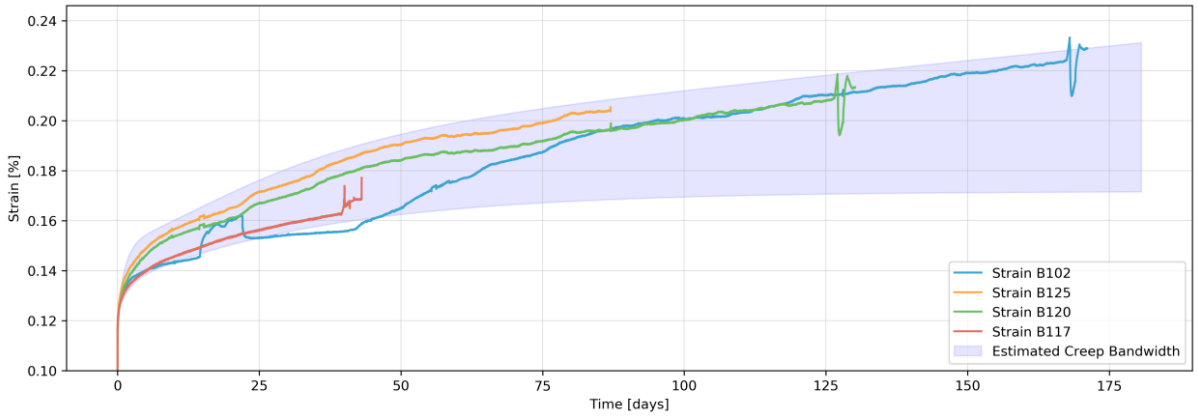

Figure 24: Creep curve flax fibre composite QI-laminate (Amsterdam, 2025)

By applying the permanent load to the structure for several days prior to service, a significant portion of the initial creep deformation can be induced in advance. This deformation can then be accounted for during manufacturing by introducing an appropriate pre-camber. Consequently, the long-term service deflection is reduced.

The values of η_{ck} and the corresponding creep coefficients for different time periods are presented in the table below.

Time [days]	η_{ck} [−]	Creep coefficient [-]
0	-	-
10	0.478	1.092
20	0.460	1.172
30	0.450	1.220
40	0.444	1.255

Table 17: Creep coefficients for different loading times

6.7 Core material[12]

The core material which needs to be used is ArmacelPET_Eco50, see Figure 25. ArmacelPET_Eco50 is a foam made from low-density polyethylene terephthalate (PET) derived entirely from recycled plastic bottles. It offers long-lasting insulation performance, maintaining low thermal conductivity over time. Its closed-cell structure makes the foam water-resistant and ensures consistent thermal efficiency. The boards are available in thicknesses ranging from 20 mm to 200 mm, with standard widths of 1000 mm or 1220 mm, and lengths from 500 mm up to 3000 mm. In the table below are the material properties of the core material shown.



Figure 25: ArmacelPET_Eco50 (ArmaPET Eco, 2023)

Core material	$\boldsymbol{\rho_c}$ $[\boldsymbol{kg/m^3}]$	$\boldsymbol{E_c}$ $[\boldsymbol{N/mm^2}]$	$\boldsymbol{G_c}$ $[\boldsymbol{N/mm^2}]$	$\boldsymbol{\tau_{13}}$ $[\boldsymbol{N/mm^2}]$	$\boldsymbol{\tau_{23}}$ $[\boldsymbol{N/mm^2}]$
ArmacelPET_Eco50	50	10	5	0.3	0.3

Table 18: Properties core material

6.8 Bonding paste[13]

The manufactured components are bonded using BÜFA 740-0110 bonding paste. The characteristic interlaminar shear strength between the Bcomp flax fibre laminates and the bonding paste is 18 MPa. The adhesive bonds do not need to be included in the FE model. However, the shear stress in the layer where the bonding paste is applied must be verified against a maximum shear stress of 1 MPa. This value is deliberately conservative to ensure that this layer does not become governing.

[12] Material properties obtained from: Basis of Design by Witteveen+Bos, “Seasaw bio-composite”, 26-5-2025
[13] Bonding paste information obtained from: Basis of Design by Witteveen+Bos, “Seasaw bio-composite”, 26-5-2025

6.9 Classical Laminate Theory (CLT)[14]

A laminate is composed of different lamella. These lamellas are often stacked in different orientations. The stiffness in a particular laminate direction will vary for each lamella. As a result, an external load leads to different internal stresses in the individual lamella, see Figure 26. A consequence of this is that, when determining the strength of a laminate, the stresses in each individual lamella must be calculated from the strains of the laminate and evaluated using a failure criterion. However, the strain of the laminate itself depends on the combined stiffnesses of the lamella. With the classical laminate theory, it is possible to determine the combined stiffnesses of the lamella, so the stiffness of the laminate. The derivations, theory and equations are given in Appendix C. (Nijsen, 2015)

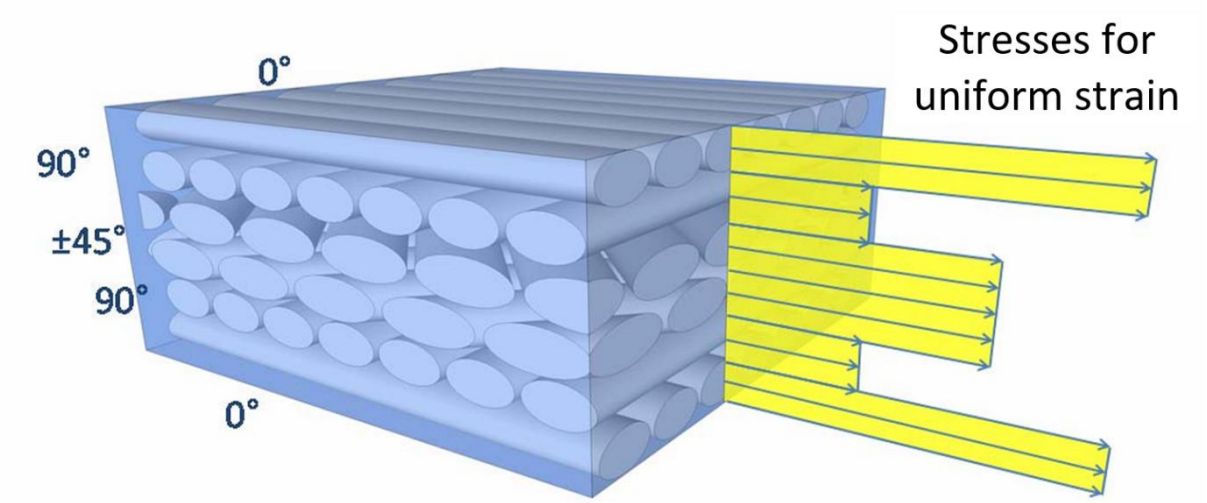

Figure 26: Stresses in a lamella depended on the lamella stiffness (Nijsen, 2015)

6.10 Durability

Durability refers to a material's ability to resist deterioration caused by both external influences and internal processes. The durability of flax fibre composites can be affected by for example fatigue and moisture absorption. Research has shown that fungal and bacterial growth in flax composites, caused by biodegradation and moisture retention, poses a significant challenge for their application as structural materials. In addition, exposure to varying weather conditions may lead to discoloration, weight loss, surface roughening, and strength reduction in natural fibre composites. (Yan, Chouw, & Jayaraman, 2013)

6.10.1 Fatigue

Fatigue is a progressive degradation process that occurs when a material is subjected to cyclic or variable loading. Even when the applied stress remains below the material's elastic limit, repeated loading can eventually lead to sudden and catastrophic failure. The fatigue limit is defined as the stress level below which a material can theoretically withstand an infinite number of load cycles without failure. However, this limit does not exist for all materials. In more ductile systems, failure may still occur at very low stress levels if the number of cycles is sufficiently high. This behaviour is observed, for example, in Aluminium and, in some cases, in natural fibre composites where plant fibres exhibit relatively limited mechanical performance. (Pavlovic, Valzania, & Minak, 2025)

[14] Equations and theory for the Classical Laminate Theory obtained from: Lecture 1 & 2 of the course AE 4509, 10-2-2014 & 14-2-2014

In composite materials, fatigue behaviour is influenced by several interacting factors.

- Fibre orientation: Fatigue resistance is not necessarily maximized when fibres are fully aligned with the applied load, as such configurations often provide poor transverse strength. Improved performance can be achieved with cross-ply laminates, fibres oriented at 90°, or with fibres placed at small angles, 5–10°, relative to the primary loading direction.
- Matrix type: Matrices with higher fatigue resistance, such as epoxy resins, generally enhance overall durability due to their hardness and resistance to deterioration.
- Fibre volume fraction: Increasing the fibre content improves fatigue performance, provided that the fibres are uniformly distributed. The S-N curve is enhanced when the fibre content increases. However, an optimal value exists. When the fibre content becomes higher or lower as a certain volume fraction the performance tends to deteriorate.
- Type of loading: Composites exhibit fatigue responses that strongly depend on the type of loading.

(Pavlovic, Valzania, & Minak, 2025)

After short periods of use with loads lower than 20% of the laminate's static tensile strength fatigue damage can occur. The fatigue damage typically initiates with the formation of cracks in lamellas whose fibres are oriented at the largest angle relative to the load direction. When the applied load exceeds approximately 25–30% of the laminate's static strength, the buildup of the cyclic loading leads to the formation of delamination cracks near the interfaces between lamellas. As these cracks propagate, they reduce the laminate's overall stiffness and increase change of failure in the weakest lamella. At this stage, the remaining service life of the laminate is often less than 10% of the component's total life. In the final stages of fatigue, cracks may also develop in lamellas with fibres aligned parallel to the load. These cracks usually originate from fibre fracture or matrix cracking. If the adhesion between the fibre and the matrix is insufficient, debonding occurs, accelerating damage progression and ultimately leading to structural failure. (Pavlovic, Valzania, & Minak, 2025)

6.10.2 Moisture absorption

In comparison with synthetic glass fibre reinforced composites, flax fibre reinforced composites generally exhibit lower resistance to moisture, because of the presence of hydroxyl and other polar groups within the fibre constituents. High moisture uptake in flax fibres weakens the interfacial bonding between the fibre and the matrix, ultimately compromising the mechanical properties of the composite. As a result, flax fibre composites are particularly sensitive to environmental factors such as and hygrothermal aging and loading, making long-term performance prediction more challenging. Hygrothermal aging refers to the degradation of materials by prolonged exposure to elevated temperatures combined with moisture. (Yan, Chouw, & Jayaraman, 2013) (Zhang, et al., 2024)

To improve performance, it is essential to enhance the hydrophobicity of flax fibres. Hydrophobicity is the physicochemical property of non-polar substances that repel water and do not mix well with aqueous solutions. This can be achieved through surface treatments using suitable coupling agents or by coating the composite with appropriate resins. Such modifications help reduce moisture absorption and improve both mechanical properties and environmental durability. For the Seasaw, the flax fibre composite components will be coated on the outside of the components. (Yan, Chouw, & Jayaraman, 2013) (Hydrophobic effect, 2025)

6.11 Coating[15]

A coating system is applied to protect the flax fibre composite structure against environmental influences and to improve its durability during the service life of the Seasaw. The proposed coating system consists of the following components:

- IJmopox HB coating, double coat
- The top part of the structure needs to be foreseen with a warning layer (under the wear layer)
- Anti-graffiti coating (PSS-20 Clear)

The IJmopox HB coating is a two-component epoxy-based coating with a polyamide hardener. It can be applied to sufficiently prepared polyester surfaces and is recommended for use in osmosis prevention for polyester. The coating has excellent mechanical properties and good resistance to chemicals and (salt) water. For the Seasaw, the coating is therefore applied to protect the polyester-based composite against moisture and environmental exposure and to reduce the risk of osmosis. (De IJssel Coatings BV, 2022)

A double coat is specified to provide sufficient protective coverage of the composite surface. Applying multiple coating layers can increase the thickness and continuity of the protective coating system, thereby reducing the likelihood that local imperfections or discontinuities in a single layer expose the underlying composite. The exact number of layers and required coating thickness should be confirmed during the detailed design and according to the coating manufacturer's specifications.

A warning layer is incorporated underneath the wear layer on the top surface of the structure. This layer provides a visual indication when the wear layer has been sufficiently worn or damaged. This allows deterioration of the walking surface to be identified before the underlying structural or protective layers are affected. The warning layer therefore supports inspection and maintenance of the deck.

Finally, a PSS-20 clear anti-graffiti coating is applied to the exposed surfaces to protect the structure against graffiti. PSS-20 is a water-based protective coating based on plant-derived polysaccharides, including cellulose and starch. After application, it forms a thin film of approximately 0.03 mm on the surface. The coating acts as a sacrificial layer, meaning that it is removed together with the graffiti during cleaning. Once the graffiti has been removed, the protective layer can be reapplied to the still-moist surface, restoring the protection against future graffiti. (PSS 20 graffiti becherming, sd)

The complete coating system therefore provides protection against moisture and environmental exposure, facilitates inspection and maintenance of the walking surface, and reduces the risk of damage caused by graffiti.

[15] Coating system obtained from: Basis of Design by Witteveen+Bos, “Seasaw bio-composite”, 26-5-2025

6.12 Hybrid Composites

Flax fibre alone is likely not sufficiently strong to be used as the sole material for the complete Seasaw structure. Therefore, hybrid composites are considered as a potential alternative for some parts of the structure.

A hybrid composite is hybridization of natural fibre with stronger and more corrosion-resistant synthetic fibre, for example, glass, carbon, or basalt fibre. This can improve the stiffness and strength of the composite. By incorporating two or more different types of fibres into a hybrid composite, the strengths of one fibre can offset the weaknesses of another. This approach enables a more optimized balance between performance and cost through careful material design. Hybrid composites are generally fabricated using two primary techniques:

- Inter-ply, which involves stacking layers of different fibre fabrics within a single laminate.
- Intra-ply, which utilizes co-woven fabrics containing alternating threads of dissimilar fibres within the same layer.

Glass, carbon, and basalt fibres were considered as potential reinforcement materials for inter-ply hybrid laminates during the material selection process. The corresponding material properties are provided in Appendix B. (Yan, Chouw, & Jayaraman, 2013) (Pavlovic, Valzania, & Minak, 2025)

7. Preliminary design

The architectural shape of the structure is defined using a Rhino 3D-model, see Figure 28.[16] This Rhino 3D-model was developed by the architectural firm MVRDV and made available by Witteveen+Bos. The overall dimensions of the structure are known, however the dimensions of the cross-section are not yet determined. Figure 27 shows the cross-section of the deck, including its different components. The dimensions of the cross-section will be determined in this chapter, to get an initial preliminary design to put in a finite element model. The width of the cross-section is approximately 1800 mm, as obtained from the Rhino model. The preliminary design will be made from Flax fibre UP-bio composite.

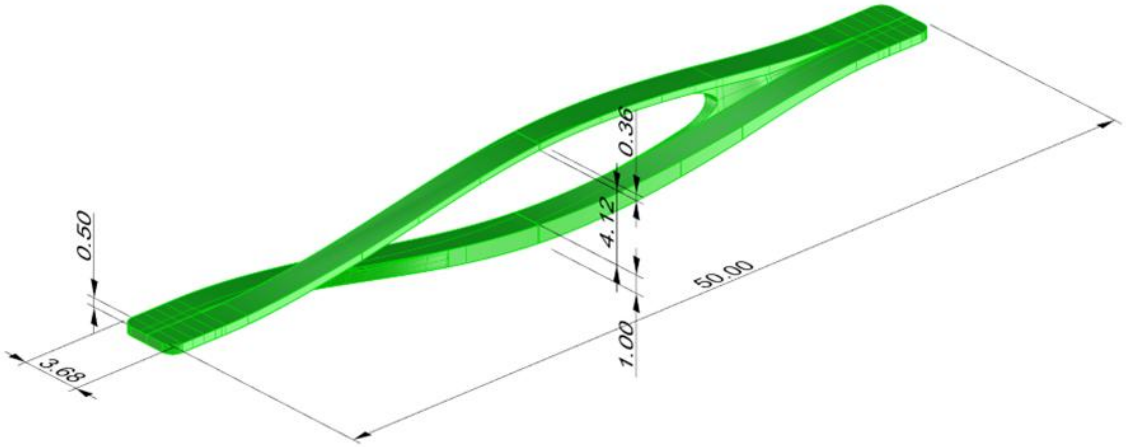

Figure 28: Rhino model with dimensions (MVRDV)[16]

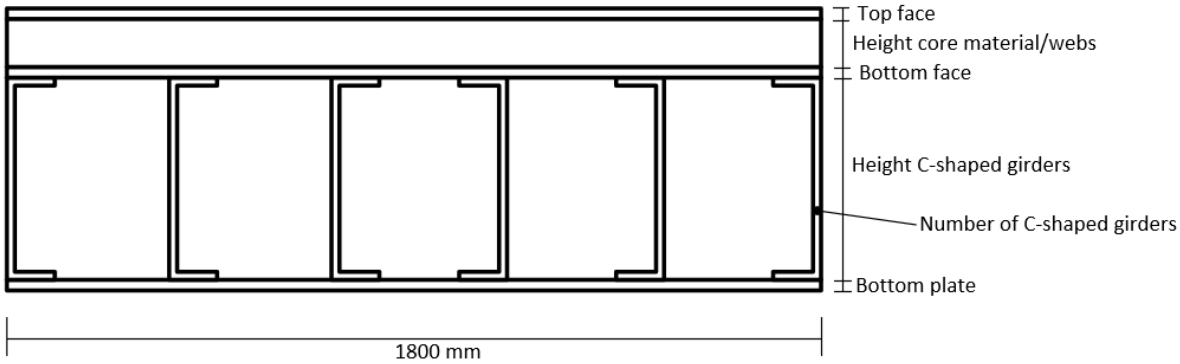

Figure 27: Cross-section deck

To determine the cross-sectional dimensions for the preliminary design, the stiffness of the composite material must be known. A Python script was developed to calculate the stiffness of a laminate based on the Classical Laminate Theory (CLT). In addition, the code includes a function to print the results and a function that plots the stacking of the laminate. Python was selected because the obtained material properties can be directly incorporated into other Python-based calculations. Although the laminate stiffness could also have been determined using existing software, using a Python script avoids manually transferring the calculated stiffness properties to the subsequent calculations and provides a consistent calculation procedure throughout the analysis. The code is provided in Appendix D, and its explanation and verification are given in Appendix E.

[16] Rhino model made by MVRDV and figure obtained from: Basis of Design by Witteveen+Bos, “Seasaw bio-composite”, 26-5-2025

For the laminate lay-up, several design rules are applied to ensure balanced mechanical behaviour. The rules are as follows:

- For the C-shaped girders, the laminate should be balanced, with approximately 25% of the lamella oriented in each of the four fibre directions (0°, 90°, +45°, and −45°). This lay-up provides high shear resistance while ensuring similar material properties in both principal directions.
- A maximum of 2-5 consecutive 0° lamella may be used. These plies should be preceded and followed by a 90°, +45°, or −45° lamella.
- Each +45° lamella should be paired with a −45° lamella, and vice versa, to maintain laminate balance.

The Python script includes functions to calculate the percentage distribution of fibre orientations and to generate symmetric laminates.

A separate Python script was developed to determine the stiffness of the cross-section shown in Figure 27. This code is provided in Appendix F, with its explanation and verification included in Appendix G. In this analysis, the webs within the core material are neglected. The script also includes a function to visualize the cross-section along with its dimensions.

7.1 Thickness C-shaped girders

The primary function of the C-shaped girders is to transfer the shear forces. The thickness of the girders is determined such that they can resist the maximum shear force in the structure. The shear resistance is verified using the unity check:

$$\frac{V_{ED}}{V_{RD}} \leq 1$$

With:

$$V_{RD} = \frac{\eta_c * A_v * \tau_{xy,Rk}}{\gamma_m}$$

Where:

γ_m	is equal to 1.38, see Chapter 6.4.2
η_c	is $\eta_{ct} * \eta_{cm} * \eta_{cr}$ with $\eta_{ct} = 0.9$, $\eta_{cm} = 0.9$ and $\eta_{cr} = 1.0$, see Chapter 6.4.3
$\tau_{xy,Rk}$	is $\gamma_{12,Rk} * G$, with $\gamma_{12,Rk} = 1.6\ \%$, see Chapter 6.4.1
A_v	is the area of the web of the cross-section

The ULS load determined in Appendix L is used for the shear design. The resulting total design load is 18 kN/m, which is obtained by combining the governing load components according to the relevant ULS load combination. The maximum shear force of the structure occurs in the middle of the bottom half of the Seasaw. In Figure 29 is shown how the maximum shear force is determined. It is assumed that the bottom half of the Seasaw can be idealised as a straight beam clamped at midspan. It is further assumed that, at the mid-region of the upper half, the load is transferred to the bottom deck via the curved connection between the upper and lower parts of the structure. As shown in Figure 29, $V_{ED} = 900\ kN$.

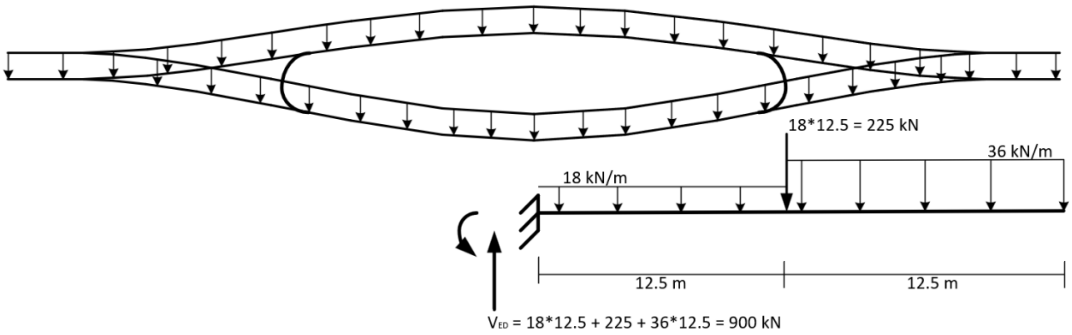

Figure 29: Schematic representation of maximum shear force

For the girders, the laminate lay-up shown in Figure 30 is assumed. The laminate lay-up of the C-shaped girders is balanced according to the design rules described earlier in this chapter. The properties used in this analysis are obtained from the laminate stiffness code (Appendix D) and are shown in Table 19. $\tau_{xy,Rk}$ of this material using the membrane properties is:

$$\tau_{xy,Rk} = \gamma_{12,Rk} * G = 0.016 * 2780 = 44.48\ N/mm^2$$

The height of the girder is not the same height as the height of the cross-section. At the middle, where the shear force is the highest, the cross-section has a height of around 1000 mm. A conservative assumption is made that the top face, core, bottom face, and bottom plate together have a height of approximately 200 mm. Consequently, a girder height of 800 mm is considered. Furthermore, four C-shaped girders are considered in the cross-section. The area of the webs of the cross-section will be:

$$A_v = h_{girder} * t_{girder} * 4 = 800 * 15.17 * 4 = 48544\ mm^2$$

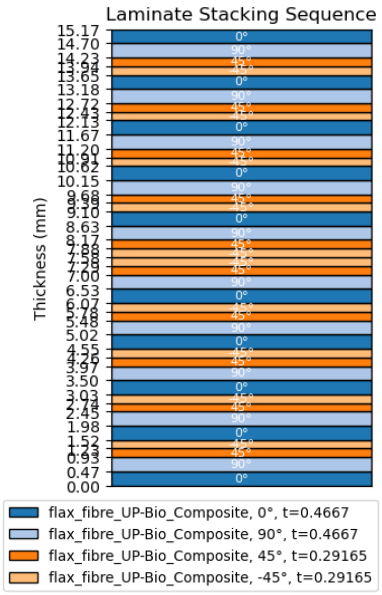

Figure 30: Stacking of the laminate for the C-shaped girders

Property	Membrane	Bending	Unit
E_1	9.308	10.328	GPa
E_2	9.308	9.174	GPa
G_{12}	2.780	2.473	GPa
υ_{12}	0.228650	0.203338	-
υ_{21}	0.228650	0.180629	-

Table 19: Material properties composite C-shaped girders

The total conversion factor is:

$$\eta_c = \eta_{ct} * \eta_{cm} * \eta_{cr} = 0.9 * 0.9 * 1.0 = 0.81, \text{ see Chapter 6.4.3}$$

The shear resistance of the cross-section is:

$$V_{RD} = \frac{\eta_c * A_v * \tau_{xy,Rk}}{\gamma_m} = \frac{0.81 * 48544 * 44.48}{1.38} = 1267.3 * 10^3\ N = 1267.3\ kN$$

Since $V_{rd} > V_{ED}$, a thickness of 15.17 mm for the C-shaped girder is sufficient for four girders in the cross-section.

7.2 Thickness bottom plate, bottom face, and top face

To determine the thickness of the bottom plate, bottom face and top face, the deflection of the top half of the bridge and the side is evaluated using the SLS load of 14 kN/m, which is obtained by combining the governing load components according to the relevant SLS load combination, see Appendix L. The schematic representation of the top half of the bridge and the side is shown in Figure 31. The top half is modelled as a beam fixed at both ends, while the side is modelled as a cantilever. The deflection of the top half can be calculated with:

$$w = \frac{1}{384} * \frac{ql^4}{EI}$$

The deflection of the sides can be calculated with:

$$w = \frac{ql^4}{8EI}$$

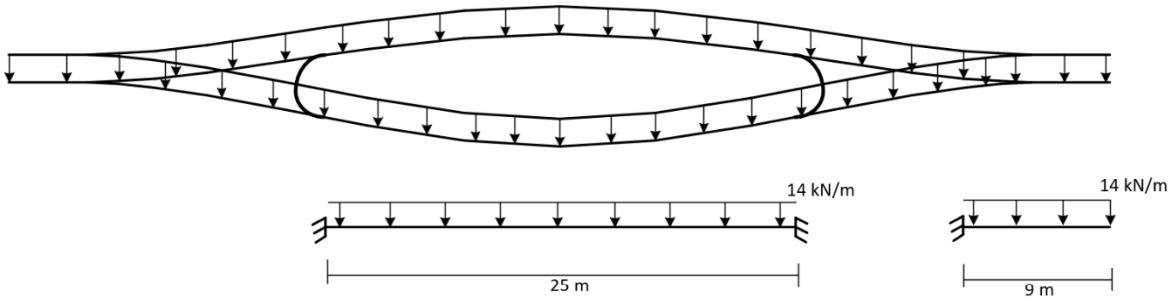

Figure 31: Schematic representation of top half bridge and side

For the maximum deflection of the top half, the following limit is applied for the determined SLS load:

$$w \leq \frac{l}{150}$$

This can be written as:

$$\frac{1}{384} * \frac{ql^4}{EI} \leq \frac{l}{150}$$

The maximum deflection for a length of 25 m is:

$$\frac{1}{384} * \frac{18 * 25000^4}{EI} \leq \frac{25000}{150} = 166.67\ mm$$

The stiffness of the deck has to be at least:

$$EI \geq \frac{1}{384} * \frac{18 * 25000^4}{166.67} = 1.09 * 10^{14}\ N/mm^2$$

The stiffness of the cross-section is determined using the Python code in Appendix F. The average thickness of the cross-section of the top half of the bridge over the span of 25 m is 400 mm. The width is 1800 mm. The girders will have a height of 330 mm. The deck of the top half has a stiffness of $1.100 * 10^{14}\ [N\ mm^2]$, which satisfies the requirement, when using a top and bottom face thickness of 27.07 mm, a core height of 75 mm, and a bottom plate thickness of 33.84 mm.

For the maximum deflection of the sides, the following limit is applied for the determined SLS load:

$$w \leq \frac{2l}{150}$$

This can be written as:

$$\frac{ql^4}{8EI} \leq \frac{2l}{150}$$

The maximum deflection for a length of 9 m is:

$$\frac{18 * 9000^4}{8EI} \leq \frac{2 * 9000}{150} = 120\ mm$$

The stiffness of the deck has to be at least:

$$EI \geq \frac{18 * 9000^4}{8 * 122.67} = 1.23 * 10^{14}\ N/mm^2$$

The stiffness is determined using the Python code in Appendix F. For the side section the cross-section has a height of 500 mm and the girders will have a height of 420 mm. The deck of the sides has a stiffness of $1.628 * 10^{14}$ $[N\ mm^2]$ which also satisfies the required stiffness. This confirms that the selected thicknesses are suitable for the preliminary design. The layering of the bottom and top face is shown in Figure 32 and the material properties are shown in Table 20. The layering of the bottom plate is shown in Figure 33 and the material properties are shown in Table 21.

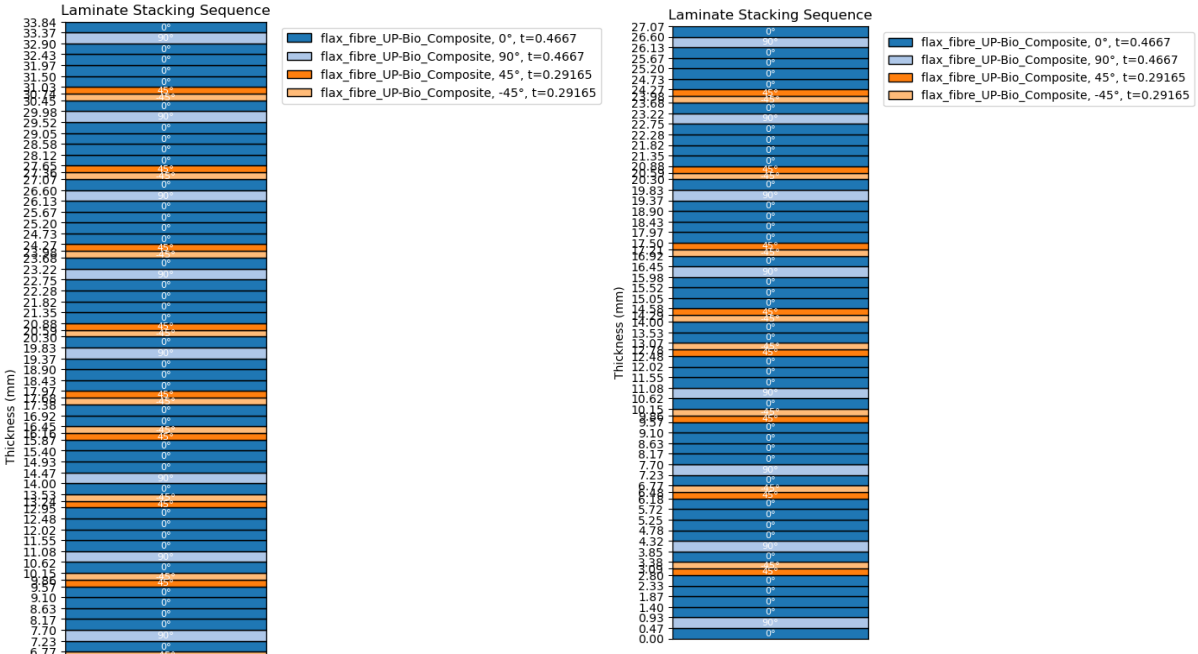

Figure 32: Stacking of the laminate for the bottom face and top face

Figure 33: Stacking of the laminate for the bottom plate

Property	Membrane	Bending	Unit
E_1	15.822	16.049	GPa
E_2	5.241	5.598	GPa
G_{12}	1.853	1.633	GPa
υ_{12}	0.246580	0.193800	-
υ_{21}	0.081680	0.067591	-

Table 20: Material properties composite bottom and top face

Property	Membrane	Bending	Unit
E_1	15.822	16.016	GPa
E_2	5.241	5.524	GPa
G_{12}	1.853	1.675	GPa
υ_{12}	0.246580	0.203556	-
υ_{21}	0.081680	0.070206	-

Table 21: Material properties composite bottom plate

7.3 Number of girders

The number of girders was initially assumed to be four. To verify that the spacing between girders is acceptable, the local deflection of the top plate between girders is analysed. The span between the girders can be obtained from Figure 34, this figure is obtained from the code in Appendix F. The span between the centre of gravity of the girders is 584 mm. The distance from the side of a girder to the side of the other girder is:

$$584 - 100 = 484\ mm$$

The top plate is assumed to be simply supported between the girders, to simplify the calculation. At first the loads on the top plate have to be determined. After the stiffness of the top deck and at last the deflection can be determined.

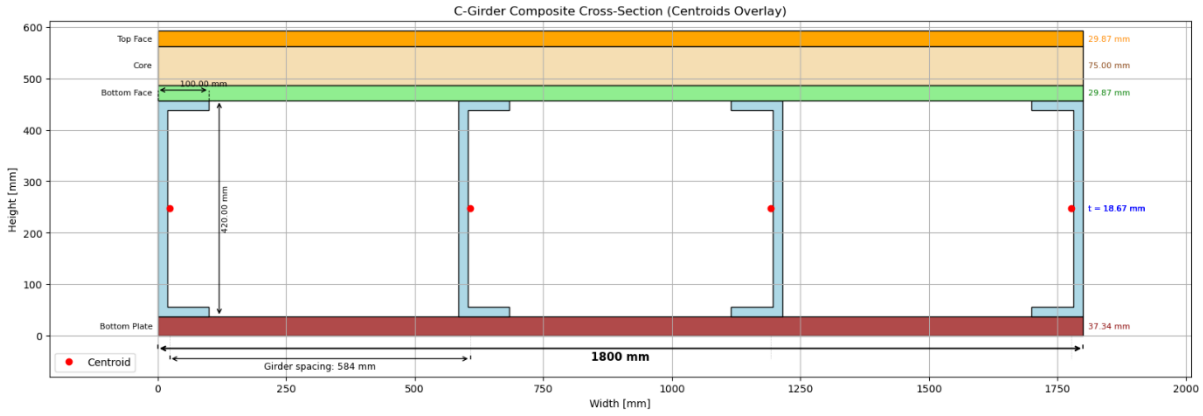

Figure 34: Spacing cross-section for 4 girders

7.3.1 Loads on top plate

The loads are determined based on Chapter 5.2.3. The total loads acting on the top plate are derived in Appendix L. In Figure 35 are the loads on the structure shown. All the loads are distributed per meter over the length of the bridge. The considered loads are:

- Distributed load and load top plate: $q_d = 4.5\ kN/m^2$
- Load of the balustrade: $F_{d,b} = 1.2\ kN/m$
- Downward wind load: $F_{d,w} = 0.18\ kN/m$

The loads are obtained by combining the governing load components according to the relevant SLS load combination.

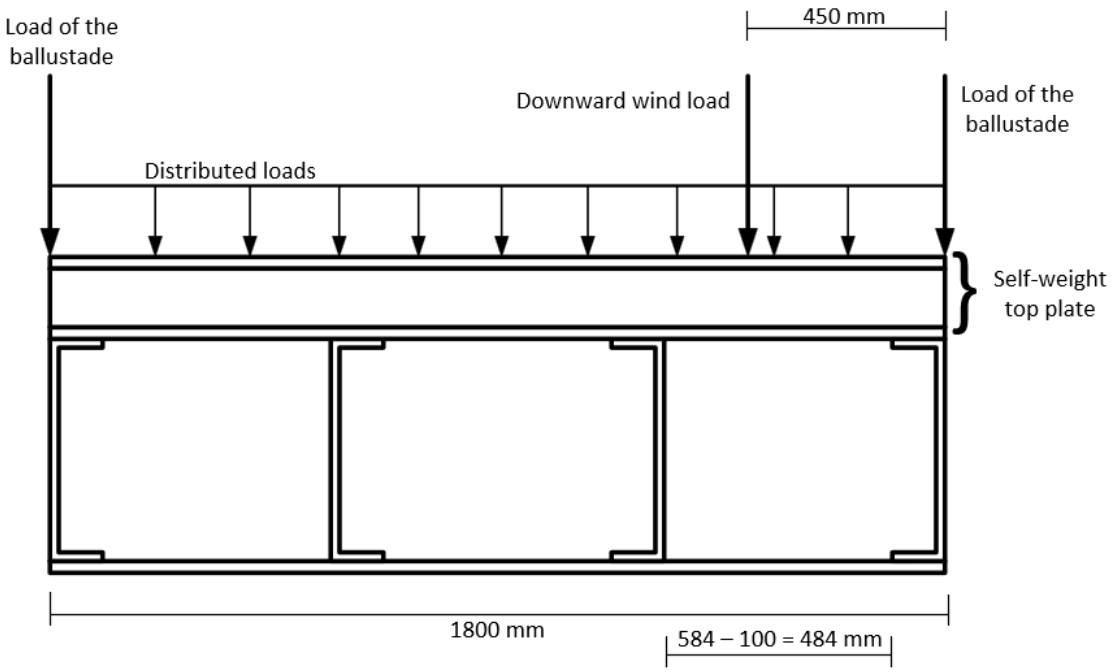

Figure 35: Loads on the top plate

7.3.2 Stiffness top plate

Since the width of the plate is as long as the bridge deck, the stiffness will be calculated for a width of 1 metre. The stiffness of the top plate can be calculated with:

$$EI_{zz} = \sum_{elements} E_{2,element} * (I_{zz,element} + A_{element} * (z_{cg} - z_{element})^2$$

Where E_2 of the material is used since the deflection will be calculated in the direction of E_2. The centre of gravity is in the middle of the top plate because the top plate is symmetric so:

$$z_{cg} = t_{bf} + \frac{1}{2} * h_{core} = 27.07 + \frac{1}{2} * 75 = 64.57\ mm$$

The stiffness of the top plate will be:

$$EI_{zz} = E_{2,bf} * (I_{zz,bf} + A_{bf} * \left(z_{cg} - z_{bf}\right)^2) + E_{core} * I_{zz,core} + E_{2,tf} * (I_{zz,tf} + A_{tf} * \left(z_{cg} - z_{tf}\right)^2)$$

$$EI_{zz} = 5241 * \left(\frac{1}{12} * 1000 * 27.07^3 + 1000 * 27.07 * \left(64.57 - \frac{1}{2} * 27.07\right)^2\right) + 10 * \frac{1}{12} * 1000 * 75^3 + 5241 * (\frac{1}{12} * 1000 * 27.07^3 + 1000 * 27.07 * \left(64.57 - \frac{1}{2} * 27.07 - 75 - 27.07\right)^2)$$

$$EI_{zz} = 7.6 * 10^{11}\ N\ mm^2$$

7.3.3 Deflection top plate

The deflection of the top plate is calculated based on the schematic representation shown in Figure 36. To simplify the analysis, the wind load with an eccentricity of 350 mm is assumed to act at the centre of the span. This assumption is conservative, as the actual load position would result in a smaller deflection. The deflection is calculated using:

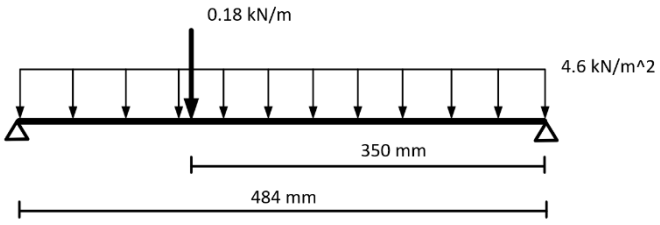

Figure 36: Schematic representation top deck span between girders

$$w = \frac{5}{384} * \frac{ql^4}{EI} + \frac{1}{48} * \frac{Fl^3}{EI}$$

The deflection is:

$$w = \frac{5}{384} * \frac{4.5 * 484^4}{7.6 * 10^{11}} + \frac{1}{48} * \frac{0.18 * 484^3}{7.6 * 10^{11}} = 4.2 * 10^{-3}\ mm$$

The calculated deflection is very small. It corresponds to approximately $8.7 * 10^{-4}$ % of the span. This indicates that increasing the number of C-shaped girders in the cross-section is not necessary, so 4 C-shaped girders will be used.

7.4 Connection upper and lower deck (De Oksel)

The upper and lower deck are connected at the sides by what is called the “Oksel” in Dutch, see Figure 39. It is a structure under the upper deck which is connected to the side of the lower deck. The structure includes vertical support plates, see Figure 37, Figure 40 and Figure 41, which are round at the bottom to create a nice transition, see Figure 38. The geometry of the support plates varies along the connection due to changes in the height difference between the upper and lower decks, as well as variations in the height of the lower deck. At the locations of the support plate in the lower deck, plates will be placed between the C-shaped girders, oriented perpendicular to them, to connect and couple the girders. These will be called stiffener plates. There will be flanges on all the sides of the support plates to connect the plates to the upper and lower deck. All the support plates are connected with each other with a side plate over the entire bottom side of the support plates and the left top side to create a nice, closed structure. The arch shown in Figure 37 is also a plate.

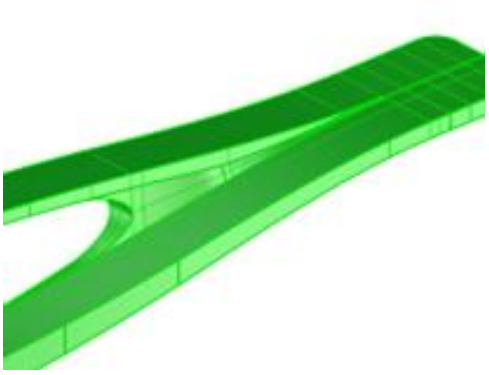

Figure 39: Connection upper and lower deck top view

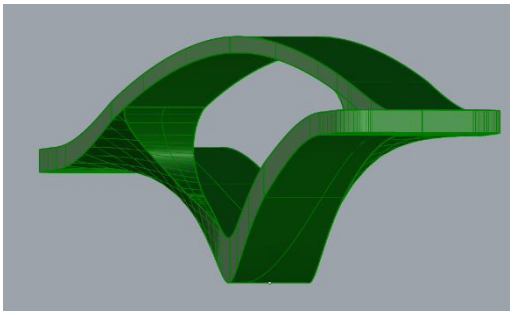

Figure 38: Connection upper and lower deck bottom view

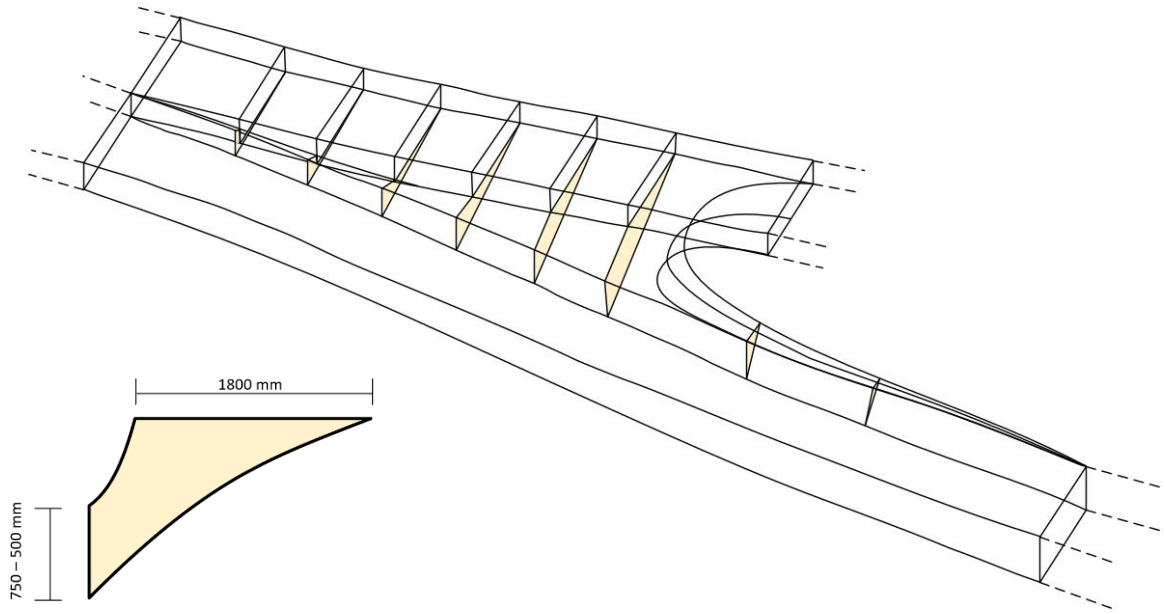

Figure 37: Structure connection upper and lower deck

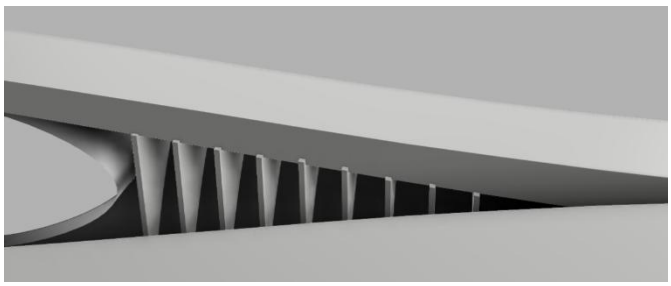

Figure 41: Side view connection upper and lower deck

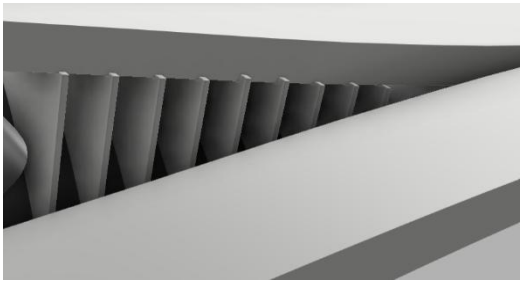

Figure 40: Connection upper and lower deck

As a first estimate of the support plates thickness, the slenderness of the plates is evaluated. The slenderness provides an indication of whether failure is governed by material strength or by elastic buckling. A slenderness value around 1.0 indicates that the material strength and the elastic buckling stress are of the same order, which is generally considered an efficient design. The slenderness of a plate is defined as:

$$\overline{\lambda_p} = \sqrt{\frac{f_{c,rk}}{\sigma_{cr,c}}}$$

Where:

$f_{c,rk}$ is the characteristic value of the compressive strength

$\sigma_{cr,c}$ is the critical elastic buckling stress

For the plate buckling assessment, the support plate is idealized as being clamped along the top-left and bottom-right edges, as illustrated in Figure 42. This idealization is based on the bonded connection between the flanges of the support plate and the adjacent side plates, which is assumed to provide sufficient rotational restraint along these edges. The critical elastic buckling stress, for a plate clamped on both sides, can be calculated with:

$$\sigma_{cr,c} = \frac{\pi^2}{tb^2}(4.35\sqrt{D_{11}D_{22}} + 2.44(D_{12} + 2D_{66}))$$

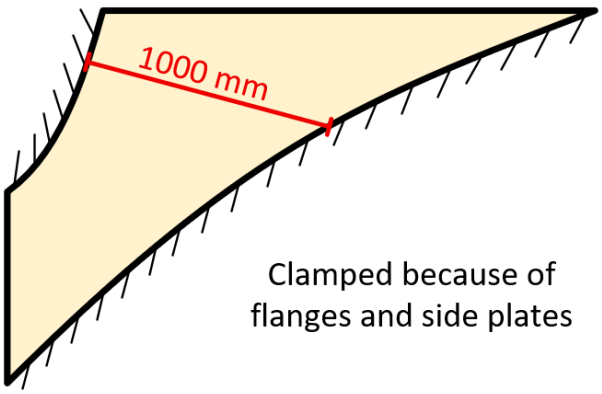

Figure 42: Schematic representation of the support plate and the assumed clamped edge conditions for the plate buckling analysis

The critical elastic buckling stress and slenderness for an orthotropic laminate plate is calculated according to CUR 96:2019.

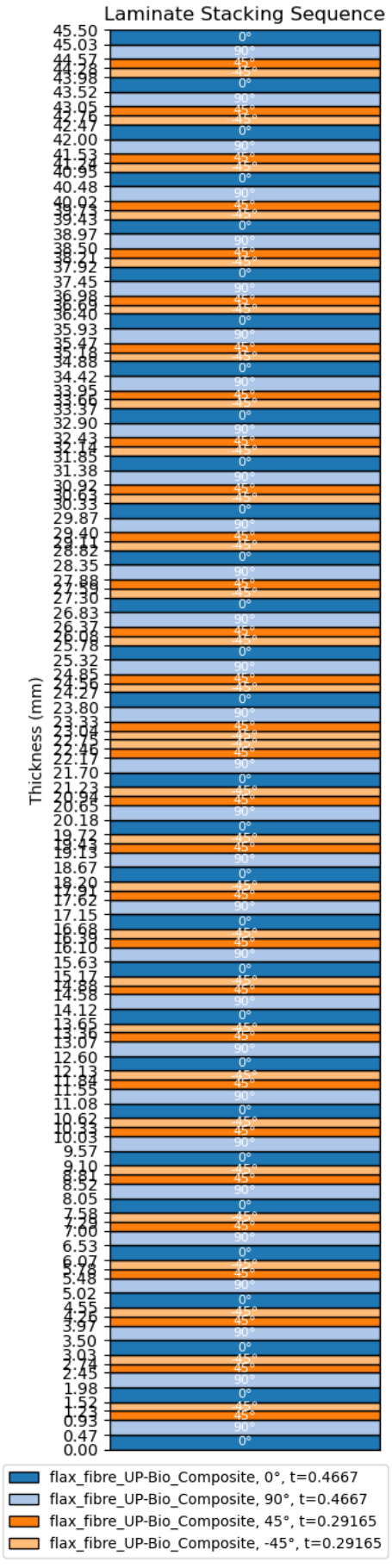

Figure 43: Stacking of the laminate for the support plates

For the support plates is the layering of the laminate shown in Figure 43 assumed, which is a well-balanced laminate. The properties shown in Table 22 are obtained from the code for the laminate stiffness, Appendix F.

The linear strain limit according to CUR 96:2019 is 1.2%, see Chapter 6.4.1. The characteristic value of the compressive strength is therefore:

$$f_{c,rk} = \varepsilon_1 * E_1 = 0.012 * 9308 = \ 111.7\ MPa$$

The bending stiffness terms of the laminate, D-matrix, are obtained from the Python code:

- $D_{11} = \ 79398235$
- $D_{22} = \ 76414149$
- $D_{12} = \ 16821369$
- $D_{66} = \ 21013653$

The parameter *b* denotes the width of the support plate. For the support plates, an average width of 1000 mm is assumed, see Figure 42. This value is adopted because the effective width of the support plates must be considered, and 1000 mm provides a representative approximation of this dimension along the varying geometry. This assumption provides a reasonable estimate for initial sizing, however buckling and stresses in the support plate should be checked in a later stage, see Chapter 9.2.1.

The critical elastic buckling stress for the laminate with a width of 1000 mm is:

$$\sigma_{cr,c} = \frac{\pi^2}{tb^2}\left(4.35\sqrt{D_{11}D_{22}} + 2.44(D_{12} + 2D_{66})\right)$$

$$\sigma_{cr,c} = \frac{\pi^2}{45.50 * 1000^2}(4.35\sqrt{79398235 * 76414149} + 2.44(16821369 + 2 * 21013653\ ))$$

$$\sigma_{cr,c} = 104.6\ MPa$$

The corresponding slenderness is:

$$\overline{\lambda_p} = \sqrt{\frac{f_{c,rk}}{\sigma_{cr,c}}} = \sqrt{\frac{177.65}{201.66}} = 0.94$$

The calculated slenderness of 0.94 indicates that the support plate is close to the transition between material failure and elastic buckling. This suggests that the chosen thickness of 45.5 mm results in a good preliminary design, where neither buckling nor material failure clearly dominates.

Property	Membrane	Bending	Unit
E_1	9.308	9.642	GPa
E_2	9.308	9.280	GPa
G_{12}	2.780	2.677	GPa
υ_{12}	0.228650	0.220098	-
υ_{21}	0.228650	0.211826	-

Table 22: Material properties composite support plates

The side plates and the plate in the arch will have the same thickness and laminate structure as the bottom plate of the deck for a preliminary design.

7.5 Stiffener plates

Between the C-shaped girders, stiffener plates will be placed at several locations in both the upper and lower decks of the structure. These plates will connect the C-shaped girders and increase the overall stiffness of the structure. The layering of the stiffener plates are shown in Figure 44 and the material properties are shown in Table 23.

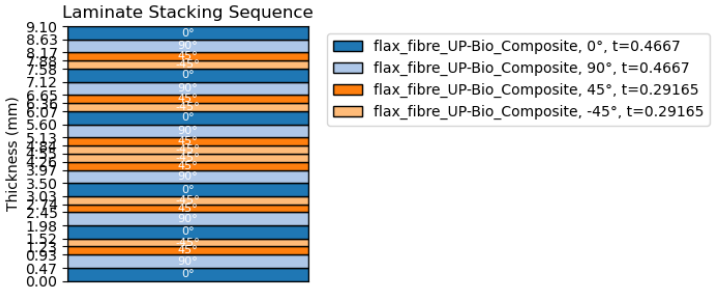

Figure 44: Stacking of the laminate for the stiffener plates

Property	Membrane	Bending	Unit
E_1	9.308	11.037	GPa
E_2	9.308	9.006	GPa
G_{12}	2.780	2.273	GPa
υ_{12}	0.228650	0.186934	-
υ_{21}	0.228650	0.152534	-

Table 23: Material properties composite stiffener plates

8. FEM model

The structural model was developed in Dlubal RFEM 6. RFEM was selected because the complex geometry of the Seasaw was already available in Rhino, which can be directly integrated with RFEM. RFEM also provides the required capabilities for static, stability and modal analyses. Furthermore, Witteveen+Bos primarily uses RFEM, allowing technical support during the study.

SCIA Engineer, DIANA and Abaqus were also considered as potential alternatives. SCIA provides similar capabilities for general structural analysis, while DIANA and Abaqus offer more advanced options for detailed and nonlinear material modelling. However, these additional capabilities are not required for this study, as the flax fibre composite is represented by an equivalent laminate stiffness based on Classical Laminate Theory (CLT). Therefore, RFEM was considered the most suitable software for the analysis.

Two models are developed in RFEM: a beam model and a plate model. These models will be compared later in this chapter. The input parameters for both models are generated using Python scripts, which are provided in Appendix H and Appendix J. A detailed explanation and validation of these scripts can be found in Appendix I and Appendix K.

For the beam model, RFEM does not allow the direct implementation of stiffness parameters such as EI_{zz}, EI_{yy}, GI_w, and EA. Instead, the software requires material properties such as E, G, ν, and geometric cross-sectional properties as input. To address this, the function *beam_model_input_RFEM* is used to convert the calculated stiffness values, obtained from the python script in Appendix F, into equivalent material and geometric properties suitable for RFEM. A comprehensive explanation and validation of this procedure are provided in Appendix I. The code was validated by comparing the maximum bending moment and deflection of a simply supported beam modelled in RFEM with hand calculations. The maximum bending moments matched the hand calculations, while the RFEM model predicted deflections 0.13% higher in the z-direction and 1.70% higher in the y-direction. The RFEM model therefore accurately reproduces the expected beam behaviour.

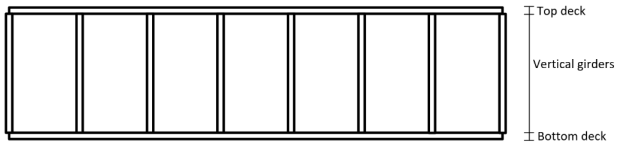

Figure 45: RFEM plate model layering

For the plate model, the cross-section is simplified into three main components: a horizontal bottom deck, vertical girders, and a horizontal top deck, see Figure 45. This approach enables an efficient representation of the structural behaviour while reducing modelling complexity. The bottom deck consists of the bottom plate combined with the lower horizontal flanges of the C-shaped girders. The vertical girders are modelled separately, retaining the material and stiffness properties of the original girders, although their height is adjusted to account for the distance between the centres of gravity of the bottom and top decks. The top deck comprises the top face, core material, bottom face, and the upper horizontal flanges of the C-shaped girders. In Figure 46 is the distribution of the top and bottom deck shown. Both the top and bottom decks are assigned an effective width, defined as the distance between the centres of gravity of the outer vertical girders. Representative stiffness and thickness values for these components are determined using dedicated Python functions. A full description of these functions, including the underlying assumptions and validation, is provided in Appendix K, with the implementation code given in Appendix J. The code was validated by comparing the maximum deflection of a simply supported plate model in RFEM with hand calculations. The model showed good agreement for bending in the *z*-direction, with a difference of 0.43%, while the difference in the *y*-direction was 8.05%. The larger difference in the *y*-direction is attributed to the bending stiffness contribution of the top and bottom decks being neglected when deriving the equivalent properties.

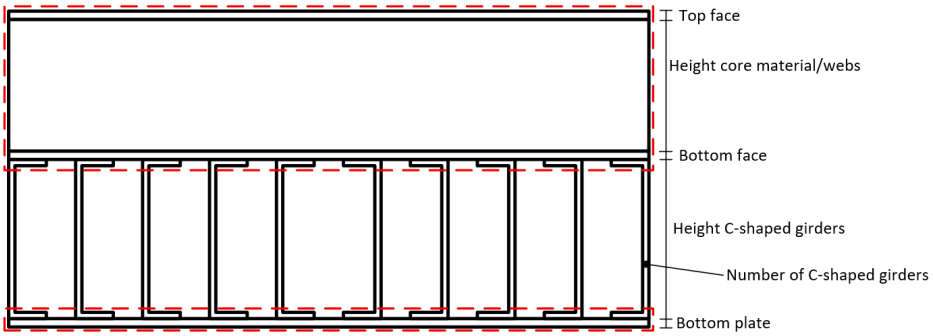

Figure 46: Distribution of the top and bottom deck

8.1 Beam model

The beam model was created by extracting several coordinates from the imported Rhino model into RFEM. The selected coordinates correspond to points located along the centreline of the deck. The cross-sections of the deck were defined by averaging the deck height within each corresponding segment. The cross-sectional geometry and corresponding properties implemented in RFEM are provided in Appendix M which are determined with the python code given in Appendix H. The RFEM model is shown in Figure 47. A detailed description of the beam model is provided in Appendix P, including the boundary conditions, applied loads, and mesh configuration.

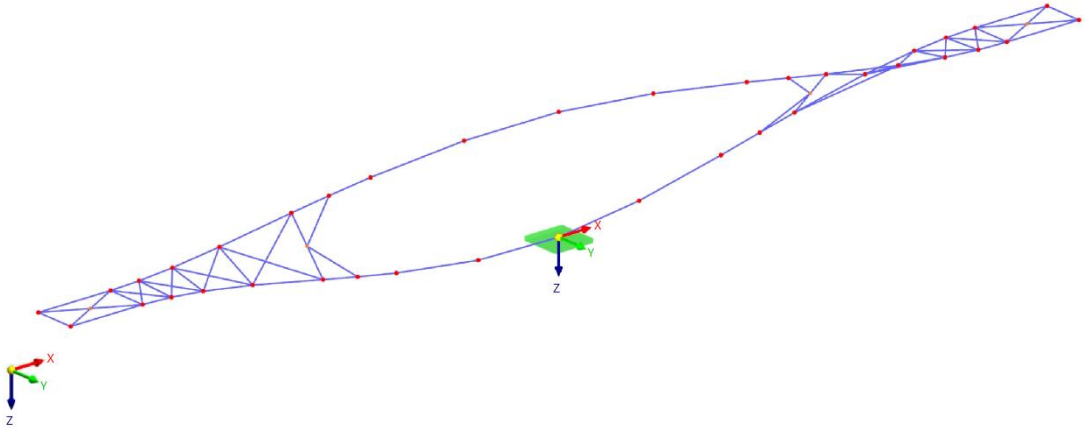

Figure 47: Beam model Seasaw

8.2 Plate model

For the plate model, the imported Rhino geometry required extensive preprocessing before it could be used in RFEM. The model was manually cleaned and repaired by removing duplicate nodes and lines, correcting geometric inconsistencies, and converting the remaining lines into polylines to create a continuous and suitable geometry for the plate model. The surfaces of the girders, bottom deck, and top deck were subsequently created using polygonal and quadrangle surfaces. The material and cross-sectional properties of the top deck, girders, and bottom deck are provided in Appendix M. Between the C-shaped girder there are stiffener plates to connect the C-shaped girders, see Figure 49. The material and cross-sectional properties of the stiffener plates are given in Appendix M and the x-coordinates of the point closest to $y = 0$ of the plates is given in Appendix N. For the connection between the upper and lower deck, support plates will be put in. These support plates are drawn in the yz-plane and are made with polygonal surfaces, see Figure 48. The x-coordinates of the support plates are given in Appendix N. The side plates are made with quadrangle surfaces and the lines from the Rhino model are used as boundaries of the plates, see Figure 48. The material and cross-sectional properties of the support plates, the bottom side plate, the top side plate, and the arch side plate are provided in Appendix M. The plate model is shown in Figure 51 and Figure 50.

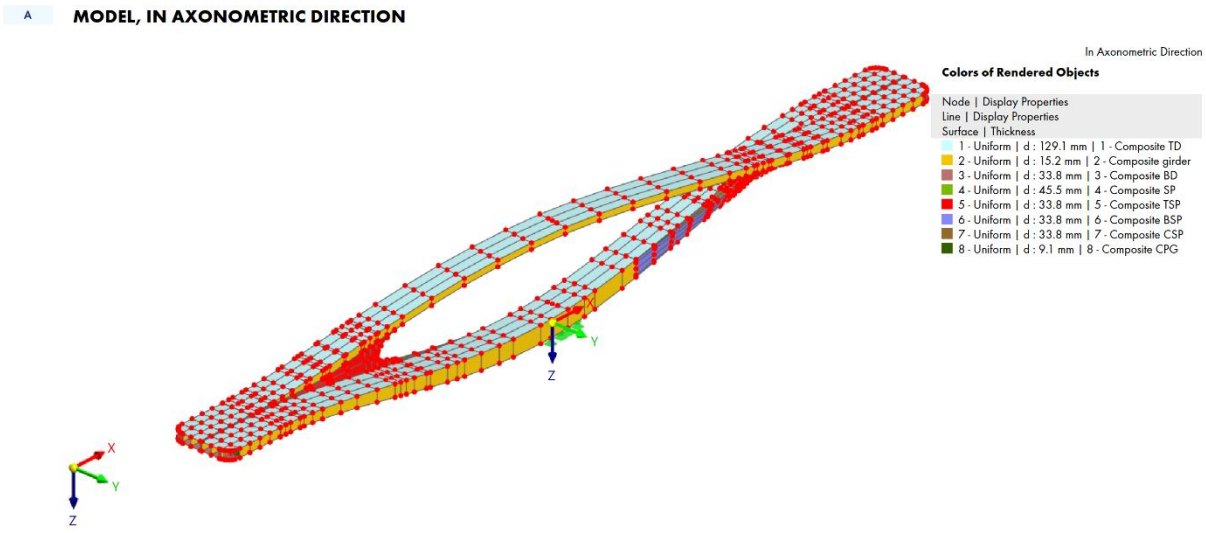

Figure 51: Plate model Seasaw

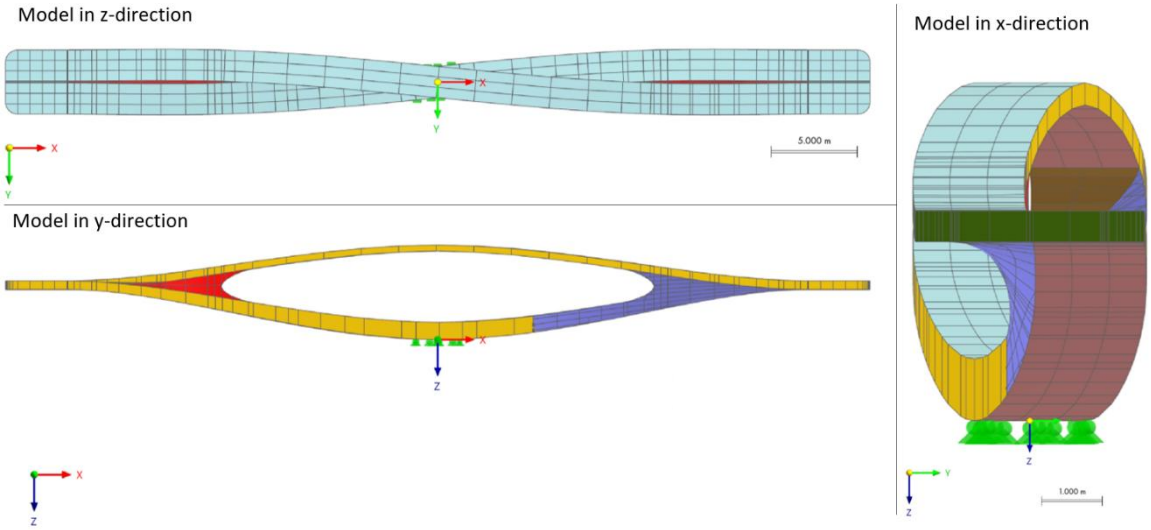

Figure 50: Plate model front, side, and top view

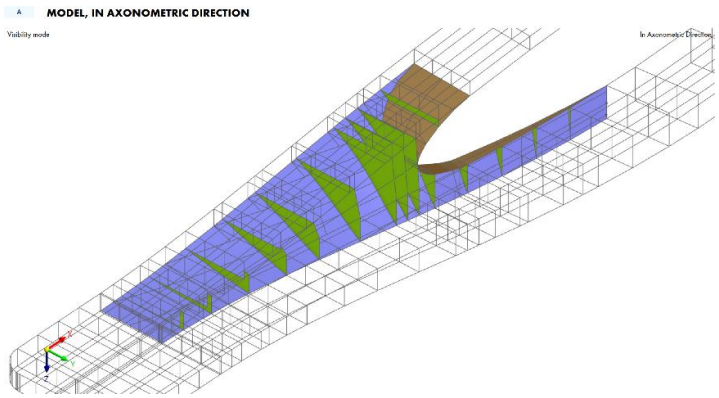

Figure 48: Plate model connection

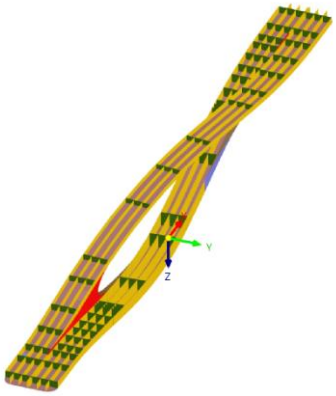

Figure 49: Plate model stiffness plates

8.2.1 Boundary conditions

At the bottom of the structure, a rectangular support region with dimensions of approximately 1.8 m by 2.7 m is present. The bottom plate of this rectangle, the surface, is fully clamped. The applied clamped boundary condition is shown in Figure 52.

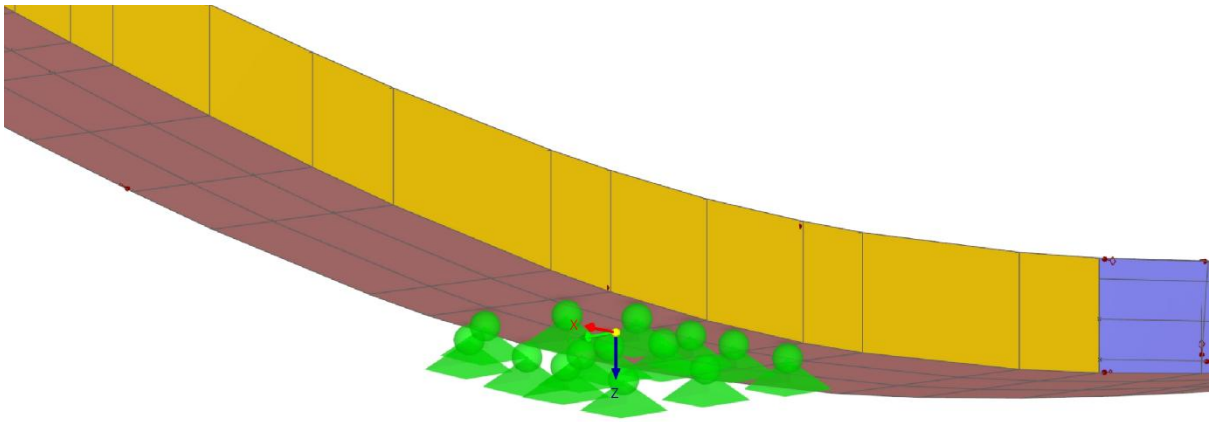

Figure 52: Plate model boundary condition

8.2.2 Loads

The load cases in RFEM are:

- Self-weight [LC1]
- Permanent loads [LC2]
- Traffic loads
  - Full deck loaded [LC3]
  - Bottom half loaded [LC14]
  - Top half loaded [LC15]
  - Loads on one side in longitudinal direction [LC16]
  - Loads on one side in transverse direction [LC17]
  - Middle top half loaded [LC18]
  - Middle bottom half loaded [LC19]
  - One side part loaded [LC20]
  - Middle top and bottom and one side part loaded [LC21]
- Pedestrian balustrade load [LC4]
- Wind load z-direction (Downward wind load) [LC5]
- Wind load moment z-direction [LC6]
- Wind load y-direction (Parallel to dike) [LC7]
- Wind load x-direction (Perpendicular to dike) [LC8]
- Wind load -y-direction (Parallel to dike) [LC9]
- Wind load -z-direction (Downward wind load) [LC10]

The load and result combinations are provided in Appendix O, including overview figures showing an overview of the different traffic load configurations. All the loads will be applied in the direction of the global coordinate system. The reason for this is that the possibility exists that not all the plates have the correct local coordinate system since this is difficult to obtain because of the many number of plates.

Self-Weight

The load in this load case is automatically computed in RFEM. RFEM uses the densities of the materials put into RFEM.

Permanent loads

Balustrade

The distributed line load of the balustrade is:

$$q_{balustrade} = 0.8\ kN/m$$

This load is applied on top of the top deck on both sides of the bridge deck in z-direction.

Wear surface

The distributed area load of the wear surface is:

$$p_{wearing} = 0.20\ kN/m^2$$

This load is applied on top of the top deck in z-direction.

Coating

The distributed area load of the coating is:

$$p_{coating} = 0.006\ kN/m^2$$

Twice this load is applied on all the plates, top deck, girders, and bottom deck, in z-direction (a plate has two side). This load is also applied on the connection between the upper and lower deck. So, the support plates and the side plates.

Bonding paste

The distributed area load of the bonding paste is:

$$p_{paste} = 0.05\ kN/m^2$$

The paste is applied at the top and bottom of the C-shaped girders. The distributed line load of the bonding paste is:

$$q_{paste} = 0.05 * 0.1 = 0.005\ kN/m$$

This load is applied at the top and bottom of the girder plates. The load is also applied on all the sides of the support plates of the connection between the upper and lower deck.

Resin absorption of the core material

The distributed area load of the resin absorption is:

$$p_{resin} = 0.005\ kN/m^2$$

This load is applied on top of the top deck in z-direction.

Traffic loads

The bridge has a length of 50 meters. The distributed traffic load is:

$$q_{fk} = 2.0 + \frac{120}{L + 30} = 2.0 + \frac{120}{50 + 30} = 3.5\left[\frac{kN}{m^2}\right]$$

This load is applied on top of the top deck in z-direction for the different configurations.

For traffic loads a horizontal force Q_{flk} should be taken into account, acting along the bridge deck axis at the pavement level. The characteristic value of the horizontal force is 10 % of the total load corresponding to the uniformly distributed load. The load is:

$$q_{fk} = 3.5 * 0.10 = 0.35\ [kN/m^2]$$

The horizontal force shall be considered as acting simultaneously with the corresponding vertical load. The load is applied on the bridge deck in x-direction in the same configurations as the distributed traffic load.

Pedestrian balustrade load

The distributed line load of pedestrians on the balustrade is:

$$q_{ped,balustrade} = 1.0\ kN/m$$

The load is applied at the top of the deck on both sides of the bridge. The vertical component acts in the z-direction, while the horizontal component acts away from the deck, directed outward from the bridge.

The distributed bending moment resulting from the horizontal balustrade load is:

$$m_{ped,balustrade} = 1 * 1.2 = 1.2\ kNm/m$$

where 1.2 m is the height of the balustrade.

This bending moment is applied along both edges of the deck at the balustrade locations. The bending moment direction is such that it causes an outward rotation of the balustrade away from the bridge deck.

Wind load in z-direction

The distributed wind load in z-direction on the bridge deck is:

$$q_{w,z} = 881.1\ [N/m] = 0.881\ [kN/m]$$

The distributed line load of the wind results in a distributed area load of:

$$q_{w,z} = \frac{0.881}{1.82} = 0.484\ [kN/m^2]$$

This load is applied in z-direction on the deck surface. The load is also applied in z-direction on the top side plate on the projected area.

Wind load moment z-direction

The distributed wind load in z-direction on the bridge deck is:

$$q_{w,z} = 881.1\ [N/m] = 0.881\ [kN/m]$$

The load has an eccentricity of $e = 450\ [mm]$. This eccentricity results in a bending moment of:

$$m_{w,x} = 0.881 * 0.450 = 0.40\ kNm/m$$

This bending moment will be applied on the deck surface by a distributed load in z-direction ranging from a value to another. To determine this value a load ranging from 1 to -1 is set on the structure. This gives a resultant load of 83.09 kNm about the x-axis. The total bending moment because of the wind of the structure is:

$$M_{w,x} = m_{w,x} * l = 0.40 * 50 = 20\ kNm$$

This means that the value 1 should be rescaled by a factor of:

$$\frac{20}{83.09} = 0.24$$

The bending moment determined before is applied on the deck surface by a distributed load ranging from -0.24 to 0.24 in y-direction, see Figure 53.

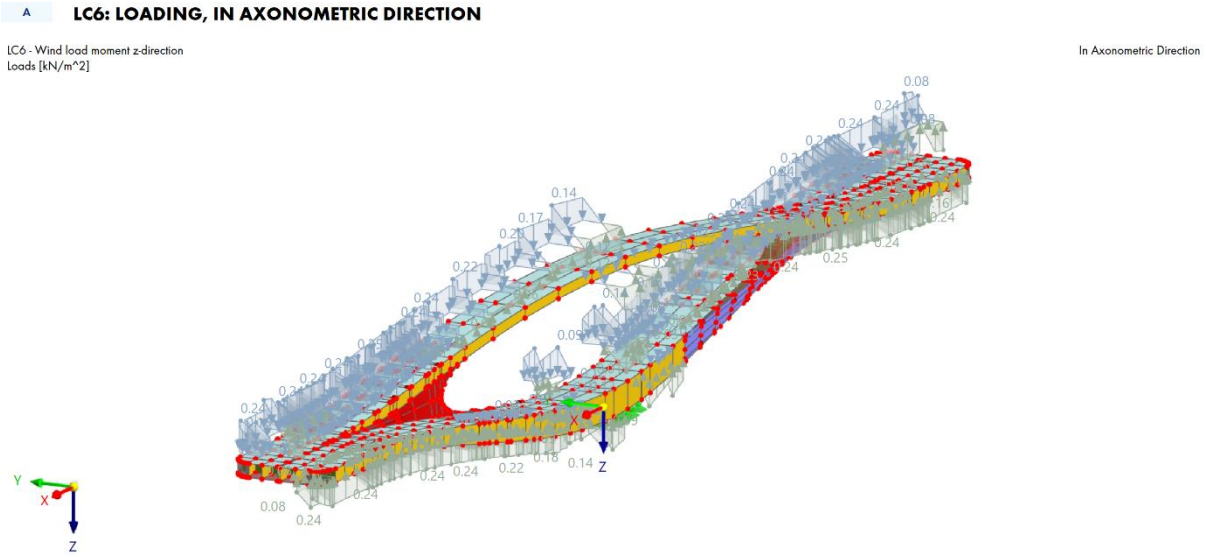

Figure 53: Bending moment wind load z-direction plate model

Wind load in y-direction

The distributed wind load in y-direction on the bridge deck is:

$$q_{w,y} = 2855.5 * d_{tot}\ [N/m] = 2.86 * d_{tot}\ [kN/m]$$

With $d_{tot} = 0.6 + d$

This results in:

$$q_{w,y} = 2.86 * (0.6 + d) = 1.716 + 2.86 * d\ [kN/m]$$

In the formula for d_{tot} correspond the 0.6 to the wind load because of the balustrade. This part of the load, 1.716 kN/m, will be applied on the top edge of the deck in positive y-direction. A load of $2.86\ [kN/m^2]$ will be applied on the negative side of the bridge in positive y-direction. The load will be applied on the girders which are not covered by the side plates of the connection, one side of the structure on the top side plate and on the other on the bottom side plate on the projected area. The height of the girders in not the real height of the bridge deck but is the height between the centre of gravity of the top deck and bottom deck. At the top of the bridge deck there is an additional height of 67.1 mm and at the bottom an additional height of 18.3 mm, obtained from the python code for the plate model. At the top of the girders there will be a distributed line load applied of $2.86 * 0.0671 = 0.2\ kN/m$ and at the bottom a load of $2.86 * 0.0183 = 0.05\ kN/m$.

Wind load in x-direction

The distributed wind load in y-direction on the bridge deck is:

$$q_{w,x} = 0.4 * q_{w,y} = 1142.2 * d_{tot}\ [N/m] = 1.14 * d_{tot}\ [kN/m]$$

With $d_{tot} = 0.6 + d$

This results in:

$$q_{w,x} = 1.14 * (0.6 + d) = 0.684 + 1.14 * d\ [kN/m]$$

In the formula for d_{tot} correspond the 0.6 to the wind load because of the balustrade. This part of the load, 0.684 kN/m, will be applied on the top edges, left and right side, of the deck in positive x-direction. Because there are two sides and the load in x-direction is 0.4 times the load in y-direction, the distributed load on the edges will be:

$$\frac{0.684}{2} = 0.342\ kN/m$$

The value for d changes over the structure. The same height distribution as the beam model will be used for the plate model, see Figure 55. The corresponding x-coordinates are shown in Figure 54.

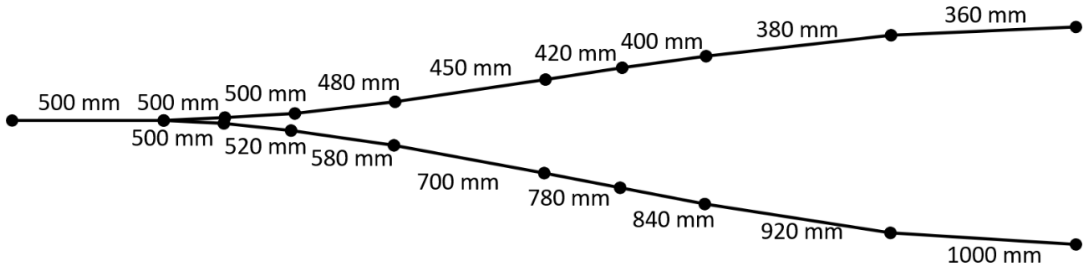

Figure 55: Height cross-section of half of the Seasaw

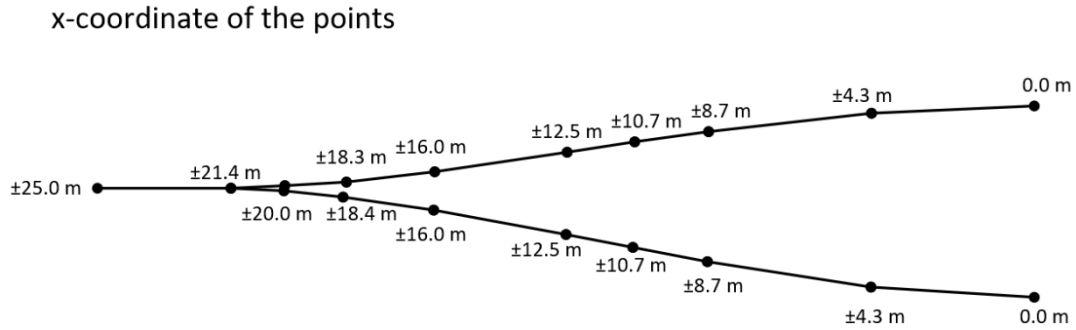

Figure 54: x-coordinates of the schematic representation of half of the Seasaw

The load is for each part of the structure different. The loads for the different parts are:

- $h = 1000\ mm$: $d = 1092.07\ [mm]$, $q_{w,x} = 1.14 * \frac{1.092}{1.82} = 0.684\ [kN/m^2]$
- $h = 920\ mm$: $d = 1012.07\ [mm]$, $q_{w,x} = 1.14 * \frac{1.012}{1.82} = 0.634\ [kN/m^2]$
- $h = 840\ mm$: $d = 932.07\ [mm]$, $q_{w,x} = 1.14 * \frac{0.932}{1.82} = 0.584\ [kN/m^2]$
- $h = 780\ mm$: $d = 872.07\ [mm]$, $q_{w,x} = 1.14 * \frac{0.872}{1.82} = 0.546\ [kN/m^2]$
- $h = 700\ mm$: $d = 792.07\ [mm]$, $q_{w,x} = 1.14 * \frac{0.792}{1.82} = 0.496\ [kN/m^2]$
- $h = 580\ mm$: $d = 672.07\ [mm]$, $q_{w,x} = 1.14 * \frac{0.672}{1.82} = 0.421\ [kN/m^2]$
- $h = 520\ mm$: $d = 612.07\ [mm]$, $q_{w,x} = 1.14 * \frac{0.612}{1.82} = 0.383\ [kN/m^2]$
- $h = 500\ mm$: $d = 592.07\ [mm]$, $q_{w,x} = 1.14 * \frac{0.592}{1.82} = 0.371\ [kN/m^2]$
- $h = 480\ mm$: $d = 572.07\ [mm]$, $q_{w,x} = 1.14 * \frac{0.572}{1.82} = 0.358\ [kN/m^2]$
- $h = 450\ mm$: $d = 542.07\ [mm]$, $q_{w,x} = 1.14 * \frac{0.542}{1.82} = 0.339\ [kN/m^2]$
- $h = 420\ mm$: $d = 512.07\ [mm]$, $q_{w,x} = 1.14 * \frac{0.512}{1.82} = 0.321\ [kN/m^2]$
- $h = 400\ mm$: $d = 492.07\ [mm]$, $q_{w,x} = 1.14 * \frac{0.492}{1.82} = 0.308\ [kN/m^2]$
- $h = 380\ mm$: $d = 472.07\ [mm]$, $q_{w,x} = 1.14 * \frac{0.472}{1.82} = 0.296\ [kN/m^2]$
- $h = 360\ mm$: $d = 452.07\ [mm]$, $q_{w,x} = 1.14 * \frac{0.452}{1.82} = 0.283\ [kN/m^2]$

These loads are applied on their corresponding parts in positive x-direction.

Wind load -y-direction

The distributed wind load in y-direction on the bridge deck is:

$$q_{w,y} = 2855.5 * d_{tot}\ [N/m] = 2.86 * d_{tot}\ [kN/m]$$

With $d_{tot} = 0.6 + d$

This results in:

$$q_{w,y} = 2.86 * (0.6 + d) = 1.716 + 2.86 * d\ [kN/m]$$

In the formula for d_{tot} correspond the 0.6 to the wind load because of the balustrade. This part of the load, 1.716 kN/m, will be applied on the top edge of the deck in negative y-direction. A load of $2.86\ [kN/m^2]$ will be applied on the positive side of the bridge in negative y-direction. The load will be applied on the girders which are not covered by the side plates of the connection, one side of the structure on the top side plate and on the other on the bottom side plate on the projected area. The height of the girders in not the real height of the bridge deck but is the height between the centre of gravity of the top deck and bottom deck. At the top of the bridge deck there is an additional height of 70.3 mm and at the bottom an additional height of 20.3 mm, obtained from the python code for the plate model. At the top of the girders there will be a distributed line load applied of $2.86 * 0.0703 = 0.2\ kN/m$ and at the bottom a load of $2.86 * 0.0203 = 0.06\ kN/m$.

Wind load -z-direction

The distributed wind load in z-direction on the bridge deck is:

$$q_{w,z} = 881.1\ [N/m] = 0.881\ [kN/m]$$

The distributed line load of the wind results in a distributed area load of:

$$q_{w,z} = \frac{0.881}{1.82} = 0.484\ [kN/m^2]$$

This load is applied in -z-direction on the deck surface on true area and on the bottom side plate on projected area.

8.2.3 Mesh

A mesh size of 0.100 m was selected, since the smallest vertical girder has a height of 360 mm, resulting in approximately four elements over the girder height. Furthermore, halving the mesh size did not lead to significant changes in the calculated deformations. For the smaller surfaces in the model, local mesh refinement was applied to ensure that at least 3–4 elements were present across the width or length of the plates. For the finite elements, triangular and quadrilateral elements are selected. Figure 56 shows the plate model together with the mesh, providing an impression of the mesh distribution. A mesh sensitivity study is performed in Appendix Q.

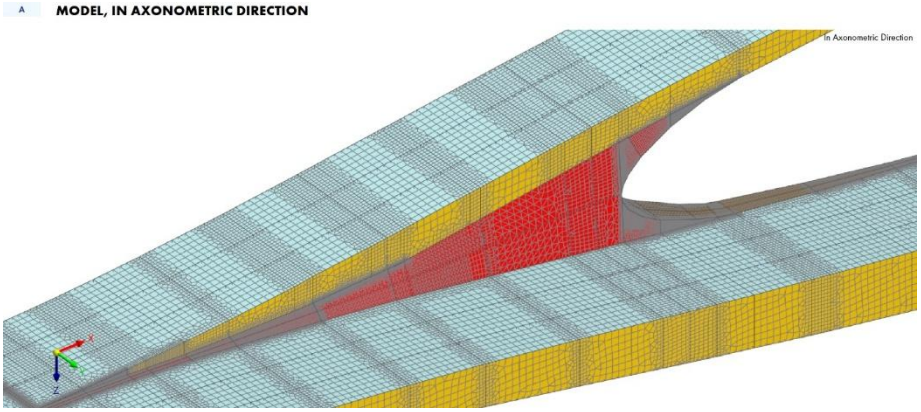

Figure 56: Mesh plate model

8.2.4 Validation of the plate model

When only the self-weight is applied, the plate model deforms as expected, see Figure 57. The upper half of the structure shows a larger deformation than the deformation at x = +/- 12.5. Similarly, the side parts of the structure exhibit greater deformation than the deformation at x = +/- 12. The deformation pattern is symmetric, which is consistent with the geometry and loading of the structure. Furthermore, no deformation occurs at the supports, as expected.

The reaction forces confirm that the model is in equilibrium. The sum of the applied loads equals the sum of the support reactions in all directions, see Table 24. In addition, the resultant reaction moments are effectively zero, with only a negligible residual reaction moment in the z-direction due to numerical rounding. This is consistent with the symmetric geometry and loading conditions.

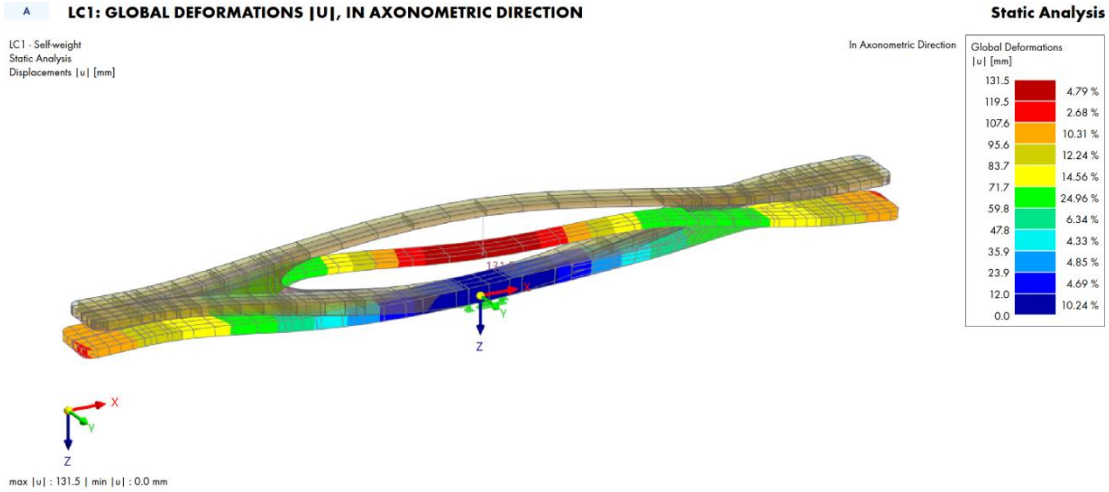

Figure 57: Deformation because of self-weight

	X	Y	Z
Sum of loads in	0.00 kN	0.00 kN	332.82 kN
Sum of support forces	0.00 kN	0.00 kN	332.82 kN
Resultant of reactions about	0.00 kNm	0.00 kNm	-0.03 kNm

Table 24: Reaction forces self-weight and loading

The deformation of the structure under wind loading in the positive x-direction is shown in Figure 58. Due to the curvature of the structure, it is expected that one side of the structure moves upward while the opposite side moves downward, resulting in a seesaw deformation. The model exhibits this behaviour, indicating that the structural response is realistic.

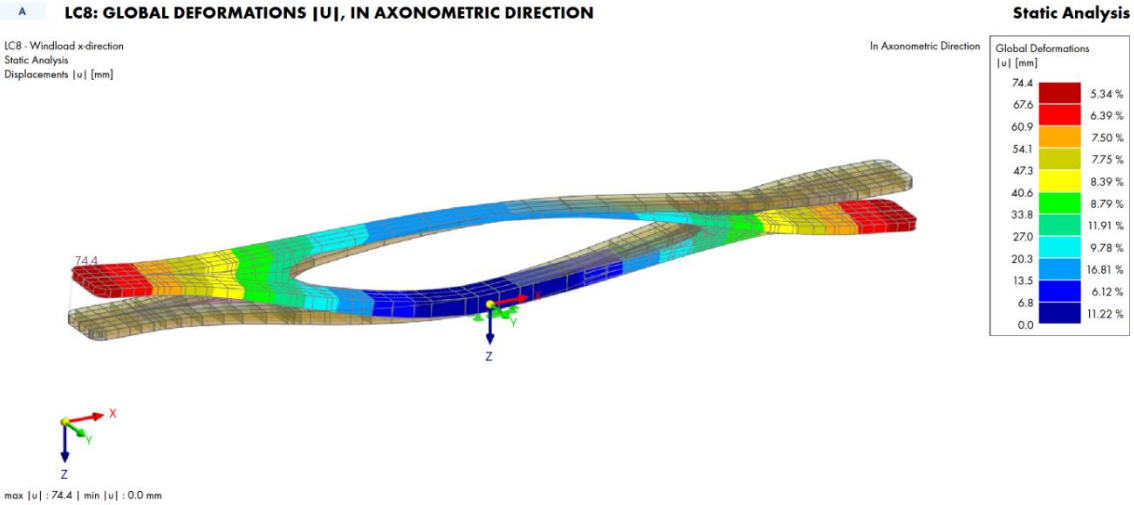

Figure 58: Deformation because of wind load in x-direction

The reaction forces also confirm equilibrium for this load case. The total applied wind load equals the total support reactions in the x-direction, see Table 25. A small resultant reaction moment about the y-axis is present, which is consistent with the observed deformation pattern and the structural geometry. Because the supports are located at the bottom of the structure while the upper part extends above them, the resultant wind load does not act through the support but with an eccentricity, generating a reaction moment about the y-axis.

	X	**Y**	**Z**
Sum of loads in	143.59 kN	0.00 kN	0.00 kN
Sum of support forces	143.59 kN	0.00 kN	0.00 kN
Resultant of reactions about	0.00 kNm	-19.82 kNm	0.00 kNm

Table 25: Reaction forces wind load in x-direction and loading

8.3 Comparison plate and beam model

The plate and beam models are compared on deflection and loads. The comparison between the loads on the beam and plate models shows that, after several modifications to the beam model, the applied loads and resultant reactions are generally in good agreement. Small remaining differences are mainly caused by the simplified representation of the geometry in the beam model, whereas the plate model explicitly includes the structural components and applies the loads at their actual locations. A detailed overview of the comparison is included in Appendix R.

8.3.1 Deflection comparison

On both the models will the same loads be applied in x-direction, y-direction, and z-direction in separate load cases. After the global deformations, $|u|, u_x, u_y \; and \; u_z$, will be compared in the middle and on both sides of the structure.

Load in z-direction

In the plate model, a distributed load of 1 kN/m² in z-direction is applied to the top deck, resulting in a total load in the z-direction of 181.61 kN. In the beam model, a distributed load of 1.8 kN/m is applied to all deck beams, yielding a total load in the z-direction of 181.57 kN. Thus, the total applied loads in both models are nearly identical. Table 26 presents the resulting deformations, while Table 27 shows the percentage differences between the beam and plate models, expressed relative to the plate model deformations. The $|u|$ are plotted for the plate model in Figure 60 and for the beam model in Figure 59.

	$\|u\|\ [mm]$		$u_x\ [mm]$		$u_y\ [mm]$		$u_z\ [mm]$	
	Beam	Plate	Beam	Plate	Beam	Plate	Beam	Plate
-x, -y side	42.4	57.8	-1.0	-3.1	-25.1	-21.7	34.1	53.5
-x, +y side	41.0	60.8	-3.6	-8.4	-25.1	-21.7	32.2	56.2
middle	41.0	75.3	0	0	0	0	41.0	75.3
+x, -y side	41.0	60.8	3.6	8.4	25.1	21.7	32.2	56.2
+x, +y side	42.4	57.8	1.0	3.1	25.1	21.7	34.1	53.5

Table 26: Deformation because of load in z-direction

	$(\lvert u_{beam} \rvert - \lvert u_{plate} \rvert) / \lvert u_{plate} \rvert$ [%]	$(u_{x,beam} - u_{x,plate}) / u_{x,plate}$ [%]	$(u_{y,beam} - u_{y,plate}) / u_{y,plate}$ [%]	$(u_{z,beam} - u_{z,plate}) / u_{z,plate}$ [%]
-x, -y side	-26.6	-67.7	15.7	-36.3
-x, +y side	-32.6	-57.1	15.7	-42.7
middle	-45.6	0.0	0.0	-45.6
+x, -y side	-32.6	-57.1	15.7	-42.7
+x, +y side	-26.6	-67.7	15.7	-36.3

Table 27: Percentual difference deformation with respect to the plate deformation because of load in z-direction

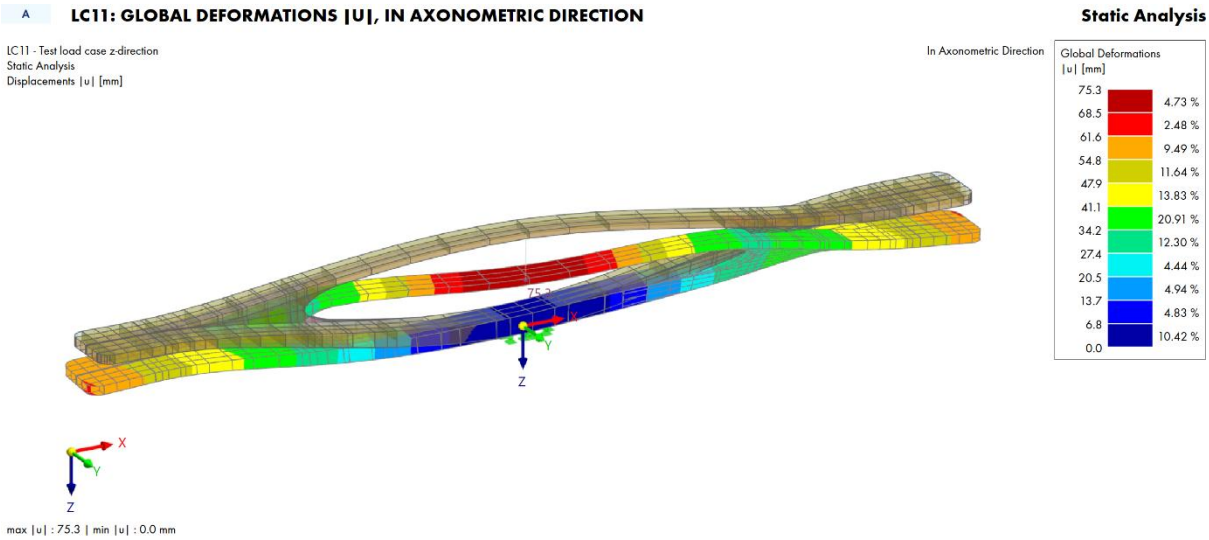

Figure 60: Deformation plate model load z-direction

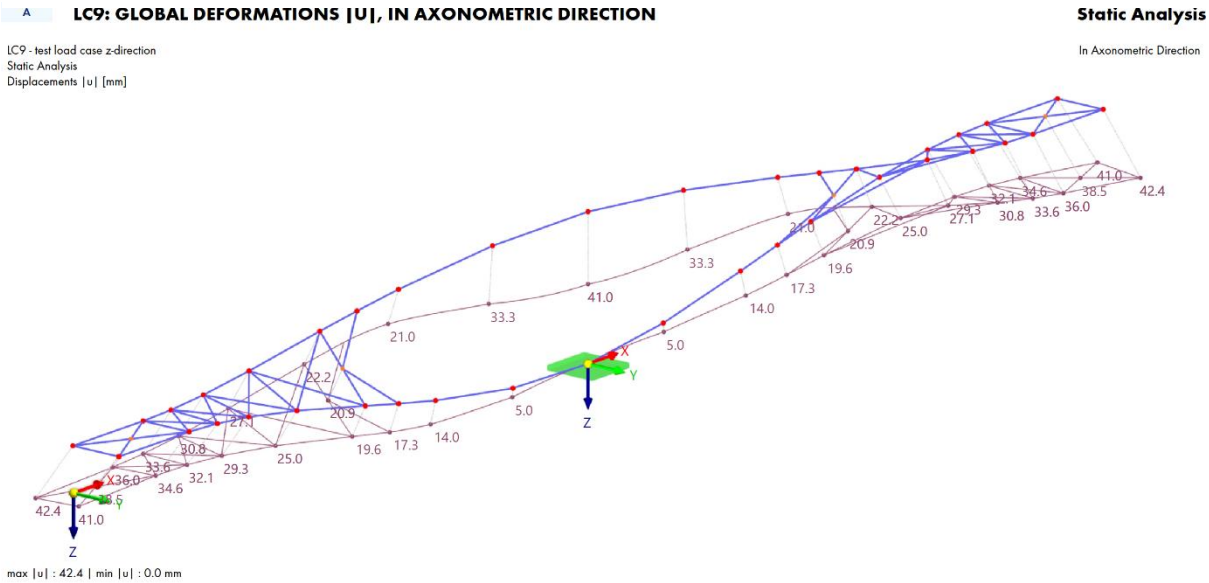

Figure 59: Deformation beam model load z-direction

The results indicate that the plate model exhibits significantly larger deformations in the middle than the beam model. The difference in deformation for the sides is less. This difference can be attributed to the modelling of the connection between the top half and bottom half of the structure. In the beam model, this connection is represented as excessively stiff, whereas in the plate model it is less stiff, resulting in a greater overall deformation.

Both models show symmetric deformation patterns, which is consistent with the symmetric geometry and loading conditions. The percentage differences in the x-direction are relatively large, suggesting that the support or connection of the beam model restrict in-plane deformation more strongly than the plate model. In the y-direction, the deformation changes sign across the structure, as expected from symmetry. However, the beam model generally predicts slightly larger magnitudes than the plate model. Finally, the differences in total displacement $|u|$ closely follow those in u_z, indicating that the discrepancy is primarily governed by vertical deformation. This is consistent with the applied loading in the z-direction, which produces the largest displacement component in that direction.

Load in y-direction

In the plate model, a distributed load of 1 kN/m² in y-direction is applied to the side girder, resulting in a total load in the y-direction of 57.94 kN. In the beam model, different distributed loads are applied to each element due to the variation in height along the structure, see Figure 61 for the loads. This results in a total load in the y-direction of 59.40 kN. The total applied loads in both models are therefore comparable, although the beam model has a slightly higher total load. Table 28 presents the resulting deformations, while Table 29 shows the percentage differences between the beam and plate models, expressed relative to the plate model deformations. The $|u|$ are plotted for the plate model in Figure 63 and for the beam model in Figure 62.

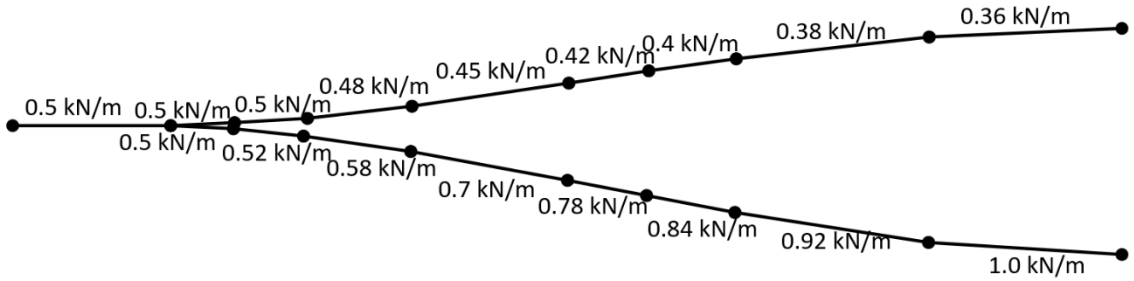

Figure 61: Loads in y-direction beam model

	$\|u\|$ $[mm]$		u_x $[mm]$		u_y $[mm]$		u_z $[mm]$	
	Beam	Plate	Beam	Plate	Beam	Plate	Beam	Plate
-x, -y side	38.3	34.2	-1.0	-2.3	37.0	32.9	-10.0	-9.0
-x, +y side	37.1	33.1	1.5	2.0	37.0	32.9	-3.4	2.7
middle	19.3	19.5	0.2	-0.6	19.3	19.5	0	0
+x, -y side	37.1	33.1	1.5	2.0	37.0	32.9	3.4	-2.7
+x, +y side	38.2	34.2	-1.0	-2.3	37.0	32.9	10.0	9.0

Table 28: Deformation because of load in y-direction

	$(\|u_{beam}\| - \|u_{plate}\|) / \|u_{plate}\|$ [%]	$(u_{x,beam} - u_{x,plate}) / u_{x,plate}$ [%]	$(u_{y,beam} - u_{y,plate}) / u_{y,plate}$ [%]	$(u_{z,beam} - u_{z,plate}) / u_{z,plate}$ [%]
-x, -y side	12.0	-56.5	12.5	11.1
-x, +y side	12.1	-25.0	12.5	-225.9
middle	-1.0	-133.3	-1.0	0.0
+x, -y side	12.1	-25.0	12.5	-225.9
+x, +y side	11.7	-56.5	12.5	11.1

Table 29: Percentual difference deformation with respect to the plate deformation because of load in y-direction

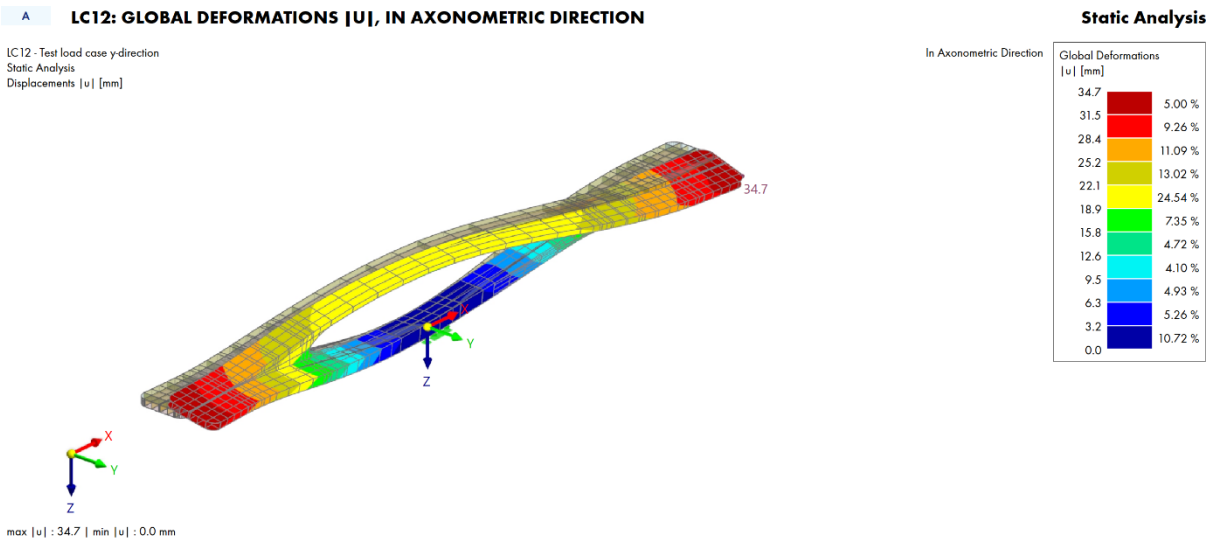

Figure 63: Deformation plate model load y-direction

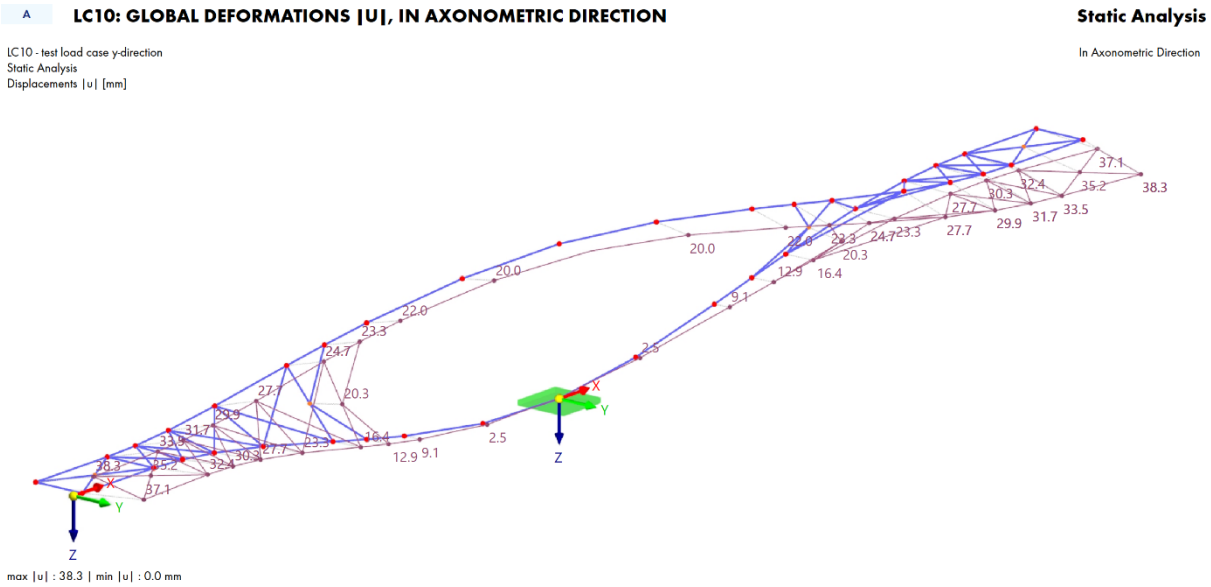

Figure 62: Deformation beam model load y-direction

The results show that the differences between the two models are smaller than those observed for loading in the z-direction, although the beam model generally predicts somewhat larger deformations than the plate model. The total displacements $|u|$ differ only slightly at the middle, although a larger deviation is observed at outer points. The response is dominated by deformation in the y-direction, which is consistent with the applied loading. The beam model generally predicts slightly bigger u_y values than the plate model, because of the bigger load. In the x-direction, the percentage differences are relatively large, despite the small absolute values. This suggests, as observed for loading in z-direction, that the support or connection of the beam model restrict in-plane deformation more strongly than the plate model. The deformation patterns in the z-direction differ between the two models. In the beam model, a sign change occurs between the $-x$ and $+x$ side, whereas in the plate model, the sign change occurs between the $-y$ and $+y$ side. This discrepancy is likely related to the modelling of the connection between the top half and bottom half of the structure.

Load in x-direction

In the plate model, a distributed load of 1 kN/m² is applied to the top deck, resulting in a total load in the x-direction of 181.61 kN. In the beam model, a distributed load of 1.8 kN/m is applied to all deck beams, yielding a total load in the x-direction of 181.57 kN. Thus, the total applied loads in both models are nearly identical. Table 30 presents the resulting deformations, while Table 31 shows the percentage differences between the beam and plate models, expressed relative to the plate model deformations. The $|u|$ are plotted for the plate model in Figure 64 and for the beam model in Figure 65.

	$\|u\|$ $[mm]$		u_x $[mm]$		u_y $[mm]$		u_z $[mm]$	
	Beam	Plate	Beam	Plate	Beam	Plate	Beam	Plate
-x, -y side	71.8	99.4	9.3	13.9	-3.6	-4.1	-71.1	-98.3
-x, +y side	68.9	96.3	8.5	12.5	-3.6	-4.1	-68.2	-95.4
middle	17.3	21.7	15.5	21.4	7.8	3.6	0	0
+x, -y side	68.9	96.3	8.5	12.5	-3.6	-4.1	68.2	95.4
+x, +y side	71.8	99.4	9.3	13.9	-3.6	-4.1	71.1	98.3

Table 30: Deformation because of load in x-direction

	$(\|u_{bar}\| - \|u_{plate}\|)/\|u_{plate}\|$ [%]	$(u_{x,bar} - u_{x,plate})/u_{x,plate}$ [%]	$(u_{y,bar} - u_{y,plate})/u_{y,plate}$ [%]	$(u_{z,bar} - u_{z,plate})/u_{z,plate}$ [%]
-x, -y side	-27.8	-33.1	-12.2	-27.7
-x, +y side	-28.5	-32.0	-12.2	-28.5
middle	-20.3	-27.6	116.7	0.0
+x, -y side	-28.5	-32.0	-12.2	-28.5
+x, +y side	-27.8	-33.1	-12.2	-27.7

Table 31: Percentual difference deformation with respect to the plate deformation because of load in x-direction

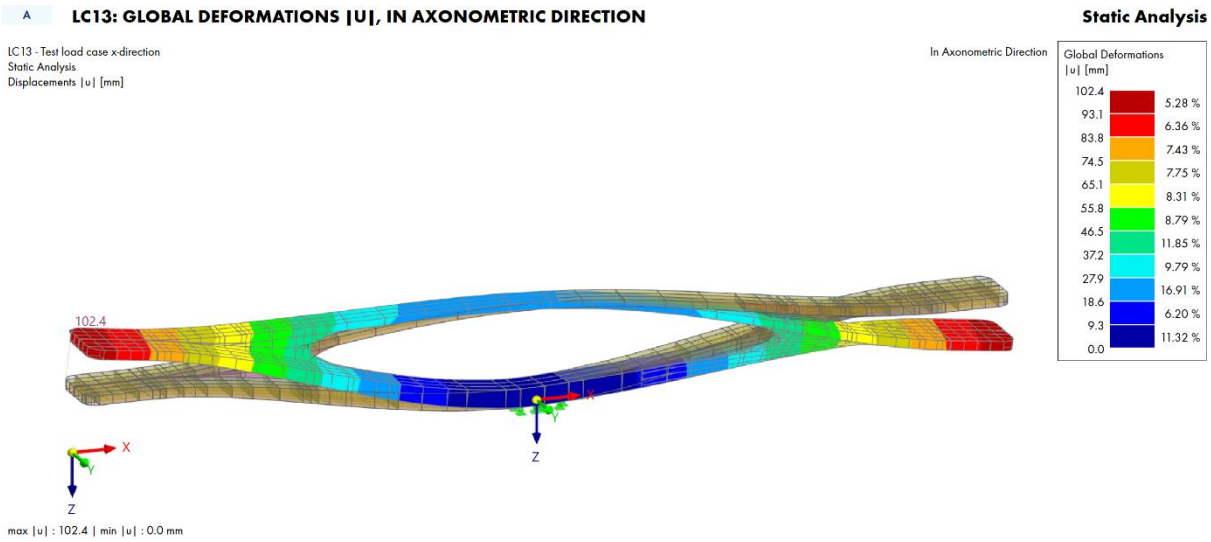

Figure 64: Deformation plate model load x-direction

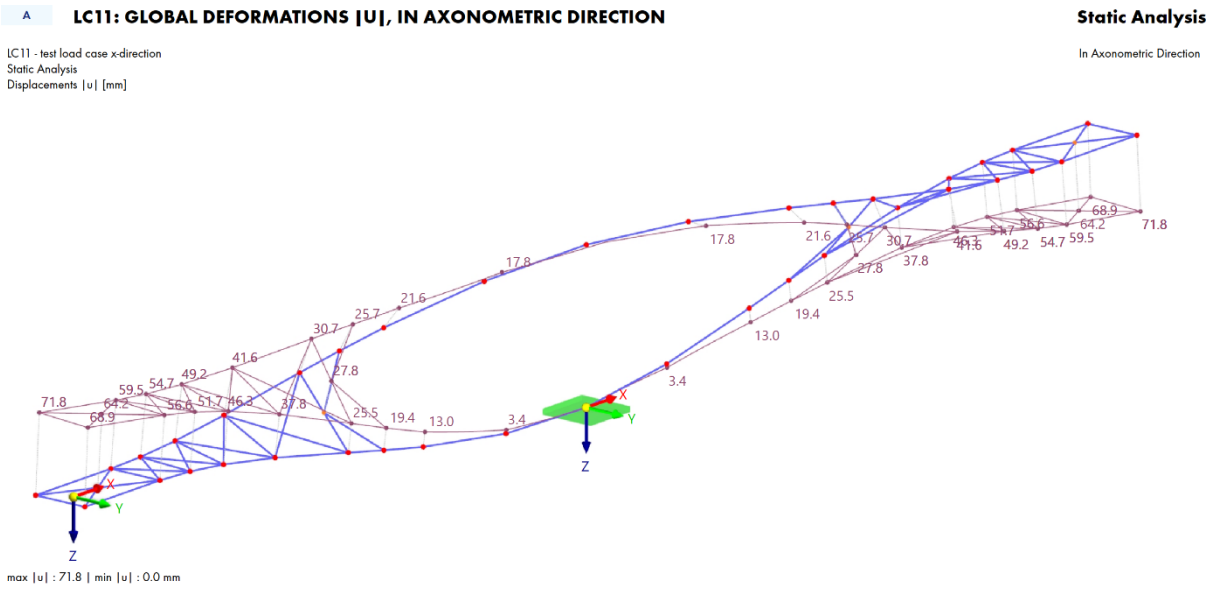

Figure 65: Deformation beam model load x-direction

The results indicate that the plate model exhibits consistently larger deformations than the beam model, although the differences are smaller than those observed for loading in the z-direction. The response is dominated by deformation in the z-direction, as the structure behaves similarly to a seesaw due to the fact that it is only clamped at the bottom. The beam model generally predicts smaller u_x values, indicating a stiffer structural response. In the y-direction, the deformations are relatively small, but the percentage differences are still notable. At midspan, a large percentage difference is observed due to the small magnitude of the plate model deformation, making the relative difference sensitive. The deformation pattern in the z-direction is symmetric, with opposite signs on the $-x$ and $+x$ sides, reflecting the rotation around the support in the bottom middle deck. The beam model again shows smaller magnitudes, suggesting that the support or connection of the beam model restrict in-plane deformation more strongly than the plate model. Overall, both models exhibit symmetric deformation patterns, consistent with the geometry and loading conditions, while the beam model consistently underestimates deformation due to its stiffer representation of structural behaviour.

8.3.2 Conclusion

The plate model predicts larger deformations for loading in the z- and x-directions, indicating a stiffer response of the beam model. For y-direction loading, the plate model predicts slightly smaller deformations, partly due to the 2.5% higher loading in the beam model and potentially differences in torsional stiffness. Overall, the beam model tends to underestimate displacements, particularly in the x- and z-directions. Both models show symmetric deformation patterns consistent with the geometry and loading, confirming the numerical consistency of the results.

The beam model is not suitable for detailed ULS, SLS, stability, or modal analyses because its simplified representation of the connections does not accurately capture the structural stiffness and load transfer. The plate model provides a more realistic representation of the structural behaviour and is therefore adopted for all subsequent analyses.

9. Static analysis

A static analysis was performed in RFEM to evaluate both the Ultimate Limit State (ULS) and the Serviceability Limit State (SLS) of the different versions of the Seasaw.

For the ULS assessment, an additional result combination was created that evaluates all ULS load combinations and automatically selects the combination resulting in the highest stresses in the structure. For the SLS assessment, the load combinations were defined to determine the deflections w_1, w_2(without creep factor), and w_3 for the characteristic, frequent, and quasi-permanent serviceability limit states. The deflections of the Seasaw are evaluated relative to other points in the structure. The relevant span lengths and allowable deflection limits are presented in Chapter 5.2.5.

This chapter presents the static analysis as an iterative design process. First, the preliminary design is evaluated for the ULS and SLS in Chapter 9.1. Based on the results, design modifications are introduced in Chapter 9.1.3. Finally, the revised design is assessed for the ULS and SLS in Chapter 9.2.

9.1 Preliminary model

9.1.1 Ultimate limit state

All structural components of the Seasaw were assessed for strength. The design strength of the laminate plates, obtained from Chapter 6.4, is calculated as:

$$R_d = \frac{\eta_c * R_k}{\gamma_M}$$

A partial material factors of 1.38 will be used, obtained from Table 14. The total conversion factor is determined as:

$$\eta_c = \eta_{ct} * \eta_{cm} * \eta_{cv} * \eta_{cf}$$

$$\eta_c = 0.9 * 0.9 * 1.0 * 1.0 = 0.81$$

To verify that the stresses remain below the allowable design stresses, the stress distributions for σ_x, σ_y, and τ_{xy}were evaluated for each component. Both the overall stress levels and local stress concentrations were examined. Non-continuous results are used because they respect the natural discontinuity of finite element surface models. In RFEM, stresses are evaluated per surface and are not artificially forced to be continuous across mesh or surface boundaries. This is important in ULS assessment because real structural behaviour includes abrupt changes in internal forces. By avoiding cross-surface averaging, this result type prevents smoothing effects that could mask local peak stresses and ensures a more realistic representation of governing design zones. Some high peak stresses occur at locations where stress singularities are present. These singularities arise from idealisations in the numerical model, such as concentrated loads, supports, sharp geometric transitions, or connections between structural components. At these locations, the calculated stresses can become unrealistically high and may increase with mesh refinement. An example of a singularity is shown in Figure 66. These local peak stresses are not considered representative of the actual structural behaviour and are disregarded in the unity check assessment. An overview of the identified singularities is provided in Appendix S.

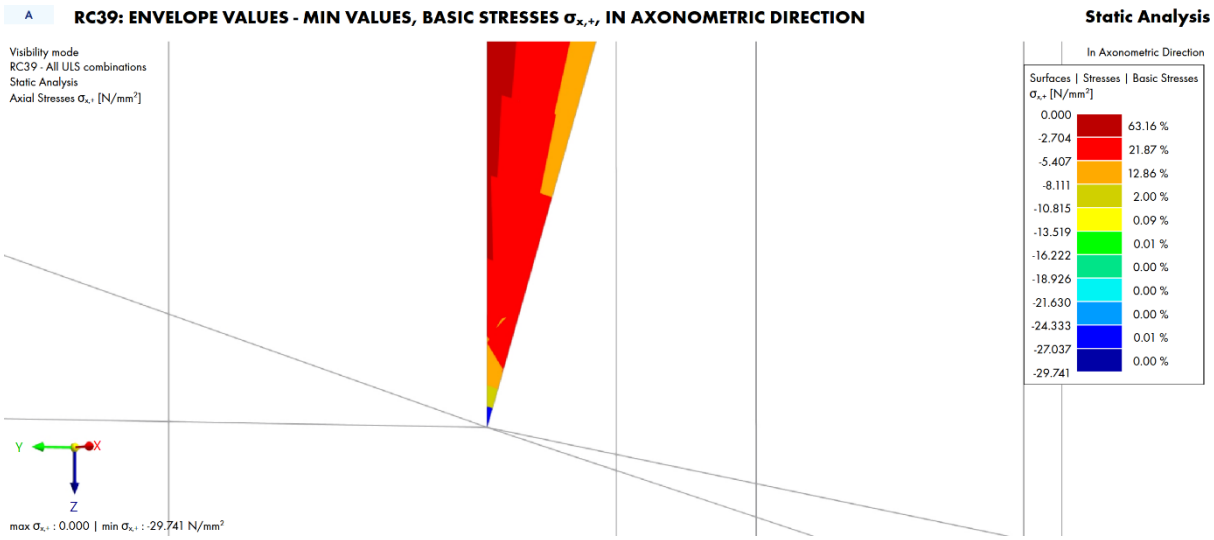

Figure 66: Example singularity in tip of support plate

The complete unity check (UC) tables for all structural components with the design stress limits are presented in Appendix T. The preliminary design does not satisfy the Ultimate Limit State (ULS) requirements, as several structural components exceed a unity check of 1.0. The support plates adjacent to the arch exhibit a maximum UC of 1.63 due to compressive stresses in the x-direction, σ_x. The side plates exceed the design limits in shear, with maximum UCs of 1.76 for the arch plate, 1.63 for the top side plate, and 1.18 for the bottom side plate. In addition, the bottom plate exceeds the allowable compressive stress, σ_x, with a maximum UC of 1.29, while the C-shaped girders and stiffener plates exceed the allowable shear stress with maximum UCs of 1.11 and 1.42, respectively.

Only the top plate satisfies all ULS requirements, with a maximum unity check of 0.41. The results indicate that the preliminary design requires modifications.

9.1.2 Serviceability limit state

As explained in Chapter 5.2.5, the bottom half of the structure can be seen as a clamped beam and the deflection is determined with the difference in deflection between the deflection at x = 0 [m] and the deflection at x = 16 [m] in the bottom half of the structure. The side part can also be seen as a clamped beam and the deflection is determined with the difference in deflection between the deflection at x = 16 [m] and the deflection at x = 25 [m]. The top half of the structure can be seen as a simply supported beam and the deflection at the middle of the top half is determined as the deflection at x = 0 [m] and the deflection at x = 12.5 [m] in the top half of the structure. The deflection plots of the entire structure can be seen in Appendix U.

Characteristic

The maximum allowable deflections for the characteristic load combination are defined as follows:

- Top half: $w_2 + w_3 \leq \frac{l_{span}}{150} = \frac{25000}{150} = 166.7\ mm$
- Side part: $w_2 + w_3 \leq \frac{2*l_{cantiliver}}{150} = \frac{2*9000}{150} = 120\ mm$
- Bottom half: $w_2 + w_3 \leq \frac{2*l_{cantiliver}}{150} = \frac{2*16000}{150} = 213.3\ mm$

The deflections of w_2 without creep factor are shown in Figure 68 and the deflections of w_3 are shown in Figure 67.

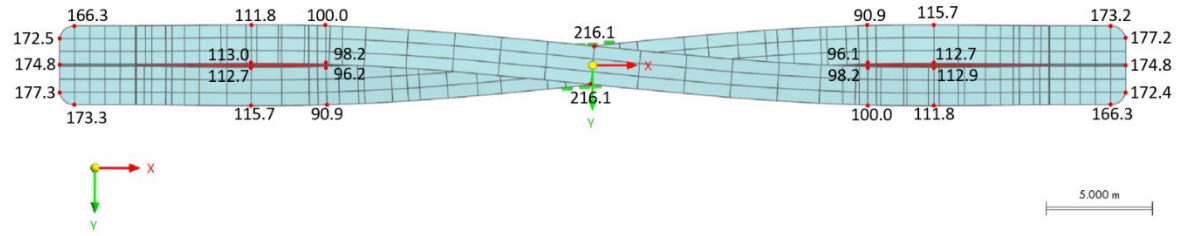

Figure 68: Deflections of w_2 without creep factor at multiple locations in mm

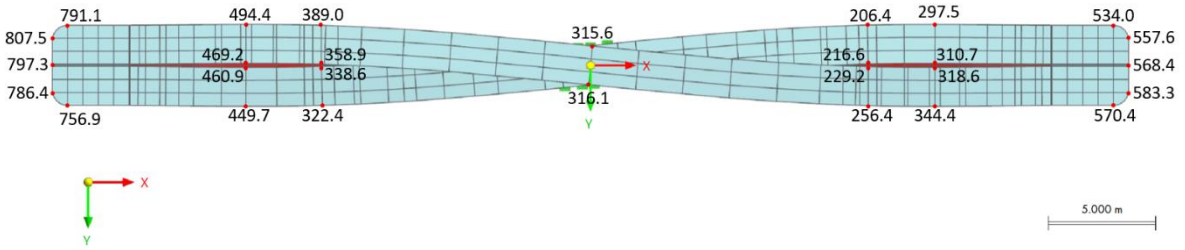

Figure 67: Deflection of w_3 at multiple locations in mm

Table 32 presents the calculated deflections for each part of the structure and compares them with the maximum allowable deflection, $w_2 + w_3$.

Deflections at multiple locations in mm						
Locations	Deflection w_2 without creep factor	Deflection w_2 with creep factor	Deflection w_3	Total deflection $w_2 + w_3$	Max allowed deflection	Check
Top half left	$216.1 - 98.2 = 117.9$	$117.9 * 2.153 = 253.8$	$315.6 - 358.9 = -43.3$	210.5	166.7	Not okay
Top half right	$216.1 - 98.2 = 117.9$	$117.9 * 2.153 = 253.8$	$316.1 - 229.2 = 86.9$	340.7	166.7	Not okay
Side part left	$174.8 - 112.7 = 62.1$	$62.1 * 2.153 = 133.7$	$797.3 - 460.9 = 336.4$	470.1	120	Not okay
Side part right	$174.8 - 112.7 = 62.1$	$62.1 * 2.153 = 133.7$	$568.4 - 310.7 = 257.7$	391.4	120	Not okay
Bottom half left	$112.7 - 0 = 112.7$	$112.7 * 2.163 = 242.64$	$460.9 - 0 = 460.9$	703.54	213.3	Not okay
Bottom half right	$112.7 - 0 = 112.7$	$112.7 * 2.163 = 242.64$	$310.7 - 0 = 310.7$	553.34	213.3	Not okay

Table 32: Characteristic deflection check

The calculated deflections exceed the allowable limits at all investigated locations. Therefore, the structure does not satisfy the characteristic deflection requirements.

Frequent

The frequent combination is used for the local deflection in the deck plate. The deck has a span between girders of 484 mm. The maximum allowed deflection in the top deck plate is:

- $w_3 \leq \frac{l_{deckplate}}{750} = \frac{484}{750} = 0.65\ mm$

The highest deflection comes from the highest combination for w_3. w_3 includes only one load with ψ_1. The traffic load is the highest variable load and for local effect the concentrated point load of 7 kN should be used. To determine the local deflection, part of the top plate is modelled with a span of 484 mm and a width of 1 meter. The top plate is assumed to be simply supported as a simplification. The load of 7 kN is applied in the middle for load case 2: concentrated traffic load and the result combination is:

$$0.8 * LC2$$

There is a mesh used of 0.02 mm. This mesh size was also halved and the results did not change. The schematic representation in RFEM is shown in Figure 69.

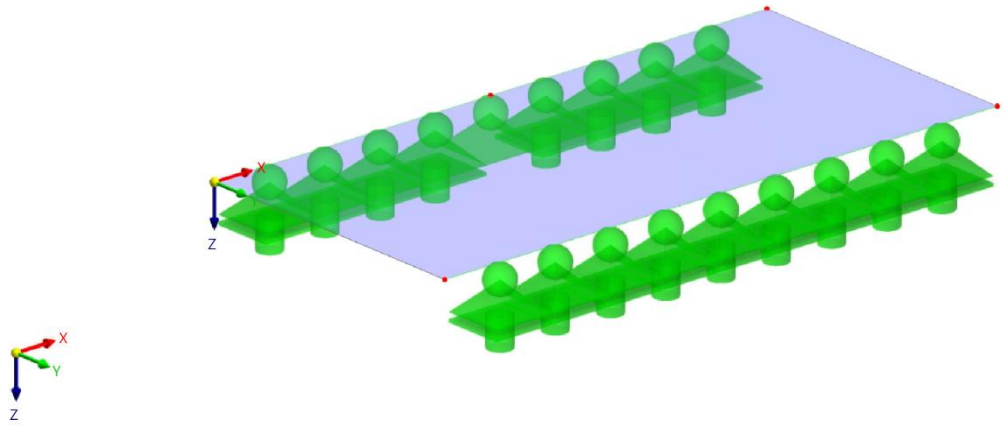

Figure 69: Model top deck plate RFEM

The result is shown in Figure 70. The maximum deflection is 0.1 mm which is smaller than the maximum allowed deflection. The stiffness of the top plate is high enough for the frequent serviceability constraint.

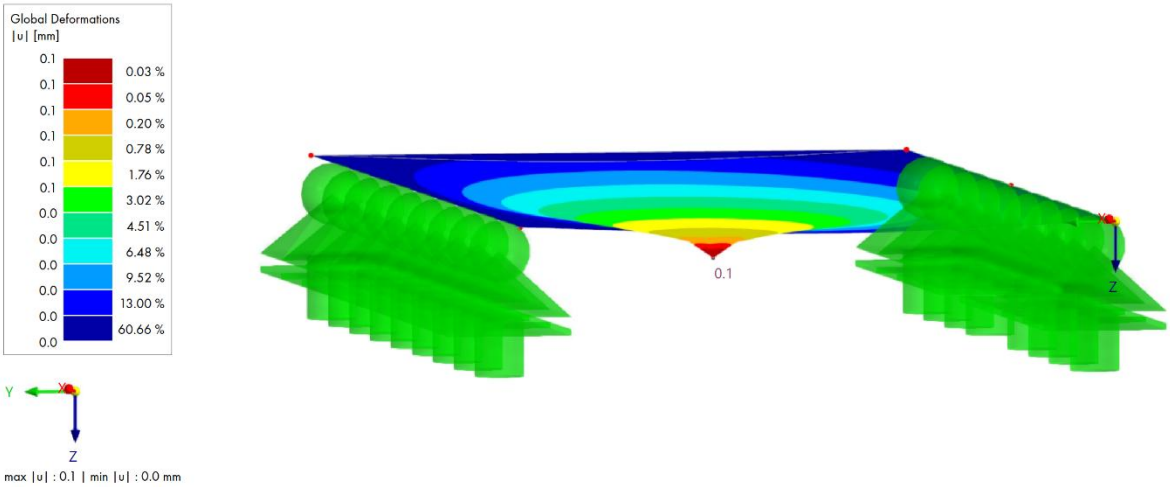

Figure 70: Deflection top deck plate

Quasi-permanent

The maximum deflections of the structure for quasi-permanent combinations are:

- Top half: $w_{max} \leq \frac{l_{span}}{250} = \frac{25000}{250} = 100\ mm$
- Side part: $w_{max} \leq \frac{2*l_{cantiliver}}{250} = \frac{2*9000}{250} = 72\ mm$
- Bottom half: $w_{max} \leq \frac{2*l_{cantiliver}}{250} = \frac{2*16000}{250} = 128\ mm$

The deflections of w_1 and the deflections of w_2 without creep factor are shown in Figure 71, the deflections are the same for both of w_1 and w_2 without creep factor as shown in the plots in Appendix U.

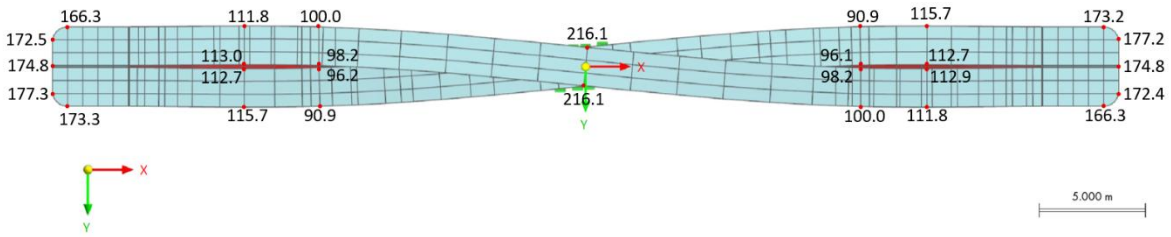

Figure 71: Deflection of w_1 and w_2 without creep factor at multiple locations in mm

Table 33 presents the calculated deflections for each part of the structure and compares them with the maximum allowable deflection, w_{max}. w_{max} is the deflection of $w_1 + w_2$ minus the pre-camber.

Deflections at multiple locations in mm					
Locations	Deflection w_1	Deflection w_2 without creep factor	Deflection w_2 with creep factor	Total deflection $w_1 + w_2$	Max allowed deflection w_{max}
Top half left	$216.1 - 98.2 = 117.9$	$216.1 - 98.2 = 117.9$	$117.9 * 2.153 = 253.8$	317.7	100
Top half right	$216.1 - 98.2 = 117.9$	$216.1 - 98.2 = 117.9$	$117.9 * 2.153 = 253.8$	317.7	100
Side part left	$174.8 - 112.7 = 62.1$	$174.8 - 112.7 = 62.1$	$62.1 * 2.153 = 133.7$	195.8	72
Side part right	$174.8 - 112.7 = 62.1$	$174.8 - 112.7 = 62.1$	$62.1 * 2.153 = 133.7$	195.8	72
Bottom half left	$112.7 - 0 = 112.7$	$112.7 - 0 = 112.7$	$112.7 * 2.163 = 242.64$	355.34	128
Bottom half right	$112.7 - 0 = 112.7$	$112.7 - 0 = 112.7$	$112.7 * 2.163 = 242.64$	355.34	128

Table 33: Quasi-permanent deflection check

The total deflection of $w_1 + w_2$ at all investigated locations exceeds the max allowed deflection. However, a pre-camber can be applied on the structure and reduce the max deflection. The pre-camper will be the deflection of $w_1 + w_2$ with creep of 10 days. In Table 34 is the maximum deflection calculated for quasi-permanent loads shown.

Deflections at multiple locations in mm					
Locations	Deflection w_1	Deflection w_2 without creep factor	Deflection w_2 with creep factor of 10 days	Pre-camber	Max deflection w_{max}
Top half left	$216.1 - 98.2 = 117.9$	$216.1 - 98.2 = 117.9$	$117.9 * 1.092 = 128.7$	247.6	70.1
Top half right	$216.1 - 98.2 = 117.9$	$216.1 - 98.2 = 117.9$	$117.9 * 1.092 = 128.7$	247.6	70.1
Side part left	$174.8 - 112.7 = 62.1$	$174.8 - 112.7 = 62.1$	$62.1 * 1.092 = 67.8$	129.9	65.9
Side part right	$174.8 - 112.7 = 62.1$	$174.8 - 112.7 = 62.1$	$62.1 * 1.092 = 67.8$	129.9	65.9
Bottom half left	$112.7 - 0 = 112.7$	$112.7 - 0 = 112.7$	$112.7 * 1.092 = 123.1$	235.8	119.55
Bottom half right	$112.7 - 0 = 112.7$	$112.7 - 0 = 112.7$	$112.7 * 1.092 = 123.1$	235.8	119.55

Table 34: Calculation max deflection

All calculated maximum deflections, including a pre-camber of $w_1 + w_2$ with creep of 10 days, remain within the allowable deflection limits. Therefore, the structure satisfies this Serviceability Limit State (SLS) requirement.

9.1.3 Changes to design

The first modification to the structure is an increase in the dimensions of the support rectangle at the base. In the preliminary design, the support measures approximately 1.8 m × 2.7 m. In the revised design, the support dimensions are increased to approximately 1.8 m × 4.4 m, resulting in a length increase in the x-direction by a factor of approximately 1.6.

This increase in support length reduces the maximum characteristic deflection, w_3, at x = -25 m by a factor of 0.82 and decreases the maximum deflection due to permanent loads at x = 0 m by a factor of 0.93. The larger support area has a more significant effect on the deflection at the ends of the structure than at the centre of the top deck. The deflection at the ends of the structure were the most problematic.

	Maximum deflection w_3 characteristic at x = -25 m [mm]	Maximum deflection due to permanent loads at x = 0 m [mm]
Preliminary design	807.7	216.1
Preliminary design with new support rectangle	661.8	201.5

Table 35: Deflection comparison different support areas

A support length of approximately 4.4 m in the x-direction is feasible because the crest of the dike is 6.5 m wide, leaving approximately 1 m of clearance on either side of the support. In the figure below is the structure with supports on top of the dike shown.

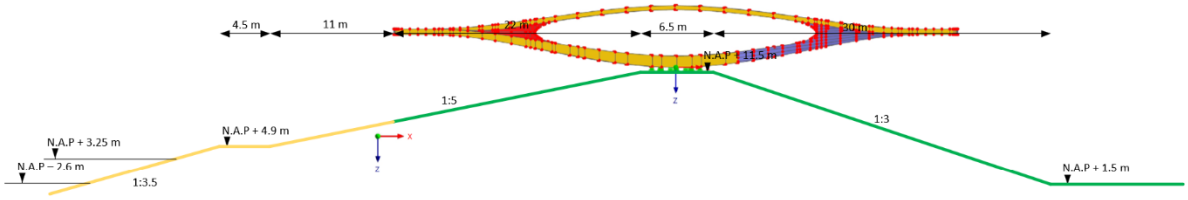

Figure 72: Side view structure with estimated dike profile on scale with new support area

Since the characteristic deflection under variable loading remains significantly larger than the allowable value, the cross-sectional height of the structure was increased. The height of the bottom deck cross-section was increased by 400 mm. In addition, the height of the top deck was increased by 400 mm between x = +/-25 m and x = +/-19.7 m. Between x = -16 m and x = 16 m, the top deck height was increased by 200 mm. A gradual transition in cross-sectional height was introduced between x = +/-19.7 m and x = +/-16 m to ensure a smooth variation in geometry. After increasing the cross-sectional height, it was found that the overlap between the upper and lower halves of the structure no longer maintained a vertical clearance of 2.0 m. Therefore, the geometry was modified slightly to restore the minimum clearance while preserving the overall structural shape as much as possible. The preliminary design side view and resulting side view are shown in Figure 74 and Figure 73. Although the revised design appears slightly bulkier, the overall geometry and the smooth transition in height are preserved.

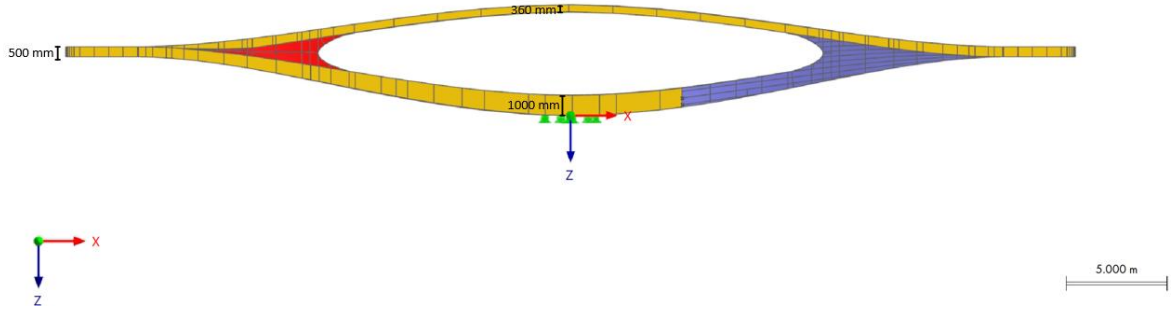

Figure 74: Side view preliminary design

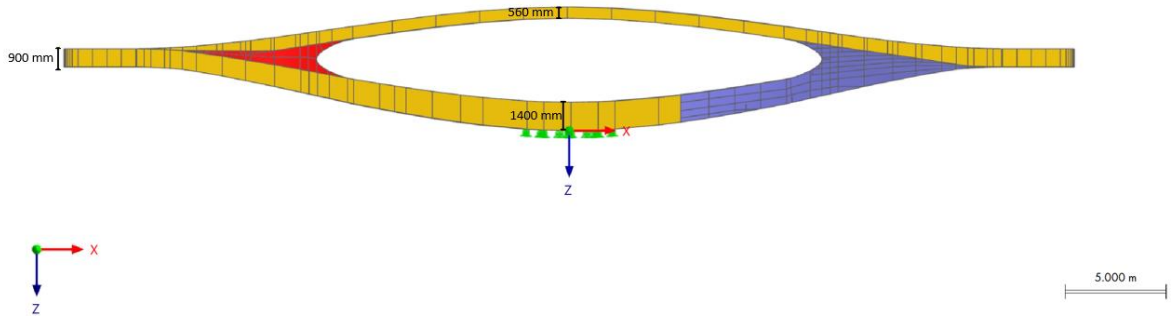

Figure 73: Side view higher cross-section

As an alternative, the structural performance was evaluated by increasing the panel thickness instead of the cross-sectional height. In this configuration, the thickness of the bottom deck was increased by a factor of approximately 2.6, while the bending stiffness of the top deck was increased by a factor of approximately 1.6. This increase in stiffness was achieved by decreasing the core thickness and increasing the face-sheet thickness.

However, this alternative proved to be less effective. The reduction in maximum characteristic deflection was smaller than that achieved by increasing the cross-sectional height, see Table 36. Furthermore, the maximum deflection due to permanent loads remained substantially higher than for the increased-height configuration.

The self-weight of the design with the increased cross-sectional height is 362.20 kN, compared with 530.79 kN for the design with increased thickness and stiffness. For reference, the self-weight of the preliminary design is 332.82 kN. These results demonstrate that increasing the panel thickness requires considerably more material while providing inferior structural performance compared with increasing the cross-sectional height.

	Maximum deflection w_3 characteristic at x = -25 m [mm]	Maximum deflection due to permanent loads at x = 0 m [mm]
Preliminary design with new support rectangle	661.8	201.5
Increased height of the cross-section	387.8	106.6
Increased thickness and stiffness	438.0	177.0

Table 36: Comparison deflection of different designs

Additional stiffener plates were incorporated into the revised design. The locations of these stiffener plates are provided in Appendix V. The added stiffeners create additional connections between the C-shaped girders, increasing the overall structural stiffness and improving the distribution of loads between the girders. Furthermore, the increased number of connections enhances the stability of the structure by providing additional restraint against local deformations and improving the overall structural behaviour, resulting in reduced deflections.

Table 37 and Table 38 present the revised plate thicknesses together with the reasoning for each modification, or the reason why no changes were made. The corresponding layer structure figures and input properties for RFEM are provided in Appendix W.

Component	Thickness [mm]	Layer direction percentages	Reason
Support plates set 1	9.10	Direction 0°: 25.00% Direction -45°: 25.00% Direction +45°: 25.00% Direction 90°: 25.00%	The unity check values for these plates are well below the allowable limit, indicating that they are significantly underutilised. Since their primary function is to support the arch plate and the bottom side plate rather than to carry substantial structural loads, their thickness was reduced considerably. Despite this reduction, the laminate configuration remains quasi-isotropic (QI), as the stresses remain well balanced in all directions.
Support plates set 2	9.10	Direction 0°: 25.00% Direction -45°: 25.00% Direction +45°: 25.00% Direction 90°: 25.00%	The thickness of support plate set 2 was reduced for the same reasons as support plate set 1.
Support plates set 3 without plate next to arch	30.33	Direction 0°: 25.00% Direction -45°: 25.00% Direction +45°: 25.00% Direction 90°: 25.00%	The unity checks values remained well below 1.0, indicating that these plates were still significantly underutilised. Therefore, a modest reduction in plate thickness was implemented. As these plates are relatively large and provide support for the upper half of the structure, only a limited reduction in thickness was considered appropriate to maintain sufficient stiffness and structural support.
Support plates set 3 with plate next to arch	51.57	Direction 0°: 25.00% Direction -45°: 25.00% Direction +45°: 25.00% Direction 90°: 25.00%	The unity check for compression exceeded 1.0 by a considerable margin, indicating that the plate did not satisfy the design requirements. Consequently, the plate thickness was increased to improve its compressive capacity. In addition, the plate was subjected to relatively high shear stresses. For this reason, the laminate configuration was retained as a quasi-isotropic (QI) lay-up to provide balanced strength and stiffness in all in-plane directions.
Support plates set 4	15.17	Direction 0°: 25.00% Direction -45°: 25.00% Direction +45°: 25.00% Direction 90°: 25.00%	The unity checks were still far below one so reduction of the thickness was applied.

Table 37: Changes in thickness and layer direction percentages components with reason

Component	Thickness [mm]	Layer direction percentages	Reason
Arch plate	35.23	Direction 0°: 51.16% Direction -45°: 16.28% Direction +45°: 16.28% Direction 90°: 16.28%	In the laminate stacking sequence, the number of 0° lamella was reduced, as the unity check for shear stress exceeded 1.0 by a considerable margin. The unity checks for compression in the x-directions was close to unity, indicating that the laminate was highly utilized in compression as well. To ensure sufficient resistance to compression in the x-direction, an adequate number of 0° lamella was still required. Therefore, a purely quasi-isotropic lay-up was not considered sufficient for this case. In addition, the overall laminate thickness was slightly increased to improve the structural capacity.
Top side plate	35.23	Direction 0°: 51.16% Direction -45°: 16.28% Direction +45°: 16.28% Direction 90°: 16.28%	The same modifications were applied as for the arch plate, for the same reasons.
Bottom side plate	35.23	Direction 0°: 51.16% Direction -45°: 16.28% Direction +45°: 16.28% Direction 90°: 16.28%	The same modifications were applied as for the arch plate, for the same reasons.
Bottom plate	40.60	Direction 0°: 62.50% Direction -45°: 12.50% Direction +45°: 12.50% Direction 90°: 12.50%	The unity check for compression exceeded 1.0 by a considerable margin, indicating that the plate did not satisfy the design requirements. Consequently, the plate thickness was increased to improve its compressive capacity.
C-shaped girders	21.33	Direction 0°: 25.00% Direction -45°: 25.00% Direction +45°: 25.00% Direction 90°: 25.00%	The unity check for shear stress exceeded 1.0 by a considerable margin, indicating that the plate did not satisfy the design requirements. Consequently, the plate thickness was increased to improve its capacity.
Top plate	129.14	Top and bottom face: Direction 0°: 62.50% Direction -45°: 12.50% Direction +45°: 12.50% Direction 90°: 12.50% H_{core}: 75 mm	The top plate satisfies all design checks and therefore remains unchanged in the revised design.
Stiffener plates	9.10	Direction 0°: 25.00% Direction -45°: 25.00% Direction +45°: 25.00% Direction 90°: 25.00%	No changes were made to the plate thickness because the addition of extra stiffener plates reduces the stresses in the existing plates by improving load distribution and increasing the overall stiffness of the structure.

Table 38: Changes in thickness and layer direction percentages components with reason

9.2 Revised design

The revised design is evaluated using the same ultimate limit state (ULS) and serviceability limit state (SLS) procedures as those applied to the preliminary design. In addition to these evaluations, the revised structure is also assessed for its buckling resistance. A stability analysis is performed in RFEM to evaluate the buckling behaviour of the structure and to identify the critical buckling modes and corresponding load factors. Furthermore, the shear stresses in the bonded connections between the C-shaped girders and the top and bottom decks are verified to ensure that they remain below the allowable value of 1 MPa, corresponding to the strength of the bonding paste. The shear stresses in the bonded connections between the support plates and the surrounding plates are also evaluated to confirm the adequacy of the adhesive joints. The same verification is performed for the bonded connections of the stiffener plates. The maximum stresses due to creep under the quasi-permanent load combination are also evaluated for all structural components.

9.2.1 Ultimate limit state

Support plates

The material and design stress limits for the support plates are given in the table below.

		CUR 96 Strain limit [%]		**Material Stress limit** $[N/mm^2]$	**Design Material Stress limit** $[N/mm^2]$
Tension	$\varepsilon_{1t,Rk}$	1.2	$\sigma_{f1t} = \varepsilon_{1t,Rk} * E_1$	111.7	65.5
	$\varepsilon_{2t,Rk;low}$	1.2	$\sigma_{f2t} = \varepsilon_{2t,Rk;low} * E_2$	111.7	65.5
Compression	$\varepsilon_{1c,Rk}$	1.0	$\sigma_{f1c} = \varepsilon_{1c,Rk} * E_1$	93.1	54.6
	$\varepsilon_{2c,Rk;low}$	1.2	$\sigma_{f2c} = \varepsilon_{2c,Rk;low} * E_2$	111.7	65.5
Shear	$\gamma_{12,Rk}$	1.6	$\tau_{f12} = \gamma_{12,Rk} * G$	44.5	26.1

Table 39: Stress limits laminate support plates

The unity checks (UC) of different support plates sets are given in the tables below. The different sets are given in Appendix S including the locations where singularities appear.

Set 1	Max stress $[N/mm^2]$	UC	Side of the plate
σ_x tensile	13	0.20	Positive
σ_x compression	17	0.31	Negative
σ_y tensile	11	0.17	Negative
σ_y compression	12	0.18	Positive
τ_{xy}	6	0.23	Membrane

Table 40: UC of support plates set 1

Set 2	Max stress $[N/mm^2]$	UC	Side of the plate
σ_x tensile	14	0.21	Positive
σ_x compression	26	0.48	Positive
σ_y tensile	26	0.40	Positive
σ_y compression	45	0.69	Positive
τ_{xy}	15	0.57	Membrane

Table 41: UC of support plates set 2

Set 3 without plate next to arch	Max stress $[N/mm^2]$	UC	Side of the plate
σ_x tensile	14	0.21	Positive
σ_x compression	20	0.37	Positive
σ_y tensile	18	0.27	Positive
σ_y compression	30	0.46	Positive
τ_{xy}	7	0.27	Membrane

Table 42: UC of support plates set 3 without plate next to arch

Set 3 plate next to arch	Max stress $[N/mm^2]$	UC	Side of the plate
σ_x tensile	13	0.20	Negative
σ_x compression	54	0.99	Positive
σ_y tensile	27	0.41	Positive
σ_y compression	27	0.41	Positive
τ_{xy}	15	0.57	Membrane

Table 43: UC of support plates set 3 with plate next to arch

Set 4	Max stress $[N/mm^2]$	UC	Side of the plate
σ_x tensile	28	0.43	Positive
σ_x compression	24	0.44	Negative
σ_y tensile	28	0.43	Positive
σ_y compression	21	0.32	Negative
τ_{xy}	5	0.19	Membrane

Table 44: UC of support plates set 4

To connect the support plates to the bottom half of the structure, the upper half of the structure, and the side plates, bonding flanges are provided along the plate edges. The required flange widths are determined from the internal force n_{xy}, the shear flow, obtained from the finite element analysis. The shear flow at the edges of the support plates is divided by the allowable adhesive shear stress of 1 MPa to determine the minimum flange width required for the bonded connection. The distributions of the maximum and minimum shear flow are presented in Figure 76 and Figure 75. The highest representative shear flow, excluding the local peaks, is 350 kN/m and occurs in the support plate adjacent to the arch plate. The required flange width is therefore:

$$\frac{350}{1} = 350\ mm$$

This flange is relatively wide, reflecting the high shear forces transferred through this connection. For the remaining support plates, the maximum representative shear flow is considerably lower, with a value of 150 kN/m. The required flange width for these plates is therefore:

$$\frac{150}{1} = 150\ mm$$

Based on these results, a flange width of 350 mm is adopted for the support plate adjacent to the arch plate, while a flange width of 150 mm is used for all other support plates. This provides sufficient bonding area to transfer the calculated shear forces without exceeding the allowable adhesive shear stress.

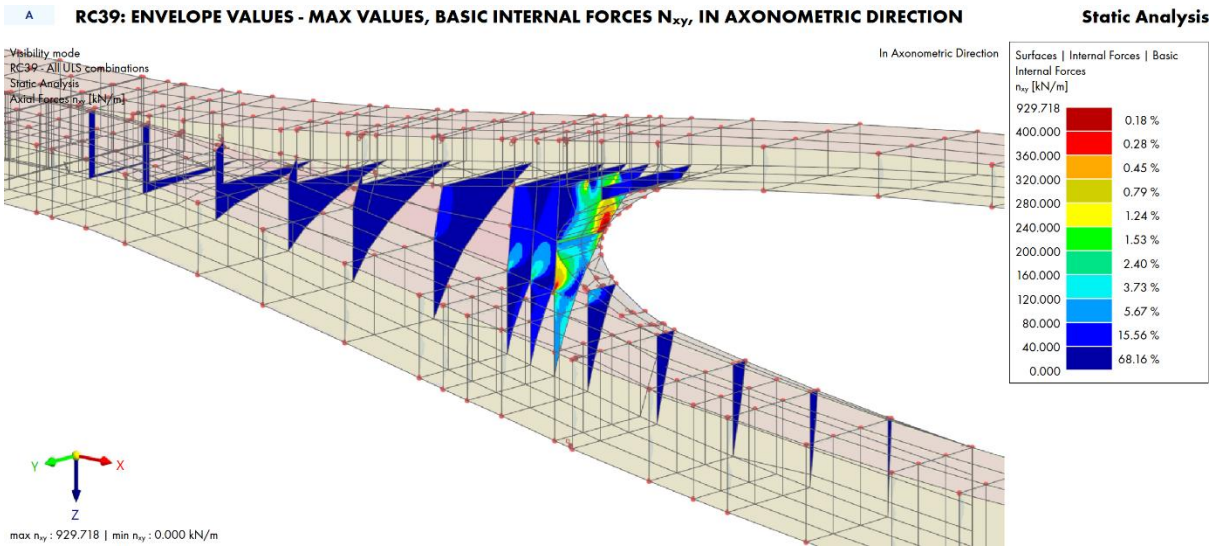

Figure 76: Max values of n_{xy} in support plates

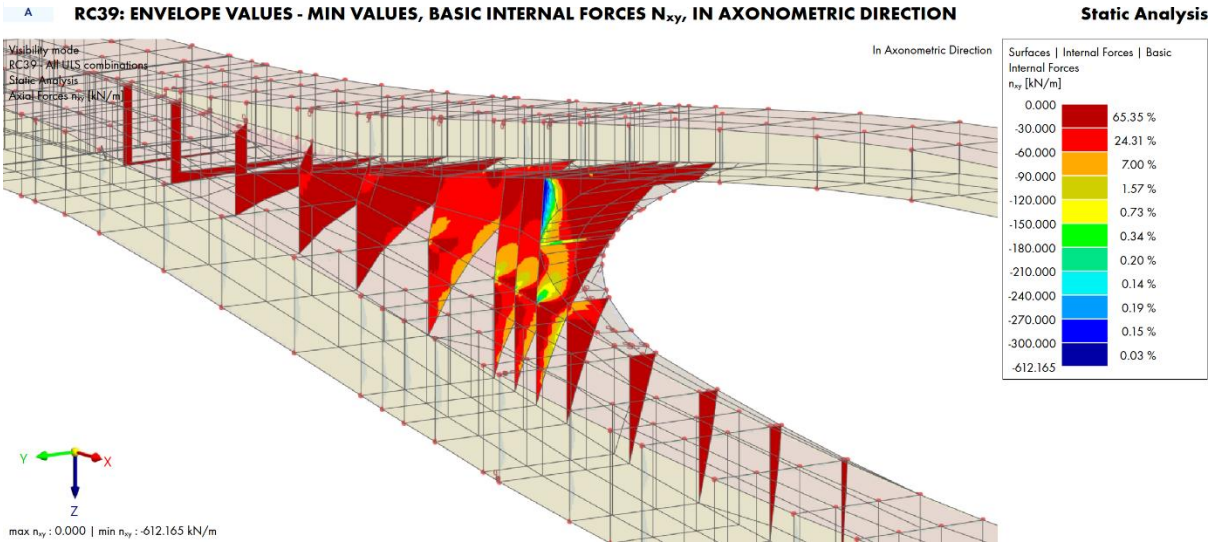

Figure 75: Min values of n_{xy} in support plates

Side plates

The material and design stress limits for the side plates are given in the table below.

		CUR 96 Strain limit [%]		Material Stress limit $[N/mm^2]$	Design Material Stress limit $[N/mm^2]$
Tension	$\varepsilon_{1t,Rk}$	1.2	$\sigma_{f1t} = \varepsilon_{1t,Rk} * E_1$	168.0	98.6
	$\varepsilon_{2t,Rk;low}$	1.2	$\sigma_{f2t} = \varepsilon_{2t,Rk;low} * E_2$	77.1	45.3
Compression	$\varepsilon_{1c,Rk}$	1.0	$\sigma_{f1c} = \varepsilon_{1c,Rk} * E_1$	140.0	82.2
	$\varepsilon_{2c,Rk;low}$	1.2	$\sigma_{f2c} = \varepsilon_{2c,Rk;low} * E_2$	77.1	45.3
Shear	$\gamma_{12,Rk}$	1.6	$\tau_{f12} = \gamma_{12,Rk} * G$	33.8	19.8

Table 45: Stress limits laminate side plates

Arch plate

The unity checks of the arch plate is given in the table below. The locations where singularities occur are shown in Appendix S.

Arch plate	Max stress $[N/mm^2]$	UC	Side of the plate
σ_x tensile	27	0.27	Positive
σ_x compression	66	0.80	Negative
σ_y tensile	44	0.97	Negative
σ_y compression	44	0.97	Positive
τ_{xy}	19	0.96	Membrane

Table 46: UC of arch plate

Top side plate

The unity checks of the top side plate is given in the table below. The locations where singularities occur are shown in Appendix S.

Top side plate	Max stress $[N/mm^2]$	UC	Side of the plate
σ_x tensile	24	0.24	Positive
σ_x compression	65	0.79	Positive
σ_y tensile	20	0.44	Positive
σ_y compression	40	0.88	Positive
τ_{xy}	15	0.76	Membrane

Table 47: UC of top side plate

Bottom side plate

The unity checks of the bottom side plate is given in the table below. The locations where singularities occur are shown in Appendix S.

Bottom side plate	Max stress $[N/mm^2]$	UC	Side of the plate
σ_x tensile	31	0.31	Positive
σ_x compression	75	0.91	Negative
σ_y tensile	17	0.38	Positive
σ_y compression	30	0.66	Negative
τ_{xy}	13	0.66	Membrane

Table 48: UC of bottom side plate

Bottom plate

The material and design stress limits for the bottom plate are given in the table below.

		CUR 96 Strain limit [%]		**Material Stress limit** $[N/mm^2]$	**Design Material Stress limit** $[N/mm^2]$
Tension	$\varepsilon_{1t,Rk}$	1.2	$\sigma_{f1t} = \varepsilon_{1t,Rk} * E_1$	189.9	111.4
	$\varepsilon_{2t,Rk;low}$	1.2	$\sigma_{f2t} = \varepsilon_{2t,Rk;low} * E_2$	62.9	36.9
Compression	$\varepsilon_{1c,Rk}$	1.0	$\sigma_{f1c} = \varepsilon_{1c,Rk} * E_1$	158.2	92.8
	$\varepsilon_{2c,Rk;low}$	1.2	$\sigma_{f2c} = \varepsilon_{2c,Rk;low} * E_2$	62.9	36.9
Shear	$\gamma_{12,Rk}$	1.6	$\tau_{f12} = \gamma_{12,Rk} * G$	29.6	15.3

Table 49: Stress limits laminate bottom plate

The unity checks of the bottom plate is given in the table below. The locations where singularities occur are shown in Appendix S.

Bottom plate	Max stress $[N/mm^2]$	UC	Side of the plate
σ_x tensile	50	0.45	Positive
σ_x compression	90	0.97	Positive
σ_y tensile	12	0.33	Positive
σ_y compression	10	0.27	Negative
τ_{xy}	12	0.78	Membrane

Table 50: UC of bottom plate

C-shaped girders

The material and design stress limits for the C-shaped girders are given in the table below.

		CUR 96 Strain limit [%]		**Material Stress limit** $[N/mm^2]$	**Design Material Stress limit** $[N/mm^2]$
Tension	$\varepsilon_{1t,Rk}$	1.2	$\sigma_{f1t} = \varepsilon_{1t,Rk} * E_1$	111.7	65.5
	$\varepsilon_{2t,Rk;low}$	1.2	$\sigma_{f2t} = \varepsilon_{2t,Rk;low} * E_2$	111.7	65.5
Compression	$\varepsilon_{1c,Rk}$	1.0	$\sigma_{f1c} = \varepsilon_{1c,Rk} * E_1$	93.1	54.6
	$\varepsilon_{2c,Rk;low}$	1.2	$\sigma_{f2c} = \varepsilon_{2c,Rk;low} * E_2$	111.7	65.5
Shear	$\gamma_{12,Rk}$	1.6	$\tau_{f12} = \gamma_{12,Rk} * G$	44.5	26.1

Table 51: Stress limits laminate C-shaped girders

The unity checks of the C-shaped girders is given in the table below. The locations where singularities occur are shown in Appendix S.

C-shaped girders	Max stress $[N/mm^2]$	UC	Side of the plate
σ_x tensile	29	0.44	Positive
σ_x compression	50	0.92	Negative
σ_y tensile	14	0.21	Negative
σ_y compression	60	0.92	Positive
τ_{xy}	25	0.96	Membrane

Table 52: UC of C-shaped girders

To verify the bonded connections between the C-shaped girders and the top and bottom decks, the shear stresses in the adhesive layer are evaluated. The verification is based on the internal force n_{xy}, the shear flow, obtained from the finite element analysis at the interface between the C-shaped girders and the deck panels. The corresponding shear flow distributions are shown in Figure 78 and Figure 77.

The maximum absolute shear flow at the edge of the girder is 265 kN/m. The peak values in the vicinity of the supports are disregarded, as these are influenced by local support effects and are not representative of the actual load transfer in the bonded connection.

Assuming that the shear flow is transferred uniformly through the adhesive joint, the average shear stress in the adhesive layer is determined by dividing the shear flow by the flange width. For the original flange width of 100 mm, the resulting shear stress is:

$$\frac{265}{100} = 2.65\ N/mm^2$$

This value exceeds the allowable adhesive shear stress of 1 MPa, indicating that the original flange width is insufficient.

To reduce the shear stress in the adhesive joint, the flange width of the C-shaped girders was increased to 265 mm. The resulting average shear stress becomes:

$$\frac{265}{265} = 1.0\ N/mm^2$$

With a flange width of 265 mm, the resulting shear stress satisfies the adopted limit of 1 MPa. Therefore, a flange width of 265 mm is considered acceptable for the revised design.

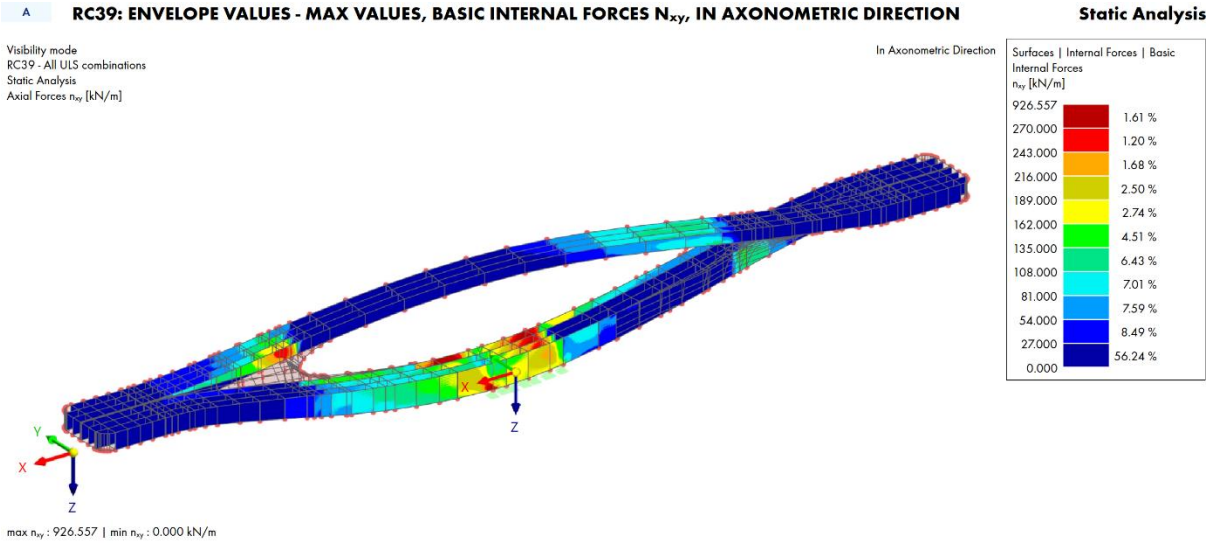

Figure 78: Max values of n_{xy} in C-shaped girders

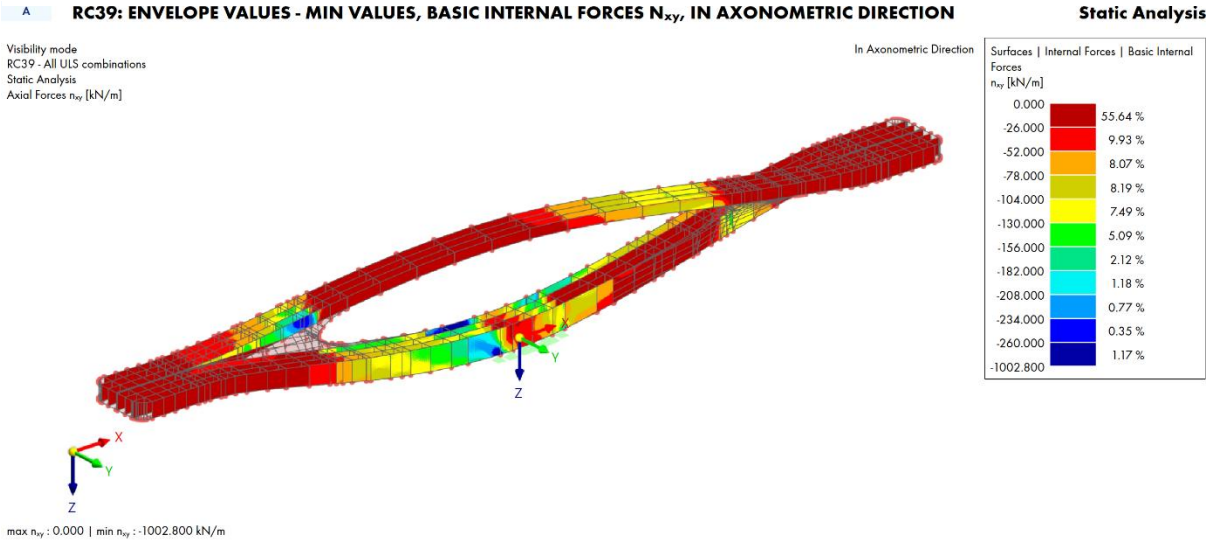

Figure 77: Min values of n_{xy} in C-shaped girders

Top plate

The material and design stress limits for the top plate are given in the table below.

		CUR 96 Strain limit [%]		**Material Stress limit** $[N/mm^2]$	**Design Material Stress limit** $[N/mm^2]$
Tension	$\varepsilon_{1t,Rk}$	1.2	$\sigma_{f1t} = \varepsilon_{1t,Rk} * E_1$	189.9	111.4
	$\varepsilon_{2t,Rk;low}$	1.2	$\sigma_{f2t} = \varepsilon_{2t,Rk;low} * E_2$	62.9	36.9
Compression	$\varepsilon_{1c,Rk}$	1.0	$\sigma_{f1c} = \varepsilon_{1c,Rk} * E_1$	158.2	92.8
	$\varepsilon_{2c,Rk;low}$	1.2	$\sigma_{f2c} = \varepsilon_{2c,Rk;low} * E_2$	62.9	36.9
Shear	$\gamma_{12,Rk}$	1.6	$\tau_{f12} = \gamma_{12,Rk} * G$	29.6	15.3

Table 53: Stress limits laminate top plate

The unity check of the top plate is given in the table below. The locations where singularities occur are shown in Appendix S.

Top plate	Max stress $[N/mm^2]$	UC	Side of the plate
σ_x tensile	26	0.23	Negative
σ_x compression	17	0.18	Negative
σ_y tensile	7	0.19	Negative
σ_y compression	9	0.24	Negative
τ_{xy}	3	0.20	Membrane

Table 54: UC of top plate

Stiffener plates

The material and design stress limits for the stiffener plates are given in the table below.

		CUR 96 Strain limit [%]		**Material Stress limit** $[N/mm^2]$	**Design Material Stress limit** $[N/mm^2]$
Tension	$\varepsilon_{1t,Rk}$	1.2	$\sigma_{f1t} = \varepsilon_{1t,Rk} * E_1$	111.7	65.5
	$\varepsilon_{2t,Rk;low}$	1.2	$\sigma_{f2t} = \varepsilon_{2t,Rk;low} * E_2$	111.7	65.5
Compression	$\varepsilon_{1c,Rk}$	1.0	$\sigma_{f1c} = \varepsilon_{1c,Rk} * E_1$	93.1	54.6
	$\varepsilon_{2c,Rk;low}$	1.2	$\sigma_{f2c} = \varepsilon_{2c,Rk;low} * E_2$	111.7	65.5
Shear	$\gamma_{12,Rk}$	1.6	$\tau_{f12} = \gamma_{12,Rk} * G$	44.5	26.1

Table 55: Stress limits laminate stiffener plates

The unity checks of all the stiffener plates are given in the tables below. The different sets are given in Appendix S including the locations where singularities appear.

Stiffener plates	Max stress $[N/mm^2]$	UC	Side of the plate
σ_x tensile	30	0.46	Positive
σ_x compression	28	0.51	Negative
σ_y tensile	20	0.31	Positive
σ_y compression	30	0.46	Positive
τ_{xy}	17	0.65	Membrane

Table 56: UC of stiffener plates

To connect the stiffener plates to the girders, bonding flanges are provided along the plate edges next to the girders. The required flange widths are determined from the internal force n_{xy}, the shear flow, obtained from the finite element analysis. The shear flow at the edges of the stiffener plates is divided by the allowable adhesive shear stress to determine the minimum flange width required for the bonded connection. The highest representative shear flow, excluding the local peaks and the peaks near the supports, is 100 kN/m. The required flange width is therefore:

$$\frac{100}{1} = 100\ mm$$

Stability of the structure

A linear stability analysis was performed in RFEM to evaluate the global and local buckling behaviour of the revised structure and to determine the critical buckling modes and corresponding load factors. The analysis was carried out using the eigenvalue method with the following settings:

- Stability analysis type: Eigen values method (linear)
- Number of lowest eigenvalues: 15
- Option I: Consider favourable effects due to tension

The following ultimate limit state load combination was used for the analysis:

$$1.35 * LC1 + 1.35 * LC2 + 1.35 * LC3 + 0.54 * LC4 + 0.45 * LC5 + 0.45 * LC6 + 0.45 * LC7$$

This load combination was selected because the traffic load is the governing variable action. Load case LC3, in which the entire structure is subjected to the pedestrian traffic load, was therefore taken as the leading variable load. To be conservative, several critical buckling modes with load factors greater than 1.0 were also evaluated in case the analysed load combination was not the governing one.

The results of the stability analysis are presented in Appendix X. A selection of some relevant results is given in Table 57. The critical buckling modes are characterised by local buckling of the C-shaped girders near the supports, together with local buckling of the adjacent stiffener plates. The corresponding critical load factors are relatively close to each other, indicating that the region around the supports is particularly sensitive to buckling. The lowest critical load factor is 0.562.

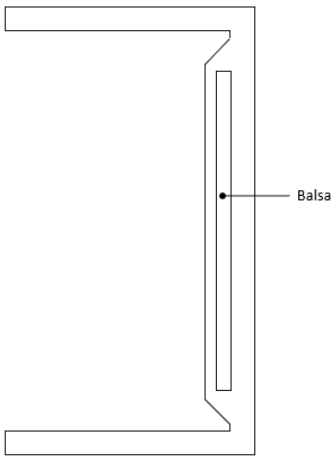

Figure 79: C-shaped girder with Balsa to increase thickness

The highest determined critical load factor is 1.293. At this load level, buckling is limited to local buckling of the C-shaped girders and the adjacent stiffener plates near the supports. No global buckling modes are observed, indicating that local instability governs the buckling behaviour of the structure.

The obtained buckling load factors are considered insufficient, the buckling resistance can be improved by increasing the thickness of these plates. An efficient solution is to add a balsa core with a few layers of flax fibre over it, creating a sandwich structure, see Figure 79. Balsa wood has a low density and relatively high mechanical properties, making it well suited for improving local buckling resistance with only a limited increase in self-weight. (Borrega, Ahvenainen, Serimaa, & Gibson, 2015)

Mode number	Critical load factor	Buckling shape
1	0.562	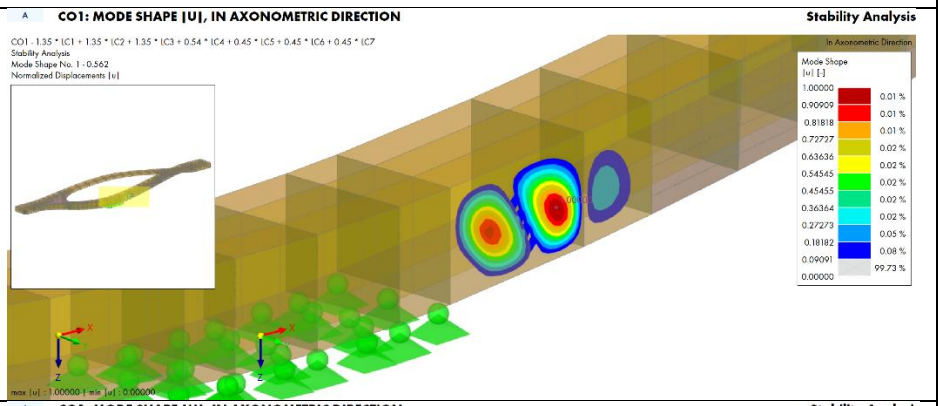
2	0.601	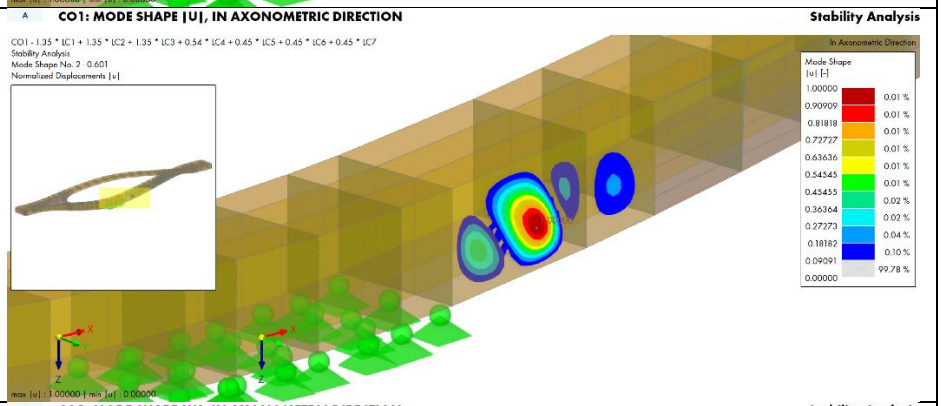
15	1.293	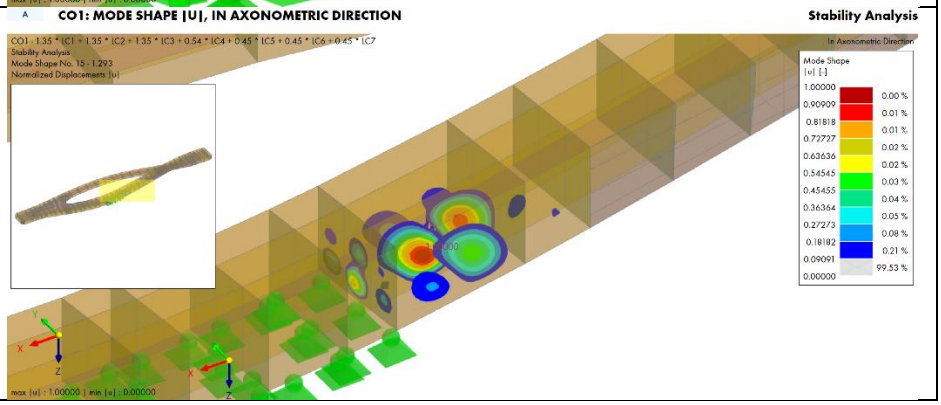

Table 57: Buckling shapes and critical load factors

Maximum creep stress check

The maximum stresses under the quasi-permanent load combination are verified against the creep constraint curve shown in Figure 80. The design is considered satisfactory when the calculated stresses remain below the boundary of this curve. The corresponding reserve factor is determined from the creep constraint curve.

The maximum absolute stress in both the x- and y-directions under quasi-permanent loading is 20 N/mm^2 and occurs adjacent to the supports. Over the majority of the structure, the maximum absolute stress is approximately 10 N/mm^2. For a design life of 50 years, the maximum allowable stress according to the creep constraint curve is 30.6 N/mm².

The resulting reserve factors are:

- 1.53 for the maximum stress near the supports, $\frac{30.6}{20}$
- 3.06 for the majority of the structure, $\frac{30.6}{10}$

Both stress levels remain below the creep constraint curve, indicating that the revised design satisfies the long-term creep requirements for the specified design life.

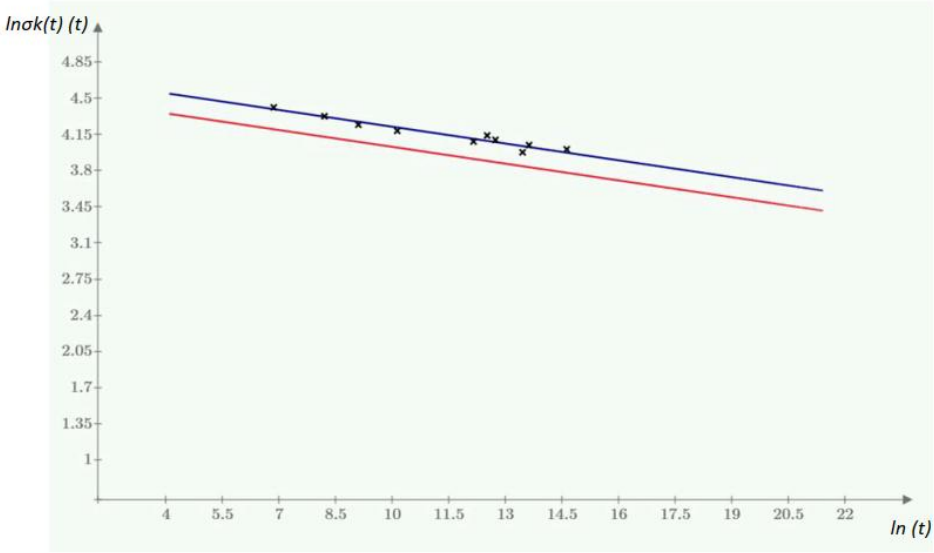

Figure 80: Creep line (blue) and characteristic creep line (red) on log-log scale for a lifetime of 50 years (Smart Circular Bridge for a circular built environment, sd)

9.2.2 Serviceability limit state

Chapter 5.2.5 explains how the deflections are determined.

Characteristic

The maximum allowable deflections for the characteristic load combination are defined as follows:

- Top half: $w_2 + w_3 \leq \frac{l_{span}}{150} = \frac{25000}{150} = 166.7\ mm$
- Side part: $w_2 + w_3 \leq \frac{2*l_{cantiliver}}{150} = \frac{2*9000}{150} = 120\ mm$
- Bottom half: $w_2 + w_3 \leq \frac{2*l_{cantiliver}}{150} = \frac{2*16000}{150} = 213.3\ mm$

The deflections of w_2 without creep factor are shown in Figure 82 and the deflections of w_3 are shown in Figure 81.

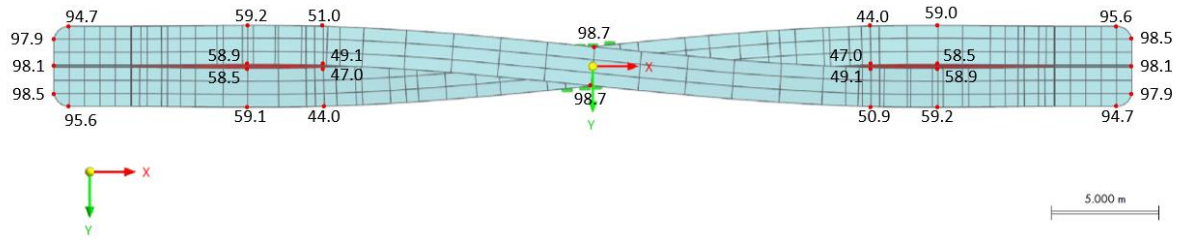

Figure 82: Deflections of w_2 without creep factor at multiple locations in mm

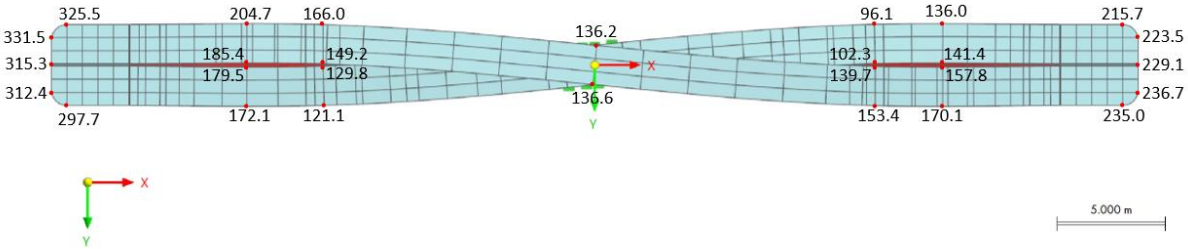

Figure 81: Deflection of w_3 at multiple locations in mm

Table 58 presents the calculated deflections for each part of the structure and compares them with the maximum allowable deflection, $w_2 + w_3$.

Locations	Deflection w_2 without creep factor	Deflection w_2 with creep factor	Deflection w_3	Total deflection $w_2 + w_3$	Max allowed deflection	Check
Top half left	$98.7 - 49.1 = 49.6$	$49.6 * 2.153 = 106.8$	$136.6 - 149.2 = -12.6$	94.2	166.7	Okay
Top half right	$98.7 - 49.1 = 49.6$	$49.6 * 2.153 = 106.8$	$136.6 - 139.7 = -3.1$	103.7	166.7	Okay
Side part left	$98.1 - 58.5 = 39.6$	$39.6 * 2.153 = 85.3$	$315.3 - 179.5 = 135.8$	221.1	120	Not okay
Side part right	$98.1 - 58.5 = 39.6$	$39.6 * 2.153 = 85.3$	$229.1 - 141.4 = 87.7$	173.0	120	Not okay
Bottom half left	$58.5 - 0 = 58.5$	$58.5 * 2.163 = 126.0$	$179.5 - 0 = 179.5$	305.5	213.3	Not okay
Bottom half right	$58.5 - 0 = 58.5$	$58.5 * 2.163 = 126.0$	$141.4 - 0 = 141.4$	267.4	213.3	Not okay

Table 58: Characteristic deflection check

Almost all calculated deflections exceed the recommended allowable limits at the investigated locations. However, the predicted deflections are still considered to provide an acceptable level of user comfort. A significant proportion of the creep deformation develops during the first days after loading. Furthermore, creep-induced deflection occurs gradually over time and is therefore not perceptible to users during usage of the structure.

The characteristic deflection w_3 due to variable loading, which represents the deformation that is noticeable during use, satisfies the recommended maximum deflection limit in almost all cases. The only exception occurs at the left side part of the structure, where the maximum allowable deflection is exceeded. This deflection results from the combination of a traffic load applied on the left side of the bridge and a contribution from the wind load. The probability of this loading combination occurring is relatively low, and the exceedance of the recommended limit is small. If the side part and the bottom part are together considered as a cantilever, the recommended maximum deflection becomes:

$$\frac{2 * l_{cantiliver}}{150} = \frac{2 * 25000}{150} = 333.3\ mm$$

The characteristic deflection w_3 on the left end is 315.3 mm, see Figure 81, which is below the maximum deflection of 333.3 mm. Consequently, although one recommended deflection limit is exceeded for a specific loading case, the predicted deformations are still considered acceptable from a user comfort perspective.

Because the given deflections result from the combination of a traffic load applied on the left side of the bridge and a contribution from the wind load, an additional analysis was performed considering only the traffic load acting on the middle section of the top half of the structure. The resulting deflections are presented in the table below. None of these deflections exceed the recommended allowable limit, with a considerable margin, indicating that the top half of the structure is sufficiently stiff.

Deflections at multiple locations in mm					
	Deflection in the middle	Deflection at $x = \pm 12.5$	Deflection w_3	Max allowed deflection	Check
Top half left	69	28.3	$69 - 28.3 = 40.7$	166.7	Okay
Top half right	69	34.5	$69 - 34.5 = 34.5$	166.7	Okay

Table 59: Deflection due to traffic load on the middle part of the top half

Frequent

The frequent serviceability limit state (SLS) is not evaluated again, as the properties of the top plate, which govern this verification, remain unchanged in the revised design.

Quasi-permanent

The maximum deflections of the structure for quasi-permanent combinations are:

- Top half: $w_{max} \leq \frac{l_{span}}{250} = \frac{25000}{250} = 100\ mm$
- Side part: $w_{max} \leq \frac{2*l_{cantiliver}}{250} = \frac{2*9000}{250} = 72\ mm$
- Bottom half: $w_{max} \leq \frac{2*l_{cantiliver}}{250} = \frac{2*16000}{250} = 128\ mm$

The deflections of w_1 and the deflections of w_2 without creep factor are shown in Figure 83, the deflections are for both the same as shown in the plots in Appendix U.

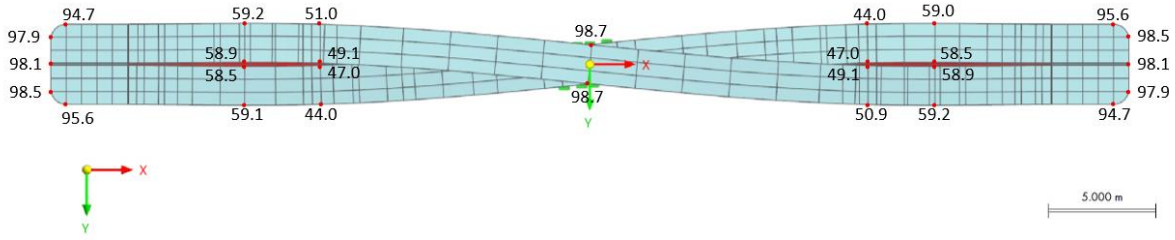

Figure 83: Deflection of w_1 and w_2 without creep factor at multiple locations in mm

The table below presents the calculated deflections for each part of the structure and compares them with the maximum allowable deflection, w_{max}. w_{max} is the deflection of $w_1 + w_2$ minus the pre-camber.

Deflections at multiple locations in mm					
Locations	Deflection w_1	Deflection w_2 without creep factor	Deflection w_2 with creep factor	Total deflection $w_1 + w_2$	Max allowed deflection w_{max}
Top half left	$98.7 - 49.1 = 49.6$	$98.7 - 49.1 = 49.6$	$49.6 * 2.153 = 106.8$	156.4	100
Top half right	$98.7 - 49.1 = 49.6$	$98.7 - 49.1 = 49.6$	$49.6 * 2.153 = 106.8$	156.4	100
Side part left	$98.1 - 58.5 = 39.6$	$98.1 - 58.5 = 39.6$	$39.6 * 2.153 = 85.3$	124.9	72
Side part right	$98.1 - 58.5 = 39.6$	$98.1 - 58.5 = 39.6$	$39.6 * 2.153 = 85.3$	124.9	72
Bottom half left	$58.5 - 0 = 58.5$	$58.5 - 0 = 58.5$	$58.5 * 2.163 = 126.0$	184.5	128
Bottom half right	$58.5 - 0 = 58.5$	$58.5 - 0 = 58.5$	$58.5 * 2.163 = 126.0$	184.5	128

Table 60: Quasi-permanent deflection check

The total deflection of $w_1 + w_2$ at all investigated locations exceeds the max allowed deflection. However, a pre-camber can be applied on the structure and reduce the max deflection. The pre-camper will be the deflection of $w_1 + w_2$ with creep of 10 days. In Table 61 is the maximum deflection calculated for quasi-permanent loads shown.

Deflections at multiple locations in mm					
Locations	Deflection w_1	Deflection w_2 without creep factor	Deflection w_2 with creep factor of 10 days	Pre-camber	Max deflection w_{max}
Top half left	$98.7 - 49.1 = 49.6$	$98.7 - 49.1 = 49.6$	$49.6 * 1.092 = 54.2$	103.8	52.6
Top half right	$98.7 - 49.1 = 49.6$	$98.7 - 49.1 = 49.6$	$49.6 * 1.092 = 54.2$	103.8	52.6
Side part left	$98.1 - 58.5 = 39.6$	$98.1 - 58.5 = 39.6$	$39.6 * 1.092 = 43.2$	82.3	42.0
Side part right	$98.1 - 58.5 = 39.6$	$98.1 - 58.5 = 39.6$	$39.6 * 1.092 = 43.2$	82.3	42.0
Bottom half left	$58.5 - 0 = 58.5$	$58.5 - 0 = 58.5$	$58.5 * 1.092 = 63.9$	122.4	62.1
Bottom half right	$58.5 - 0 = 58.5$	$58.5 - 0 = 58.5$	$58.5 * 1.092 = 63.9$	122.4	62.1

Table 61: Calculation max deflection

All calculated maximum deflections, including a pre-camber of $w_1 + w_2$ with creep of 10 days, remain within the allowable deflection limits. Therefore, the structure satisfies the Serviceability Limit State (SLS) requirements.

10. Modal analysis

A modal analysis was performed for the revised design to determine the natural frequencies and corresponding mode shapes of the Seasaw. The analysis was performed using the Lanczos eigenvalue solver. The Lanczos method is widely used in structural dynamics because it efficiently reduces large finite element systems while maintaining a high level of accuracy for the dominant vibration characteristics. This makes the method particularly suitable for determining the lowest natural frequencies and mode shapes that govern the dynamic behaviour of footbridges. (Nour-Omid & Regelbrugge, 1989)

A consistent mass matrix was adopted for the analysis. In a consistent mass formulation, the mass distribution follows the element shape functions and is therefore represented more accurately than in a lumped (diagonal) mass matrix. This approach provides a more realistic prediction of both translational and torsional vibration modes, which is important for slender bridge structures. (Entities: Consistent vs Lumped Mass, sd)

Mass participation was considered in all translational directions (X, Y and Z) and all rotational directions (RX, RY and RZ). This ensures that all relevant global vibration modes, including vertical bending, lateral bending and torsional modes, are captured within the eigenvalue analysis. Since pedestrian bridges can be sensitive to both vertical and lateral dynamic excitation, consideration of all translational and rotational degrees of freedom is considered appropriate.

The analysis was configured to determine 10 eigenmodes. This number was selected to ensure that all relevant global vibration modes are identified. The resulting modes were subsequently reviewed to identify the governing vertical, lateral and torsional frequencies of the structure.

The mass model was based on the characteristic permanent actions and the quasi-permanent portion of the pedestrian live load in accordance with NEN-EN 1990. The structural mass was therefore determined using:

$$M = G_k + 0.4 * Q_k$$

where G_k represents the characteristic permanent actions and Q_k represents the characteristic pedestrian load. The factor 0.4 corresponds to the quasi-permanent combination factor ψ_2 applicable to pedestrian loading. This mass representation is considered appropriate for evaluating the dynamic characteristics of the bridge under normal operating conditions.

The calculated natural frequencies were compared with the critical frequency ranges specified for pedestrian bridges. When a natural frequency falls within one of these critical ranges, a further assessment of pedestrian comfort is required. In addition, for frequencies within the critical range for intentional excitation, an ultimate limit state (ULS) verification should be performed.

Vibration type	Critical frequency range
Vertical vibrations	Pedestrian comfort: $1.25 < natural\ frequency < 2.3$ Jogger comfort: $1.9 < natural\ frequency < 3.5$ ULS: $1.7 < natural\ frequency < 3.0$
Longitudinal vibrations	Pedestrian comfort: $1.25 < natural\ frequency < 2.3$
Lateral vibrations	Pedestrian comfort: $0.5 < natural\ frequency < 1.2$
Torsional vibrations	Pedestrian comfort: $0.5 < natural\ frequency < 1.2$

Table 62: Critical frequency ranges, obtained from NEN-EN 1990

The table below summarises the calculated modal properties and indicates whether each natural frequency falls within a critical frequency range. The corresponding mode shapes are presented in Appendix Y. Mode shape 1 is shown in Figure 84.

Mode number	Eigenvalue $\lambda\ [1/s^2]$	Angular frequency $\omega\ [rad/s]$	Natural frequency $f\ [Hz]$	Natural period $T\ [s]$	Vibration type	Verification critical frequency range
1	23.607	4.859	0.773	1.293	Vertical	Outside range
2	27.013	5.197	0.827	1.209	Torsional	Inside range
3	34.662	5.887	0.937	1.067	Lateral	Inside range
4	108.249	10.404	1.656	0.604	Lateral	Outside range
5	109.974	10.487	1.669	0.599	Vertical	Inside range
6	388.406	19.708	3.137	0.319	Torsional	Outside range
7	693.217	26.329	4.190	0.239	Vertical	Outside range
8	969.275	31.133	4.955	0.202	Torsional	Outside range
9	1324.185	36.389	5.792	0.173	Torsional	Outside range
10	1416.882	37.641	5.991	0.167	Vertical	Outside range

Table 63: Modes with modal properties

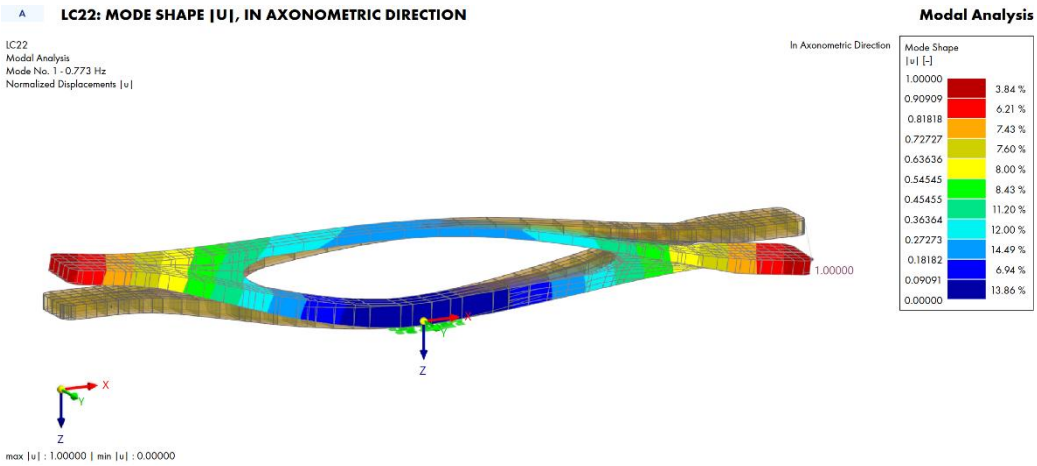

Figure 84: Mode shape 1

The natural frequencies of modes 2, 3 and 5 fall within the critical frequency ranges and therefore require a detailed pedestrian comfort assessment. The natural frequency of mode 5 is also close to the lower bound of the critical frequency ranges for jogger comfort and intentional excitation (ULS). The remaining modes lie outside the critical frequency ranges and do not require further dynamic verification.

A detailed pedestrian comfort assessment is beyond the scope of this study and should be carried out during a later stage of the design process. Nevertheless, the relatively low natural frequencies indicate that the bridge is likely to be susceptible to pedestrian-induced vibrations. It is therefore expected that vibration mitigation measures, such as tuned mass dampers (TMDs) (see Figure 88 and Figure 89), will be required to satisfy the applicable comfort criteria in the final design. Examples of TMD installations in pedestrian bridges are shown in Figure 87, Figure 86 and Figure 85.

For the Seasaw, sufficient space is available between the C-shaped girders to accommodate TMDs. Potential locations include the middle section of the top half of the structure and the left and right-side sections, where the vibration amplitudes are expected to be relatively large. During the detailed design stage, the additional mass introduced by the TMDs should be taken into account, and the surrounding structural components should be designed accordingly to safely transfer the additional loads.

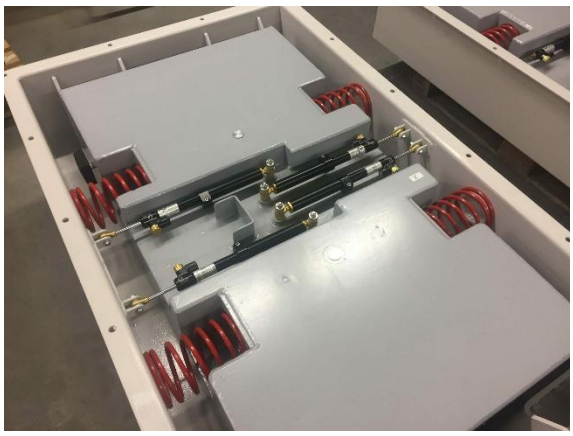

Figure 88: Example of horizontal tuned mass damper (Tuned Mass Damper, sd)



Figure 89: Example of tuned mass damper for bridges (Tuned Mass Damper, sd)



Figure 87: Installation of tuned mass damper (Tuned Mass Damper for bridges, sd)



Figure 86: Tuned mass damper installed in a bridge (Tuned Mass Damper for bridges, sd)



Figure 85: Tuned mass damper installed under a bridge (Tuned Mass Damper for bridges, sd)

11. Validation

The evaluation criteria defined in Chapter 5.3 are shown in the table below. In this chapter, each criterion is evaluated and it is explained whether and how it has been satisfied. If a criterion is not met, recommendations are provided to improve the design and achieve compliance.

Service life	The structure achieves a design service life of 50 years
User safety	The design provides a safe environment for pedestrians under normal use, minimising risks related to falling, slipping and loss of balance.
Usability and comfort (SLS)	The structural behaviour, geometry, and movements of the Seasaw do not cause discomfort, fear, or uncertainty for users during pedestrian traffic.
Structural safety (ULS)	The structure safely resists all relevant design actions and load combinations without collapse or loss of structural integrity.
Stability (ULS)	The structure remains stable under all relevant design situations, including unfavourable loading and environmental actions.
Serviceability performance (SLS)	Deformations and vibrations remain within acceptable limits under characteristic load combinations, ensuring adequate comfort and usability.
Robustness	Localised damage or unforeseen events do not lead to disproportionate or progressive collapse of the structure.
Durability	Material degradation over the design working life does not impair structural performance, considering environmental exposure and maintenance.
Sustainability	The design limits adverse environmental, societal, and economic impacts over the full life cycle of the structure.
Appearance of the Seasaw	The design of the Seasaw should retain the overall layout and appearance of the original concept, with only minor changes to its visual appearance.

Table 64: Evaluation criteria

11.1 Service life

The service life criterion is satisfied by designing and verifying the structure for a 50-year design life. All creep calculations and allowable long-term stresses are based on the 50-year creep constraint curve. In addition, the wind loads are determined for a design return period corresponding to a 50-year design life.

11.2 User safety

The user safety criterion is satisfied by incorporating several measures into the design. The walking surface is provided with an anti-slip deck to reduce the risk of slipping, while guardrails are installed along the edges of the bridge to prevent pedestrians from falling.

At the location with the smallest vertical distance between the top half and the bottom half of the structure, there is a minimum clearance of 2.0 m. At this location, the overlap between the top and bottom halves is small, approximately 10 cm. In regions where the overlap increases to approximately 30 cm, the vertical clearance increases to around 2.5 m.

11.3 Usability and comfort

The route from the entrance, via the middle of the bottom half of the structure, to one of the side sections has a length of 21.414 m and overcomes a height difference of 2.642 m, resulting in an average gradient of 12.3% (approximately 1:8). The route from a side section to the middle of the top half also has a length of 21.414 m but overcomes a height difference of 2.071 m, corresponding to an average gradient of 9.7% (approximately 1:10).

Although the first gradient is steeper than is generally recommended for accessible pedestrian routes, it is considered appropriate for the intended function of the Seasaw as a tourist attraction. The structure is designed exclusively for pedestrians and is not intended to accommodate wheelchair users, pushchairs, or persons with limited mobility. Consequently, the gradients do not compromise the intended safe use of the structure.

The gradual transitions in slope and continuous geometry contribute to a stable and predictable walking experience, reducing the likelihood of discomfort or uncertainty during use.

11.4 Structural safety (ULS)

All unity checks were below 1.0, indicating that the structure satisfies the ultimate limit state requirements for the considered load combinations. However, stress singularities occurred in the vicinity of the supports due to the simplified support modelling adopted in the finite element model. These local peak stresses were therefore excluded from the assessment, as they are not considered representative of the actual structural behaviour. In a subsequent design stage, the support regions should be evaluated in more detail using a different support model to obtain more realistic stress distributions.

11.5 Stability

Only local instability was observed, namely buckling of the C-shaped girders and adjacent stiffener plates in the regions near the supports. No global instability modes were identified within the investigated load combinations, indicating that the overall structural stability is maintained.

The observed local instability can be mitigated by increasing the local plate stiffness, for example by introducing sandwich panels with a balsa core and additional flax fibre layers. This improves the buckling resistance of the affected components without significantly increasing the self-weight of the structure.

11.6 Serviceability performance (SLS)

The serviceability assessment shows that most calculated deflections slightly exceed the recommended allowable limits at certain locations. However, these exceedances are generally small and are considered acceptable from a user comfort perspective. A significant portion of the long-term creep deformation develops in the initial days after loading and occurs gradually over time, making it imperceptible during normal use of the structure.

The characteristic variable-load deflection w_3 satisfies the recommended limits in almost all cases. Only the left side of the structure shows a limited exceedance due to a combined effect of traffic and wind loading. When this region is conservatively treated as a cantilever, the corresponding allowable deflection is 333.3 mm, while the calculated value of 315.3 mm remains within this limit. Additional checks with only traffic loading on the top half confirm that deflections remain well below the allowable limits, demonstrating sufficient stiffness in this part of the structure.

A detailed pedestrian comfort assessment is outside the scope of this study but should be performed in a later design stage. The relatively low natural frequencies indicate a likelihood of pedestrian-induced vibrations, meaning that vibration mitigation measures such as tuned mass dampers (TMDs) will likely be required. Sufficient space is available between the C-shaped girders to accommodate such devices, with potential placement in the middle of the top half and the side parts where vibration amplitudes are expected to be the highest.

11.7 Robustness

A detailed robustness assessment was not carried out within the scope of this study. However, the cross-section consists of multiple C-shaped girders, and stiffener plates are distributed throughout the structure. In addition, the connection between the upper and lower halves includes multiple support plates, creating multiple alternative load paths within the structural system.

As a result, local damage can be redistributed through other structural components, reducing the likelihood of disproportionate or progressive collapse. Consequently, these features contribute positively to the overall robustness of the design.

11.8 Durability

The durability of the structure is ensured by applying a protective coating to the flax fibre composite components. This coating reduces moisture absorption and thereby improves both the mechanical properties and the long-term environmental resistance of the material over the design working life. The coating will need to be reapplied periodically during the design life as part of the maintenance strategy to ensure continued protection.

11.9 Sustainability

No full life cycle assessment was performed within the scope of this study. However, the design incorporates flax fibre composites as a bio-based material, which can reduce environmental impact compared to conventional composite materials.

From a societal perspective, the Seasaw contributes to more sustainable construction practices and enhances the public space in Den Helder by strengthening the connection between land and sea. It may also support local tourism and economic activity and strengthen the city's identity as a location associated with innovation and sustainability.

Potential negative sustainability aspects mainly relate to increased maintenance demands and the need for coordination with dike management authorities to avoid interference with flood defence operations. Overall, the design is considered to contribute positively to sustainability at a conceptual level.

11.10 Design of the Seasaw

The design of the Seasaw retains the overall layout and appearance of the original concept, with only limited local modifications introduced to meet structural performance requirements. The cross-sectional height was increased in several regions to reduce excessive deflections under characteristic variable loading, while gradual transitions were applied to preserve the original geometric form.

Minor local adjustments were required to maintain a vertical clearance of 2.0 m between the upper and lower halves, but these do not affect the global shape of the structure. Overall, the revised design preserves the characteristic appearance and layout of the Seasaw, with only minor visual changes compared to the original concept.

12. Comparison of flax and glass fibre composites

The Seasaw is currently designed using flax fibre composite. However, it is relevant to explore whether a glass fibre composite alternative could offer advantages or disadvantages from a structural perspective. Glass fibre composites are generally stiffer than flax fibre composites, which may allow for lower required plate thicknesses.

To evaluate this trade-off, a comparative Seasaw design using glass fibre composite will be developed. In this analysis, the thickness of each structural component will be designed and assessed, together with key performance indicators such as stability, deflection, eigenfrequencies and modal shapes. The material properties of the glass fibre composite are provided in Appendix B.

12.1 Design in glass fibre composite

The design of the flax fibre version will be used as a basis. The cross-section height of the revised design will be used and the flange width of the C-shaped girder will be, for a first estimate, 100 mm. As a first estimate for the thicknesses of the different components in the Seasaw, the values from the flax fibre composite design will be scaled. This scaling is based on the relative stiffness of the two materials, since stiffness is the governing parameter in the structural design of the Seasaw.

The modulus ratio is given by:

$$\frac{E_{x,flax\ composite}}{E_{x,glass\ composite}} = \frac{21.1}{37.2} \approx 0.6$$

Since glass fibre has a higher Young's modulus than flax fibre, the required thicknesses can be reduced accordingly. Therefore, the initial glass fibre design is obtained by multiplying the flax fibre thicknesses by approximately 0.6 as a first approximation.

12.1.1 Thickness structure different components

The plate thicknesses were determined by multiplying the thicknesses of the flax fibre design by a factor of 0.6 and selecting a laminate configuration with a thickness equal to or slightly greater than the calculated value, while maintaining the same stacking sequence as the flax fibre design. For the top plate, only the face thickness was modified. The original face thickness of 27.07 mm was reduced to approximately 16.24 mm, the adopted face thickness is 19.20 mm for both the top and bottom faces.

The resulting thicknesses of all structural components are presented in Table 65. The corresponding laminate configurations and RFEM input data are provided in Appendix Z.

Component	Flax fibre version thickness [mm]	Flax fibre version Layer direction percentages	Glas fibre version thickness [mm]	Glass fibre version Layer direction percentages
Support plates set 1 and set 2	9.10	Direction 0°: 25.00% Direction -45°: 25.00% Direction +45°: 25.00% Direction 90°: 25.00%	5.76	Direction 0°: 25.00% Direction -45°: 25.00% Direction +45°: 25.00% Direction 90°: 25.00%
Support plates set 3 without plate next to arch	30.33	Direction 0°: 25.00% Direction -45°: 25.00% Direction +45°: 25.00% Direction 90°: 25.00%	19.20	Direction 0°: 25.00% Direction -45°: 25.00% Direction +45°: 25.00% Direction 90°: 25.00%
Support plates set 3 with plate next to arch	51.57	Direction 0°: 25.00% Direction -45°: 25.00% Direction +45°: 25.00% Direction 90°: 25.00%	30.72	Direction 0°: 25.00% Direction -45°: 25.00% Direction +45°: 25.00% Direction 90°: 25.00%
Support plates set 4	15.17	Direction 0°: 25.00% Direction -45°: 25.00% Direction +45°: 25.00% Direction 90°: 25.00%	9.60	Direction 0°: 25.00% Direction -45°: 25.00% Direction +45°: 25.00% Direction 90°: 25.00%
Arch plate	35.23	Direction 0°: 51.16% Direction -45°: 16.28% Direction +45°: 16.28% Direction 90°: 16.28%	23.52	Direction 0°: 50.82% Direction -45°: 16.39% Direction +45°: 16.39% Direction 90°: 16.39%
Top side plate	35.23	Direction 0°: 51.16% Direction -45°: 16.28% Direction +45°: 16.28% Direction 90°: 16.28%	23.52	Direction 0°: 50.82% Direction -45°: 16.39% Direction +45°: 16.39% Direction 90°: 16.39%
Bottom side plate	35.23	Direction 0°: 51.16% Direction -45°: 16.28% Direction +45°: 16.28% Direction 90°: 16.28%	23.52	Direction 0°: 50.82% Direction -45°: 16.39% Direction +45°: 16.39% Direction 90°: 16.39%
Bottom plate	40.60	Direction 0°: 62.50% Direction -45°: 12.50% Direction +45°: 12.50% Direction 90°: 12.50%	26.88	Direction 0°: 62.50% Direction -45°: 12.50% Direction +45°: 12.50% Direction 90°: 12.50%
C-shaped girders	21.33	Direction 0°: 25.00% Direction -45°: 25.00% Direction +45°: 25.00% Direction 90°: 25.00%	13.44	Direction 0°: 25.00% Direction -45°: 25.00% Direction +45°: 25.00% Direction 90°: 25.00%
Top plate	129.14	Top and bottom face: Direction 0°: 62.50% Direction -45°: 12.50% Direction +45°: 12.50% Direction 90°: 12.50% H_{core}: 75 mm	113.40	Top and bottom face: Direction 0°: 62.50% Direction -45°: 12.50% Direction +45°: 12.50% Direction 90°: 12.50% H_{core}: 75 mm
Stiffener plates	9.10	Direction 0°: 25.00% Direction -45°: 25.00% Direction +45°: 25.00% Direction 90°: 25.00%	5.76	Direction 0°: 25.00% Direction -45°: 25.00% Direction +45°: 25.00% Direction 90°: 25.00%

Table 65: New thicknesses for glass fibre design

12.2 Static analysis

The glass fibre design is evaluated using the same ultimate limit state (ULS) and serviceability limit state (SLS) procedures as those applied to the flax fibre design.

12.2.1 Ultimate limit state

The conversion factor and partial material factor are the same as for flax fibre. The factors are:

- Conversion factor: 0.81
- Partial material factor: 1.38

Unity checks

The structural verification of the different laminate components was performed using the adopted material stress limits. All investigated components satisfy the stress criteria, with unity checks below 1.0. The highest unity checks are found for the arch plate under compressive stress in the y-direction (UC = 0.88), the support plate adjacent to the arch plate under compressive stress in the x-direction (UC = 0.87), and the bottom plate under compressive stress in the x-direction (UC = 0.87). The bottom side plate reaches a maximum UC of 0.85 for compressive stress in the x-direction, while the remaining components have lower unity checks. The detailed stress limits and unity checks are provided in Appendix AA.

Flange design

The required flange widths are determined from the internal force , the shear flow, obtained from the finite element analysis. The shear flow at the edges of the plates is divided by the allowable adhesive shear stress of 1 MPa to determine the minimum flange width required for the bonded connection. For the support plates, the highest shear flow occurs in the support plate adjacent to the arch plate, resulting in a required flange width of 350 mm. The remaining support plates have a lower maximum shear flow, resulting in a required flange width of 150 mm. For the C-shaped girders, a required flange width of 300 mm is obtained and for the stiffener plates, a required flange width of 120 mm is obtained. The shear-flow distributions and flange-width calculations are provided in Appendix AA.

Stability of the structure

A linear stability analysis was performed in RFEM to evaluate the global and local buckling behaviour of the glass fibre structure and to determine the critical buckling modes and corresponding load factors. The analysis was carried out using the eigenvalue method with the following settings:

- Stability analysis type: Eigen values method (linear)
- Number of lowest eigenvalues: 40
- Option I: Consider favourable effects due to tension

The following ultimate limit state load combination was used for the analysis:

$$1.35 * LC1 + 1.35 * LC2 + 1.35 * LC3 + 0.54 * LC4 + 0.45 * LC5 + 0.45 * LC6 + 0.45 * LC7$$

This load combination was selected because the traffic load is the governing variable action. Load case LC3, in which the entire structure is subjected to the pedestrian traffic load, was therefore taken as the leading variable load. To be conservative, several critical buckling modes with load factors greater than 1.0 were also evaluated in case the analysed load combination was not the governing one.

The results of the stability analysis are presented in Appendix BB. A selection of some relevant results is given in Table 66. The critical buckling modes are characterised by local buckling of the C-shaped girders near the supports, together with local buckling of the adjacent stiffener plates. The

corresponding critical load factors are relatively close to each other, indicating that the region around the supports is particularly sensitive to buckling. The lowest critical load factor is 0.447 and there are 21 critical load factors below 1.0.

The highest determined critical load factor is 1.236. At this load level, buckling is limited to local buckling of the C-shaped girders and the adjacent stiffener plates near the supports except for critical load factor 1.232. There the buckling is observed in a stiffener plate above the connection. No global buckling modes are observed, indicating that local instability governs the buckling behaviour of the structure.

Mode	Critical load factor	Buckling shape or buckling location
1	0.447	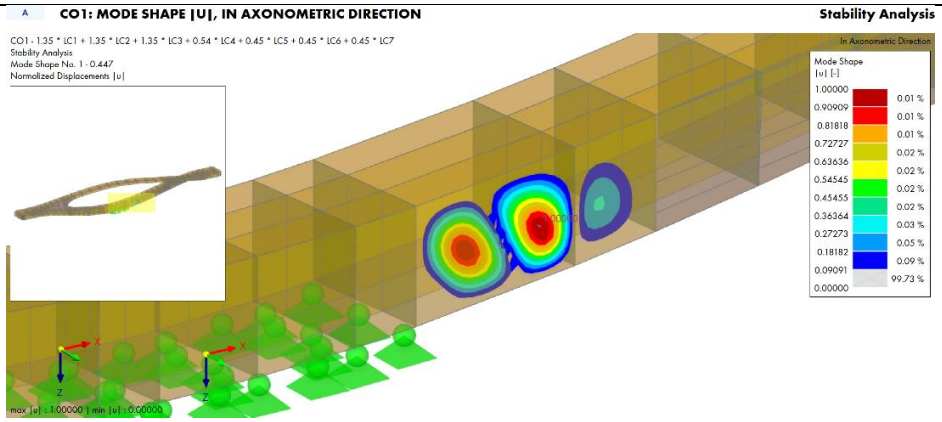 Similar buckling mode as the flax fibre design with critical load factor 0.562
2	0.478	Location: next to support Similar buckling mode as the flax fibre design with critical load factor 0.601
3	0.569	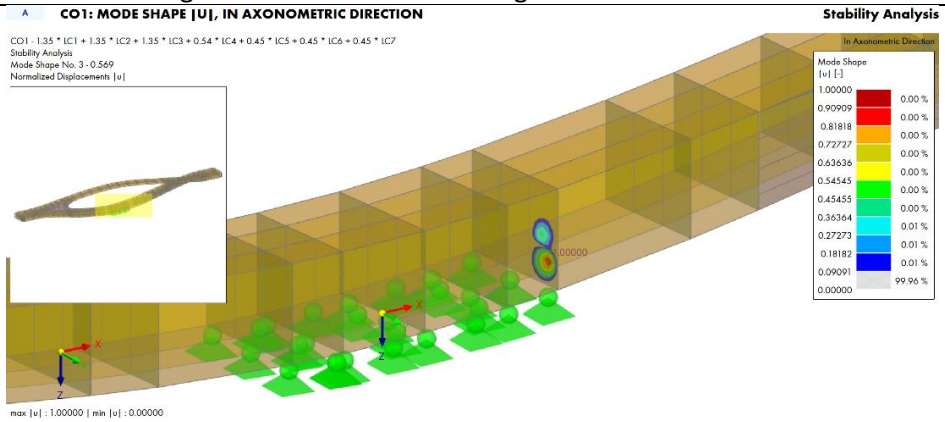
4	0.588	Location: next to support in C-shaped girder Similar buckling mode as the flax fibre design with critical load factor 0.740
39	1.232	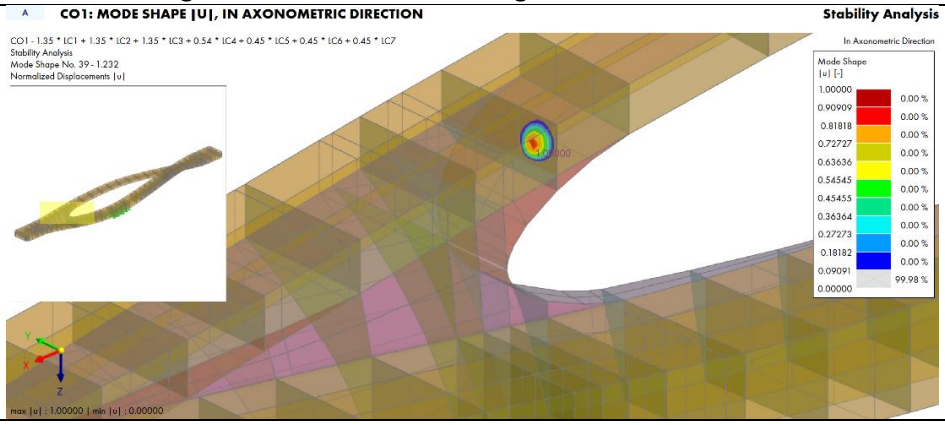

Table 66: Buckling shapes/location and critical load factors of the glass fibre design

Maximum creep stress check

The maximum stresses under the quasi-permanent load combination are verified against the maximum allowable stress due to creep, as determined in Appendix CC. For a design life of 50 years, the maximum allowable stress is 70.6 N/mm². The design is considered satisfactory when the calculated stresses remain below this value. The corresponding reserve factor is determined as the ratio of the allowable stress to the calculated stress.

The maximum absolute stress in both the x- and y-directions under the quasi-permanent load combination is 30 N/mm² and occurs adjacent to the supports. Over the majority of the structure, the maximum absolute stress is approximately 18 N/mm².

The corresponding reserve factors are:

- 2.35 for the maximum stress near the supports, $\frac{70.6}{30}$
- 3.92 for the majority of the structure, $\frac{70.6}{18}$

Both stress levels remain well below the maximum allowable creep stress, demonstrating that the glass fibre design satisfies the long-term strength requirements for the specified 50-year design life.

12.2.2 Serviceability limit state

Chapter 5.2.5 explains how the deflections are determined.

Characteristic

The maximum allowable deflections for the characteristic load combination are defined as follows:

- Top half: $w_2 + w_3 \leq \frac{l_{span}}{150} = \frac{25000}{150} = 166.7\ mm$
- Side part: $w_2 + w_3 \leq \frac{2*l_{cantiliver}}{150} = \frac{2*9000}{150} = 120\ mm$
- Bottom half: $w_2 + w_3 \leq \frac{2*l_{cantiliver}}{150} = \frac{2*16000}{150} = 213.3\ mm$

The deflections of w_2 without creep factor are shown in Figure 91 and the deflections of w_3 are shown in Figure 90.

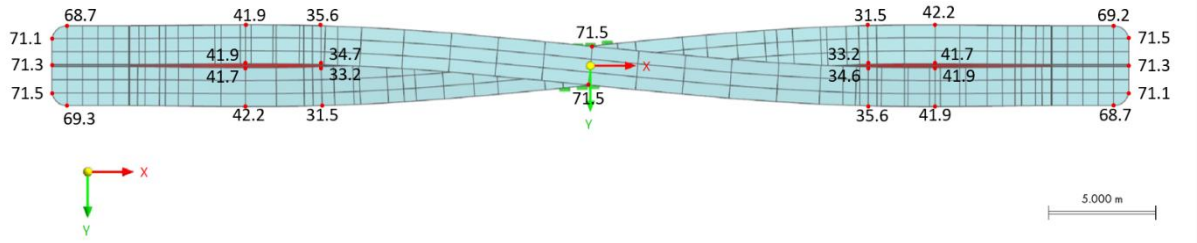

Figure 91: Deflections of w_2 without creep factor at multiple locations in mm

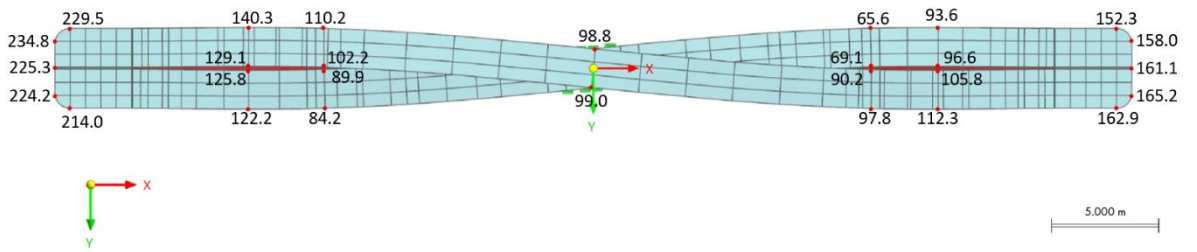

Figure 90: Deflection of w_3 at multiple locations in mm

The table below presents the calculated deflections for each part of the structure and compares them with the maximum allowable deflection, $w_2 + w_3$. The creep factor is given in Appendix CC.

Locations	Deflection w_2 without creep factor	Deflection w_2 with creep factor	Deflection w_3	Total deflection $w_2 + w_3$	Max allowed deflection	Check
Top half left	$71.5 - 34.7 = 36.8$	$36.8 * 1.32 = 48.6$	$99.0 - 102.2 = -3.2$	45.4	166.7	Okay
Top half right	$71.5 - 34.6 = 36.9$	$36.9 * 1.32 = 48.7$	$99.0 - 90.2 = 8.8$	57.5	166.7	Okay
Side part left	$71.3 - 41.7 = 29.6$	$29.6 * 1.32 = 39.1$	$225.3 - 125.8 = 99.5$	138.6	120	Not okay
Side part right	$71.3 - 41.7 = 29.6$	$29.6 * 1.32 = 39.1$	$161.1 - 96.6 = 64.5$	103.6	120	Okay
Bottom half left	$41.7 - 0 = 41.7$	$41.7 * 1.32 = 55.0$	$125.8 - 0 = 125.8$	180.8	213.3	Okay
Bottom half right	$41.7 - 0 = 41.7$	$41.7 * 1.32 = 55.0$	$96.6 - 0 = 96.6$	151.6	213.3	Okay

Table 67: Characteristic deflection check

Almost all calculated deflections are below the recommended allowable limits at the investigated locations. However, the predicted deflections are still considered to provide an acceptable level of user comfort. A significant proportion of the creep deformation develops during the first days after loading. Furthermore, creep-induced deflection occurs gradually over time and is therefore not perceptible to users during usage of the structure.

The characteristic deflection w_3 due to variable loading, which represents the deformation that is noticeable during use, satisfies the recommended maximum deflection limit in all cases. Consequently, the predicted deformations are still considered acceptable from a user comfort perspective.

Because the given deflections result from the combination of a traffic load applied on the left side of the bridge and a contribution from the wind load, an additional analysis was performed considering only the traffic load acting on the middle section of the top half of the structure. The resulting deflections are presented in the table below. None of these deflections exceed the recommended allowable limit, with a considerable margin, indicating that the top half of the structure is sufficiently stiff.

Deflections at multiple locations in mm					
	Deflection in the middle	Deflection at $x = \pm 12.5$	Deflection w_3	Max allowed deflection	Check
Top half left	50.9	19.9	$50.9 - 19.9 = 31.0$	166.7	Okay
Top half right	50.9	24.2	$50.9 - 24.2 = 26.7$	166.7	Okay

Table 68: Deflection due to traffic load on the middle part of the top half

Frequent

The frequent combination is used for the local deflection in the top plate. The top plate has a span between girders of 484 mm. The maximum allowed deflection in the top deck plate is:

- $w_3 \leq \frac{l_{deckplate}}{750} = \frac{484}{750} = 0.65\ mm$

The highest deflection comes from the highest combination for w_3. w_3 includes only one load with ψ_1. The traffic load is the highest variable load and for local effect the concentrated point load of 7 kN should be used. To determine the local deflection part of the plate is modelled with a span of 484 mm and a width of 1 meter. The plate is assumed to be simply supported as a simplification. The load of 7 kN is applied in the middle for load case 2: concentrated traffic load and the result combination is:

$$0.8 * LC2$$

There is a mesh used of 0.02 mm. This mesh size was also halved and the results did not change. The schematic representation in RFEM is shown in Figure 92.

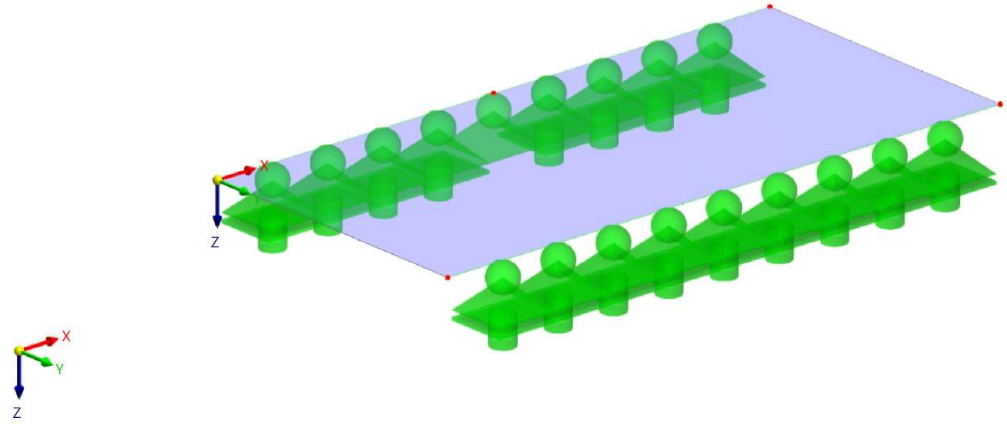

Figure 92: Model top deck plate RFEM

The result is shown in Figure 93. The maximum deflection is 0.1 mm which is smaller than the maximum allowed deflection. The stiffness of the top plate is high enough for the frequent serviceability constraint.

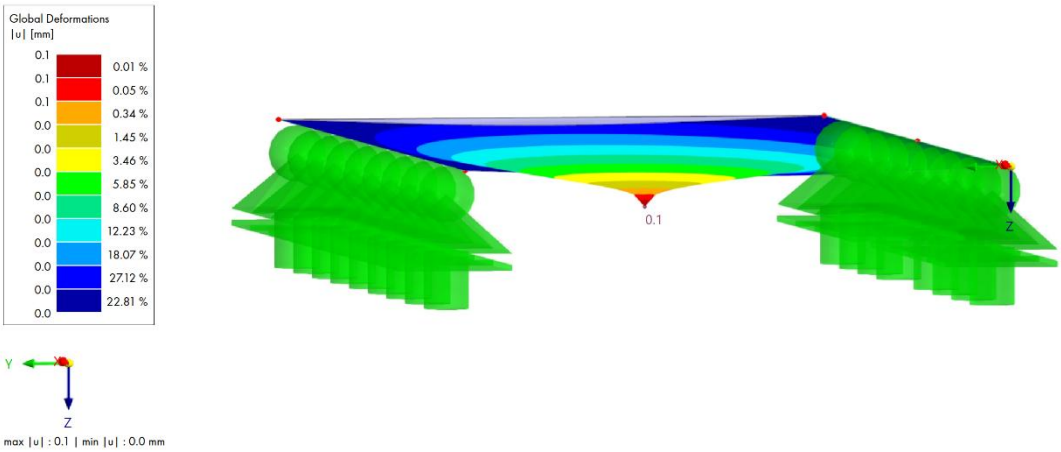

Figure 93: Deflection top deck plate

Quasi-permanent

The maximum deflections of the structure for quasi-permanent combinations are:

- Top half: $w_{max} \leq \frac{l_{span}}{250} = \frac{25000}{250} = 100\ mm$
- Side part: $w_{max} \leq \frac{2*l_{cantiliver}}{250} = \frac{2*9000}{250} = 72\ mm$
- Bottom half: $w_{max} \leq \frac{2*l_{cantiliver}}{250} = \frac{2*16000}{250} = 128\ mm$

The deflections of w_1 and the deflections of w_2 without creep factor are shown in Figure 94, the deflections are for both the same as shown in the plots in Appendix U.

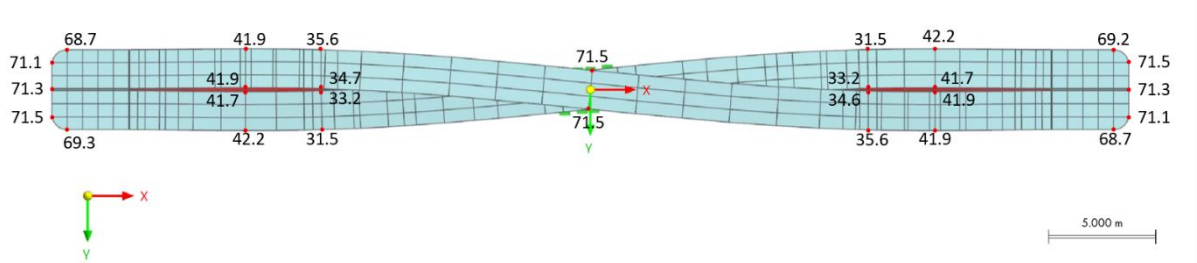

Figure 94: Deflection of w_1 and w_2 without creep factor at multiple locations in mm

The table below presents the calculated deflections for each part of the structure and compares them with the maximum allowable deflection, w_{max}. w_{max} is the deflection of $w_1 + w_2$ minus the pre-camber.

Deflections at multiple locations in mm					
Locations	Deflection w_1	Deflection w_2 without creep factor	Deflection w_2 with creep factor	Total deflection $w_1 + w_2$	Max allowed deflection w_{max}
Top half left	$71.5 - 34.7 = 36.8$	$71.5 - 34.7 = 36.8$	$36.8 * 1.32 = 48.6$	85.4	100
Top half right	$71.5 - 34.6 = 36.9$	$71.5 - 34.6 = 36.9$	$36.9 * 1.32 = 48.7$	85.6	100
Side part left	$71.3 - 41.7 = 29.6$	$71.3 - 41.7 = 29.6$	$29.6 * 1.32 = 39.1$	68.7	72
Side part right	$71.3 - 41.7 = 29.6$	$71.3 - 41.7 = 29.6$	$29.6 * 1.32 = 39.1$	68.7	72
Bottom half left	$41.7 - 0 = 41.7$	$41.7 - 0 = 41.7$	$41.7 * 1.32 = 55.0$	96.7	128
Bottom half right	$41.7 - 0 = 41.7$	$41.7 - 0 = 41.7$	$41.7 * 1.32 = 55.0$	96.7	128

Table 69: Quasi-permanent deflection check

All total deflection $w_1 + w_2$ are below the maximum allowed deflection w_{max}. Therefore, no pre-camber is required for the glass fibre design.

12.3 Modal analysis

The same analysis settings as those used for the modal analysis of the flax fibre design were adopted. The calculated natural frequencies were compared with the critical frequency ranges specified for pedestrian bridges. When a natural frequency falls within one of these critical ranges, a further assessment of pedestrian comfort is required. In addition, for frequencies within the critical range for intentional excitation, an ultimate limit state (ULS) verification should be performed.

Vibration type	Critical frequency range
Vertical vibrations	Pedestrian comfort: $1.25 < natural\ frequency < 2.3$ Jogger comfort: $1.9 < natural\ frequency < 3.5$ ULS: $1.7 < natural\ frequency < 3.0$
Longitudinal vibrations	Pedestrian comfort: $1.25 < natural\ frequency < 2.3$
Lateral vibrations	Pedestrian comfort: $0.5 < natural\ frequency < 1.2$
Torsional vibrations	Pedestrian comfort: $0.5 < natural\ frequency < 1.2$

Table 70: Critical frequency ranges, obtained from NEN-EN 1990

The table below summarises the calculated modal properties and indicates whether each natural frequency falls within a critical frequency range. The corresponding mode shapes are presented in Appendix DD. Mode shape 1 is shown in Figure 95.

Mode number	Eigenvalue $\lambda\ [1/s^2]$	Angular frequency $\omega\ [rad/s]$	Natural frequency $f\ [Hz]$	Natural period $T\ [s]$	Vibration type	Verification critical frequency range
1	34.057	5.836	0.929	1.077	Vertical	Outside range
2	39.510	6.286	1.000	1.000	Torsional	Inside range
3	51.226	7.157	1.139	0.878	Lateral	Inside range
4	150.437	12.265	1.952	0.512	Vertical	Inside range
5	174.985	13.228	2.105	0.475	Lateral	Outside range
6	542.528	23.292	3.707	0.270	Torsional	Outside range
7	971.614	31.171	4.961	0.202	Vertical	Outside range
8	1495.898	38.677	6.156	0.162	Torsional	Outside range
9	1989.397	44.603	7.099	0.141	Vertical	Outside range
10	2063.060	45.421	7.229	0.138	Torsional	Outside range

Table 71: Modes with modal properties of glass fibre design

The natural frequencies of modes 2, 3 and 4 fall within the critical frequency ranges and therefore require a detailed pedestrian comfort assessment. The natural frequency of mode 4 is also just above the lower bound of the critical frequency ranges for jogger comfort and intentional excitation (ULS). The remaining modes lie outside the critical frequency ranges and do not require further dynamic verification.

A detailed pedestrian comfort assessment is beyond the scope of this study and should be carried out during a later stage of the design process. Nevertheless, the relatively low natural frequencies indicate that the bridge is likely to be susceptible to pedestrian-induced vibrations. It is therefore expected that vibration mitigation measures, such as tuned mass dampers (TMDs) (see Figure 88 and Figure 89), will be required to satisfy the applicable comfort criteria in the final design.

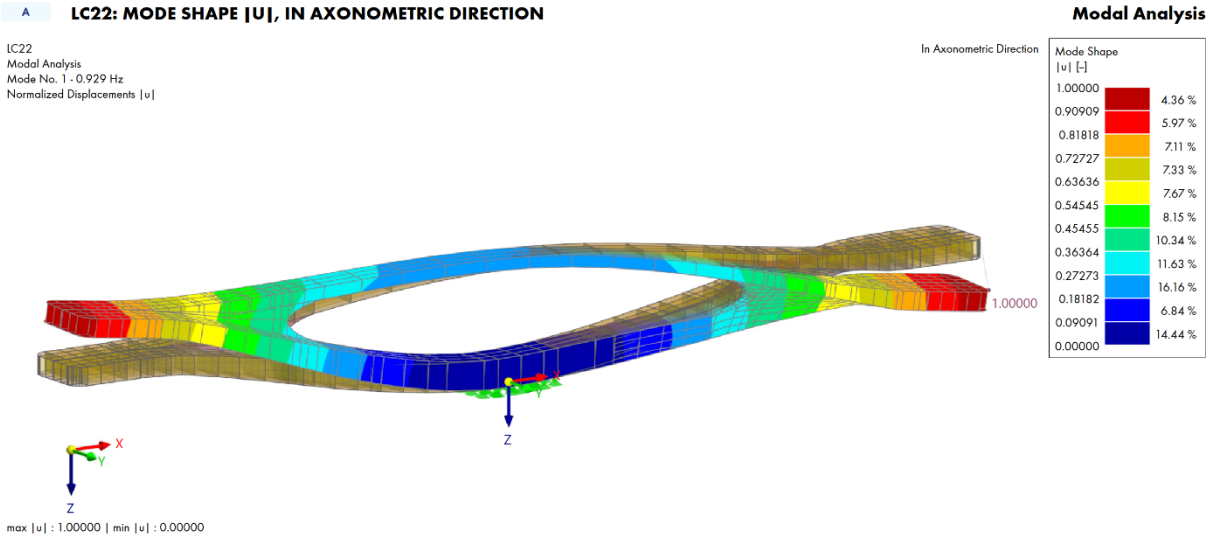

Figure 95: Mode shape 1 of the glass fibre design

12.4 Comparison

This section compares the structural performance of the flax fibre and glass fibre designs. The comparison focuses on the differences in plate thicknesses, self-weight, stability behaviour, deflections, and dynamic characteristics. The aim is to evaluate the advantages and limitations of replacing the flax fibre composite with a glass fibre composite while maintaining the same overall structural concept. The material properties used for the flax fibre and glass fibre composites are presented in Table 72. The glass fibre composite has a higher longitudinal tensile modulus (E_1), transverse modulus (E_2), and shear modulus (G) than the flax fibre composite, which results in a higher structural stiffness. The implications of these differences for the structural performance are discussed in the following sections.

Material	V_f $[-]$	E_1 $[GPa]$	E_2 $[GPa]$		G $[Gpa]$	ν $[-]$
Flax fibre composite	40%	21.1	$E_{2,low}$ 1.7	$E_{2,high}$ 5.0	1.1	0.33
Glass fibre composite	50%	37.2	11.4		3.4	0.29

Table 72: Material properties flax fibre composite and glass fibre composite

12.4.1 Thickness of the plates

Table 73 compares the plate thicknesses of the flax fibre and glass fibre designs. Most thickness ratios are between 0.60 and 0.70. The ratios are generally slightly higher than 0.60 because the calculated laminate thicknesses for the glass fibre design, $0.6 * t_{plate\ flax\ fibre\ deisgn}$, were rounded up to the nearest feasible stacking sequence while maintaining the same laminate configuration as the flax fibre design.

All unity checks for the glass fibre design are below 1.0, indicating that the selected plate thicknesses satisfy the ultimate limit state requirements. In general, the unity checks are lower than those of the corresponding flax fibre design, suggesting that several components could potentially be further optimized by reducing their thickness while still meeting the design requirements.

Component		Flax fibre version thickness [mm]	Glas fibre version thickness [mm]	Ratio: $\frac{t_{plate\ glass\ fibre\ deisgn}}{t_{plate\ flax\ fibre\ deisgn}}$
Support plates set 1 and set 2		9.10	5.76	0.633
Support plates set 3 without plate next to arch		30.33	19.20	0.633
Support plates set 3 with plate next to arch		51.57	30.72	0.596
Support plates set 4		15.17	9.60	0.633
Arch plate		35.23	23.52	0.668
Top side plate		35.23	23.52	0.668
Bottom side plate		35.23	23.52	0.668
Bottom plate		40.60	26.88	0.662
C-shaped girders		21.33	13.44	0.630
Top plate	Total thickness	129.14	113.40	0.878
	Thickness face	27.07	19.20	0.709
	Thickness core	75	75	1.000
Stiffener plates		9.10	5.76	0.633

Table 73: Comparison of the thicknesses of the plates

12.4.2 Self-weight

The density of the flax fibre composite is:

$$\rho_{com} = V_f \rho_f + \left(100\% - V_f\right) * \rho_r = 0.4 * 1500 + (1 - 0.4) * 1200 = 1320\ kg/m^3$$

The density of the glass fibre composite is:

$$\rho_{com} = V_f \rho_f + \left(100\% - V_f\right) * \rho_r = 0.5 * 2550 + (1 - 0.5) * 1200 = 1875\ kg/m^3$$

The calculated self-weights of both designs are presented in Table 74. Although the density of the glass fibre composite is considerably higher than that of the flax fibre composite, the total self-weight of the glass fibre design is 11.08 kN lower. This reduction is achieved because the glass fibre design requires significantly thinner plates, resulting in a lower overall material volume.

The ratio between the densities of the flax fibre and glass fibre composites is:

$$\frac{\rho_{com,flax\ fibre}}{\rho_{com,glass\ fibre}} = \frac{1320}{1875} = 0.7$$

This density ratio is slightly higher than the thickness ratios adopted for most plates (approximately 0.60–0.67). As a result, despite the higher material density, the reduced plate thicknesses lead to a lower overall self-weight of the glass fibre design.

Self-weight flax fibre design [kN]	Self-weight glass fibre design [kN]
389.61	378.53

Table 74: Self-weight comparison

12.4.3 Stability

The critical load factors of the glass fibre design are lower than those of the flax fibre design. The glass fibre design has 21 critical load factors below 1.0, compared to 9 for the flax fibre design. Several buckling modes are similar between the two designs; for example, mode 1 is identical for both designs.

The lower critical load factors of the glass fibre design can be explained by the reduced plate thicknesses. Although the stiffness of the glass fibre composite is higher, the buckling resistance is strongly influenced by the plate thickness, which has a cubic relationship with the critical buckling load. Therefore, the reduction in thickness has a larger negative effect on the buckling resistance than the increase in material stiffness provides.

12.4.4 Deflections

The glass fibre design shows lower deflections compared to the flax fibre design for all investigated load combinations. This is mainly due to the higher stiffness of the glass fibre composite, which allows for a thinner but stiffer structural design.

For the characteristic load combination, the glass fibre design satisfies the allowable deflection limits at almost all investigated locations. Only the left side part slightly exceeds the recommended limit, with a deflection of 138.6 mm compared to the allowable 120 mm. In contrast, the flax fibre design exceeds the allowable limits at four of the six investigated locations. The noticeable deflection caused by the variable load, w_3, remains within the allowable limits for the glass fibre design, while the flax fibre design has a local exceedance at the left side part.

For the quasi-permanent load combination, all calculated deflections of the glass fibre design remain below the allowable limits without pre-camber, meaning that no pre-camber is required. The flax fibre design exceeds the limits at all investigated locations without pre-camber. Although a pre-camber enables the flax fibre design to satisfy the allowable limits, the glass fibre design achieves superior long-term deformation behaviour without requiring pre-camber.

The same cross-sectional height was used for both designs to allow a direct comparison. However, due to the lower deflections and higher stiffness of the glass fibre design, the cross-sectional height could potentially be reduced compared to the current design. This indicates that the glass fibre design could be further optimized by reducing the structural height while still satisfying the serviceability requirements. The cross-sectional height of the preliminary design may potentially be sufficient for the glass fibre design.

A comparison of the maximum deflections under individual load cases is presented in Table 75. The glass fibre design shows lower deflections for all considered loading directions. The reduction in maximum deflection varies between 26.1% and 29.4% compared to the flax fibre design. The largest reduction occurs for the load in the *x*-direction, while the smallest reduction occurs for the load in the *z*-direction. This confirms the increased stiffness of the glass fibre design, resulting in improved deformation behaviour.

Loads	Maximum deflection flax fibre design [mm]	Maximum deflection glass fibre design [mm]	Relative difference $\frac{\lvert w_{glass} - w_{flax} \rvert}{w_{flax}} * 100\%$	Location
1 kN/m^2 in +z-direction	31.4	23.2	26.1%	Middle top
1 kN/m^2 in +y-direction	40.9	28.9	29.3%	End right side
1 kN/m^2 in +x-direction	45.2	31.9	29.4%	End left side

Table 75: Comparison of maximum deflections for individual load cases

12.4.5 Eigenfrequencies and modal shapes

Table 76 compares the first ten natural frequencies and corresponding mode shapes of the flax fibre and glass fibre designs. The glass fibre design exhibits consistently higher natural frequencies than the flax fibre design, indicating an increase in global stiffness. The corresponding mode shapes remain essentially unchanged. Minor differences are limited to the plotting direction of some mode shapes and the interchange in the order of modes 4 and 5, and modes 9 and 10, which have very similar frequencies.

Mode number	Flax fibre design natural frequency $f\ [Hz]$	Glass fibre design natural frequency $f\ [Hz]$	Comparison mode shapes
1	0.773	0.929	The mode shapes are identical.
2	0.827	1.000	The mode shapes are identical.
3	0.937	1.139	The mode shapes are similar but are plotted in the opposite direction.
4	1.656	1.952	Mode shape 4 of the flax fibre design closely corresponds to mode shape 5 of the glass fibre design but is plotted in the opposite direction.
5	1.669	2.105	Mode shape 5 of the flax fibre design closely corresponds to mode shape 4 of the glass fibre design but is plotted in the opposite direction.
6	3.137	3.707	The mode shapes are similar but are plotted in the opposite direction.
7	4.190	4.961	The mode shapes are identical.
8	4.955	6.156	The mode shapes are identical.
9	5.792	7.099	Mode shape 9 of the flax fibre design closely corresponds to mode shape 10 of the glass fibre design but is plotted in the opposite direction.
10	5.991	7.229	Mode shape 10 of the flax fibre design closely corresponds to mode shape 9 of the glass fibre design but is plotted in the opposite direction.

Table 76: Comparison of natural frequencies and modal shapes

13. Eurocode wind loads against RWIND wind loads

Although the Seasaw is not a bridge, the Eurocodes for bridges are used to determine the design requirements and the design wind loads. Because of the unique geometry of the Seasaw, the applicability of these Eurocode wind load provisions is assessed using wind simulations in RWIND, integrated within RFEM. The simulations are performed for the preliminary design of the Seasaw.

The assessment is carried out in three steps. First, a test structure is analysed to assess the selected RWIND modelling approach. The full wind analysis of the test structure, including the Eurocode loads and the comparison with the RWIND results, is provided in Appendix EE. Next, the standalone Seasaw, without a modelled dike, is analysed for two wind directions, see Figure 96. Finally, the analysis is repeated for the Seasaw with a modelled dike for one wind direction, see Figure 97, to investigate the influence of the dike representation on the calculated wind loading. The simulation settings for the Seasaw wind simulations are provided in Appendix FF while the Eurocode wind loads used for comparison are presented in Appendix HH.

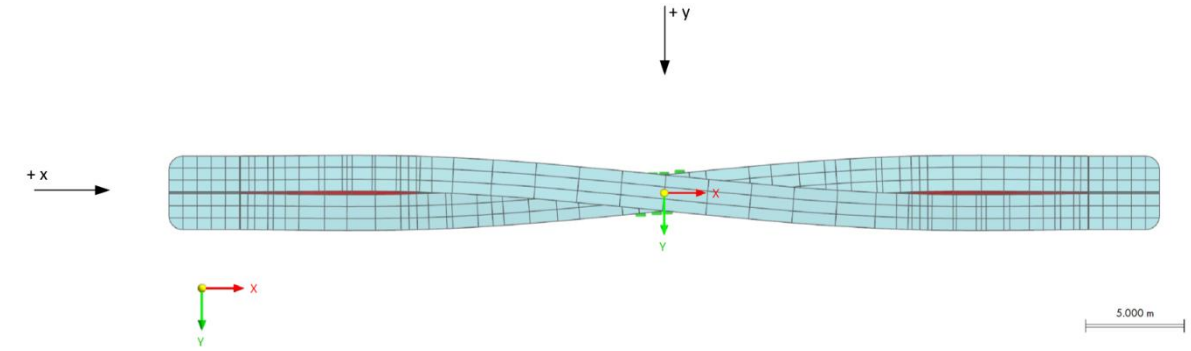

Figure 96: Wind directions for simulation without modelled dike

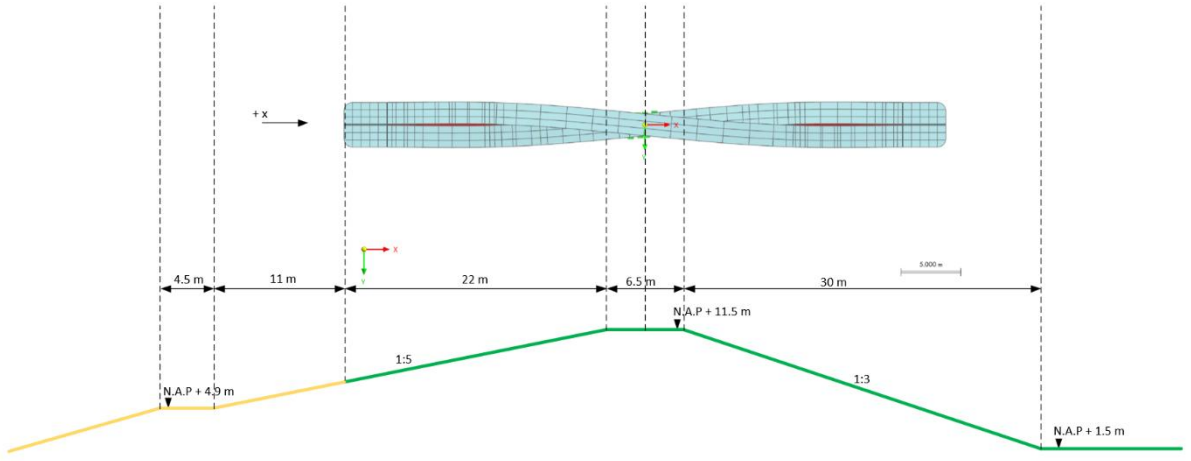

Figure 97: Wind directions for simulation with modelled dike

13.1 Testing of RWIND with simple structure

Before applying RWIND to the Seasaw, the modelling approach and selected RWIND settings were checked using a simple structure with a known geometry. The structure is 3 m high, 4 m wide, and 5 m long. The walls, top and bottom plates are made of 50 mm thick C30/45 concrete. The structure is fully clamped at the bottom plate and is shown in Figure 98. The structure is assumed to be located near the coast in Den Helder.

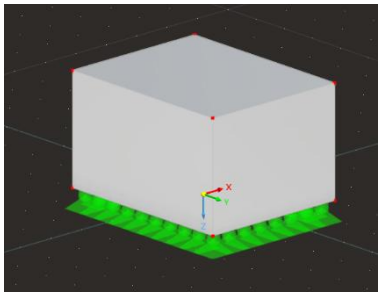

Figure 98: Test structure wind simulation

The wind loads obtained from the RWIND simulation, see Figure 99, were compared with wind loads calculated according to NEN-EN 1991-1-4. The Eurocode calculation was used as a reference, with the wind zones shown in Figure 100. The full wind analysis, including the Eurocode loads and the comparison with the RWIND results, is provided in Appendix EE.

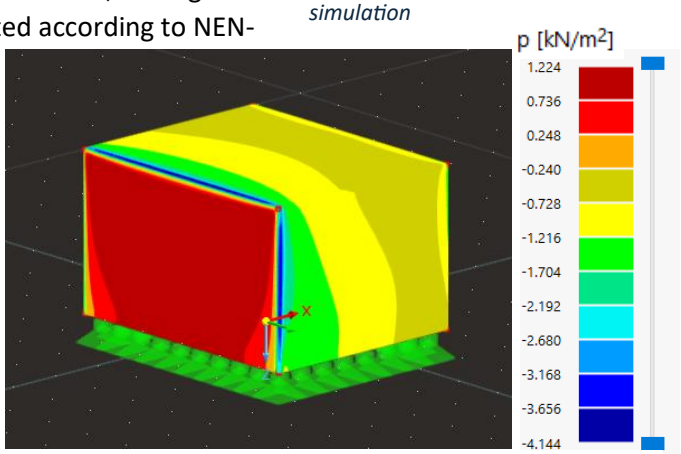

Figure 99: Results test wind simulation

The comparison showed good agreement between the RWIND simulation and the Eurocode for most wind pressure zones. The RWIND simulation produces a more detailed and non-uniform pressure distribution than the simplified pressure distribution assumed by the Eurocode. Nevertheless, the average pressures in zones A, B, D, E, G, and H were close to the corresponding Eurocode values.

The total forces in the x- and y-directions also showed good agreement between the two methods. The total force in the y-direction was approximately zero for both methods, while the difference in the x-direction was only 0.198 kN. This indicates that, for the tested structure, the applied RWIND setup produces global wind forces of the same order of magnitude as the Eurocode calculation.

The largest difference was observed in the z-direction. The RWIND simulation predicted a higher total force than the Eurocode calculation. This difference is attributed primarily to the pressure distribution in zone I and the non-uniform pressure distribution obtained from the numerical simulation compared with the simplified Eurocode approach.

Overall, the comparison provided a check of the selected RWIND modelling approach and the interpretation of its results. The good agreement in the global forces and pressure values provides confidence in the selected RWIND setup as a basis for the subsequent wind-load analysis of the Seasaw.

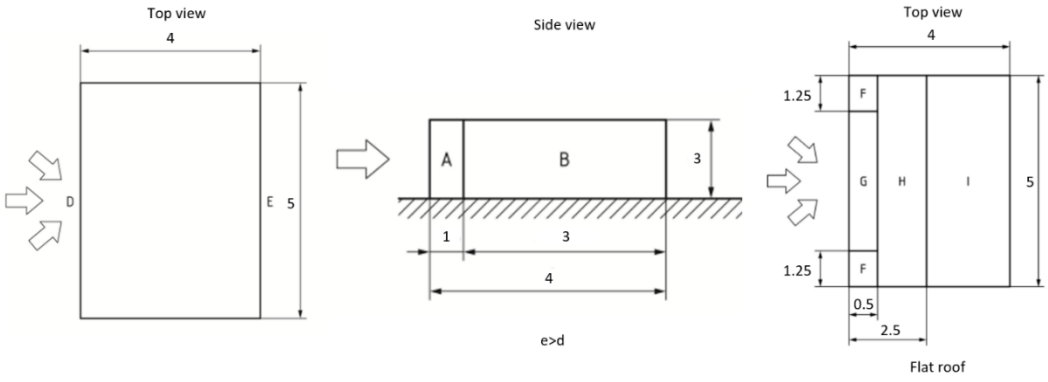

Figure 100: Wind zones Eurocode for e>d and flat roof with lengths in meters

13.2 RWIND simulation Seasaw without modelled dike in x-direction

In this section, wind simulations are performed for the standalone Seasaw structure without a modelled dike, for wind acting in the x-direction. The simulation settings are provided in Appendix FF. First, the simulation results are presented, after which the results are compared with the wind loads obtained from the Eurocode. Both the Eurocode for wind loads on a bridge and on a canopy are considered separately in the comparison and are presented in Appendix HH.

13.2.1 Results of the wind simulations

The simulation configuration is shown in Figure 101. According to the RWIND 3 online manual, a simulation is considered to have converged satisfactorily when the graph of the residual quantity over time no longer changes (or only very little), or it periodically oscillates around a certain mean value. The results indicate that the present simulation satisfies this convergence criterion. (Online Manuals RWIND 3: Troubleshooting, sd)

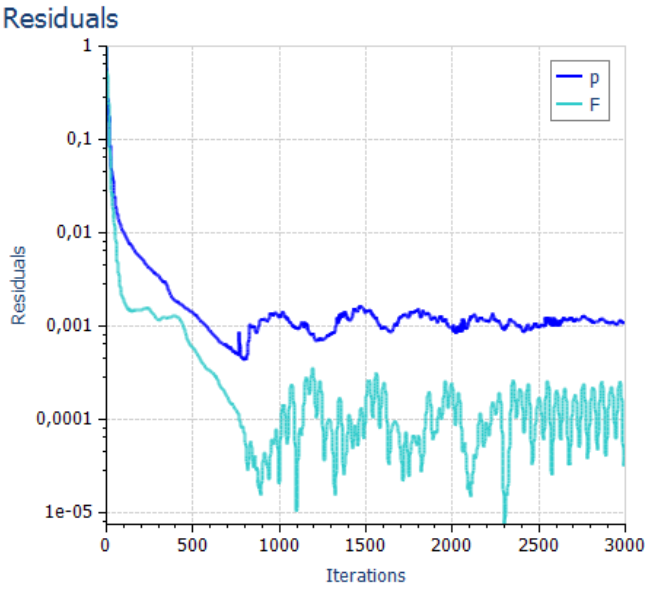

Figure 101: Residuals configurations wind simulation Seasaw x-direction without modelled dike

The streamlines obtained from the simulation are shown in Figure 102.

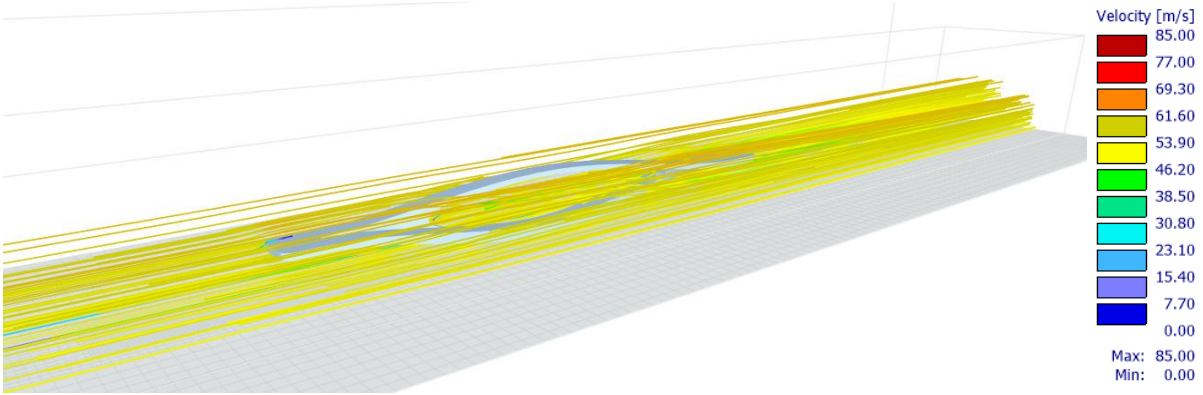

Figure 102: Streamlines wind simulation Seasaw x-direction without modelled dike

The resulting drag forces in the three coordinate directions are presented in Table 77, while the pressure distribution on the structure is shown in Figure 104 and Figure 103.

Wind load component	Value [kN]
Drag force in x	11.169
Drag force in y	4.236
Drag force in z	-1.361
Resultant drag force	12.022

Table 77: Results Seasaw with wind in x-direction without modelled dike

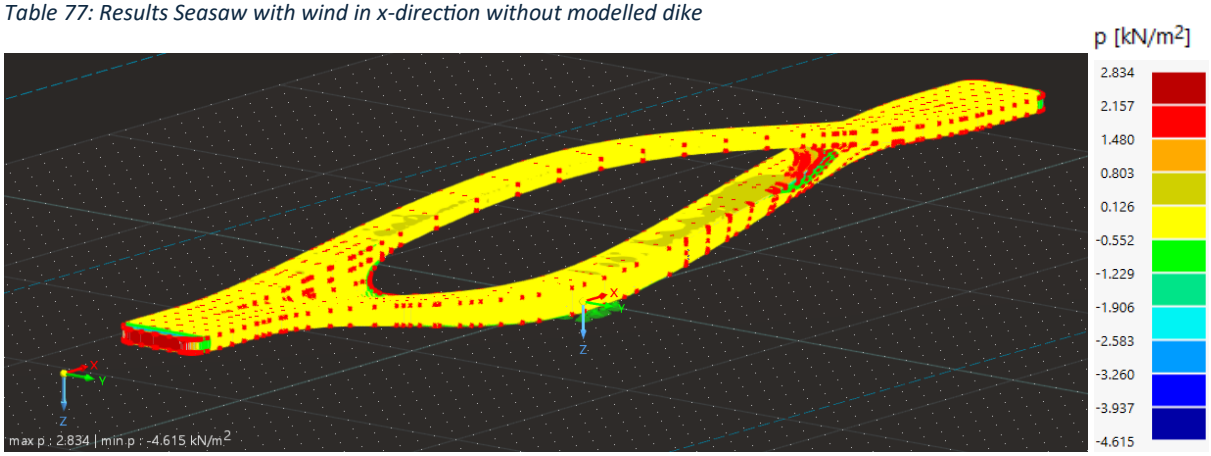

Figure 104: Pressure on front side Seasaw for wind simulation in x-direction without dike

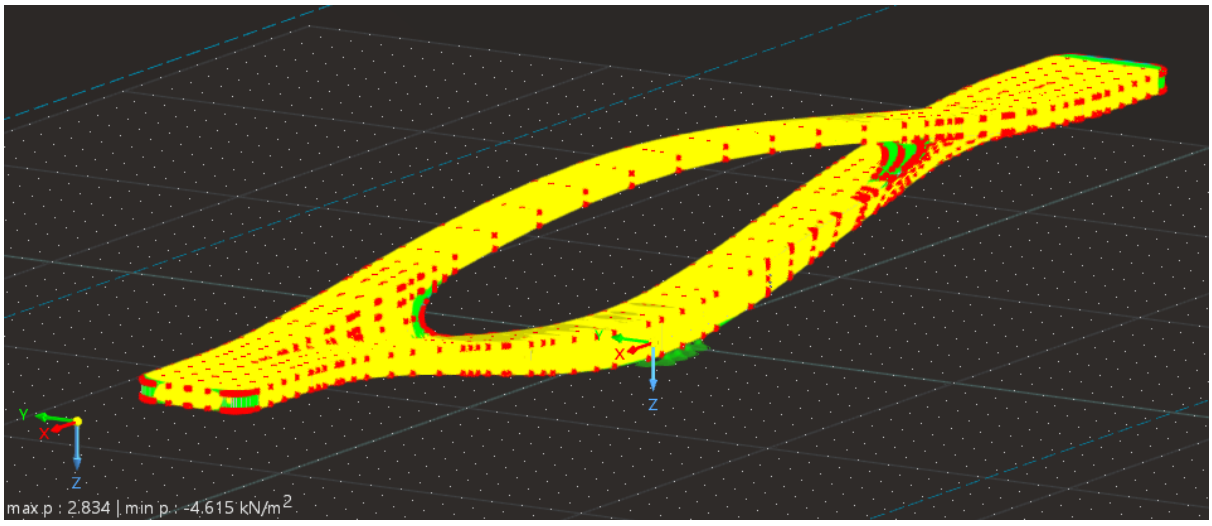

Figure 103: Pressure on back side Seasaw for wind simulation in x-direction without dike

The resulting deformation of the structure under the simulated wind loading is shown in Figure 105.

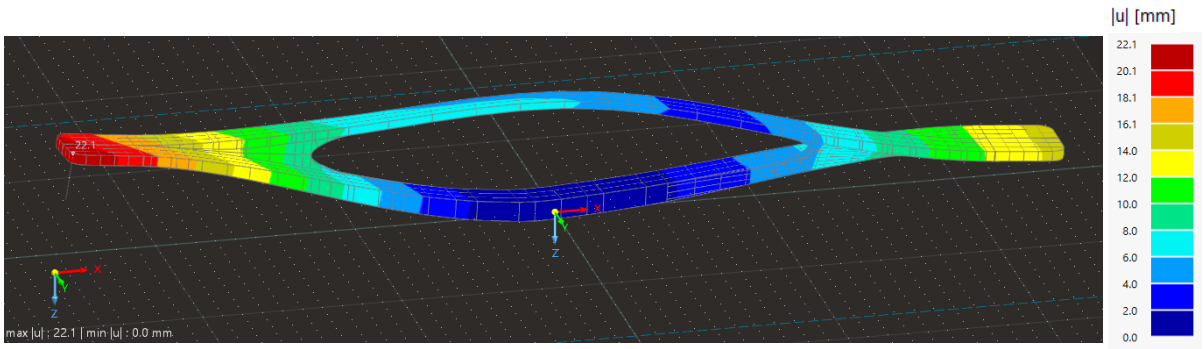

Figure 105: Deformation Seasaw wind simulation in x-direction without dike

The sum of loads and the resultant of reactions obtained from RFEM are given in the table below. The sum of loads represents the total applied wind load on the structural model. The corresponding support forces are equal in magnitude. The resultant of reactions represents the resulting moments of the support reactions. The terminology in this table follows the terminology used in RFEM.

Sum of loads in:	[kN]
X	12.22
Y	4.45
Z	-1.47
Resultant of reactions about:	[kNm]
X	-20.43
Y	-95.67
Z	-2.27

Table 78: The sum of loads and resultant of reactions of the wind simulation in x-direction without modelled dike

A global assessment of the stress distribution, excluding local singularities, resulted in the approximate stress ranges shown in Table 79.

Stress component	Stress range $[N/mm^2]$
σ_x, local x-direction	-2 to +2
σ_y, local y-direction	-1 to +1
τ_{xy}, shear stress	-1 to +1

Table 79: Approximate global stress ranges for the RWIND load case in the x-direction without a modelled dike

13.2.2 Comparison with Eurocode loads

To compare the wind simulation results with the Eurocode load models, the average net pressure was determined for the different deck regions shown in Figure 106. The pressures on the top and bottom surfaces of the deck were used to calculate the net pressure acting on each region. The net pressure determined from the wind simulation acts perpendicular to the local deck surface. Consequently, the direction of the simulated pressure is not necessarily aligned with the global coordinate directions. For the Eurocode bridge load model, the wind load is applied as a global load in the x-direction and may be applied in either the positive or negative x-direction. The Eurocode canopy provisions define net pressures perpendicular to the canopy surface. The canopy provisions define different pressure coefficients for specific zones of the canopy. However, these zones do not correspond directly to the zones identified in the RWIND simulation. Therefore, the overall canopy pressure ranges are used for comparison. No surface roughness factors were applied to the surfaces in the wind simulation and their influence is therefore not included in the present comparison. The results are summarized in Table 80.

Zone	Wind simulation (net pressure) $[kN/m^2]$	Eurocode wind load bridge (load in x-direction) $[kN/m^2]$	Eurocode wind load canopies (net pressure) $[kN/m^2]$	Comparison
A	Approximately: -0.1	+/- 0.371	+0.488 (all φ) -0.854 ($\varphi = 0$) -1.708 ($\varphi = 1$)	The magnitude of the simulated pressure is lower than the Eurocode bridge load and the load is in a different direction. The canopy values are considerably larger in magnitude.
B	Approximately: +0.2 to +0.4	+/- 0.35	+0.488 (all φ) -0.854 ($\varphi = 0$) -1.586 ($\varphi = 1$)	The simulated pressure is of a similar order of magnitude to the Eurocode bridge load, but the load has a different direction. The positive canopy value is also similar, but a bit bigger.
C	Approximately: +0.2 to +0.3	+/- 0.31	+0.488 (all φ) -0.854 ($\varphi = 0$) -1.586 ($\varphi = 1$)	The simulated pressure is of a similar order of magnitude to the Eurocode bridge load, but the load has a different direction. The positive canopy value is also similar, but a bit higher.
D	Approximately: -0.3 to -0.5	+/- 0.31	+0.488 (all φ) -0.854 ($\varphi = 0$) -1.586 ($\varphi = 1$)	The simulated pressure is of a similar order of magnitude to or slightly higher in magnitude than the Eurocode bridge load, but the load has a different direction. The negative canopy values are higher.
E	Approximately: +0.3	+/- 0.35	+0.488 (all φ) -0.854 ($\varphi = 0$) -1.586 ($\varphi = 1$)	The simulated pressure is slightly lower in magnitude than the Eurocode bridge load and the load is in a different direction. The positive canopy value is somewhat higher.
F	Approximately: -0.1	+/- 0.371	+0.488 (all φ) -0.854 ($\varphi = 0$) -1.708 ($\varphi = 1$)	The magnitude of the simulated pressure is lower than the Eurocode bridge load and the load is in a different direction. The canopy values are considerably larger in magnitude.
G	Approximately: -0.5 to -0.7	+/- 0.4	+0.488 (all φ) -0.732 ($\varphi = 0$) -1.708 ($\varphi = 1$)	The simulated pressure is higher in magnitude than the Eurocode bridge load and the load is applied in a different direction. The negative canopy values for $\varphi = 0$ is similar in magnitude.

H	Approximately: -0.3 Next to zone I: -1.2	+/- 0.6	+0.488 (all φ) -0.732 ($\varphi = 0$) -1.708 ($\varphi = 1$)	The simulated pressure varies significantly within the zone. For −0.3 kN/m², the magnitude is lower than the Eurocode bridge load and for −1.2 kN/m², it is considerably higher. The direction of the applied load is also different. The canopy values are considerably larger in magnitude compared to -0.3 kN/m². The magnitude of the pressure next to zone I is in between the values for the different φ.
I	Approximately: +0.2	+/- 0.684	+0.488 (all φ) -0.732 ($\varphi = 0$) -1.708 ($\varphi = 1$)	The simulated pressure is considerably lower in magnitude than the Eurocode bridge load and the load is applied in a different direction. The positive value for the canopies is more than twice as high.
J	Approximately: +0.4 to +0.6	+/- 0.6	+0.488 (all φ) -0.732 ($\varphi = 0$) -1.708 ($\varphi = 1$)	The simulated pressure is of a similar order of magnitude to the Eurocode bridge load, but applied in a different direction. The positive value for canopies is similar.
K	Approximately: +0.1	+/- 0.4	+0.488 (all φ) -0.732 ($\varphi = 0$) -1.708 ($\varphi = 1$)	The magnitude of the simulated pressure is considerably lower than the Eurocode bridge load and applied in a different direction. The positive canopy value is higher.

Table 80: Comparison between Eurocode load and wind simulation load on the deck

The pressure comparison shows that the RWIND simulation and the Eurocode provisions can produce substantially different local pressure distributions. In several regions, the simulated pressures are of a similar order of magnitude to the Eurocode bridge load in x-direction, while in other regions the simulated pressure is higher. The canopy wind loads also result in pressure values that differ from the RWIND results. In some zones the magnitude of the pressure is higher than the values obtained from the simulation.

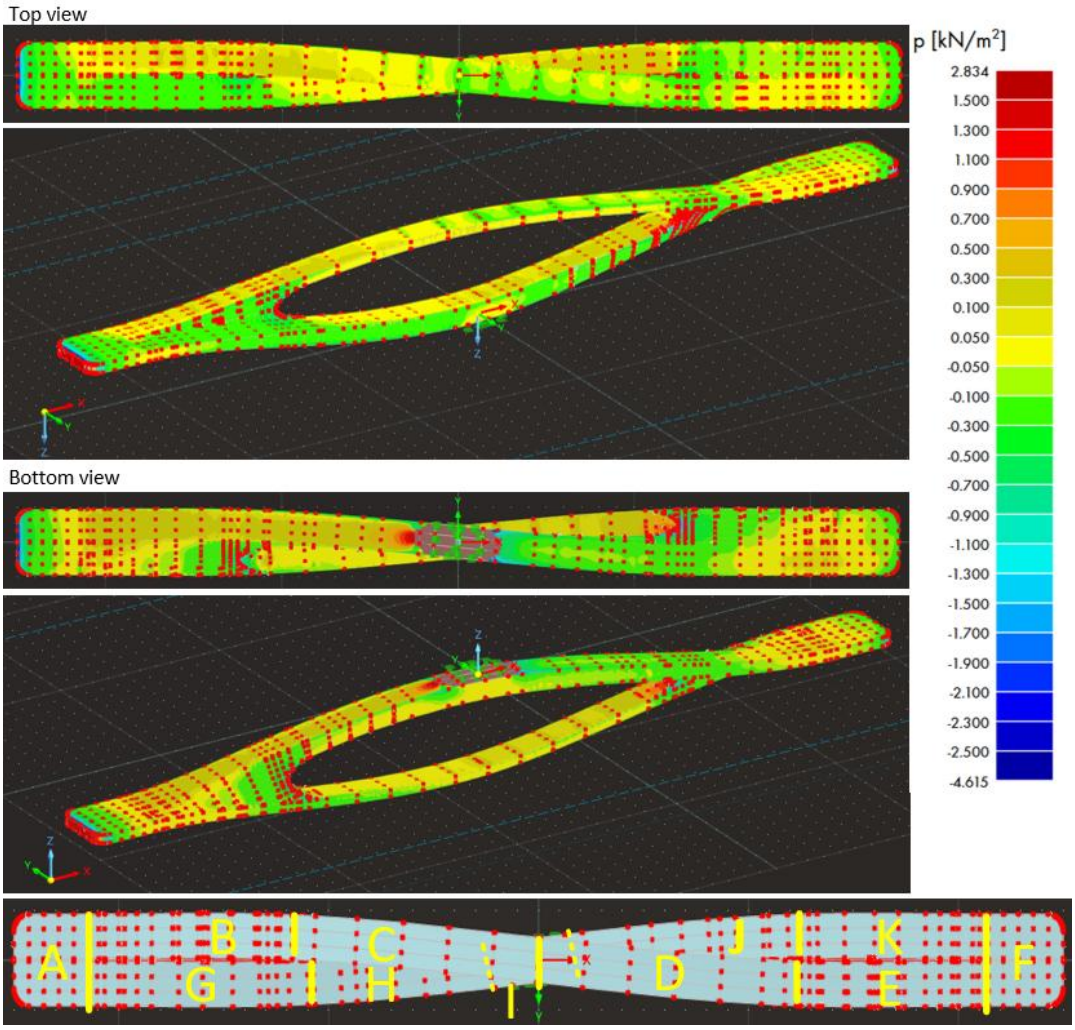

Figure 106: Pressure on the top and bottom side of the deck with a zone indication

On the side surfaces of the structure, the wind simulation predicts pressures of approximately −0.3 kN/m² on the −y side and −0.2 kN/m² on the +y side, see Figure 107. These pressures act perpendicular to the local side surfaces and therefore are not directed entirely in the global y-direction. In comparison, the Eurocode bridge load model applies a load of 1.142 kN/m² in the global y-direction. The Eurocode value is therefore substantially higher than the local pressures obtained from the wind simulation. However, the two values are not directly equivalent because the RWIND pressures act normal to the local surfaces, whereas the Eurocode load is defined in the global y-direction.

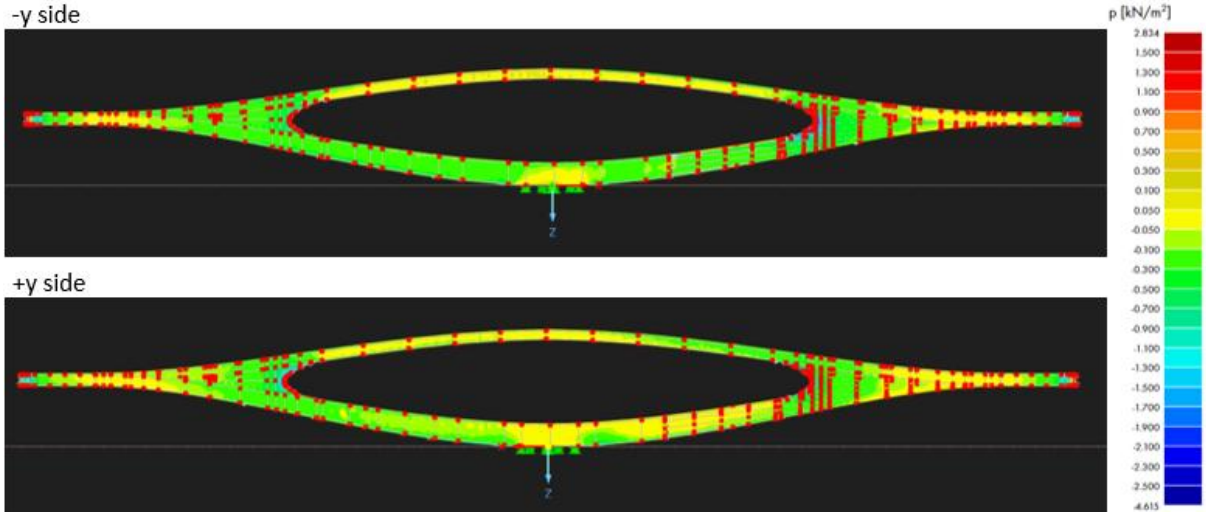

Figure 107: Pressure on the sides of the structure

A comparison of the pressure distributions also shows differences between the Eurocode load model and the RWIND simulation. At the locations indicated by the red arrows in Figure 108, no wind loads are applied according to the Eurocode load model for bridges and canopies, whereas the RWIND simulation predicts wind pressures at these locations. Furthermore, the RWIND simulation shows relatively high pressures at the locations indicated in the left figure. This demonstrates that the spatial variation of wind pressure over the Seasaw is not fully captured by the simplified Eurocode load models.

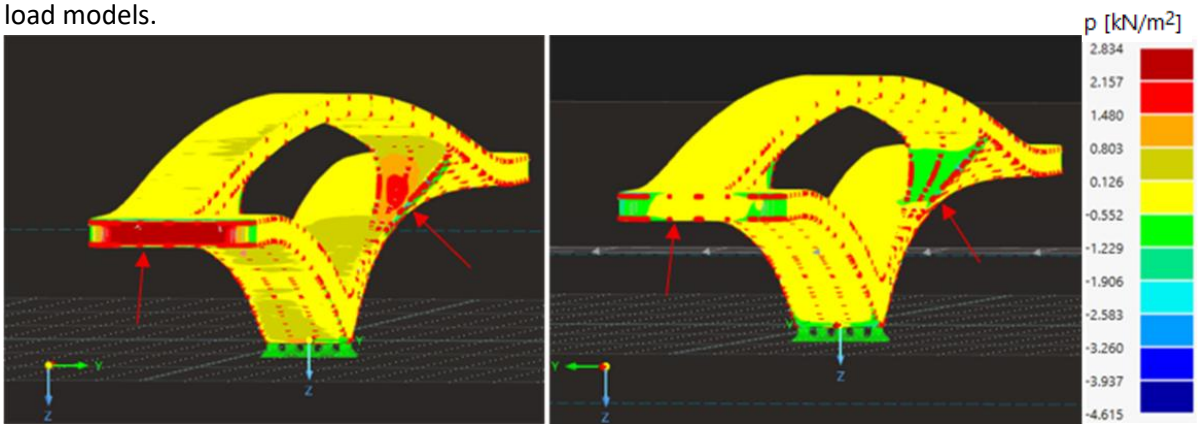

Figure 108: Locations where no loads are applied according to the Eurocode for bridges and canopies

The global wind loads obtained from the Eurocode bridge load model is substantially higher than those obtained from the wind simulation, see Table 81. The sum of loads for the Eurocode bridge load model is approximately 12 times higher in the x-direction and 31 times higher in the y-direction. The wind simulation also predicts a small sum of loads in the z-direction, which is not included in the Eurocode bridge load model. The difference in the y-direction is particularly pronounced because the Eurocode load is applied as a global load to one side of the structure, whereas the RWIND simulation predicts pressures on both sides of the structure. These pressures act normal to the local surfaces and therefore partly oppose each other when expressed in the global y-direction. The resulting reaction moments also differ considerably. The wind simulation produces larger moments about the x- and y-axes, whereas the Eurocode bridge load model produces a substantially larger moment about the z-axis. The Eurocode bridge load model also includes the effect of the balustrade, whereas the wind simulation does not. Therefore, a comparison based on global force magnitude alone is not sufficient to determine which load model is more conservative for the structural response.

The deformation patterns also differ between the two approaches. Under the wind simulation, the structure primarily deforms in a seesaw-like motion, with a maximum deformation of 22.1 mm. Under the Eurocode bridge wind loads, the structure also exhibits seesaw-like deformation but additionally rotates about the x-axis, resulting in a larger maximum deformation of 130.5 mm. This difference results from both the substantially higher total loads and the different spatial distribution of the applied loads. However, the difference in deformation alone does not determine whether wind loading is governing for the structural design. The influence of wind loading should instead be assessed based on its effect on the governing stresses.

Sum of loads in:	Wind simulation [kN]	Eurocode bridge [kN]
X	12.22	143.59
Y	4.45	136.19
Z	-1.47	0.0
Resultant of reactions about:	Wind simulation [kNm]	Eurocode bridge [kNm]
X	-20.43	-4.70
Y	-95.67	-19.82
Z	-2.27	114.50

Table 81: Sum of loads and resultant of reactions comparison

The global stress distributions obtained from the RWIND simulation and the Eurocode bridge load model were compared to assess the influence of the different wind load models on the structural response. Local stress singularities were excluded from the comparison. The resulting approximate stress ranges are presented in Table 82. The Eurocode bridge load case results in higher stress ranges than the RWIND load case for all three considered stress components. The calculated stress ranges were compared with the design material stress limits used for the laminate configurations considered in the preliminary design. For the local x-direction, the design material stress limits are 65.5 and 111.4 N/mm² in tension and 54.6 and 92.8 N/mm² in compression, depending on the laminate configuration.. For the local y-direction, the corresponding limits are 36.9 and 65.5 N/mm² in both tension and compression depending on the laminate configuration, while the design shear stress limits are 15.3 and 26.1 N/mm² depending on the laminate configuration. The Eurocode bridge load case therefore remains well below the design material stress limits for all considered stress components. The highest stress-to-limit ratio is obtained for shear, at approximately 26% of the lowest design shear stress limit. The results indicate that wind loading does not govern the material strength of the preliminary design for the investigated load case.

Stress component	Stress range RWIND $[N/mm^2]$	Stress range Eurocode bridge $[N/mm^2]$
σ_x, local x-direction	-2 to +2	-7 to +7
σ_y, local y-direction	-1 to +1	-3 to +3
τ_{xy}, shear stress	-1 to +1	-4 to +4

Table 82: Approximate stress ranges comparison

Overall, the comparison shows that the Eurocode bridge load model predicts substantially higher global horizontal wind loads than the RWIND simulation for the investigated Seasaw configuration. Therefore, the two approaches cannot be considered directly comparable in terms of their global load magnitude. The RWIND simulation provides additional information on the spatial distribution and direction of local wind pressures over the complex deck geometry, which is not fully captured by the simplified Eurocode bridge load model. The higher global Eurocode wind loads also result in a more critical global stress response; however, the resulting stress ranges remain well below the design material stress limits for the laminate configurations considered in the preliminary design. Therefore, wind loading does not govern the material strength of the preliminary design for the investigated load case.

13.3 RWIND simulation Seasaw without modelled dike in y-direction

In this section, wind simulations are performed for the standalone Seasaw structure without a modelled dike in the y-direction. The simulation settings are provided in Appendix FF. First, the simulation results are presented, after which the simulation results are compared with the wind loads obtained from the Eurocode. The Eurocode wind loads for bridge structures used for the comparison are presented in Appendix HH.

13.3.1 Results of the wind simulations

The simulation configuration is shown in Figure 109. According to the RWIND 3 online manual, a simulation is considered to have converged satisfactorily when the graph of the residual quantity over time no longer changes (or only very little), or it periodically oscillates around a certain mean value. The results indicate that this criterion is satisfied for the present simulation. (Online Manuals RWIND 3: Troubleshooting, sd)

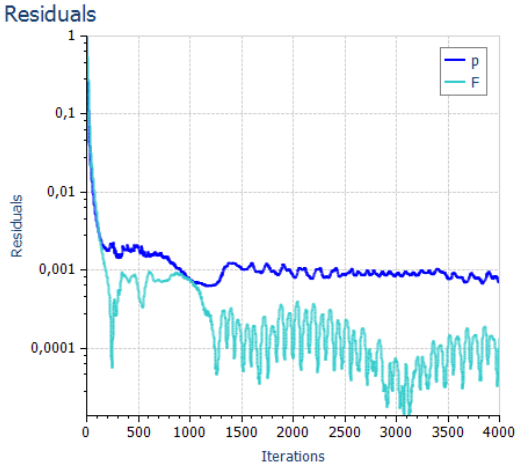

Figure 109: Residuals configurations wind simulation Seasaw y-direction without modelled dike

The streamlines obtained from the simulation are shown in Figure 110.

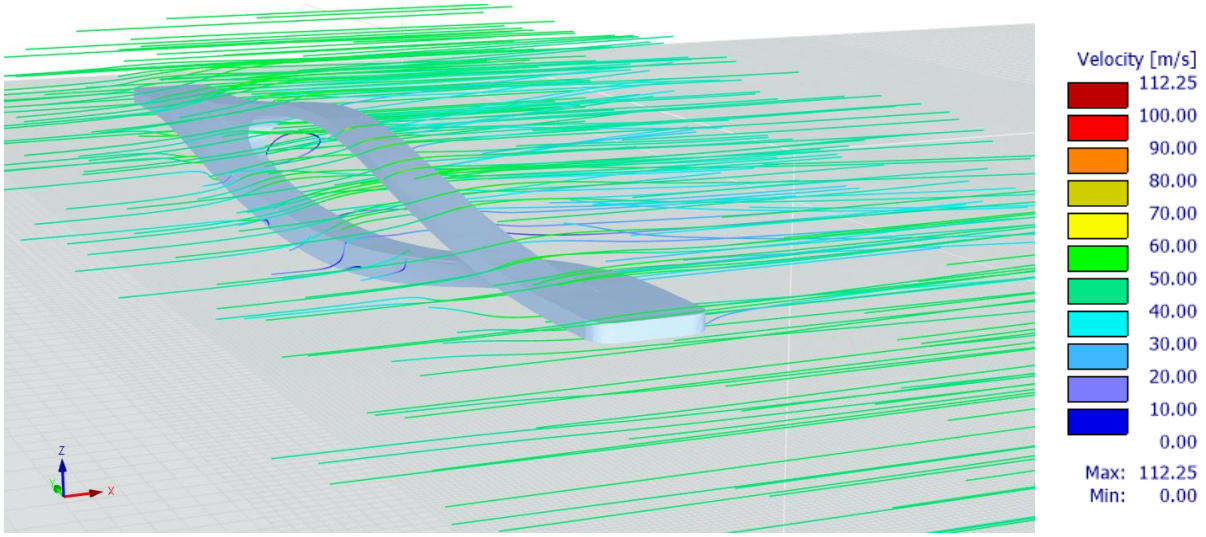

Figure 110: Streamlines wind simulation Seasaw y-direction without modelled dike

The resulting drag forces in the three coordinate directions are presented in Table 83, while the pressure distribution on the structure is shown in Figure 111 and Figure 112.

Wind load component	Value [kN]
Drag force in x	3.199
Drag force in y	134.604
Drag force in z	-41.846
Resultant drag force	140.995

Table 83: Results Seasaw with wind in y-direction without modelled dike

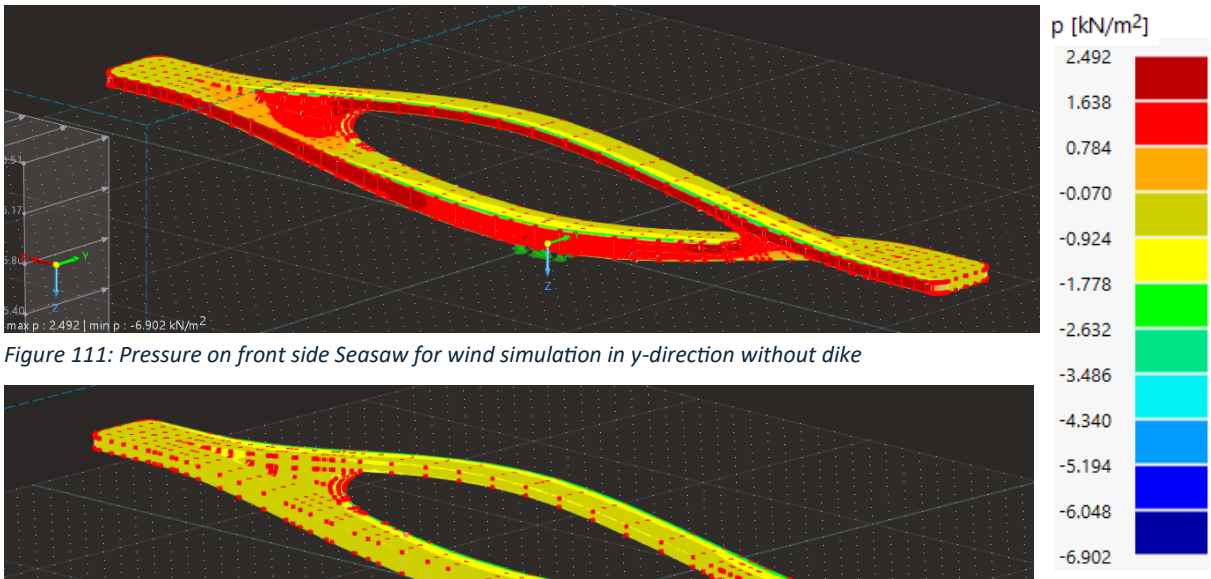

Figure 111: Pressure on front side Seasaw for wind simulation in y-direction without dike

Figure 112: Pressure on back side Seasaw for wind simulation in y-direction without dike

The resulting deformation of the structure under the simulated wind loading is shown in Figure 113.

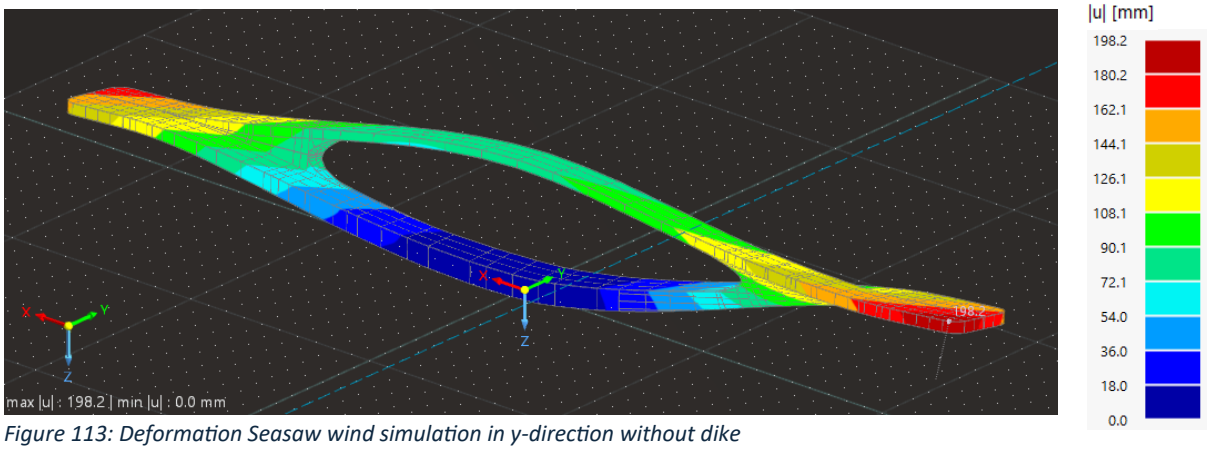

Figure 113: Deformation Seasaw wind simulation in y-direction without dike

The sum of loads and the resultant of reactions obtained from RFEM are given in the table below. The sum of loads represents the total applied wind load on the structural model. The corresponding support forces are equal in magnitude. The resultant of reactions represents the resulting moments of the support reactions. The terminology in this table follows the terminology used in RFEM.

Sum of loads in:	[kN]
X	3.25
Y	156.12
Z	-40.97
Resultant of reactions about:	[kNm]
X	-20.29
Y	-925.11
Z	92.06

Table 84: The sum of loads and resultant of reactions of the wind simulation in y-direction without dike

A global assessment of the stress distribution, excluding local singularities, resulted in the approximate stress ranges shown in Table 85.

Stress component	Stress range $[N/mm^2]$
σ_x, local x-direction	-8 to +8
σ_y, local y-direction	-5 to +5
τ_{xy}, shear stress	-6 to +6

Table 85: Approximate global stress ranges for the RWIND load case in the y-direction without a modelled dike

13.3.2 Comparison with Eurocode loads

On the front and back surfaces of the structure, the wind simulation predicts pressures of approximately +1.8 kN/m² on the +y side and −0.6 kN/m² on the -y side, see Figure 115. These pressures act perpendicular to the local side surfaces and therefore are not directed entirely in the global y-direction. The corresponding pressure difference between the two sides is approximately $2.4\ \mathrm{kN/m^2}$. In comparison, the Eurocode bridge load model applies a load of $2.856\ \mathrm{kN/m^2}$ in the global y-direction. The two pressure values are therefore not directly equivalent, because the RWIND pressure acts normal to the local surfaces, whereas the Eurocode load is defined directly in the global y-direction. Due to the inclination of the Seasaw surfaces, only a component of the resulting RWIND force acts in the global y-direction.

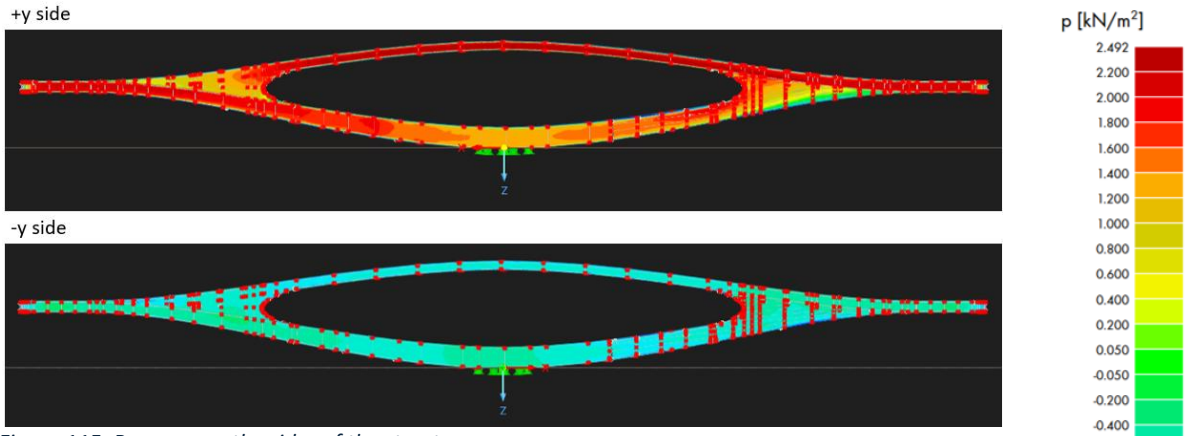

Figure 115: Pressure on the sides of the structure

The average net pressure on the deck in the z-direction, determined from the difference between the pressures on the top and bottom surfaces of the deck, is approximately 0.2 kN/m², see Figure 114. However, significant local variations occur near the connections. Near the left connection, the net pressure is approximately 1.6 kN/m² upward, while near the right connection it is approximately 1 kN/m² downward. In comparison, the Eurocode bridge load model specifies a uniformly distributed load of 0.484 kN/m² in the z-direction. The RWIND simulation therefore indicates a substantially more non-uniform pressure distribution, with local net pressures near the connections exceeding the magnitude of the uniformly distributed Eurocode load.

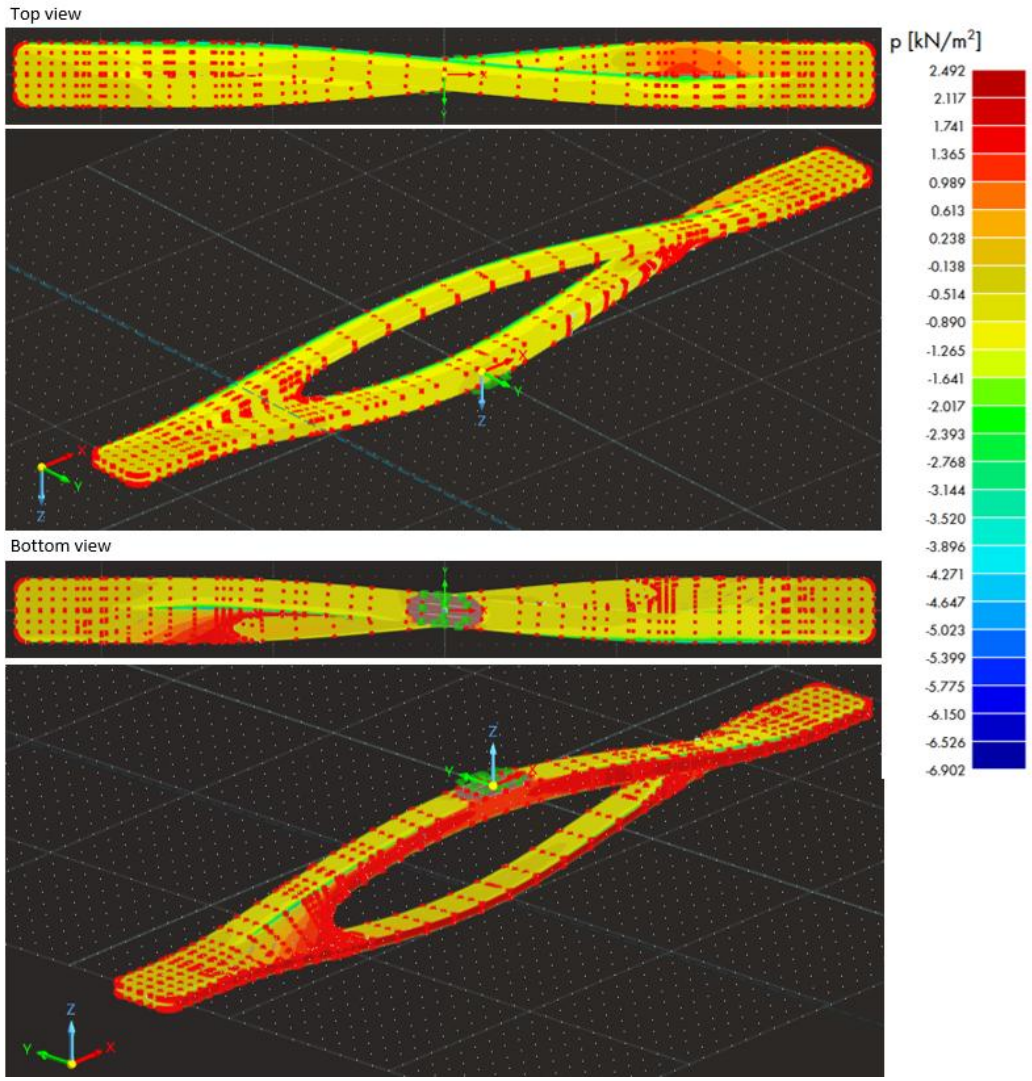

Figure 114: Pressure on the top and bottom side of the deck

A comparison of the pressure distributions also shows differences between the Eurocode load model and the RWIND simulation. At the locations indicated by the red arrows in Figure 116, no wind loads are applied according to the Eurocode load model for bridges, whereas the RWIND simulation predicts small wind pressures at these locations. This illustrates that the simplified Eurocode load model does not reproduce the detailed spatial distribution of the pressures obtained from the RWIND simulation.

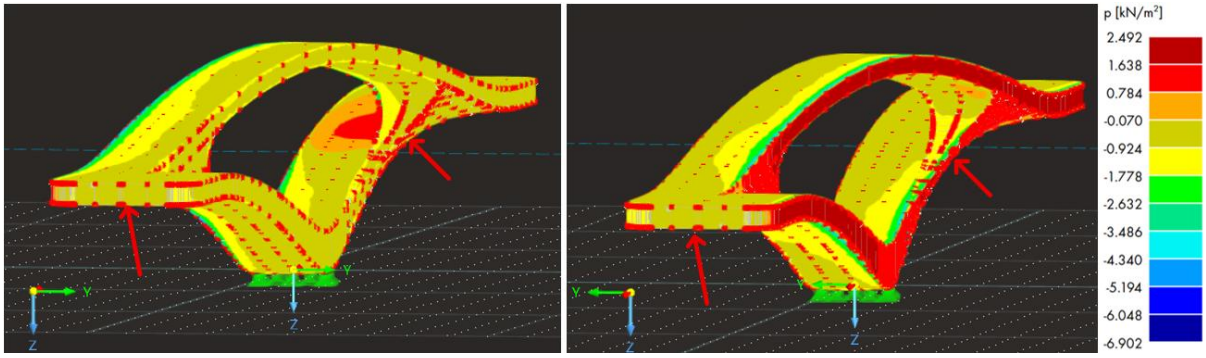

Figure 116: Locations where no loads are applied according to the Eurocode for bridges

The sum of loads and resultant reaction moments obtained from both approaches are summarized in Table 86. The Eurocode bridge load model results in a substantially higher total load in the y-direction than the RWIND simulation. The Eurocode load in the y-direction is approximately 2.2 times the corresponding RWIND load. This difference is partly related to the inclusion of the balustrade load in the Eurocode load model, which is not included in the RWIND simulation, and to differences in the applied pressure distribution on the side surfaces of the structure. The Eurocode model also results in higher loads in the z-direction, whereas the RWIND simulation predicts a load in the opposite direction. Unlike the Eurocode bridge load model, which applies loads directly in the global coordinate directions, the wind simulation predicts pressures acting perpendicular to the local surfaces. As a result, the pressures on the inclined surfaces of the Seasaw generate force components in the global x-, y-, and z-directions. The small load in the global x-direction is therefore a consequence of the inclination of the structure rather than a direct wind pressure acting in that direction. The reaction moments differ considerably between the two approaches. In particular, the RWIND simulation produces a substantially larger moment about the y-axis. This may be related to the non-uniform distribution of the pressure around the connections. The Eurocode load model, in contrast, applies simplified distributed loads and therefore does not capture these local variations. The Eurocode model also produces a larger moment about the z-axis, which is partly associated with the applied balustrade loads and their asymmetric distribution over the structure.

The deformation patterns also differ between the two approaches. Both models result in a deformation pattern in which the structure rotates predominantly in the y-direction. However, the deformation shape is not identical, which is consistent with the differences in the magnitude and spatial distribution of the applied loads and resulting moments. The maximum deformation is 198.2 mm for the RWIND simulation and 245.5 mm for the Eurocode bridge load model.

Sum of loads in:	Wind simulation [kN]	Eurocode bridge [kN]
X	3.25	0.0
Y	156.12	340.47
Z	-40.97	89.25
Resultant of reactions about:	Wind simulation [kNm]	Eurocode bridge [kNm]
X	-20.29	9.99
Y	-925.11	0.33
Z	92.06	286.24

Table 86: Sum of loads and resultant of reactions comparison

The global stress distributions obtained from the RWIND simulation and the Eurocode bridge load model were compared to assess the influence of the different wind load models on the structural response. Local stress singularities were excluded from the comparison. The resulting approximate stress ranges are presented in Table 87. The Eurocode bridge load case results in higher stress ranges than the RWIND load case for all three considered stress components. The calculated stress ranges were compared with the design material stress limits used for the laminate configurations considered in the preliminary design. For the local x-direction, the design material stress limits are 65.5 or 111.4 N/mm² in tension and 54.6 or 92.8 N/mm² in compression depending on the laminate configuration. For the local y-direction, the corresponding limits are 36.9 or 65.5 N/mm² in both tension and compression depending on the laminate configuration, while the design shear stress limit is 15.3 or 26.1 N/mm² depending on the laminate configuration. The Eurocode bridge load case remains below the applicable design material stress limits for all considered stress components. The highest stress-to-limit ratio is obtained for shear stress in the C-shaped girders, where the maximum global shear stress of approximately 10 N/mm² corresponds to approximately 38.3% of the applicable design shear stress limit of 26.1 N/mm². The results indicate that wind loading does not govern the material strength of the preliminary design for the investigated load case.

Stress component	Stress range RWIND $[N/mm^2]$	Stress range Eurocode bridge $[N/mm^2]$
σ_x, local x-direction	-8 to +8	-14 to +14
σ_y, local y-direction	-5 to +5	-7 to +9
τ_{xy}, shear stress	-6 to +6	-10 to +10

Table 87: Approximate global stress ranges for the RWIND and Eurocode bridge load cases

Overall, the comparison shows that the Eurocode bridge load model predicts a substantially higher global load in the y-direction than the RWIND simulation for the investigated Seasaw configuration. The Eurocode load in the y-direction is approximately 2.2 times the corresponding RWIND load. However, the RWIND simulation produces substantially larger reaction moments about the y-axis due to its non-uniform pressure distribution, while the Eurocode load model produces a larger reaction moment about the z-axis, partly due to the inclusion of the balustrade load. This demonstrates that the two approaches result in different global load distributions despite both representing the same wind direction.

The RWIND simulation additionally provides a more detailed representation of the spatial pressure distribution, including local pressure variations on the inclined deck and around the connections that are not captured by the simplified Eurocode load model. Despite these differences, the higher global stress response obtained for the Eurocode bridge load case remains below the applicable design material stress limits. Therefore, for the investigated y-direction wind load case, the Eurocode bridge load model provides a conservative basis for assessing the material strength of the preliminary design.

13.4 RWIND simulation Seasaw with modelled dike in x-direction

In this section, wind simulations are performed for the standalone Seasaw structure with a modelled dike in the x-direction, see Figure 117. The simulation settings are provided in Appendix FF. First, the simulation results are presented, after which the simulation results are compared with the wind loads obtained from the Eurocode. The Eurocode wind loads for bridge and canopy structures used for the comparison are presented in Appendix HH.



Figure 117: Seasaw with dike modelled

13.4.1 Results of the wind simulations

The simulation configuration is shown in Figure 118. According to the RWIND 3 online manual, a simulation is considered to have converged satisfactorily when the graph of the residual quantity over time no longer changes (or only very little), or it periodically oscillates around a certain mean value. The results indicate that this criterion is satisfied for the present simulation. (Online Manuals RWIND 3: Troubleshooting, sd)

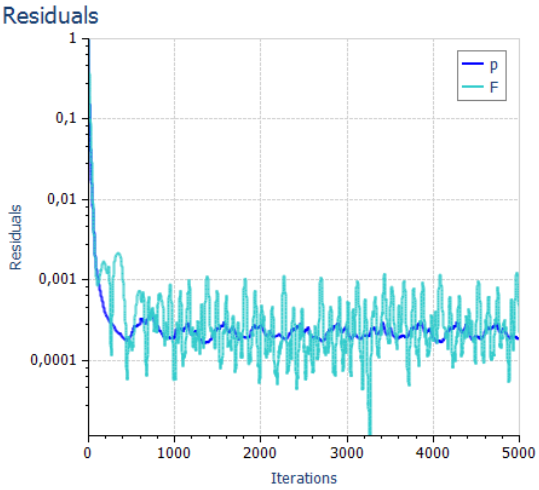

Figure 118: Residuals configurations wind simulation Seasaw x-direction with modelled dike

The streamlines obtained from the simulation are shown in Figure 119.

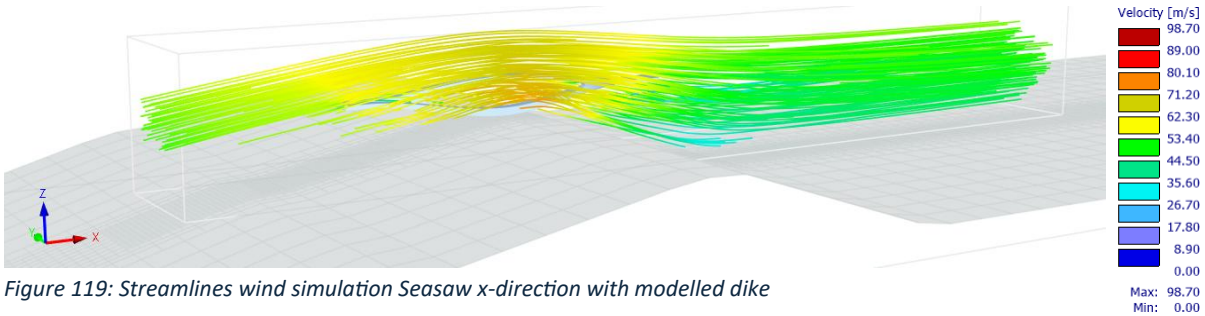

Figure 119: Streamlines wind simulation Seasaw x-direction with modelled dike

The resulting drag forces in the three coordinate directions are presented in Table 88, while the pressure distribution on the structure is shown in Figure 121 and Figure 120.

Wind load component	Value [kN]
Drag force in x	16.397
Drag force in y	18.166
Drag force in z	7.481
Resultant drag force	25.590

Table 88: Results Seasaw with wind in x-direction with modelled dike

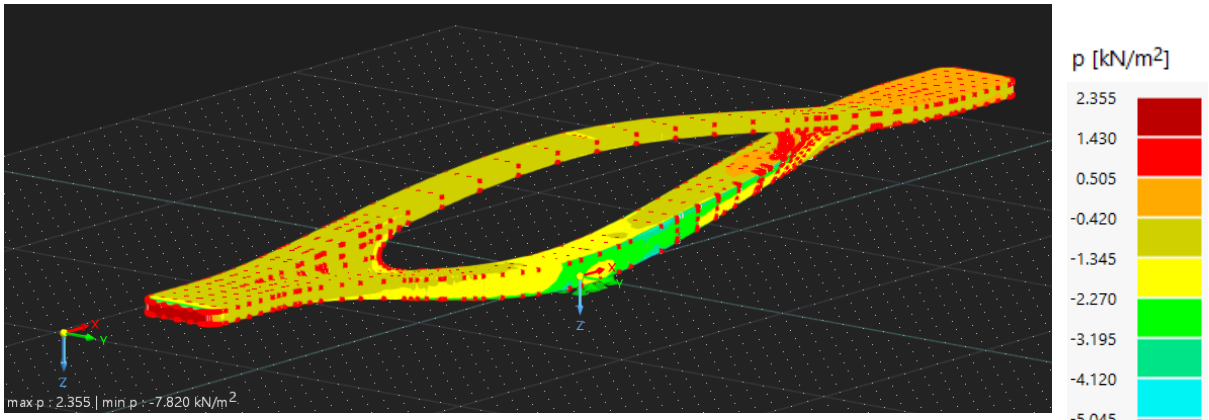

Figure 121: Pressure on front side Seasaw for wind simulation in x-direction with dike

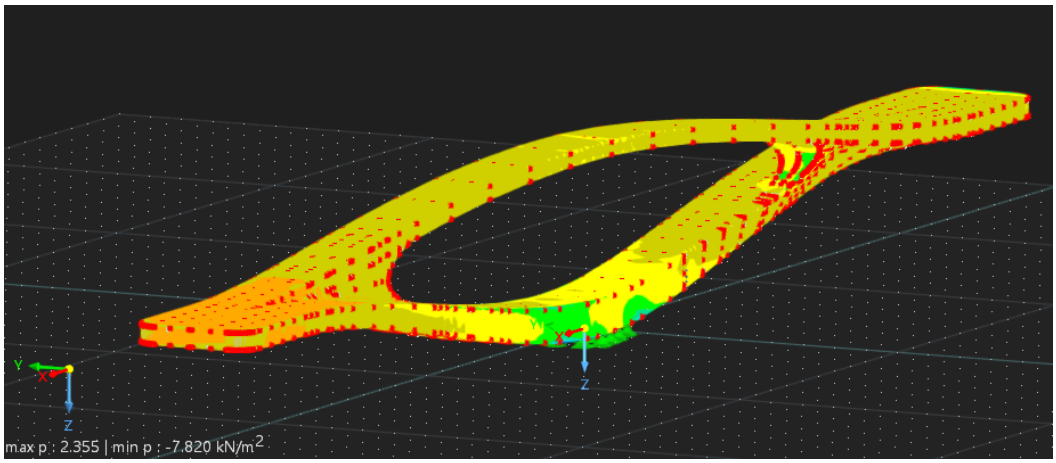

Figure 120: Pressure on back side Seasaw for wind simulation in x-direction with dike

The resulting deformation of the structure under the simulated wind loading is shown in Figure 122.

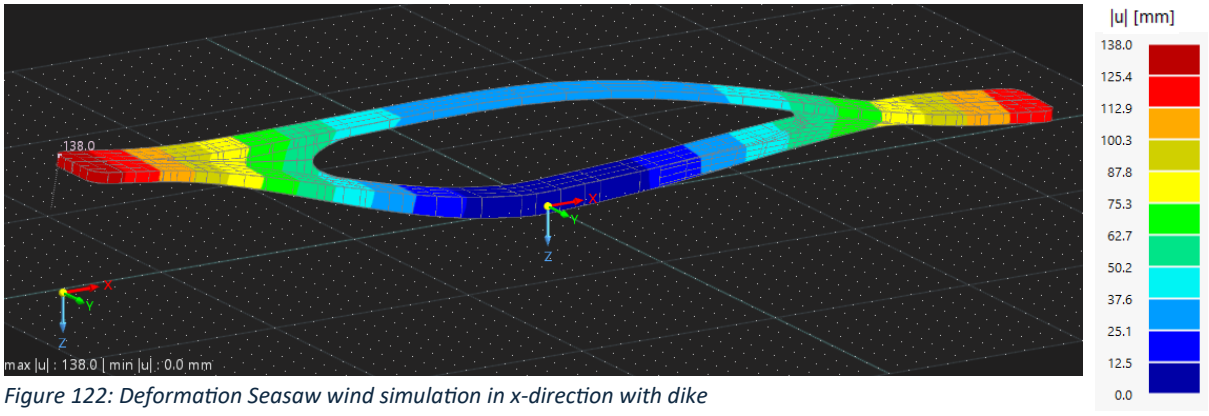

Figure 122: Deformation Seasaw wind simulation in x-direction with dike

The sum of loads and the resultant of reactions obtained from RFEM are given in Table 89. The sum of loads represents the total applied wind load on the structural model. The corresponding support forces are equal in magnitude and opposite in direction for a structure in equilibrium. The resultant of reactions represents the resulting moments of the support reactions. The terminology in this table follows the terminology used in RFEM.

Sum of loads in:	[kN]
X	17.42
Y	20.16
Z	7.73
Resultant of reactions about:	[kNm]
X	-52.75
Y	-827.28
Z	-11.99

Table 89: The sum of loads and resultant of reactions of the wind simulation in x-direction with dike

A global assessment of the stress distribution, excluding local singularities, resulted in the approximate stress ranges shown in Table 90.

Stress component	Stress range $[N/mm^2]$
σ_x, local x-direction	-4 to +4
σ_y, local y-direction	-4 to +4
τ_{xy}, shear stress	-5 to +2

Table 90: Approximate global stress ranges for the RWIND load case in the x-direction with a modelled dike

13.4.2 Comparison with Eurocode loads

To compare the wind simulation results with the Eurocode load models, the average net pressure was determined for the different deck regions shown in Figure 123. The pressures on the top and bottom surfaces of the deck were used to calculate the net pressure acting on each region. The net pressure determined from the wind simulation acts perpendicular to the local deck surface. For the Eurocode bridge load model, the wind load is applied as a global load in the x-direction and may be applied in either the positive or negative x-direction. The Eurocode canopy provisions define net pressures perpendicular to the canopy surface. The canopy provisions define different pressure coefficients for specific zones of the canopy. However, these zones do not correspond directly to the zones identified in the RWIND simulation. Therefore, the overall canopy pressure ranges are used for comparison. No surface roughness factors were applied to the surfaces in the wind simulation. The results are summarized in Table 91.

Zone	Wind simulation (net pressure) $[kN/m^2]$	Eurocode wind load bridge (load in x-direction) $[kN/m^2]$	Eurocode wind load canopies (net pressure) $[kN/m^2]$	Comparison
A	Approximately: -1.0	+/- 0.371	+0.488 (all φ) -0.854 ($\varphi = 0$) -1.708 ($\varphi = 1$)	The magnitude of the simulated pressure is considerably higher than the Eurocode bridge load and the direction is different. The negative canopy value for $\varphi = 0$ is slightly lower, while the value for $\varphi = 1$ is higher in magnitude.
B	Approximately: -0.5 to -0.9	+/- 0.35	+0.488 (all φ) -0.854 ($\varphi = 0$) -1.586 ($\varphi = 1$)	The magnitude of the simulated pressure is higher than the Eurocode bridge load and the direction is different. The negative canopy value for $\varphi = 0$ is within the simulated range, while the value for $\varphi = 1$ is higher in magnitude.

C	Approximately: +0.2 to +0.5	+/- 0.31	+0.488 (all φ) -0.854 ($\varphi = 0$) -1.586 ($\varphi = 1$)	The simulated pressure is similar in magnitude to the Eurocode bridge load, but in a different direction. The positive canopy value is also similar.
D	Approximately: +0.2 to +0.4	+/- 0.31	+0.488 (all φ) -0.854 ($\varphi = 0$) -1.586 ($\varphi = 1$)	The simulated pressure is similar in magnitude to the Eurocode bridge load, but in a different direction. The positive canopy value is also similar.
E	Approximately: +0.5	+/- 0.35	+0.488 (all φ) -0.854 ($\varphi = 0$) -1.586 ($\varphi = 1$)	The simulated pressure is higher in magnitude to the Eurocode bridge load and applied in a different direction. The positive canopy value is similar.
F	Approximately: +0.1	+/- 0.371	+0.488 (all φ) -0.854 ($\varphi = 0$) -1.708 ($\varphi = 1$)	The simulated pressure is lower in magnitude to the Eurocode bridge load and applied in a different direction. The positive canopy value is higher.
G	Approximately: -0.5 to -0.7	+/- 0.4	+0.488 (all φ) -0.732 ($\varphi = 0$) -1.708 ($\varphi = 1$)	The magnitude of the simulated pressure is higher than the Eurocode bridge load and the direction is different. The negative canopy value for $\varphi = 0$ is similar, while the value for $\varphi = 1$ is higher in magnitude.
H	Approximately: -0.5 Next to zone I: -1.5	+/- 0.6	+0.488 (all φ) -0.732 ($\varphi = 0$) -1.708 ($\varphi = 1$)	The simulated pressure varies significantly. The −0.5 value is slightly lower than the Eurocode bridge load, while the −1.5 value is considerably higher. The loads are also applied in different direction. The canopy values are generally higher than −0.5 but the −1.5 is comparable to the negative value for $\varphi = 1$.
I	Approximately: -1.5	+/- 0.684	+0.488 (all φ) -0.732 ($\varphi = 0$) -1.708 ($\varphi = 1$)	The magnitude of the simulated pressure is higher than the Eurocode bridge load and the direction is different. The value of the simulated pressure falls within the range of the negative canopy values for $\varphi = 0$ and $\varphi = 1$.

J	Approximately: +1 to +1.7	+/- 0.6	+0.488 (all φ) -0.732 ($\varphi = 0$) -1.708 ($\varphi = 1$)	The simulated pressure is considerably higher in magnitude than the Eurocode bridge load and applied in a different direction. The simulated range is higher than the positive value for the canopies.
K	Approximately: +1.0	+/- 0.4	+0.488 (all φ) -0.732 ($\varphi = 0$) -1.708 ($\varphi = 1$)	The simulated pressure is considerably higher in magnitude than the Eurocode bridge load and applied in a different direction. The simulated range is higher than the positive value for the canopies.

Table 91: Comparison between Eurocode load and wind simulation load on the deck

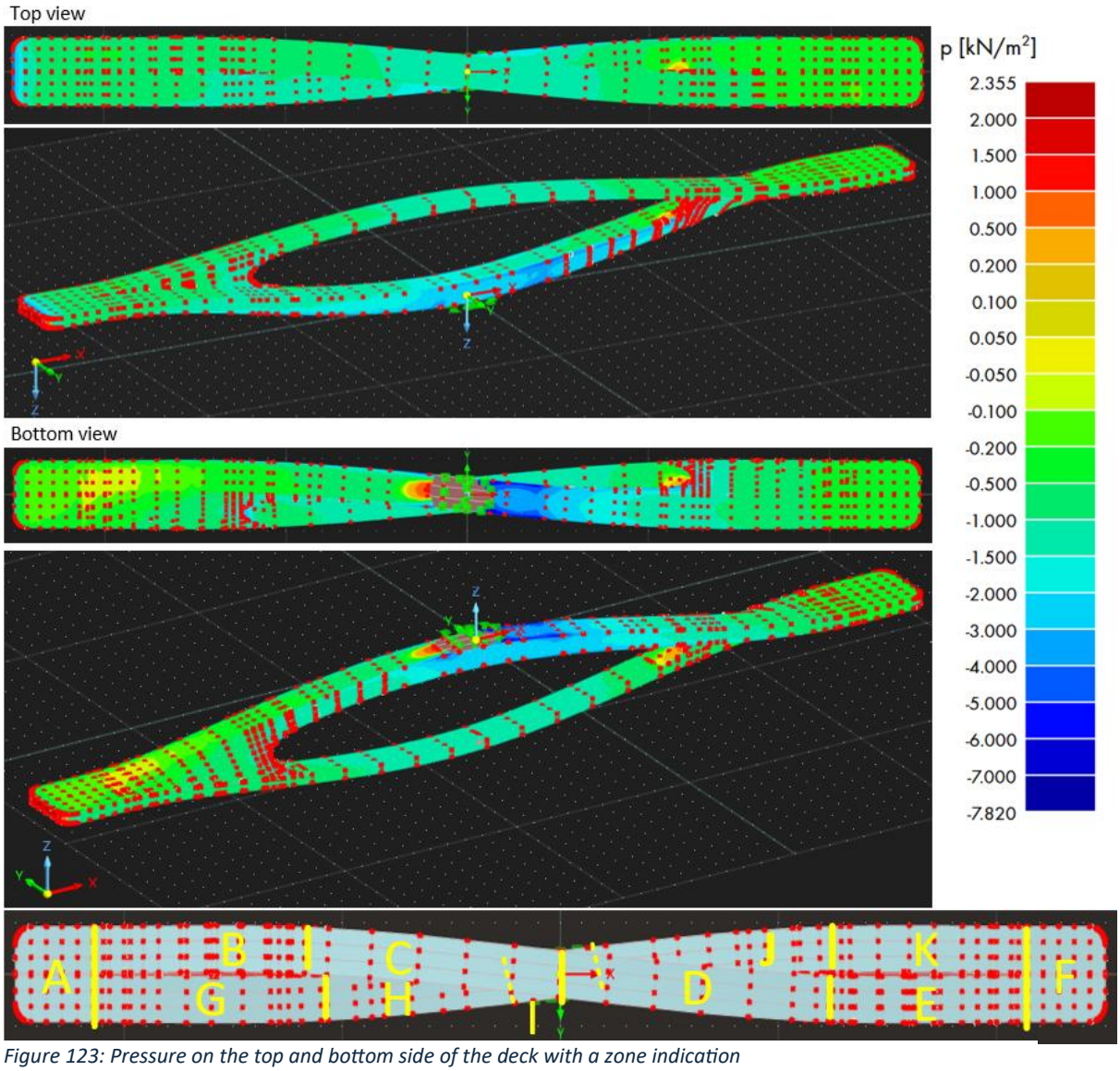

Figure 123: Pressure on the top and bottom side of the deck with a zone indication

On the side surfaces of the structure, the wind simulation predicts pressures of approximately −1.5 kN/m² on the −y side and −1.3 kN/m² on the +y side, see Figure 124. These pressures act perpendicular to the local side surfaces and therefore are not directed entirely in the global y-direction. In comparison, the Eurocode bridge load model applies a load of 1.142 kN/m² in the global y-direction. Although the local pressures from the wind simulation are higher in magnitude, the Eurocode load is applied only to one side of the structure, whereas the wind simulation predicts pressures on both sides. As a result, the contributions from the two sides partially balance each other, resulting in a net load of approximately 0.2 kN/m² in the y-direction, which is considerably lower than the load predicted by the Eurocode bridge load model.

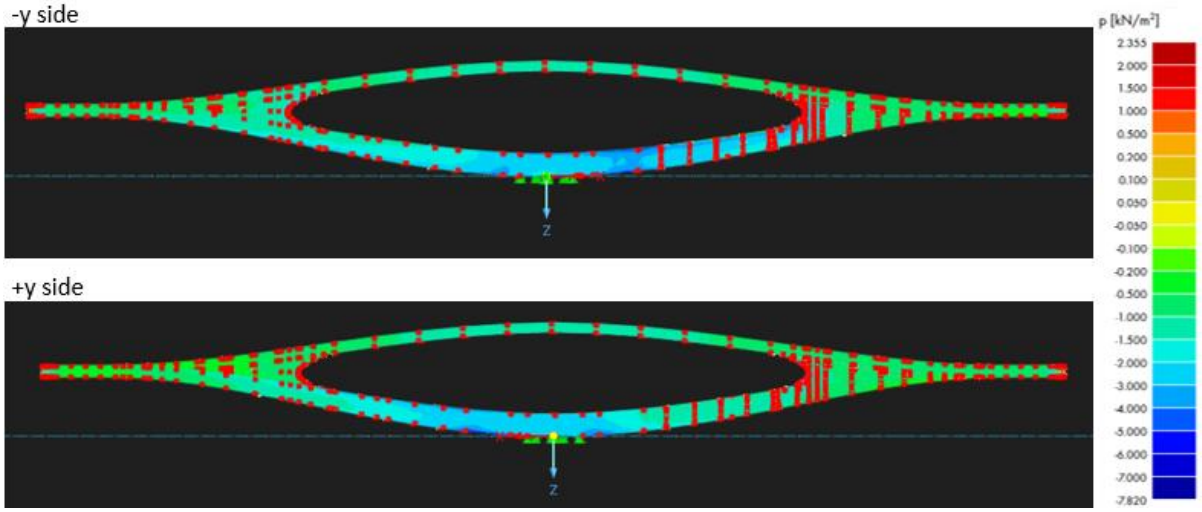

Figure 124: Pressure on the sides of the structure

A comparison of the pressure distributions also shows differences between the Eurocode load model and the RWIND simulation. At the locations indicated by the red arrows in Figure 125, no wind loads are applied according to the Eurocode load model for bridges and canopies, whereas the RWIND simulation predicts wind pressures at these locations. Furthermore, the RWIND simulation shows relatively high pressures at the locations indicated in the left figure. This indicates that the spatial distribution of the pressure obtained from the RWIND simulation differs substantially from the simplified distribution assumed by the Eurocode load models.

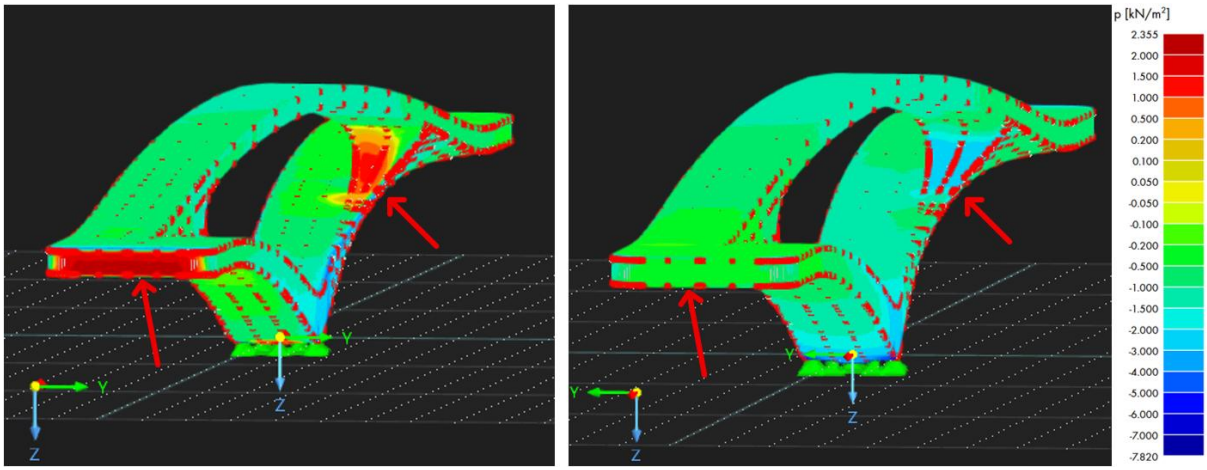

Figure 125: Locations where no loads are applied according to the Eurocode for bridges and canopies

The sum of loads obtained from the Eurocode bridge load model is considerably higher than those obtained from the RWIND simulation, see Table 92. The Eurocode loads are approximately 8 times higher in the x-direction and 7 times higher in the y-direction. The RWIND simulation also predicts a load of 7.73 kN in the z-direction, which is not included in the Eurocode bridge load model. The resultant reaction moments differ substantially as well. The RWIND simulation produces considerably larger moments about the x- and y-axes, particularly about the y-axis, whereas the Eurocode bridge load model produces a substantially larger moment about the z-axis. The Eurocode bridge load model also includes the effect of the balustrade, which is not considered in the RWIND simulation. Consequently, the Eurocode model gives substantially higher global horizontal forces, whereas the RWIND model can produce larger moments about certain axes due to its non-uniform pressure distribution.

The deformation patterns also differ between the two approaches. Under the wind simulation, the structure primarily deforms in a seesaw-like motion, with a maximum deformation of 138.0 mm. Under the Eurocode bridge wind loads, the structure also exhibits seesaw-like deformation, combined with rotation about the x-axis, resulting in a slightly lower maximum deformation of 130.5 mm. The similar maximum deformations despite the substantially different total loads can be attributed to the differences in the spatial distribution and direction of the applied loads, as reflected by the significantly different resultant reaction moments.

Sum of loads in:	Wind simulation [kN]	Eurocode bridge [kN]
X	17.42	143.59
Y	20.16	136.19
Z	7.73	0.0
Resultant of reactions about:	Wind simulation [kNm]	Eurocode bridge [kNm]
X	-52.75	-4.70
Y	-827.28	-19.82
Z	-11.99	114.50

Table 92: Sum of loads and resultant of reactions comparison

The global stress distributions obtained from the RWIND simulation and the Eurocode bridge load model were compared to assess the influence of the different wind load models on the structural response. Local stress singularities were excluded from the comparison. The resulting approximate stress ranges are presented in Table 93. The Eurocode bridge load case results in a higher stress range in the local x-direction, whereas the RWIND load case results in a slightly higher stress range in the local y-direction. For shear stress, the RWIND load case results in a larger negative stress magnitude, while the Eurocode bridge load case results in a larger positive stress magnitude. The calculated stress ranges were compared with the design material stress limits used for the laminate configurations considered in the preliminary design. For the local x-direction, the design material stress limits are 65.5 and 111.4 N/mm² in tension and 54.6 and 92.8 N/mm² in compression, depending on the laminate configuration. For the local y-direction, the corresponding limits are 36.9 and 65.5 N/mm² in both tension and compression depending on the laminate configuration, while the design shear stress limits are 15.3 and 26.1 N/mm² depending on the laminate configuration. The Eurocode bridge load case remains below the applicable design material stress limits for all considered stress components. The highest stress-to-limit ratio is obtained for the maximum negative shear stress in the C-shaped girders for the wind simulation. The approximate global shear stress of 5 N/mm² corresponds to approximately 19.2% of the applicable design shear stress limit of 26.1 N/mm². The results indicate that wind loading does not govern the material strength of the preliminary design for the investigated load case.

Stress component	Stress range RWIND $[N/mm^2]$	Stress range Eurocode bridge $[N/mm^2]$
σ_x, local x-direction	-4 to +4	-7 to +7
σ_y, local y-direction	-4 to +4	-3 to +3
τ_{xy}, shear stress	-5 to +2	-4 to +4

Table 93: Approximate global stress ranges for the RWIND and Eurocode bridge load cases

Overall, the comparison shows that the Eurocode bridge load model predicts substantially higher global horizontal loads than the RWIND simulation for the investigated configuration. However, the RWIND simulation produces substantially different reaction moments due to the spatially varying pressure distribution. The RWIND simulation therefore cannot be considered simply more or less conservative than the Eurocode model based on the global loads alone. The global stress comparison shows that the two load models result in different stress distributions, but the resulting stresses remain below the applicable design material stress limits. Therefore, wind loading does not govern the material strength of the preliminary design for the investigated load case.

Furthermore, the relatively high local pressures obtained in the simulation with the modelled dike should be interpreted with caution, as the flow pattern around the dike and Seasaw may introduce local acceleration effects that are not representative of the actual wind conditions. The results of the simulation with the modelled dike are therefore primarily used to assess the sensitivity of the wind loads to the representation of the surrounding geometry, rather than as a definitive representation of the design wind loading.

13.5 Comparison RWIND simulations in x-direction with and without dike modelled

To investigate the influence of explicitly modelling the dike on the wind loading of the Seasaw, the RWIND results obtained with and without the dike geometry included in the computational domain are compared. In the simulation without the explicitly modelled dike, the influence of the dike on the wind profile is accounted for through an orography factor. The comparison therefore assesses the difference between representing the dike through an adjusted wind profile and modelling the dike geometry directly in the wind simulation. The average net pressures in the different deck regions are given in Table 94. The corresponding zones are shown in Figure 126.

Zone	Wind simulation without dike modelled (net pressure) $[kN/m^2]$	Wind simulation with dike modelled (net pressure) $[kN/m^2]$	Comparison
A	Approximately: -0.1	Approximately: -1.0	The magnitude increases considerably when the dike is explicitly modelled.
B	Approximately: +0.2 to +0.4	Approximately: -0.5 to -0.9	The pressure changes sign and increases in magnitude.
C	Approximately: +0.2 to +0.3	Approximately: +0.2 to +0.5	The pressure remains positive and increases slightly.
D	Approximately: -0.3 to -0.5	Approximately: +0.2 to +0.4	The pressure changes sign and decreases in magnitude.
E	Approximately: +0.3	Approximately: +0.5	The magnitude increases slightly.
F	Approximately: -0.1	Approximately: +0.1	The pressure changes sign but remains relatively small.
G	Approximately: -0.5 to -0.7	Approximately: -0.5 to -0.7	The pressure remains approximately unchanged.
H	Approximately: -0.3 Next to I: -1.2	Approximately: -0.5 Next to I: -1.5	The magnitude increases slightly, including the local pressure near zone I.
I	Approximately: +0.2	Approximately: -1.5	The pressure changes sign and increases considerably in magnitude.
J	Approximately: +0.4 to +0.6	Approximately: +1 to +1.7	The magnitude increases considerably.
K	Approximately: +0.1	Approximately: +1.0	The magnitude increases considerably.

Table 94: Comparison of net pressures in the different zones

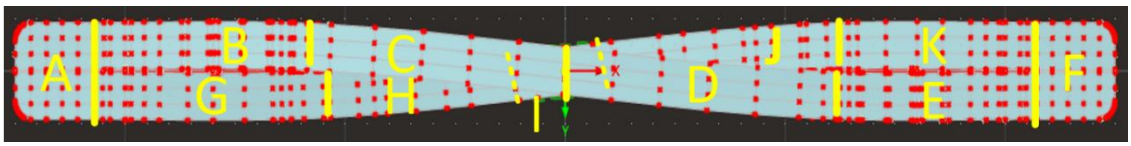

Figure 126: Zones for net pressures on deck

The results show that explicitly modelling the dike significantly changes the pressure distribution over the Seasaw compared with representing the dike influence only through the orography factor. The largest changes occur in zones A, B, I, J and K, where the pressure either changes sign or increases substantially in magnitude. In contrast, the pressure in zone G remains approximately unchanged. This indicates that the orography factor accounts for the general influence of the elevated terrain on the wind profile but does not capture the local flow effects resulting from the interaction between the dike and the Seasaw.

The difference is also evident on the side surfaces. The pressure on the +y side increases from approximately −0.2 kN/m² without the explicitly modelled dike to −1.3 kN/m² with the dike explicitly modelled. On the −y side, the pressure increases from approximately −0.3 kN/m² to −1.5 kN/m². This indicates that explicitly modelling the dike substantially increases the calculated local pressures on the side surfaces.

However, the increased pressures obtained with the modelled dike should be interpreted with caution. The streamlines in Figure 119 indicate a strong local flow acceleration in the narrow gap between the crest of the dike and the Seasaw. The streamlines become increasingly concentrated as the flow approaches the narrowed region, while the calculated velocity increases from approximately 50 m/s in the free stream to approximately 70–90 m/s in the narrowed region. This indicates a Venturi-like acceleration effect in the computational model. As a result, the high local pressures obtained with the modelled dike may be influenced by the geometry-induced acceleration and may not be representative of the actual wind conditions around the Seasaw.

The total loads and resultant reaction moments are summarized in Table 95.

Sum of loads in:	Wind simulation without dike modelled [kN]	Wind simulation with dike modelled [kN]
X	12.22	17.42
Y	4.45	20.16
Z	-1.47	7.73
Resultant of reactions about:	Wind simulation without dike modelled [kNm]	Wind simulation with dike modelled [kNm]
X	-20.43	-52.75
Y	-95.67	-827.28
Z	-2.27	-11.99

Table 95: Comparison of total loads and resultant of reactions with and without the modelled dike

Explicitly modelling the dike increases the total load in the x-direction by approximately 43% and the y-direction load by approximately 353%, corresponding to a factor of 4.5. The increase in the y-direction is particularly pronounced, indicating that the calculated wind loading is highly sensitive to the representation of the dike and the surrounding geometry. The reaction moments also increase considerably, particularly the moment about the y-axis, which increases by a factor of approximately 8.6.

Although the overall deformation shapes of the two simulations are similar, with both showing a seesaw-like deformation pattern, the magnitude of the deformation differs considerably. The maximum deformation increases from 22.1 mm without the modelled dike to 138.0 mm with the dike modelled. This further illustrates the sensitivity of the calculated structural response to the selected wind-load representation.

The influence of the modelled dike is also reflected in the global stress distribution. As shown in Table 96, the approximate global stress ranges increase when the dike is explicitly modelled. Despite these increases, the calculated global stresses remain below the applicable design material stress limits used for the preliminary design. The results therefore indicate that, although explicitly modelling the dike increases the calculated structural response, wind loading does not govern the material strength of the preliminary design for the investigated configuration.

Stress component	Stress range RWIND without modelled dike in x-direction $[N/mm^2]$	Stress range RWIND with modelled dike in x-direction $[N/mm^2]$
σ_x, local x-direction	-2 to +2	-4 to +4
σ_y, local y-direction	-1 to +1	-4 to +4
τ_{xy}, shear stress	-1 to +1	-5 to +2

Table 96: Approximate global stress ranges for the wind simulation without and with dike modelled

Overall, the comparison demonstrates that explicitly modelling the dike has a substantial influence on the calculated wind pressures, global loads, reaction moments, and structural response of the Seasaw. The orography factor accounts for the general influence of the elevated terrain on the wind profile but does not reproduce the local pressure distribution resulting from the interaction between the dike and the Seasaw. However, the high local pressures obtained with the explicitly modelled dike should be interpreted with caution. The calculated flow field shows strong local acceleration in the narrow gap between the dike and the Seasaw, resulting in a Venturi-like acceleration effect that may be influenced by the specific geometry and modelling assumptions of the computational domain. Therefore, the simulation with the explicitly modelled dike is not considered sufficiently reliable to serve as the definitive design wind load. Instead, the comparison demonstrates the sensitivity of the calculated wind loading to the representation of the surrounding geometry. A more reliable assessment of the wind loading around the dike and Seasaw would require a specialised wind engineering study, including an appropriate representation and validation of the surrounding terrain and flow field.

13.6 Overall assessment of the Eurocode wind-load provisions

Overall, the results indicate that the Eurocode wind-load provisions provide a suitable basis for the preliminary assessment of the global wind response of the Seasaw. The Eurocode bridge load model generally predicts higher global wind loads than the RWIND simulations, particularly for wind acting in the x-direction. The resulting stresses remain below the applicable design material stress limits, indicating that wind loading does not govern the material strength of the preliminary design for the investigated load cases.

The comparison also shows that the simplified Eurocode load models do not fully capture the local pressure distribution over the complex geometry of the Seasaw. The RWIND simulations provide additional information on the spatial distribution of local pressures, particularly around the connections between the top and bottom half of the structure. However, the results are sensitive to the modelling of the surrounding geometry, as demonstrated by the substantial differences between the RWIND simulations with and without the explicitly modelled dike. The strong local flow acceleration observed in the simulation with the dike further introduces uncertainty in the representativeness of the calculated pressures.

Based on the investigated load cases, the Eurocode wind-load provisions can therefore be considered applicable for the preliminary global structural assessment, while the RWIND simulations provide additional insight into local wind-pressure effects and the sensitivity of the results to the surrounding geometry.

14. Discussion

The analyses performed in this thesis demonstrate the structural feasibility of the Seasaw using flax fibre composite. However, several assumptions were made during the modelling, material characterization, and design process that influence the interpretation of the results. This chapter discusses the main limitations and uncertainties of the research, including the reliability of the finite element model, the uncertainty in material properties, the optimization potential of the design, practical aspects related to the future realization of the Seasaw and the reliability of the wind simulations.

14.1 Finite element model reliability

The finite element model provides a realistic representation of the global structural behaviour of the Seasaw. However, several modelling assumptions influence the accuracy of the local results. The supports were modelled as fully fixed boundary conditions at the bottom plate, resulting in stress singularities near the support locations. These local stresses are not representative of the actual structural behaviour because the supports are assumed to be infinitely stiff. A more realistic support model, for example incorporating support flexibility or a detailed connection model, would likely reduce these stress concentrations and provide a more accurate stress distribution.

Additional numerical difficulties occurred in the side plates surrounding the connections. These side plates were modelled using quadrilateral plate elements because of their curved geometry. The arch plate consists of multiple small plate segments, meaning that the boundaries of the top and bottom side plates are composed of many short line segments, see Figure 127. This complex geometry complicates the meshing of the quadrangle plates, resulting in overlapping mesh elements and local stress singularities in the plates adjacent to the arch. Furthermore, several side plates were modelled using triangular shaped plates to create the shape of the structure. Stress singularities are also commonly observed in the sharp corners of these triangles and should therefore be regarded as numerical artefacts rather than representative local stresses.

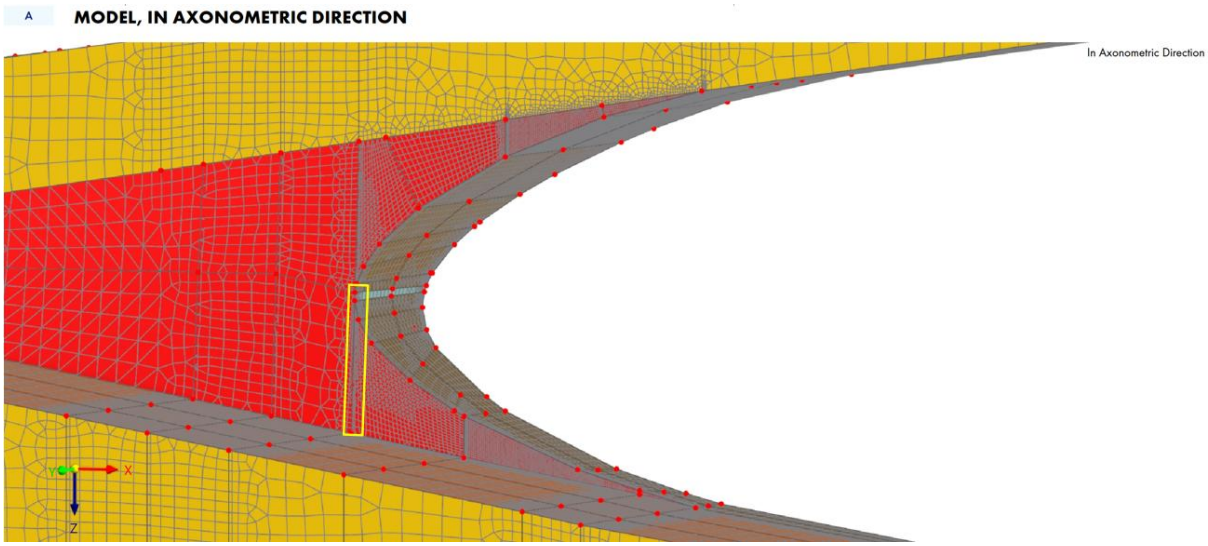

Figure 127: Connection of the top and bottom half with meshing

14.2 Finite element model mesh error

During the development of the plate model, a meshing error initially occurred, as shown in Figure 129. The error consisted of an abrupt transition from small mesh elements to elements that were twice as large, resulting in an invalid mesh. For comparison, Figure 128 shows the mesh without the error. The issue most likely originated from the mesh refinement in the top side plate (red plate), which was not correctly integrated with the girder plates (yellow plates). To resolve this issue, the end of the girder plate was aligned exactly with the end of the top side plate and the girder plate was split along the interface between the two plates. Before this modification, the girder plate extended over the full girder height, including the portion located behind the red plate. These modifications ensured proper mesh continuity between the connected components.

After these modifications, the meshing error no longer occurred for the adopted mesh settings. Although the error could still reappear for extremely fine mesh refinements, this issue was resolved by disabling the 'Independent mesh preferred' option. These observations illustrate that complex geometries can make mesh generation sensitive to modelling choices. Consequently, careful verification of the generated mesh is essential before interpreting the numerical results.

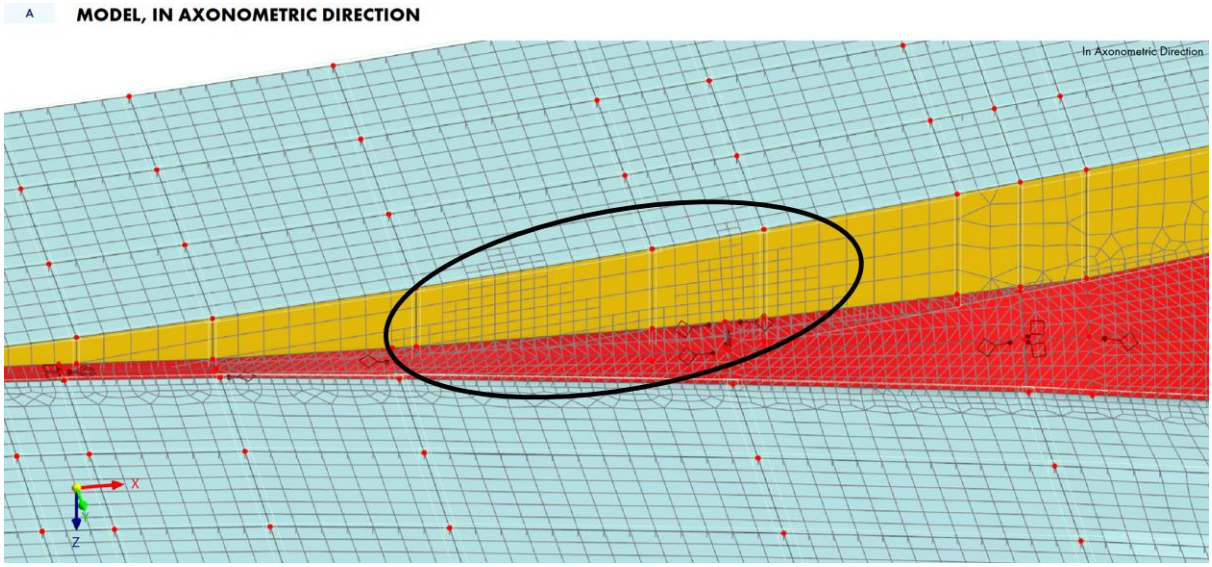

Figure 129: Mesh error plate model

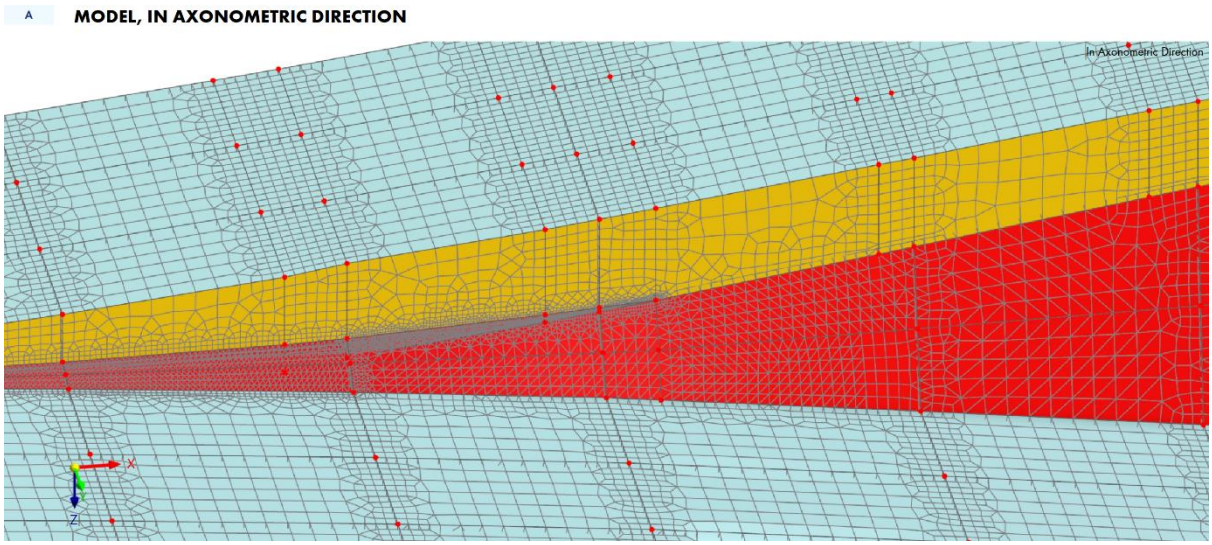

Figure 128: Mesh without error

14.3 Material properties uncertainty

The material properties of the individual flax fibre lamellas were obtained from experimental testing. The stiffness properties of the structural laminate configurations were subsequently determined using Classical Laminate Theory (CLT) based on the selected stacking sequences. Although CLT is a well-established method for predicting the behaviour of laminated composites, the calculated laminate properties have not been experimentally validated for the specific laminates used in the Seasaw. Manufacturing imperfections, such as variations in fibre volume fraction, fibre orientation, laminate thickness, and void content, may therefore lead to differences between the predicted and actual structural stiffness.

Furthermore, the characteristic strength values were estimated using the simplified strain criterion from CUR 96:2019, which was originally developed for glass fibre composites. These strength values should therefore be regarded as preliminary and should be verified through experimental testing and statistical evaluation in accordance with NEN-EN 1990 Appendix D7 before a final design is completed.

14.4 Applicability to different environmental conditions

The environmental conversion factors adopted in this study are based on the environmental conditions considered for the proposed Seasaw location in Den Helder. The structural concept may potentially be applied at other locations; however, the applicability of the adopted conversion factors depends on the environmental conditions at the new location.

Recent experimental research by Perruchoud et al. (2026) demonstrates that the mechanical behaviour of flax fibre-reinforced epoxy composites is sensitive to temperature and relative humidity. For a [0/90/0]S flax FRP laminate, the tensile modulus decreased from 17.1 GPa at 20 °C and 50% relative humidity to 14.5 GPa at 50 °C and 50% relative humidity, 11.3 GPa at 20 °C and 90% relative humidity, and 8.4 GPa at 50 °C and 90% relative humidity. Relative to the reference condition of 20 °C and 50% relative humidity, these values correspond to stiffness reduction factors of approximately 0.85, 0.66 and 0.49, respectively. (Perruchoud, Prapavesis, Alderliesten, & Mosleh, 2026)

These experimentally derived factors are not directly applicable as design conversion factors for the Seasaw, as the tested laminate, material system and exposure conditions differ from those considered in this study. The experimental results demonstrate that the effects of temperature and humidity can differ between material properties and laminate configurations.

Nevertheless, the factors provide an indication of the potential sensitivity of the structural response to environmental conditions. To illustrate this sensitivity, the three experimentally derived stiffness factors were applied in a hypothetical sensitivity analysis of the Seasaw. The resulting unity checks are presented in Figure 130.

For a factor of 0.85, all investigated structural components remain below a unity check of 1.0. When the factor is reduced to 0.66, the support plates, arch plate, top side plate, bottom side plate, bottom plate and C-shaped girders exceed a unity check of 1.0. For a factor of 0.49, the stiffener plates also exceed a unity check of 1.0. These results indicate that the structural utilisation is sensitive to reductions in the assumed material properties.

The results should, however, be interpreted as a sensitivity analysis rather than a prediction of the structural performance under these environmental conditions. The factors are derived from tensile modulus measurements and are not validated strength reduction factors for the Seasaw material. Nevertheless, they demonstrate that substantially more severe environmental conditions could have a significant influence on the required structural capacity and plate thicknesses.

The experimental study further shows that combined temperature and moisture exposure can result in reduced stiffness and strength, with the combined hot–wet condition producing substantial reductions in the investigated flax FRP laminates. Therefore, a location with simultaneously higher temperatures and humidity than Den Helder should not be considered equivalent to the environmental conditions assumed in the current design. (Perruchoud, Prapavesis, Alderliesten, & Mosleh, 2026)

Consequently, the Seasaw concept should not be considered restricted to Den Helder. However, its direct application to locations with substantially different environmental conditions cannot be justified solely using the conversion factors adopted in this study. For application at another location, the expected temperature, humidity and wetting conditions should first be established, after which the corresponding environmental reduction factors should be verified using experimental data or validated material models. In particular, locations with simultaneously high temperature and humidity require additional assessment because of the combined influence of these environmental conditions on flax FRP.

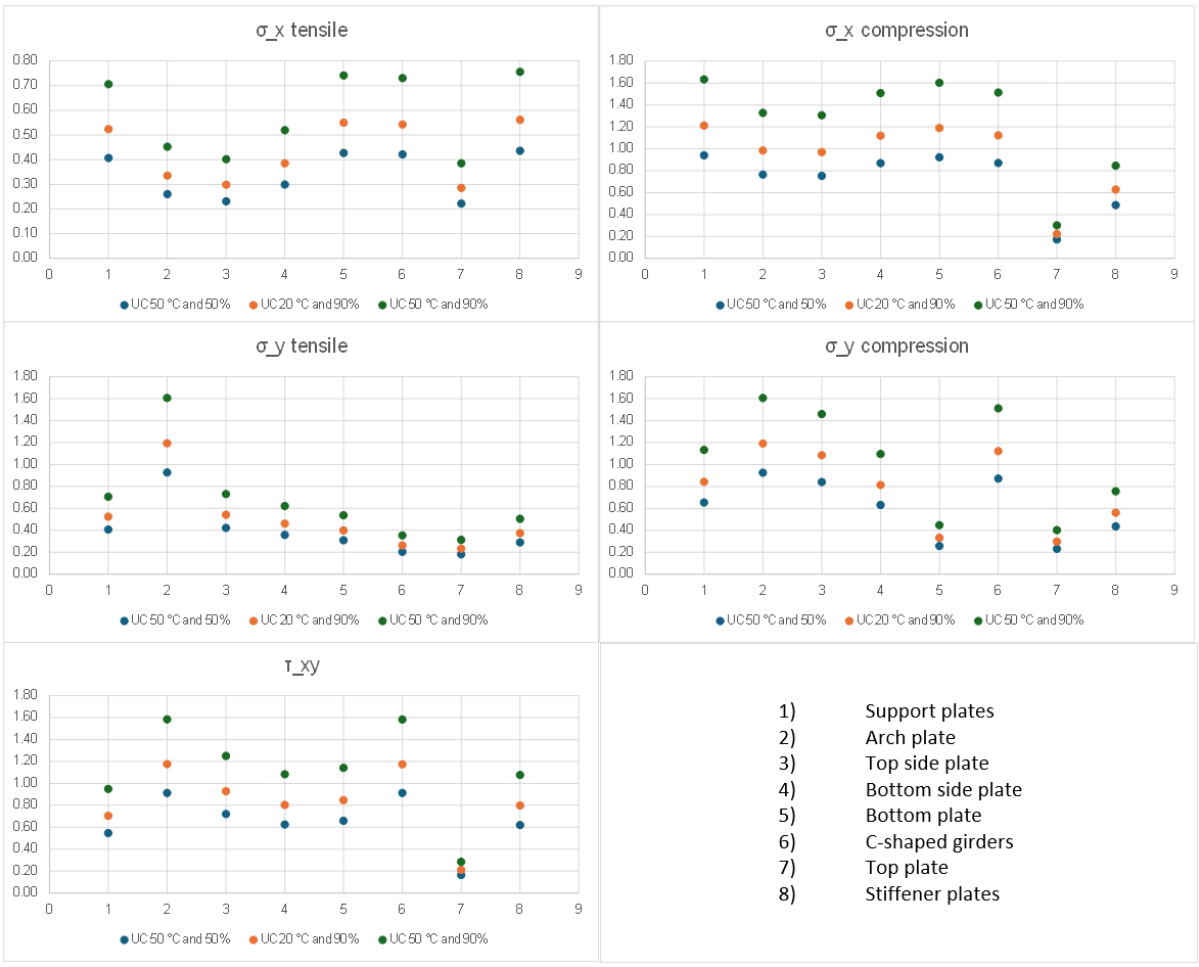

Figure 130: Graphs of unity check of the Seasaw with different reduction factors

14.5 Structural optimization and design efficiency

The final design demonstrates the structural feasibility of the Seasaw but should not be considered fully optimized. The plate thicknesses were selected per structural component to satisfy the design requirements; however, each component was assigned a constant thickness over its entire length. In reality, the internal forces and utilization vary throughout the structure, meaning that some regions are overdesigned while others are more highly utilized.

Further optimization could therefore be achieved by varying the plate thickness locally according to the structural demand. Such an approach could reduce material consumption and self-weight without compromising structural safety. However, any reduction in plate thickness should be evaluated carefully, as it may increase deflections, reduce local buckling resistance, and lower the natural frequencies of the structure.

14.6 Practical implementation of the Seasaw

The research focused primarily on the structural feasibility of the Seasaw and the verification of its structural behaviour using finite element analyses. However, several practical aspects that could influence the final design were outside the scope of this study. The manufacturing of large-scale flax fibre composite components requires further investigation, as production tolerances, laminate quality, and connection details may affect the actual structural performance.

Furthermore, the construction sequence and logistics were not considered. The division of the structure into transportable components, the transportation of these components to the dike location, and the assembly process on site may impose additional requirements on the structural design and connections. These aspects should be considered in further design stages to ensure that the proposed structural concept can be practically manufactured, transported, and assembled.

In addition, the interaction between the structure, foundation, and dike was not investigated in detail. The foundation system and the mechanism enabling the tidal-responsive movement of the Seasaw may introduce additional loads, constraints, and maintenance requirements that could influence the final structural design.

14.7 Wind simulation reliability

The wind simulations were performed for the preliminary design of the Seasaw structure. During the design process, the structure was revised by increasing the cross-sectional dimensions and making several local modifications. As a result, the pressure distribution and the resulting wind loads on the final design may differ from those obtained from the simulations presented in this study. Consequently, the wind simulation results should be regarded as representative for the preliminary design and as an indication of the expected wind behaviour rather than the exact wind loads acting on the final structure.

In addition, there was limited prior experience with computational fluid dynamics (CFD) before performing the wind simulations. Consequently, many of the default settings in RWIND were adopted without extensive sensitivity analyses. Although mesh sensitivity and convergence studies were carried out, other modelling parameters, such as turbulence modelling and boundary conditions, were not investigated in detail. As a result, the accuracy of the simulated wind loads cannot be fully quantified.

Another source of uncertainty is the determination of the net pressure acting on the structure. RWIND does not directly provide the net pressure between the upper and lower surfaces of the deck. Therefore, the net pressure was estimated by visually interpreting the pressure contour plots and determining representative average pressures on the upper and lower surfaces. This approach introduces a degree of subjectivity, as the selected averaging regions may influence the resulting pressure difference.

Furthermore, no roughness factor was applied directly to the structure in the wind simulation. Consequently, the simulated wind loads may differ from those prescribed by the Eurocode. The wind simulations should therefore primarily be regarded as an indication of the pressure distribution on the structure rather than an exact representation of the design wind loads.

Despite these limitations, the simulations provide valuable insight into the behaviour of the wind around the Seasaw structure. They show the locations of high suction and pressure, and illustrate the influence of the complex geometry on the wind flow.

Finally, the wind simulations did not include the balustrades. Since these elements can significantly influence the local flow field and pressure distribution, the simulated loads may differ from those acting on the final structure.

15. Conclusion

This chapter summarizes the main findings of the thesis and evaluates the feasibility of designing the Seasaw using flax fibre composite. The conclusions are divided into four main parts: the development and validation of the finite element models, the validation of the final design, the comparison between flax and glass fibre composites, and the wind load assessment of the structure.

15.1 Finite element model development and validation

Two finite element models were developed for the structural analysis of the Seasaw: a beam model and a plate model. Python scripts were developed to determine the required RFEM input parameters, including the equivalent material properties, plate thicknesses, and cross-sectional properties. The generated properties were verified using simply supported beam models and compared with hand calculations, showing good agreement. The beam model accurately reproduced the beam behaviour, with differences of 0.13% and 1.70% in the calculated deflections in the z- and y-directions, respectively, compared with the hand calculations. The plate model showed excellent agreement for bending in the z-direction, with a difference of 0.43%, while the difference in the y-direction was 8.05%. The lower accuracy in the y-direction is attributed to the bending stiffness contribution of the top and bottom plates being neglected when deriving the equivalent properties. (see page 66)

The plate model was successfully validated by verifying the deformation patterns and support reactions. The calculated structural response was consistent with the geometry, support conditions, and applied loads, while the reaction forces confirmed static equilibrium. The plate model therefore provides a realistic representation of the structural behaviour.

A comparison between the two models showed that the beam model represents a stiffer structural response than the plate model, particularly for loading in the x- and z-directions, resulting in underestimated deformations. For loading in the z-direction, the beam model predicted up to 45.6% lower deformation than the plate model, while for loading in the x-direction, the deformation was up to 28.5% lower (see Chapter 8.3). As a result, the beam model is not suitable for detailed ULS, SLS, stability, or modal analyses. The plate model was therefore adopted for all subsequent structural analyses.

15.2 Validation of the design

The validation demonstrates that it is structurally feasible to build the Seasaw using flax fibre composite. The revised design satisfies the majority of the predefined design criteria, including the requirements for service life, user safety, structural safety, durability, and appearance. Although local buckling occurs near the supports, this can be mitigated by locally increasing the plate stiffness (see page 99).

The serviceability assessment shows that the total characteristic deflections exceed the recommended limits at four of the six investigated locations, with a maximum exceedance of 101.1 mm. However, the variable-load deflection (w_3), which is most relevant to user comfort, exceeds the limit only at the left side part by 15.8 mm. When the side and bottom parts are considered as one cantilever, the maximum deflection of 315.3 mm remains below the limit of 333.3 mm. For quasi-permanent loading, all deflections satisfy the allowable limits when pre-camber is applied. Overall, the predicted deflections are considered acceptable (see Chapter 9.2.2).

The modal analysis indicates that the natural frequencies of modes 2, 3, and 5 fall within the critical ranges for pedestrian-induced vibrations: 0.5–1.2 Hz for lateral and torsional vibrations and 1.25–2.3 Hz for vertical vibrations (see Chapter 10). Consequently, vibration mitigation measures, such as tuned mass dampers, are required in the final design.

Overall, the analyses show that a flax fibre composite Seasaw is feasible, provided that local buckling is addressed and appropriate vibration mitigation measures are incorporated during the detailed design stage.

15.3 Comparison of flax and glass fibre composite

The comparison between the flax fibre and glass fibre designs shows that the glass fibre composite provides superior structural performance. Despite its higher material density, the glass fibre design has a 2.8% lower self-weight due to the reduced plate thicknesses, while also exhibiting 26.1-29.4% smaller deflections and higher natural frequencies. However, the thinner plates result in lower buckling resistance, with 21 critical load factors below 1.0 for the glass fibre design compared with 9 for the flax fibre design, making local stability more critical than for the flax fibre design (see page 113).

15.4 Wind simulation

Wind simulations were performed in RWIND to verify whether the wind load provisions of the Eurocodes for bridges are applicable to the unique geometry of the Seasaw. The results showed that the flow around the structure is significantly affected by its unconventional geometry, leading to non-uniform pressure distributions over the deck. Although the simulation results deviated from the Eurocode provisions, the Eurocode remains a conservative basis for overall safety. Ultimately, the results indicate that wind loading does not govern the material strength of the preliminary design for the investigated load cases.

15.5 Recommendations for further development

Although the analyses proof the feasibility of building the Seasaw using flax fibre composite, several aspects require further investigation before a final design can be achieved. The following recommendations are proposed:

- Validation of material properties: The characteristic stress limits used for the flax fibre composite are based on available data and should be validated through experimental testing and statistical evaluation according to NEN-EN 1990 Appendix D7.
- Improved support modelling and local reinforcement: The simplified support modelling resulted in stress concentrations and local buckling near the supports. A more detailed support model should be developed to obtain more realistic stresses and optimize local reinforcement, for example using sandwich plates with a balsa core or additional flax fibre layers.
- Structural optimization: The current design uses similar plate thicknesses for multiple components. A detailed design phase should optimize the thicknesses while considering strength, stability, and deflection requirements. The laminate should also be tested on lamella level.
- Fatigue assessment: The influence of repeated wind loading on the long-term performance of the structure should be evaluated.
- Pedestrian comfort and vibration control: A detailed pedestrian comfort assessment should be performed, followed by the design and positioning of tuned mass dampers if required.
- Additional assessments: Robustness and railing design were outside the scope of this study and should be addressed in a further design stage.
- Foundation and movement mechanism: The foundation design and tidal movement mechanism were outside the scope of this research. Further studies should investigate the interaction between the structure, foundation, and dike, as well as the influence of the movement mechanism on structural behaviour, durability, and maintenance.

- Sustainability assessment: A life cycle assessment should be performed to quantify the environmental impact of the Seasaw, including production, maintenance, and end-of-life scenarios.

References

Amsterdam, E. v. (2025). *Creep Behaviour of Flax Fibre Composites.* Delft. Retrieved from https://resolver.tudelft.nl/uuid:4b3a285f-5567-450e-9e28-0a2237abf0ff

ARK Basalt Fibre. (n.d.). *Mechanische eigenschappen*. Retrieved from ARK Basalt Fibre: https://basaltfiberchina.com/properties/mechanical-properties/

ArmaPET Eco. (2023). Retrieved from Materialiecososostenibili: http://materialiecososostenibili.com/collections/materiali

Barré, S., Chotard, T., & Benzeggagh, M. (1996). *Comparative study of strain rate effects on mechanical properties of glass fibre-reinforced thermoset matrix composite.* Compiègne: Elsevier. Retrieved from https://www.sciencedirect.com/science/article/pii/1359835X96000759

Basalt woven fabrics. (n.d.). Retrieved from Basaltex: https://www.basaltex.com/products/woven-fabrics

Blaauwendraad, J. (2010). *Plates and FEM.* Ontario: Delft. Retrieved from https://phoogenboom.nl/boek%20blaauwendraad.pdf

Borrega, M., Ahvenainen, P., Serimaa, R., & Gibson, L. (2015). *Composition and structure of balsa (Ochroma pyramidale) wood.* Retrieved from https://link.springer.com/article/10.1007/s00226-015-0700-5

Chand, N., & Fahim, M. (2021). *Tribology of Natural Fiber Polymer Composites.* Woodhead publishing. Retrieved from https://www.sciencedirect.com/science/chapter/monograph/pii/B9780128189832000116

Composite Calculator. (2019). Retrieved from Composite Construction Materials: https://composite-designers.com/composite-theory/

CYC Fiberglass Unidirectional Fabric (UD Fabric). (n.d.). Retrieved from CYC Composites: https://www.cyccomposites.net/sale-8445967-e-glass-unidirectional-fiberglass-fabric-ud-fabric.html

De IJssel Coatings BV. (2022). *IJMOPOX HB COATING.* Retrieved from https://de-ijssel-coatings.s3.eu-central-1.amazonaws.com/uploads/tib/nl/352.pdf

Entities: Consistent vs Lumped Mass. (n.d.). Retrieved from strand7: https://www.strand7.com/strand7r3help/Content/Topics/Elements/ElementsMassMatrix.htm

Flax Fibre Reinforcement in Composites. (n.d.). Retrieved from Easycomposites: https://www.easycomposites.eu/learning/flax-fibre-in-composites

Hoogenboom, P. (2023). *Notes on torsion.* Hoogmade. Retrieved from https://phoogenboom.nl/dictaatwringingEng.pdf

Hydrophobic effect. (2025, 5 25). Retrieved from Wikipedia: https://en.wikipedia.org/wiki/Hydrophobic_effect#:~:text=The%20hydrophobic%20effect%20is%20the,observed%20are%20known%20as%20hydrophobes.

Jörg Franke, J., Hellsten, A., Schlünzen, H., & Carissimo, B. (2007). *Best practice guideline for the CFD simulation of flows in the urban environment.* COST European Cooperation in Science. Retrieved from https://hal.science/hal-04181390/

Kiron, M. I. (2025, 9 6). *What is Basalt Fiber: Properties, Manufacturing and Applications*. Retrieved from Textilelearner: https://textilelearner.net/what-is-basalt-fiber-properties-manufacturing-and-applications/

Koolstofvezel. (2024, 11 18). Retrieved from Wikipedia: https://nl.wikipedia.org/wiki/Koolstofvezel

Mallick, P. (2007). *FIBER REINFORCED COMPOSITES.* Taylor & Francis Group. Retrieved from https://ia803204.us.archive.org/24/items/IntroductionToBasicManufacturingProcessAndWorkshopTechnology/Fibre_Reinforced_Composites.pdf

Maps. (2026). Retrieved from Google: https://www.google.com/maps/@52.9256074,4.8225299,11z?entry=ttu&g_ep=EgoyMDI2MDgwNS4xIKXMDSoASAFQAw%3D%3D

Morvan, C., Andème-Onzighi, C., Girault, R., Himmelsbach, D. S., Driouich, A., & Akin, D. E. (2003). *Building flax fibres: more than one brick in the walls.* Elsevier. Retrieved from https://www.sciencedirect.com/science/article/pii/S0981942803001529

NEN. (2016). *Guidance for the Design of FRP Bridges.* NEN.

Nijsen, R. (2015). *Composieten basiskennis.* VKCN.

Nour-Omid, B., & Regelbrugge, M. E. (1989). *Lanczos method for dynamic analysis of damped structural systems.* Retrieved from https://onlinelibrary-wiley-com.tudelft.idm.oclc.org/doi/abs/10.1002/eqe.4290180802

Online Manuals RWIND 3: Troubleshooting. (n.d.). Retrieved from Dlubal: https://www.dlubal.com/en/downloads-and-information/documents/online-manuals/rwind-3/005662

OSMOSE, WAT IS HET EN HOE KUNT U HET VOORKOMEN OF BEHANDELEN? (n.d.). Retrieved from vanbaars expert pleziervaartuigen: https://www.expertpleziervaart.nl/artikel/osmose-wat-is-het-hoe-voorkomen-of-behandelen

Pavlovic, A., Valzania, L., & Minak, G. (2025). *Effects of Moisture Absorption on the Mechanical and Fatigue Properties of Natural Fiber Composites: A Review.* Basel. Retrieved from https://pmc.ncbi.nlm.nih.gov/articles/PMC12299171/

Perruchoud, V., Alderliesten, R., & Mosleh, Y. (2025). *Tailoring the fatigue response of flax FRP composites by exploiting Micro-structural re-arrangements and auxiliary loading sequences.* Delft: Elsevier Ltd.

Perruchoud, V., Prapavesis, A., Alderliesten, R., & Mosleh, Y. (2026). *Combined and isolated effects of humidity and temperature on monotonic and fatigue response of flax fibre/epoxy composites.* Elsevier. Retrieved from https://www.sciencedirect.com/science/article/pii/S1359836826004622#sec3.1.4

Pisupati, A., Bonnaud, L., Deléglise-Lagardère, M., & Hae Park, C. (2021). *Influence of Environmental Conditions on the Mechanical Properties of Flax Fiber Reinforced Thermoset Composites.* Retrieved from https://link.springer.com/article/10.1007/s10443-021-09885-z

Pitarresi, G., Tumino, D., & Mancuso, A. (2015). *Thermo-Mechanical Behaviour of Flax-Fibre Reinforced Epoxy Laminates for Industrial Applications.* Retrieved from https://www.mdpi.com/1996-1944/8/11/5384

Plymouth University. (n.d.). *Reinforcement fibres.* Retrieved from Composites Design and Manufacture: https://ecm-academics.plymouth.ac.uk/jsummerscales/MATS347/MATS347C1%20fibres.htm

PSS 20 graffiti becherming. (n.d.). Retrieved from AZS Nederland: https://www.azsnederland.nl/pss-20-graffiti-becherming/

Section builder. (n.d.). Retrieved from SkyCiv: https://platform.skyciv.com/section-builder

Shahmirzaloo, A. (2025). *Flax Fiber Polyester Resin in Bridge Construction.* Eindhoven University of Technology, Eindhoven. Retrieved from https://pure.tue.nl/ws/portalfiles/portal/355129970/20250409_Shahmirzaloo_hf.pdf

Shelton, S. (n.d.). *How to Grow Flax: Advice from Farmers*. Retrieved from Piedmont Fibershed: https://www.piedmontfibershed.org/whats-new/how-to-grow-flax-advice-from-farmers

Smart Circular Bridge for a circular built environment. (n.d.). Retrieved from Interreg North-West Europe Smart Circular Bridge: https://vb.nweurope.eu/projects/project-search/smart-circular-bridge-scb-for-pedestrians-and-cyclists-in-a-circular-built-environment/#tab-4

Stainless steel. (2015, 12 25). Retrieved from Wikipedia: https://en.wikipedia.org/wiki/Stainless_steel

Stamboulis, A., Baillie, C. A., Garkhail, S. K., van Melick, H. G., & Peijs, T. (2000). *Environmental Durability of Flax Fibres and their Composites based on Polypropylene Matrix.* Kluwer Academic Publishers. Retrieved from https://link.springer.com/article/10.1023/A:1026581922221

Togeby, S. (2025, 8 16). *A Bridge Made of Flax Fibres Can Carry 24 Tons – and Plays Music When You Walk on It*. Retrieved from Institut for Bæredygtighed og Planlægning: https://www.plan.aau.dk/a-bridge-made-of-flax-fibres-can-carry-24-tons-n140657

Tuned Mass Damper. (n.d.). Retrieved from Flow engineering: https://flow-engineering.com/tuned-mass-dampers-tmd/

Tuned Mass Damper for bridges. (n.d.). Retrieved from Flow engineering: https://flow-engineering.com/tuned-mass-damper-bridge/

UD Carbon Fiber Cloth. (n.d.). Retrieved from CA Composites: https://cacomposites.com/product/ud-carbon-fiber-cloth/

Vacuum Resin Infusion Process Explained. (n.d.). Retrieved from Smarttech: https://smartechonline.com/resources/vacuum-resin-infusion-process/

Valentino, P., Furgiuele, F., Romano, M., Ehrlich, I., & Gebbeken, N. (2013). *Mechanical characterization of basalt fibre reinforced plastic with different fabric reinforcements – Tensile tests and FE-calculations with representative volume elements (RVEs).* Rome. Retrieved from https://d1wqtxts1xzle7.cloudfront.net/47715210/10914-41710-1-PB-libre.pdf?1470120095=&response-content-disposition=inline%3B+filename%3DMechanical_characterization_of_basalt_fi.pdf&Expires=1773650032&Signature=IBvCJRybblmjTGH0WxB9ctS6uOclOa9QzMdCxs4Eh6Ppi

Viscocity of air, Dynamic and Kinematic. (n.d.). Retrieved from Engineers edge: https://www.engineersedge.com/physics/viscosity_of_air_dynamic_and_kinematic_14483.htm

Yan, L., Chouw, N., & Jayaraman, K. (2013). *Flax fibre and its composites – A review.* The University of Auckland, Auckland. Retrieved from https://www.sciencedirect.com/science/article/pii/S1359836813004228#s0010

Zhang, Y., Yan, S., Wang, X., Guan, Y., Du, C., Fan, T., . . . Zhai, J. (2024). *An Experimental Investigation of the Mechanism of Hygrothermal Aging and Low-Velocity Impact Performance of Resin Matrix Composites.* Basel. Retrieved from https://pmc.ncbi.nlm.nih.gov/articles/PMC11174897/#:~:text=Their%20research%20shows%20that%20hygrothermal,fiber%20interface%20using%20molecular%20dynamics.

Zweben, C. (2005). *Composites: Overview.* Devon: Elsevier. Retrieved from https://www.sciencedirect.com/science/chapter/referencework/abs/pii/B0123694019005453

Appendix A: Strength verification composites

According to CUR 96:2019, the structural verification of composite materials may be performed at lamina, laminate, and cross-sectional level, depending on the required level of detail and the governing failure mechanism.

Lamella level strength verification

For laminates subjected to multi-axial stress states, or laminates composed of different fibre reinforcement materials within a single stacking sequence, see Chapter 6.12, strength verification shall be performed at the lamella level.

In a lamella-level analysis, laminate failure is assessed based on the progressive failure of the individual plies. Initial failure is defined by the failure of the first ply. If first ply failure is considered acceptable within the design philosophy, a progressive failure analysis may be performed in which failed plies are successively removed from the stiffness matrix until the last ply fails, which defines ultimate laminate failure. The contribution of failed plies to the residual stiffness and strength shall be neglected, typically by reducing their stiffness properties to zero or to a negligible value.

The stresses and strains in each ply may be determined using either:

- an analytical approach based on Classical Laminate Theory (CLT); or
- a numerical approach using a Finite Element Method (FEM) model.

For each individual lamina, the combined stress state must be evaluated using an appropriate failure criterion. Commonly used criteria include the Tsai–Hill failure criterion, the Tsai–Wu failure criterion, and the Puck Action Plane Fracture Model. The Von Mises criterion is not considered suitable for fibre-reinforced polymer composites.

The Tsai-Hill failure criterion is given by:

$$\left(\frac{\sigma_{1,Ed}}{f_{1,Rd}}\right)^2 + \left(\frac{\sigma_{2,Ed}}{f_{2,Rd}}\right)^2 + \left(\frac{\tau_{12,Ed}}{\tau_{12,Rd}}\right)^2 - \frac{\sigma_{1,Ed} * \sigma_{2,Ed}}{f_{1,Rd}^2} \leq 1.0$$

The Tsai-Wu failure criterion is given by:[17]

$$\frac{\sigma_{1,Ed}^2}{f_{1t,Rd} * f_{1c,Rd}} + \frac{\sigma_{2,Ed}^2}{f_{2t,Rd} * f_{2c,Rd}} - \sqrt{\frac{1}{f_{1t,Rd} * f_{1c,Rd}} * \frac{1}{f_{2t,Rd} * f_{2c,Rd}}} * \sigma_{1,Ed} * \sigma_{2,Ed} + \left(\frac{1}{f_{1t,Rd}} - \frac{1}{f_{1c,Rd}}\right)$$
$$* \sigma_{1,Ed} + \left(\frac{1}{f_{2t,Rd}} - \frac{1}{f_{2c,Rd}}\right) * \sigma_{2,Ed} + \left(\frac{\tau_{12,Ed}}{\tau_{12,Rd}}\right)^2 \leq 1.0$$

Where:

$\sigma_{1,Ed}$	is the normal stress parallel to the fibre direction
$\sigma_{1,Ed}$	is the normal stress perpendicular to the fibre direction
$\tau_{12,Ed}$	is the shear stress

[17] Equations Tsai-Wu failure criterion is obtained from: Lecture 1 & 2 of the course AE 4509, 10-2-2014 & 14-2-2014

The design capacity parallel to the fibre direction is defined as:

$$f_{1,Rd} = \frac{\eta_c * \varepsilon_{1,Rk} * E_1}{\gamma_M}$$

Where:

$f_{1,Rd} = f_{1t,Rd}$ and $\varepsilon_{1,Rd} = \varepsilon_{1t,Rd}$ if $\sigma_{1,Ed} \geq 0.0$ (tension)

$f_{1,Rd} = f_{1c,Rd}$ and $\varepsilon_{1,Rd} = \varepsilon_{1c,Rd}$ if $\sigma_{1,Ed} < 0.0$ (compression)

The design capacity perpendicular to the fibre direction is defined as:

$$f_{2,Rd} = \frac{\eta_c * \varepsilon_{2,Rk} * E_2}{\gamma_M}$$

Where:

$f_{2,Rd} = f_{2t,Rd}$ and $\varepsilon_{2,Rd} = \varepsilon_{2t,Rd}$ if $\sigma_{2,Ed} \geq 0.0$ (tension)

$f_{2,Rd} = f_{2c,Rd}$ and $\varepsilon_{2,Rd} = \varepsilon_{2c,Rd}$ if $\sigma_{2,Ed} < 0.0$ (compression)

The design shear stress capacity is defined as:

$$\tau_{12,Rd} = \frac{\eta_c * \gamma_{12,Rk} * G_{12}}{\gamma_M}$$

Laminate level strength verification

In a laminate-level analysis, the failure of the composite laminate is assessed based on a stress or strain criterion applied to the laminate as a whole, rather than to the individual plies.

For a uniaxial stress state or pure in-plane shear, the laminate shall satisfy the following strength criteria:

$$\frac{\sigma_{i,Ed}}{f_{i,Rd}} \leq 1.0 \text{ and } \frac{\tau_{kl,Ed}}{\tau_{kl,Rd}} \leq 1.0$$

Where:

$\sigma_{i,Ed}$	is the applied normal stress in the considered loading direction
$\tau_{kl,Ed}$	is the applied shear stress in the considered plane
$f_{i,Rd}$	is the design strength of the laminate in the considered loading direction
$\tau_{kl,Rd}$	is the design shear strength of the laminate in the considered plane
i, k, l	are coordinate axes corresponding to the considered directions

The laminate strength should be determined experimentally which will not be done in this report.

For fibre-reinforced laminates, containing at least 12.5% fibre reinforcement in each principal material direction and satisfying the boundary conditions specified in CUR 96:2019, a simplified strain criterion may be applied. For uniaxial loading or pure in-plane shear with respect to the laminate axes x and y, the following limits apply:

$$\varepsilon_{x,Ed} \leq \frac{\eta_c * 1.2\%}{\gamma_M}$$

$$\varepsilon_{y,Ed} \leq \frac{\eta_c * 1.2\%}{\gamma_M}$$

$$\gamma_{x,Ed} \leq \frac{\eta_c * 1.6\%}{\gamma_M}$$

For multi-axial stress states, or for laminates consisting of different fibre reinforcement materials within one laminate, the laminate-level stress or strain criterion may be derived according to the general methodology in 'Lamella level strength verification'. For a specific laminate lay-up, this procedure may be used to derive a three-dimensional stress or strain failure envelope, representing the allowable combined loading domain of the laminate.

Cross-sectional level strength verification

As an alternative for structural members, strength verification may be performed at the cross-sectional level, where the resistance is evaluated in terms of the internal forces and bending moments acting on the section. In this approach, the design resistance of the cross-section as a whole shall be used.

The design values of the applied section forces shall not exceed the corresponding design resistances. When multiple section forces act simultaneously, their combined effect shall not exceed the cross-sectional resistance for that load combination.

As a conservative approach, the interaction between the different load effects may be assessed using a linear interaction criterion:

$$\frac{N_{Ed}}{N_{Rd}} + \frac{M_{y,Ed}}{M_{y,Rd}} + \frac{M_{z,Ed}}{M_{z,Rd}} + \frac{V_{y,Ed}}{V_{y,Rd}} + \frac{V_{z,Ed}}{V_{z,Rd}} + \frac{\tau_{Ed}}{\tau_{Rd}} \leq 1.0$$

Where N_{Ed}, $M_{y,Ed}$, $M_{z,Ed}$, $V_{y,Ed}$, $V_{z,Ed}$ en τ_{Ed} are the design values of the applied internal forces and bending moments and N_{Rd}, $M_{y,Rd}$, $M_{z,Rd}$, $V_{y,Rd}$, $V_{z,Rd}$ en τ_{Rd} are the corresponding cross-sectional design resistances.

The cross-sectional resistance should preferably be determined experimentally, which will not be done in this report. Alternatively, it may be derived analytically from the laminate-level material properties.

Appendix B: Material properties of different fibre composites

This appendix provides an overview of the material properties of the fibre composites considered for use in the hybrid composites, namely glass fibre, carbon fibre, and basalt fibre composites. For each material, the general characteristics are briefly described, followed by the mechanical properties of the fibres and the material properties of the corresponding fibre composite, including the elastic modulus and strength limits. Finally, the thickness of a unidirectional (UD) lamella is determined based on the fibre density and a fibre volume fraction of 50%.

Glass fibre

Glass fibre is made from silicon dioxide (SiO_2), which is primarily obtained from sand. To produce glass fibres, silicon dioxide is heated together with various additives to temperatures above its melting point. The molten glass is then directed into channels that contain small openings at the bottom, each with a diameter of approximately 2 mm. The molten material flows through these openings and forms continuous filaments. (Nijsen, 2015)

These viscous filaments are wound onto a rotating spool at very high speeds. As a result of this rapid winding process, the filaments are stretched significantly, reducing their diameter to about 20 micrometres. Immediately after leaving the extrusion bushings, made from a platinum-rhodium alloy that can withstand extremely high temperatures, the fibres are sprayed with water to cool and solidify them quickly. The water contains additives that facilitate the subsequent processing of the fibres. (Nijsen, 2015)

There are different types of glass, each with specific material properties. Each type is designated by a letter. The most common type is E-glass, which is widely used due to its low cost and low thermal and electrical conductivity. Other types include:

- S-glass, which offers higher strength and stiffness
- C-glass, which provides improved chemical resistance
- D-glass, which has a low dielectric constant and is therefore particularly suitable for applications such as radar domes

The type of glass is determined by its chemical composition. The material properties of E-glass fibres are shown in Table 97. (Nijsen, 2015) (Zweben, 2005)

Property	**E-glass**
Stiffness [GPa]	70-80
Tensile strength [MPa]	2400
Strain at break [%]	2.6
Density [kg/m^3]	2500-2600
Break length [km]	96

Table 97: Properties of E-glass fibres (Nijsen, 2015)

The material properties of a UD lamella of E-glass fibre UP composite according to CUR96 are shown in Table 98 and Table 99.

V_f [−]	E_1 [Gpa]	E_2 [Gpa]	G [Gpa]	ν [−]
50%	37.2	11.4	3.4	0.29

Table 98: Material properties of a UD lamella of E-glass fibre UP composite

		CUR 96 Strain limit [%]		Material Stress limit $[N/mm^2]$
Tension	$\varepsilon_{1t,Rk}$	1.2	$\sigma_{f1t} = \varepsilon_{1t,Rk} * E_1$	446.4
	$\varepsilon_{2t,Rk;low}$	1.2	$\sigma_{f2t} = \varepsilon_{2t,Rk;low} * E_{2,low}$	136.8
Compression	$\varepsilon_{1c,Rk}$	1.0	$\sigma_{f1c} = \varepsilon_{1c,Rk} * E_1$	372
	$\varepsilon_{2c,Rk;low}$	1.2	$\sigma_{f2c} = \varepsilon_{2c,Rk;low} * E_{2,low}$	136.8
Shear	$\gamma_{12,Rk}$	1.6	$\tau_{f12} = \gamma_{12,Rk} * G$	54.4

Table 99: Stress limit of a UD lamella of E-glass fibre UP composite

The unidirectional lamella of E-glass fibre has a weight of 300 gram/m^2, the ECY-UDT300-1270 was chosen. (CYC Fiberglass Unidirectional Fabric (UD Fabric), sd) The thickness of a glass fibre lamella for a density of 2550 kg/m^3 and a fibre volume fraction of 50% is:

- $t_{300} = \frac{300}{2550*0.50} = 0.24\ mm$

Carbon fibre

Carbon fibre is composed of extremely fine filaments of carbon, typically 5–10 micrometres in diameter, made of elongated carbon crystals mostly aligned along the fibre axis. The fibres exhibit very low elongation before fracture, resulting in high tensile strength and stiffness in the fibre direction. (Koolstofvezel, 2024)

Carbon fibres are produced from carbon-rich raw materials such as PAN (polyacrylonitrile), pitch, or cellulose. PAN is a semi-finished product with consistent properties, while pitch is a natural material that is more cost-effective but less uniform. (Nijsen, 2015)

Filaments are drawn from the PAN or pitch, and then they undergo three processing steps:

1. Oxidation at around 200°C, imparts the characteristic black colour to the fibres.
2. Carbonization at 800–1600°C, removes non-carbon elements such as nitrogen.
3. Graphitization finalizes the carbon structure and properties of the fibre.

During processing, fibres are stretched to align the carbon chains with the fibre axis, producing an anisotropic structure. Carbon fibres are typically transversely isotropic, with stiffness and strength much higher along the fibre length than across it. The material properties of carbon fibres are shown in Table 100. There are many grades of carbon fibre, with some optimized for high strength and others for high stiffness. This explains the relatively wide range of reported material properties. (Nijsen, 2015)

Property	Carbon
Stiffness [GPa]	160-440
Tensile strength [MPa]	2000-5300
Strain at break [%]	1-1.5
Density [kg/m^3]	1800-2000
Break length [km]	187

Table 100: Properties of Carbon fibres (Nijsen, 2015)

The material properties of Carbon fibre HS obtained from CUR96 are shown in Table 101.

Fibre	ρ_f $[kg/m^3]$	E_{f1} $[N/mm^2]$	E_{f2} $[N/mm^2]$	G_f $[N/mm^2]$	ν_f $[-]$
Carbon fibres HS	1790	238000	15000	50000	0.30

Table 101: Material properties of Carbon fibre HS obtained from CUR96

The material properties of a lamella of Carbon fibre UP composite are shown in Table 102 and Table 103. The properties of the lamella are calculated with the following formulas:

$$E_1 = E_f * V_f + E_r * V_r = 238 * 0.5 + 3.350 * 0.5 = 120.67\ GPa$$

$$E_2 = \frac{E_f E_r}{E_f V_r + E_r V_f} = \frac{238 * 3.350}{238 * 0.5 + 3.350 * 0.5} = 6.6\ GPa$$

$$G = \frac{G_f G_r}{G_f V_r + G_r V_f} = \frac{50 * 1.350}{50 * 0.5 + 1.350 * 0.5} = 2.6\ GPa$$

$$\nu = \nu_f V_f + \nu_r V_r = 0.3 * 0.5 + 0.38 * 0.5 = 0.34$$

(Mallick, 2007)

$\boldsymbol{V_f}$ [−]	$\boldsymbol{E_1}$ $[\boldsymbol{GPa}]$	$\boldsymbol{E_2}$ $[\boldsymbol{GPa}]$	$\boldsymbol{G}$ $[\boldsymbol{Gpa}]$	$\boldsymbol{\nu}$ [−]
50%	120.67	6.6	2.6	0.34

Table 102: Material properties of a UD lamella of Carbon fibre UP composite

		CUR 96 Strain limit [%]		**Material Stress limit** $[\boldsymbol{N/mm^2}]$
Tension	$\varepsilon_{1t,Rk}$	1.2	$\sigma_{f1t} = \varepsilon_{1t,Rk} * E_1$	1448.04
	$\varepsilon_{2t,Rk;low}$	1.2	$\sigma_{f2t} = \varepsilon_{2t,Rk;low} * E_{2,low}$	79.2
Compression	$\varepsilon_{1c,Rk}$	1.0	$\sigma_{f1c} = \varepsilon_{1c,Rk} * E_1$	1206.7
	$\varepsilon_{2c,Rk;low}$	1.2	$\sigma_{f2c} = \varepsilon_{2c,Rk;low} * E_{2,low}$	79.2
Shear	$\gamma_{12,Rk}$	1.6	$\tau_{f12} = \gamma_{12,Rk} * G$	41.6

Table 103: Stress limit of a UD lamella of Carbon fibre UP composite

The unidirectional lamella of carbon fibre has a weight of 200, 300, 400, 450 and 600 gram/m^2. A weight of 300 gram/m^2 will be chosen. (UD Carbon Fiber Cloth, sd) The thickness of carbon fibre lamella for a density of 1800 kg/m^3 and a fibre volume fraction of 50% is:

- $t_{300} = \frac{300}{1800 * 0.50} = 0.33\ mm$

Basalt fibre

Basalt is an igneous rock formed from the solidification of volcanic magma. The manufacturing process of basalt fibre is similar to that of glass fibre. Like glass, basalt is heated in a furnace until it melts, after which fibres are drawn from the molten material. Unlike glass production, this process does not require the mixing of additional components, as basalt naturally contains the necessary minerals. The composition of basalt varies depending on its geographical source, which limits the supply. In addition, basalt is more difficult to melt than glass, requiring higher processing temperatures. The material properties of basalt fibre are shown in Table 104.

Property	Basalt
Stiffness [GPa]	79-93
Tensile strength [MPa]	3000-4840
Strain at break [%]	2-3.2
Density [kg/m^3]	2600-2800
Break length [km]	113
Poisson ratio [-]	0.26
Shear modulus [GPa]	21.7

Table 104: Properties of basalt fibres (Kiron, 2025), (Plymouth University, sd), (ARK Basalt Fibre, sd), (Valentino, Furgiuele, Romano, Ehrlich, & Gebbeken, 2013)

The material properties of a lamella of Basalt fibre UP composite are shown in Table 105 and Table 106. The given shear modulus and Poisson ratio given in the table above belong to a stiffness of 89 GPa. (Valentino, Furgiuele, Romano, Ehrlich, & Gebbeken, 2013) The properties of the lamella are calculated with the following formulas:

$$E_1 = E_f * V_f + E_r * V_r = 89 * 0.5 + 3.350 * 0.5 = 46.17\ GPa$$

$$E_2 = \frac{E_f E_r}{E_f V_r + E_r V_f} = \frac{89 * 3.350}{89 * 0.5 + 3.350 * 0.5} = 6.5\ GPa$$

$$G = \frac{G_f G_r}{G_f V_r + G_r V_f} = \frac{21.7 * 1.350}{21.7 * 0.5 + 1.350 * 0.5} = 2.5\ GPa$$

$$\nu = \nu_f V_f + \nu_r V_r = 0.26 * 0.5 + 0.38 * 0.5 = 0.32$$

(Mallick, 2007)

$\boldsymbol{V_f}$ $[-]$	$\boldsymbol{E_1}$ $[\boldsymbol{GPa}]$	$\boldsymbol{E_2}$ $[\boldsymbol{GPa}]$	$\boldsymbol{G}$ $[\boldsymbol{Gpa}]$	$\boldsymbol{\nu}$ $[-]$
50%	46.17	6.5	2.5	0.32

Table 105: Material properties of a UD lamella of Basalt fibre UP composite

		CUR 96 Strain limit [%]		Material Stress limit $[\boldsymbol{N/mm^2}]$
Tension	$\varepsilon_{1t,Rk}$	1.2	$\sigma_{f1t} = \varepsilon_{1t,Rk} * E_1$	554.04
	$\varepsilon_{2t,Rk;low}$	1.2	$\sigma_{f2t} = \varepsilon_{2t,Rk;low} * E_{2,low}$	77.5
Compression	$\varepsilon_{1c,Rk}$	1.0	$\sigma_{f1c} = \varepsilon_{1c,Rk} * E_1$	461.7
	$\varepsilon_{2c,Rk;low}$	1.2	$\sigma_{f2c} = \varepsilon_{2c,Rk;low} * E_{2,low}$	77.5
Shear	$\gamma_{12,Rk}$	1.6	$\tau_{f12} = \gamma_{12,Rk} * G$	40.7

Table 106: Stress limit of a UD lamella of Basalt fibre UP composite

The unidirectional lamella of basalt fibre has a weight of 400 gram/m^2. (Basalt woven fabrics, sd) The thickness of a basalt fibre lamella for a density of 2700 kg/m^3 and a fibre volume fraction of 50% is:

$$t_{400} = \frac{400}{2700 * 0.50} = 0.30\ mm$$

Appendix C: Classical Laminate Theory (CLT)

The equations and theory for the Classical Laminate Theory is obtained from Lecture 1 & 2 of the course AE 4509, 10-2-2014 & 14-2-2014. The equations, theory and derivation are given below.

Stress-strain relations lamella

The constitutive relation, stress-strain relation, for a single lamella is:

$$\begin{bmatrix}\sigma_x\\ \sigma_y\\ \sigma_z\\ \tau_{yz}\\ \tau_{xz}\\ \tau_{xy}\end{bmatrix} = \begin{bmatrix}E_{11} & E_{12} & E_{13} & 0 & 0 & 0\\ E_{12} & E_{23} & E_{23} & 0 & 0 & 0\\ E_{13} & E_{23} & E_{33} & 0 & 0 & 0\\ 0 & 0 & 0 & E_{44} & 0 & 0\\ 0 & 0 & 0 & 0 & E_{55} & 0\\ 0 & 0 & 0 & 0 & 0 & E_{66}\end{bmatrix} \begin{bmatrix}\varepsilon_x\\ \varepsilon_y\\ \varepsilon_z\\ \gamma_{yz}\\ \gamma_{xz}\\ \gamma_{xy}\end{bmatrix}$$

If a laminate is thin enough then:

$$\sigma_z \approx \tau_{yz} \approx \tau_{xz} \approx 0$$

Then:

$$\sigma_x = E_{11} * \varepsilon_x + E_{12} * \varepsilon_y + E_{13} * \varepsilon_z$$

$$\sigma_y = E_{12} * \varepsilon_x + E_{22} * \varepsilon_y + E_{23} * \varepsilon_z$$

$$\sigma_z = E_{13} * \varepsilon_x + E_{23} * \varepsilon_y + E_{33} * \varepsilon_z = 0$$

$$\tau_{yz} = E_{44} * \gamma_{yz} = 0$$

$$\tau_{xz} = E_{55} * \gamma_{xz} = 0$$

$$\tau_{xy} = E_{66} * \gamma_{xy}$$

For a coordinate system with one axis aligned with the fibres, the equations above can be reduced to:

$$\sigma_x = (E_{11} - \frac{E_{13}^2}{E_{33}}) * \varepsilon_x + (E_{12} - \frac{E_{13}E_{23}}{E_{33}}) * \varepsilon_y$$

$$\sigma_y = (E_{12} - \frac{E_{13}E_{23}}{E_{33}}) * \varepsilon_x + (E_{12} - \frac{E_{23}^2}{E_{33}}) * \varepsilon_y$$

$$\tau_{xy} = E_{66} * \gamma_{xy}$$

The equations above can be written in matrix notation as:

$$\begin{bmatrix}\sigma_x\\ \sigma_y\\ \tau_{xy}\end{bmatrix}=\begin{bmatrix}Q_{xx} & Q_{xy} & 0\\ Q_{xy} & Q_{yy} & 0\\ 0 & 0 & Q_{ss}\end{bmatrix}\begin{bmatrix}\varepsilon_x\\ \varepsilon_y\\ \gamma_{xy}\end{bmatrix}$$

With:

$$Q_{xx}=(E_{11}-\frac{E_{13}^2}{E_{33}})$$

$$Q_{yy}=(E_{12}-\frac{E_{23}^2}{E_{33}})$$

$$Q_{xy}=(E_{12}-\frac{E_{13}E_{23}}{E_{33}})$$

$$Q_{ss}=E_{66}$$

The young's modulus parallel to the fibre, E_L, can be determined by the test setup on the left in Figure 131. The transverse young's modulus, E_T can be determined from the test setup in the middle. And by a shear test, the test setup on the right, the shear modulus, G_{LT} can be determined. From the test setup on the left the poison ratio, υ_{LT}, can be determined by a strain gauge in the transverse direction.

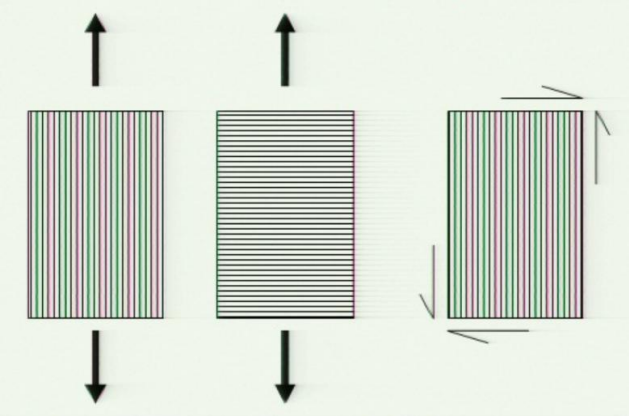

Figure 131: Test setups to determine material properties

The E_L is the same as E_1 in the tables for the lamella of flax fibre composite, E_T is the same as E_2 and υ_{LT} is the same as the given ν in the tables for the lamella of flax fibre composite.

The Q_{xx}, Q_{yy}, Q_{xy} and Q_{ss} can also be written with E_L, E_T, G_{LT} and υ_{LT} as:

$$Q_{xx}=\frac{E_L}{1-\upsilon_{LT}\upsilon_{TL}}$$

$$Q_{yy}=\frac{E_T}{1-\upsilon_{LT}\upsilon_{TL}}$$

$$Q_{xy}=\frac{\upsilon_{LT}E_T}{1-\upsilon_{LT}\upsilon_{TL}}=\frac{\upsilon_{TL}E_L}{1-\upsilon_{LT}\upsilon_{TL}}$$

$$Q_{ss}=G_{LT}$$

Where:

$\upsilon_{LT}E_T=\upsilon_{TL}E_L$, so $\upsilon_{TL}=\upsilon_{LT}\frac{E_T}{E_L}$

Transformation of stress

The stress-strain relation of a lamella determined above is for when the direction of the fibres is in the x-direction. When the direction of the fibres is under an angle θ, see Figure 132, the stresses need to be transformed. The stresses can be transformed with:

$$\begin{bmatrix}\sigma_1\\ \sigma_2\\ \tau_{12}\end{bmatrix} = \begin{bmatrix}(\cos(\theta))^2 & (\sin(\theta))^2 & 2\sin(\theta)\cos(\theta)\\ (\sin(\theta))^2 & (\cos(\theta))^2 & -2\sin(\theta)\cos(\theta)\\ -\sin(\theta)\cos(\theta) & \sin(\theta)\cos(\theta) & ((\cos(\theta))^2-(\sin(\theta))^2)\end{bmatrix}\begin{bmatrix}\sigma_x\\ \sigma_y\\ \tau_{xy}\end{bmatrix}$$

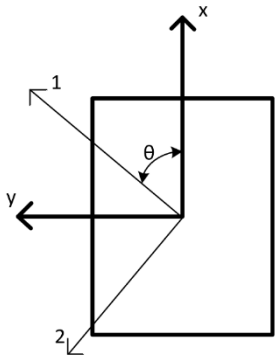

Figure 132: Coordinate system transformation

For a lamella for any direction the stress-strain relation with the coordinate systems given in Figure 133 is:

$$\begin{bmatrix}\sigma_1\\ \sigma_2\\ \tau_{12}\end{bmatrix} = \begin{bmatrix}Q_{11} & Q_{12} & Q_{16}\\ Q_{12} & Q_{22} & Q_{26}\\ Q_{16} & Q_{26} & Q_{66}\end{bmatrix}\begin{bmatrix}\varepsilon_1\\ \varepsilon_2\\ \gamma_{12}\end{bmatrix}$$

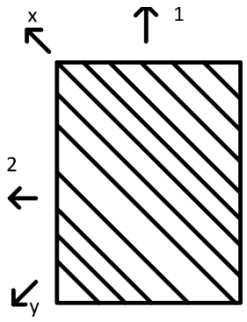

Figure 133: Coordinate systems fibre orientation

With:

$$Q_{11}^{(\theta)} = m^4Q_{xx} + n^4Q_{yy} + 2m^2n^2Q_{xy} + 4m^2n^2Q_{ss}$$

$$Q_{22}^{(\theta)} = n^4Q_{xx} + m^4Q_{yy} + 2m^2n^2Q_{xy} + 4m^2n^2Q_{ss}$$

$$Q_{12}^{(\theta)} = m^2n^2Q_{xx} + m^2n^2Q_{yy} + (m^4 + n^4)Q_{xy} - 4m^2n^2Q_{ss}$$

$$Q_{66}^{(\theta)} = m^2n^2Q_{xx} + m^2n^2Q_{yy} - 2m^2n^2Q_{xy} + (m^2 - n^2)^2Q_{ss}$$

$$Q_{16}^{(\theta)} = m^3nQ_{xx} - mn^3Q_{yy} + (mn^3 - m^3n)Q_{xy} + 2(mn^3 - m^3n)Q_{ss}$$

$$Q_{26}^{(\theta)} = mn^3Q_{xx} - m^3nQ_{yy} + (m^3n - mn^3)Q_{xy} + 2(m^3n - mn^3)Q_{ss}$$

Where:

$$m = \cos(\theta)$$

$$n = \sin(\theta)$$

From lamella to laminate

The equations above only describe a single lamella. The cross-section of a laminate is built up by multiple layers. When a strain is applied on a laminate, see Figure 134, then the strain in a lamella is the same as the strain in a laminate. So:

$$\varepsilon_i = \varepsilon_a$$

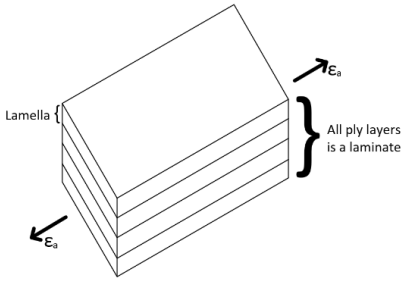

Figure 134: Laminate with strain

Where:

ε_i is the strain in a lamella

ε_a is the applied strain

The strain is equal to the force divided by the area and the E-modulus, so the equation above can be written as:

$$\frac{F_i}{E_i A_i} = \frac{F_{tot}}{E_{laminate} A_{laminate}}$$

Where:

F_i	is the force on a lamella
E_i	is the E-modulus of a lamella
A_i	is the area of a lamella
F_{tot}	is the total force on the laminate
$E_{laminate}$	is the E-modulus of the laminate
$A_{laminate}$	is the area of the laminate

The total force can be calculated with:

$$\sum F_i = F_{tot}$$

The equations above can be rewritten. To make it easier this will be done with an example of 2 lamella. The total force will then be:

$$F_{tot} = F_1 + F_2$$

The strain will be:

$$\varepsilon_1 = \varepsilon_2 = \varepsilon_a$$

$$\frac{F_1}{E_1 A_1} = \frac{F_2}{E_2 A_2} = \frac{F_{tot}}{E_{laminate} A_{laminate}}$$

The force F_2 can be written as:

$$F_2 = \frac{E_2 A_2}{E_1 A_1} F_1$$

The total force equation can then be rewritten as:

$$F_{tot} = F_1 + \frac{E_2 A_2}{E_1 A_1} F_1$$

Then the force F_1 can be written as:

$$F_1 = \frac{E_1 A_1}{E_1 A_1 + E_2 A_2} F_{tot}$$

In general, the equation above can be written as:

$$F_i = \frac{E_i A_i}{\sum E_i A_i} F_{tot}$$

And the total force can be calculated with:

$$F_{tot} = \frac{\sum E_i A_i}{E_i A_i} F_i$$

The applied strain can be calculated with:

$$\varepsilon_a = \frac{F_{tot}}{E_{laminate}A_{laminate}}$$

Which can be rewritten to:

$$E_{laminate}A_{laminate} = \frac{F_{tot}}{\varepsilon_a}$$

For F_{tot} can the equation from before filled in and for ε_a can the equation $\varepsilon_i = \frac{F_i}{E_i A_i}$ filled in since $\varepsilon_i = \varepsilon_a$. The equation for $E_{laminate}A_{laminate}$ can then be rewritten as:

$$E_{laminate}A_{laminate} = \frac{\sum \frac{E_i A_i}{E_i A_i} F_i}{\frac{F_i}{E_i A_i}} = \sum E_i A_i$$

So, the equivalent stiffness $(EA)_{eq}$, $E_{laminate}A_{laminate}$, is given as the sum of the individual EA, $E_i A_i$, components. This means that we can use the transformation equations to get the stiffness of each lamella in the axis system of interest and multiply by the lamella cross-sectional area:

$$(EA)_{lamella,i} = (Q_{ij})_{lamella,i} * A_{lamella,i} = \left(Q_{ij}\right)_{lamella,i} * t^{(i)} * w$$

$$(EA)_{laminate} = \sum_{i=1}^{n} (EA)_{lamella,i}$$

Stress resultant

As a good approximation it is possible to average stresses over the laminates thickness. This is possible because laminates are very thin compared to their in-plane dimensions. Then, instead of stresses, which change from lamella to lamella, it is possible to work with stress resultants: n_x, n_y, n_{xy}, m_x, m_y and m_{xy}, see Figure 135.

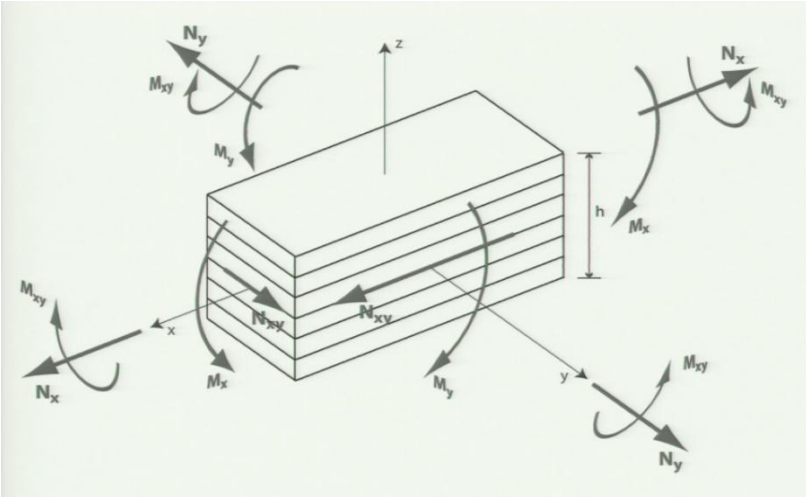

Figure 135: Forces on a laminate

The stress resultants are:

$$n_x = \int_{-\frac{h}{2}}^{\frac{h}{2}} \sigma_x dz$$

$$n_y = \int_{-\frac{h}{2}}^{\frac{h}{2}} \sigma_y dz$$

$$n_{xy} = \int_{-\frac{h}{2}}^{\frac{h}{2}} \tau_{xy} dz$$

$$m_x = \int_{-\frac{h}{2}}^{\frac{h}{2}} \sigma_x z dz$$

$$m_y = \int_{-\frac{h}{2}}^{\frac{h}{2}} \sigma_y z dz$$

$$m_{xy} = \int_{-\frac{h}{2}}^{\frac{h}{2}} \tau_{xy} z dz$$

The force and bending moment resultants are forces and bending moments per unit width.

For the case of uniaxial tension, see Figure 136, the average applied stress, σ_o, is:

$$\sigma_o = \frac{F}{wh}$$

By definition, the average applied stress is:

$$\sigma_o = \frac{1}{h} \int_{-\frac{h}{2}}^{\frac{h}{2}} \sigma_x dz$$

Using the definition for n_x, the equation becomes:

$$\sigma_o = \frac{n_x}{h}$$

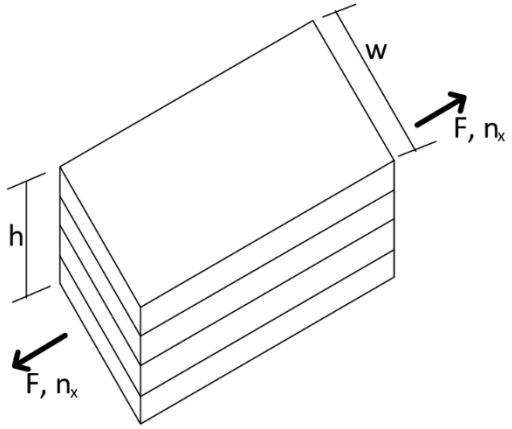

Figure 136: Uniaxial tension on a laminate

The ABD-matrix

The ABD-matrix is a matrix that describes the relation between the stress resultants and the strain and the curvatures. Based on standard plate theory, the strains are assumed to be almost linear through the thickness:

$$\varepsilon_x = \varepsilon_{xo} - \frac{\partial^2 w}{\partial x^2} z = \varepsilon_{xo} + z\kappa_x$$

$$\varepsilon_y = \varepsilon_{yo} - \frac{\partial^2 w}{\partial y^2} z = \varepsilon_{yo} + z\kappa_y$$

$$\gamma_{xy} = \gamma_{xyo} - 2\frac{\partial^2 w}{\partial x \partial y} z = \gamma_{xyo} + z\kappa_{xy}$$

To obtain the ABD-matrix, there will be looked at the case in-plane loads and no bending, the case of pure bending and the case of bending-stretching coupling.

In-plane loads and no bending

Because the loads are in-plane and there is no bending the strains, ε_1, ε_2 and γ_{12}, are constant through the thickness and equal to the midplane strain, ε_{1o}, ε_{2o} and γ_{12o}. To obtain the A-matrix of the ABD-matrix the equation $\sigma_1 = Q_{11}\varepsilon_{1o} + Q_{12}\varepsilon_{2o} + Q_{16}\gamma_{12o}$ will be integrated with respect to z:

$$\int_{-\frac{h}{2}}^{\frac{h}{2}} \sigma_{11} dz = \int_{-\frac{h}{2}}^{\frac{h}{2}} Q_{11}\varepsilon_{xo} dz + \int_{-\frac{h}{2}}^{\frac{h}{2}} Q_{12}\varepsilon_{yo} dz + \int_{-\frac{h}{2}}^{\frac{h}{2}} Q_{16}\gamma_{xyo} dz$$

Because $n_x = \int_{-\frac{h}{2}}^{\frac{h}{2}} \sigma_x dz$ the equation above becomes:

$$n_x = \int_{-\frac{h}{2}}^{\frac{h}{2}} Q_{11}\varepsilon_{xo} dz + \int_{-\frac{h}{2}}^{\frac{h}{2}} Q_{12}\varepsilon_{yo} dz + \int_{-\frac{h}{2}}^{\frac{h}{2}} Q_{16}\gamma_{xyo} dz$$

$$n_x = \int_{-\frac{h}{2}}^{\frac{h}{2}} Q_{11} dz\, \varepsilon_{xo} + \int_{-\frac{h}{2}}^{\frac{h}{2}} Q_{12} dz\, \varepsilon_{yo} + \int_{-\frac{h}{2}}^{\frac{h}{2}} Q_{16} dz\, \gamma_{xyo}$$

Where:

$$\int_{-\frac{h}{2}}^{\frac{h}{2}} Q_{11} dz = A_{11}$$

$$\int_{-\frac{h}{2}}^{\frac{h}{2}} Q_{12} dz = A_{12}$$

$$\int_{-\frac{h}{2}}^{\frac{h}{2}} Q_{16} dz = A_{16}$$

Similarly, the equation for σ_2 and τ_{12} can be integrated with respect to z. Putting the equations together gives:

$$\begin{bmatrix} n_x \\ n_y \\ n_{xy} \end{bmatrix} = \begin{bmatrix} A_{11} & A_{12} & A_{16} \\ A_{12} & A_{22} & A_{26} \\ A_{16} & A_{26} & A_{66} \end{bmatrix} \begin{bmatrix} \varepsilon_x \\ \varepsilon_y \\ \gamma_{xy} \end{bmatrix}$$

Where A_{ij} is given by :

$$A_{ij} = \int_{-\frac{h}{2}}^{\frac{h}{2}} Q_{ij} dz$$

Because Q_{ij} is constant in each lamella the integral can be substituted by a summation:

$$A_{ij} = \sum_{k=1}^{N} \left(Q_{ij}\right)^k (z_k - z_{k-1})$$

Where $(z_k - z_{k-1})$ is the lamella thickness, k denotes the kth lamella, z_0 is at the bottom of the laminate and N is the total number of lamellas.

Pure bending

For the case of pure bending, there are no in-plane strains so $\varepsilon_{xo} = \varepsilon_{yo} = \gamma_{xyo} = 0$, so for pure bending the strains are:

$$\varepsilon_x = -\frac{\partial^2 w}{\partial x^2} z$$

$$\varepsilon_y = -\frac{\partial^2 w}{\partial y^2} z$$

$$\gamma_{xy} = -2\frac{\partial^2 w}{\partial x \partial y} z$$

To obtain the D-matrix of the ABD-matrix the equation $\sigma_1 = Q_{11}(-\frac{\partial^2 w}{\partial x^2} z) + Q_{12}(-\frac{\partial^2 w}{\partial y^2} z) + Q_{16}(-2\frac{\partial^2 w}{\partial x \partial y} z)$ will be multiplied on both sides and integrated through the thickness with respect to z:

$$\int_{-\frac{h}{2}}^{\frac{h}{2}} z\sigma_{11} dz = \int_{-\frac{h}{2}}^{\frac{h}{2}} Q_{11} z(-\frac{\partial^2 w}{\partial x^2} z) dz + \int_{-\frac{h}{2}}^{\frac{h}{2}} Q_{12} z(-\frac{\partial^2 w}{\partial y^2} z) dz + \int_{-\frac{h}{2}}^{\frac{h}{2}} Q_{16} z(-2\frac{\partial^2 w}{\partial x \partial y} z)\, dz$$

Because $m_x = \int_{-\frac{h}{2}}^{\frac{h}{2}} \sigma_x z dz$ the equation above becomes:

$$m_x = -\int_{-\frac{h}{2}}^{\frac{h}{2}} Q_{11} z^2 \frac{\partial^2 w}{\partial x^2} dz - \int_{-\frac{h}{2}}^{\frac{h}{2}} Q_{12} z^2 \frac{\partial^2 w}{\partial y^2} dz - \int_{-\frac{h}{2}}^{\frac{h}{2}} 2Q_{16} z^2 \frac{\partial^2 w}{\partial x \partial y}\, dz$$

For pure bending the curvatures, $-\frac{\partial^2 w}{\partial x^2}$, $-\frac{\partial^2 w}{\partial x^2}$ and $-\frac{\partial^2 w}{\partial x \partial y}$, are constant and can be taken out of the integral:

$$m_x = \kappa_x \int_{-\frac{h}{2}}^{\frac{h}{2}} Q_{11} z^2 dz + \kappa_y \int_{-\frac{h}{2}}^{\frac{h}{2}} Q_{12} z^2 dz + \kappa_{xy} \int_{-\frac{h}{2}}^{\frac{h}{2}} Q_{16} z^2\, dz$$

Where:

$$\int_{-\frac{h}{2}}^{\frac{h}{2}} Q_{11} z^2 dz = D_{11}$$

$$\int_{-\frac{h}{2}}^{\frac{h}{2}} Q_{12} z^2 dz = D_{12}$$

$$\int_{-\frac{h}{2}}^{\frac{h}{2}} Q_{16} z^2\, dz = D_{16}$$

Similarly, the equation for σ_2 and τ_{12} can be multiplied on both sides and integrated through the thickness with respect to z. Putting the equations together gives:

$$\begin{bmatrix} m_x \\ m_y \\ m_{xy} \end{bmatrix} = \begin{bmatrix} D_{11} & D_{12} & D_{16} \\ D_{12} & D_{22} & D_{26} \\ D_{16} & D_{26} & D_{66} \end{bmatrix} \begin{bmatrix} \kappa_x \\ \kappa_y \\ \kappa_{xy} \end{bmatrix}$$

Where D_{ij} is given by :

$$D_{ij} = \int_{-\frac{h}{2}}^{\frac{h}{2}} Q_{ij} z^2 dz$$

Because Q_{ij} is constant in each lamella the integral can be substituted by a summation:

$$D_{ij} = \sum_{k=1}^{N} (Q_{ij})^k \frac{z_k^3 - z_{k-1}^3}{3}$$

Bending-stretching coupling

It is possible, for some laminates, to undergo bending or twisting under in-loads or undergo stretching under applied bending or torsional moments. For this case, the strains are:

$$\varepsilon_x = \varepsilon_{xo} + z\kappa_x$$

$$\varepsilon_y = \varepsilon_{yo} + z\kappa_y$$

$$\gamma_{xy} = \gamma_{xyo} + z\kappa_{xy}$$

To obtain the B-matrix of the ABD-matrix the equation $\sigma_x = Q_{11}(\varepsilon_{xo} + z\kappa_x) + Q_{12}(\varepsilon_{yo} + z\kappa_y) + Q_{16}(\gamma_{xyo} + z\kappa_{xy})$ will be integrated through the thickness with respect to z:

$$\int_{-\frac{h}{2}}^{\frac{h}{2}} z\sigma_x dz = \int_{-\frac{h}{2}}^{\frac{h}{2}} Q_{11}(\varepsilon_{xo} + z\kappa_x) dz + \int_{-\frac{h}{2}}^{\frac{h}{2}} Q_{12}(\varepsilon_{yo} + z\kappa_y) dz + \int_{-\frac{h}{2}}^{\frac{h}{2}} Q_{16}(\gamma_{xyo} + z\kappa_{xy})\, dz$$

Writing the integrals above with more integrals, using $n_x = \int_{-\frac{h}{2}}^{\frac{h}{2}} \sigma_x dz$ and because the curvatures and midplane stain are constant, the equation above becomes:

$$n_x = \int_{-\frac{h}{2}}^{\frac{h}{2}} Q_{11} dz\, \varepsilon_{xo} + \int_{-\frac{h}{2}}^{\frac{h}{2}} Q_{11} z dz\, \kappa_x + \int_{-\frac{h}{2}}^{\frac{h}{2}} Q_{12} dz\, \varepsilon_{yo} + \int_{-\frac{h}{2}}^{\frac{h}{2}} Q_{12} z dz\, \kappa_y + \int_{-\frac{h}{2}}^{\frac{h}{2}} Q_{16}\, dz\, \gamma_{xyo} + \int_{-\frac{h}{2}}^{\frac{h}{2}} Q_{16} z\, dz\, \kappa_{xy}$$

Using the definition for A_{ij}, the equation becomes:

$$n_x = A_{11}\varepsilon_{xo} + \int_{-\frac{h}{2}}^{\frac{h}{2}} Q_{11} z dz\, \kappa_x + A_{12}\varepsilon_{yo} + \int_{-\frac{h}{2}}^{\frac{h}{2}} Q_{12} z dz\, \kappa_y + A_{16}\gamma_{xyo} + \int_{-\frac{h}{2}}^{\frac{h}{2}} Q_{16} z\, dz\, \kappa_{xy}$$

The three integrals can be turned into summations:

$$n_x = A_{11}\varepsilon_{xo} + A_{12}\varepsilon_{yo} + A_{16}\gamma_{xyo} + \kappa_x \sum_{k=1}^{N} (Q_{11})^k \frac{z_k^2 - z_{k-1}^2}{2} + \kappa_y \sum_{k=1}^{N} (Q_{12})^k \frac{z_k^2 - z_{k-1}^2}{2} + \kappa_{xy} \sum_{k=1}^{N} (Q_{16})^k \frac{z_k^2 - z_{k-1}^2}{2}$$

Where:

$$\sum_{k=1}^{N}(Q_{11})^k \frac{z_k^2 - z_{k-1}^2}{2} = B_{11}$$

$$\sum_{k=1}^{N}(Q_{12})^k \frac{z_k^2 - z_{k-1}^2}{2} = B_{12}$$

$$\sum_{k=1}^{N}(Q_{16})^k \frac{z_k^2 - z_{k-1}^2}{2} = B_{16}$$

Similarly, the equation for σ_x and τ_{xy} can be integrated with respect to z. In general, it can be said that:

$$B_{ij} = \sum_{k=1}^{N}\left(Q_{ij}\right)^k \frac{z_k^2 - z_{k-1}^2}{2}$$

The general ABD-matrix

The equivalent stress-strain relation for a laminate is:

$$\begin{bmatrix} n_x \\ n_y \\ n_{xy} \\ m_x \\ m_y \\ m_{xy} \end{bmatrix} = \begin{bmatrix} A_{11} & A_{12} & A_{16} & B_{11} & B_{12} & B_{16} \\ A_{12} & A_{22} & A_{26} & B_{12} & B_{22} & B_{26} \\ A_{16} & A_{26} & A_{66} & B_{16} & B_{26} & B_{66} \\ B_{11} & B_{12} & B_{16} & D_{11} & D_{12} & D_{16} \\ B_{12} & B_{22} & B_{26} & D_{12} & D_{22} & D_{26} \\ B_{16} & B_{26} & B_{66} & D_{16} & D_{26} & D_{66} \end{bmatrix} \begin{bmatrix} \varepsilon_{xo} \\ \varepsilon_{yo} \\ \gamma_{xyo} \\ \kappa_x \\ \kappa_y \\ \kappa_{xy} \end{bmatrix}$$

Where:

$$A_{ij} = \sum_{k=1}^{N}\left(Q_{ij}\right)^k (z_k - z_{k-1})$$

$$B_{ij} = \sum_{k=1}^{N}\left(Q_{ij}\right)^k \frac{z_k^2 - z_{k-1}^2}{2}$$

$$D_{ij} = \sum_{k=1}^{N}\left(Q_{ij}\right)^k \frac{z_k^3 - z_{k-1}^3}{3}$$

For symmetric laminates, the B-matrix is zero. For balanced laminates, for each +θ there is a -θ somewhere, $A_{16} = A_{26} = 0$. Usually, the strains and curvature are not known, but the forces and bending moments are known. Then it is better to use the inverted relations:

$$\begin{bmatrix} \varepsilon_{xo} \\ \varepsilon_{yo} \\ \gamma_{xyo} \\ \kappa_x \\ \kappa_y \\ \kappa_{xy} \end{bmatrix} = \begin{bmatrix} \alpha_{11} & \alpha_{12} & \alpha_{16} & \beta_{11} & \beta_{12} & \beta_{16} \\ \alpha_{12} & \alpha_{22} & \alpha_{26} & \beta_{21} & \beta_{22} & \beta_{26} \\ \alpha_{16} & \alpha_{26} & \alpha_{66} & \beta_{61} & \beta_{62} & \beta_{66} \\ \beta_{11} & \beta_{12} & \beta_{16} & \delta_{11} & \delta_{12} & \delta_{16} \\ \beta_{21} & \beta_{22} & \beta_{26} & \delta_{12} & \delta_{22} & \delta_{26} \\ \beta_{61} & \beta_{62} & \beta_{66} & \delta_{16} & \delta_{26} & \delta_{66} \end{bmatrix} \begin{bmatrix} n_x \\ n_y \\ n_{xy} \\ m_x \\ m_y \\ m_{xy} \end{bmatrix}$$

Where:

$$[\alpha] = [A]^{-1} + [A]^{-1}[B][[D] - [B][A]^{-1}[B]]^{-1}[B][A]^{-1}$$

$$[\beta] = -[A][B][[D] - [B][A]^{-1}[B]]^{-1}$$

$$[\delta] = [[D] - [B][A]^{-1}[B]]^{-1}$$

For a symmetric laminate, the matrix equation above becomes:

$$\begin{bmatrix} \varepsilon_{xo} \\ \varepsilon_{yo} \\ \gamma_{xyo} \\ \kappa_x \\ \kappa_y \\ \kappa_{xy} \end{bmatrix} = \begin{bmatrix} a_{11} & a_{12} & a_{16} & 0 & 0 & 0 \\ a_{12} & a_{22} & a_{26} & 0 & 0 & 0 \\ a_{16} & a_{26} & a_{66} & 0 & 0 & 0 \\ 0 & 0 & 0 & d_{11} & d_{12} & d_{16} \\ 0 & 0 & 0 & d_{12} & d_{22} & d_{26} \\ 0 & 0 & 0 & d_{16} & d_{26} & d_{66} \end{bmatrix} \begin{bmatrix} n_x \\ n_y \\ n_{xy} \\ m_x \\ m_y \\ m_{xy} \end{bmatrix}$$

In general, $a_{ij} \neq \alpha_{ij}$ and $d_{ij} \neq \delta_{ij}$, they are only the same for symmetric laminates.

Young's modules for a laminate

For a symmetric laminate under uniaxial tension: $n_y = n_{xy} = 0$, see Figure 137. Then from the ABD-matrix equation:

$$n_x = A_{11}\varepsilon_{xo} + A_{12}\varepsilon_{yo}$$

$$n_y = A_{12}\varepsilon_{xo} + A_{22}\varepsilon_{yo} = 0$$

Solve for ε_{yo} and substitute in the equation for n_x to obtain:

$$n_x = (A_{11} - \frac{A_{12}^2}{A_{22}})\varepsilon_{xo}$$

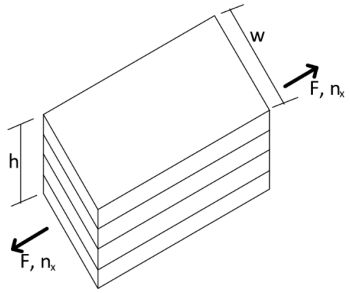

Figure 137: Laminate under uniaxial tension

Using the equation between n_x and applied stress, see Figure 138:

$$\sigma_o = \frac{F}{wh} = \frac{n_x}{h}$$

$$\sigma_o = \frac{F}{wh} = \frac{1}{h}\left[\frac{A_{11}A_{22} - A_{12}^2}{A_{22}}\right]\varepsilon_{xo}$$

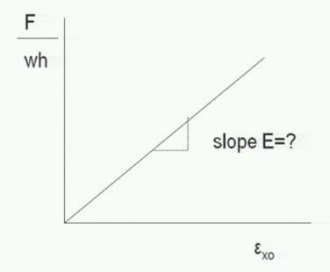

Figure 138: Graph for stiffness E

Where:

$$\left[\frac{A_{11}A_{22} - A_{12}^2}{A_{22}}\right] = a_{11}$$

So, the equation of the applied stress becomes:

$$\sigma_o = \frac{1}{ha_{11}}\varepsilon_{xo}$$

From which the membrane laminate modulus in stretching is:

$$E_{1m} = \frac{1}{ha_{11}}$$

Similarly, it is possible to show that:

$$E_{1m} = \frac{1}{ha_{11}} \qquad E_{1b} = \frac{12}{h^3 d_{11}}$$

$$E_{2m} = \frac{1}{ha_{22}} \qquad E_{2b} = \frac{12}{h^3 d_{22}}$$

$$G_{12m} = \frac{1}{ha_{66}} \qquad G_{12b} = \frac{12}{h^3 d_{66}}$$

$$\nu_{12m} = -\frac{a_{12}}{a_{11}} \qquad \nu_{12b} = -\frac{d_{12}}{d_{11}}$$

$$\nu_{21m} = -\frac{a_{12}}{a_{22}} \qquad \nu_{21b} = -\frac{d_{12}}{d_{22}}$$

Where the terms with subscript m are for pure stretching and with subscript b are for pure bending. The moduli will be different for pure stretching and pure bending and there needs to be decided which are appropriate for the problem. The most used is the most conservative.

Appendix D: Python code for the Classical Laminate Theory (CLT)

The code for the Classical Laminate Theory (CLT) is provided below. An explanation and validation of the code are provided in Appendix E.

```
import numpy as np
import pandas as pd
import matplotlib.pyplot as plt
from matplotlib.patches import Patch
from matplotlib.patches import Rectangle, Polygon
import scipy as sc

# -------------------------
# Material Library function
# -------------------------
# Define material properties for the different materials used in the cross-section
def material_properties(material_name):
    if material_name == 'flax_fibre_UP-Bio_Composite':
        E1 = 21.1  # GPa
        E2 = 1.7  # GPa
        G12 = 1.1 # GPa
        nu12 = 0.33
    elif material_name == 'flax_fibre_epoxy-Bio_Composite':
        E1 = 25.0  # GPa
        E2 = 2  # GPa
        G12 = 1.4 # GPa
        nu12 = 0.32
    elif material_name == 'E-glass_fibre_UP_composite':
        E1 = 30.4 # Gpa
        E2 = 8.9 # Gpa
        G12 = 2.7 # Gpa
        nu12 = 0.3
    elif material_name == 'basalt_fibre_UP_composite':
        E1 = 37.61 # Gpa
        E2 = 5.2 # Gpa
        G12 = 2.2 # Gpa
        nu12 = 0.33
    elif material_name == 'Carbon_fibre_UP_composite':
        E1 = 97.21 # Gpa
        E2 = 5.5 # Gpa
        G12 = 2.2 # Gpa
        nu12 = 0.31

    return E1, E2, G12, nu12

# -------------------------------------------
# Transforming stiffness to X and Y directions
# -------------------------------------------
```

```
# Calculate the stiffness matrix Q for a unidirectional composite lamina based
on its material properties
def Q_x_y(E1, E2, G12, nu12):
    E_L = E1
    E_T = E2
    G_LT = G12
    nu_LT = nu12
    nu_TL = (nu_LT * E_T) / E_L
    Q_xx = E_L / (1 - nu_LT * nu_TL)
    Q_yy = E_T / (1 - nu_LT * nu_TL)
    Q_xy = (nu_LT * E_T) / (1 - nu_LT * nu_TL)
    Q_ss = G_LT
    return Q_xx, Q_yy, Q_xy, Q_ss

# ------------------------------------------------
# Transforming stiffness to  principal directions
# ------------------------------------------------
# Transform the stiffness matrix Q for a lamina oriented at an angle theta to
the reference axes
def transform_Q(Q_xx, Q_yy, Q_xy, Q_ss, theta_deg):
    # Convert angle to radians
    theta = np.radians(theta_deg)

    # Compute m = cos(theta), n = sin(theta)
    m = np.cos(theta)
    n = np.sin(theta)

    # Transformed Q components
    Q11 = m**4 * Q_xx + n**4 * Q_yy + 2*m**2*n**2*Q_xy + 4*m**2*n**2*Q_ss
    Q22 = n**4 * Q_xx + m**4 * Q_yy + 2*m**2*n**2*Q_xy + 4*m**2*n**2*Q_ss
    Q12 = m**2*n**2*Q_xx + m**2*n**2*Q_yy + (m**4 + n**4)*Q_xy -
4*m**2*n**2*Q_ss
    Q66 = m**2*n**2*Q_xx + m**2*n**2*Q_yy - 2*m**2*n**2*Q_xy + (m**2 -
n**2)**2 * Q_ss
    Q16 = m**3*n*Q_xx - m*n**3*Q_yy + (m*n**3 - m**3*n)*Q_xy + 2*(m*n**3 -
m**3*n)*Q_ss
    Q26 = m*n**3*Q_xx - m**3*n*Q_yy + (m**3*n - m*n**3)*Q_xy + 2*(m**3*n -
m*n**3)*Q_ss

    return Q11, Q22, Q12, Q66, Q16, Q26

# ----------------------------------------
# Creating a z-axis through the thickness
# ----------------------------------------
# Calculate the z-coordinates of the bottom and top of each ply in the
laminate based on the thicknesses of the plies
def z_values(ply_thickness):
    h = sum(ply_thickness)
    z_bottom = [-h/2]  # bottom of first ply
    z_top = []
```

```
    for t in ply_thickness:
        z_top.append(z_bottom[-1] + t)
        z_bottom.append(z_top[-1])
    z_bottom = z_bottom[:-1]  # remove last extra bottom
    return z_bottom, z_top

# -------------------
# Compute ABD-matrix
# -------------------
# Compute the A matrix for the laminate by integrating the transformed
stiffness matrix Q over the thickness of the laminate
def compute_A_matrix(laminate_layers):
    A11 = 0
    A22 = 0
    A12 = 0
    A66 = 0
    A16 = 0
    A26 = 0

    for layer in laminate_layers:
        Q11 = layer['Q11']
        Q22 = layer['Q22']
        Q12 = layer['Q12']
        Q66 = layer['Q66']
        Q16 = layer['Q16']
        Q26 = layer['Q26']

        A11 += Q11 * (layer['z_top'] - layer['z_bottom'])
        A22 += Q22 * (layer['z_top'] - layer['z_bottom'])
        A12 += Q12 * (layer['z_top'] - layer['z_bottom'])
        A66 += Q66 * (layer['z_top'] - layer['z_bottom'])
        A16 += Q16 * (layer['z_top'] - layer['z_bottom'])
        A26 += Q26 * (layer['z_top'] - layer['z_bottom'])
    A = np.array([
        [A11, A12, A16],
        [A12, A22, A26],
        [A16, A26, A66]
    ])
    return A

# Compute the D matrix for the laminate by integrating the transformed
stiffness matrix Q multiplied by z^2 over the thickness of the laminate
def compute_D_matrix(laminate_layers):
    D11 = 0
    D22 = 0
    D12 = 0
    D66 = 0
    D16 = 0
    D26 = 0
```

```
    for layer in laminate_layers:
        Q11 = layer['Q11']
        Q22 = layer['Q22']
        Q12 = layer['Q12']
        Q66 = layer['Q66']
        Q16 = layer['Q16']
        Q26 = layer['Q26']

        D11 += Q11 * (layer['z_top']**3 - layer['z_bottom']**3) / 3
        D22 += Q22 * (layer['z_top']**3 - layer['z_bottom']**3) / 3
        D12 += Q12 * (layer['z_top']**3 - layer['z_bottom']**3) / 3
        D66 += Q66 * (layer['z_top']**3 - layer['z_bottom']**3) / 3
        D16 += Q16 * (layer['z_top']**3 - layer['z_bottom']**3) / 3
        D26 += Q26 * (layer['z_top']**3 - layer['z_bottom']**3) / 3
    D = np.array([
        [D11, D12, D16],
        [D12, D22, D26],
        [D16, D26, D66]
    ])
    return D

# Compute the B matrix for the laminate by integrating the transformed
stiffness matrix Q multiplied by z over the thickness of the laminate
def compute_B_matrix(laminate_layers):
    B11 = 0
    B22 = 0
    B12 = 0
    B66 = 0
    B16 = 0
    B26 = 0

    for layer in laminate_layers:
        Q11 = layer['Q11']
        Q22 = layer['Q22']
        Q12 = layer['Q12']
        Q66 = layer['Q66']
        Q16 = layer['Q16']
        Q26 = layer['Q26']

        B11 += Q11 * (layer['z_top']**2 - layer['z_bottom']**2) / 2
        B22 += Q22 * (layer['z_top']**2 - layer['z_bottom']**2) / 2
        B12 += Q12 * (layer['z_top']**2 - layer['z_bottom']**2) / 2
        B66 += Q66 * (layer['z_top']**2 - layer['z_bottom']**2) / 2
        B16 += Q16 * (layer['z_top']**2 - layer['z_bottom']**2) / 2
        B26 += Q26 * (layer['z_top']**2 - layer['z_bottom']**2) / 2
    B = np.array([
        [B11, B12, B16],
        [B12, B22, B26],
        [B16, B26, B66]
    ])
```

```
    return B

# Compute the A, B, and D matrices for the laminate by calling the respective
functions
def compute_ABD_matrices(laminate_layers):
    A = compute_A_matrix(laminate_layers)
    B = compute_B_matrix(laminate_layers)
    D = compute_D_matrix(laminate_layers)
    return A, B, D

# ---------------------------
# Compute α, β, and δ-matrix
# ---------------------------
# Compute the α, β, and δ matrices for the laminate based on the A, B, and D
matrices using the given formulas
def compute_alpha_beta_delta(A, B, D):
    # Inverse van A
    A_inv = np.linalg.inv(A)

    # Hulpmatrix: D - B A^-1 B
    D_eff = D - B @ A_inv @ B
    D_eff_inv = np.linalg.inv(D_eff)

    # Berekening van α, β, δ
    alpha = A_inv + A_inv @ B @ D_eff_inv @ B @ A_inv
    beta = -A_inv @ B @ D_eff_inv
    delta = D_eff_inv

    return alpha, beta, delta

# ----------------------------------
# Compute stiffnesses of the laminate
# ----------------------------------
# Calculate the stiffnesses E_1m, E_2m, G_12m, nu_12m, nu_21m for the membrane
# and E_1b, E_2b, G_12b, nu_12b, nu_21b for the bending based on the α and δ
matrices and the thickness of the laminate
def stiffnesses(alpha, beta, delta, h_laminate):
    threshold = 1e-6  # define what "really small" means

    # Check if any entry in beta is larger than the threshold
    if np.any(np.abs(beta) > threshold):
        print("Warning: the Laminate is not symmetric or balanced.")

    E_1m = 1 / (h_laminate * alpha[0, 0])
    E_2m = 1 / (h_laminate * alpha[1, 1])
    G_12m = 1 / (h_laminate * alpha[2, 2])
    nu_12m = -alpha[0, 1] / alpha[0, 0]
    nu_21m = -alpha[1, 0] / alpha[1, 1]

    E_1b = 12/(h_laminate**3 * delta[0, 0])
```

```
    E_2b = 12/(h_laminate**3 * delta[1, 1])
    G_12b = 12/(h_laminate**3 * delta[2, 2])
    nu_12b = -delta[0, 1] / delta[0, 0]
    nu_21b = -delta[1, 0] / delta[1, 1]

    stiffness_list = [E_1m, E_2m, G_12m, nu_12m, nu_21m,
                      E_1b, E_2b, G_12b, nu_12b, nu_21b]

    return stiffness_list

# -------------------------
# Final laminate stiffness
# -------------------------
# Main function to calculate the laminate stiffness based on the layer
structure, thickness structure, and material properties
def laminate_stiffness(layer_structure, thickness_structure, material_name):
    laminate_layers = []

    z_bottom, z_top = z_values(thickness_structure)
    h_laminate = np.sum(thickness_structure)

    for i in range(len(layer_structure)):
        E1, E2, G12, nu12 = material_properties(material_name[i])
        E1 = E1 * 1000  # Convert from GPa to MPa
        E2 = E2 * 1000  # Convert from GPa to MPa
        G12 = G12 * 1000  # Convert from GPa to MPa
        Q_xx, Q_yy, Q_xy, Q_ss = Q_x_y(E1, E2, G12, nu12)
        Q11, Q22, Q12, Q66, Q16, Q26 = transform_Q(Q_xx, Q_yy, Q_xy, Q_ss,
layer_structure[i])

        layer_info = {
            'material': material_name[i],
            'theta': layer_structure[i],
            'z_bottom': z_bottom[i],
            'z_top': z_top[i],
            'Q11': Q11,
            'Q22': Q22,
            'Q12': Q12,
            'Q66': Q66,
            'Q16': Q16,
            'Q26': Q26
        }

        laminate_layers.append(layer_info)

    A, B, D = compute_ABD_matrices(laminate_layers)
    alpha, beta, delta = compute_alpha_beta_delta(A, B, D)
    stiffness_list = stiffnesses(alpha, beta, delta, h_laminate)
    stiffness_list = np.array(stiffness_list, dtype=float)  # make sure it's a
NumPy array
```

```
    indices_to_convert = [0, 1, 2, 5, 6, 7]
    stiffness_list[indices_to_convert] = stiffness_list[indices_to_convert] /
1000 # Convert from MPa to GPa for membrane stiffnesses
    return stiffness_list

# ------------------
# Requirement check
# ------------------
def requirement_direction(layer_structure):
    # Count the number of layers in each direction
    lam_0 = 0
    lam_min_45 = 0
    lam_plus_45 = 0
    lam_90 = 0
    for layer in layer_structure:
        if layer == 0:
            lam_0 += 1
        elif layer == -45:
            lam_min_45 += 1
        elif layer == 45:
            lam_plus_45 += 1
        elif layer == 90:
            lam_90 += 1

    # Calculate the percentage of layers in each direction
    pc_0 = lam_0 / len(layer_structure) * 100
    pc_min_45 = lam_min_45 / len(layer_structure) * 100
    pc_plus_45 = lam_plus_45 / len(layer_structure) * 100
    pc_90 = lam_90 / len(layer_structure) * 100

    # Check if any direction has less than 12.5% of the layers and print a
warning if so
    if pc_0 < 12.5 or pc_min_45 < 12.5 or pc_plus_45 < 12.5 or pc_90 < 12.5:
        print("Warning: the laminate does not meet the requirement of having
at least 12.5% of each direction.")
        print(f"Direction 0°: {pc_0:.2f}%")
        print(f"Direction -45°: {pc_min_45:.2f}%")
        print(f"Direction +45°: {pc_plus_45:.2f}%")
        print(f"Direction 90°: {pc_90:.2f}%")

    elif pc_0 >= 20 and pc_min_45 >= 20 and pc_plus_45 >= 20 and pc_90 >= 20:
        print('The laminate is well balanced')
        print(f"Direction 0°: {pc_0:.2f}%")
        print(f"Direction -45°: {pc_min_45:.2f}%")
        print(f"Direction +45°: {pc_plus_45:.2f}%")
        print(f"Direction 90°: {pc_90:.2f}%")

    elif pc_0 >= 12.5 and pc_min_45 >= 12.5 and pc_plus_45 >= 12.5 and pc_90
>= 12.5:
```

```
        print('The laminate meets the requirement of having at least 12.5% of
each direction, but it is not well balanced.')
        print(f"Direction 0°: {pc_0:.2f}%")
        print(f"Direction -45°: {pc_min_45:.2f}%")
        print(f"Direction +45°: {pc_plus_45:.2f}%")
        print(f"Direction 90°: {pc_90:.2f}%")

# ---------------
# Overview table
# ---------------
# Function to print stiffness values in a table with Membrane and Bending
columns and a separate Unit column
def print_stiffness_overview(stiffness_list):
    # Unpack values
    E_1m, E_2m, G_12m, nu_12m, nu_21m, E_1b, E_2b, G_12b, nu_12b, nu_21b =
stiffness_list

    # Header
    print(f"{'Property':<8} {'Membrane':>12} {'Bending':>12} {'Unit':>8}")
    print("-" * 45)

    # Moduli
    properties = ["E1", "E2", "G12"]
    moduli_m = [E_1m, E_2m, G_12m]
    moduli_b = [E_1b, E_2b, G_12b]
    for i, prop in enumerate(properties):
        print(f"{prop:<8} {moduli_m[i]:>12.3f} {moduli_b[i]:>12.3f}
{'GPa':>8}")

    # Poisson ratios
    properties = ["nu12", "nu21"]
    poiss_m = [nu_12m, nu_21m]
    poiss_b = [nu_12b, nu_21b]
    for i, prop in enumerate(properties):
        print(f"{prop:<8} {poiss_m[i]:>12.6f} {poiss_b[i]:>12.6f} {'-':>8}")

# --------------
# Plot laminate
# --------------
# Function to plot a laminate stacking sequence from bottom to top.
# Parameters:
# - full_layer_structure: list of fiber directions (degrees)
# - full_thickness_structure: list of layer thicknesses
# - full_material_name: list of materials per layer
def plot_laminate(full_layer_structure, full_thickness_structure,
full_material_name):

    # Safety check
    if not (len(full_layer_structure) ==
            len(full_thickness_structure) ==
```

```
            len(full_material_name)):
        raise ValueError("All input lists must have the same length.")

    # Define unique layer types (material, angle, thickness)
    layer_types = list(zip(full_material_name,
                           full_layer_structure,
                           full_thickness_structure))
    unique_types = list(dict.fromkeys(layer_types))  # preserve order

    # Assign colors
    colors = plt.cm.tab20.colors
    type_color_map = {
        ut: colors[i % len(colors)]
        for i, ut in enumerate(unique_types)
    }

    # Create figure
    y_height = sum(full_thickness_structure)*0.35 # Adjust height based on
total thickness
    fig, ax = plt.subplots(figsize=(3, y_height))

    bottom = 0
    cumulative = [0]

    # Plot layers
    for mat, angle, thick in layer_types:
        color = type_color_map[(mat, angle, thick)]

        ax.bar(0, thick,
               bottom=bottom,
               color=color,
               edgecolor='black',
               width=1)

        # Angle label in center of ply
        ax.text(0,
                bottom + thick / 2,
                f"{angle}°",
                ha='center',
                va='center',
                fontsize=8,
                color='white')

        bottom += thick
        cumulative.append(bottom)

    total_thickness = sum(full_thickness_structure)

    # Remove extra white space
    ax.set_ylim(0, total_thickness)
```

```
    # Show cumulative thickness values
    ax.set_yticks(cumulative)
    ax.set_yticklabels([f"{c:.2f}" for c in cumulative])

    ax.set_xlim(-0.5, 0.5)
    ax.set_xticks([])
    ax.set_ylabel("Thickness (mm)")
    ax.set_title("Laminate Stacking Sequence")

    # Legend
    legend_patches = [
        Patch(facecolor=type_color_map[ut],
              edgecolor='black',
              label=f"{ut[0]}, {ut[1]}°, t={ut[2]}")
        for ut in unique_types
    ]

    ax.legend(handles=legend_patches,
              bbox_to_anchor=(1.05, 1),
              loc='upper left')

    plt.tight_layout()
    plt.show()

# ---------------------
# Symmetrical laminate
# ---------------------
# Function to create a symmetric laminate by mirroring the half-layer
structure, thickness structure, and material name lists.
def sym_laminate(half_layer_structure, half_thickness_structure,
half_material_name):
    full_layer_structure = half_layer_structure +  half_layer_structure[::-1]
    full_thickness_structure = half_thickness_structure +
half_thickness_structure[::-1]
    full_material_name = half_material_name + half_material_name[::-1]

    return full_layer_structure, full_thickness_structure, full_material_name

# --------------------
# Laminate properties
# --------------------
# Calculate the equivalent Young's modulus of the laminate in the 1 and 2
directions,
# The equivalent shear modulus, and the equivalent Poisson's ratios using the
minimum of the membrane and bending stiffnesses for each property
def laminate_properties(stiffness_list, thickness_structure):
    # Unpack values
    E_1m, E_2m, G_12m, nu_12m, nu_21m, E_1b, E_2b, G_12b, nu_12b, nu_21b =
stiffness_list
```

```
    laminate_properties_info = {
        'E_1': E_1m * 1000,       # Change [Gpa] to [Mpa]
        'E_2': E_2m * 1000,       # Change [Gpa] to [Mpa]
        'G_12': G_12m * 1000,    # Change [Gpa] to [Mpa]
        'nu_12': nu_12m,
        'nu_21': nu_21m,
        't_laminate': np.sum(thickness_structure)
    }
    return laminate_properties_info
```

Appendix E: Explanation and validation of the CLT python code

The Classical Laminate Theory (CLT) code is provided in Appendix D. The CLT code is structured such that several intermediate functions are first defined, which are then used in a final function. This final function generates a list containing the laminate properties $\mathrm{E_{1m}}, \mathrm{E_{2m}}, \mathrm{G_{12m}}, \upsilon_{12\mathrm{m}}, \upsilon_{21\mathrm{m}}, \mathrm{E_{1b}}, \mathrm{E_{2b}}, \mathrm{G_{12b}}, \upsilon_{12\mathrm{b}}$ and $\upsilon_{21\mathrm{b}}$. In the python code the function requirement_direction calculates the percentages of the lamella directions in the laminate with the formula:

$$percentage = \frac{Number\ layers\ of\ in\ a\ certain\ direction}{len(layer_structure)} * 100\%$$

These percentages are then evaluated using several if-statements, after which the results are printed.

- The first check verifies whether all percentages are above 12.5%. If this condition is not met, a warning is printed indicating that the laminate layering does not meet the requirements.
- The second check evaluates whether the laminate is well balanced by verifying if all percentages are above 20%. A value of 20% was chosen because achieving exactly 25% in each principal direction is often difficult in practice.
- The final check again verifies whether all percentages are above 12.5%, ensuring that the minimum directional requirement is satisfied.

The sym_laminate function generates the full stacking sequence of the laminate by mirroring the provided half-sequence. The print_stiffness_overview function outputs the laminate properties in a structured tabular format. Additionally, the plot_laminate function visualizes the stacking sequence of the laminate.

Material library function

The first function stores the material properties of the different lamellas. The material properties can be obtained by providing the material name as an input in the function. The function then returns the constants $E_1, E_2, G_{12}\ and\ \upsilon_{12}$ of the material.

Stiffness matrix Q

This Q_x_y function takes the $E_1, E_2, G_{12}\ and\ \upsilon_{12}$ as input and calculates the stiffness matrix components $Q_{xx}, Q_{yy}, Q_{xy}\ and\ Q_{ss}$ using the functions:

$$Q_{xx} = \frac{E_L}{1 - \upsilon_{LT}\upsilon_{TL}}$$

$$Q_{yy} = \frac{E_T}{1 - \upsilon_{LT}\upsilon_{TL}}$$

$$Q_{xy} = \frac{\upsilon_{LT}E_T}{1 - \upsilon_{LT}\upsilon_{TL}} = \frac{\upsilon_{TL}E_L}{1 - \upsilon_{LT}\upsilon_{TL}}$$

$$Q_{ss} = G_{LT}$$

Where: $E_L = E_1$, $E_T = E_2$, $G_{LT} = G_{12}$ and $\upsilon_{LT} = \upsilon_{12}$

Transformation matrix

The transform_Q function takes the $Q_{xx}, Q_{yy}, Q_{xy}, Q_{ss}$ and the lamella orientation angle as input. It then calculates the transformed stiffness components $Q_{11}, Q_{22}, Q_{12}, Q_{66}, Q_{16}\ and\ Q_{26}$ using the following equations:

$$Q_{11}^{(\theta)} = m^4 Q_{xx} + n^4 Q_{yy} + 2m^2 n^2 Q_{xy} + 4m^2 n^2 Q_{ss}$$

$$Q_{22}^{(\theta)} = n^4 Q_{xx} + m^4 Q_{yy} + 2m^2 n^2 Q_{xy} + 4m^2 n^2 Q_{ss}$$

$$Q_{12}^{(\theta)} = m^2 n^2 Q_{xx} + m^2 n^2 Q_{yy} + (m^4 + n^4) Q_{xy} - 4m^2 n^2 Q_{ss}$$

$$Q_{66}^{(\theta)} = m^2 n^2 Q_{xx} + m^2 n^2 Q_{yy} - 2m^2 n^2 Q_{xy} + (m^2 - n^2)^2 Q_{ss}$$

$$Q_{16}^{(\theta)} = m^3 n Q_{xx} - m n^3 Q_{yy} + (m n^3 - m^3 n) Q_{xy} + 2(m n^3 - m^3 n) Q_{ss}$$

$$Q_{26}^{(\theta)} = m n^3 Q_{xx} - m^3 n Q_{yy} + (m^3 n - m n^3) Q_{xy} + 2(m^3 n - m n^3) Q_{ss}$$

Where: $m = \cos(\theta)$ and $n = \sin(\theta)$

z-values function

To compute the ABD-matrix, the z coordinates of the top and bottom of each lamella in the laminate must be known. The coordinate system is defined such that z = 0 is located at the mid-plane of the laminate. Since only the thickness of the individual lamella's are known, the coordinates are determined by first calculating the total thickness of the laminate. The z-coordinate of the bottom of the lowest lamella, is then equal to −½ of the total laminate thickness, and this value is stored in an array. Next, a for-loop iterates through the thickness-array. During each iteration, the z-coordinate of the top of the current lamella is calculated as the z-coordinate of the bottom of the lamella plus its thickness, and this value is stored in an array. The bottom z-coordinate of the next lamella is equal to the top z-coordinate of the current lamella, and this value is stored in the array containing the bottom coordinates. After the for-loop, the last value in the bottom-coordinate array is removed, since it corresponds to an additional coordinate for a non-existent next layer. This procedure is implemented in the z_values function, which takes the thickness structure as input and returns two lists: one containing the bottom z-coordinates and one containing the top z-coordinates of the lamella.

Compute ABD-matrix

To compute the ABD-matrix, separate functions are implemented to calculate the A-matrix, B-matrix, and D-matrix. A final function then combines these functions to compute the A,B and D-matrices.

A-matrix

The compute_A_matrix function takes laminate_layers as input. This variable is a dictionary that contains the Q-values of each lamella and the arrays with the z-coordinates. The function returns the A-matrix. First, all A-components are initialized to zero. The function then loops through the laminate layers and adds the contribution of each layer to the different A-components. The contribution of each layer is calculated using:

$$A_{ij} += Q_{ij}(z_k - z_{k-1})$$

Where: z_k is the top z-coordinate and z_{k-1} is the bottom z-coordinate.

B-matrix

The compute_B_matrix function takes laminate_layers as input and returns the B-matrix. Similar to the A-matrix calculation, the function first initializes all B-components to zero and then loops through the laminate layers, adding the contribution of each layer. The contribution of each layer is calculated using:

$$B_{ij} += Q_{ij} \frac{z_k^2 - z_{k-1}^2}{2}$$

Where: z_k is the top z-coordinate and z_{k-1} is the bottom z-coordinate.

D-matrix

The compute_D_matrix function takes laminate_layers as input and returns the D-matrix. The procedure is similar to the previous functions. All D-components are first initialized to zero, after which the function loops through the laminate layers and sums the contribution of each layer. The contribution of each layer is calculated using:

$$D_{ij} += Q_{ij} \frac{z_k^3 - z_{k-1}^3}{3}$$

Where: z_k is the top z-coordinate and z_{k-1} is the bottom z-coordinate.

Final ABD-matrix function

The compute_ABD_matrix function takes laminate_layers as input and returns the A, B, and D matrices simultaneously. The function calculates these matrices by calling the compute_A_matrix, compute_B_matrix, and compute_D_matrix functions described above.

Compute α, β, and δ-matrix

The compute_alpha_beta_delta function takes the A, B and D matrix as input and calculates the α, β, and δ-matrix using the functions:

$$[\alpha] = [A]^{-1} + [A]^{-1}[B][[D] - [B][A]^{-1}[B]]^{-1}[B][A]^{-1}$$

$$[\beta] = -[A][B][[D] - [B][A]^{-1}[B]]^{-1}$$

$$[\delta] = [[D] - [B][A]^{-1}[B]]^{-1}$$

Compute stiffness of the laminate

The stiffnesses function takes the α, β, and δ-matrix and the height of the laminate as input. It calculates $\mathrm{E_{1m}}, \mathrm{E_{2m}}, \mathrm{G_{12m}}, \upsilon_{12m}, \upsilon_{21m}, \mathrm{E_{1b}}, \mathrm{E_{2b}}, \mathrm{G_{12b}}, \upsilon_{12b}$ and υ_{21b}, and returns these values in a list. These values are calculated with:

$$E_{1m} = \frac{1}{h a_{11}} \qquad E_{1b} = \frac{12}{h^3 d_{11}}$$

$$E_{2m} = \frac{1}{h a_{22}} \qquad E_{2b} = \frac{12}{h^3 d_{22}}$$

$$G_{12m} = \frac{1}{h a_{66}} \qquad G_{12b} = \frac{12}{h^3 d_{66}}$$

$$\nu_{12m} = -\frac{a_{12}}{a_{11}} \qquad \nu_{12b} = -\frac{d_{12}}{d_{11}}$$

$$\nu_{21m} = -\frac{a_{12}}{a_{22}} \qquad \nu_{21b} = -\frac{d_{12}}{d_{22}}$$

Final laminate stiffness

The laminate_stiffness function takes as input the layer_structure, thickness_structure and material_name arrays of the laminate and returns a list containing $E_{1m}, E_{2m}, G_{12m}, \upsilon_{12m}, \upsilon_{21m}, E_{1b}, E_{2b}, G_{12b}, \upsilon_{12b}$ and υ_{21b}. The function first computes the total laminate height by summing the values in thickness_structure. After, the z-coordinates are determined with the z-values function. The function then loops through each layer using a for-loop to:

- Retrieve the material properties using the material library function
- Computes the Q-matrix with the function Q_x_y
- Computes the transformed Q-matrix using the function transform_Q
- Stores the transformed Q-matrix, material, orientation, z-coordinates for every layer in a dictionary

After completing the loop, the A, B and D-matrices are computed using the function compute_ABD_matrices, followed by the calculation of the α, β, and δ-matrices with the function compute_alpha_beta_delta. Finally, the stiffnesses function is used to compute $E_{1m}, E_{2m}, G_{12m}, \upsilon_{12m}, \upsilon_{21m}, E_{1b}, E_{2b}, G_{12b}, \upsilon_{12b}$ and υ_{21b}, which are returned as a list.

Validation of the function

By testing the final function, the other functions are also tested, since they are all used within the final function. The function is tested by defining a laminate layup and comparing the calculated laminate properties with the results from the app Composite Construction Materials (Composite Calculator, 2019), which determines laminate stiffness using the Classical Laminate Theory. In the app the material properties were entered, shown in Figure 142. The laminate layup used is [0/90/45/-45]s, which is a symmetric laminate, shown in Figure 141. The layup configuration is shown in Figure 140, including the materials used in each layer. In total, the laminate consists of eight layers, which becomes visible when the table in the app is scrolled down. The resulting laminate properties calculated by the app are shown in Figure 139.



Figure 142: CLT app material properties

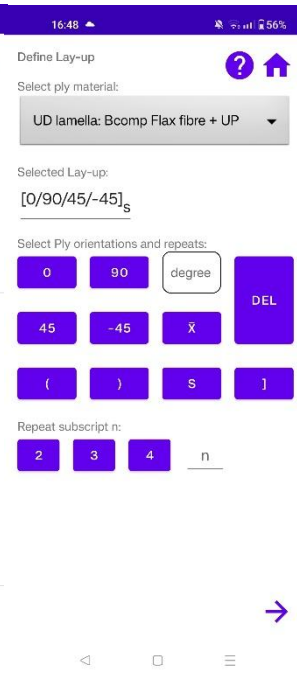

Figure 141: CLT app laminate layup input

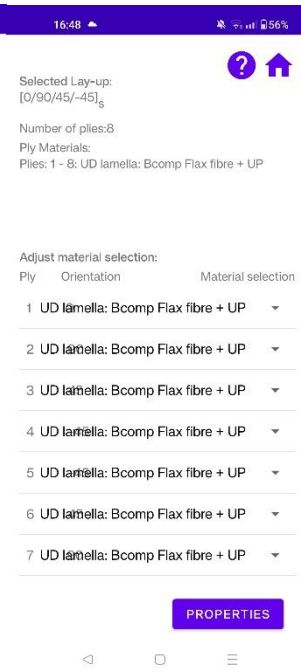

Figure 140: CLT app laminate layup overview



Figure 139: CLT app results

To test the laminate_stiffness function the following arrays are filled in the function sym_laminate:

- half_layer_structure = [0, 90, +45, -45] # direction lamella
- half_thickness_structure = [0.4667] * len(half_layer_structure) # thickness lamella [mm]
- half_material_name = ['flax_fibre_UP-Bio_Composite'] * len(half_layer_structure) # material lamella

The first array contains the stacking sequence of the lamella orientations. The second array defines the thickness of each layer, and the third array specifies the material used in each layer. These arrays only contain half of the laminate, but the function sym_laminate completes them by mirroring the stacking sequence to create a symmetric laminate. The resulting full layer structure, full thickness structure and full material name arrays are then used as input in the laminate_stiffness function. The calculated laminate properties are shown in the table below. The laminate layering is shown in Figure 143. These values match the results obtained from the app. The only difference is that the app rounds the values to two decimal places.

Property	Membrane	Bending	Unit
E_1	8.506	13.459	GPa
E_2	8.506	8.004	GPa
G_{12}	3.284	1.609	GPa
υ_{12}	0.295122	0.121867	-
υ_{21}	0.295122	0.072467	-

Table 107: Results test layering

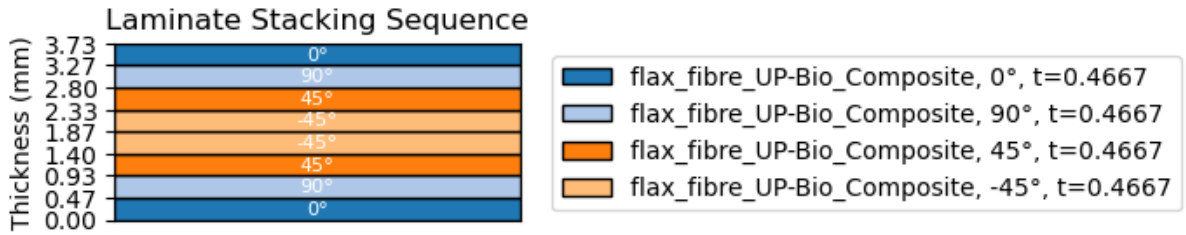

Figure 143: Layering of test laminate

Function for dictionary of laminate properties

The laminate_properties function creates a dictionary containing $E_1, E_2, G_{12}, \upsilon_{12}$ and the thickness of the laminate. The function takes as input the stiffness_list, determined with the laminate_stiffness function, and the thickness_structure array. In the stiffness_list there are two values for $E_1, E_2, G_{12}, \upsilon_{12}$ one corresponding to pure stretching and one correspong to pure bending. The pure stretching stiffness is chosen since in the top plates and bottom plate there are mainly membrane forces because of bending. The total thickness of the laminate is calculated by summing over the thickness_structure array. The function returns a dictionary containing the conservative stiffness values and the laminate thickness.

Validation of the function

To validate the function, a test laminate structure is entered into the laminate_stiffness function. The output of this function is then used as input for the laminate_properties function. The results of both functions are printed and evaluated. The following code lines are entered in a Python code cell:

```
half_layer_structure_test = [0, 90, +45, -45] # direction lamella
half_thickness_structure_test = [0.5] * len(half_layer_structure_test) #
thickness lamella [mm]
half_material_name_test = ['flax_fibre_UP-Bio_Composite'] *
len(half_layer_structure_test) # material lamella

# Calculation properties
full_layer_structure_test, full_thickness_structure_test,
full_material_name_test = sym_laminate(half_layer_structure_test,
half_thickness_structure_test, half_material_name_test)
stiffness_list_test = laminate_stiffness(full_layer_structure_test,
full_thickness_structure_test, full_material_name_test)
laminate_properties_info_test = laminate_properties(stiffness_list_test,
full_thickness_structure_test)
```

The results of the laminate_stiffness function are shown in Table 108.

Property	Membrane	Bending	Unit
E_1	8.506	13.459	GPa
E_2	8.506	8.004	GPa
G_{12}	3.284	1.609	GPa
υ_{12}	0.295122	0.121867	-
υ_{21}	0.295122	0.072467	-

Table 108: Results test layering

The results for the laminate_properties function are:

E_1: 8505.68 MPa
E_2: 8505.68 MPa
G_{12}: 3.284 MPa
υ_{12}: 0.295 MPa
Total thickness of the laminate: 4.00 mm

When comparing these results with the values in Table 108, it can be seen that the values of the membrane properties are selected in each case, which is the intended behaviour of the laminate_properties function. The calculated laminate thickness is also correct, as shown in Figure 144.

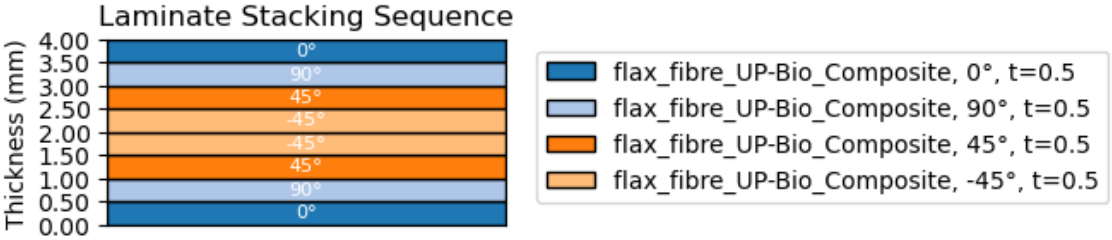

Figure 144: Test laminate stacking

Appendix F: Python code for the stiffness of the cross-section

The code for the stiffness of the cross-section is provided below. An explanation and validation of the code are provided in Appendix G.

```
# cross_section_beam_model.py
import matplotlib.pyplot as plt
from matplotlib.patches import Rectangle, Polygon

# ------------------------------
# C-Girder Functions
# ------------------------------
# Area of the cross-section of the C-girder
def area_c_girders(h_c_girder, w_c_girder, t_c_girder):
    tw = tf = t_c_girder

    # Areas
    Aw = tw * (h_c_girder - 2*tf)   # Area of the web
    Af = w_c_girder * tf          # Area of each flange
    A = Aw + 2*Af   # Total area of the cross-section
    return A

# I_zz is the moment of inertia about the z-axis (the axis parallel to the
hight of the girder)
def I_zz_c_girders(h_c_girder, w_c_girder, t_c_girder):
    tw = tf = t_c_girder

    # Areas
    Aw = tw * (h_c_girder - 2*tf)
    Af = w_c_girder * tf
    A = Aw + 2*Af

    # I_zz
    I_zz_web = tw * (h_c_girder - 2*tf)**3 / 12 # I_zz of the web
    d = h_c_girder/2 - tf/2 # distance from the center of the flange to the
neutral axis (assuming it's at mid-height)
    I_zz_flange = (w_c_girder * tf**3)/12 + Af * d**2 # I_zz of each flange
using parallel axis theorem
    I_zz = I_zz_web + 2*I_zz_flange # Total I_zz is the sum of the web and the
two flanges
    return I_zz

# Center of gravity of the cross-section in the y-direction (the direction of
the width of the girder)
def center_of_gravity_y_c_girder(w_c_girder, tw, Af, Aw, orientation):
    if orientation == 'right':  # Assuming the web is on the right side, the
center of the web is at w_c_girder - tw/2
        z_w = w_c_girder - tw/2
    elif orientation == 'left': # Assuming the web is on the left side, the
center of the web is at tw/2
        z_w = tw/2
```

```
    else:
        raise ValueError("orientation must be 'left' or 'right'")

    z_f = w_c_girder/2  # Assuming the center of the flange is at the midpoint
of the width of the girder
    z_cog = (2*Af*z_f + Aw*z_w) / (2*Af + Aw)   # Center of gravity using the
formula: z_cog = (sum of (area * distance to reference axis)) / total area
    return z_cog, z_f, z_w

# I_yy is the moment of inertia about the y-axis (the axis parallel to the
width of the girder)
def I_yy_c_girders(h_c_girder, w_c_girder, t_c_girder, orientation):
    tw = tf = t_c_girder

    #Areas
    Aw = tw * (h_c_girder - 2*tf)
    Af = w_c_girder * tf

    z_cog, z_f, z_w = center_of_gravity_y_c_girder(w_c_girder, tw, Af, Aw,
orientation)

    # I_yy
    I_yy_web = (h_c_girder - 2*tf) * tw**3 / 12 + Aw * (z_cog - z_w)**2 # I_yy
of the web using parallel axis theorem
    I_yy_flange = (tf * w_c_girder**3)/12 + Af * (z_cog - z_f)**2   # I_yy of
each flange using parallel axis theorem
    I_yy = I_yy_web + 2*I_yy_flange # Total I_yy is the sum of the web and the
two flanges
    return I_yy

# ----------------------------
# Plate/Core Functions
# ----------------------------
# Area of the cross-section of the plate and core
def area_plate_core(w_plate_core, t_plate_core):
    A = w_plate_core * t_plate_core
    return A

# I_zz is the moment of inertia about the z-axis (the axis parallel to the
hight of the girder)
def I_zz_plate_core(w_plate_core, t_plate_core):
    I_zz = w_plate_core * t_plate_core**3 / 12
    return I_zz

# I_yy is the moment of inertia about the y-axis (the axis parallel to the
width of the girder)
def I_yy_plate_core(w_plate_core, t_plate_core):
    I_yy = t_plate_core * w_plate_core**3 / 12
    return I_yy
```

```
# ------------------------------
# Z-Coordinates & Center of Gravity
# ------------------------------
# Z-coordinates of the different components of the cross-section (bottom
plate, c-girder, bottom flange, core, top flange)
def z_coordinates(h_c_girder, t_bp, t_bf, h_core, t_tf):

    z_coords = {
        'bp': t_bp / 2, # Center of the bottom plate is at half its thickness
        'c_girder': t_bp + h_c_girder / 2,  # Center of the c-girder is at the
bottom plate thickness plus half the height of the c-girder
        'bf': t_bp + h_c_girder + t_bf / 2, # Center of the bottom flange is
at the bottom plate thickness plus the height of the c-girder plus half the
thickness of the bottom flange
        'core': t_bp + h_c_girder + t_bf + h_core / 2,  # Center of the core
is at the bottom plate thickness plus the height of the c-girder plus the
thickness of the bottom flange plus half the height of the core
        'tf': t_bp + h_c_girder + t_bf + h_core + t_tf / 2  # Center of the
top flange is at the bottom plate thickness plus the height of the c-girder
plus the thickness of the bottom flange plus the height of the core plus half
the thickness of the top flange
    }
    return z_coords

# Calculate the z-coordinate of the center of gravity of the cross-section
using the formula:
# z_cg = (sum of (E * A * z)) / (sum of (E * A)
# where E is the Young's modulus, A is the area of the cross-section, and z is
the z-coordinate of the center of gravity of each component)
def center_of_gravity_z(E_bp, a_bp,
                        E_c_girder, a_c_girder, n_o_g,
                        E_bf, a_bf,
                        E_core, a_core,
                        E_tf, a_tf,
                        z_coords):

    numerator = (E_bp*a_bp*z_coords['bp'] +     # Contribution of the bottom
plate
                 E_c_girder*a_c_girder*z_coords['c_girder']*n_o_g +     #
Contribution of the c-girders (multiplied by the number of girders)
                 E_bf*a_bf*z_coords['bf'] +     # Contribution of the bottom
flange
                 E_core*a_core*z_coords['core'] +       # Contribution of the
core
                 E_tf*a_tf*z_coords['tf'])    # Contribution of the top flange

    denominator = (E_bp*a_bp +      # Contribution of the bottom plate
                   E_c_girder*a_c_girder*n_o_g +    # Contribution of the c-
girders (multiplied by the number of girders)
                   E_bf*a_bf +     # Contribution of the bottom flange
```

```
                  E_core*a_core +     # Contribution of the core
                  E_tf*a_tf)    # Contribution of the top flange

    return numerator / denominator

# ----------------------------
# Y-Coordinates of C-girders
# ----------------------------
# Y-coordinates of the center of gravity of the c-girders, ensuring they are
evenly spaced across the width of the cross-section
# and that the flanges of the middle two girders do not overlap
def y_coordinates(w, h_c_girder, w_c_girder, t_c_girder, n_o_g):
    if n_o_g % 2 != 0:  # Ensure the number of girders is even to avoid a
single middle girder
        raise ValueError("Number of girders must be even.")

    tw = tf = t_c_girder

    # Areas for centroid calculation
    Aw = tw * (h_c_girder - 2*tf)
    Af = w_c_girder * tf

    y_cog_dis,_,_ = center_of_gravity_y_c_girder(   # Calculate the distance
from the outer edge to the center of gravity of the web
                w_c_girder, tw, Af, Aw, 'left'
                )

    spacing = (w - 2 * y_cog_dis) / (n_o_g - 1) # Calculate the spacing
between the centers of gravity of the girders

    y_positions = []    # List to store the y-coordinates of the centers of
gravity of the girders
    orientations = []   # List to store the orientation of the girders (left
or right)

    for i in range(n_o_g):

        # Calculate the y-coordinate of the center of gravity of the current
girder
        y_loc_global = y_cog_dis + i * spacing

        # Determine orientation (opening inward)
        if y_loc_global < w/2:
            orientation = 'left'
        else:
            orientation = 'right'

        y_positions.append(y_loc_global)
        orientations.append(orientation)
```

```
    if y_positions[n_o_g//2-1] + y_cog_dis >= y_positions[n_o_g//2] +
y_cog_dis - w_c_girder:   # Check if the flanges of the middle two girders
overlap
        print('The flanges of the middle two girders overlap')
    return y_positions, orientations

# ----------------------------
# Structural Properties
# ----------------------------
# Calculate the total bending stiffness EI_zz of the cross-section using the
formula:
# EI_zz = sum of (E * (I_zz + A * (z_cg - z_component)**2))
# where E is the Young's modulus, I_zz is the moment of inertia about the z-
axis,
# A is the area of the cross-section, z_cg is the z-coordinate of the center
of gravity of the cross-section,
# and z_component is the z-coordinate of the center of gravity of each
component
def EI_zz_total_cross_section(w, bottom_plate_laminate, girder_laminate,
n_o_g, h_girder, w_girder, bottom_face_laminate, h_core, E_core,
top_face_laminate):
    if n_o_g % 2 != 0:  # Ensure the number of girders is even to maintain a
symmetric layout
        raise ValueError("Number of girders (n_o_g) must be even for symmetric
layout.")

    # Calculate areas and moments of inertia for each component
    a_bp = area_plate_core(w, bottom_plate_laminate['t_laminate'])
    I_zz_bp = I_zz_plate_core(w, bottom_plate_laminate['t_laminate'])

    a_c_girder = area_c_girders(h_girder, w_girder,
girder_laminate['t_laminate'])
    I_zz_girder = I_zz_c_girders(h_girder, w_girder,
girder_laminate['t_laminate'])

    a_bf = area_plate_core(w, bottom_face_laminate['t_laminate'])
    I_zz_bf = I_zz_plate_core(w, bottom_face_laminate['t_laminate'])

    a_core = area_plate_core(w, h_core)
    I_zz_c = I_zz_plate_core(w, h_core)

    a_tf = area_plate_core(w, top_face_laminate['t_laminate'])
    I_zz_tf = I_zz_plate_core(w, top_face_laminate['t_laminate'])

    # Calculate z-coordinates of the centers of gravity of the components
    z_coords = z_coordinates(h_girder, bottom_plate_laminate['t_laminate'],
bottom_face_laminate['t_laminate'], h_core, top_face_laminate['t_laminate'])
    # Calculate the z-coordinate of the center of gravity of the cross-section
    cog_z = center_of_gravity_z(bottom_plate_laminate['E_1'], a_bp,
                                girder_laminate['E_1'], a_c_girder, n_o_g,
```

```
                                bottom_face_laminate['E_1'], a_bf,
                                E_core, a_core,
                                top_face_laminate['E_1'], a_tf,
                                z_coords)

    # Calculate the total bending stiffness EI_zz of the cross-section
    EI_zz = (bottom_plate_laminate['E_1'] * (I_zz_bp + a_bp * (cog_z -
z_coords['bp'])**2) +
             girder_laminate['E_1'] * n_o_g * (I_zz_girder + a_c_girder *
(cog_z - z_coords['c_girder'])**2) +
             bottom_face_laminate['E_1'] * (I_zz_bf + a_bf * (cog_z -
z_coords['bf'])**2) +
             E_core * (I_zz_c + a_core * (cog_z - z_coords['core'])**2) +
             top_face_laminate['E_1'] * (I_zz_tf + a_tf * (cog_z -
z_coords['tf'])**2))

    return EI_zz

# Calculate the total bending stiffness EI_yy of the cross-section using the
formula:
# EI_yy = sum of (E * (I_yy + A * (y_cg - y_component)**2))
# where E is the Young's modulus, I_yy is the moment of inertia about the y-
axis,
# A is the area of the cross-section, y_cg is the y-coordinate of the center
of gravity of the cross-section,
# and y_component is the y-coordinate of the center of gravity of each
component.
# For the c-girders, the y-coordinate of the center of gravity is different
for each girder
# and is calculated to ensure they are evenly spaced across the width of the
cross-section and that the flanges of the middle two girders do not overlap.
def EI_yy_total_cross_section(w, bottom_plate_laminate, girder_laminate,
n_o_g, h_girder, w_girder, bottom_face_laminate, h_core, E_core,
top_face_laminate):
    if n_o_g % 2 != 0:
        raise ValueError("Number of girders (n_o_g) must be even for symmetric
layout.")

    # Calculate areas and moments of inertia for each component
    a_c_girder = area_c_girders(h_girder, w_girder,
girder_laminate['t_laminate'])

    I_yy_bp = I_yy_plate_core(w, bottom_plate_laminate['t_laminate'])

    I_yy_bf = I_yy_plate_core(w, bottom_face_laminate['t_laminate'])

    I_yy_tf = I_yy_plate_core(w, top_face_laminate['t_laminate'])

    I_yy_core = I_yy_plate_core(w, h_core)
```

```
    # Calculate y-coordinates of the centers of gravity of the c-girders,
    # ensuring they are evenly spaced across the width of the cross-section
and that the flanges of the middle two girders do not overlap
    y_coords, orientation = y_coordinates(w, h_girder, w_girder,
girder_laminate['t_laminate'], n_o_g)

    # The cross-section is symmetric in y-direction so the center of gravity
is in the middle of the width
    y_cg = w / 2

    # Calculate the total bending stiffness EI_yy of the cross-section
    EI_yy = bottom_plate_laminate['E_1'] * I_yy_bp +
bottom_face_laminate['E_1'] * I_yy_bf + E_core * I_yy_core +
top_face_laminate['E_1'] * I_yy_tf

    for i in range(n_o_g):
        I_yy_girder = I_yy_c_girders(h_girder, w_girder,
girder_laminate['t_laminate'], orientation[i])
        EI_yy += girder_laminate['E_1'] * (I_yy_girder + a_c_girder * (y_cg -
y_coords[i])**2)

    return EI_yy

# Calculate the total axial stiffness EA of the cross-section using the
formula:
# EA = sum of (E * A)
# where E is the Young's modulus and A is the area of the cross-section of
each component.
def EA_total_cross_section(w, bottom_plate_laminate, girder_laminate, n_o_g,
h_girder, w_girder, bottom_face_laminate, h_core, E_core, top_face_laminate):
    a_bp = area_plate_core(w, bottom_plate_laminate['t_laminate'])
    a_c_girder = area_c_girders(h_girder, w_girder,
girder_laminate['t_laminate'])
    a_bf = area_plate_core(w, bottom_face_laminate['t_laminate'])
    a_core = area_plate_core(w, h_core)
    a_tf = area_plate_core(w, top_face_laminate['t_laminate'])

    EA = (bottom_plate_laminate['E_1'] * a_bp +
          girder_laminate['E_1'] * n_o_g * a_c_girder +
          bottom_face_laminate['E_1'] * a_bf +
          E_core * a_core +
          top_face_laminate['E_1'] * a_tf)

    return EA

# Calculate the total shear stiffness GI_w of the cross-section using the
formula:
# GI_w = 4 * A^2 / (sum of (s_i / (G_i * h_i)))
# where A is the area of the cross-section for GI_w calculation,
# s_i is the length of the shear flow path through each component,
```

```
# G_i is the shear modulus of each component,
# and h_i is the thickness of each component in the direction of the shear
flow.
def GI_w_total_cross_section(w, bottom_plate_laminate, girder_laminate, n_o_g,
h_girder, w_girder, bottom_face_laminate, h_core, G_core, top_face_laminate):
    h_cs = bottom_plate_laminate['t_laminate'] + h_girder +
bottom_face_laminate['t_laminate'] + h_core + top_face_laminate['t_laminate']
# Total height of the cross-section
    h_w_cs = h_cs - 0.5 * bottom_plate_laminate['t_laminate'] - 0.5 *
(bottom_face_laminate['t_laminate'] + h_core +
top_face_laminate['t_laminate']) # Height for area of GI_w calculation
    b_w_cs = w - girder_laminate['t_laminate'] # Width for area of GI_w
calculation
    A_w_cs = h_w_cs * b_w_cs # Area of the cross-section for GI_w calculation
    s_Gh = 0
    for i in range(4):
        if i == 0: # Contribution of the bottom plate
            s_i = b_w_cs
            G_h_i = bottom_plate_laminate['G_12'] *
bottom_plate_laminate['t_laminate']
        elif i == 1: # Contribution of the c-girders right side
            s_i = h_w_cs
            G_h_i = girder_laminate['G_12'] * girder_laminate['t_laminate']
        elif i == 2: # Contribution of the bottom face, core and top face
            s_i = b_w_cs
            G_h_i = G_core * h_core + bottom_face_laminate['G_12'] *
bottom_face_laminate['t_laminate'] + top_face_laminate['G_12'] *
top_face_laminate['t_laminate']
        elif i == 3: # Contribution of c-girders left side
            s_i = h_w_cs
            G_h_i = girder_laminate['G_12'] * girder_laminate['t_laminate']

        s_Gh += s_i / (G_h_i)

    GI_w = 4 * A_w_cs**2 / s_Gh
    return GI_w

# Calculate both EI_zz, EI_yy, EA and GI_w of the cross-section and return
them as a tuple
def EI_zz_yy_EA_GI_w_total_cross_section(w, bottom_plate_laminate,
girder_laminate, n_o_g, h_girder, w_girder, bottom_face_laminate, h_core,
E_core, G_core, top_face_laminate):
    EI_zz = EI_zz_total_cross_section(w, bottom_plate_laminate,
girder_laminate, n_o_g, h_girder, w_girder, bottom_face_laminate, h_core,
E_core, top_face_laminate)
    EI_yy = EI_yy_total_cross_section(w, bottom_plate_laminate,
girder_laminate, n_o_g, h_girder, w_girder, bottom_face_laminate, h_core,
E_core, top_face_laminate)
```

```
    EA = EA_total_cross_section(w, bottom_plate_laminate, girder_laminate,
n_o_g, h_girder, w_girder, bottom_face_laminate, h_core, E_core,
top_face_laminate)
    GI_w = GI_w_total_cross_section(w, bottom_plate_laminate, girder_laminate,
n_o_g, h_girder, w_girder, bottom_face_laminate, h_core, G_core,
top_face_laminate)
    return EI_zz, EI_yy, EA, GI_w

# -------------------
# Area cross-section
# -------------------
def area_total_cross_section(w, bottom_plate_laminate, girder_laminate, n_o_g,
h_girder, w_girder, bottom_face_laminate, h_core, top_face_laminate):
    a_bp = area_plate_core(w, bottom_plate_laminate['t_laminate'])
    a_c_girder = area_c_girders(h_girder, w_girder,
girder_laminate['t_laminate'])
    a_bf = area_plate_core(w, bottom_face_laminate['t_laminate'])
    a_core = area_plate_core(w, h_core)
    a_tf = area_plate_core(w, top_face_laminate['t_laminate'])

    total_area = a_bp + n_o_g * a_c_girder + a_bf + a_core + a_tf
    return total_area

# ---------------------
# Height cross-section
# ---------------------
def height_total_cross_section(bottom_plate_laminate, h_girder,
bottom_face_laminate, h_core, top_face_laminate):
    h_cross_section = bottom_plate_laminate['t_laminate'] + h_girder +
bottom_face_laminate['t_laminate'] + h_core + top_face_laminate['t_laminate']
    return h_cross_section

# ----------------------------
# Plotting
# ----------------------------
# Plot the cross-section of the sandwich structure,
# showing the bottom plate, c-girders, bottom face, core, and top face with
their respective thicknesses and labels.
def plot_cross_section(
    w, bottom_plate_laminate, girder_laminate, n_o_g, h_girder, w_girder,
    bottom_face_laminate, h_core, E_core, top_face_laminate):

    t_bp = bottom_plate_laminate['t_laminate']
    t_g = girder_laminate['t_laminate']
    t_bf = bottom_face_laminate['t_laminate']
    t_tf = top_face_laminate['t_laminate']

    fig, ax = plt.subplots(figsize=(20, 10))

    title_offset = -10  # more space for left titles
```

```
    thickness_offset = 10  # horizontal offset for thickness labels

    # Bottom plate
    ax.add_patch(Rectangle((0, 0), w, t_bp, facecolor='#b04a4a',
edgecolor='black', linewidth=1))
    ax.text(title_offset, t_bp/2, 'Bottom Plate', ha='right', va='center',
fontsize=8)
    ax.text(w + thickness_offset, t_bp/2, f'{t_bp:.2f} mm', ha='left',
va='center', fontsize=8, color='darkred')

    # Compute y-coordinates (centroids) and orientations
    y_cogs, orientations = y_coordinates(w, h_girder, w_girder, t_g, n_o_g)

    tw = tf = t_g
    hw = h_girder - 2*tf
    Aw = tw * hw
    Af = w_girder * tf

    # Draw each C-girder polygon
    for i, (y_cog, orientation) in enumerate(zip(y_cogs, orientations)):
        z_cog_local, z_f, z_w = center_of_gravity_y_c_girder(w_girder, tw, Af,
Aw, orientation)

        if orientation == 'left':
            y_left = y_cog - z_cog_local
            points = [
                (y_left, t_bp),
                (y_left + w_girder, t_bp),
                (y_left + w_girder, t_bp + tf),
                (y_left + tf, t_bp + tf),
                (y_left + tf, t_bp + hw + tf),
                (y_left + w_girder, t_bp + hw + tf),
                (y_left + w_girder, t_bp + h_girder),
                (y_left, t_bp + h_girder)
            ]
        else:
            y_right = y_cog - z_cog_local + w_girder
            points = [
                (y_right, t_bp),
                (y_right - w_girder, t_bp),
                (y_right - w_girder, t_bp + tf),
                (y_right - tf, t_bp + tf),
                (y_right - tf, t_bp + hw + tf),
                (y_right - w_girder, t_bp + hw + tf),
                (y_right - w_girder, t_bp + h_girder),
                (y_right, t_bp + h_girder)
            ]

        poly = Polygon(points, facecolor='lightblue', edgecolor='black',
linewidth=1)
```

```
        ax.add_patch(poly)
        ax.plot(y_cog, t_bp + h_girder/2, 'ro', label='Centroid' if i == 0
else "")

        # Thickness label to the right of the girder
        ax.text(w + thickness_offset, t_bp + h_girder/2, f't = {t_g:.2f} mm',
ha='left', va='center', fontsize=8, color='blue')

        if i == 0:
            dim_offset = 20  # distance away from girder for dimension lines

            if orientation == 'left':
                x_start = y_left
                x_end = y_left + w_girder
            else:
                x_start = y_right - w_girder
                x_end = y_right

            y_bottom = t_bp
            y_top = t_bp + h_girder

            # -------------------------
            # Horizontal dimension (width)
            # -------------------------
            y_dim = y_top + dim_offset

            ax.annotate('', xy=(x_start, y_dim), xytext=(x_end, y_dim),
                        arrowprops=dict(arrowstyle='<->'))
            ax.text((x_start + x_end)/2 + 40, y_dim + 5,
                    f'{w_girder:.2f} mm',
                    ha='center', va='bottom', fontsize=8)

            # Extension lines
            ax.plot([x_start, x_start], [y_top, y_dim], 'k--', linewidth=0.8)
            ax.plot([x_end, x_end], [y_top, y_dim], 'k--', linewidth=0.8)

            # -------------------------
            # Vertical dimension (height)
            # -------------------------
            x_dim = x_end + dim_offset

            ax.annotate('', xy=(x_dim, y_bottom), xytext=(x_dim, y_top),
                        arrowprops=dict(arrowstyle='<->'))
            ax.text(x_dim + 5, (y_bottom + y_top)/2,
                    f'{h_girder:.2f} mm',
                    ha='left', va='center', rotation=90, fontsize=8)

            # Extension lines
            ax.plot([x_end, x_dim], [y_bottom, y_bottom], 'k--',
linewidth=0.8)
```

```
            ax.plot([x_end, x_dim], [y_top, y_top], 'k--', linewidth=0.8)

    # Bottom face
    y_bf = t_bp + h_girder
    ax.add_patch(Rectangle((0, y_bf), w, t_bf, facecolor='lightgreen',
edgecolor='black', linewidth=1))
    ax.text(title_offset, y_bf + t_bf/2, 'Bottom Face', ha='right',
va='center', fontsize=8)
    ax.text(w + thickness_offset, y_bf + t_bf/2, f'{t_bf:.2f} mm', ha='left',
va='center', fontsize=8, color='green')

    # Core
    y_core = y_bf + t_bf
    ax.add_patch(Rectangle((0, y_core), w, h_core, facecolor='wheat',
edgecolor='black', linewidth=1))
    ax.text(title_offset, y_core + h_core/2, 'Core', ha='right', va='center',
fontsize=8)
    ax.text(w + thickness_offset, y_core + h_core/2, f'{h_core:.2f} mm',
ha='left', va='center', fontsize=8, color='saddlebrown')

    # Top face
    y_tf = y_core + h_core
    ax.add_patch(Rectangle((0, y_tf), w, t_tf, facecolor='orange',
edgecolor='black', linewidth=1))
    ax.text(title_offset, y_tf + t_tf/2, 'Top Face', ha='right', va='center',
fontsize=8)
    ax.text(w + thickness_offset, y_tf + t_tf/2, f'{t_tf:.2f} mm', ha='left',
va='center', fontsize=8, color='darkorange')

    # -------------------------
    # Bottom measurement bar
    # -------------------------
    y_main = -25
    y_sub = -45
    tick = 6

    # Total width of the cross-section
    ax.annotate('', xy=(0, y_main), xytext=(w, y_main),
                arrowprops=dict(arrowstyle='<->', linewidth=1.5))

    ax.plot([0, 0], [y_main, y_main + tick], 'k-', linewidth=1.2)
    ax.plot([w, w], [y_main, y_main + tick], 'k-', linewidth=1.2)

    ax.text(w/2, y_main - 5,
            f'{w:.0f} mm',
            ha='center', va='top', fontsize=11, fontweight='bold')


    # Girder spacing
    # Take first spacing (they are equal anyway)
```

```
    spacing = y_cogs[1] - y_cogs[0]

    # Show it only between first two girders
    x1 = y_cogs[0]
    x2 = y_cogs[1]

    ax.annotate('', xy=(x1, y_sub), xytext=(x2, y_sub),
                arrowprops=dict(arrowstyle='<->', linewidth=1.0))

    ax.plot([x1, x1], [y_sub, y_sub + tick], 'k-', linewidth=1.0)
    ax.plot([x2, x2], [y_sub, y_sub + tick], 'k-', linewidth=1.0)

    ax.text((x1 + x2)/2, y_sub - 5,
            f'Girder spacing: {spacing:.0f} mm',
            ha='center', va='top', fontsize=9)


    # Light guidelines
    for x in y_cogs:
        ax.plot([x, x], [0, y_sub], 'k--', linewidth=0.5, alpha=0.2)

    # Axes settings
    ax.set_xlim(title_offset - 200, w + thickness_offset + 200)  # extend left
to fit titles
    ax.set_ylim(-80, y_tf + t_tf + 20)
    ax.set_aspect('equal')
    ax.set_xlabel('Width [mm]')
    ax.set_ylabel('Height [mm]')
    ax.set_title('C-Girder Composite Cross-Section (Centroids Overlay)')
    ax.grid(True)
    ax.legend()
    plt.show()
```

Appendix G: Explanation and validation of the stiffness of the cross-section code

The code for calculating the cross-sectional stiffness is provided in Appendix F. The cross-section for which the stiffness of the cross-section code was made is shown in Figure 145. The stiffness of the cross-section code is structured such that several intermediate functions are first defined, which are then used in a final function. This final function generates values for EI_{zz}, EI_{yy}, EA and GI_w. The plot_cross_section function plots the cross-section with its dimensions.

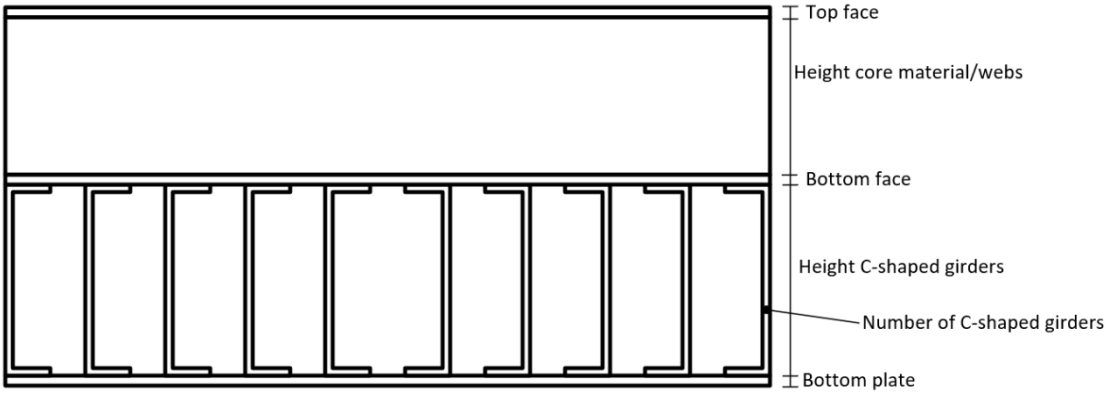

Figure 145: Cross-section deck

Area and moment of inertia of C-shaped girder

Area of C-shaped girder

The area_c_girders function takes as input the height, width, and thickness of the C-shaped girder. The function first calculates the areas of the web and flanges with:

$$A_w = t_w * (h_{c-girder} - 2 * t_f)$$

$$A_f = w_{c-girder} * \ t_f$$

With: $t_w = t_f = t_{c-girder}$

The total area is then:

$$A = A_w + A_f$$

The value for A is returned.

Moment of inertia about the z-axis (I_{zz})

The I_zz_c_girders function takes as input the height, width, and thickness of the C-shaped girder. First, the areas of the web and flanges are calculated as above. Then, the moments of inertia about the z-axis are calculated:

$$I_{zz,web} = \frac{1}{12} * t_w * (h_{c-girder} - 2 * t_f)^3$$

$$d = \frac{h_{c-girder}}{2} - \frac{t_f}{2}$$

$$I_{zz,flange} = \frac{1}{12} * w_{c-girder} * {t_f}^3 + A_f * d^2$$

$$I_{zz} = \ I_{zz,web} + 2 * I_{zz,flange}$$

The values for I_{zz} is returned.

Centre of gravity of the cross-section in the y-direction

The center_of_gravity_y_c_girder function takes the width and thickness of the C-shaped girder, the areas of the web and flanges and the orientation of the web (left or right) as input. First, the location of the centre of the web is determined. If the orientation is right, the centre of the web is located at:

$$z_w = w_{c-girder} - \frac{t_w}{2}$$

If the orientation is left, the centre of the web is located at:

$$z_w = \frac{t_w}{2}$$

The centre of the flange is assumed to be located at the midpoint of the girder width:

$$z_f = \frac{w_{c-girder}}{2}$$

The centroid of the entire cross-section is calculated using the formula:

$$z_{cog} = \frac{2A_f z_f + A_w z_w}{2A_f + A_w}$$

The function returns z_{cog}, z_f, and z_w.

Moment of inertia about the y-axis (I_{yy})

The I_yy_c_girders function takes as input the height, width and thickness of the C-shaped girder and orientation of the web. First, the areas of the web and flanges are calculated as area of C-shaped girder. After the centroid is determined by calling center_of_gravity_y_c_girder. Then, the moment of inertia about the y-axis is computed using the parallel axis theorem:

$$I_{yy,web} = \frac{1}{12} * (h_{c-girder} - 2t_f) \cdot t_w^3 + A_w \cdot (z_{cog} - z_w)^2$$
$$I_{yy,flange} = \frac{1}{12} * (t_f \cdot w_{c-girder}^3) + A_f \cdot (z_{cog} - z_f)^2$$
$$I_{yy} = I_{yy,web} + 2 \cdot I_{yy,flange}$$

The function returns the total I_{yy}.

Validation of the functions

The functions described above are validated using the website SkyCiv, (Section builder, sd). In SkyCiv, the cross-section shown in Figure 148 is defined. The section has a height of 250 mm, a width of 100 mm, and a thickness of 10 mm. The results obtained from SkyCiv are shown in Figure 147 and Figure 146.

Area	ⓘ	4300	mm^2
C_z	ⓘ	25.9302	mm
C_y	ⓘ	125	mm

Figure 147: Results SkyCiv test C-girder Geometric properties

I_z	ⓘ	38.9558×10^6	mm^4
I_y	ⓘ	3.85211×10^6	mm^4

Figure 146: Results SkyCiv test C-girder moment of inertia

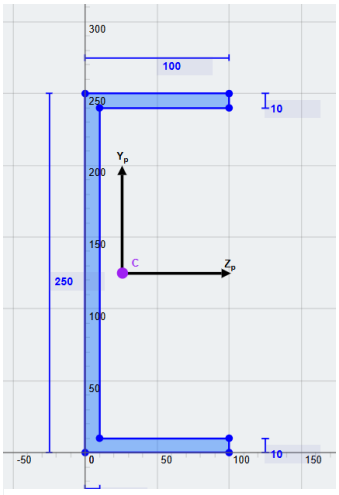

Figure 148: Cross-section test C-girder in SkyCiv

The following code lines are entered in a Python code cell:

```
h_girder_test = 250 # [mm]
w_girder_test = 100 # [mm]
t_girder_test = 10 # [mm]
area_flange_test = t_girder_test * w_girder_test
area_web_test = t_girder_test * (h_girder_test - 2*t_girder_test)

area_c_girders_test = area_c_girders(h_girder_test, w_girder_test,
t_girder_test)
I_yy_c_girders_test = I_yy_c_girders(h_girder_test, w_girder_test,
t_girder_test, 'left')
I_zz_c_girders_test = I_zz_c_girders(h_girder_test, w_girder_test,
t_girder_test)
y_cog_girder_test, y_flange_test, y_web_test =
center_of_gravity_y_c_girder(w_girder_test, t_girder_test, area_flange_test,
area_web_test, 'left')
```

The obtained results are:

Area of the flange: $1000.00\ mm^2$
Area of the web: $2300.00\ mm^2$
Area of the girder: $4300.00\ mm^2$
I_{yy}: $3852112.40\ mm^4$
I_{zz}: $38955833.33\ mm^4$
y-coordinate of the center of gravity of the flange: 50.00 mm
y-coordinate of the center of gravity of the web: 5.00 mm
y-coordinate of the center of gravity of the girder: 25.93 mm

The area of the girder calculated with the code is the same as the area calculated with SkyCiv. The value of I_{yy} calculated with the code is equal to the value of I_y obtained from SkyCiv. Similarly, the value of I_{zz} calculated with the code matches the value of I_z from SkyCiv. The value c_z reported by SkyCiv corresponds to the y-coordinate of the center of gravity of the girder in the python code, because the assumed y- and z-axes are reversed compared to SkyCiv. The value of c_z is the same as the y-coordinate calculated with the code. Based on this comparison, the functions area_c_girders, I_zz_c_girders, center_of_gravity_y_c_girder, and I_yy_c_girders are correct.

Area and moment of inertia of plates and core

Area plate or core

The area_plate_core function takes as input the width and thickness of the plate or core. The area is calculated with:

$$A = w * t$$

The function returns the value of A.

Moment of inertia about the z-axis (I_{zz})

The I_zz_plate_core function takes as input the width and thickness of the plate or core. The moment of inertia is calculated with:

$$I_{zz} = \frac{1}{12} * w * t^3$$

The function returns the value of I_{zz}.

Moment of inertia about the y-axis (I_{yy})

The I_yy_plate_core function takes as input the width and thickness of the plate or core. The moment of inertia is calculated with:

$$I_{yy} = \frac{1}{12} * t * w^3$$

The function returns the value of I_{yy}.

Validation of the functions

The functions above are tested with the program SkyCiv, (Section builder, sd). In SkyCiv, the cross-section shown in Figure 149 is defined. The height of the plate is 10 mm and the width is 1800 mm. The results obtained from SkyCiv are shown in Figure 150 and Figure 151.

Area		18 x10^3 mm^2

Figure 151: Results SkyCiv test plate geometric properties

I_z		150 x10^3 mm^4
I_y		4.86 x10^9 mm^4

Figure 150: Results SkyCiv test plate moment of inertia

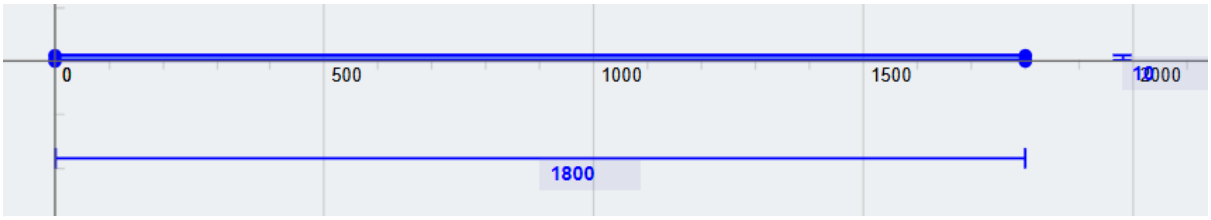

Figure 149: Cross-section test plate in SkyCiv

The following code lines are entered in a Python code cell:

```
h_plate_test = 10 # [mm]
w_plate_test = 1800 # [mm]
area_plate_test = area_plate_core(w_plate_test, h_plate_test)
I_yy_plate_test = I_yy_plate_core(w_plate_test, h_plate_test)
I_zz_plate_test = I_zz_plate_core(w_plate_test, h_plate_test)
```

The obtained results are:

Area of the plate: $18000.00\ mm^2$
I_{yy} of the plate: $4860000000.00\ mm^4$
I_{zz} of the plate: $150000.00\ mm^4$

The area of the plate calculated with the code is the same as the area calculated with SkyCiv. The value of I_{yy} calculated with the code is equal to the value of I_y obtained from SkyCiv. The value of I_{zz} calculated with the code is also equal to the value of I_z obtained from SkyCiv. Based on this comparison, the area_plate_core, I_zz_plate_core, and I_yy_plate_core are verified to be correct.

z-coordinates centre of gravity elements

The z_coordinates function determines the centre of gravity of all cross-sectional elements with respect to the bottom of the cross-section and stores these values in a dictionary. The function takes as input the height of the C-shaped girders, the thickness of the bottom plate, the thickness of the bottom face, the height of the core and the thickness of the top face. The z-coordinates are calculated as follows:

Bottom plate: $z = \frac{t_{bp}}{2}$

C-girder: $z = t_{bp} + \frac{h_{c-girder}}{2}$

Bottom face: $z = t_{bp} + h_{c-girder} + \frac{t_{bf}}{2}$

Core: $z = t_{bp} + h_{c-girder} + t_{bf} + \frac{h_{core}}{2}$

Top face: $z = t_{bp} + h_{c-girder} + t_{bf} + h_{core} + \frac{t_{tf}}{2}$

The function returns these z-coordinates in a dictionary.

Validation of the function

To test the function, test values are entered into the function in Python. The used values are then drawn to scale with bars together with the results of the function to verify whether the calculated values are reasonable. This visual check helps confirm that the function performs as intended and that the calculated z-values are logical. The following code lines are entered in a Python code cell:

```
h_c_girder_test = 100 # [mm]
t_bp_test = 10 # [mm]
t_bf_test = 5 # [mm]
h_core_test = 20 # [mm]
t_tf_test = 5 # [mm]

z_coords_test = z_coordinates(h_c_girder_test, t_bp_test, t_bf_test,
h_core_test, t_tf_test)
```

The results are:

z-coordinate of the centre of gravity of the bottom plate: 5 mm
z-coordinate of the centre of gravity of the girder: 60 mm
z-coordinate of the centre of gravity of the bottom face: 112.50 mm
z-coordinate of the centre of gravity of the core: 125 mm
z-coordinate of the centre of gravity of the top face: 137.50 mm

In Figure 152 the heights of the elements are drawn to scale with bars. On the left-hand side of the drawing, the dimension lines of the elements are shown. On the right-hand side of the drawing, the results of the function are indicated with lines. From the figure it can be concluded that the calculated z-coordinates correspond correctly with the geometry of the cross-section.

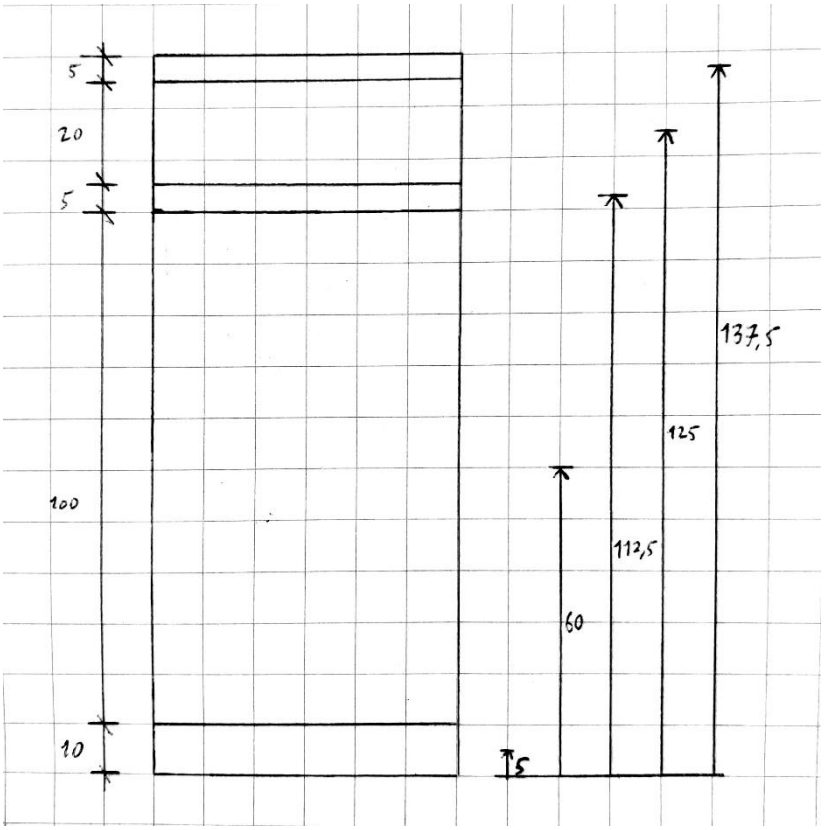

Figure 152: To scale drawing of the elements heights in bars with results in [mm]

z-coordinate centre of gravity of the cross-section

The center_of_gravity_z function takes as input the Young's modulus and area of all the cross-sectional elements, the number of C-girders and the z-coordinates determined with the z-coordinates function. The centre of gravity is calculated using the standard weighted-average formula:

$$z_{cg} = \frac{\sum_{elements} E_{1,element} * A_{element} * z_{element}}{\sum_{elements} E_{1,element} * A_{element}}$$

The function returns the value of z_{cg}.

Test of the function

To test the function, test values are entered into the function and afterwards a hand calculation is performed and compared with the result from the function. The following code lines are entered in a Python code cell:

```
E_bp_test = 17000 # [MPa]
w_plate_test = 1800 # [mm]
t_bp_test = 10 # [mm]
a_bp_test = area_plate_core(w_plate_test, t_bp_test)
E_c_girder_test = 14000 # [MPa]
h_c_girder_test = 250 # [mm]
w_girder_test = 100 # [mm]
```

```
t_girder_test = 10 # [mm]
a_c_girder_test = area_c_girders(h_c_girder_test, w_girder_test,
t_girder_test)
n_o_g_test = 4
E_bf_test = 16000 # [MPa]
t_bf_test = 5 # [mm]
a_bf_test = area_plate_core(w_plate_test, t_bf_test)
E_core_test = 10 # [MPa]
h_core_test = 20 # [mm]
a_core_test = area_plate_core(w_plate_test, h_core_test)
E_tf_test = 16000 # [MPa]
t_tf_test = 5 # [mm]
a_tf_test = area_plate_core(w_plate_test, t_tf_test)

z_coordinates_test = z_coordinates(h_c_girder_test, t_bp_test, t_bf_test,
h_core_test, t_tf_test)
cog_test = center_of_gravity_z(E_bp_test, a_bp_test,
                               E_c_girder_test, a_c_girder_test, n_o_g_test,
                               E_bf_test, a_bf_test,
                               E_core_test, a_core_test,
                               E_tf_test, a_tf_test,
                               z_coordinates_test)
```

The results are:

- The areas are: 18000.00 mm^2 for the bottom plate, 4300.00 mm^2 for the girder, 9000.00 mm^2 for the bottom face, 36000.00 mm^2 for the core, and 9000.00 mm^2 for the top face.
- The z-coordinates of the elements are: {'bp': 5.0, 'c_girder': 135.0, 'bf': 262.5, 'core': 275.0, 'tf': 287.5}
- Test result for z-coordinate of the center of gravity of the cross-section: 135.71 mm

Below is the hand calculation. The final result of the hand calculation is identical to the value obtained from the Python code, confirming the correctness of the function.

$$z_{cg} = \frac{\sum_{elements} E_{1,element} * A_{element} * z_{element}}{\sum_{elements} E_{1,element} * A_{element}}$$

$$z_{cg} = (E_{1,bp} * A_{bp} * z_{bp} + E_{1,c,gir} * A_{c,gir} * z_{c,gir} * n_o_g + E_{1,bf} * A_{bf} * z_{bf} + E_{1,core} * A_{core} * z_{core} + E_{1,tf} * A_{tf} * z_{tf}) / (E_{1,bp} * A_{bp} + E_{1,c,gir} * A_{c,gir} * n_o_g + E_{1,bf} * A_{bf} + E_{1,core} * A_{core} + E_{1,tf} * A_{tf})$$

$$z_{cg} = (17000 * 18000 * 5 + 14000 * 4300 * 135 * 4 + 16000 * 9000 * 262.5 + 10 * 36000 * 275 + 16000 * 9000 * 287.5) / (17000 * 18000 + 14000 * 4300 * 4 + 16000 * 9000 + 10 * 36000 + 16000 * 9000)$$

$$z_{cg} \approx 135.707$$

Location C-shaped girders

The y_coordinates function determines the y-coordinates of the centroids of the C-shaped girders in the cross-section. It ensures that the girders are evenly spaced across the width and that the flanges of the middle two girders do not overlap. The function takes as input the width of the cross-section, the height, width and thickness of a C-shaped girder and the number of girders. First, the function ensures that the number of girders is even, to avoid having a single middle girder. The areas of the web and flanges are calculated for centroid determination:

$$A_w = t_w * (h_{c-girder} - 2 * t_f)$$

$$A_f = w_{c-girder} * \ t_f$$

The function then calls center_of_gravity_y_c_girder to calculate the distance from the outer edge to the centroid of the web, which is used to determine the spacing between the centres of gravity of the girders:

$$spacing = \frac{w - 2 * y_{cog,c-girder}}{number\ of\ girders\ - 1}$$

A for-loop iterates over the number of girders. For each girder:

- The global y-coordinate of the centroid is calculated as: $y_{loc} = z_{cog,c-girder} + i \cdot$ spacing
- The orientation of the web of the girder is determined:
    - left if the girder is on the left side of the cross-section
    - right if the girder is on the right side

The y-coordinates and orientations of all girders are stored in separate lists. Finally, the function checks whether the flanges of the middle two girders overlap. If they do, a warning is printed. The function returns the list of y-coordinates and the corresponding orientations of the girders.

Validation of the function

To test the function, test values are entered into the function and afterwards a hand calculation is performed to evaluate the results. The following code lines are entered in a Python code cell:

```
w_test = 1800 # [mm]
h_c_girder_test = 250 # [mm]
w_c_girder_test = 100 # [mm]
t_c_girder_test = 10 # [mm]
n_o_g_test = 4

y_coord_test = y_coordinates(w_test, h_c_girder_test, w_c_girder_test,
t_c_girder_test, n_o_g_test)
```

Test results for y-coordinates of the centres of gravity and orientations of the C-girders:

- Girder 1: y-coordinate of the centre of gravity = 25.93 mm, orientation = left
- Girder 2: y-coordinate of the centre of gravity = 608.64 mm, orientation = left
- Girder 3: y-coordinate of the centre of gravity = 1191.36 mm, orientation = right
- Girder 4: y-coordinate of the centre of gravity = 1774.07 mm, orientation = right

To verify the placement of the first girder, the y-coordinate of the center of gravity relative to the side of a left-oriented C-girder is calculated:

```
area_flange_test = t_girder_test * w_girder_test
area_web_test = t_girder_test * (h_girder_test - 2*t_girder_test)
y_cog_girder_test, y_flange_test, y_web_test =
center_of_gravity_y_c_girder(w_girder_test, t_girder_test, area_flange_test,
area_web_test, 'left')
```

The calculated y-coordinate of the centre of gravity relative to the side of the C-girder is 25.93 mm, which matches the y-coordinate obtained from the y_coordinates function. This confirms that the first girder is correctly positioned, with its left side aligned with the edge of the full cross-section.

Similarly, the distance of the fourth girder from the right side of the cross-section is: $1800 - 1774.07 = 25.93\ mm$. This confirms that the fourth girder is also correctly positioned.

The spacing between the girders is:

- The distance between the first and second girder is: $608.64 - 25.93 = 582.71$
- The distance between the second and third girder is: $1191.36 - 608.64 = 582.72$
- The distance between the third and fourth girder is: $1774.07 - 1191.36 = 582.71$

The slight difference between the spacing of the second and third girders is likely due to rounding. Since the spacing is almost identical across all girders, it can be concluded that the y_coordinates function works correctly.

EI_{zz} of total cross-section

The EI_zz_total_cross_section calculates the bending stiffness about the z-axis of the total cross-section, the EI_{zz}. The function takes as input the width of the cross-section, the laminate properties of the bottom plate, the laminate properties of the C-girder, the number of C-girders, the height and width of the C-girder, the laminate properties of the bottom face, the height and elastic modulus of the core material and the laminate properties of the top face. First, the function raised an error if the number of girders is uneven, since a symmetric layout is assumed. Then, the function determines the areas and moments of inertia of all the elements. The area_plate_core and I_zz_plata_core functions are used for the bottom plate, the bottom face, the core, and the top face. The area_c_girders and I_zz_c_girders functions are used for the C-girders. After the z-coordinates of the elements are determined using the z_coordinates function and the z-coordinate of the centre of gravity of the cross-section (z_{cg}) is determined using the center_of_gravity_z function. At last, the EI_{zz} is calculated using the parallel axis theorem:

$$EI_{zz} = \sum_{elements} E_{1,element} * (I_{zz,element} + A_{element} * (z_{cg} - z_{element})^2$$

The function returns the value of EI_{zz}

EI_{yy} of total cross-section

The EI_yy_total_cross_section determines the bending stiffness about the y-axis of the total cross-section, the EI_{yy}. The function takes the same input as EI_zz_total_cross_section. It first raises an error if the number of C-girders is uneven. Then, the function determines the area of the C-girders and moments of inertia of the bottom plate, the bottom face, the core, and the top face. The I_yy_plata_core function is used for the bottom plate, the bottom face, the core, and the top face. The area_c_girders function is used for the C-girders. Then the y-coordinates of the centres of gravity of the C-girders and their orientations are determined using the y_coordinates function and

the coordinate of the centre of gravity of the cross-section is calculated with: $y_{cg} = \frac{w}{2}$, since the cross-section is symmetric. The EI_{zz} is calculated with:

$$EI_{yy} = \sum_{elements} E_{1,element} * (I_{yy,element} + A_{element} * (y_{cg} - y_{element})^2$$

The $y_{element}$ of the bottom plate, the bottom face, the core, and the top face is the same as y_{cg} and for the C-girders the value changes. First, the contribution of the bottom plate, the bottom face, the core, and the top face are summed. After, with a for-loop over the number of girders are the contributions of the C-girders added. In the for loop are also the values for the moments of inertia of the C-girder determined with the I_yy_c_girders function. The function returns the value of EI_{yy}.

EA of total cross-section

The EA_total_cross_section function determines the axial stiffness of total cross-section, the EA. The function takes the same input as EI_zz_total_cross_section. It first determines the areas of the elements in the cross-section. The area_plata_core function is used for the bottom plate, the bottom face, the core, and the top face. The area_c_girders function is used for the C-girders. Then the EA is calculated with:

$$EA = \sum_{elements} E_{1,element} * A_{element}$$

The function returns the value of EA.

GI_w of total cross-section

The GI_w_total_cross_section determines the torsional stiffness of the total cross-section. The function takes almost the same input as EI_zz_total_cross_section, it just takes G_core instead of E_core. It calculates the torsional stiffness with Bredt's second formula:

$$GI_t = \frac{4A^2}{\sum_i \frac{s_i}{G_i h_i}}$$

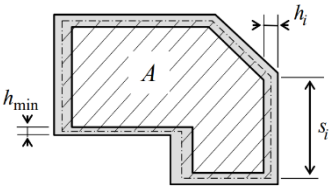

Figure 153: Box girder example (Hoogenboom, 2023)

The formula is for closed thin wall beams that have just one cell, see Figure 153. (Hoogenboom, 2023)

For the cross-section in Figure 154 will the torsional stiffness be determined. The middle C-shaped girders are left out since they do not contribute much to the torsional stiffness and otherwise Bredt's second formula cannot be used.

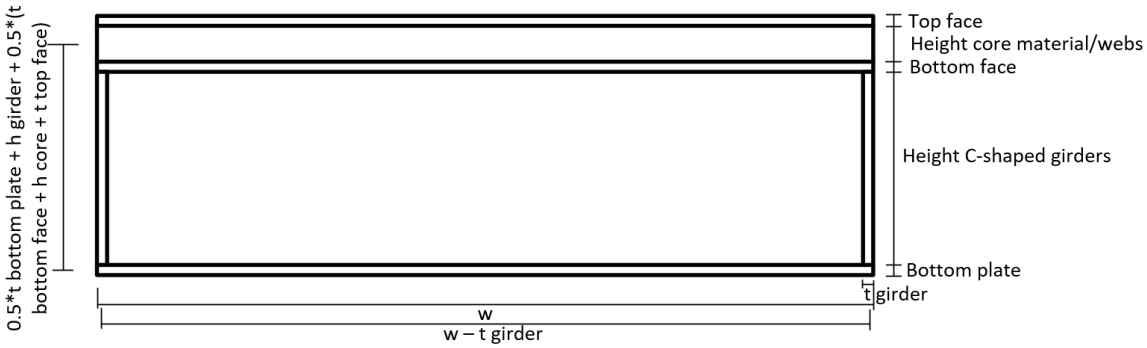

Figure 154: Representative cross-section for torsional stiffness

The torsional stiffness of the cross-section will be:

$$GI_t = \frac{4A^2}{\sum_i \frac{s_i}{G_i h_i}}$$

With:

$$\sum_i \frac{s_i}{G_i h_i} = \frac{w - t_{girder}}{G_{bp} * t_{bp}} + 2 * \frac{0.5 * t_{bp} + h_{girder} + 0.5(t_{bf} + h_{core} + t_{tf})}{G_{girder} * t_{girder}} + \frac{w - t_{girder}}{G_{bf} * t_{bf} + G_{core} * h_{core} + G_{tf} * t_{tf}}$$

$$A = (w - t_{girder}) * (0.5 * t_{bp} + h_{girder} + 0.5(t_{bf} + h_{core} + t_{tf}))$$

The function returns the value of GI_t.

Final function for the stiffness of the total cross-section

The EI_zz_yy_EA_GI_w_total_cross_section function calculates the EI_{zz}, EI_{yy}, EA and GI_t of total cross-section. The function takes the same inputs as the individual stiffness functions. The function calculates the EI_{zz}, EI_{yy}, EA and GI_t with the functions: EI_zz_total_cross_section, EI_yy_total_cross_section, EA _total_cross_section and GI_w_total_cross_section. The function returns the values of EI_{zz}, EI_{yy}, EA and GI_t.

Validation of the function

The functions: EI_zz_total_cross_section, EI_yy_total_cross_section, EA _total_cross_section and GI_w_total_cross_section are also validated when the EI_zz_yy_EA_GI_w_total_cross_section function is validated. The function will be evaluated by filling in test values in the function such that every element has the same elastic modulus and performing hand calculations. The hand calculations determine the stiffnesses of a rectangular cross-section with the same width and height as the total cross-section, as well as the stiffnesses of a cross-section without the C-shaped girders. The results obtained from the Python code are then compared with the hand calculations. The values of EI_{zz}, EI_{yy}, EA and GI_t of a rectangular cross-section should be bigger as the results from the code and the values for a cross-section without the C-shaped girders should be lower as the results from the code. The following code lines are entered in a Python code cell:

```
w = 1800 # [mm]
half_layer_structure_bp = [0, 90, 0, 0, 0, +45, -45, 0, 90, 0, 0, 0, +45, -45,
0] # direction lamella
half_thickness_structure_bp = [0.4667] * len(half_layer_structure_bp) #
thickness lamella [mm]
half_material_name_bp = ['flax_fibre_UP-Bio_Composite'] *
len(half_layer_structure_bp) # material lamella
full_layer_structure_bp, full_thickness_structure_bp, full_material_name_bp =
sym_laminate(half_layer_structure_bp, half_thickness_structure_bp,
half_material_name_bp)
stiffness_list_bp = laminate_stiffness(full_layer_structure_bp,
full_thickness_structure_bp, full_material_name_bp)
bottom_plate_laminate = laminate_properties(stiffness_list_bp,
full_thickness_structure_bp)

n_o_g = 2 # Number of girders
h_girder = 250 # [mm]
```

```
w_girder = 100 # [mm]
half_layer_structure_girder = [0, 90, 0, 0, 0, +45, -45, 0, 90, 0, 0, 0, +45,
-45, 0] # direction lamella
half_thickness_structure_girder = [0.4667] * len(half_layer_structure_girder)
# thickness lamella [mm]
half_material_name_girder = ['flax_fibre_UP-Bio_Composite'] *
len(half_layer_structure_girder) # material lamella
full_layer_structure_girder, full_thickness_structure_girder,
full_material_name_girder = sym_laminate(half_layer_structure_girder,
half_thickness_structure_girder, half_material_name_girder)
stiffness_list_girder = laminate_stiffness(full_layer_structure_girder,
full_thickness_structure_girder, full_material_name_girder)
girder_laminate = laminate_properties(stiffness_list_girder,
full_thickness_structure_girder)

half_layer_structure_bf = [0, 90, 0, 0, 0, +45, -45, 0, 90, 0, 0, 0, +45, -45,
0] # direction lamella
half_thickness_structure_bf = [0.4667] * len(half_layer_structure_bf) #
thickness lamella [mm]
half_material_name_bf = ['flax_fibre_UP-Bio_Composite'] *
len(half_layer_structure_bf) # material lamella
full_layer_structure_bf, full_thickness_structure_bf, full_material_name_bf =
sym_laminate(half_layer_structure_bf, half_thickness_structure_bf,
half_material_name_bf)
stiffness_list_bf = laminate_stiffness(full_layer_structure_bf,
full_thickness_structure_bf, full_material_name_bf)
bottom_face_laminate = laminate_properties(stiffness_list_bf,
full_thickness_structure_bf)

h_core = 50 # [mm]
E_core = 14384 # [MPa] (This is the same stiffness as the stiffness from the
composite)
G_core = 2264.65 # MPA (This is the same stiffness as the stiffness from the
composite)

half_layer_structure_tf = [0, 90, 0, 0, 0, +45, -45, 0, 90, 0, 0, 0, +45, -45,
0] # direction lamella
half_thickness_structure_tf = [0.4667] * len(half_layer_structure_tf) #
thickness lamella [mm]
half_material_name_tf = ['flax_fibre_UP-Bio_Composite'] *
len(half_layer_structure_tf) # material lamella
full_layer_structure_tf, full_thickness_structure_tf, full_material_name_tf =
sym_laminate(half_layer_structure_tf, half_thickness_structure_tf,
half_material_name_tf)
stiffness_list_tf = laminate_stiffness(full_layer_structure_tf,
full_thickness_structure_tf, full_material_name_tf)
top_face_laminate = laminate_properties(stiffness_list_tf,
full_thickness_structure_tf)
```

```
EI_zz, EI_yy, EA, GI_w = EI_zz_yy_EA_GI_w_total_cross_section(w,
bottom_plate_laminate, girder_laminate, n_o_g, h_girder, w_girder,
bottom_face_laminate, h_core, E_core,  G_core, top_face_laminate)
```

The obtained results from the code are:

The EI_{zz} is equal to 3.169e+13 $[N\ mm^2]$
The EI_{yy} is equal to 7.727e+14 $[N\ mm^2]$
The EA is equal to 2.552e+09 [N]
The GI_t is equal to 1.314e+13 $[N\ mm^2]$

The cross-section is shown in Figure 155. The total height of the cross-section is $14.00 + 250.00 + 14.00 + 50.00 + 14.00 = 342.00\ \ mm$. The rectangular cross-section will have a width of 1800 mm, a height of 342 mm, an elastic modulus of 14384 N/mm^2 and a shear modulus of 2264.65 N/mm^2. The ratio $\frac{b}{h} = \frac{1800}{342} = 5.2$ this is approximately 5, so from table 1 of (Hoogenboom, 2023) gives $\frac{I_t}{bh^3} = 0.292$.

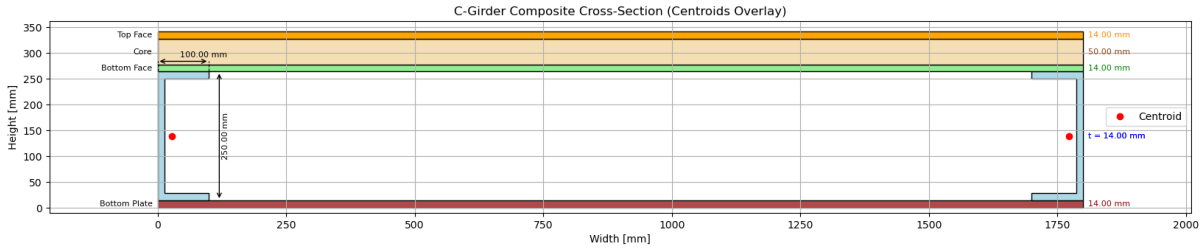

Figure 155: Test cross-section

The rectangular cross-section has the following stiffnesses:

$$EI_{zz} = E * \frac{1}{12} * w * h^3 = 14384 * \frac{1}{12} * 1800 * 342^3 = 8.63 * 10^{13}\ [N\ mm^2]$$

$$EI_{yy} = E * \frac{1}{12} * h * w^3 = 14384 * \frac{1}{12} * 342 * 1800^3 = 2.39 * 10^{15}\ [N\ mm^2]$$

$$EA = E * w * h = 14384 * 1800 * 342 = 8.85 * 10^{9}\ [N]$$

$$GI_t = G * 0.292 * b * h^3 = 2264.65 * 0.292 * 1800 * 342^3 = 4.76 * 10^{13} [N\ mm^2]$$

The stiffnesses will also be determined for the cross-section shown in Figure 156. The centre of gravity of the cross-section is:

$$z_{cg} = \frac{\sum_{elements} A_{element} * z_{element}}{\sum_{elements} A_{element}}$$

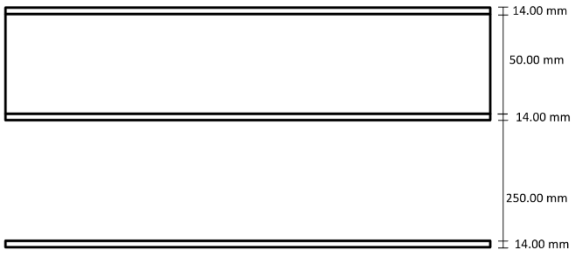

Figure 156: Cross-section without C-girders

$$z_{cg} = \frac{14 * 1800 * 7 + 14 * 1800 * 271 + 50 * 1800 * 303 + 14 * 1800 * 335}{14 * 1800 + 14 * 1800 + 50 * 1800 + 14 * 1800} = 257.957\ [mm]$$

The EI_{zz} of the cross-section is:

$$EI_{zz} = \sum_{elements} E * (I_{zz,element} + A_{element} * (z_{cg} - z_{element})^2$$

$$EI_{zz} = 14384 * (\frac{1}{12} * 1800 * 14^3 + (1800 * 14) * (257.957 - 7)^2 + \frac{1}{12} * 1800 * 14^3 + (1800 * 14) * (257.957 - 271)^2 + \frac{1}{12} * 1800 * 50^3 + (1800 * 50) * (257.957 - 303)^2 + \frac{1}{12} * 1800 * 14^3 + (1800 * 14) * (257.957 - 335)^2)$$

$$EI_{zz} = 2.793 * 10^{13}\ [N\ mm^2]$$

The EI_{yy} of the cross-section is:

$$EI_{yy} = E * \sum_{elements} I_{yy,element}$$

$$EI_{yy} = 14384 * (\frac{1}{12} * 14 * 1800^3 + \frac{1}{12} * 14 * 1800^3 + \frac{1}{12} * 50 * 1800^3 + \frac{1}{12} * 14 * 1800^3)$$

$$EI_{yy} = 6.428 * 10^{14}\ [N\ mm^2]$$

The EA of the cross-section is:

$$EA = E * \sum_{elements} A_{element}$$

$$EA = 14384 * (1800 * 14 + 1800 * 14 + 1800 * 50 + 1800 * 14)$$

$$EA = 2.38 * 10^9\ [N]$$

The values for EI_{zz}, EI_{yy} and EA obtained from the python code fall between the values calculated for a rectangular cross-section with the same width and height of the total cross-section and for a cross-section without the C-shaped girders, as expected. Specifically:

- The code values are smaller than those of the full rectangular cross-section
- The code values are larger than those of the cross-section without C-girders

The value for GI_t obtained from the python code is smaller as the value obtained from the hand calculation as expected.

This confirms that the functions EI_zz_total_cross_section, EI_yy_total_cross_section, EA_total_cross_section, and EI_zz_yy_EA_total_cross_section are working correctly.

Appendix H: Python code for the input for a beam model in RFEM

The code for the input for a beam model is provided below. An explanation and validation of the code are provided in Appendix I.

```
#----------------------------
# Input RFEM for a beam model
#----------------------------
def beam_model_input_RFEM(w, EI_yy, EI_zz, EA, GI_w, laminate, V_f, rho_f,
rho_r, total_area, rho_core, h_core, h_cross_section):
    E = EA / total_area
    nu_12 = laminate['nu_12']
    G = E/(2*(1+nu_12))
    rho_com = V_f/100 * rho_f + (1 - V_f/100) * rho_r
    area_core = area_plate_core(w, h_core)
    percentage_core = area_core / total_area * 100
    percentage_composite = 100 - percentage_core
    rho_total = percentage_composite / 100 * rho_com + percentage_core / 100 *
rho_core
    gamma_total = rho_total * 10 / 1000 # Convert from kg/m^3 to kN/m^3
    A = total_area/100 # Convert from mm^2 to cm^2
    A_y = A_z = total_area/100 # Convert from mm^2 to cm^2 for shear area
approximation
    I_zz = EI_zz / E / 1e4 # Convert from mm^4 to cm^4
    I_yy = EI_yy / E / 1e4 # Convert from mm^4 to cm^4
    I_t = GI_w / G / 1e4 # Convert from mm^4 to cm^4
    b = w
    h = h_cross_section
    print(f"Material properties for RFEM input:")
    print(f"Young's modulus (E): {E:.2f} [MPa]")
    print(f"Shear modulus (G): {G:.2f} [MPa]")
    print(f"Poisson's ratio (nu_12): {nu_12:.6f}")
    print(f"Total density of the cross-section (rho_total): {rho_total:.2f}
[kg/m^3]")
    print(f"Weight of the cross-section (gamma_total): {gamma_total:.4f}
[kN/m^3]")
    print(f"Total area of the cross-section (A): {A:.4f} [cm^2]")
    print(f"A_y (shear area approximation): {A_y:.4f} [cm^2]")
    print(f"A_z (shear area approximation): {A_z:.4f} [cm^2]")
    print(f"Torsional constant (I_t): {I_t:.2f} [cm^4]")
    print(f"Moment of inertia about y-axis (I_zz) (I_y): {I_zz:.2f} [cm^4]")
    print(f"Moment of inertia about z-axis (I_yy) (I_z): {I_yy:.2f} [cm^4]")
    print(f"Width b: {b:.2f} [mm]")
    print(f"Height h: {h:.4f} [mm]")
```

Appendix I: Explanation and validation of the input for a beam model in RFEM code

The code for the input for a beam model in RFEM is provided in Appendix H. In RFEM, it is not possible to directly input the stiffness parameters EI_{zz}, EI_{yy}, GI_w and EA as calculated above. Instead, RFEM requires material and cross-sectional properties such as E, G, ν and geometric properties as input for a beam element. The input fields for a beam in RFEM are shown in Figure 157 and Figure 158. The beam_model_input_RFEM function takes as input w, EI_yy, EI_zz, EA, GI_w, laminate, V_f, rho_f, rho_r, total_area, rho_core, h_core, h_cross_section. The variable laminate contains the laminate properties of the bottom plate, bottom face, or top face, as determined using the laminate_properties function. The total area is calculated with the area_total_cross_section function which takes as input: w, bottom_plate_laminate, girder_laminate, n_o_g, h_girder, w_girder, bottom_face_laminate, h_core and top_face_laminate, where n_o_g is the number of girders. This function computes the areas of the individual components with the functions for the areas of the different components and sums the areas:

$$A_{total\ cross-section} = A_{bp} + n.o.g * A_{girder} + A_{bf} + A_{core} + A_{tf}$$

The height of the cross-section is calculated with the height_total_cross_section function which takes as input: bottom_plate_laminate, h_girder, bottom_face_laminate, h_core, and top_face_laminate. The function calculates the height with the equation:

$$h_{total\ cross-section} = t_{bp} + h_{girder} + t_{bf} + h_{core} + t_{tf}$$

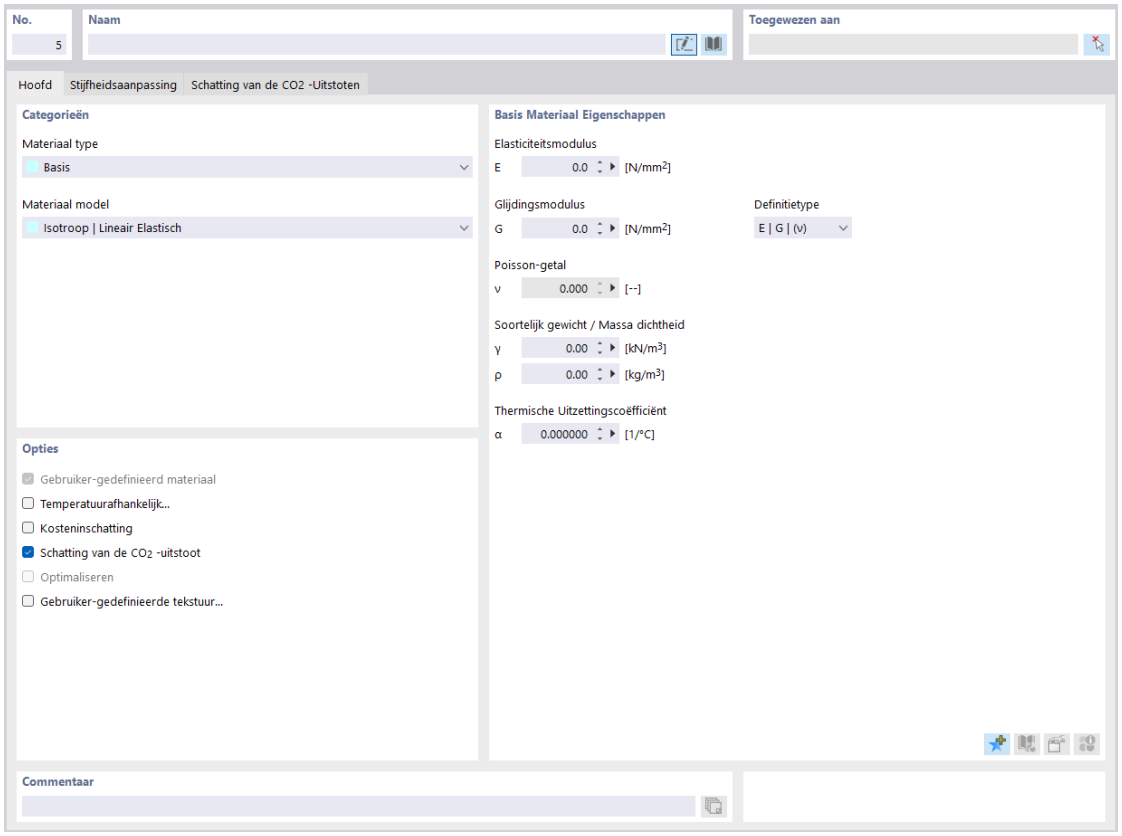

Figure 157: Input field material properties

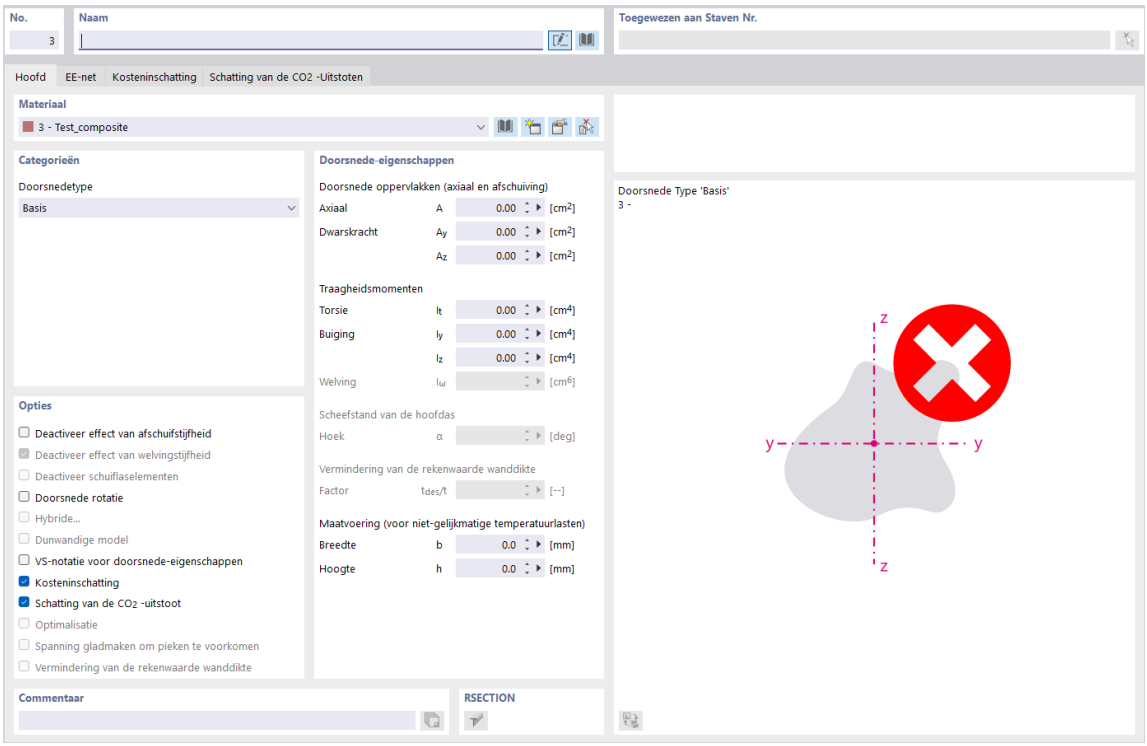

Figure 158: Input field cross-sectional properties

Material properties

The elastic modulus is determined from:

$$E = \frac{EA}{A_{total\ cross-section}}$$

In RFEM, the material properties must satisfy:

$$G = \frac{E}{2 * (1 + \upsilon)}$$

The Poisson ratio is taken from either the bottom plate, bottom face or top face laminate and the shear modulus is calculated using the relation above.

Density and specific weight

The specific weight and density of the material is used in RFEM to determine the self-weight of the structure. To determine the density of the representative materials of the cross-section, first the density of the composite will be determined with the equation:

$$\rho_{com} = V_f \rho_f + \left(100\% - V_f\right) * \rho_r$$

Next, the percentage core material in the cross-section is determined and the percentage of the composite material. Then the percentages are multiplied by the densities of the materials.

$$percentatge\ core\ material = \frac{A_{core}}{A_{total\ cross-section}} * 100\%$$

$$percentatge\ composite\ material = 100\% - \ percentatge\ core\ material$$

(The total cross-section is 100% so the percentage composite material can be calculated as above)

$$\rho_{total\ cross-section} = \frac{percentatge\ core}{100} * \rho_{core} + \frac{percentatge\ composite}{100} * \rho_{com}$$

The specific weight assuming a gravitational acceleration of 10 m/s² is:

$$\gamma_{total\ cross-section} = \rho_{total\ cross-section} * 10$$

Cross-sectional properties

For the RFEM input, the cross-sectional properties are defined as follows:

- **Cross-sectional area:** The total area A of the section is used for all three values A, A_y, and A_z. This simplification is acceptable because $A_y$and $A_z$are primarily used to calculate shear stresses, which are not the main focus of this model. The primary goal is to determine internal forces and deflection.
- **Torsional constant:** The torsional constant I_t is calculated from the section's torsional stiffness:

  $$I_t = \frac{GI_w}{G}$$
- **Moments of inertia:** The moments of inertia about the y- and z-axes are derived from the bending stiffnesses:

  $$I_y = \frac{EI_{zz}}{E}, I_z = \frac{EI_{yy}}{E}$$

  The moments of inertia are differently defined in RFEM as in the python script.
- **Section dimensions:** The width b and total height h of the cross-section are used directly as input.

Test of the RFEM input

To test the input for RFEM, a simply supported beam is modelled with a length of 20 meters and three load cases. The considered load cases are:

- a load case in the z-direction with a q-load of 5 kN/m
- a load case in the y-direction with a q-load of 5 kN/m
- a load case with the self-weight (automatically computed in RFEM)

The resulting deflections and bending moments from the RFEM model are compared with hand calculations.

The cross-section will have the following properties:

```
# Changeable parameters
w = 1800 # [mm]
V_f = 50 # [%]
rho_f = 1500 # [kg/m^3]
rho_r = 1200 # [kg/m^3]
half_layer_structure_bp = [0, 90, 0, 0, 0, +45, -45, 0, 90, 0, 0, 0, +45, -45,
0] # direction lamella
half_thickness_structure_bp = [0.4667] * len(half_layer_structure_bp) #
thickness lamella [mm]
half_material_name_bp = ['flax_fibre_UP-Bio_Composite'] *
len(half_layer_structure_bp) # material lamella

# Calculation properties
full_layer_structure_bp, full_thickness_structure_bp, full_material_name_bp =
lm.sym_laminate(half_layer_structure_bp, half_thickness_structure_bp,
half_material_name_bp)
lm.requirement_direction(full_layer_structure_bp)
```

```
stiffness_list_bp = lm.laminate_stiffness(full_layer_structure_bp,
full_thickness_structure_bp, full_material_name_bp)

bottom_plate_laminate = lm.laminate_properties(stiffness_list_bp,
full_thickness_structure_bp)

lm.print_stiffness_overview(stiffness_list_bp)
lm.plot_laminate(full_layer_structure_bp, full_thickness_structure_bp,
full_material_name_bp)
# Changeable parameters
n_o_g = 6 # Number of girders
h_girder = 280 # [mm]
w_girder = 100 # [mm]
half_layer_structure_girder = [0, 90, +45, -45, 0, 90, +45, -45, 0, 90, +45, -
45] # direction lamella
half_thickness_structure_girder = [0.4667] * len(half_layer_structure_girder)
# thickness lamella [mm]
half_material_name_girder = ['flax_fibre_UP-Bio_Composite'] *
len(half_layer_structure_girder) # material lamella

# Calculation properties
full_layer_structure_girder, full_thickness_structure_girder,
full_material_name_girder = lm.sym_laminate(half_layer_structure_girder,
half_thickness_structure_girder, half_material_name_girder)
lm.requirement_direction(full_layer_structure_girder)
stiffness_list_girder = lm.laminate_stiffness(full_layer_structure_girder,
full_thickness_structure_girder, full_material_name_girder)

girder_laminate = lm.laminate_properties(stiffness_list_girder,
full_thickness_structure_girder)

lm.print_stiffness_overview(stiffness_list_girder)
lm.plot_laminate(full_layer_structure_girder, full_thickness_structure_girder,
full_material_name_girder)
# Changeable parameters
half_layer_structure_bf = [0, 90, 0, 0, 0, +45, -45, 0] # direction lamella
half_thickness_structure_bf = [0.4667] * len(half_layer_structure_bf) #
thickness lamella [mm]
half_material_name_bf = ['flax_fibre_UP-Bio_Composite'] *
len(half_layer_structure_bf) # material lamella

# Calculation properties
full_layer_structure_bf, full_thickness_structure_bf, full_material_name_bf =
lm.sym_laminate(half_layer_structure_bf, half_thickness_structure_bf,
half_material_name_bf)
lm.requirement_direction(full_layer_structure_bf)
stiffness_list_bf = lm.laminate_stiffness(full_layer_structure_bf,
full_thickness_structure_bf, full_material_name_bf)
```

```
bottom_face_laminate = lm.laminate_properties(stiffness_list_bf,
full_thickness_structure_bf)

lm.print_stiffness_overview(stiffness_list_bf)
lm.plot_laminate(full_layer_structure_bf, full_thickness_structure_bf,
full_material_name_bf)
# Changeable parameters
h_core = 50 # [mm]
E_core = 10 # [MPa]
G_core = 5 # [MPa]
rho_core = 50 # [kg/m^3]
# Changeable parameters
half_layer_structure_tf = [0, 90, 0, 0, 0, +45, -45, 0] # direction lamella
half_thickness_structure_tf = [0.4667] * len(half_layer_structure_tf) #
thickness lamella [mm]
half_material_name_tf = ['flax_fibre_UP-Bio_Composite'] *
len(half_layer_structure_tf) # material lamella

# Calculation properties
full_layer_structure_tf, full_thickness_structure_tf, full_material_name_tf =
lm.sym_laminate(half_layer_structure_tf, half_thickness_structure_tf,
half_material_name_tf)
lm.requirement_direction(full_layer_structure_tf)
stiffness_list_tf = lm.laminate_stiffness(full_layer_structure_tf,
full_thickness_structure_tf, full_material_name_tf)

top_face_laminate = lm.laminate_properties(stiffness_list_tf,
full_thickness_structure_tf)

lm.print_stiffness_overview(stiffness_list_tf)
lm.plot_laminate(full_layer_structure_tf, full_thickness_structure_tf,
full_material_name_tf)
```

The stiffness and geometric properties from the code are:

- $EI_{zz} = 2.268 * 10^{13}\ [N\ mm^2]$
- $EI_{yy} = 2.992 * 10^{14}\ [N\ mm^2]$
- $EA = \ 1.023 * 10^{9}\ [N]$
- $GI_{w} = \ 1.020 * 10^{13}\ [N\ mm^2]$
- Total cross-sectional area: $A = 1.728 * 10^{5}\ [mm^2]$
- Total height of the cross-section $h \ = \ 358.94\ [mm]$

Self-Weight

The load for self-weight can be determined by multiplying the different components of the cross-section by their corresponding density. The width of the cross-section is 1800 mm, the height of the girders is 280 mm, the width of the girders is 100 mm, the number of girders is 6 and the thicknesses of the plates, girders and core are:

- $t_{tf} = 7.467\ mm$
- $h_{core} = 50\ mm$
- $t_{bf} = 7.467\ mm$
- $t_{girder} = 11.201\ mm$
- $t_{bp} = 14.001\ mm$

The areas of the components of the cross-section are:

$$A_{tf} = w * t_{tf} = 1800 * 7.467 = \ 13440.96\ mm^2$$

$$A_{core} = w * h_{core} = 1800 * 50 = 90000\ mm^2$$

$$A_{bf} = w * t_{bf} = 1800 * 7.467 = 13440.96\ mm^2$$

$$A_{girder} = 2 * w_{girder} * t_{girder} + h_{girder} * t_{girder} = 2 * 100 * 11.201 + 280 * 11.201 = 5125.47\ mm^2$$

$$A_{bp} = w * t_{bp} = 1800 * 14.001 = 25201.8\ mm^2$$

The density of the core material is 50 kg/m^3. The density of the laminate can be calculated with:

$$\rho_{com} = V_f \rho_f + \left(100\% - V_f\right) * \rho_r$$

For the laminate is $\rho_f = 1500\ kg/m^3$, $V_f = 50\ \%$ and $\rho_r = 1200\ kg/m^3$. The density of the laminate is:

$$\rho_{com} = 0.50 * 1500 + 0.5 * 1200 = 1350\ kg/m^3$$

The weight of the cross-section in kg/m will be:

$$weight_{cs} = (A_{tf} + A_{bf} + n.o.g * A_{girder} + A_{bp}) * \rho_{com} + A_{core} * \rho_{core}$$

$$= (2 * 13440.96 + 6 * 5125.47 + 25201.8\ )/10^6 * 1350 + 90000/10^6 * 50 = 116.33\ kg/m$$

The q-load for self-weight will be:

$$q_{sw} = weight_{cs} * 10 = 116.33 * 10 = 1163.3\ N/m = \ 1.163\ kN/m$$

The total load in the z-direction due to self-weight is equal to:

$$q_{sw} * l = 1.163 * 20 = 23.26\ kN$$

Load case z-direction

The maximum bending moment of a simply supported beam with a q-load in z-direction is:

$$M_{max} = \frac{1}{8} q l^2 = \frac{1}{8} * 5 * 20^2 = 250\ kNm$$

The maximum deflection of a simply supported beam with a q-load in z-direction is:

$$w_{max} = \frac{5}{384} * \frac{q * l^4}{EI_{zz}} = \frac{5}{384} * \frac{5 * (20 * 10^3)^4}{2.268 * 10^{13}} = 459.3\ mm$$

Load case y-direction

The maximum bending moment of a simply supported beam with a q-load in y-direction is:

$$M_{max} = \frac{1}{8}ql^2 = \frac{1}{8} * 5 * 20^2 = 250\ kNm$$

The maximum deflection of a simply supported beam with a q-load in y-direction is:

$$w_{max} = \frac{5}{384} * \frac{q * l^4}{EI_{yy}} = \frac{5}{384} * \frac{5 * (20 * 10^3)^4}{2.992 * 10^{14}} = 34.8\ mm$$

Load case self-weight

The maximum bending moment of a simply supported beam with the load because of self-weight is:

$$M_{max} = \frac{1}{8}ql^2 = \frac{1}{8} * 1.163\ * 20^2 = 58.16\ kNm$$

The maximum deflection of a simply supported beam with the load because of self-weight is:

$$w_{max} = \frac{5}{384} * \frac{q * l^4}{EI_{zz}} = \frac{5}{384} * \frac{1.163\ * (20 * 10^3)^4}{2.268 * 10^{13}} = 106.86\ mm$$

RFEM model

Below are the input fields of the material and cross-sectional properties shown and the models for the load cases.

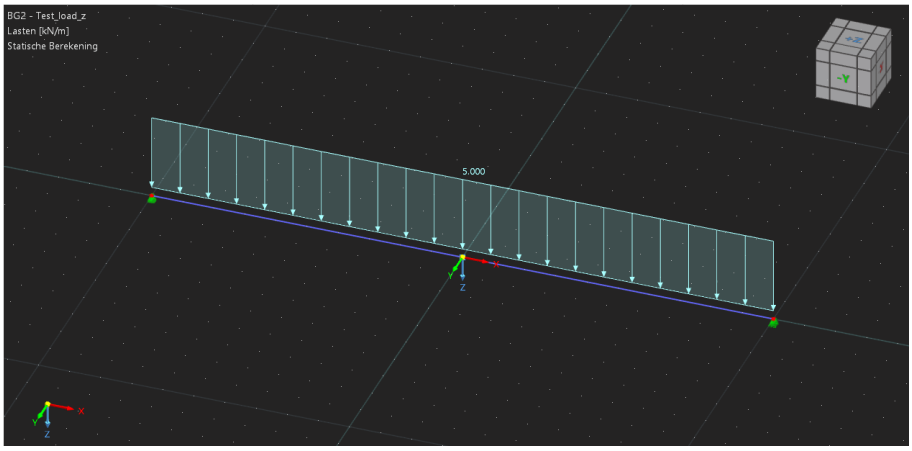

Figure 159: RFEM model load case z-direction

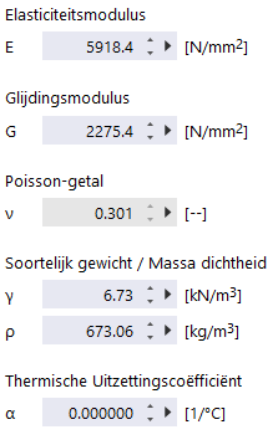

Figure 162: Input material properties



Figure 161: Input cross-sectional properties

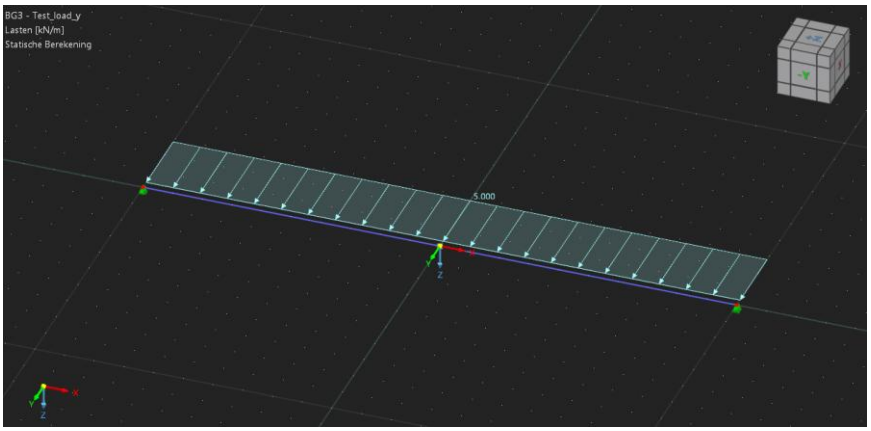

Figure 160: RFEM model load case y-direction

For the left support are the $u_x, u_y, u_z \; and \; \varphi_x$ fixed and for the right support are the $u_x, u_y \; and \; \varphi_x$ fixed. A mesh with a length of 0.500 meters is used.

The results from the model are shown in Figure 163, Figure 164, Figure 165, Figure 166, Figure 167 and Figure 168.

- z-direction load:
  - The maximum bending moment is: 250 kNm
  - The maximum deflection is: 459.9 mm
- y-direction load:
  - The maximum bending moment is: 250 kNm
  - The maximum deflection is: 35.4 mm
- Self-weight:
  - The maximum bending moment is: 58.16 kNm
  - The maximum deflection is: 107.0 mm

Reducing the mesh length by half does not lead to any change in the computed displacements.

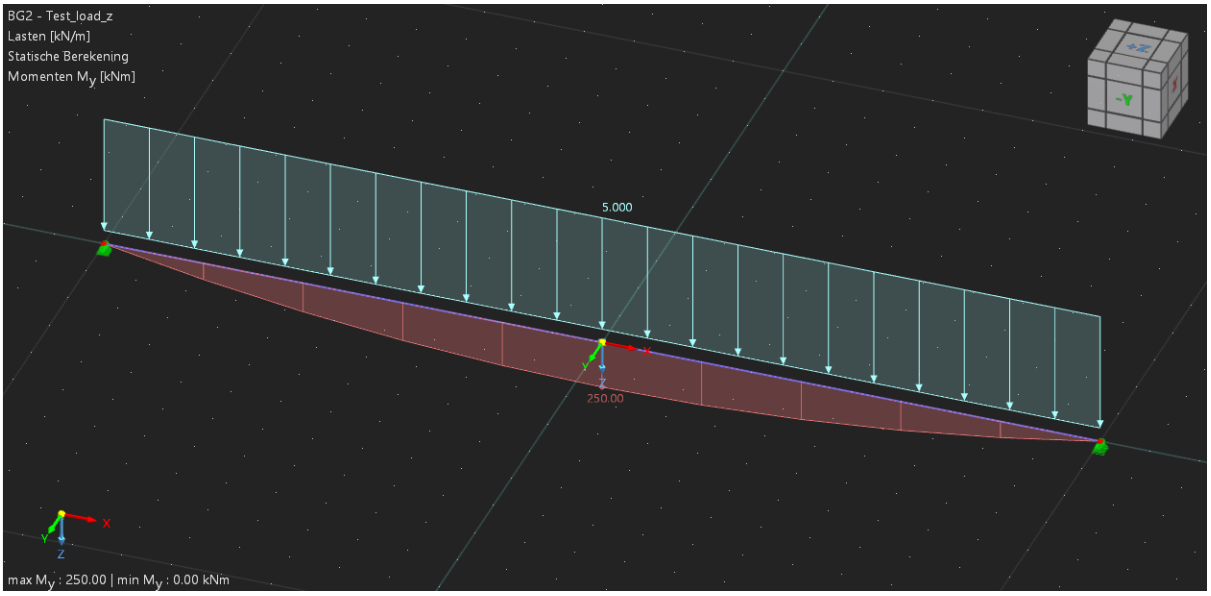

Figure 163: Bending moment line load case z-direction

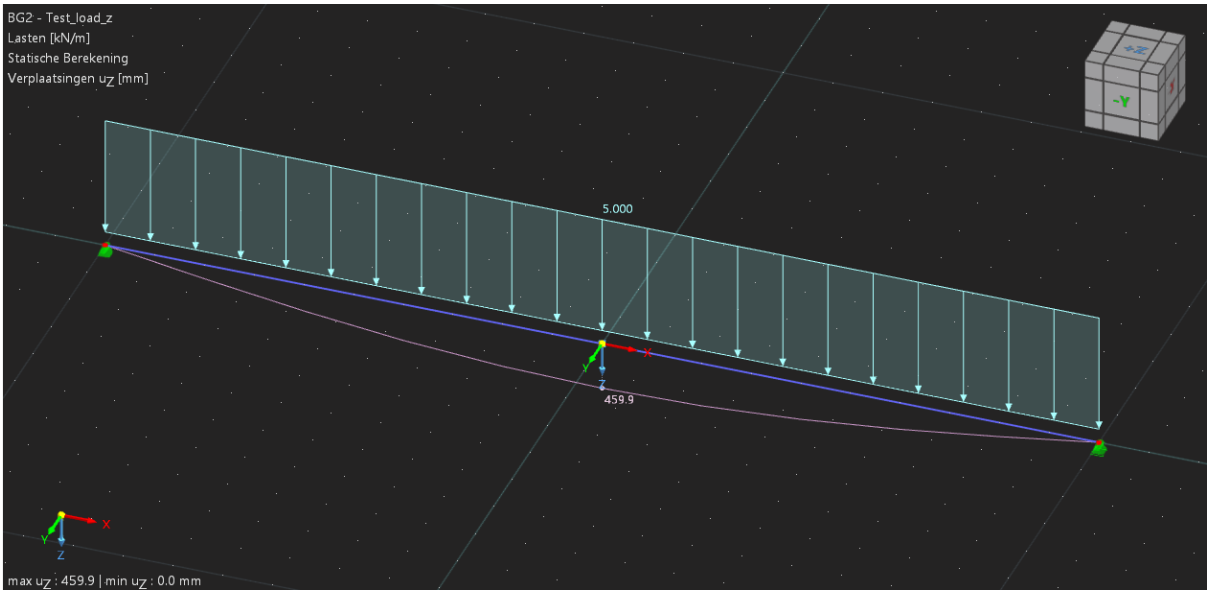

Figure 164: Deflection load case z-direction

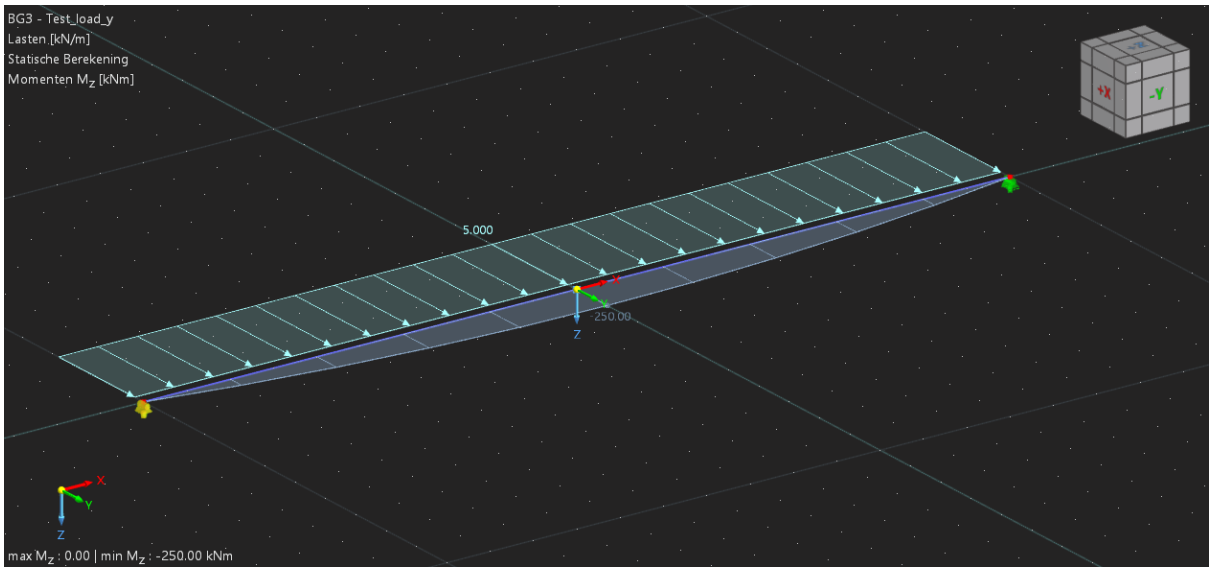

Figure 167: Bending moment line load case y-direction

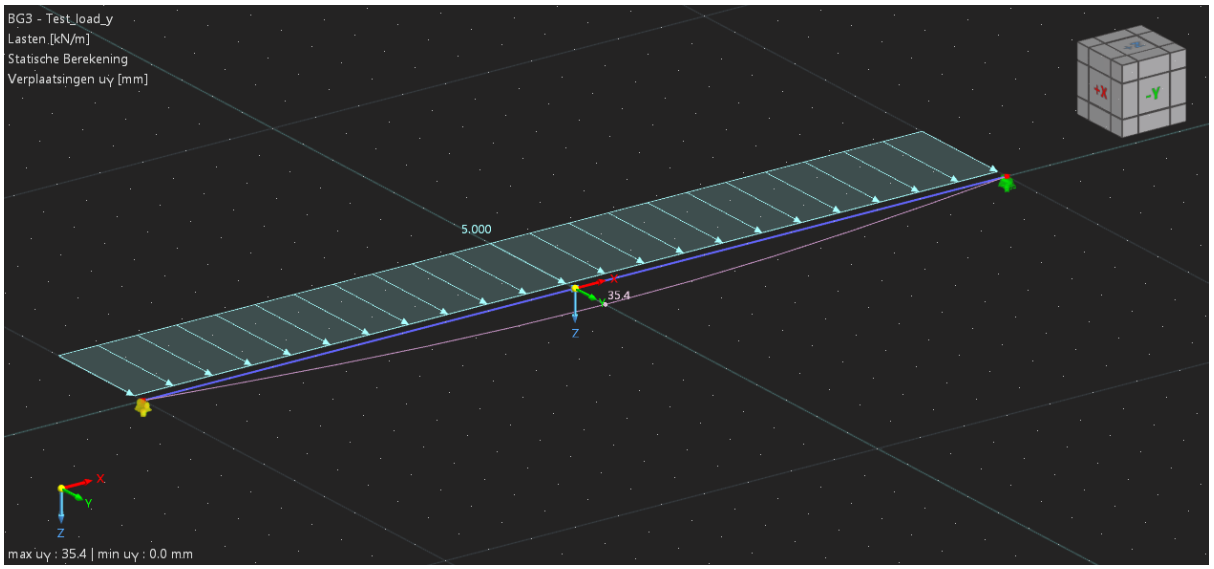

Figure 166: Deflection load case y-direction

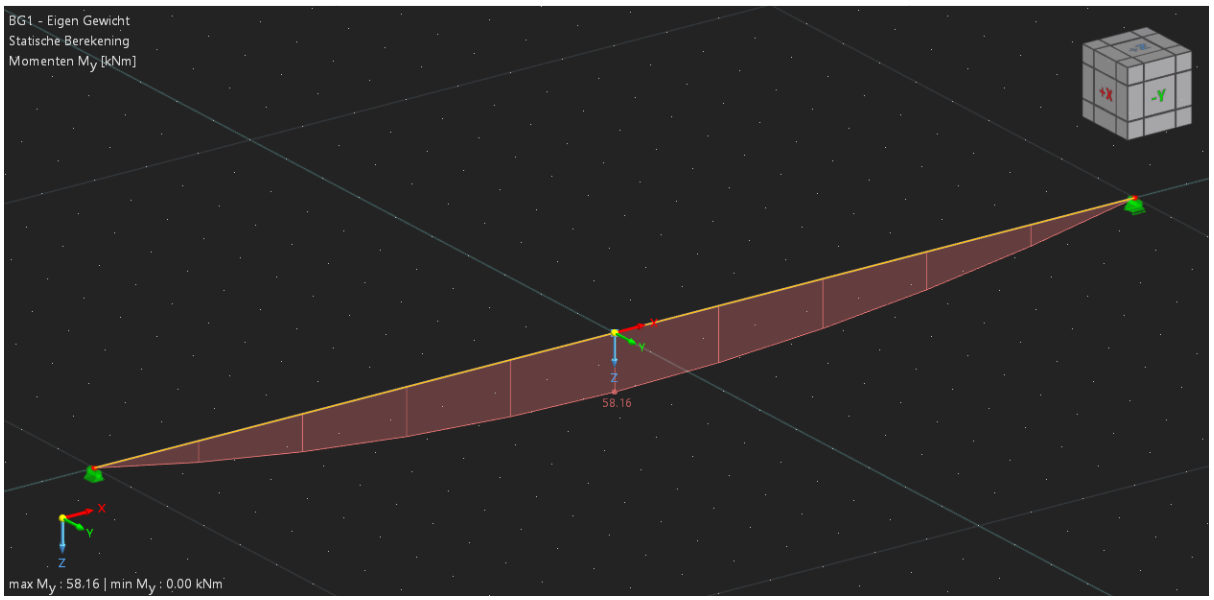

Figure 165: Bending moment line of self-weight

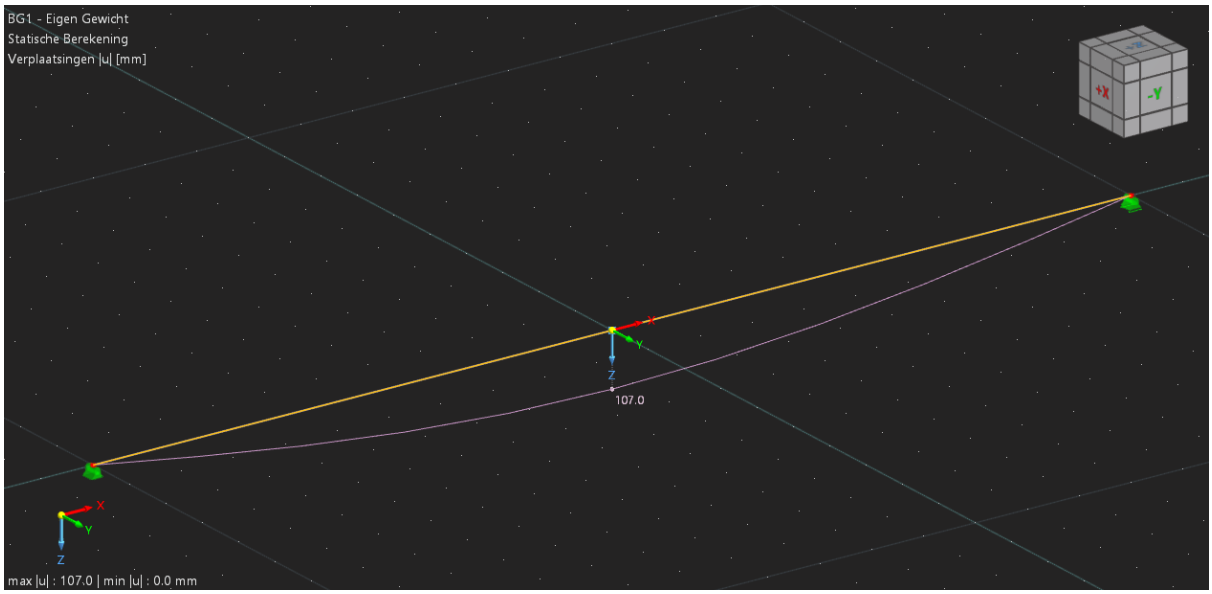

Figure 168: Deflection of self-weight

Conclusion

The maximum bending moment of the q-load in the z-direction from the model matches exactly with the hand calculation. The corresponding deflection from the model is slightly larger than the hand calculation, with a difference of 0.6 mm, which is 0.13% higher ($\frac{0.6}{459.3} * 100$) than the hand calculation. For the load case in the y-direction, the maximum bending moment from the model is also identical to the hand calculation. However, the deflection in the y-direction is slightly larger in the model, with a difference of 0.6 mm, which is 1.7% higher ($\frac{0.6}{34.8} * 100$) than the hand calculation. Overall, the RFEM model slightly overestimates deflections compared to hand calculations, which is conservative.

The maximum bending moment due to self-weight from the model is identical to the hand calculation. The total load in the z-direction due to self-weight is 23.27 kN, closely matching the hand calculation. The small difference of 0.01 kN is likely due to rounding. This accurate representation of self-weight confirms that the density input in RFEM is correct.

Appendix J: Python code for the input for a plate model in RFEM

The code for the input for a plate model in RFEM is provided below. An explanation and validation of the code are provided in Appendix K.

```
# cross_section_plate_model.py
import matplotlib.pyplot as plt
from matplotlib.patches import Rectangle, Polygon

# ------------------------------
# Plate/Core Functions
# ------------------------------
# Area of the cross-section of the plate and core
def area_plate_core(w_plate_core, t_plate_core):
    A = w_plate_core * t_plate_core
    return A

# ---------------------------------
# Center of gravity C-shaped girder
# ---------------------------------
# Center of gravity of the cross-section in the y-direction (the direction of
the width of the girder)
def center_of_gravity_y_c_girder(w_c_girder, tw, Af, Aw, orientation):
    if orientation == 'right':  # Assuming the web is on the right side, the
center of the web is at w_c_girder - tw/2
        z_w = w_c_girder - tw/2
    elif orientation == 'left': # Assuming the web is on the left side, the
center of the web is at tw/2
        z_w = tw/2
    else:
        raise ValueError("orientation must be 'left' or 'right'")

    z_f = w_c_girder/2  # Assuming the center of the flange is at the midpoint
of the width of the girder
    z_cog = (2*Af*z_f + Aw*z_w) / (2*Af + Aw)   # Center of gravity using the
formula: z_cog = (sum of (area * distance to reference axis)) / total area
    return z_cog, z_f, z_w

# ------------------------------------------------------------------------
# Center of gravity bottom plate and bottom horizontal part C-shaped girder
# ------------------------------------------------------------------------
def C_o_G_BD(bottom_plate_laminate, girder_laminate, a_bp, a_girder, n_o_g):
    z_bp = 1/2 * bottom_plate_laminate['t_laminate']
    z_girder = bottom_plate_laminate['t_laminate'] + 1/2 *
girder_laminate['t_laminate']
    z_cog = (bottom_plate_laminate['E_1'] * a_bp * z_bp +
girder_laminate['E_1'] * a_girder * z_girder * n_o_g) /
(bottom_plate_laminate['E_1'] * a_bp + girder_laminate['E_1'] * a_girder *
n_o_g)
```

```
    return z_cog, z_bp, z_girder

# ------------------------------------------------------------------------
# Center of gravity top deck and top horizontal part C-shaped girder
# ------------------------------------------------------------------------
def C_o_G_TD(girder_laminate, bottom_face_laminate, E_core, h_core,
top_face_laminate, a_girder, a_bf, a_core, a_tf, n_o_g):
    z_tf = 1/2 * top_face_laminate['t_laminate']
    z_core = top_face_laminate['t_laminate'] + 1/2 * h_core
    z_bf = top_face_laminate['t_laminate'] + h_core + 1/2 *
bottom_face_laminate['t_laminate']
    z_girder = top_face_laminate['t_laminate'] + h_core +
bottom_face_laminate['t_laminate'] + 1/2 * girder_laminate['t_laminate']
    z_tel = (top_face_laminate['E_1'] * a_tf * z_tf +
             E_core * a_core * z_core +
             bottom_face_laminate['E_1'] * a_bf * z_bf +
             girder_laminate['E_1'] * a_girder * z_girder * n_o_g)
    z_num = (top_face_laminate['E_1'] * a_tf +
             E_core * a_core +
             bottom_face_laminate['E_1'] * a_bf +
             girder_laminate['E_1'] * a_girder * n_o_g)
    z_cog = z_tel/z_num
    return z_cog, z_tf, z_core, z_bf, z_girder

# ------------------------------------------------
# Y-coordinates of the center of gravity girders
# ------------------------------------------------
# Y-coordinates of the center of gravity of the representative girders,
ensuring they are evenly spaced across the width of the cross-section
# and that the flanges of the middle two girders do not overlap
def rep_girder_loc(w, h_c_girder, w_c_girder, t_c_girder, n_o_g):
    if n_o_g % 2 != 0:  # Ensure the number of girders is even to avoid a
single middle girder
        raise ValueError("Number of girders must be even.")

    tw = tf = t_c_girder

    # Areas for centroid calculation
    Aw = tw * (h_c_girder - 2*tf)
    Af = w_c_girder * tf

    y_cog_dis,_,_ = center_of_gravity_y_c_girder(   # Calculate the distance
from the outer edge to the center of gravity of the web
                w_c_girder, tw, Af, Aw, 'left'
                )

    spacing = (w - 2 * y_cog_dis) / (n_o_g - 1) # Calculate the spacing
between the centers of gravity of the girders
```

```
    y_positions = []    # List to store the y-coordinates of the centers of
gravity of the girders
    orientations = []   # List to store the orientation of the girders (left
or right)
    y_positions_rep_girder = []

    for i in range(n_o_g):

        # Calculate the y-coordinate of the center of gravity of the current
girder
        y_loc_global = y_cog_dis + i * spacing

        # Determine orientation (opening inward)
        if y_loc_global < w/2:
            orientation = 'left'
            y_rep_girder_loc = y_loc_global - y_cog_dis + 1/2 * t_c_girder
        else:
            orientation = 'right'
            y_rep_girder_loc = y_loc_global + y_cog_dis - 1/2 * t_c_girder

        y_positions.append(y_loc_global)
        orientations.append(orientation)
        y_positions_rep_girder.append(y_rep_girder_loc)

    if y_positions[n_o_g//2-1] + y_cog_dis >= y_positions[n_o_g//2] +
y_cog_dis - w_c_girder:   # Check if the flanges of the middle two girders
overlap
        print('The flanges of the middle two girders overlap')

    return y_positions_rep_girder

# ------------------
# Density composite
# ------------------
def density_composite(V_f, rho_f, rho_r):
    rho_com = V_f/100 * rho_f + (100 - V_f)/100 * rho_r
    return rho_com

# ----------------------
# Input RFEM bottom deck
# ----------------------
def rep_t_E_1_prop_BD(bottom_plate_laminate, girder_laminate, w_girder, n_o_g,
w, V_f, rho_f, rho_r):
    t_rep_BD = bottom_plate_laminate['t_laminate']
    a_girder_hp = area_plate_core(w_girder, girder_laminate['t_laminate'])
    a_bp = area_plate_core(w, bottom_plate_laminate['t_laminate'])

    E_1_rep_BD = (bottom_plate_laminate['E_1'] *
bottom_plate_laminate['t_laminate'] +
```

```
                  (n_o_g * girder_laminate['E_1'] * a_girder_hp)/w * (1 -
bottom_plate_laminate['nu_12']*bottom_plate_laminate['nu_21'])) / t_rep_BD

    w_RFEM = w - girder_laminate["t_laminate"]

    rho_com = density_composite(V_f, rho_f, rho_r)
    rho_BD_RFEM = rho_com * (a_bp + n_o_g * a_girder_hp) / (t_rep_BD * w_RFEM)
    gamma_BD_RFEM = rho_BD_RFEM * 10 / 1000

    print('Input for RFEM plate model for bottom deck:')
    print(f'E_x = {E_1_rep_BD:.3f} [N/mm^2]')
    print(f'E_y = {bottom_plate_laminate['E_2']:.3f} [N/mm^2]')
    print(f'G_yz = {bottom_plate_laminate['G_12']:.3f} [N/mm^2]')
    print(f'G_xz = {bottom_plate_laminate['G_12']:.3f} [N/mm^2]')
    print(f'G_xy = {bottom_plate_laminate['G_12']:.3f} [N/mm^2]')
    print(f'nu_xy = {bottom_plate_laminate['nu_12']:.3f} [-]')
    print(f'Density of the bottom deck = {rho_BD_RFEM:.3f} [kg/m^3]')
    print(f'Weight of the bottom deck = {gamma_BD_RFEM:.3f} [kN/m^3]')
    print(f'Thickness = {t_rep_BD:.3f} [mm]')
    print(f'The width of the plate is {w} [mm]')
    print(f'The width of the plate from girder to girder is {w_RFEM:.3f}
[mm]')

# -------------------
# Input RFEM girders
# -------------------
def rep_girder_prop(top_face_laminate, bottom_face_laminate,
bottom_plate_laminate, girder_laminate, w, h_girder, w_girder, n_o_g, E_core,
h_core, h_cross_section, V_f, rho_f, rho_r):
    y_rep_girders = rep_girder_loc(w, h_girder, w_girder,
girder_laminate['t_laminate'], n_o_g)
    rep_h_girder = h_girder - 2 * girder_laminate['t_laminate']

    a_girder_hp = area_plate_core(w_girder, girder_laminate['t_laminate'])
    a_bp = area_plate_core(w, bottom_plate_laminate['t_laminate'])
    a_bf = area_plate_core(w, bottom_face_laminate['t_laminate'])
    a_core = area_plate_core(w, h_core)
    a_tf = area_plate_core(w, top_face_laminate['t_laminate'])

    z_cog_BD,_,_ = C_o_G_BD(bottom_plate_laminate, girder_laminate, a_bp,
a_girder_hp, n_o_g)
    z_cog_TD,_,_,_,_ = C_o_G_TD(girder_laminate, bottom_face_laminate, E_core,
h_core, top_face_laminate, a_girder_hp, a_bf, a_core, a_tf, n_o_g)
    rep_h_girder_RFEM = h_cross_section - z_cog_TD - z_cog_BD

    rho_com = density_composite(V_f, rho_f, rho_r)
    rep_rho_girder = rho_com * area_plate_core(rep_h_girder,
girder_laminate['t_laminate']) / area_plate_core(rep_h_girder_RFEM,
girder_laminate['t_laminate'])
    rep_gamma_girder = rep_rho_girder * 10 / 1000
```

```
    print('Input for RFEM plate model for girders is:')
    print(f'E_x = {girder_laminate['E_1']:.3f} [N/mm^2]')
    print(f'E_y = {girder_laminate['E_2']:.3f} [N/mm^2]')
    print(f'G_yz = {girder_laminate['G_12']:.3f} [N/mm^2]')
    print(f'G_xz = {girder_laminate['G_12']:.3f} [N/mm^2]')
    print(f'G_xy = {girder_laminate['G_12']:.3f} [N/mm^2]')
    print(f'nu_xy = {girder_laminate['nu_12']:.3f} [-]')
    print(f'Density of the bottom deck = {rep_rho_girder:.3f} [kg/m^3]')
    print(f'Weight of the bottom deck = {rep_gamma_girder:.3f} [kN/m^3]')
    print(f'Thickness = {girder_laminate['t_laminate']:.3f} [mm]')
    print(f'The representative height of the girders is
{rep_h_girder_RFEM:.3f}')
    print(f'The centre of gravity of the bottom deck is located at
{z_cog_BD:.3f} [mm] from the bottom of the cross-section')
    print(f'The centre of gravity of the top deck is located at {z_cog_TD:.3f}
[mm] from the top of the cross-section')
    print(f'The locations of the girders with respect to the left side of the
cross-section is:')
    for i in range(len(y_rep_girders)):
        print(f'Girder {i+1} is located at {y_rep_girders[i]:.3f} [mm]')
    print(f'The distance between the girders is:')
    for i in range(len(y_rep_girders)-1):
        print(f'Between girder {i+1} and girder {i+2} is {y_rep_girders[i+1] -
y_rep_girders[i]:.3f} [mm]')

# --------------------
# Input RFEM top deck
# --------------------
def rep_t_E_G_prop_TD(girder_laminate, w_girder, bottom_face_laminate,
top_face_laminate, E_core, G_core, h_core, w, n_o_g, V_f, rho_f, rho_r,
rho_core):
    nu_core = E_core/(2*G_core)-1
    t_rep_TD = bottom_face_laminate['t_laminate'] + h_core +
top_face_laminate['t_laminate']
    a_girder_hp = area_plate_core(w_girder, girder_laminate['t_laminate'])
    a_bf = area_plate_core(w, bottom_face_laminate['t_laminate'])
    a_core = area_plate_core(w, h_core)
    a_tf = area_plate_core(w, top_face_laminate['t_laminate'])

    E_1_rep_TD = (bottom_face_laminate['E_1'] *
bottom_face_laminate['t_laminate'] +
                (E_core * h_core)/(1 - nu_core**2) * (1 -
bottom_face_laminate['nu_12']*bottom_face_laminate['nu_21']) +
                (top_face_laminate['E_1'] *
top_face_laminate['t_laminate'])/(1 -
top_face_laminate['nu_12']*top_face_laminate['nu_21']) * (1 -
bottom_face_laminate['nu_12']*bottom_face_laminate['nu_21']) +
                (n_o_g * girder_laminate['E_1'] * a_girder_hp)/w * (1 -
bottom_face_laminate['nu_12']*bottom_face_laminate['nu_21'])) / t_rep_TD
```

```
    E_2_rep_TD = (bottom_face_laminate['E_2'] *
bottom_face_laminate['t_laminate'] +
                (E_core * h_core)/(1 - nu_core**2) * (1 -
bottom_face_laminate['nu_12']*bottom_face_laminate['nu_21']) +
                (top_face_laminate['E_2'] *
top_face_laminate['t_laminate'])/(1 -
top_face_laminate['nu_12']*top_face_laminate['nu_21']) * (1 -
bottom_face_laminate['nu_12']*bottom_face_laminate['nu_21'])
                )/ t_rep_TD

    G_rep = (bottom_face_laminate['G_12'] * bottom_face_laminate['t_laminate']
+
             G_core * h_core +
             top_face_laminate['G_12'] * top_face_laminate['t_laminate'])/
t_rep_TD

    w_RFEM = w - girder_laminate["t_laminate"]

    rho_com = density_composite(V_f, rho_f, rho_r)
    rho_com = density_composite(V_f, rho_f, rho_r)
    rho_TD_RFEM = (rho_com * (a_tf + a_bf + n_o_g * a_girder_hp) + rho_core *
a_core)/ (t_rep_TD * w_RFEM)
    gamma_TD_RFEM = rho_TD_RFEM * 10 / 1000

    print('Input for RFEM plate model for top deck:')
    print(f'E_x = {E_1_rep_TD:.3f} [N/mm^2]')
    print(f'E_y = {E_2_rep_TD:.3f} [N/mm^2]')
    print(f'G_yz = {G_rep:.3f} [N/mm^2]')
    print(f'G_xz = {G_rep:.3f} [N/mm^2]')
    print(f'G_xy = {G_rep:.3f} [N/mm^2]')
    print(f'nu_xy = {bottom_face_laminate['nu_12']:.3f} [-]')
    print(f'nu_yx = {bottom_face_laminate['nu_21']:.3f} [-]')
    print(f'Density of the bottom deck = {rho_TD_RFEM:.3f} [kg/m^3]')
    print(f'Weight of the bottom deck = {gamma_TD_RFEM:.3f} [kN/m^3]')
    print(f'Thickness = {t_rep_TD:.3f} [mm]')
    print(f'The width of the plate is {w} [mm]')
    print(f'The width of the plate from girder to girder is {w_RFEM:.3f}
[mm]')
```

Appendix K: Explanation and validation of the input for a plate model in RFEM code

For a plate model in RFEM, the cross-section is simplified by modelling three main components: a horizontal bottom deck, vertical girders, and a horizontal top deck (see Figure 169). This approach allows for an efficient representation of the structural behaviour while reducing modelling complexity. The bottom deck consists of the bottom plate combined with the lower horizontal flanges of the C-shaped girders. The vertical girders are modelled separately and retain the same material and stiffness properties as the original C-shaped girders. However, their height is adjusted to account for the distance between the centres of gravity of the bottom and the top deck. The top deck consists of multiple components: the top face, core material, bottom face, and the upper horizontal flanges of the C-shaped girders. A schematic overview of the distribution between the top and bottom decks is shown in Figure 170. Both the top and bottom decks are assigned a reduced width, defined as the distance between the centres of gravity of the outer vertical girders, so the plates. To determine the representative stiffness and thickness values for both the top and bottom decks, functions are implemented in Python. The Python script of the functions is provided in Appendix J.

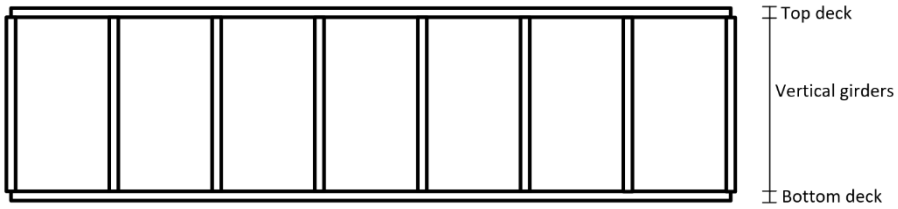

Figure 169: RFEM plate model layering

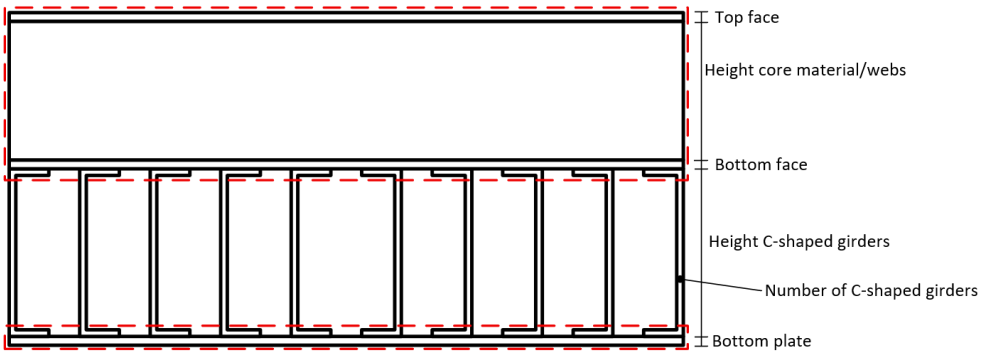

Figure 170: Distribution of top and bottom deck

Representative stiffness and thickness bottom deck

The bottom deck can be represented as a plate with stiffeners, see Figure 171. The stiffness matrix of a plate with stiffeners can be expressed as (Blaauwendraad, 2010):

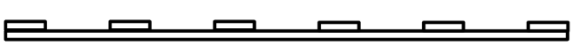

Figure 171: Schematic representation of bottom deck

$$D = \begin{bmatrix} \frac{Et}{1-v^2} + \frac{EA_a}{a} & \frac{Et}{1-v^2} & 0 \\ \frac{Et}{1-v^2} & \frac{Et}{1-v^2} + \frac{EA_b}{b} & 0 \\ 0 & 0 & Gt \end{bmatrix}$$

This stiffness formulation represents a membrane plate with stiffeners, see Figure 172. For the total cross-section, the bottom deck primarily carries membrane forces rather than bending moments. This is due to the large distance between the top and bottom decks, which creates a significant lever arm. As a result, global bending is resisted mainly by the separation of the decks, while the individual plates are primarily subjected to membrane forces.

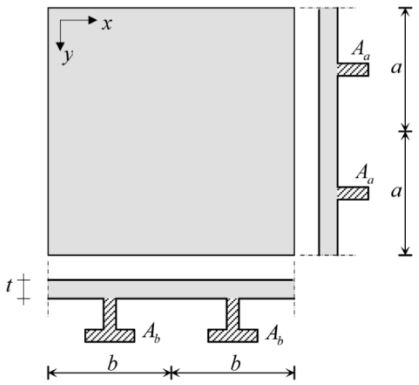

Figure 172: Example of orthotropic membrane plate (Blaauwendraad, 2010)

For the bottom deck, no stiffeners are present in the y-direction. Additionally, instead of using the stiffener spacing a, the contribution of the stiffeners is expressed over the full width of the cross-section:

$$\frac{E * A_a}{a} = \frac{n.o.g * E * A_a}{w}$$

Where n.o.g is the number of girders and w is the total width of the cross-section.

Since the composite material is orthotropic, the isotropic formulation above is not applicable. The stiffness matrix is therefore written as:

$$D = \begin{bmatrix} \frac{E_x t}{1 - \nu_{xy}\nu_{yx}} + \frac{E_x A_a}{a} & \frac{\nu_{xy} E_y t}{1 - \nu_{xy}\nu_{yx}} & 0 \\ \frac{\nu_{yx} E_x t}{1 - \nu_{xy}\nu_{yx}} & \frac{E_y t}{1 - \nu_{xy}\nu_{yx}} & 0 \\ 0 & 0 & G_{xy} t \end{bmatrix}$$

With:

$$E_x = E_1$$

$$E_y = E_2$$

$$G_{xy} = G_{12}$$

$$\nu_{xy} = \nu_{12}$$

$$\nu_{yx} = \nu_{21}$$

In RFEM, the stiffness properties and thickness cannot be defined simultaneously, the thickness is specified separately. Therefore, representative material properties must be derived. Input fields for orthotropic materials for plates and thickness for plates are shown in Figure 173 and Figure 174. The properties E_y, G_{xy}, ν_{xy} and ν_{yx}, can be directly taken from the laminate properties of the bottom plate, provided that the bottom plate thickness is used as the representative thickness t_{rep}.

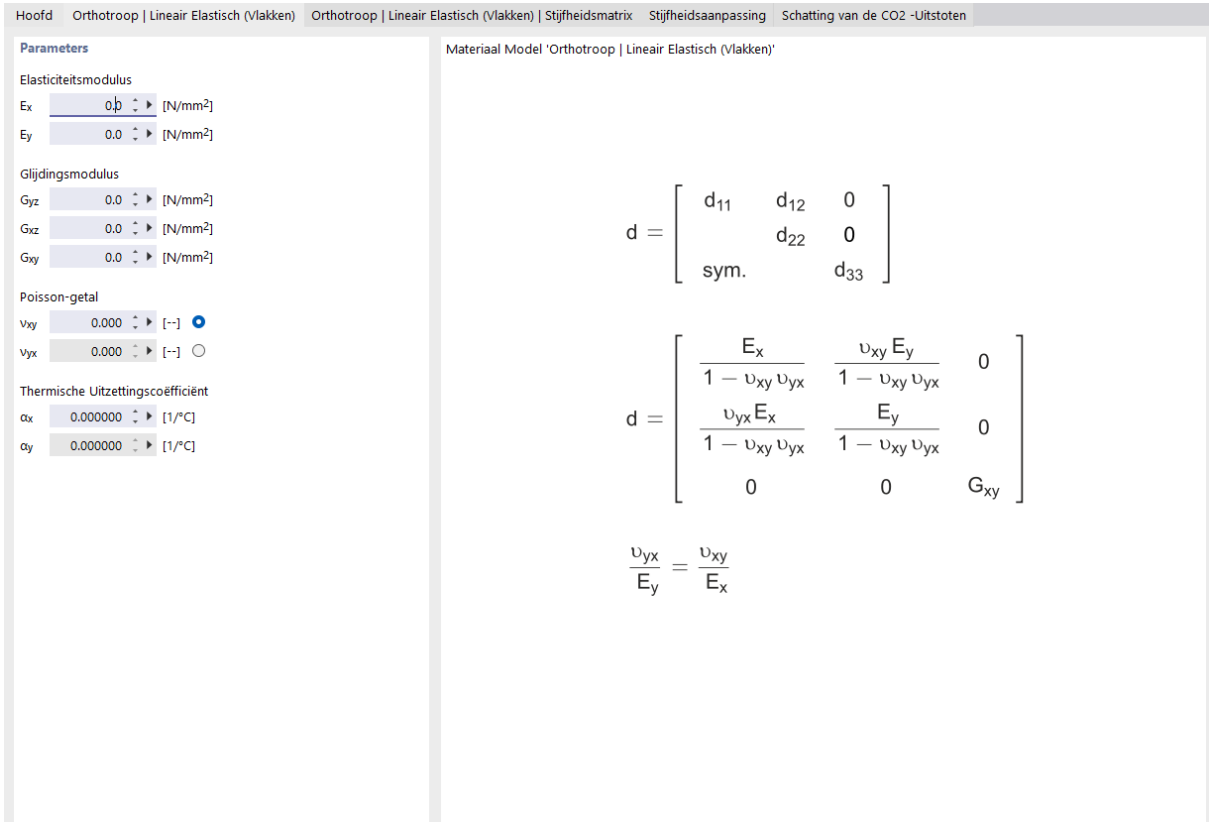

Figure 173: RFEM input field material stiffness

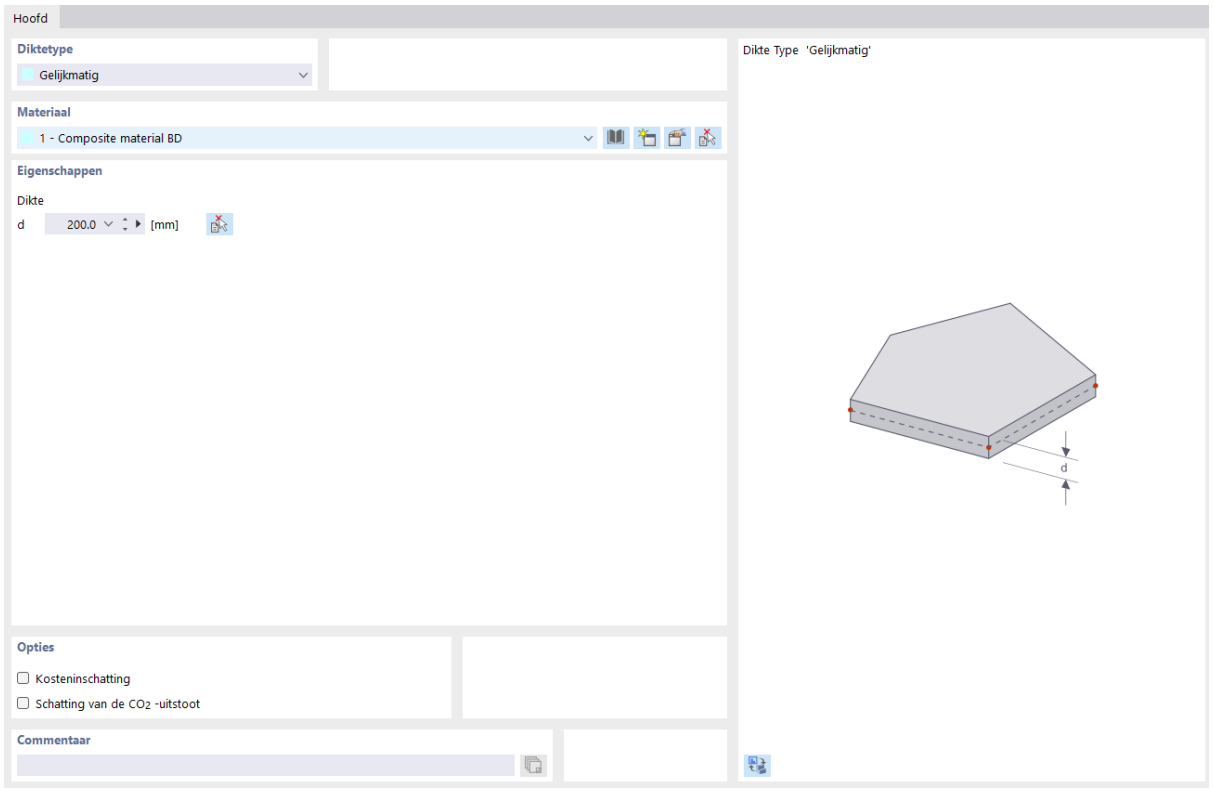

Figure 174: RFEM input field plate thickness

For E_x, the following term must be converted into an equivalent form:

$$\frac{E_x t}{1 - \nu_{xy}\nu_{yx}} + \frac{E_x * A_a}{a}$$

The expression can be rewritten as:

$$= \frac{E_{x,bp} t}{1 - \nu_{xy,bp}\nu_{yx,bp}} + \frac{n.o.g * E_{x,girder} * A_a}{w}$$

Rewriting this expression:

$$\frac{E_{x,bp} t}{1 - \nu_{xy,bp}\nu_{yx,bp}} + \frac{\frac{n.o.g * E_{x,girder} * A_a}{w}}{1 - \nu_{xy,bp}\nu_{yx,bp}} * (1 - \nu_{xy,bp}\nu_{yx,bp})$$

$$= \frac{E_{x,bp} t + \frac{n.o.g * E_{x,girder} * A_a}{w} * (1 - \nu_{xy,bp}\nu_{yx,bp})}{1 - \nu_{xy,bp}\nu_{yx,bp}}$$

The numerator can be interpreted as the equivalent product of representative stiffness and thickness:

$$E_{x,rep} * t_{rep} = E_{x,bp} t + \frac{n.o.g * E_{x,girder} * A_a}{w} * (1 - \nu_{xy,bp}\nu_{yx,bp})$$

Thus, the representative stiffness becomes:

$$E_{x,rep} = \frac{E_{x,bp} t + \frac{n.o.g * E_{x,girder} * A_a}{w} * (1 - \nu_{xy,bp}\nu_{yx,bp})}{t_{rep}}$$

Where:

$E_{x,rep}$ is the representative stiffness modulus in x-direction for RFEM

t_{rep} is the representative thickness for RFEM (the thickness of the bottom plate)

A_a is the area of a lower horizontal flange of a C-shaped girder

The equation of $E_{x,rep}$ is implemented in the function rep_t_E_1_prop_BD. The function prints the properties of the representative bottom deck, which can be used in RFEM.

The width of the bottom deck is:

$$w_{rep} - t_{girder}$$

Representative stiffness and thickness top deck

The top deck can be represented as a plate with stiffeners, similar to the bottom deck, see Figure 175. The stiffness matrix of a plate with stiffeners can be expressed as (Blaauwendraad, 2010):



Figure 175: Schematic representation of top deck

$$D = \begin{bmatrix} \frac{Et}{1-v^2} + \frac{EA_a}{a} & \frac{Et}{1-v^2} & 0 \\ \frac{Et}{1-v^2} & \frac{Et}{1-v^2} + \frac{EA_b}{b} & 0 \\ 0 & 0 & Gt \end{bmatrix}$$

This stiffness formulation represents a membrane plate with stiffeners. Similar to the bottom deck, the top deck primarily resists membrane forces rather than bending moments, due to global bending. This is due to the overall structural behaviour of the cross-section, where the large distance between the top and bottom decks creates a significant lever arm, allowing global bending to be resisted at the system level. The sandwich structure of the top deck is designed to transfer and distribute local loads across the cross-section, ensuring efficient load sharing between the different structural components. Therefore, for a model whose goal is to evaluate forces at the global level, representing the deck using membrane stiffnesses provides an appropriate and effective approximation.

For the top deck, just like the bottom deck, no stiffeners are present in the y-direction. Additionally, instead of using the stiffener spacing a, the contribution of the stiffeners is expressed over the full width of the cross-section:

$$\frac{E * A_a}{a} = \frac{n.o.g * E * A_a}{w}$$

Where n.o.g is the number of girders and w is the total width of the cross-section.

Since the composite material is orthotropic, the isotropic formulation above is not applicable. The stiffness matrix is therefore written as:

$$D = \begin{bmatrix} \frac{E_x t}{1 - \nu_{xy}\nu_{yx}} + \frac{E_x A_a}{a} & \frac{\nu_{xy} E_y t}{1 - \nu_{xy}\nu_{yx}} & 0 \\ \frac{\nu_{yx} E_x t}{1 - \nu_{xy}\nu_{yx}} & \frac{E_y t}{1 - \nu_{xy}\nu_{yx}} & 0 \\ 0 & 0 & G_{xy} t \end{bmatrix}$$

With:

$$E_x = E_1$$

$$E_y = E_2$$

$$G_{xy} = G_{12}$$

$$\nu_{xy} = \nu_{12}$$

$$\nu_{yx} = \nu_{21}$$

In RFEM, the stiffness properties and thickness cannot be defined simultaneously, the thickness is specified separately. Therefore, representative material properties must be derived. The representative thickness of the top plate will be the thickness of the bottom face plus the thickness of the top face plus the height of the core.

Stiffness modulus in x-direction

The expression $\frac{E_x t}{1-\nu_{xy}\nu_{yx}} + \frac{E_x * A_a}{a}$, can be rewritten for the top deck as:

$$\frac{E_{x,tf}t_{tf}}{1-\nu_{xy,tf}\nu_{yx,tf}} + \frac{E_{x,core}h_{core}}{1-\nu_{xy,core}\nu_{yx,core}} + \frac{E_{x,bf}t_{bf}}{1-\nu_{xy,bf}\nu_{yx,bf}} + \frac{n.o.g * E_{x,girder} * A_a}{w}$$

Because ν_{xy} and ν_{yx} are different for the different components, the core, top face, and girders will all be multiplied and divided by $1-\nu_{xy,bf}\nu_{yx,bf}$, because than the ν_{xy} and ν_{yx} from the bottom face can be used as input for the material properties. The expression will be:

$$\frac{E_{x,tf}t_{tf}}{1-\nu_{xy,tf}\nu_{yx,tf}} * \frac{1-\nu_{xy,bf}\nu_{yx,bf}}{1-\nu_{xy,bf}\nu_{yx,bf}} + \frac{E_{x,core}h_{core}}{1-\nu_{xy,core}\nu_{yx,core}} * \frac{1-\nu_{xy,bf}\nu_{yx,bf}}{1-\nu_{xy,bf}\nu_{yx,bf}} + \frac{E_{x,bf}t_{bf}}{1-\nu_{xy,bf}\nu_{yx,bf}} + \frac{n.o.g * E_{x,girder} * A_a}{w} * \frac{1-\nu_{xy,bf}\nu_{yx,bf}}{1-\nu_{xy,bf}\nu_{yx,bf}}$$

$$= (\frac{E_{x,tf}t_{tf}}{1-\nu_{xy,tf}\nu_{yx,tf}} * (1-\nu_{xy,bf}\nu_{yx,bf}) + \frac{E_{x,core}h_{core}}{1-\nu_{xy,core}\nu_{yx,core}} * (1-\nu_{xy,bf}\nu_{yx,bf}) + E_{x,bf}t_{bf} + \frac{n.o.g * E_{x,girder} * A_a}{w} * (1-\nu_{xy,bf}\nu_{yx,bf}))/(1-\nu_{xy,bf}\nu_{yx,bf})$$

The numerator can be interpreted as the equivalent product of representative stiffness and thickness:

$$E_{x,rep} * t_{rep} = \frac{E_{x,tf}t_{tf}}{1-\nu_{xy,tf}\nu_{yx,tf}} * (1-\nu_{xy,bf}\nu_{yx,bf}) + \frac{E_{x,core}h_{core}}{1-\nu_{xy,core}\nu_{yx,core}} * (1-\nu_{xy,bf}\nu_{yx,bf}) + E_{x,bf}t_{bf} + \frac{n.o.g * E_{x,girder} * A_a}{w} * (1-\nu_{xy,bf}\nu_{yx,bf})$$

Thus, the representative stiffness becomes:

$$E_{x,rep} = (\frac{E_{x,tf}t_{tf}}{1-\nu_{xy,tf}\nu_{yx,tf}} * (1-\nu_{xy,bf}\nu_{yx,bf}) + \frac{E_{x,core}h_{core}}{1-\nu_{xy,core}\nu_{yx,core}} * (1-\nu_{xy,bf}\nu_{yx,bf}) + E_{x,bf}t_{bf} + \frac{n.o.g * E_{x,girder} * A_a}{w} * (1-\nu_{xy,bf}\nu_{yx,bf}))/t_{rep}$$

Where:

$E_{x,rep}$ is the representative stiffness modulus in x-direction for RFEM

t_{rep} is the representative thickness for RFEM (The thickness of the bottom face plus the top face plus the core)

A_a is the area of an upper horizontal flange of a C-shaped girder

Stiffness modulus y-direction

The expression $\frac{E_y t}{1-\nu_{xy}\nu_{yx}}$ can be written for the top deck as:

$$\frac{E_{y,tf}t_{tf}}{1-\nu_{xy,tf}\nu_{yx,tf}} + \frac{E_{y,core}h_{core}}{1-\nu_{xy,core}\nu_{yx,core}} + \frac{E_{y,bf}t_{bf}}{1-\nu_{xy,bf}\nu_{yx,bf}}$$

For the same reason as before the core and top face will all be multiplied and divided by $(1-\nu_{xy,bf}\nu_{yx,bf})$. The expression will be:

$$\frac{E_{y,tf}t_{tf}}{1-\nu_{xy,tf}\nu_{yx,tf}} * \frac{1-\nu_{xy,bf}\nu_{yx,bf}}{1-\nu_{xy,bf}\nu_{yx,bf}} + \frac{E_{y,core}h_{core}}{1-\nu_{xy,core}\nu_{yx,core}} * \frac{1-\nu_{xy,bf}\nu_{yx,bf}}{1-\nu_{xy,bf}\nu_{yx,bf}} + \frac{E_{y,bf}t_{bf}}{1-\nu_{xy,bf}\nu_{yx,bf}}$$

$$= \frac{\frac{E_{y,tf}t_{tf}}{1-\nu_{xy,tf}\nu_{yx,tf}} * \left(1-\nu_{xy,bf}\nu_{yx,bf}\right) + \frac{E_{y,core}h_{core}}{1-\nu_{xy,core}\nu_{yx,core}} * \left(1-\nu_{xy,bf}\nu_{yx,bf}\right) + E_{y,bf}t_{bf}}{1-\nu_{xy,bf}\nu_{yx,bf}}$$

The numerators of both parts can be interpreted as the equivalent product of representative stiffness and thickness:

$$E_{y,rep} * t_{rep} = \frac{E_{y,tf}t_{tf}}{1-\nu_{xy,tf}\nu_{yx,tf}} * \left(1-\nu_{xy,bf}\nu_{yx,bf}\right) + \frac{E_{y,core}h_{core}}{1-\nu_{xy,core}\nu_{yx,core}} * \left(1-\nu_{xy,bf}\nu_{yx,bf}\right) + E_{y,bf}t_{bf}$$

Thus, the representative stiffness becomes:

$$E_{y,rep} = \frac{\frac{E_{y,tf}t_{tf}}{1-\nu_{xy,tf}\nu_{yx,tf}} * \left(1-\nu_{xy,bf}\nu_{yx,bf}\right) + \frac{E_{y,core}h_{core}}{1-\nu_{xy,core}\nu_{yx,core}} * \left(1-\nu_{xy,bf}\nu_{yx,bf}\right) + E_{y,bf}t_{bf}}{t_{rep}}$$

Where:

$E_{y,rep}$ is the representative stiffness modulus in y-direction for RFEM

t_{rep} is the representative thickness for RFEM (The thickness of the bottom face plus the top face)

Shear stiffness

The expression $G_{xy}t$ can be written for the top deck as:

$$G_{xy,rep}t_{rep} = G_{xy,tf}t_{tf} + G_{xy,core}h_{core} + G_{xy}t_{bf}$$

The representative shear stiffness will be:

$$G_{xy,rep} = \frac{G_{xy,tf}t_{tf} + G_{xy,core}h_{core} + G_{xy}t_{bf}}{t_{rep}}$$

The equations of $E_{x,rep}$, $E_{y,rep}$ and $G_{xy,rep}$ are implemented in the function rep_t_E_G_prop_TD. The function prints the properties of the representative top deck, which can be used in RFEM.

The width of the top deck is:

$$w_{rep} = w - t_{girder}$$

Positioning, height, and properties girders

The positioning and height of the plates is important for the overall stiffness of the model. The centre of gravity of the representative bottom deck must coincide with the centre of gravity of the real bottom deck. The same requirement applies to the top deck. To achieve this, the height of the c-shaped girders is adjusted. The hight of the c-shaped girders is the distance between the centres of gravity of the top and bottom deck. The girders will have a thickness of t_{girder} and the same material properties as the girder laminate. The girders are positioned at the same location as in the total cross-section.

Height girders

The height of the girders will be calculated by subtracting the distance of the centre of gravity of the top deck to the top of the cross-section and the distance of the centre of gravity of the bottom deck to the bottom of the cross-section, see Figure 176. The distance of the centre of gravity of the bottom deck to the bottom of the cross-section is:

$$z_{cg,bd} = \frac{z_{bp} * E_{1,bp} * t_{bp} * w + z_{girder\ flange} * E_{1,girder} * t_{girder} * w_{girder} * n.o.g}{E_{1,bp} * t_{bp} * w + E_{1,girder} * t_{girder} * w_{girder} * n.o.g}$$

Where:

z_{bp} is equal to $\frac{1}{2} * t_{bp}$

$z_{girder\ flange}$ is equal to $t_{bp} + \frac{1}{2} * t_{girder}$

The distance of the centre of gravity of the top deck to the top of the cross-section is:

$$z_{cg,td} = (z_{tf} * E_{1,tf} * t_{tf} * w + z_{core} * E_{core} * h_{core} * w + z_{bf} * E_{1,bf} * t_{bf} * w + z_{girder\ flange} * E_{1,girder} * t_{girder} * w_{girder} * n.o.g)/(E_{1,tf} * t_{tf} * w + E_{core} * h_{core} * w + E_{1,bf} * t_{bf} * w + E_{1,girder} * t_{girder} * w_{girder} * n.o.g)$$

Where:

z_{tf} is equal to $\frac{1}{2} * t_{tf}$

z_{core} is equal to $t_{tf} + \frac{1}{2} * h_{core}$

z_{bf} is equal to $t_{tf} + h_{core} + \frac{1}{2} * t_{bf}$

$z_{girder\ flange}$ is equal to $t_{tf} + h_{core} + t_{bf} + \frac{1}{2} * t_{girder}$

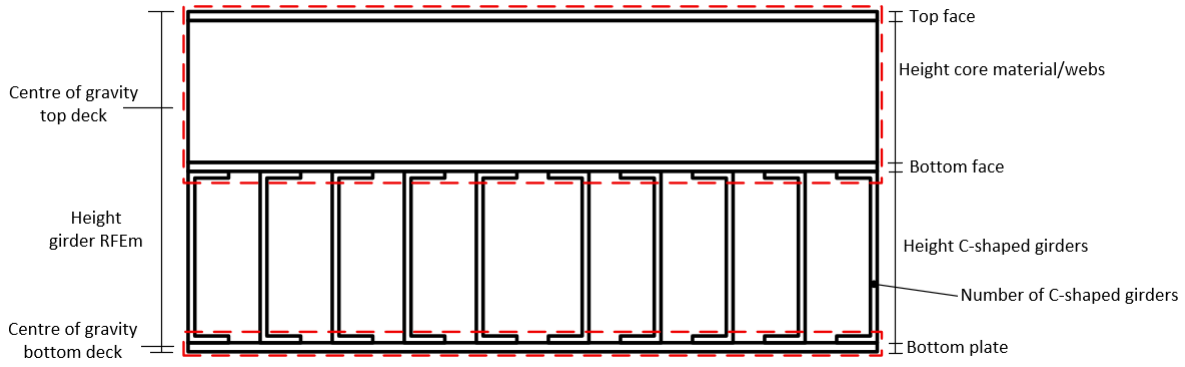

Figure 176: Schematic representation height girders

The height of the girders is:

$$h_{rep,girder} = h_{cross-section} - z_{cg,td} - z_{cg,bd}$$

This equation is implemented in the function rep_girder_prop.

Position girders

The y_coordinates function from the stiffness Python script can be modified to determine the locations for the representative rectangular girders. The original function determines the y-coordinates of the centroids of the C-shaped girders in the cross-section. However, for the rectangular representation, the centre of gravity does not correspond to the centre of gravity of the complete C-shaped girders. Therefore, the y-coordinates determined with the y_coordinates function must be adjusted. For girders on the left side of the cross-section, the correction distance, the distance between the centre of gravity of the C-shaped girders and the representative rectangular girder, must be subtracted from the y-coordinates determined with the function and for the right side the correction distance must be added to the y-coordinates. The function rep_girder_loc determines the corrected positions of the representative girders, while rep_girder_prop outputs their properties and locations.

Density of components

Representative densities for the bottom deck, girders, and top deck must be determined such that the product of the representative area and the representative density equal the actual weight of each component. The function density_composite computes the density of a composite material using:

$$\rho_{com} = V_f \rho_f + \left(100\% - V_f\right) * \rho_r$$

C-shaped girders

The density of the representative girders is not equal to the density of the composite, ρ_{com}, since the girders are higher as the real girder is. The part of the real girders which is not included in the top or bottom deck is:

$$h_{girder\ without\ flanges} = h_{girder} - 2 * t_{girder}$$

The density of the representative girders is calculated such that its total mass equals the mass of the actual bottom deck components. It is given by:

$$\rho_{rep,girder} = \rho_{com} * \frac{h_{girder\ \ without\ flanges} * t_{girder}}{h_{rep,girder} * t_{girder}}$$

This equation is implemented in the function rep_girder_prop.

Bottom deck

The density of the representative bottom deck is calculated such that its total mass equals the mass of the actual bottom deck components. It is given by:

$$\rho_{bd} = \rho_{com} * \frac{A_{bp} + A_a * n.o.g}{A_{rep,bd}}$$

Where:

A_{bp} is the area of the bottom plate

A_a is the area of a lower horizontal flange of a C-shaped girder

$n.o.g$ is the number of girders

A_{rep} is the area of the representative bottom deck ($t_{rep,bd} * w_{rep}$)

This equation is implemented in the function rep_t_E_1_prop_BD.

Top deck

The density of the representative top deck is determined by including both the composite faces and the core material:

$$\rho_{td} = \frac{\rho_{com} * (A_{tf} + A_{bf} + A_a * n.o.g) + \rho_{core} * A_{core}}{A_{rep,td}}$$

Where:

A_{tf} is the area of the top face

A_{bf} is the area of the bottom face

ρ_{core} is the density of the core

A_{core} is the area of the core

A_a is the area of an upper horizontal flange of a C-shaped girder

$n.o.g$ is the number of girders

A_{rep} is the area of the representative bottom deck ($t_{rep,td} * w_{rep}$)

This equation is implemented in the function rep_t_E_G_prop_TD.

Test of the functions

To validate the implemented functions, a plate model is created with the same properties as the model used for testing the RFEM input of the beam model. This plate model will be compared to hand calculations. The plate model has a length of 20 metres. A load of 5 kN/m in the z-direction is distributed over the width of the top plate, while a load of 5 kN/m in the y-direction is distributed over the height of the representative girder. The top and bottom plates both have a width of 1788 mm. The representative girder has a height of 313 mm. The properties of the top deck are:

- $thickness = 64.9\ mm$
- $E_x = 3885.323\ [N/mm^2]$
- $E_y = 1234.802\ [N/mm^2]$
- $G_{yz} = 507.962\ [N/mm^2]$
- $G_{xz} = 507.962\ [N/mm^2]$
- $G_{xy} = 507.962\ [N/mm^2]$
- $\upsilon_{xy} = 0.301\ [-]$
- $\rho = 429.283\ [kg/m^3]$

The properties of the girders are:

- $thickness = 11.2\ mm$
- $E_x = 8505.675[N/mm^2]$
- $E_y = 8505.675\ [N/mm^2]$
- $G_{yz} = 3283.735\ [N/mm^2]$
- $G_{xz} = 3283.735\ [N/mm^2]$
- $G_{xy} = 3283.735\ [N/mm^2]$
- $\upsilon_{xy} = 0.295\ [-]$
- $\rho = 1111.120\ [kg/m^3]$

The properties of the bottom deck are:

- $thickness = 14.0mm$
- $E_x = 16573.038\ [N/mm^2]$
- $E_y = 5568.544\ [N/mm^2]$
- $G_{yz} = 2264.659\ [N/mm^2]$
- $G_{xz} = 2264.659\ [N/mm^2]$
- $G_{xy} = 2264.659\ [N/mm^2]$
- $\upsilon_{xy} = 0.300\ [-]$
- $\rho = 1720.707[kg/m^3]$

The y-coordinates of the girders are: -0.894, -0.544, -0.194, 0.194, 0.544 and 0.894, with $y = 0$ at the middle of the plate model. At the left and right edges of the model the bottom plate is supported with a line support where $c_{u,z}$ is fixed. On the left side of the model the bottom plate is in the middle supported with a node support where $u_x, u_y\ and\ u_z$ are fixed and on the right side the $u_x\ and\ u_y$ are fixed. Star plates are placed on the left and right sides of the model to better replicate the behaviour of the beam model. A mesh with a length of 0.100 meters is used

The load in z-direction will be:

$$\frac{5\frac{kN}{m}}{\frac{1788\ mm}{1000}} = 2.80\ kN/m^2$$

The load in y-direction will be:

$$\frac{5\frac{kN}{m}}{\frac{313\ mm}{1000}} = 15.97\ kN/m^2$$

The model for the load case in z-direction is shown in Figure 177 and the model for the load case in y-direction is shown in Figure 178. There is also a load case for the self-weight determined in RFEM with the densities.

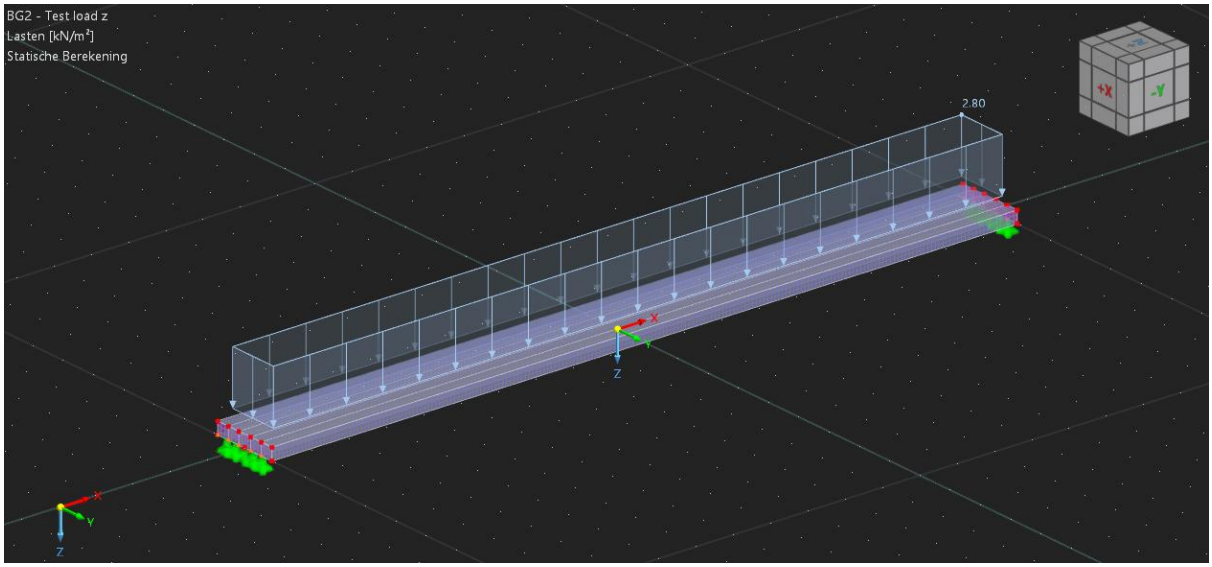

Figure 177: Test model load in z-direction

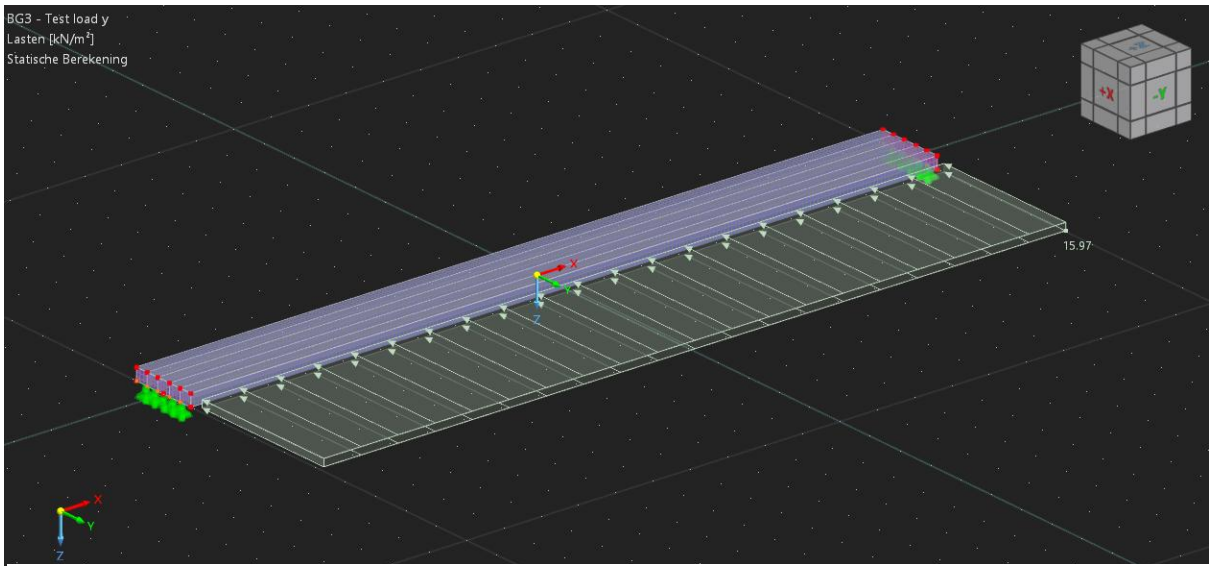

Figure 178: Test model load in y-direction

The results for the deflection of both the loads are shown in Figure 179 and Figure 180. The deflection because of the load in z-direction is 461.3 mm and the deflection because of the load in y-direction is 37.6 mm.

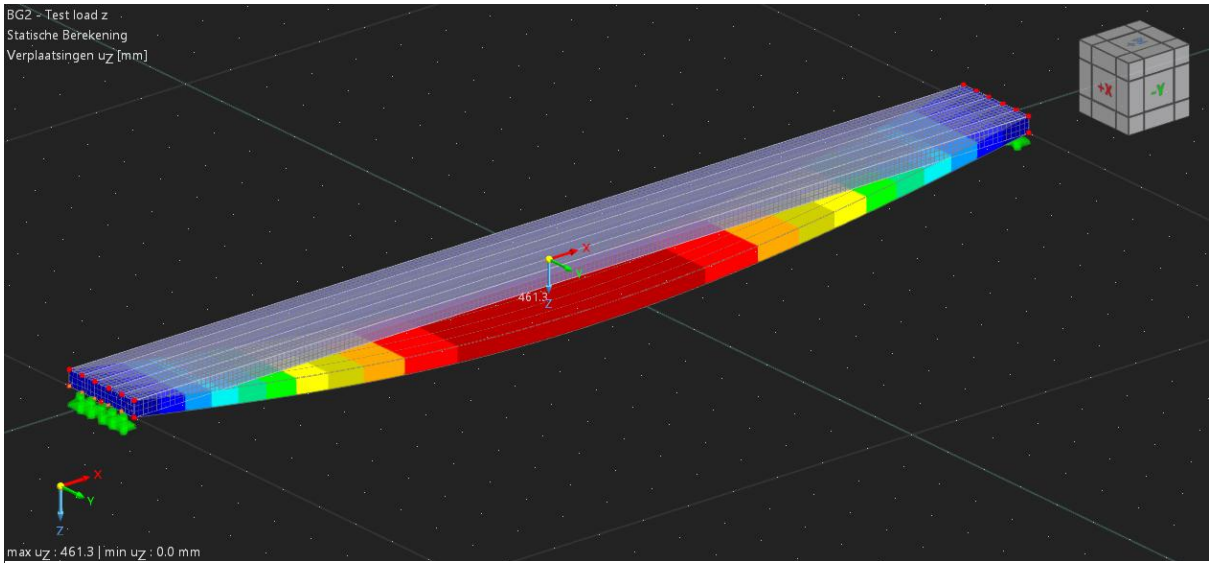

Figure 180: Test model deflection in z-direction because of load in z-direction

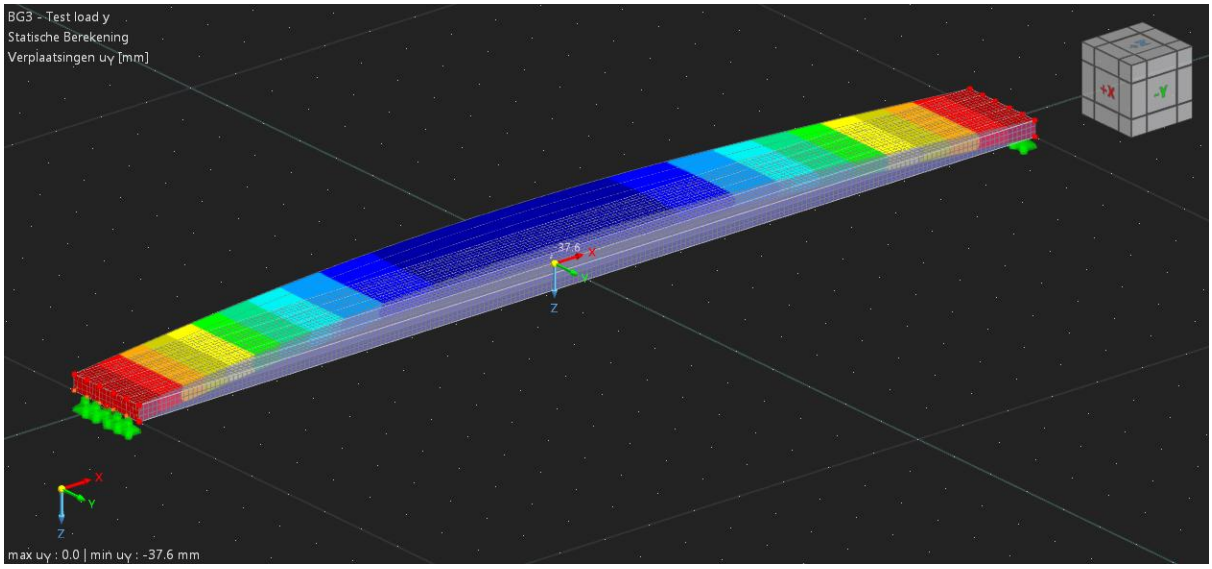

Figure 179: Test model deflection in y-direction because of load in y-direction

Hand calculation

The deflection calculated for the beam model test is identical to that of the plate model, since the plate model is also hinged in both directions. The maximum deflection of a simply supported beam with a q-load in z-direction is:

$$w_{max} = \frac{5}{384} * \frac{q * l^4}{EI_{zz}} = \frac{5}{384} * \frac{5 * (20 * 10^3)^4}{2.268 * 10^{13}} = 459.3\ mm$$

The maximum deflection in the y-direction, based on a hand calculation with hinged edges, is:

$$w_{max} = \frac{5}{384} * \frac{q * l^4}{EI_{yy}} = \frac{5}{384} * \frac{5 * (20 * 10^3)^4}{2.992 * 10^{14}} = 34.8\ mm$$

Conclusion

The deflection under the load in the z-direction is 2.0 mm higher than that of the hand calculation. The deflection is 0.43 % ($\frac{2}{459.3} * 100$) higher as the hand calculation. This difference can be explained by the modelling assumption that the stiffness of the top and bottom decks is governed only by membrane behaviour. In reality, these decks also contribute to bending stiffness, which is not accounted for in the simplified plate model.

For the load in the y-direction, the deflection is 2.8 mm higher than that of the hand calculation. The deflection is 8.05 % ($\frac{2.8}{34.8} * 100$) higher as the hand calculation. This difference can be attributed to the same modelling assumption, namely the neglect of the bending stiffness contribution of the top and bottom decks.

The total load in the z-direction due to self-weight is equal to 23.26 kN, which is exactly the same as the hand calculation. The correct representation of self-weight confirms that the density input in RFEM is accurate.

Appendix L: Design loads preliminary design

The design loads for the complete structure and the resulting design loads on the top plate are presented below.

Design load's total structure

The load types considered in the preliminary design are all loads acting in the z-direction:

- Self-weight
- Permanent loads
- Traffic loads
- Balustrade
- Wind load z-direction (Downward wind load)

Self-Weight

The self-weight is determined for a cross-section with a height of approximately 1000 mm. The self-weight is calculated by multiplying the cross-sectional area of the different components by their corresponding densities.

The cross-section has a width of 1800 mm. The girders have a height of 850 mm and a width of 100 mm. The number of girders is 4. The thicknesses of the plates, girders, and core are:

- $t_{bp} = 40\ mm$
- $t_{girder} = 20\ mm$
- $t_{bf} = 30\ mm$
- $h_{core} = 75\ mm$
- $t_{tf} = 30\ mm$

The areas of the components of the cross-section are:

$$A_{tf} = w * t_{tf} = 1800 * 30 = 54000\ mm^2$$

$$A_{core} = w * h_{core} = 1800 * 75 = 135000\ mm^2$$

$$A_{bf} = w * t_{bf} = 1800 * 30 = 54000\ mm^2$$

$$A_{girder} = 2 * w_{girder} * t_{girder} + h_{girder} * t_{girder} = 2 * 100 * 20 + 850 * 20 = 21000\ mm^2$$

$$A_{bp} = w * t_{bp} = 1800 * 40 = 72000\ mm^2$$

The density of the core material is 50 kg/m^3. The density of the laminate is calculated with:

$$\rho_{com} = V_f \rho_f + \left(100\% - V_f\right) * \rho_r$$

With:

- $\rho_f = 1500\ kg/m^3$
- $V_f = 50\ \%$
- $\rho_r = 1200\ kg/m^3$.

The density of the laminate is:

$$\rho_{com} = 0.50 * 1500 + 0.5 * 1200 = 1350\ kg/m^3$$

The weight per meter of the cross-section is:

$$weight_{cs} = (A_{tf} + A_{bf} + n.o.g * A_{girder} + A_{bp}) * \rho_{com} + A_{core} * \rho_{core}$$

$$= (2 * 54000 + 4 * 21000 + 72000\ )/10^6 * 1350 + 135000/10^6 * 50 = 363.15\ kg/m$$

The corresponding distributed load is:

$$q_{sw} = weight_{cs} * 10 = 363.15 * 10 = 3631.5\ N/m = \ 3.63\ kN/m \approx 3.7\ kN/m$$

For the self-weight, a load of 3.7 kN/m is assumed, which represents a conservative overestimation.

Permanent loads

Balustrade

The distributed line load of the balustrade is:

$$q_{balustrade} = 0.8\ kN/m$$

This load is applied twice, as balustrades are present on both sides of the deck.

Wear surface

The distributed area load of the wear surface is:

$$p_{wearing} = 0.20\ kN/m^2$$

The distributed line load of the wear surface is:

$$q_{wearing} = 0.20 * 1.8 = 0.36\ kN/m$$

Coating

The distributed area load of the coating is:

$$p_{coating} = 0.006\ kN/m^2$$

The coating is applied to all the elements in the bridge deck and the load will be different for the different heights of the cross-section. The load per different height cross-section can be calculated with:

$$q_{coating} = 0.006 * \left(b_{bp} * 2 + b_{tf} * 2 + 4 * h_{girder} * 2\right)\ [kN/m]$$

$$q_{coating} = 0.006 * \left(1.8 * 2 + 1.8 * 2 + 4 * h_{girder} * 2\right)\ [kN/m]$$

$$q_{coating} = 0.044 + 0.048 * h_{girder}\ [kN/m]$$

For a cross-section with a girder height of 850 mm the load is:

$$q_{coating} = 0.044 + 0.048 * 0.850 = 0.085$$

Bonding paste

The distributed area load of the bonding paste is:

$$p_{paste} = 0.05\ kN/m^2$$

The distributed line load of the bonding paste is:

$$q_{paste} = 0.05 * 0.1 = 0.005\ kN/m$$

The paste is applied at the bottom and top of the C-shaped girders. The total load is:

$$q_{paste} = 0.005 * 4 * 2 = 0.04\ kN/m$$

Resin absorption of the core material

The distributed area load of the bonding paste is:

$$p_{resin} = 0.005\ kN/m^2$$

The distributed line load of the bonding paste is:

$$q_{resin} = 0.005 * 1.83 = 0.0092\ kN/m$$

Total permanent load

The total permanent load is:

$$q_{per} = \ 2 * 0.8 + 0.36 + 0.085 + 0.04 + 0.0092 = 2.1\ kN/m$$

Traffic loads

The bridge has a length of 50 meters. The distributed traffic load is:

$$q_{fk} = 2.0 + \frac{120}{L + 30} = 2.0 + \frac{120}{50 + 30} = 3.5\left[\frac{kN}{m^2}\right]$$

Converted to a line load:

$$q_{fk} = 3.5 * 1.83 = 6.41\ kN/m$$

Balustrade

The distributed line load of pedestrians on the balustrade is:

$$q_{ped,balustrade} = 1.0\ kN/m$$

This load is applied twice, as balustrades are present on both sides of the deck.

Wind load in z-direction

The distributed wind load in z-direction on the bridge deck is:

$$q_{w,z} = 881.1\ [N/m] = 0.881\ [kN/m]$$

Total load ULS

The load for ULS can be calculated with:

$$\sum F_d = \sum_i \gamma_{G,i} G_{k,i} + \gamma_{Q,1} Q_{k,1} + \sum_{j>1} \gamma_{Q,j} \psi_{0,j} Q_{k,j}$$

The load combination will be the highest when $Q_{k,1}$ is equal to the traffic load. The ULS load for the preliminary design is:

$$q_{ULS} = 1.35 * 3.7 + 1.35 * 2.1 + 1.35 * 6.41 + 0.54 * 2 * 1 + 0.45 * 0.881 = 17.96\ kN/m$$

$$q_{ULS} \approx 18\ kN/m$$

Total load SLS

The load on the structure for the characteristic combination for SLS can be determined with the equation:

$$\sum F_d = \sum_i G_{k,i} + Q_{k,1} + \sum_{j>1} \psi_{0,j} Q_{k,j}$$

This equation will be used for a simplified deflection calculation for the preliminary design. The load combination will be the highest when $Q_{k,1}$ is equal to the traffic load. The SLS load for the preliminary design is:

$$q_{SLS} = 3.7 + 2.1 + 6.41 + 0.4 * 2 * 1 + 0.3 * 0.881 = 13.27\ kN/m\ \approx 14\ kN/m$$

Design loads on top deck

The loads are derived from Chapter 5.2.3. In Figure 181 are the loads on the structure shown. All the loads are distributed per meter over the length of the bridge.

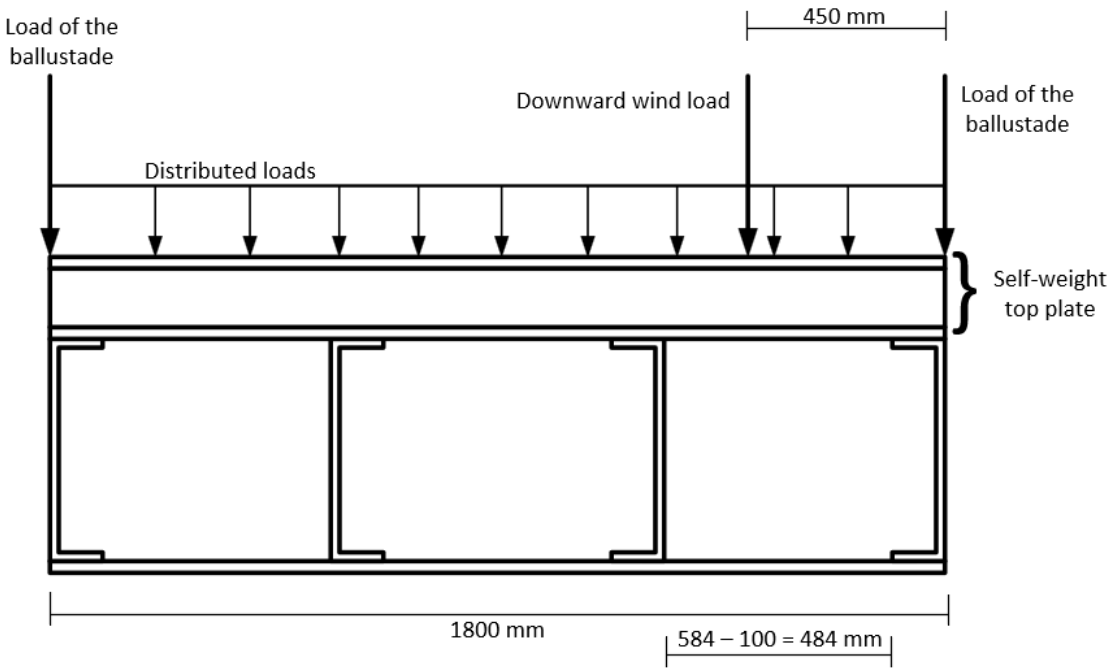

Figure 181: Loads on the top plate

Distributed loads

The distributed loads include the permanent loads on the top plate and the traffic load. The permanent loads are:

- Wear surface: $0.20\ kN/m^2$
- Coating: $2 * 0.006\ kN/m^2$
- Resin absorption core material: $0.005\ kN/m^2$

The uniformly distributed traffic load can be calculated with the following formula:

$$q_{fk} = 2.0 + \frac{120}{L + 30}\ \left[\frac{kN}{m^2}\right]$$

$$\text{with } q_{fk} \geq 2.5\ [kN/m^2]\ and\ \ q_{fk} \leq 5.0\ [kN/m^2]$$

Where

L is the length of the unfavourable part of influence surface in [m]

The L is 50 m so the traffic load will be:

$$q_{fk} = 2.0 + \frac{120}{50 + 30} = 3.5\ \left[\frac{kN}{m^2}\right]$$

Downward wind load

The wind load downward is:

$$F_{w,z} = \frac{1}{2} * \rho * v_b^2 * C * A_{ref,x} = \frac{1}{2} * 1.25 * 29.5^2 * 0.9 * 1.8 * L$$

The distributed wind load on the bridge deck will be:

$$q_{w,z} = \frac{1}{2} * 1.25 * 29.5^2 * 0.9 * 1.8 = 8811.1\ N/m = 0.88\ kN/m$$

The load downward has to be applied with an eccentricity in the x-direction. The eccentricity is $e = \frac{b}{4} = \frac{1800}{4} = 450\ mm.$

Load of the balustrade

The load of the balustrade is the self-weight of the balustrade and the variable load of pedestrians on the balustrade. The line force applied horizontally or vertically on the top of the pedestrian balustrade should be a minimum force of 1.0 kN/m for footbridges and the self-weight is 0.8 kN/m.

Self-Weight

The load for self-weight of the top plate can be determined by multiplying the height of the different components of the top plate by their corresponding density. The width of the cross-section is 1800 mm and the following dimensions are assumed for the top plate:

- $t_{tf} = 27.07\ mm$
- $h_{core} = 75\ mm$
- $t_{bf} = 27.07\ \ mm$

The density of the core material is 50 kg/m^3. The density of the laminate can be calculated with:

$$\rho_{com} = V_f \rho_f + \left(100\% - V_f\right) * \rho_r$$

For the laminate is $\rho_f = 1500\ kg/m^3$, $V_f = 50\ \%$ and $\rho_r = 1200\ kg/m^3$. The density of the laminate is:

$$\rho_{com} = 0.50 * 1500 + 0.5 * 1200 = 1350\ kg/m^3$$

The distributed self-weight of the top plate is:

$$weight = 2 * \frac{29.87}{1000} * 1350 + \frac{75}{1000} * 50 = 76.84\ kg/m^2$$

The distributed load of the top plate is:

$$q_{tp} = 76.84 * 10 = 768.4\ N/m^2 = 0.7684\ kN/m^2$$

Total loads

The total loads in SLS can be calculated with:

$$\sum F_d = \sum_i G_{k,i} + Q_{k,1} + \sum_{j>1} \psi_{0,j} Q_{k,j}$$

For $Q_{k,1}$ will the traffic load be chosen, because this is the biggest load.

Distributed load and load top plate

The total distributed load for SLS is:

$$q_d = (0.7684\ \ +\ \ 0.2 + 2 * 0.006 + 0.005) + 3.5 = 4.5\ kN/m^2$$

Load of the balustrade

The total load because of the balustrade for SLS is:

$$F_{d,b} = 0.8 + 0.4 * 1.0 = 1.2\ kN/m$$

Downward wind load

The total wind load with safety factors for SLS is:

$$F_{d,w} = 0.2 * 0.88 = 0.18\ kN/m$$

Appendix M: Cross-sections preliminary design and RFEM input

The cross-sections heights obtained from the model are shown in Figure 182. Since the transformed Rhino model will also be used for the plate model, these heights are assigned to the vertical girders. This approach avoids the need to modify the deck height within the model.

For the same reason, the width of the cross-section is slightly increased. A width of 1830 mm is adopted in order to achieve an effective width of 1800 mm in the plate model.

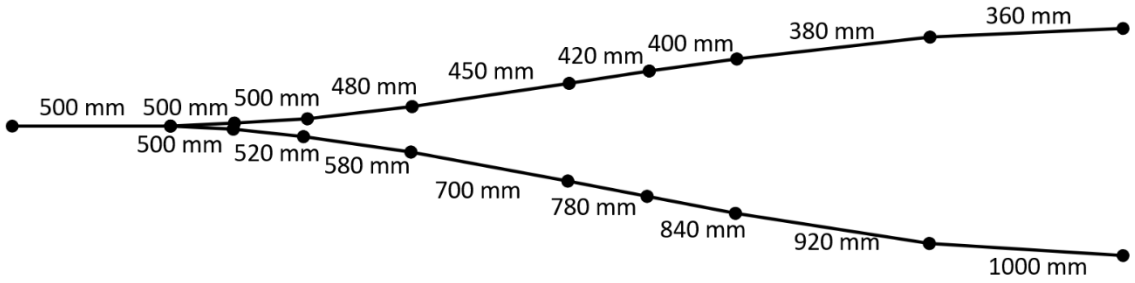

Figure 182: Cross-section heights of half the Seasaw

Input beam model

The input of the properties for the beam models corresponding to the different cross-sections is provided in the following subsections. The input of the properties for the very stiff members is also provided in the following subsections.

Height of 360 mm

The cross-section is shown in Figure 183.

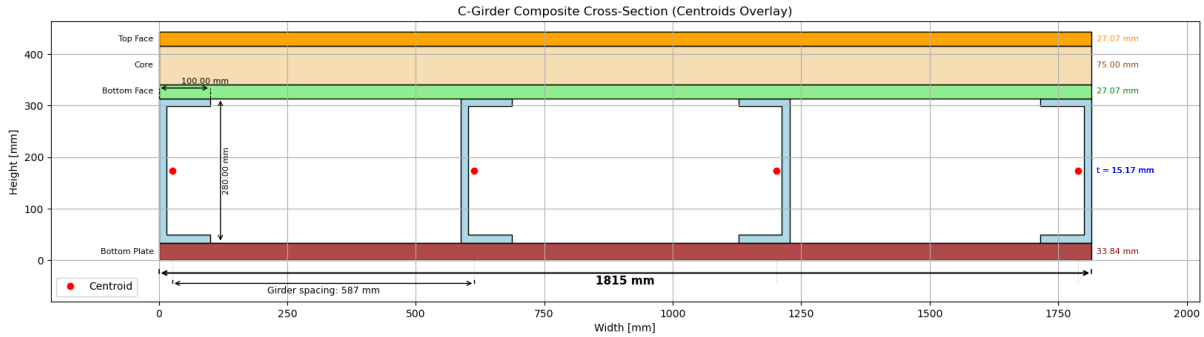

Figure 183: Cross-section height 360 mm

Material properties for RFEM input beam model:

- Young's modulus (E): 8609.62 [MPa]
- Shear modulus (G): 3453.30 [MPa]
- Poisson's ratio (nu_12): 0.246580
- Total density of the cross-section (rho_total): 802.25 [kg/m^3]
- Weight of the cross-section (gamma_total): 8.0225 [kN/m^3]
- Total area of the cross-section (A): 3230.7270 [cm^2]
- A_y (shear area approximation): 3230.7270 [cm^2]
- A_z (shear area approximation): 3230.7270 [cm^2]
- Torsional constant (I_t): 769325.53 [cm^4]

- Moment of inertia about y-axis (I_zz) (I_y): 1000090.80 [cm^4]
- Moment of inertia about z-axis (I_yy) (I_z): 9333626.74 [cm^4]
- Width b: 1815.00 [mm]
- Height h: 442.9710 [mm]

Height of 380 mm

The cross-section is shown in Figure 184.

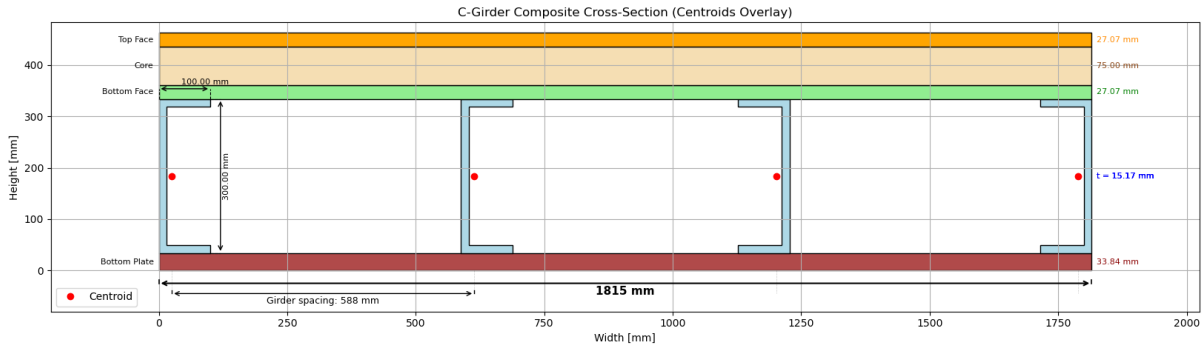

Figure 184: Cross-section height 380 mm

Material properties for RFEM input beam model:

- Young's modulus (E): 8612.23 [MPa]
- Shear modulus (G): 3454.34 [MPa]
- Poisson's ratio (nu_12): 0.246580
- Total density of the cross-section (rho_total): 804.30 [kg/m^3]
- Weight of the cross-section (gamma_total): 8.0430 [kN/m^3]
- Total area of the cross-section (A): 3242.8606 [cm^2]
- A_y (shear area approximation): 3242.8606 [cm^2]
- A_z (shear area approximation): 3242.8606 [cm^2]
- Torsional constant (I_t): 843985.59 [cm^4]
- Moment of inertia about y-axis (I_zz) (I_y): 1110128.34 [cm^4]
- Moment of inertia about z-axis (I_yy) (I_z): 9389818.03 [cm^4]
- Width b: 1815.00 [mm]
- Height h: 462.9710 [mm]

Height of 400 mm

The cross-section is shown in Figure 185.

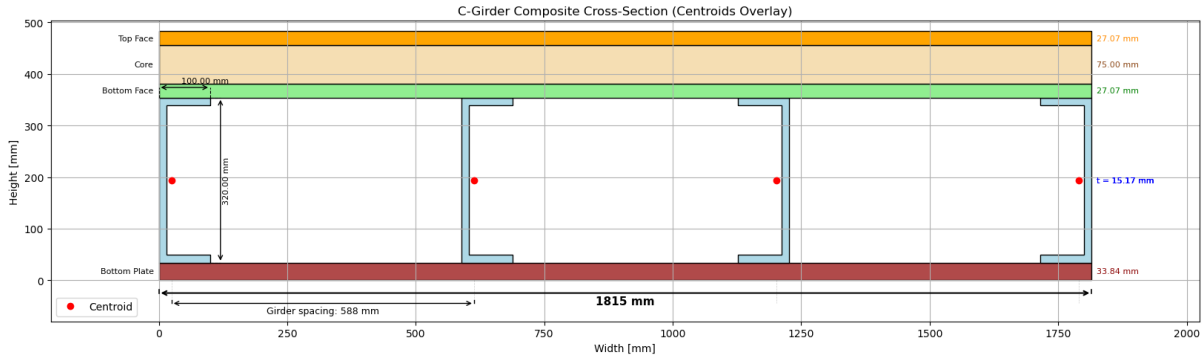

Figure 185: Cross-section height 400 mm

Material properties for RFEM input beam model:

- Young's modulus (E): 8614.83 [MPa]
- Shear modulus (G): 3455.38 [MPa]
- Poisson's ratio (nu_12): 0.246580
- Total density of the cross-section (rho_total): 806.34 [kg/m^3]
- Weight of the cross-section (gamma_total): 8.0634 [kN/m^3]
- Total area of the cross-section (A): 3254.9942 [cm^2]
- A_y (shear area approximation): 3254.9942 [cm^2]
- A_z (shear area approximation): 3254.9942 [cm^2]
- Torsional constant (I_t): 921008.73 [cm^4]
- Moment of inertia about y-axis (I_zz) (I_y): 1226365.26 [cm^4]
- Moment of inertia about z-axis (I_yy) (I_z): 9445994.97 [cm^4]
- Width b: 1815.00 [mm]
- Height h: 482.9710 [mm]

Height of 420 mm

The cross-section is shown in Figure 186.

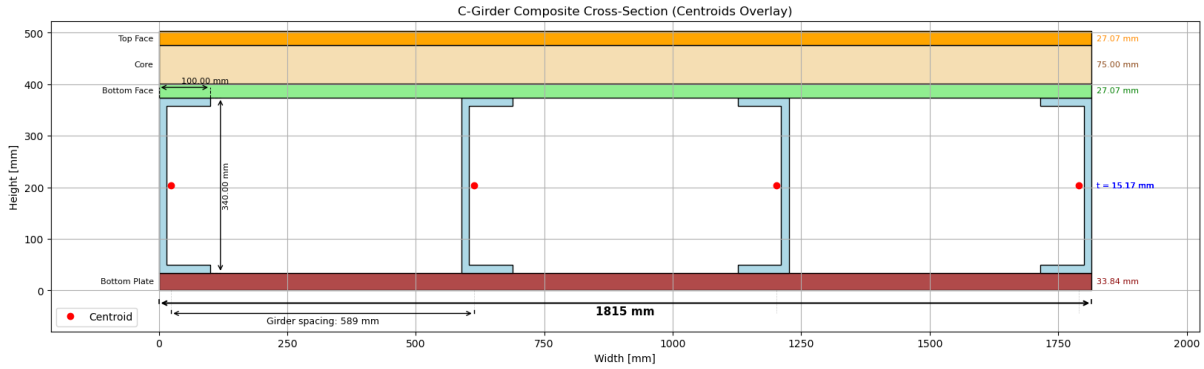

Figure 186: Cross-section height 420 mm

Material properties for RFEM input beam model:

- Young's modulus (E): 8617.40 [MPa]
- Shear modulus (G): 3456.42 [MPa]
- Poisson's ratio (nu_12): 0.246580
- Total density of the cross-section (rho_total): 808.35 [kg/m^3]
- Weight of the cross-section (gamma_total): 8.0835 [kN/m^3]
- Total area of the cross-section (A): 3267.1278 [cm^2]
- A_y (shear area approximation): 3267.1278 [cm^2]
- A_z (shear area approximation): 3267.1278 [cm^2]
- Torsional constant (I_t): 1000290.47 [cm^4]
- Moment of inertia about y-axis (I_zz) (I_y): 1348825.59 [cm^4]
- Moment of inertia about z-axis (I_yy) (I_z): 9502157.92 [cm^4]
- Width b: 1815.00 [mm]
- Height h: 502.9710 [mm]

Height of 450 mm

The cross-section is shown in Figure 187.

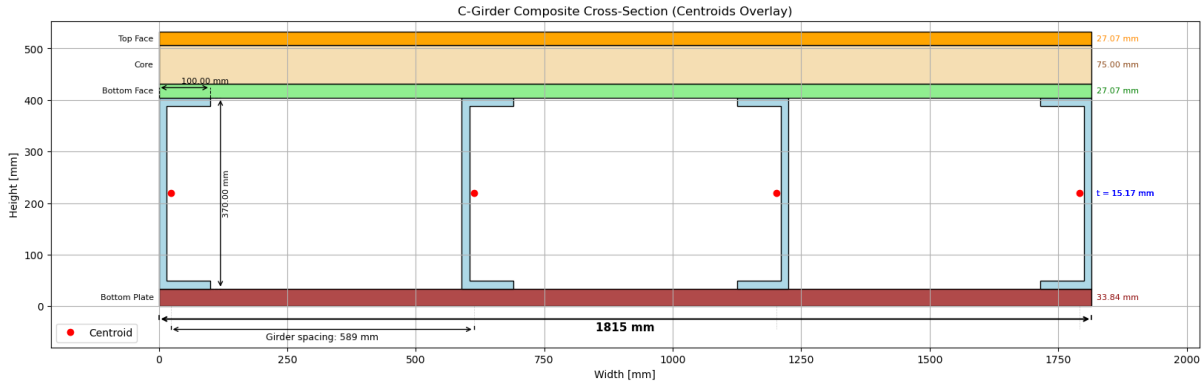

Figure 187: Cross-section height 450 mm

Material properties for RFEM input beam model:

- Young's modulus (E): 8621.23 [MPa]
- Shear modulus (G): 3457.95 [MPa]
- Poisson's ratio (nu_12): 0.246580
- Total density of the cross-section (rho_total): 811.36 [kg/m^3]
- Weight of the cross-section (gamma_total): 8.1136 [kN/m^3]
- Total area of the cross-section (A): 3285.3282 [cm^2]
- A_y (shear area approximation): 3285.3282 [cm^2]
- A_z (shear area approximation): 3285.3282 [cm^2]
- Torsional constant (I_t): 1123233.91 [cm^4]
- Moment of inertia about y-axis (I_zz) (I_y): 1544237.53 [cm^4]
- Moment of inertia about z-axis (I_yy) (I_z): 9586376.77 [cm^4]
- Width b: 1815.00 [mm]
- Height h: 532.9710 [mm]

Height of 480 mm

The cross-section is shown in Figure 188.

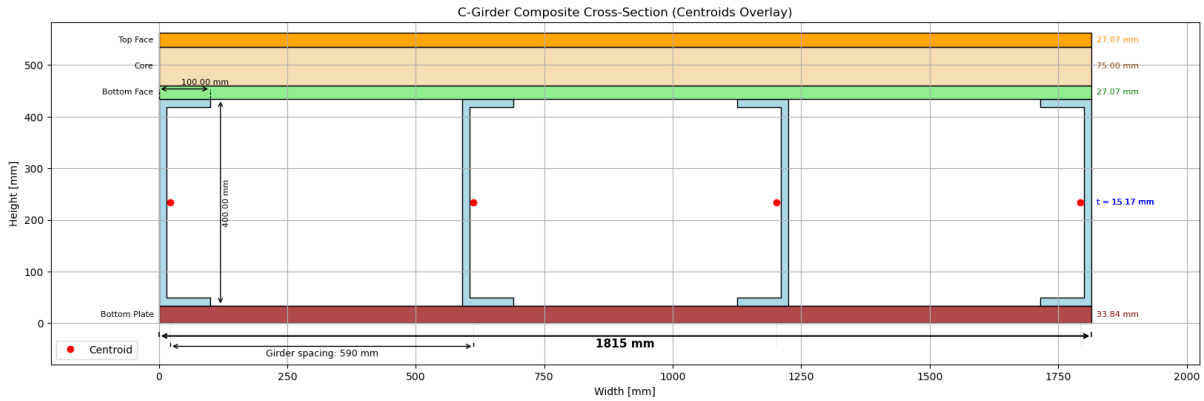

Figure 188: Cross-section height 480 mm

Material properties for RFEM input beam model:

- Young's modulus (E): 8625.01 [MPa]
- Shear modulus (G): 3459.47 [MPa]
- Poisson's ratio (nu_12): 0.246580
- Total density of the cross-section (rho_total): 814.32 [kg/m^3]
- Weight of the cross-section (gamma_total): 8.1432 [kN/m^3]
- Total area of the cross-section (A): 3303.5286 [cm^2]
- A_y (shear area approximation): 3303.5286 [cm^2]
- A_z (shear area approximation): 3303.5286 [cm^2]
- Torsional constant (I_t): 1250729.02 [cm^4]
- Moment of inertia about y-axis (I_zz) (I_y): 1753787.28 [cm^4]
- Moment of inertia about z-axis (I_yy) (I_z): 9670565.78 [cm^4]
- Width b: 1815.00 [mm]
- Height h: 562.9710 [mm]

Height of 500 mm

The cross-section is shown in Figure 189.

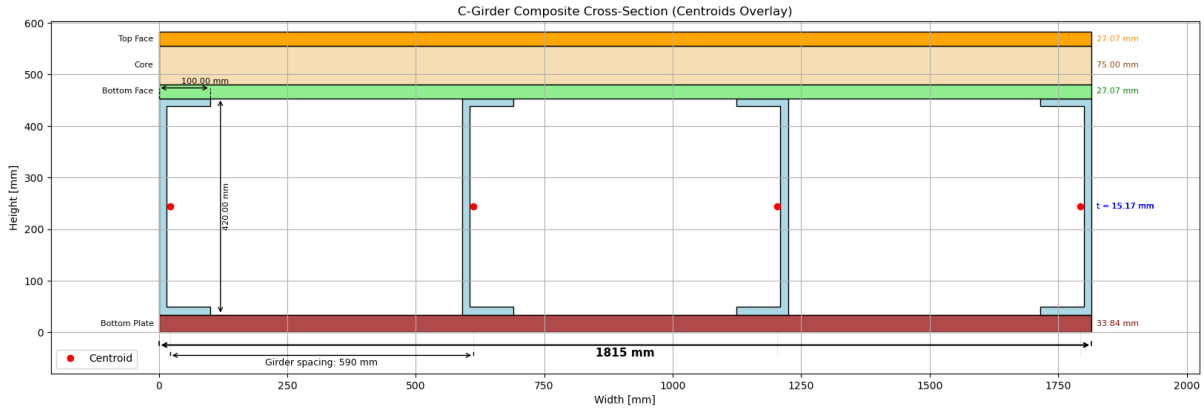

Figure 189: Cross-section height 500 mm

Material properties for RFEM input beam model:

- Young's modulus (E): 8627.51 [MPa]
- Shear modulus (G): 3460.47 [MPa]
- Poisson's ratio (nu_12): 0.246580
- Total density of the cross-section (rho_total): 816.28 [kg/m^3]
- Weight of the cross-section (gamma_total): 8.1628 [kN/m^3]
- Total area of the cross-section (A): 3315.6622 [cm^2]
- A_y (shear area approximation): 3315.6622 [cm^2]
- A_z (shear area approximation): 3315.6622 [cm^2]
- Torsional constant (I_t): 1338112.95 [cm^4]
- Moment of inertia about y-axis (I_zz) (I_y): 1901381.48 [cm^4]
- Moment of inertia about z-axis (I_yy) (I_z): 9726675.62 [cm^4]
- Width b: 1815.00 [mm]
- Height h: 582.9710 [mm]

Height of 520 mm

The cross-section is shown in Figure 190.

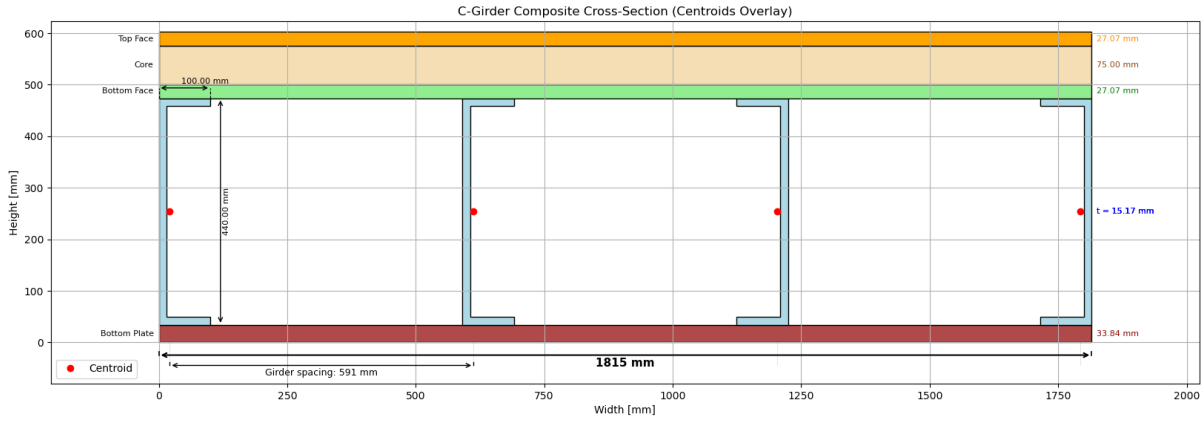

Figure 190: Cross-section height 520 mm

Material properties for RFEM input beam model:

- Young's modulus (E): 8629.99 [MPa]
- Shear modulus (G): 3461.47 [MPa]
- Poisson's ratio (nu_12): 0.246580
- Total density of the cross-section (rho_total): 818.23 [kg/m^3]
- Weight of the cross-section (gamma_total): 8.1823 [kN/m^3]
- Total area of the cross-section (A): 3327.7958 [cm^2]
- A_y (shear area approximation): 3327.7958 [cm^2]
- A_z (shear area approximation): 3327.7958 [cm^2]
- Torsional constant (I_t): 1427314.25 [cm^4]
- Moment of inertia about y-axis (I_zz) (I_y): 2055319.21 [cm^4]
- Moment of inertia about z-axis (I_yy) (I_z): 9782772.82 [cm^4]
- Width b: 1815.00 [mm]
- Height h: 602.9710 [mm]

Height of 580 mm

The cross-section is shown in Figure 191.

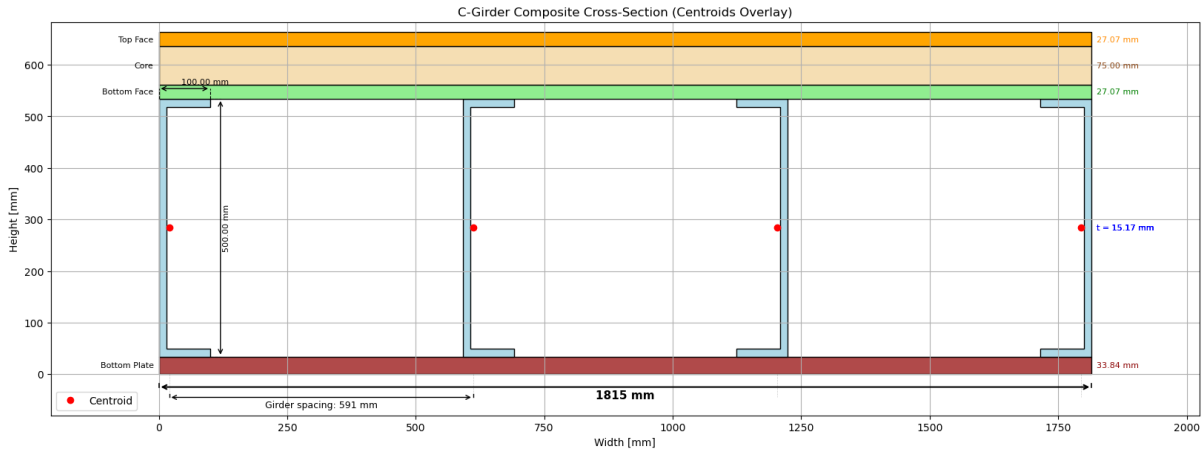

Figure 191: Cross-section height 580 mm

Material properties for RFEM input beam model:

- Young's modulus (E): 8637.32 [MPa]
- Shear modulus (G): 3464.41 [MPa]
- Poisson's ratio (nu_12): 0.246580
- Total density of the cross-section (rho_total): 823.98 [kg/m^3]
- Weight of the cross-section (gamma_total): 8.2398 [kN/m^3]
- Total area of the cross-section (A): 3364.1966 [cm^2]
- A_y (shear area approximation): 3364.1966 [cm^2]
- A_z (shear area approximation): 3364.1966 [cm^2]
- Torsional constant (I_t): 1705096.96 [cm^4]
- Moment of inertia about y-axis (I_zz) (I_y): 2555433.86 [cm^4]
- Moment of inertia about z-axis (I_yy) (I_z): 9950990.59 [cm^4]
- Width b: 1815.00 [mm]
- Height h: 662.9710 [mm]

Height of 700 mm

The cross-section is shown in Figure 192.

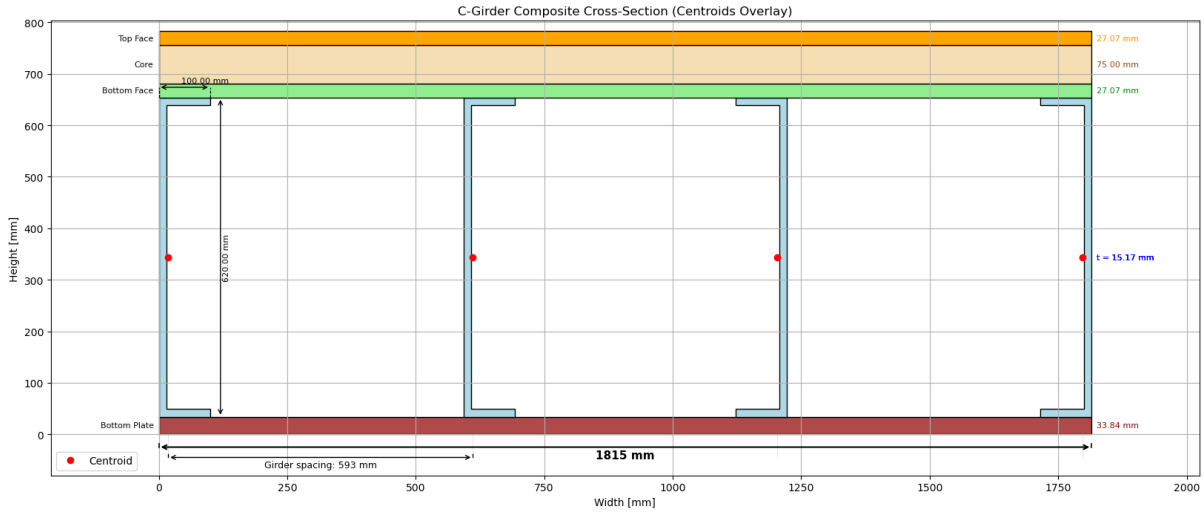

Figure 192: Cross-section height 700 mm

Material properties for RFEM input beam model:

- Young's modulus (E): 8651.52 [MPa]
- Shear modulus (G): 3470.10 [MPa]
- Poisson's ratio (nu_12): 0.246580
- Total density of the cross-section (rho_total): 835.12 [kg/m^3]
- Weight of the cross-section (gamma_total): 8.3512 [kN/m^3]
- Total area of the cross-section (A): 3436.9982 [cm^2]
- A_y (shear area approximation): 3436.9982 [cm^2]
- A_z (shear area approximation): 3436.9982 [cm^2]
- Torsional constant (I_t): 2300801.47 [cm^4]
- Moment of inertia about y-axis (I_zz) (I_y): 3730182.42 [cm^4]
- Moment of inertia about z-axis (I_yy) (I_z): 10287110.73 [cm^4]
- Width b: 1815.00 [mm]
- Height h: 782.9710 [mm]

Height of 780 mm

The cross-section is shown in Figure 193.

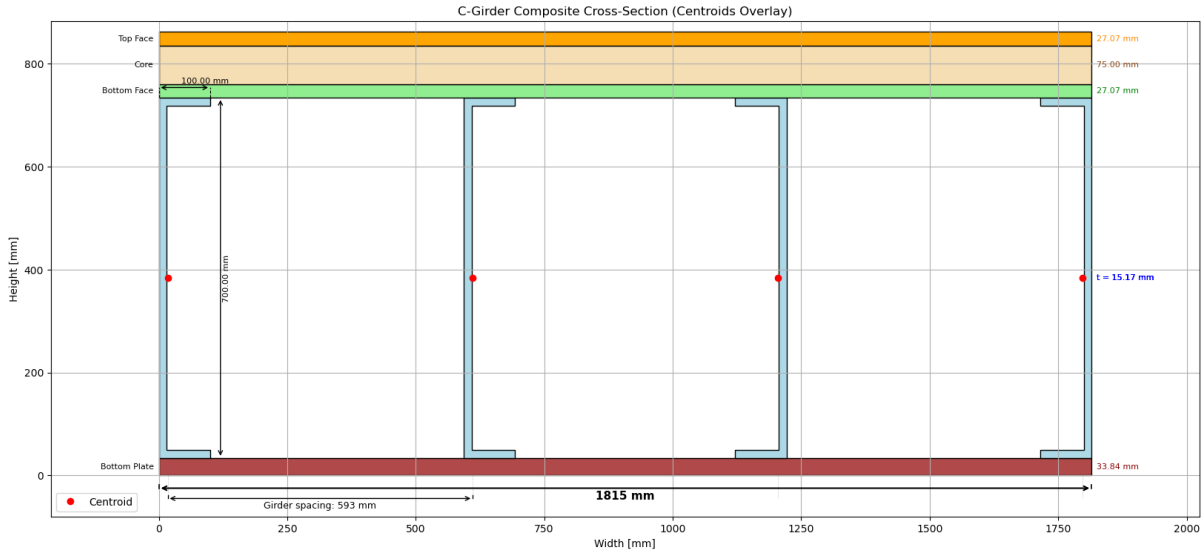

Figure 193: Cross-section height 780 mm

Material properties for RFEM input beam model:

- Young's modulus (E): 8660.66 [MPa]
- Shear modulus (G): 3473.77 [MPa]
- Poisson's ratio (nu_12): 0.246580
- Total density of the cross-section (rho_total): 842.29 [kg/m^3]
- Weight of the cross-section (gamma_total): 8.4229 [kN/m^3]
- Total area of the cross-section (A): 3485.5326 [cm^2]
- A_y (shear area approximation): 3485.5326 [cm^2]
- A_z (shear area approximation): 3485.5326 [cm^2]
- Torsional constant (I_t): 2723091.81 [cm^4]
- Moment of inertia about y-axis (I_zz) (I_y): 4644704.62 [cm^4]
- Moment of inertia about z-axis (I_yy) (I_z): 10510971.17 [cm^4]
- Width b: 1815.00 [mm]
- Height h: 862.9710 [mm]

Height of 840 mm

The cross-section is shown in Figure 194.

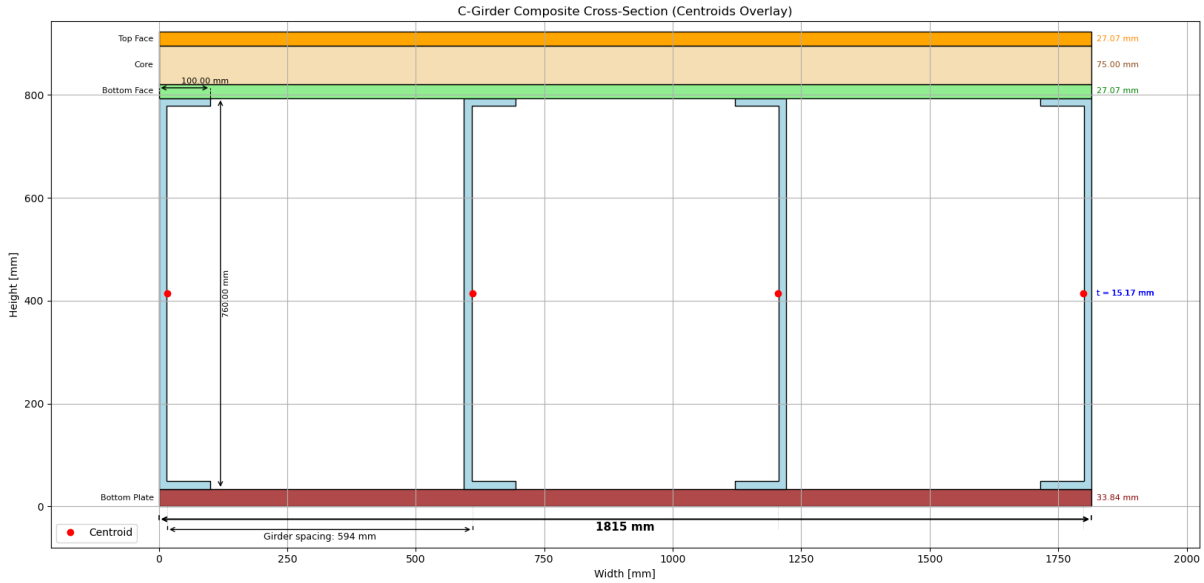

Figure 194: Cross-section height 840 mm

Material properties for RFEM input beam model:

- Young's modulus (E): 8667.35 [MPa]
- Shear modulus (G): 3476.45 [MPa]
- Poisson's ratio (nu_12): 0.246580
- Total density of the cross-section (rho_total): 847.54 [kg/m^3]
- Weight of the cross-section (gamma_total): 8.4754 [kN/m^3]
- Total area of the cross-section (A): 3521.9334 [cm^2]
- A_y (shear area approximation): 3521.9334 [cm^2]
- A_z (shear area approximation): 3521.9334 [cm^2]
- Torsional constant (I_t): 3051039.33 [cm^4]
- Moment of inertia about y-axis (I_zz) (I_y): 5400652.23 [cm^4]
- Moment of inertia about z-axis (I_yy) (I_z): 10678757.62 [cm^4]
- Width b: 1815.00 [mm]
- Height h: 922.9710 [mm]

Height of 920 mm

The cross-section is shown in Figure 195.

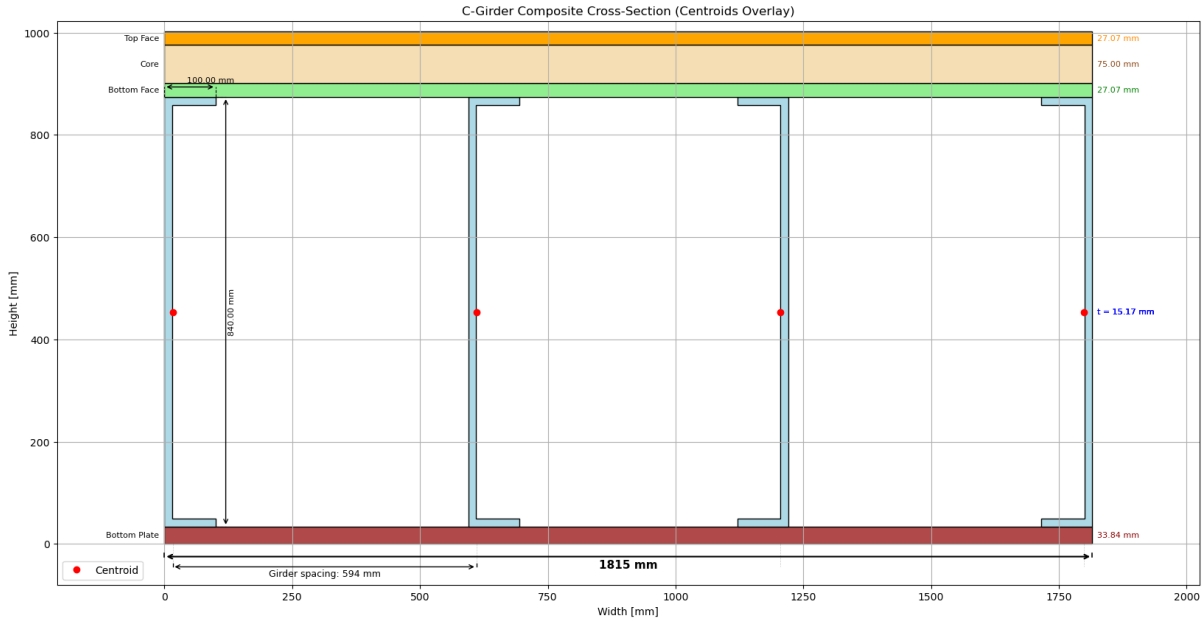

Figure 195: Cross-section height 920 mm

Material properties for RFEM input beam model:

- Young's modulus (E): 8676.05 [MPa]
- Shear modulus (G): 3479.94 [MPa]
- Poisson's ratio (nu_12): 0.246580
- Total density of the cross-section (rho_total): 854.37 [kg/m^3]
- Weight of the cross-section (gamma_total): 8.5437 [kN/m^3]
- Total area of the cross-section (A): 3570.4678 [cm^2]
- A_y (shear area approximation): 3570.4678 [cm^2]
- A_z (shear area approximation): 3570.4678 [cm^2]
- Torsional constant (I_t): 3501450.71 [cm^4]
- Moment of inertia about y-axis (I_zz) (I_y): 6503224.63 [cm^4]
- Moment of inertia about z-axis (I_yy) (I_z): 10902334.21 [cm^4]
- Width b: 1815.00 [mm]
- Height h: 1002.9710 [mm]

Height of 1000 mm

The cross-section is shown in Figure 196.

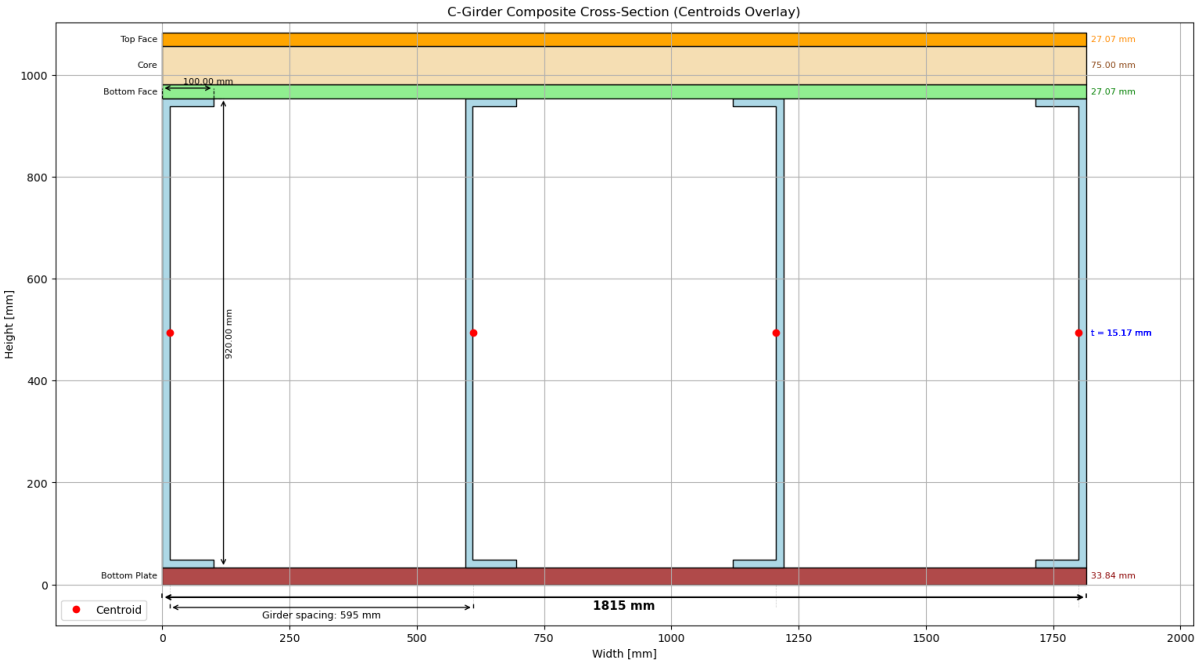

Figure 196:Cross-section height 1000 mm

Material properties for RFEM input beam model:

- Young's modulus (E): 8684.53 [MPa]
- Shear modulus (G): 3483.34 [MPa]
- Poisson's ratio (nu_12): 0.246580
- Total density of the cross-section (rho_total): 861.02 [kg/m^3]
- Weight of the cross-section (gamma_total): 8.6102 [kN/m^3]
- Total area of the cross-section (A): 3619.0022 [cm^2]
- A_y (shear area approximation): 3619.0022 [cm^2]
- A_z (shear area approximation): 3619.0022 [cm^2]
- Torsional constant (I_t): 3965123.77 [cm^4]
- Moment of inertia about y-axis (I_zz) (I_y): 7715370.54 [cm^4]
- Moment of inertia about z-axis (I_yy) (I_z): 11125759.09 [cm^4]
- Width b: 1815.00 [mm]
- Height h: 1082.9710 [mm]

Very stiff member

Material properties for RFEM input beam model for very stiff member:

- Young's modulus (E): 210000.0 [MPa]
- Shear modulus (G): 81000.0 [MPa]
- Poisson's ratio (nu_12): 0.296
- Total area of the cross-section (A): 100000.0 [cm^2]
- A_y (shear area approximation): 100000.0 [cm^2]
- A_z (shear area approximation): 100000.0 [cm^2]
- Torsional constant (I_t): 1000000.0 [cm^4]
- Moment of inertia about y-axis (I_zz) (I_y): 1000000.0 [cm^4]
- Moment of inertia about z-axis (I_yy) (I_z): 1000000.0 [cm^4]

- Width b: 5000 [mm]
- Height h: 500 [mm]

Input plate model

Input for RFEM plate model for bottom deck:

- E_x = 16722.981 [N/mm^2]
- E_y = 5241.034 [N/mm^2]
- G_yz = 1852.932 [N/mm^2]
- G_xz = 1852.932 [N/mm^2]
- G_xy = 1852.932 [N/mm^2]
- nu_xy = 0.247 [-]
- Density of the bottom deck = 1495.868 [kg/m^3]
- Weight of the bottom deck = 14.959 [kN/m^3]
- Thickness = 33.835 [mm]
- The width of the plate is 1815 [mm]
- The width of the plate from girder to girder is 1799.833 [mm]

Input for RFEM plate model for girders is:

- E_x = 9307.781 [N/mm^2]
- E_y = 9307.781 [N/mm^2]
- G_yz = 2779.664 [N/mm^2]
- G_xz = 2779.664 [N/mm^2]
- G_xy = 2779.664 [N/mm^2]
- nu_xy = 0.229 [-]
- Density of the girders = 1203.923 [kg/m^3]
- Weight of the girders = 12.039 [kN/m^3]
- Thickness = 15.167 [mm]
- The representative height of the girders is 997.613
- The locations of the girders with respect to the left side of the cross-section is:
    - Girder 1 is located at 7.583 [mm]
    - Girder 2 is located at 602.338 [mm]
    - Girder 3 is located at 1212.662 [mm]
    - Girder 4 is located at 1807.417 [mm]
- The distance between the girders is:
    - Between girder 1 and girder 2 is 594.754 [mm]
    - Between girder 2 and girder 3 is 610.325 [mm]
    - Between girder 3 and girder 4 is 594.754 [mm]

(The spacing between the girders and their locations varies slightly; however, the properties of the 1000 mm cross-section have been adopted. The density also varies slightly, and the density of the 1000 mm cross-section has been selected, as this value is the maximum.)

Input for RFEM plate model for top deck:

- E_x = 6874.605 [N/mm^2]
- E_y = 2202.821 [N/mm^2]
- G_yz = 779.684 [N/mm^2]
- G_xz = 779.684 [N/mm^2]
- G_xy = 779.684 [N/mm^2]
- nu_xy = 0.247 [-]
- nu_yx = 0.082 [-]
- Density of the top deck = 635.234 [kg/m^3]
- Weight of the top deck = 6.352 [kN/m^3]
- Thickness = 129.136 [mm]
- The width of the plate is 1815 [mm]
- The width of the plate from girder to girder is 1799.833 [mm]

Input for RFEM plate model for support plate:

- E_x = 9307.781 [N/mm^2]
- E_y = 9307.781 [N/mm^2]
- G_yz = 2779.664 [N/mm^2]
- G_xz = 2779.664 [N/mm^2]
- G_xy = 2779.664 [N/mm^2]
- nu_xy = 0.229 [-]
- nu_yx = 0.229 [-]
- Density of the support plate = 1320.0 [kg/m^3]
- Weight of the support plate = 13.20 [kN/m^3]
- Thickness = 45.50 [mm]

Input for RFEM plate model for top side plate:

- E_x = 15822 [N/mm^2]
- E_y = 5241 [N/mm^2]
- G_yz = 1853 [N/mm^2]
- G_xz = 1853 [N/mm^2]
- G_xy = 1853 [N/mm^2]
- nu_xy = 0.247 [-]
- nu_yx = 0.082 [-]
- Density of the side plate = 1320.0 [kg/m^3]
- Weight of the side plate = 13.20 [kN/m^3]
- Thickness = 33.84 [mm]

Input for RFEM plate model for bottom side plate:

- E_x = 15822 [N/mm^2]
- E_y = 5241 [N/mm^2]
- G_yz = 1853 [N/mm^2]
- G_xz = 1853 [N/mm^2]
- G_xy = 1853 [N/mm^2]
- nu_xy = 0.247 [-]
- nu_yx = 0.082 [-]
- Density of the side plate = 1320.0 [kg/m^3]
- Weight of the side plate = 13.20 [kN/m^3]
- Thickness = 33.84 [mm]

Input for RFEM plate model for arch side plate:

- E_x = 15822 [N/mm^2]
- E_y = 5241 [N/mm^2]
- G_yz = 1853 [N/mm^2]
- G_xz = 1853 [N/mm^2]
- G_xy = 1853 [N/mm^2]
- nu_xy = 0.247 [-]
- nu_yx = 0.082 [-]
- Density of the side plate = 1320.0 [kg/m^3]
- Weight of the side plate = 13.20 [kN/m^3]
- Thickness = 33.84 [mm]

Input for RFEM plate model for stiffener plates:

- E_x = 9307.781 [N/mm^2]
- E_y = 9307.781 [N/mm^2]
- G_yz = 2779.664 [N/mm^2]
- G_xz = 2779.664 [N/mm^2]
- G_xy = 2779.664 [N/mm^2]
- nu_xy = 0.229 [-]
- nu_yx = 0.229 [-]
- Density of the side plate = 1320.0 [kg/m^3]
- Weight of the side plate = 13.20 [kN/m^3]
- Thickness = 9.10 [mm]

Appendix N: x-coordinates support and stiffener plates preliminary design

The support plates lie in the yz-plane; therefore, a single x-coordinate defines the position of each entire support plate. The x-coordinates given for the stiffener plates correspond to the points on the plates closest to $y = 0$, since the stiffener plates do not lie in the yz-plane.

Support plates x-coordinate [m]	Stiffener plates x-coordinate (for points closest to y = 0) [m]
	-24.288 (Side deck)
	-22.145 (Side deck)
-20.672	-20.672 (Lower deck) (Upper deck)
-19.718	-19.718 (Lower deck)
-18.428	-18.428 (Lower deck) (Upper deck)
-17.143	-17.143 (Lower deck)
-16.003	-16.003 (Lower deck) (Upper deck)
-14.584	-14.584 (Lower deck)
-13.306	-13.306 (Lower deck)
-12.905	-12.905 (Lower deck) (Upper deck)
-12.499	-12.499 (Lower deck)
-11.926 (Below side arch)	
-11.733 (On top side arch)	
-10.751 (Below side arch)	
	-10.706 (Upper deck)
-9.472 (Below side arch)	
-8.191 (Below side arch)	-8.191 (Bottom side arch) (Lower deck)
-6.908 (Below side arch)	
	-4.371 (Upper deck)
	-1.373 (Lower deck)
	0.000 (Upper deck)
	1.373 (Lower deck)
	4.371 (Upper deck)
6.908 (Below side arch)	
8.191 (Below side arch)	8.191 (Bottom side arch) (Lower deck)
9.472 (Below side arch)	
	10.706 (Upper deck)
10.751 (Below side arch)	
11.733 (On top side arch)	
11.926 (Below side arch)	
12.499	12.499 (Lower deck)
12.905	12.905 (Lower deck) (Upper deck)
13.306	13.306 (Lower deck)
14.584	14.584 (Lower deck)
16.003	16.003 (Lower deck) (Upper deck)
17.143	17.143 (Lower deck)
18.428	18.428 (Lower deck) (Upper deck)
19.718	19.718 (Lower deck)
20.672	20.672 (Lower deck) (Upper deck)
	-22.145 (Side deck)
	-24.288 (Side deck)

Table 109: x-coordinates support and stiffener plates preliminary design

Appendix O: Load combinations RFEM

The load cases in RFEM are:

- Self-weight [LC1]
- Permanent loads [LC2]
- Traffic loads
    - Full deck loaded [LC3]
    - Bottom half loaded [LC12]
    - Top half loaded [LC13]
    - Loads on one side in longitudinal direction [LC14]
    - Loads on one side in transverse direction [LC15]
    - Middle top half loaded [LC16]
    - Middle bottom half loaded [LC17]
    - One side part loaded [LC18]
    - Middle top and bottom and one side part loaded [LC19]
- Pedestrian balustrade load [LC4]
- Wind load z-direction (Downward wind load) [LC5]
- Wind load moment z-direction [LC6]
- Wind load y-direction (Parallel to dike) [LC7]
- Wind load x-direction (Perpendicular to dike) [LC8]

The traffic loads are all combined with 'OR' statements and in the equations for ULS and SLS corresponds RC38 to the combined traffic loads. Figure 197 shows the different traffic load configurations.

Table 110 shows the different combination factors for footbridges, obtained from NEN-EN 1990 annex A.2.7.5. These factors can be used in the equations for ULS and SLS. The wind load in z-direction is applied with a wind load in y-direction and a wind load in x-direction is applied with a wind load equal to the wind load in x-direction in y-direction. In the result combinations is for the plate model the -LC7 is actually LC9 and -LC5 is LC10.

Action	**Symbol**	ψ_0	ψ_1	ψ_2
Traffic loads	gr1	0.40	0.80	0.4
	gr2	0.40	0.80	0
	gr3	0.0	0.80	0
Wind forces	F_{Wk}	0.3	0.6	0
Thermal actions	T_k	0.3	0.8	0.3
Snow loads	$Q_{Sn,k}$ Persistent design situations	0	0	0

Table 110: Combination factors for footbridges, obtained from NEN-EN 1990 NB13

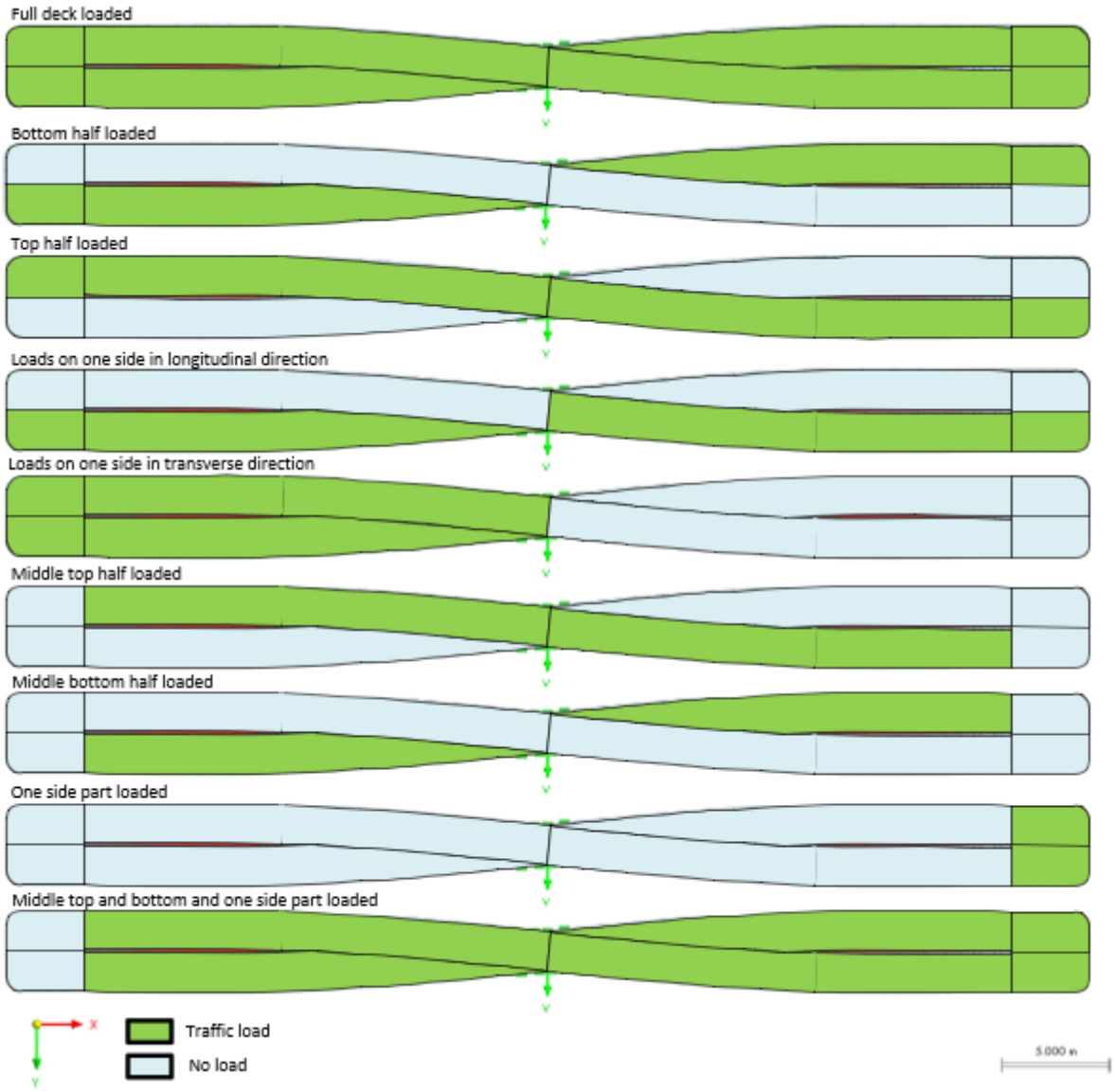

Figure 197: Overview of the different traffic load configurations

Ultimate Limit State (ULS)

According to NEN EN 1990, the load on the structure for ULS can be determined with the equation:

$$\sum F_d = \sum_i \gamma_{G,i} G_{k,i} + \gamma_{Q,1} Q_{k,1} + \sum_{j>1} \gamma_{Q,j} \psi_{0,j} Q_{k,j}$$

Where:

$G_{k,i}$	is the characteristic value of permanent action i
$\gamma_{G,i}$	is the partial factor for permanent action i
$Q_{k,1}$	is the characteristic value of the leading variable action 1
$\gamma_{Q,1}$	is the partial factor for the leading variable action 1
$Q_{k,j}$	is the characteristic value of an accompanying variable action j
$\gamma_{Q,j}$	is the partial factor for the variable action j
$\psi_{0,\mathrm{j}}$	is the combination factor for the variable action j

The combination factors are shown in Table 110 and the partial factors are shown in Table 111. When variations in the magnitude or spatial variation of permanent actions from the same source are significant, ultimate limit states that involve loss of static equilibrium should be verified using partial factors for verification cases VC2(a) and VC2(b) using whichever gives the less favourable design outcome. Verification of verification case VC2(b) may be omitted when it is obvious that verification using verification case VC2(a) governs the design outcome.

Action or effect				Partial factors γ_F and γ_E for verification cases		
Type	Group	Symbol	Resulting effect	Structural resistance	Combined structural resistance and static equilibrium / uplift	
Verification case				VC1	VC2(a)	VC2(b)
Permanent action (G_k)	All	γ_G	unfavourable/ destabilizing	1.35	1.35	1.0
Variable action (Q_k)	Road/ pedestrian traffic		unfavourable	1.35	1.35	1.35
	Other	γ_Q	unfavourable	1.5	1.5	1.5
	All	$\gamma_{Q,fav}$	favourable	0		

Table 111: Partial factors, obtained from NEN-EN 1990

The result combinations for ULS are:

$$1.35 * LC1 + 1.35 * LC2 + 1.35 * RC38 + 0.54 * LC4 + 0.45 * (+LC5\ or - LC5) + 0.45 * (+LC6\ or - LC6) + 0.45 * (+LC7\ or - LC7)$$

$$1.35 * LC1 + 1.35 * LC2 + 1.35 * RC38 + 0.54 * LC4 + 0.18 * (+LC7\ or - LC7) + 0.45 * (+LC8\ or - LC8)$$

$$1.35 * LC1 + 1.35 * LC2 + 0.54 * RC38 + 1.35 * LC4 + 0.45 * (+LC5\ or - LC5) + 0.45 * (+LC6\ or - LC6) + 0.45 * (+LC7\ or - LC7)$$

$$1.35 * LC1 + 1.35 * LC2 + 0.54 * RC38 + 1.35 * LC4 + 0.18 * (+LC7\ or - LC7) + 0.45 * (+LC8\ or - LC8)$$

$$1.35 * LC1 + 1.35 * LC2 + 0.54 * RC38 + 0.54 * LC4 + 1.5 * (+LC5\ or - LC5) + 1.5 * (+LC6\ or - LC6) + 0.45 * (+LC7\ or - LC7)$$

$$1.35 * LC1 + 1.35 * LC2 + 0.54 * RC38 + 0.54 * LC4 + 0.45 * (+LC5\ or - LC5) + 0.45 * (+LC6\ or - LC6) + 1.5 * (+LC7\ or - LC7)$$

$$1.35 * LC1 + 1.35 * LC2 + 0.54 * RC38 + 0.54 * LC4 + 0.6 * (+LC7\ or - LC7) + 1.5 * (+LC8\ or - LC8)$$

Serviceability limit state (SLS)

For the serviceability limit state there are three different combinations the characteristic, frequent and quasi-permanent combination, according to NEN EN 1990. The characteristic combination is used for irreversible limit state, the frequent combination is used for reversible limit state and the quasi-permanent combination is used for long-term effects and for the appearance of the structure.

Characteristic combination

The load on the structure for the characteristic combination can be determined with the equation:

$$\sum F_d = \sum_i G_{k,i} + Q_{k,1} + \sum_{j>1} \psi_{0,j} Q_{k,j}$$

Where:

$G_{k,i}$ is the characteristic value of permanent action i

$Q_{k,1}$ is the characteristic value of the leading variable action 1

$Q_{k,j}$ is the characteristic value of an accompanying variable action j

$\psi_{0,\mathrm{j}}$ is the combination factor for the variable action j

The result combinations for SLS characteristic are:

$$1 * LC1 + 1 * LC2 + 1 * RC38 + 0.4 * LC4 + 0.3 * (+LC5\ or - LC5) + 0.3 * (+LC6\ or - LC6) + 0.3 * (+LC7\ or - LC7)$$

$$1 * LC1 + 1 * LC2 + 1 * RC38 + 0.4 * LC4 + 0.12 * (+LC7\ or - LC7) + 0.3 * (+LC8\ or - LC8)$$

$$1 * LC1 + 1 * LC2 + 0.4 * RC38 + 1 * LC4 + 0.3 * (+LC5\ or - LC5) + 0.3 * (+LC6\ or - LC6) + 0.3 * (+LC7\ or - LC7)$$

$$1 * LC1 + 1 * LC2 + 0.4 * RC38 + 1 * LC4 + 0.12 * (+LC7\ or - LC7) + 0.3 * (+LC8\ or - LC8)$$

$$1 * LC1 + 1 * LC2 + 0.4 * RC38 + 0.4 * LC4 + 1 * (+LC5\ or - LC5) + 1 * (+LC6\ or - LC6) + 0.3 * (+LC7\ or - LC7)$$

$$1 * LC1 + 1 * LC2 + 0.4 * RC38 + 0.4 * LC4 + 0.3 * (+LC5\ or - LC5) + 0.3 * (+LC6\ or - LC6) + 1 * (+LC7\ or - LC7)$$

$$1 * LC1 + 1 * LC2 + 0.4 * RC38 + 0.4 * LC4 + 0.4 * (+LC7\ or - LC7) + 1 * (+LC8\ or - LC8)$$

Frequent combination

The load on the structure for the frequent combination can be determined with the equation:

$$\sum F_d = \sum_i G_{k,i} + \psi_{1,1} Q_{k,1} + \sum_{j>1} \psi_{2,j} Q_{k,j}$$

Where:

$G_{k,i}$ is the characteristic value of permanent action i

$Q_{k,1}$ is the characteristic value of the leading variable action 1

$\psi_{1,1}$ is the combination factor for the variable action 1

$Q_{k,j}$ is the characteristic value of an accompanying variable action j

$\psi_{2,j}$ is the combination factor for the variable action j

The result combinations for SLS frequent are:

$$1 * LC1 + 1 * LC2 + 0.8 * RC38$$

$$1 * LC1 + 1 * LC2 + 0.4 * RC38 + 0.8 * LC4$$

$$1 * LC1 + 1 * LC2 + 0.4 * RC38 + 0.6 * (+LC5\ or - LC5) + 0.6 * (+LC6\ or - LC6)$$

$$1 * LC1 + 1 * LC2 + 0.4 * RC38 + 0.6 * (+LC7\ or - LC7)$$

Quasi-permanent combination

The load on the structure for the quasi-permanent combination can be determined with the equation:

$$\sum F_d = \sum_i G_{k,i} + \sum_j \psi_{2,j} Q_{k,j}$$

Where:

$G_{k,i}$ is the characteristic value of permanent action i

$Q_{k,j}$ is the characteristic value of an accompanying variable action j

$\psi_{2,j}$ is the combination factor for the variable action j

The result combinations for SLS quasi-permanent are:

$$1 * LC1 + 1 * LC2$$

Appendix P: Description of the beam model

The beam model was created by extracting several coordinates from the imported Rhino model into RFEM. The selected coordinates correspond to points located along the centreline of the deck. The cross-sections of the deck were defined by averaging the deck height within each corresponding segment. The resulting heights are shown in Figure 198. Since the transformed Rhino model will also be used for the plate model, these heights are equal to the height of the vertical girders of the plate model. This approach avoids the need to modify the deck height within the model. For the same reason, the width of the cross-section is slightly increased. A width [b] of 1815 mm is adopted in order to achieve an effective width of 1800 mm in the plate model. The cross-sectional geometry and corresponding properties implemented in RFEM are provided in Appendix M which are determined with the python code given in Appendix H. The RFEM model is shown in Figure 199.

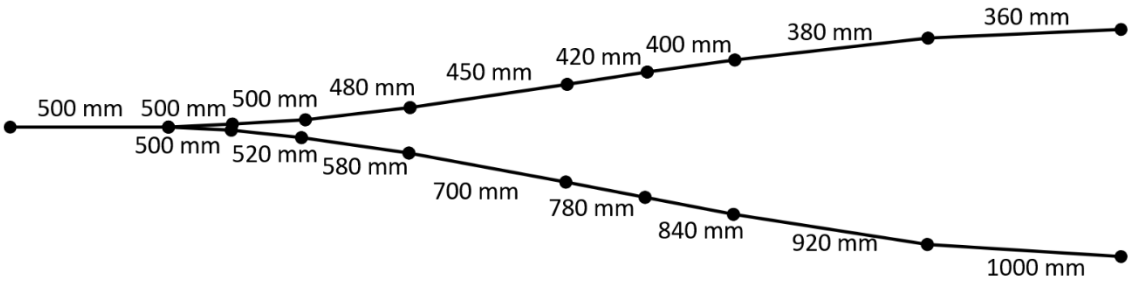

Figure 198: Height cross-section of half of the Seasaw

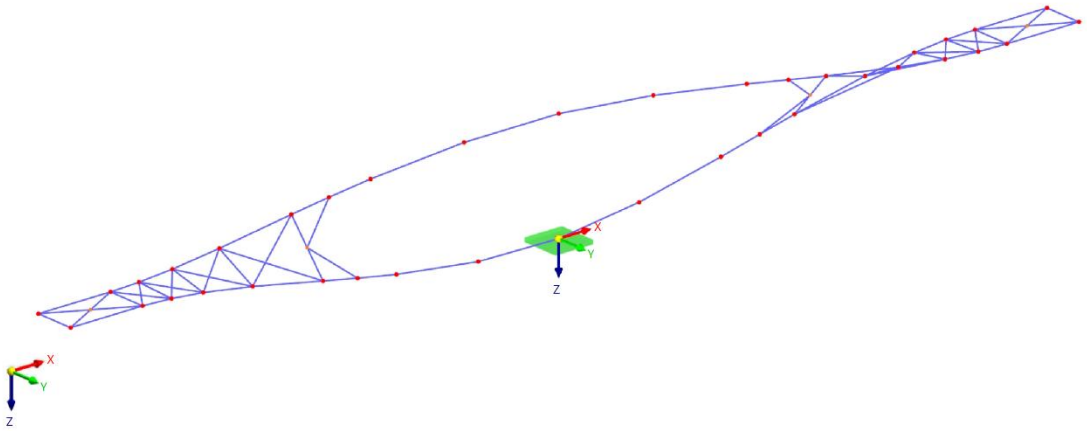

Figure 199: Beam model Seasaw

Boundary conditions

The model is fully clamed at the lowest point [0, 0, 0]. This boundary condition restrains all translational and rotational degrees of freedom, ensuring a fixed support at the base of the system.

The upper and lower parts of the Seasaw are connected to each other using very stiff members without density, which provide structural continuity between both components. The properties of these members are given in Appendix M. These members transfer forces and bending moments between the two parts, ensuring that the system behaves as a single integrated structure rather than as separate elements. These members are only applied on locations where the upper and lower parts of the structure are connected, see Figure 199.

Loads

The load cases in RFEM are:

- Self-weight [LC1]
- Permanent loads [LC2]
- Traffic loads
  - Full deck loaded [LC3]
  - Bottom half loaded [LC12]
  - Top half loaded [LC13]
  - Loads on one side in longitudinal direction [LC14]
  - Loads on one side in transverse direction [LC15]
  - Middle top half loaded [LC16]
  - Middle bottom half loaded [LC17]
  - One side part loaded [LC18]
  - Middle top and bottom and one side part loaded [LC19]
- Pedestrian balustrade load [LC4]
- Wind load z-direction (Downward wind load) [LC5]
- Wind load moment z-direction [LC6]
- Wind load y-direction (Parallel to dike) [LC7]
- Wind load x-direction (Perpendicular to dike) [LC8]

The load and result combinations are provided in Appendix O, including overview figures showing an overview of the different traffic load configurations. All the loads are applied in the directions of the global coordinate system to get a good comparison to the plate model were also all loads are applied in the direction of the global coordinate system.

Self-Weight

The load in this load case is automatically computed in RFEM. RFEM uses the densities of the materials put into RFEM.

Permanent loads

Balustrade

The distributed line load of the balustrade is:

$$q_{balustrade} = 0.8\ kN/m$$

This load is applied twice on the bridge deck in z-direction.

Wear surface

The distributed area load of the wear surface is:

$$p_{wearing} = 0.20\ kN/m^2$$

The distributed line load of the wear surface is:

$$q_{wearing} = 0.20 * 1.82 = 0.364\ kN/m$$

This load is applied on the bridge deck in z-direction.

Coating

The distributed area load of the coating is:

$$p_{coating} = 0.006\ kN/m^2$$

The coating is applied to all the elements in the bridge deck and the load will be different for the different heights of the cross-section. The load per different height cross-section can be calculated with:

$$q_{coating} = 0.006 * \left(b_{bp} * 2 + b_{tf} * 2 + 4 * h_{girder} * 2\right) [kN/m]$$

$$q_{coating} = 0.006 * \left(1.82 * 2 + 1.82 * 2 + 4 * h_{girder} * 2\right) [kN/m]$$

$$q_{coating} = 0.044 + 0.048 * h_{girder} [kN/m]$$

The loads for the cross-sections are:

- $h = 1000\ mm$: $q_{coating} = 0.092\ kN/m$
- $h = 920\ mm$: $q_{coating} = 0.088\ kN/m$
- $h = 840\ mm$: $q_{coating} = 0.084\ kN/m$
- $h = 780\ mm$: $q_{coating} = 0.081\ kN/m$
- $h = 700\ mm$: $q_{coating} = 0.078\ kN/m$
- $h = 580\ mm$: $q_{coating} = 0.072\ kN/m$
- $h = 520\ mm$: $q_{coating} = 0.069\ kN/m$
- $h = 500\ mm$: $q_{coating} = 0.068\ kN/m$
- $h = 480\ mm$: $q_{coating} = 0.067\ kN/m$
- $h = 450\ mm$: $q_{coating} = 0.066\ kN/m$
- $h = 420\ mm$: $q_{coating} = 0.064\ kN/m$
- $h = 400\ mm$: $q_{coating} = 0.063\ kN/m$
- $h = 380\ mm$: $q_{coating} = 0.062\ kN/m$
- $h = 360\ mm$: $q_{coating} = 0.061\ kN/m$

These distributed line loads are applied on their corresponding bridge deck in z-direction.

Bonding paste

The distributed area load of the bonding paste is:

$$p_{paste} = 0.05\ kN/m^2$$

The distributed line load of the bonding paste is:

$$q_{paste} = 0.05 * 0.1 = 0.005\ kN/m$$

The paste is applied at the bottom and top of the C-shaped girders. The load which is applied on the bridge deck in z-direction is:

$$q_{paste} = 0.005 * 4 * 2 = 0.04\ kN/m$$

Resin absorption of the core material

The distributed area load of the resin absorption is:

$$p_{resin} = 0.005\ kN/m^2$$

The distributed line load of the resin absorption is:

$$q_{resin} = 0.005 * 1.82 = 0.0091\ kN/m$$

This load is applied on the bridge deck in z-direction.

Traffic loads

The bridge has a length of 50 meters. The distributed traffic load is:

$$q_{fk} = 2.0 + \frac{120}{L + 30} = 2.0 + \frac{120}{50 + 30} = 3.5 \left[\frac{kN}{m^2}\right]$$

The distributed traffic load in [kN/m] is:

$$q_{fk} = 3.5 * 1.8 = 6.3\ kN/m$$

This load is applied on the bridge deck in z-direction for the different configurations.

For traffic loads a horizontal force Q_{flk} should be taken into account, acting along the bridge deck axis at the pavement level. The characteristic value of the horizontal force is 10 % of the total load corresponding to the uniformly distributed load. The load is:

$$q_{fk} = 6.3 * 0.10 = 0.63\ kN/m$$

The horizontal force shall be considered as acting simultaneously with the corresponding vertical load. The load is applied on the bridge deck in x-direction in the same configurations as the distributed traffic load.

Pedestrian balustrade load

The distributed line load of pedestrians on the balustrade is:

$$q_{ped,balustrade} = 1.0\ kN/m$$

This load is applied twice on the bridge deck in z-direction.

Wind load in z-direction

The distributed wind load in z-direction on the bridge deck is:

$$q_{w,z} = 881.1\ [N/m] = 0.881\ [kN/m]$$

This load is applied on the bridge deck in z-direction.

Wind load moment z-direction

The distributed wind load in z-direction on the bridge deck is:

$$q_{w,z} = 881.1\ [N/m] = 0.881\ [kN/m]$$

The load has an eccentricity of $e = 450\ [mm]$. This eccentricity results in a bending moment of:

$$m_{w,x} = 0.881 * 0.450 = 0.40\ kNm/m$$

This bending moment is applied on the structure with a load downwards at one side and upwards on the other. To determine the size of the load a value of 1 for the load is used on one side and -1 on the other. This results in a bending moment of 76.32 kN/m. The total bending moment because of the wind of the structure is:

$$M_{w,x} = m_{w,x} * l = 0.40 * 50 = 20\ kNm$$

This means that the value 1 should be rescaled by a factor of:

$$\frac{20}{76.32} = 0.26$$

A load of 0.26 kN/m in z-direction is applied on the negative y side of the structure and a load of -0.26 in z-direction on the positive y side, see Figure 200.

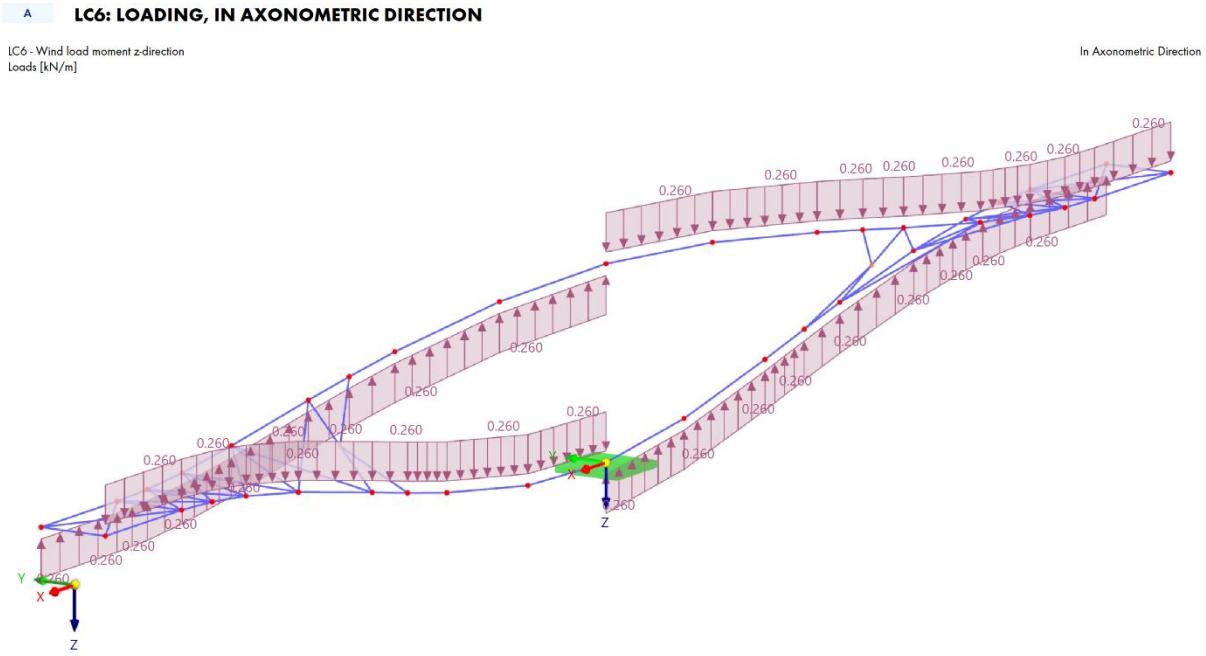

Figure 200: Bending moment wind load z-direction beam model

Wind load in y-direction

The distributed wind load in y-direction on the bridge deck is:

$$q_{w,x} = 2855.5 * d_{tot}\ [N/m] = 2.8555 * d_{tot}\ [kN/m]$$

With $d_{tot} = 0.6 + d\ [m]$

The load is for each cross-section different. The loads for the cross-sections are:

- $h = 1000\ mm$: $d = 1092.07\ [mm]$, $d_{tot} = 1.692\ [m]$, $q_{w,x} = 4.83\ [kN/m]$
- $h = 920\ mm$: $d = 1012.07\ [mm]$, $d_{tot} = 1.612\ [m]$, $q_{w,x} = 4.60\ [kN/m]$
- $h = 840\ mm$: $d = 932.07\ [mm]$, $d_{tot} = 1.532\ [m]$, $q_{w,x} = 4.38\ [kN/m]$
- $h = 780\ mm$: $d = 872.07\ [mm]$, $d_{tot} = 1.472\ [m]$, $q_{w,x} = 4.20\ [kN/m]$
- $h = 700\ mm$: $d = 792.07\ [mm]$, $d_{tot} = 1.392\ [m]$, $q_{w,x} = 3.98\ [kN/m]$
- $h = 580\ mm$: $d = 672.07\ [mm]$, $d_{tot} = 1.272\ [m]$, $q_{w,x} = 3.63\ [kN/m]$
- $h = 520\ mm$: $d = 612.07\ [mm]$, $d_{tot} = 1.212\ [m]$, $q_{w,x} = 3.46\ [kN/m]$
- $h = 500\ mm$: $d = 592.07\ [mm]$, $d_{tot} = 1.192\ [m]$, $q_{w,x} = 3.40\ [kN/m]$
- $h = 480\ mm$: $d = 572.07\ [mm]$, $d_{tot} = 1.172\ [m]$, $q_{w,x} = 3.35\ [kN/m]$
- $h = 450\ mm$: $d = 542.07\ [mm]$, $d_{tot} = 1.142\ [m]$, $q_{w,x} = 3.26\ [kN/m]$
- $h = 420\ mm$: $d = 512.07\ [mm]$, $d_{tot} = 1.112\ [m]$, $q_{w,x} = 3.18\ [kN/m]$
- $h = 400\ mm$: $d = 492.07\ [mm]$, $d_{tot} = 1.092\ [m]$, $q_{w,x} = 3.12\ [kN/m]$
- $h = 380\ mm$: $d = 472.07\ [mm]$, $d_{tot} = 1.072\ [m]$, $q_{w,x} = 3.06\ [kN/m]$
- $h = 360\ mm$: $d = 452.07\ [mm]$, $d_{tot} = 1.052\ [m]$, $q_{w,x} = 3.00\ [kN/m]$

These distributed line loads are applied on their corresponding bridge deck in y-direction.

Wind load in x-direction

The distributed wind load in x-direction on the bridge deck is:

$$q_{w,y} = 0.4 * q_{w,x} = 1142.2 * d_{tot}\ [N/m] = 1.1422 * d_{tot}\ [kN/m]$$

The load is for each cross-section different. The loads for the cross-sections are:

- $h = 1000\ mm$: $q_{w,y} = 1.93\ [kN/m]$
- $h = 920\ mm$: $q_{w,y} = 1.84\ [kN/m]$
- $h = 840\ mm$: $q_{w,y} = 1.75\ [kN/m]$
- $h = 780\ mm$: $q_{w,y} = 1.68\ [kN/m]$
- $h = 700\ mm$: $q_{w,y} = 1.59\ [kN/m]$
- $h = 580\ mm$: $q_{w,y} = 1.45\ [kN/m]$
- $h = 520\ mm$: $q_{w,y} = 1.38\ [kN/m]$
- $h = 500\ mm$: $q_{w,y} = 1.36\ [kN/m]$
- $h = 480\ mm$: $q_{w,y} = 1.34\ [kN/m]$
- $h = 450\ mm$: $q_{w,y} = 1.30\ [kN/m]$
- $h = 420\ mm$: $q_{w,y} = 1.27\ [kN/m]$
- $h = 400\ mm$: $q_{w,y} = 1.25\ [kN/m]$
- $h = 380\ mm$: $q_{w,y} = 1.22\ [kN/m]$
- $h = 360\ mm$: $q_{w,y} = 1.20\ [kN/m]$

These distributed line loads are applied on their corresponding bridge deck in x-direction.

Mesh

A mesh size of 0.200 m was selected, since the shortest member is approximately 1.4 m long. A smaller mesh size of 0.100 m was also applied, but this did not result in any significant change in the deformations compared to the 0.200 m mesh size.

Appendix Q: Mesh sensitivity study

To assess the influence of mesh density on the numerical results, a mesh sensitivity study was performed. The objective of this study was to verify that the calculated structural response is independent of the selected mesh size and that the chosen mesh provides an adequate balance between computational efficiency and accuracy.

The reference mesh consisted of a global element size of 0.100 m. This mesh size was selected because the smallest vertical girder, with a height of 360 mm, was discretized by approximately four elements over its height, providing sufficient resolution of the structural behaviour. In addition, local mesh refinements were applied to smaller surfaces within the model to ensure that at least three to four elements were present across the width or length of the plates. The local refinement levels used in the reference mesh were 0.050 m, 0.025 m, 0.020 m, and 0.010 m. Both triangular and quadrilateral shell elements were employed throughout the model.

Two additional meshes were generated by systematically refining the global and local element sizes. The first refinement level was obtained using a refinement factor of 0.7, resulting in a global element size of 0.070 m and corresponding local refinement sizes of 0.035 m, 0.0175 m, 0.014 m, and 0.007 m. The second refinement level was generated using a refinement factor of 0.5, resulting in a global element size of 0.050 m and local refinement sizes of 0.025 m, 0.0125 m, 0.010 m, and 0.005 m.

The deformations obtained from the different mesh configurations for a load of 1 kN/m^2 on the top deck in x-, y- and z-direction were subsequently compared to evaluate mesh convergence and determine whether further refinement would significantly influence the numerical results. The Deformations are given in the table below.

	Global mesh of 0.100 m	Global mesh of 0.070 m	Global mesh of 0.050 m	Difference between global mesh of 0.100 m and 0.070 m	Difference between global mesh of 0.070 m and 0.050 m
Max deformation load x-direction	102.4 mm	102.5 mm	102.6	0.10%	0.10%
Max deformation load y-direction	34.7 mm	34.7 mm	34.7 mm	0%	0%
Max deformation load z-direction	75.3 mm	75.4 mm	75.4 mm	0.13%	0%

Table 112: Different deformations for different mesh sizes

The max deformation is for the different mesh sizes almost the same, the biggest difference is 0.13% between a global mesh of 0.100 m and a global mesh of 0.070 m.

In addition to the deformation results, the stress distribution was evaluated for the different mesh configurations. The comparison was performed using the normal stress in the x-direction on the positive side of the plate elements, resulting from the load applied in the z-direction. Since local stress singularities are present in the model, the maximum stress values are expected to increase with decreasing element size and therefore do not provide a reliable measure for mesh convergence. To minimise the influence of these singularities, the stress distribution was assessed by comparing the percentage of the model area falling within predefined stress intervals ranging from -8 to 8 N/mm². The results are shown in Table 113.

Load z-direction $\sigma_{x,+}$ $[\frac{N}{mm^2}]$	Global mesh of 0.100 m	Global mesh of 0.070 m	Global mesh of 0.050 m	Difference between global mesh of 0.100 m and 0.070 m	Difference between global mesh of 0.070 m and 0.050 m
8.000 – max	0.00%	0.00%	0.00%	0%	0%
6.222 – 8.000	0.02%	0.01%	0.01%	50%	0%
4.444 – 6.222	1.08%	1.08%	1.08%	0%	0%
2.667 – 4.444	1.53%	1.53%	1.53%	0%	0%
0.889 – 2.667	12.02%	12.03%	12.04%	0.08%	0.08%
-0.889 – 0.889	68.54%	68.54%	68.54%	0%	0%
-2.667 – -0.889	10.92%	10.91%	10.92%	0.09%	0.09%
-4.444 – -2.667	3.61%	3.59%	3.60%	0.55%	0.28%
-6.222 – -4.444	1.21%	1.21%	1.20%	0%	0.83%
-8.000 – -6.222	0.78%	0.78%	0.78%	0%	0%
Min – -8.000	0.30%	0.30%	0.30%	0%	0%

Table 113: Differences in percentages of stresses within a stress range between different mesh size

The results show that the stress distributions are nearly identical for all mesh sizes. For the majority of the stress intervals, the differences between the meshes are less than 0.1%. Slightly larger relative differences are observed in the highest tensile stress range (6.222–8.000 N/mm²). However, this range represents only 0.01–0.02% of the total model area and therefore has a negligible influence on the overall structural response.

The largest portion of the model experiences stresses between -0.889 and 0.889 N/mm², accounting for approximately 68.5% of the total area for all mesh configurations. Furthermore, the percentages within the remaining stress intervals remain virtually unchanged as the mesh is refined, indicating a stable stress distribution.

The mesh sensitivity study shows that the results are largely independent of the mesh size. The maximum difference in deformation between the investigated meshes was only 0.13%, while the stress distributions remained nearly identical. Therefore, the reference mesh with a global element size of 0.100 m and local refinements of 0.050 m, 0.025 m, 0.020 m, and 0.010 m was considered sufficiently accurate and was adopted for the subsequent analyses.

Appendix R: Load comparison plate and beam model

The loads applied on the models on both models will be compared. The resulting loads in x-, y-, and z-direction are compared for all load cases. Resultant loads that are not listed are equal to zero.

Self-weight

The resulting loads for the self-weight load case are shown in the table below.

Sum of loads in:	Beam model [kN]	Plate model [kN]
X	0	0
Y	0	0
Z	280.36	332.82
Resultant of reactions about:	Beam model [kNm]	Plate model [kNm]
X	0	0.00
Y	0	0.00
Z	0	-0.03

Table 114: Resulting loads for the load case self-weight

The self-weight of the plate model is higher because the weight of the connection is included in the model. In addition, the stiffener plates are also modelled explicitly in the plate model, although their contribution is relatively small. The difference in self-weight between the two models is 52.46 kN, corresponding to 26.23 kN for each connection on each side of the structure. To account for this difference in the beam model, additional point loads will be applied at several locations, see Figure 201, which in total are about equal to 26.23 kN. The largest loads are applied near the arch supports, since these locations contain the highest number of support plates. After applying these additional point loads, the sum of loads in z becomes 332.82 kN, which corresponds closely to the plate model. The small resultant moment about the z-axes in the plate model are most likely caused by the loads being applied at their exact geometric locations and by minor asymmetries in the plate model geometry and meshing. In contrast, the beam model is fully symmetrical, and the loads are only applied at member locations, resulting in zero resultant moments.

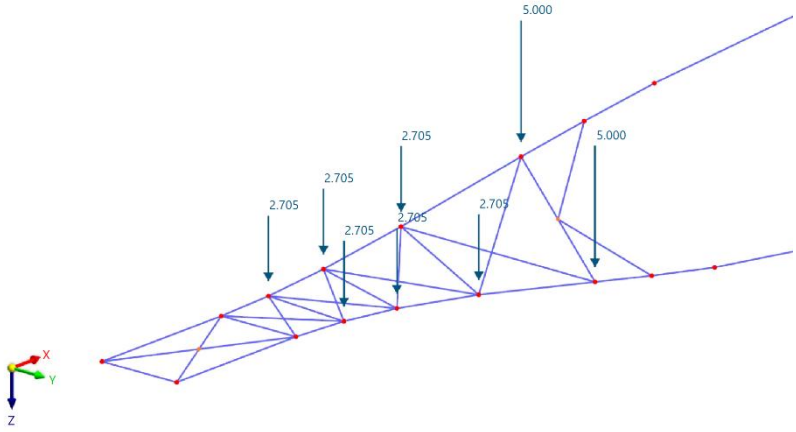

Figure 201: Loads connection self-weight

Permanent loads

The resulting loads for the permanent load case are shown in the table below.

Sum of loads in:	Beam model [kN]	Plate model [kN]
X	0	0
Y	0	0
Z	210.37	205.48
Resultant of reactions about:	Beam model [kNm]	Plate model [kNm]
X	0	-0.02
Y	0	0.11
Z	0	-0.02

Table 115: Resulting loads for the load case permanent loads

The total permanent load in the beam model is slightly higher than in the plate model, with a difference of 4.89 kN. This difference is mainly caused by the modelling of the balustrade load. When only the balustrade load is considered, the total vertical load in the z-direction is 161.40 kN for the beam model and 154.82 kN for the plate model, resulting in a difference of 6.58 kN, which is a larger difference as before. This larger difference is partly caused by the coating load, which is also applied to the connections in the plate model. In the original beam model, the balustrade load is, just like the entire structure, on the sides of the model, last 3.571 m of the upper and lower half on both sides, applied as a distributed load of 1.6 kN/m. However, this is not the actual load on this part of the structure because between the upper and lower halves, at the sides, there is no balustrade in the middle, but there is a balustrade at the outer edge in y-direction. The load on the plate model on one side of the structure, last 3.571 m, is around 8.8 kN in total and for the beam model this is 11.4, the difference is around 2.7 kN. This accounts for approximately half of the total difference in the sum of loads. To improve the agreement between the models, the balustrade load in the beam model is modified from a distributed load of 1.6 kN/m to a distributed load of 0.8 kN/m combined with a point load at the end of the upper and lower half, on each side of the structure, of 1.5 kN. The point load is determined as:

$$3.707 * \frac{0.8}{2} = 1.5\ kN$$

After this modification, the sum of loads in z caused by the balustrade becomes 155.97 kN in the beam model. Consequently, the total vertical load for the permanent load case becomes 204.94 kN, which corresponds closely to the plate model result of 205.48 kN. The small resultant moments about the axes in the plate model are most likely caused by the loads being applied at their exact geometric locations and by minor geometric or meshing asymmetries in the model, similar to the observations made for the self-weight load case.

Traffic loads

The resulting loads for the traffic load case for the full deck are shown in the table below.

Sum of loads in:	Beam model [kN]	Plate model [kN]
X	63.55	63.56
Y	0	0
Z	635.51	635.64
Resultant of reactions about:	Beam model [kNm]	Plate model [kNm]
X	0	0.00
Y	-6.07	-21.81
Z	0	-0.05

Table 116: Resulting loads for the load case traffic loads

The sum of loads in z for the beam and plate models is almost identical, with a difference of only 0.13 kN and the sum of loads in x for the beam and plate models is also almost identical, with a difference of only 0.01 kN. This indicates that the traffic loads are represented consistently in both models.

Small resultant moments about the axes are again present in the plate model. Similar to the self-weight load case, these moments are most likely caused by the loads being applied at their exact geometric locations and by minor geometric or meshing asymmetries in the plate model. In contrast, the beam model is fully symmetrical and the loads are applied directly to the structural members, resulting in zero resultant moments. For the beam model, the resultant reaction about the y-axis is lower than that of the plate model. This is mainly because the loads are applied at their actual elevations in the plate model, while in the beam model they are applied at the beam axis, resulting in a smaller moment about the y-axis.

Pedestrian balustrade load

The resulting loads for the pedestrian balustrade load case are shown in the table below.

Sum of loads in:	Beam model [kN]	Plate model [kN]
X	0	0.03
Y	0	0.08
Z	201.75	193.53
Resultant of reactions about:	Beam model [kNm]	Plate model [kNm]
X	0	0.14
Y	0	-0.06
Z	0	-2.06

Table 117: Resulting loads for the load case pedestrian balustrade load

The total pedestrian balustrade load in the beam model is slightly higher than in the plate model, with a difference of 8.22 kN. This difference is caused by the same modelling approach as discussed for the permanent load case. To improve the agreement between the models, the pedestrian balustrade load in the beam model on the sides of the model, last 3.571 m of the upper and lower half on both sides, is modified from a distributed load of 2.0 kN/m to a distributed load of 1.0 kN/m combined with a point load at the end of the upper and lower half, on each side of the structure, of 1.85 kN. The point load is determined as:

$$3.707 * \frac{1.0}{2} = 1.85\ kN$$

After this modification, the sum of loads in z-direction becomes 194.87 kN, which corresponds closely to the plate model result of 193.53 kN. The small resultant moments about the axes in the plate model are most likely caused by the loads being applied at their exact geometric locations and by minor geometric or meshing asymmetries in the model, similar to the observations made for the self-weight load case.

Wind load in z-direction

The resulting loads for the wind load case in the z-direction are shown in the table below.

Sum of loads in:	Beam model [kN]	Plate model [kN] (+z)	Plate model [kN] (-z)
X	0	0	0
Y	0	0	0
Z	88.87	89.25	-90.66
Resultant of reactions about:	Beam model [kNm]	Plate model [kNm] (+z)	Plate model [kNm] (-z)
X	0	0.00	0.00
Y	0	-0.01	-0.01
Z	0	-0.01	-0.01

Table 118: Resulting loads for the load case wind load in z-direction

The total wind loads in the z-direction for the beam and plate models are in close agreement for both the positive and negative loading directions. The plate model gives slightly larger values than the beam model. This difference is most likely caused by the explicit modelling of the small gap between the upper and lower half of the structure and the side plates of the connections between the upper and lower half of the structure, which are also subjected to wind loading. The small difference between the loads acting in the −z-direction and +z-direction in the plate model is likely caused by the load in the +z-direction being applied to the top of the structure, whereas the load in the −z-direction is applied to the bottom. As a result, a slight difference in the plate areas on the top and bottom sides of the structure might lead to the observed difference in the applied loads. Small resultant moments about the axes are again present in the plate model. Similar to the previous load cases, these moments are most likely caused by the loads being applied at their exact geometric locations and by minor geometric or meshing asymmetries in the plate model. In contrast, the beam model is fully symmetrical and the loads are applied directly to the structural members, resulting in zero resultant moments.

Wind load moment in z-direction

The resulting loads for the wind load bending moment in the z-direction are shown in the table below.

Resultant of reactions about:	Beam model [kNm]	Plate model [kNm]
X	-19.84	19.99
Y	-0.55	0.42
Z	0	0.08

Table 119: Resulting loads for the load case wind load moment in z-direction

The resultant reactions about the x-axis are almost identical for both models and are approximately equal to 20 kNm, which corresponds to the applied bending moment caused by the eccentricity of the wind load. The difference in sign is caused by the loads being applied in opposite directions in the two models. This sign difference is not relevant for the final assessment, since both loading directions are considered in the load combinations by applying a factor of -1.

The resultant reactions about the y- and z-axes are also small and show close agreement between the two models. For both models, the sums of loads in the x-, y-, and z-directions are equal to zero, as expected for a pure bending moment load case.

Wind load in y-direction

The resulting loads for the wind load case in the y-direction are shown in the table below.

Sum of loads in:	Beam model [kN]	Plate model [kN] (+y)	Plate model [kN] (-y)
X	0	0	0
Y	368.83	340.47	-338.28
Z	0	0	0
Resultant of reactions about:	Beam model [kNm]	Plate model [kNm] (+z)	Plate model [kNm] (-z)
X	-50.26	-50.91	50.85
Y	0	3.01	-2.88
Z	0	273.04	245.41

Table 120: Resulting loads for the load case wind load in y-direction

The wind load in the y-direction for the beam model is higher than for the plate model. This is most likely caused by the modelling approach in the beam model, where the structure height is averaged and may locally overestimate the exposed area in certain parts of the structure. In addition, at the sides of the structure is a wind load applied at the upper half of the structure and on the lower half. In reality, this is not fully accurate, since these parts are located next to each other at the same height and do not both represent separate exposed wind surfaces. The wind loads on the upper and lower half of the structure should be halved, this results in a sum of loads in y of 344.55 kN, which is closer to the plate model. The resultant reaction around X changes to -56.39 kNm for the beam model with the new loads. The resultant reaction around X is similar for both models. The reactions about the y-axis are also small and comparable. However, a clear difference is observed in the reactions about the z-axis. In the beam model, this resultant is zero due to perfect symmetry between the left and right sides when viewed in the y-direction. In contrast, the plate model shows a significant moment about the z-axis. This is caused by asymmetries introduced by the loading of the structure and the connection in the plate model, which breaks the ideal symmetry loading assumed in the beam model. In the plate model, the connection between the top and bottom halves of the structure covers a part of the bottom half of the structure and one side where the railing is located. This wind load on the balustrade is not included in that part of the structure and is included in is the beam model.

The small difference between the loads acting in the −y-direction and +y-direction in the plate model is likely caused by the loads being applied to opposite sides of the structure. As a result, slight differences in the plate areas of the two side plates might lead to the observed difference in the applied loads.

Wind load in x-direction

The resulting loads for the wind load case in the x-direction are shown in the table below.

Sum of loads in:	Beam model [kNm]	Plate model [kNm]
X	147.41	143.59
Y	0	0
Z	0	0
Resultant of reactions about:	[kNm]	[kNm]
X	0	0.00
Y	21.33	-19.82
Z	0	0.00

Table 121: Resulting loads for the load case wind load in x-direction

There is a small difference between the total loads in the x-direction for the beam and plate models. This difference is likely caused by numerical rounding and minor differences in how the wind load is distributed in both modelling approaches.

The resultant reactions show some differences between the models, particularly for the moment about the y-axis. These deviations are relatively small compared to the overall load magnitude and are mainly attributed to differences in load application and geometric idealisation between the beam and plate models.

Appendix S: Overview figures components and singularities

Very high local stresses may occur at geometric discontinuities, such as sharp corners and load application regions. These stress concentrations are numerical singularities resulting from the idealized finite element model and do not represent the actual structural behaviour. Their localized nature was verified by the mesh sensitivity study, which showed that the peak stresses increase with mesh refinement while remaining confined to a very small region. Therefore, these local peak stresses are not considered representative for the structural assessment and are excluded from the evaluation of the unity checks. The singularities and overview figures of the components are presented in Table 122.

Support plates

Support plates set 1

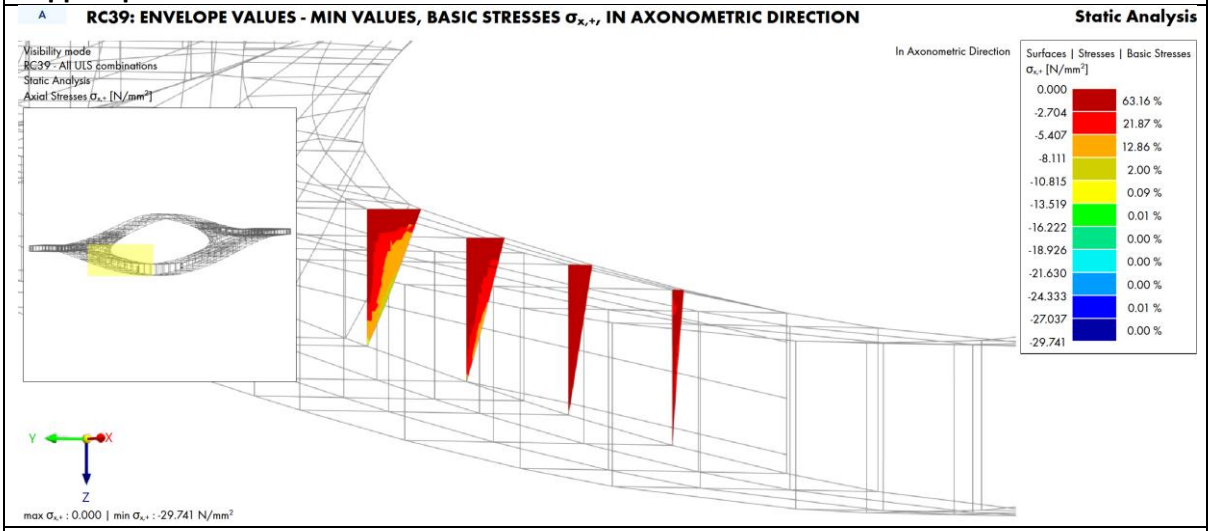

Very high local stresses occur at the bottom corners of the plates. These stress concentrations are numerical singularities caused by the modelling approach and are therefore not considered representative of the actual structural behaviour.

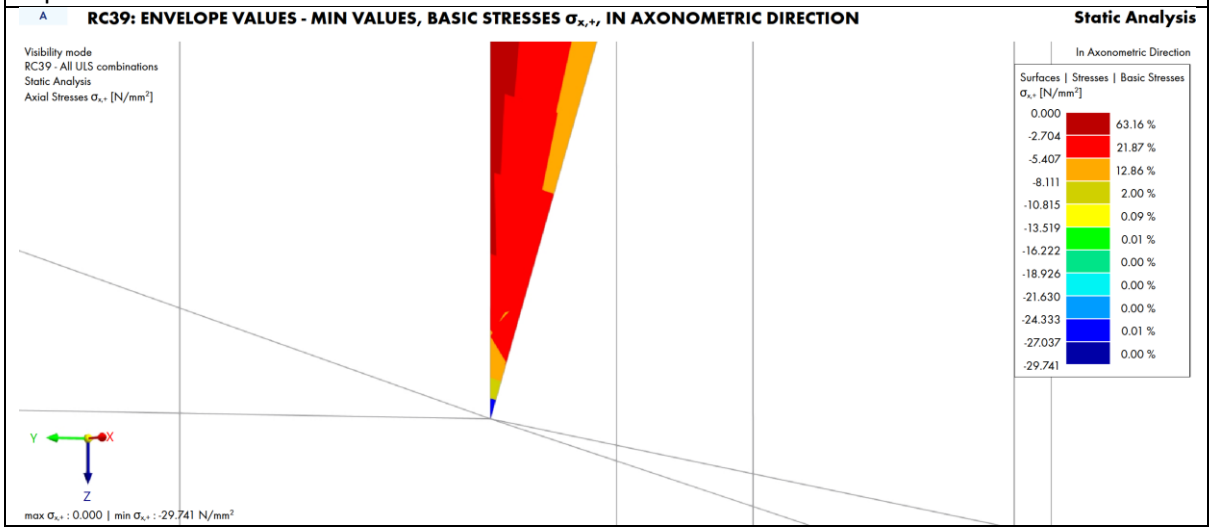

At the top corners of the plates, the abrupt increase in stress is also a numerical singularity and is therefore not representative of the actual structural behaviour.

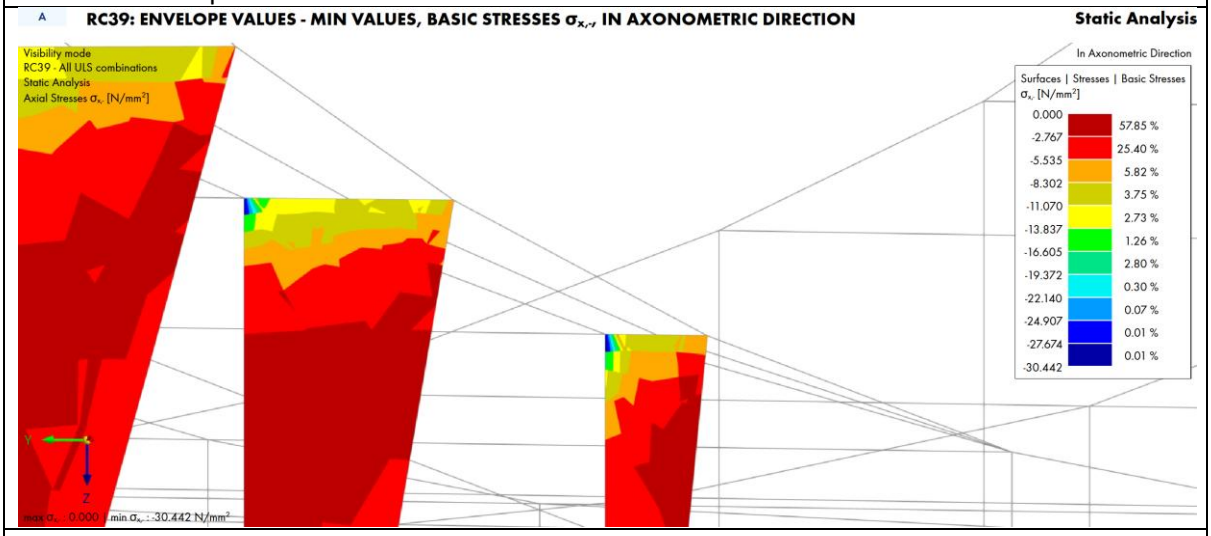

Support plates set 2

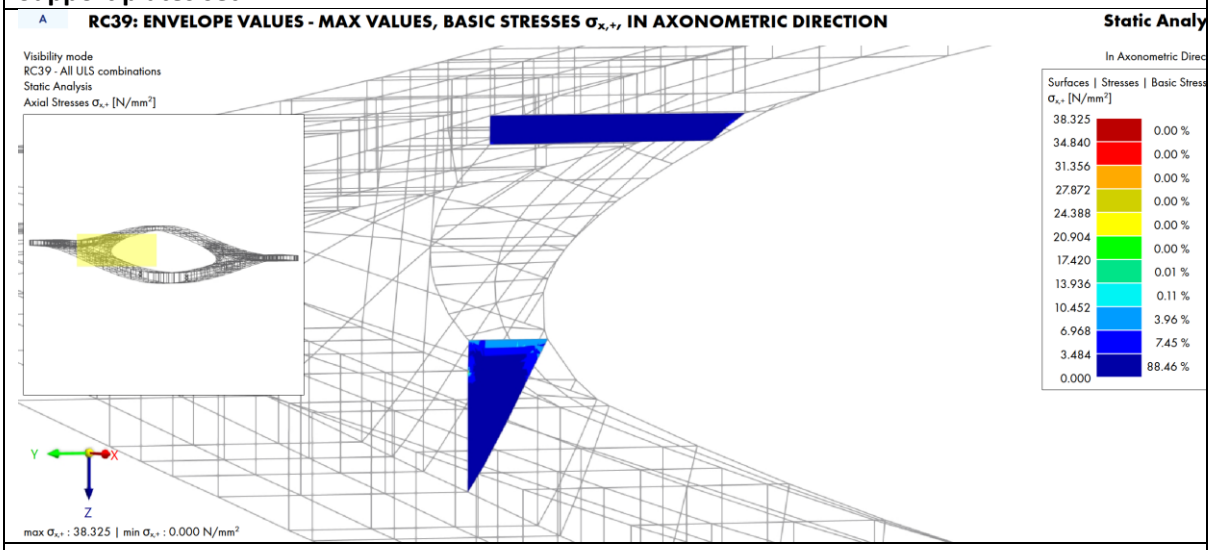

At the connection between the support plate and the top plate, the stress increases abruptly from approximately 15 to 40 N/mm². This local stress peak is a numerical singularity and is therefore not representative of the actual structural behaviour.

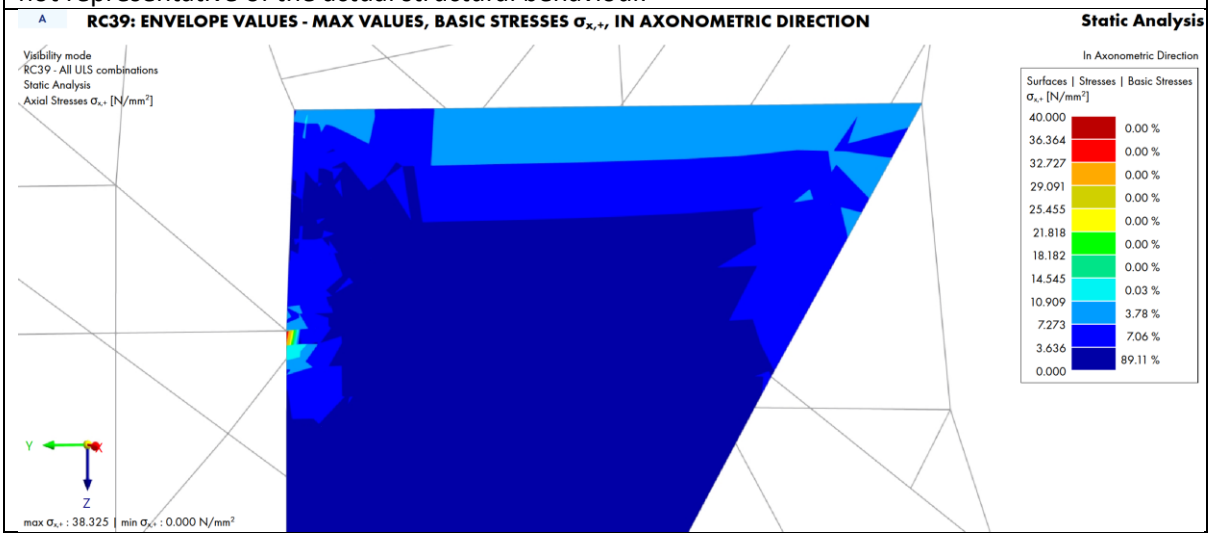

Supports plate set 3

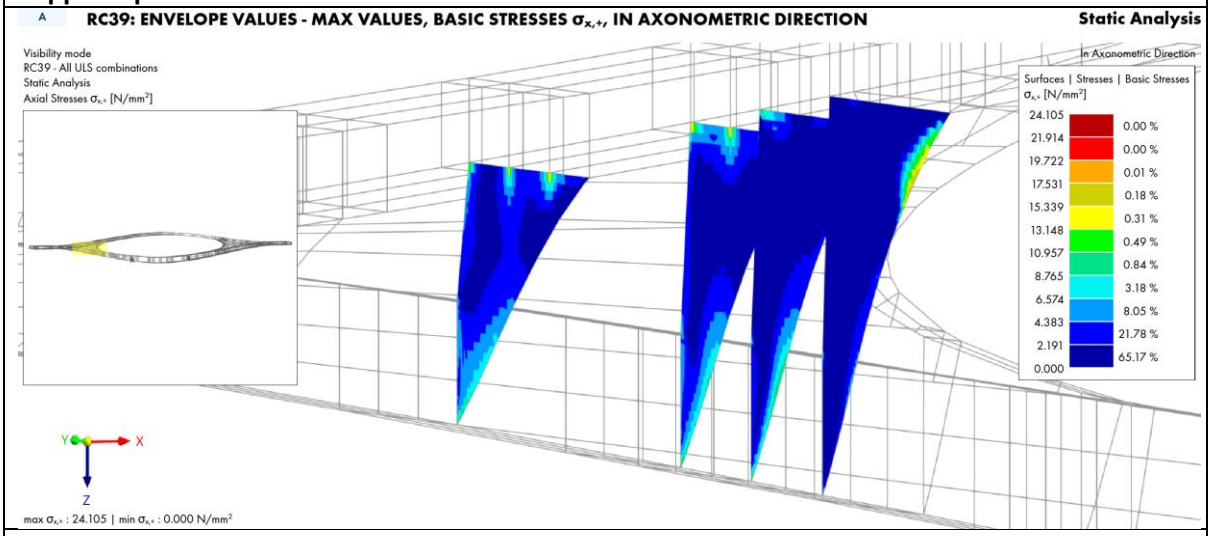

At the connection between the support plate and the top plate, the stress increases abruptly from approximately 25 to 58 N/mm². This local stress peak is a numerical singularity and is therefore not representative of the actual structural behaviour.

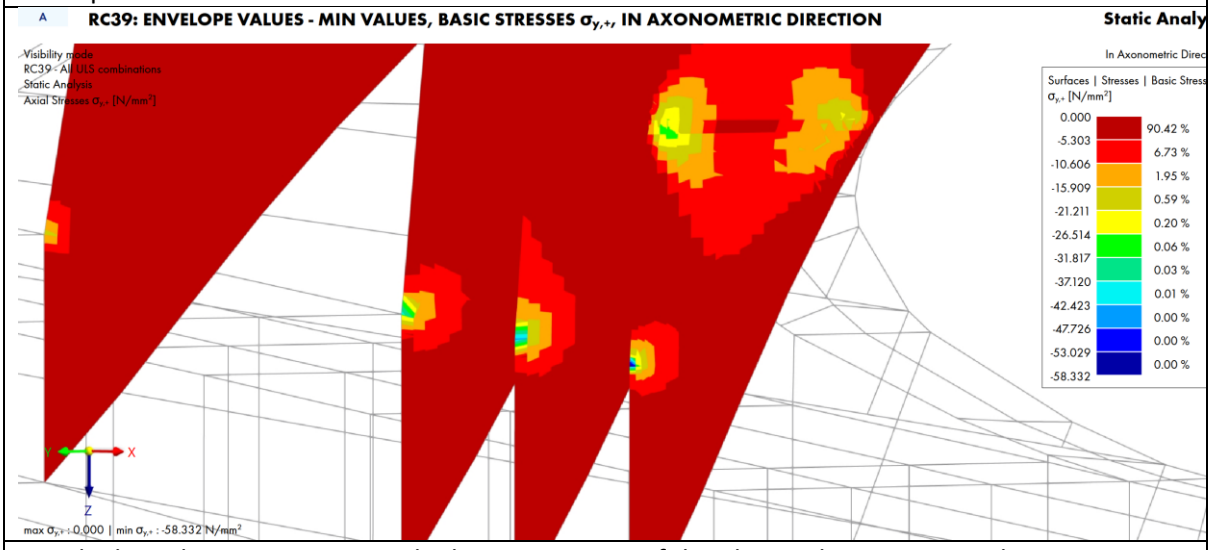

Very high peak stresses occur at the bottom corners of the plates. These stress peaks are numerical singularities and are therefore not representative of the actual structural behaviour.

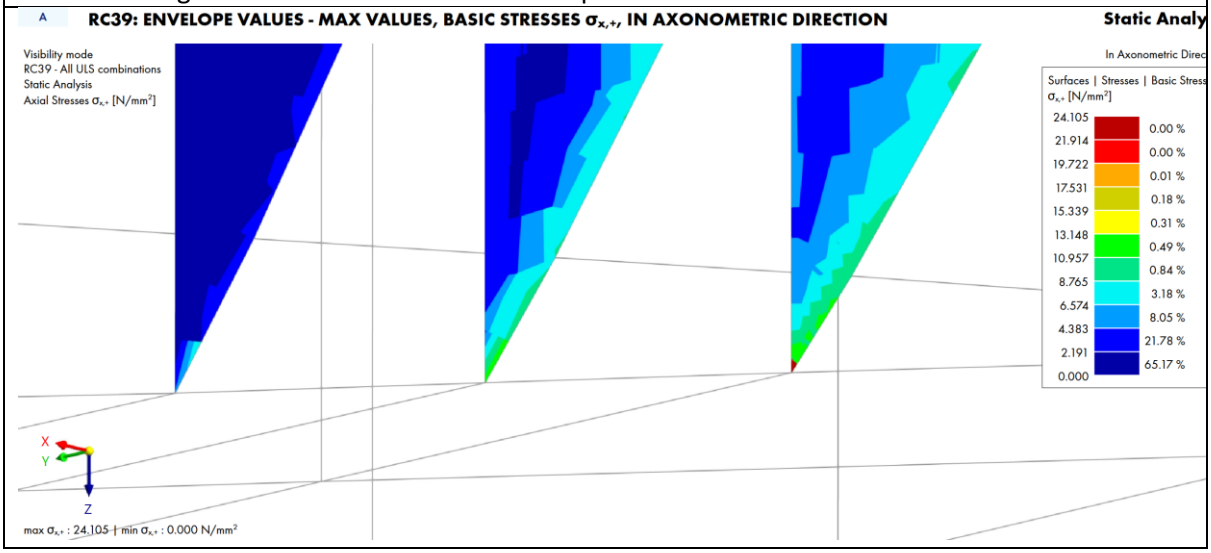

The plate shown below is connected to the arch plate. At the connection between the arch plate and the top side plate, the stress increases from approximately 36 to 80 N/mm². This stress concentration is also present when a refined mesh is used, indicating that it is not caused by mesh discretisation. Therefore, this stress is considered in the assessment.

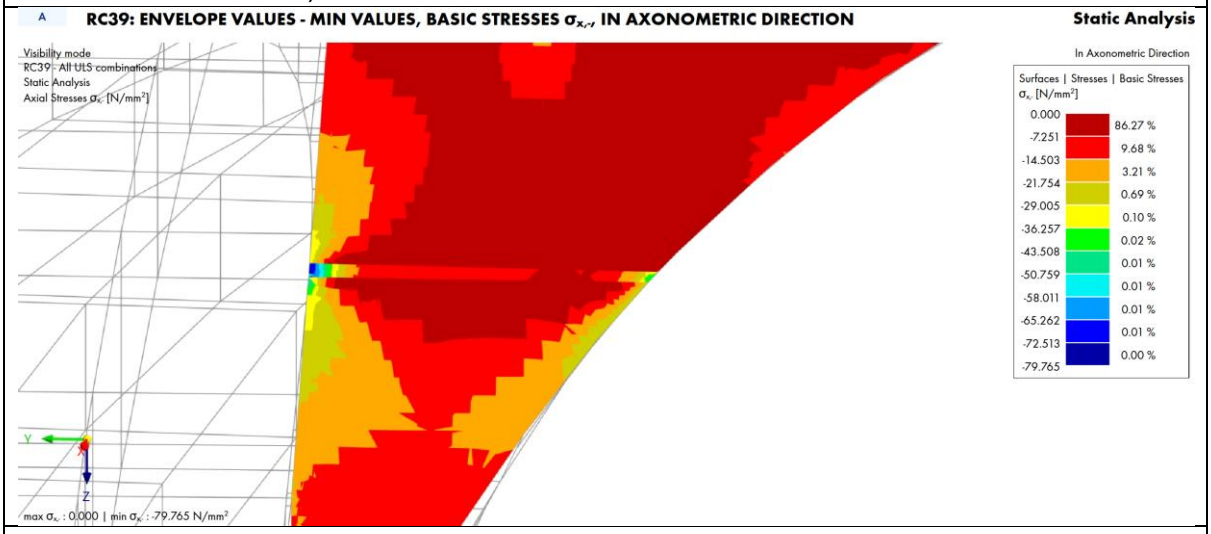

Supports plate set 4

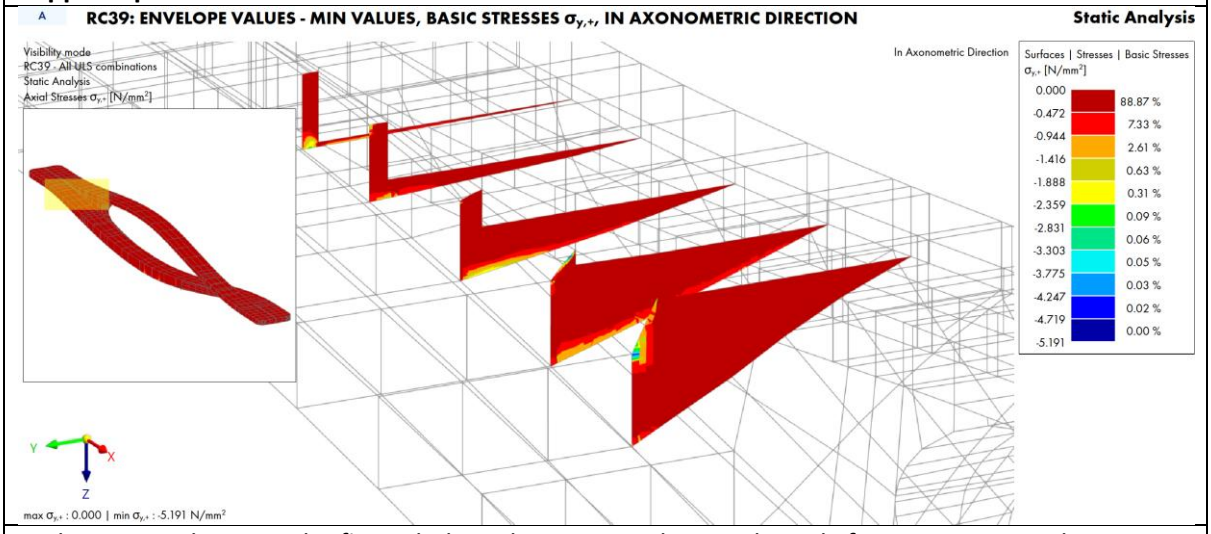

In the corner shown in the figure below, the stresses change abruptly from approximately -2 to -9 N/mm² within a few mesh elements. This local stress peak is a numerical singularity and is therefore not representative of the actual structural behaviour.

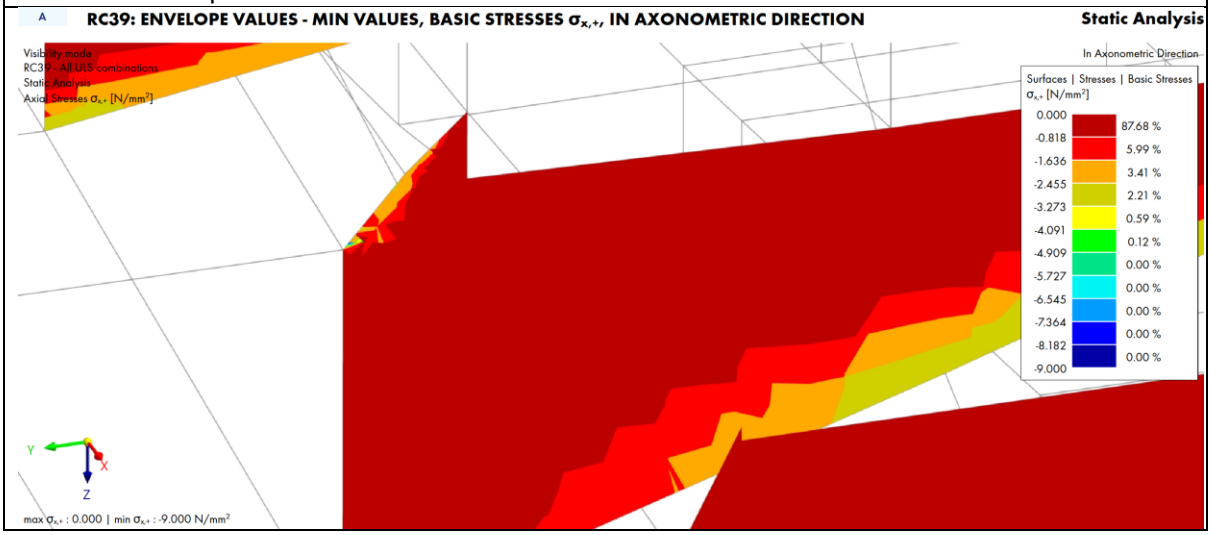

The stresses in the corner shown below increase from approximately 15 to 30 N/mm² within a small area. This local stress peak is a numerical singularity and is therefore not representative of the actual structural behaviour.

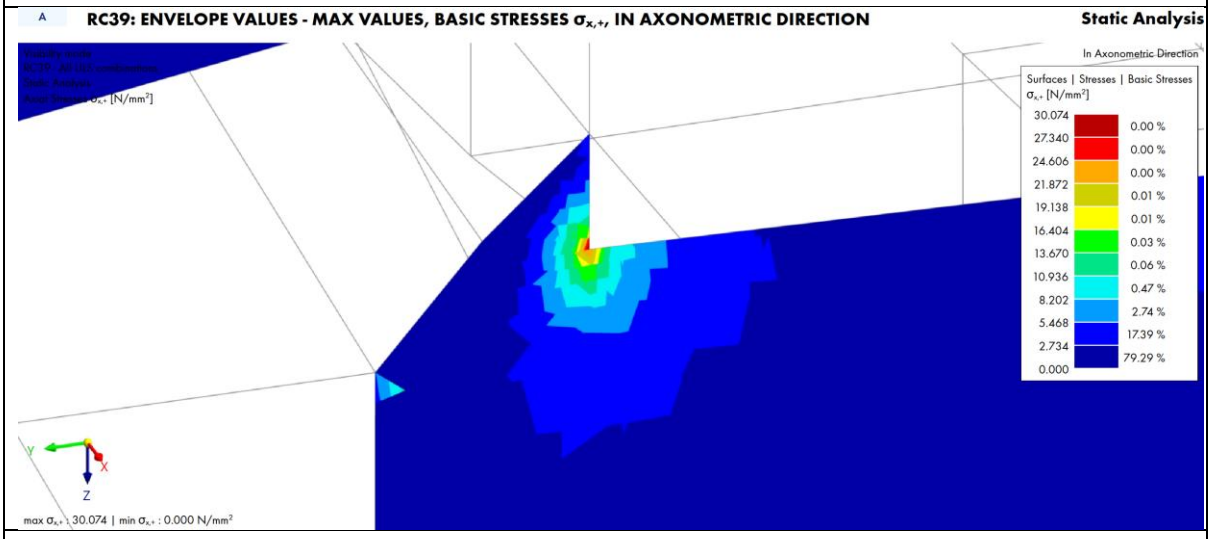

Side plates

Arch plate

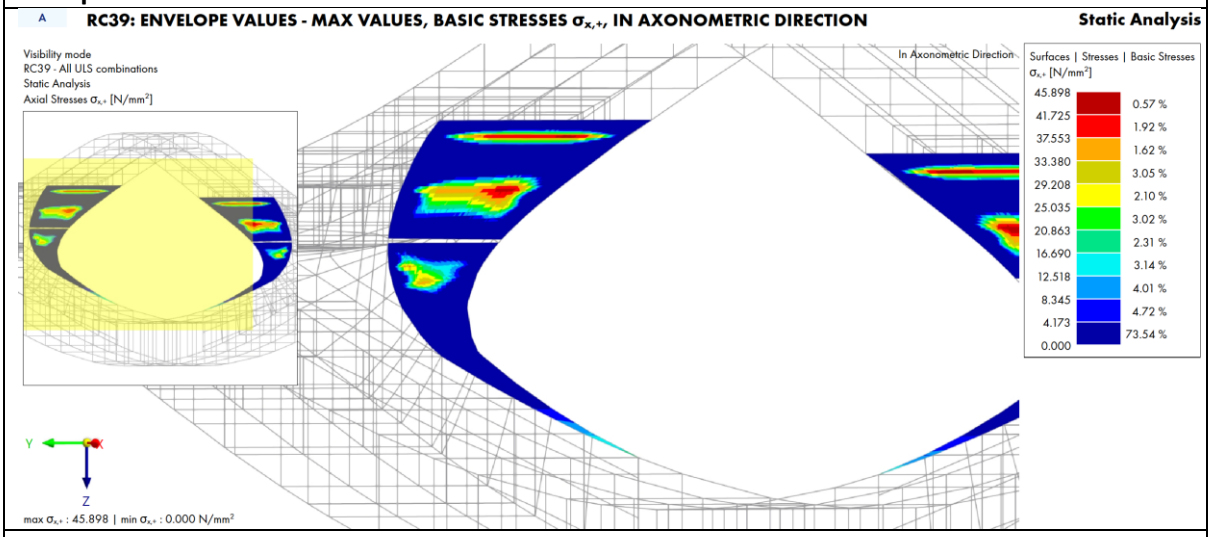

At the sides of the plate shown in the figure below, high stresses are observed. These stresses are not representative of the actual behaviour of the side plates, as the mesh quality is insufficient in these regions. Furthermore, mesh refinement results in increasing stress values, indicating a stress singularity.

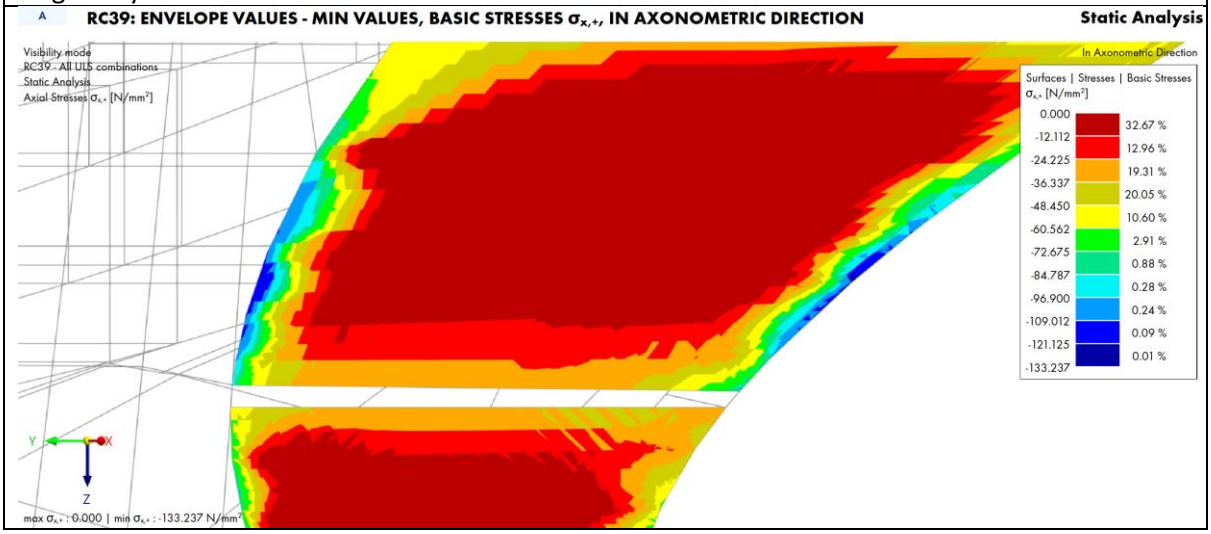

The figure below shows a small region with elevated stresses. The stress increases from approximately 28 to 44 N/mm² over a few mesh elements, indicating a singularity.

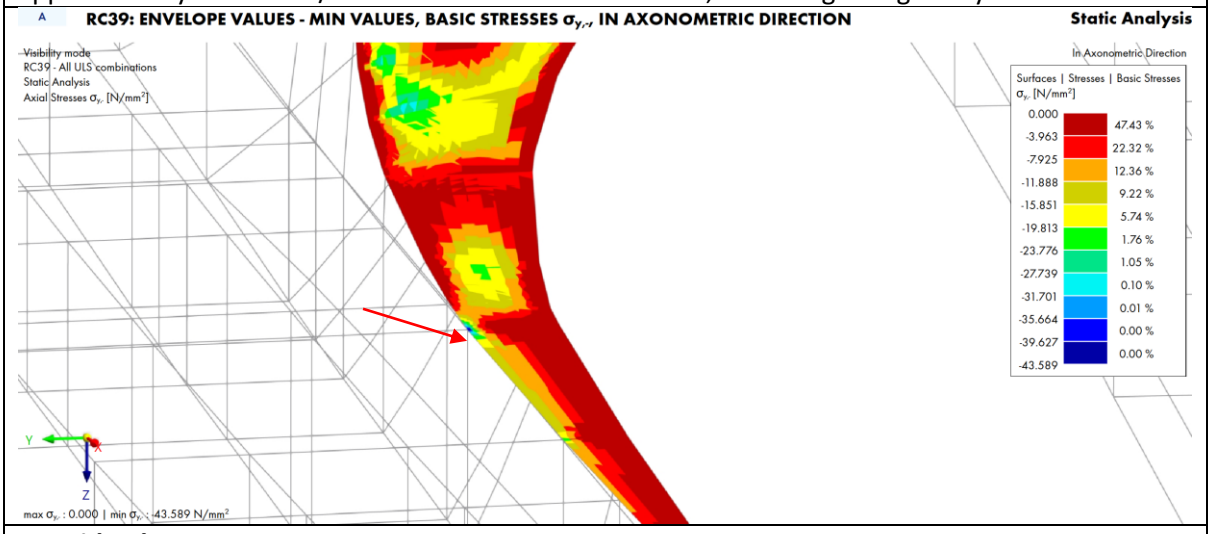

Top side plate

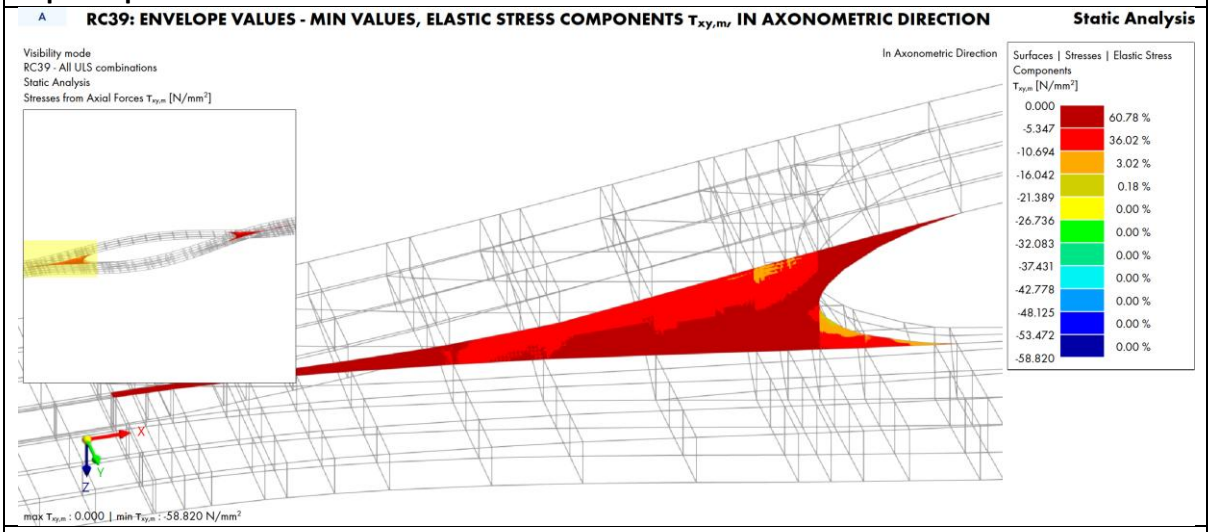

The figure below shows the corner next to the arch. Very high stresses occur along a vertical line in this region. These stresses are caused by poor meshing of the plates and are considered numerical singularities.

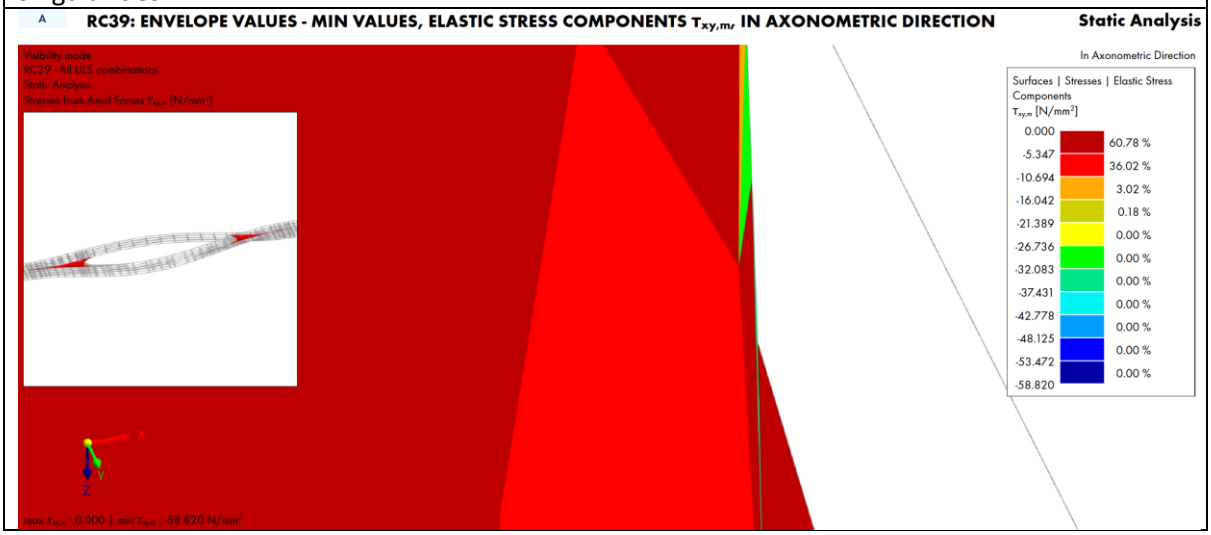

In the corner next to the arch of the top side plate, the stresses are locally higher than the surrounding stresses. This is caused by the arch plates being modelled with separate polylines rather than continuous lines, resulting in stress peaks at the connection nodes.

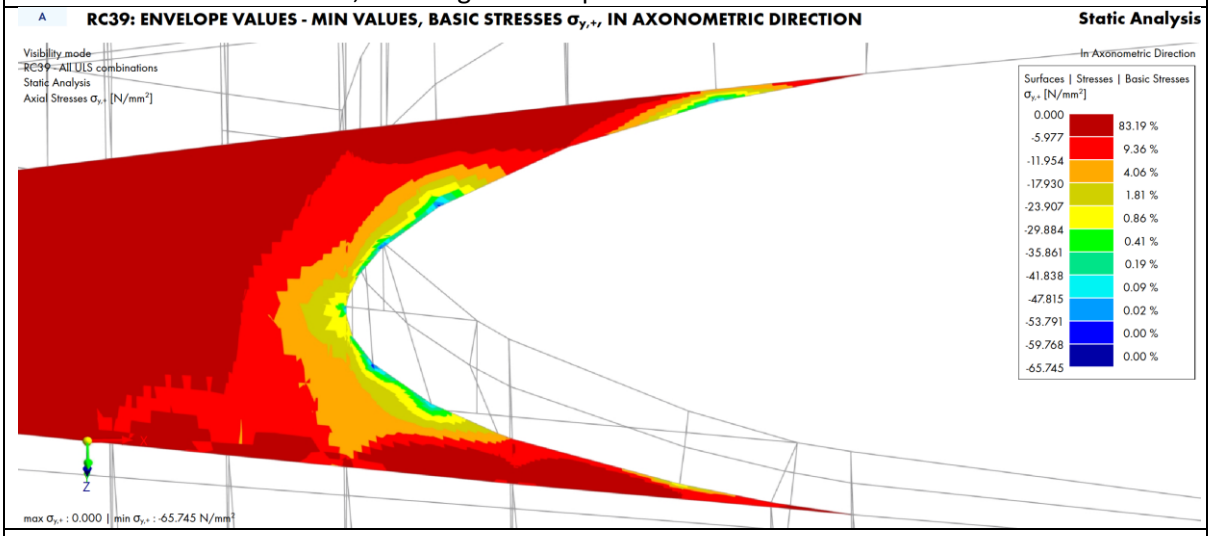

In the point high stresses occur due to a numerical singularity and are therefore not representative of the actual structural behaviour.

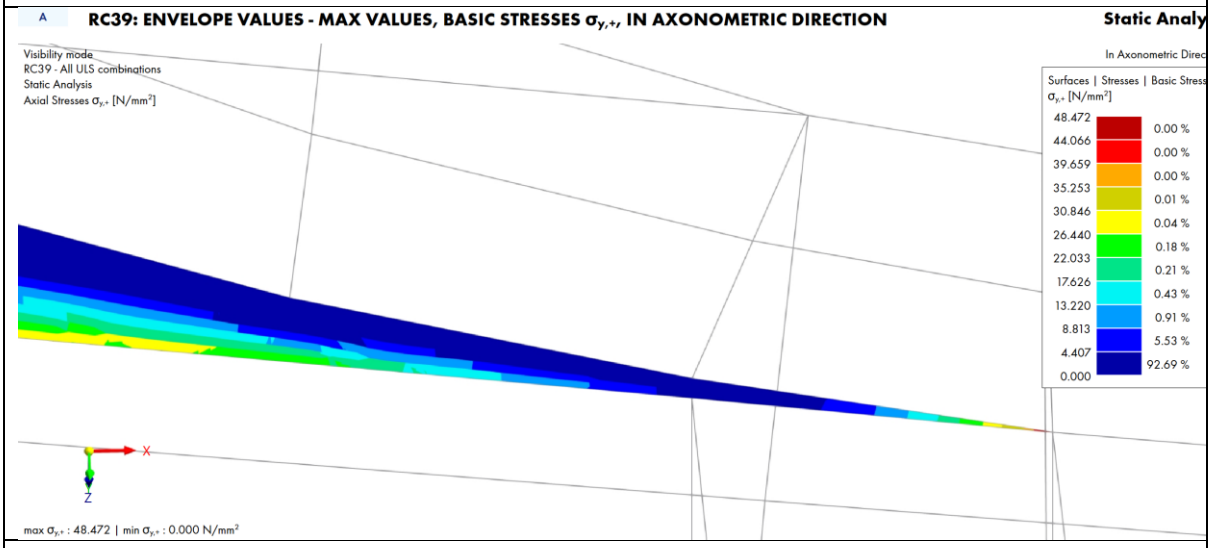

Bottom side plate



At the corner, the stresses increase from approximately 36 to 54 N/mm². This local stress peak is a numerical singularity and is therefore not representative of the actual structural behaviour.

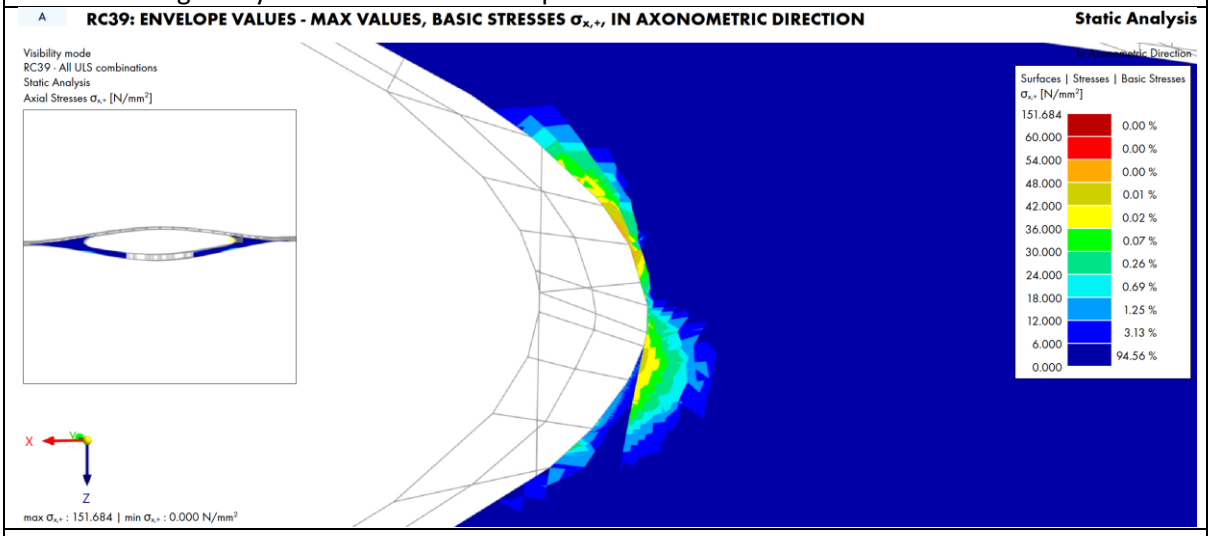

In the corner, high stresses occur within a few mesh elements. This local stress peak is a numerical singularity and is therefore not representative of the actual structural behaviour.

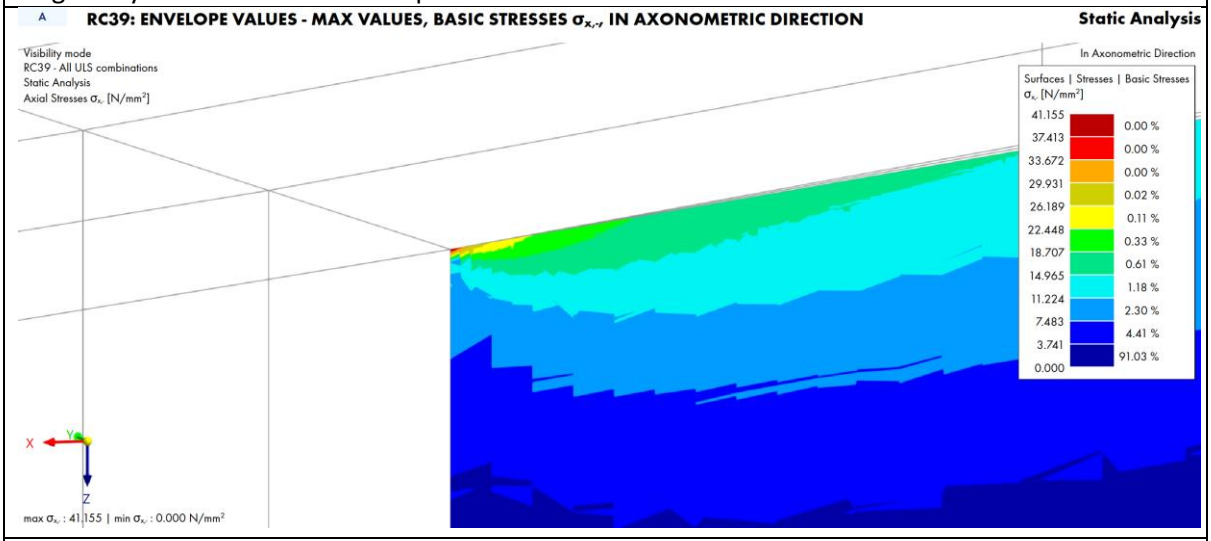

Bottom plate

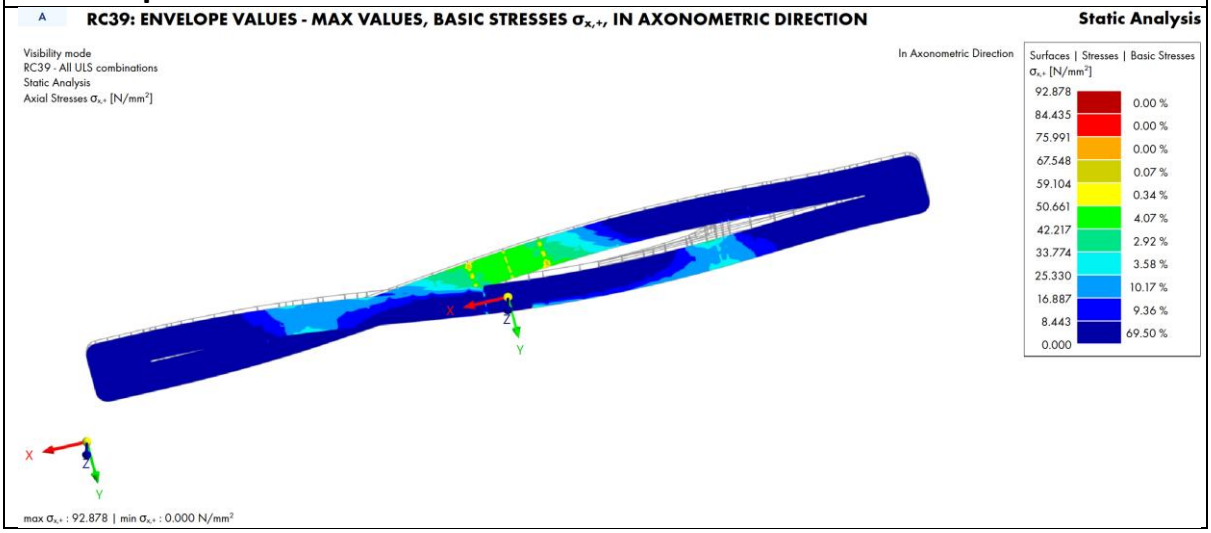

In the corner next to the plate with a fully clamped boundary condition, high stresses occur in a small region. This is considered a numerical singularity. The same applies to the entire side near the supports and the neighbouring plates, as these stresses are influenced by the support modelling approach. In a detailed design stage, these stress concentrations should be further investigated using a different support model.

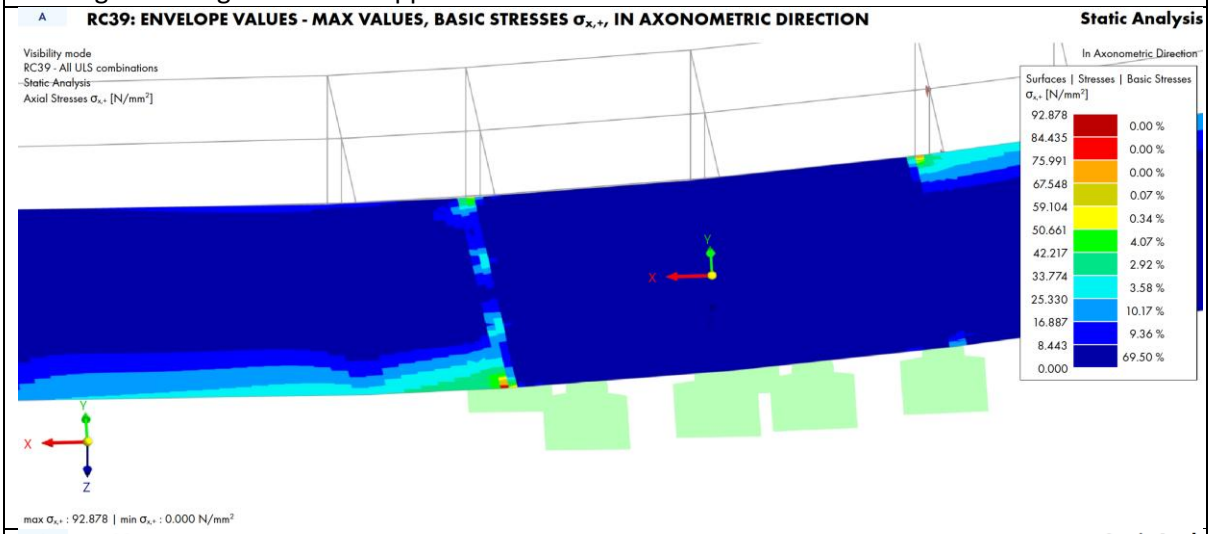

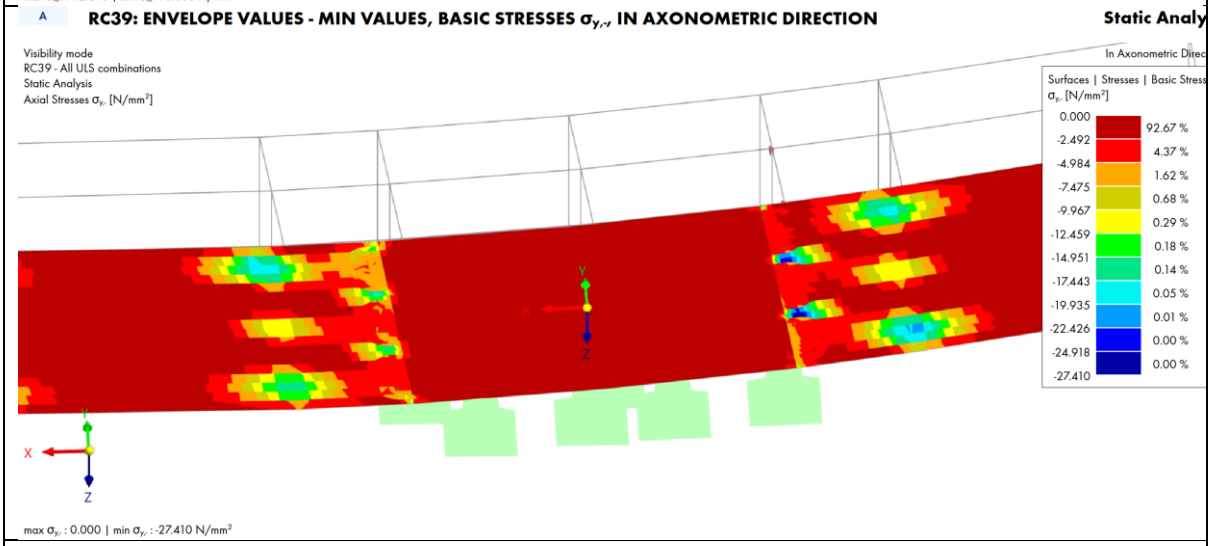

C-shaped girders

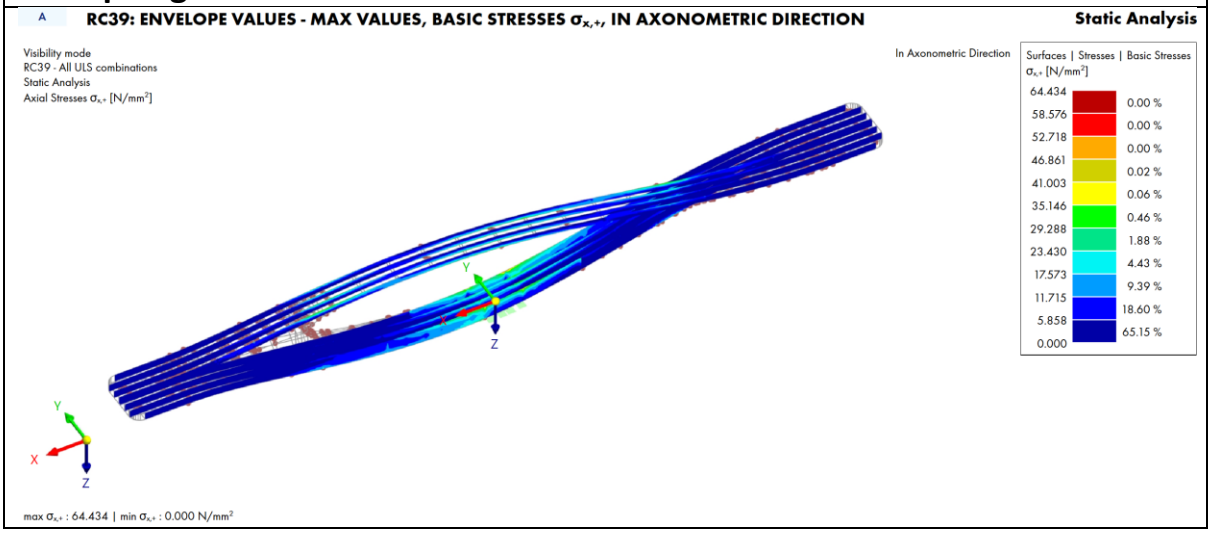

Similar to the bottom plate, higher stresses occur around the supports due to the support modelling. The peak stresses are not considered representative and are therefore ignored. In a detailed design stage, these stress concentrations should be further investigated using a different support model.

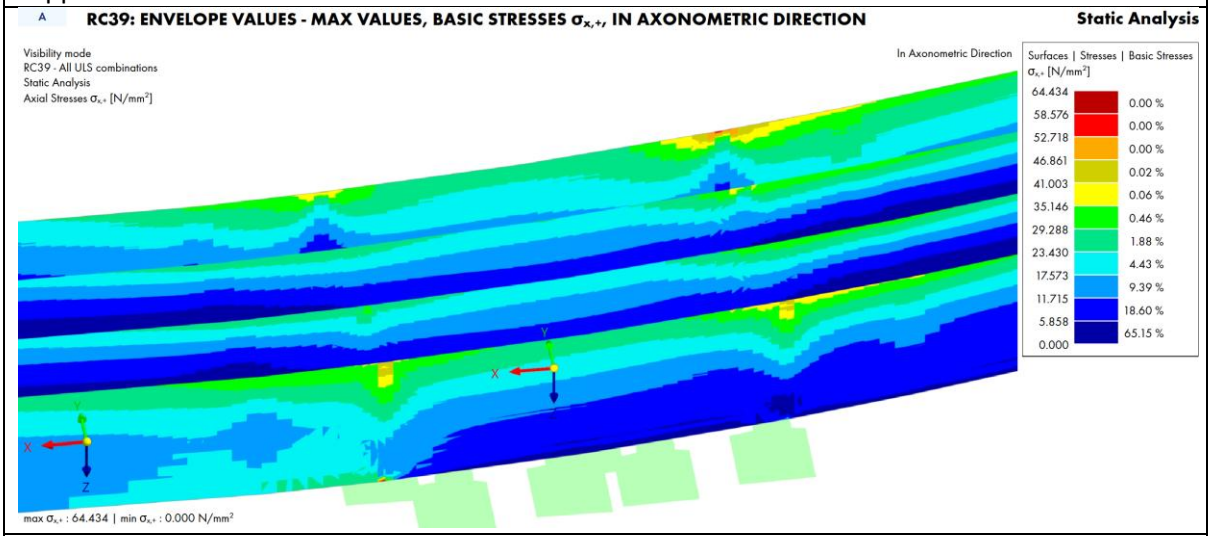

Top plate

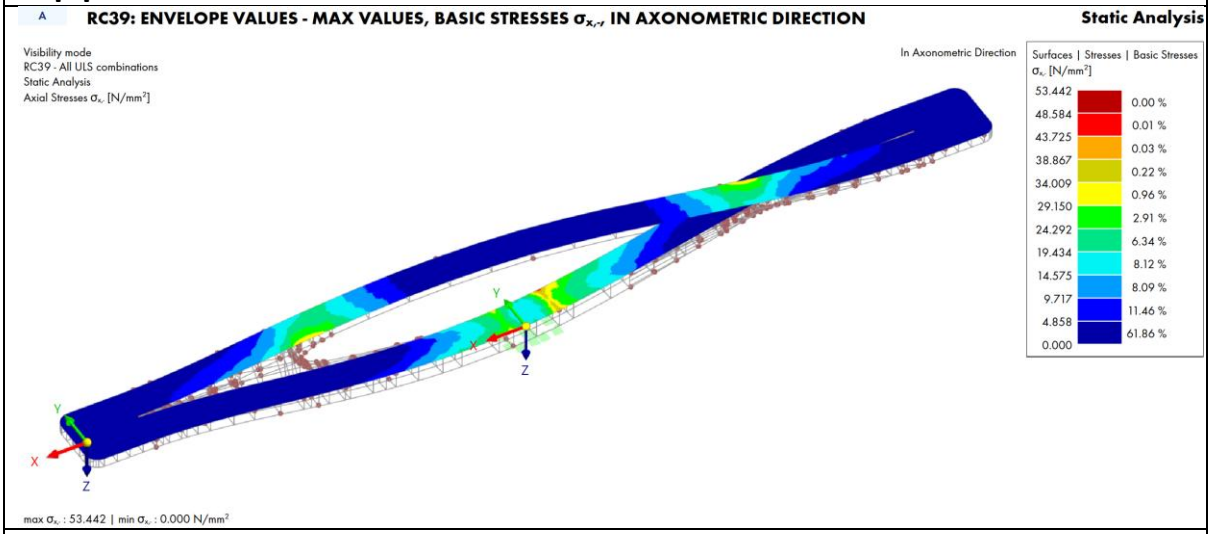

Similar to the bottom plate and C-shaped girders, higher stresses occur around the supports due to the support modelling. The peak stresses are ignored, as they are influenced by the way the supports are modelled. In a detailed design stage, these stress concentrations should be further investigated using a different support model.

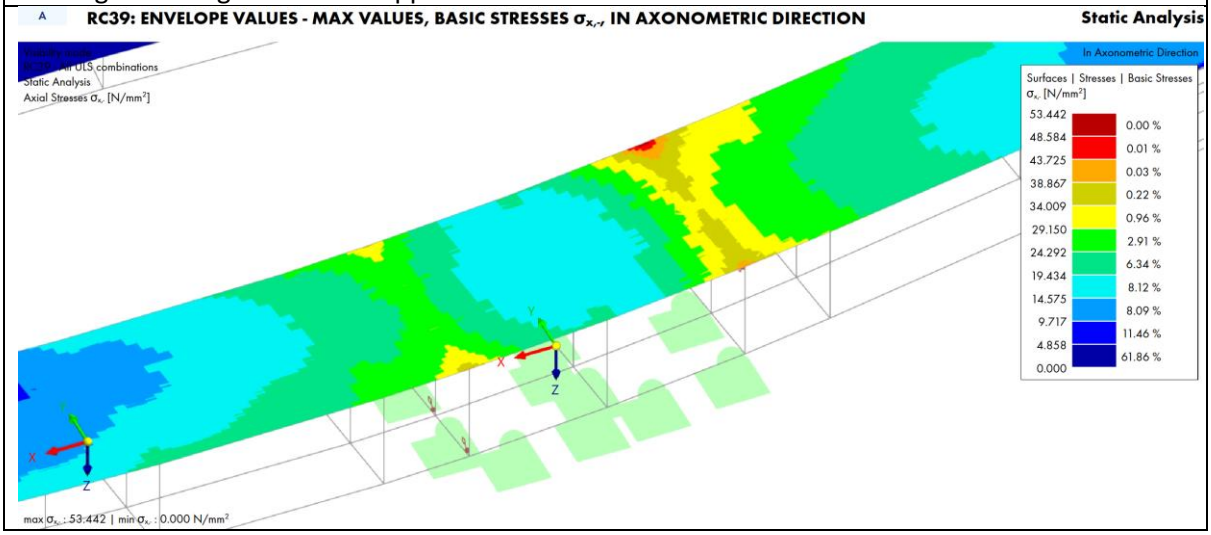

Stiffener plates

Stiffener plates set 1

The plates near the supports are strongly influenced by the support modelling. The stresses obtained from the analysis in these regions are therefore not considered representative of the actual stresses in the plates. In a detailed design stage, these stress concentrations should be further investigated using a different support model.

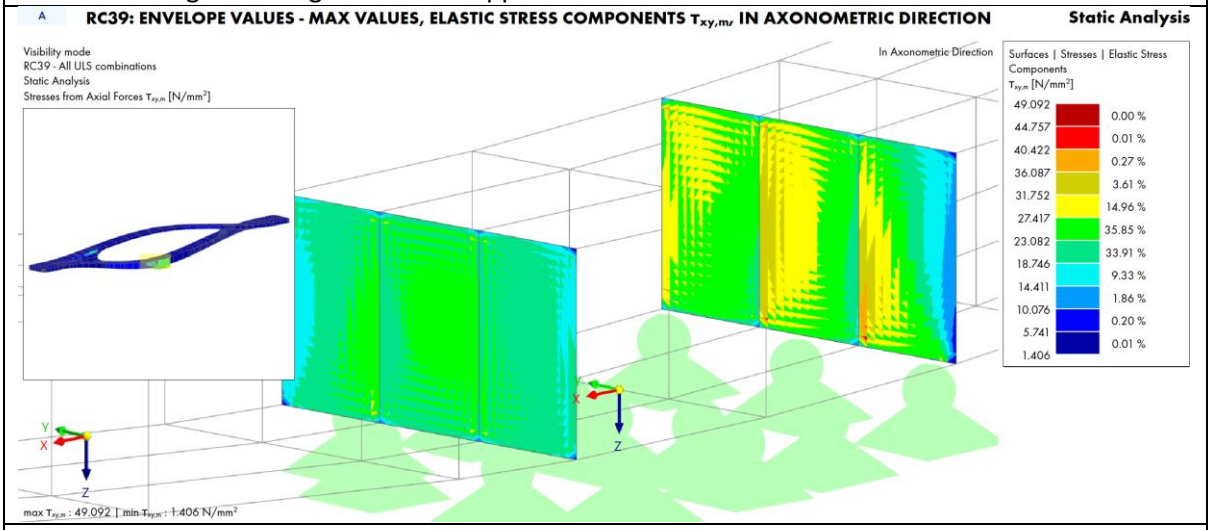

Stiffener plates set 2

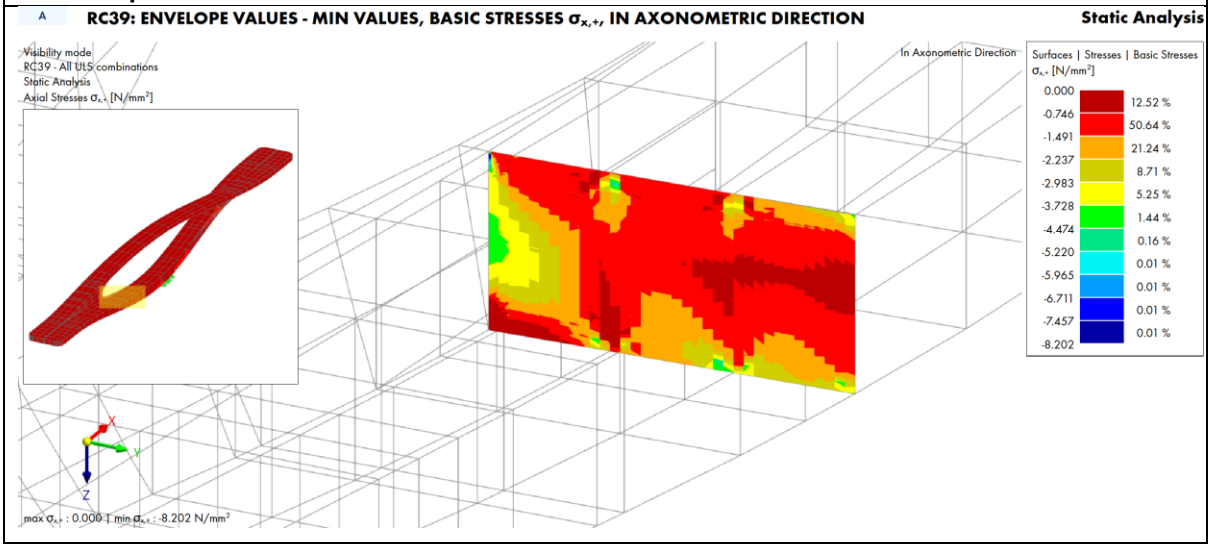

In the corner of the stiffener plate shown below, the stresses increase within a few mesh elements. This local stress peak is a numerical singularity and is therefore not representative of the actual structural behaviour.

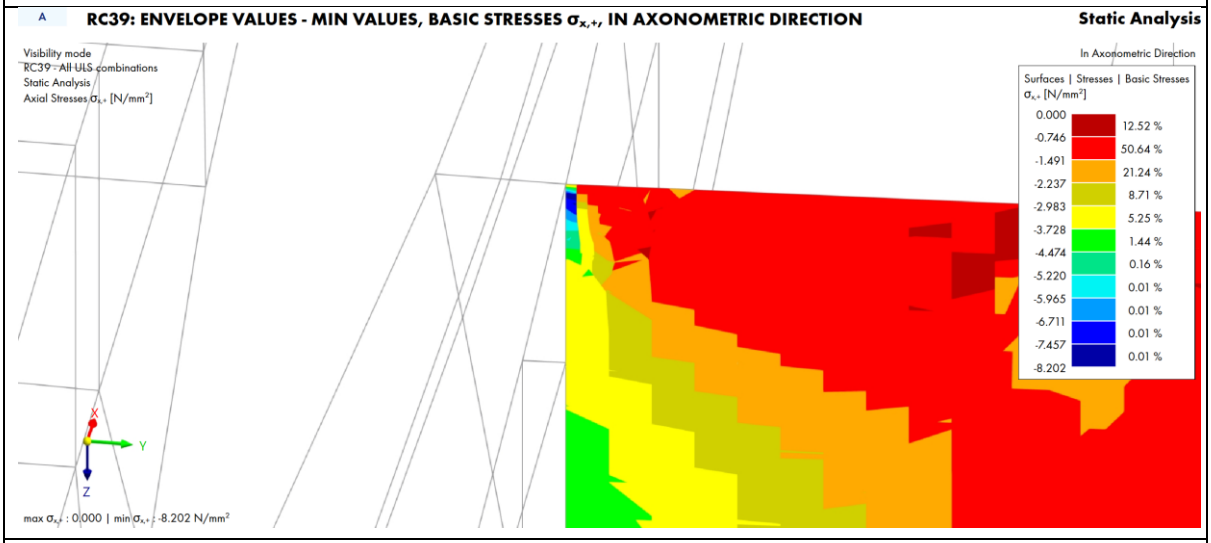

In the corner of the stiffener plate shown below, the stresses increase within a few mesh elements. This local stress peak is a numerical singularity and is therefore not representative of the actual structural behaviour.

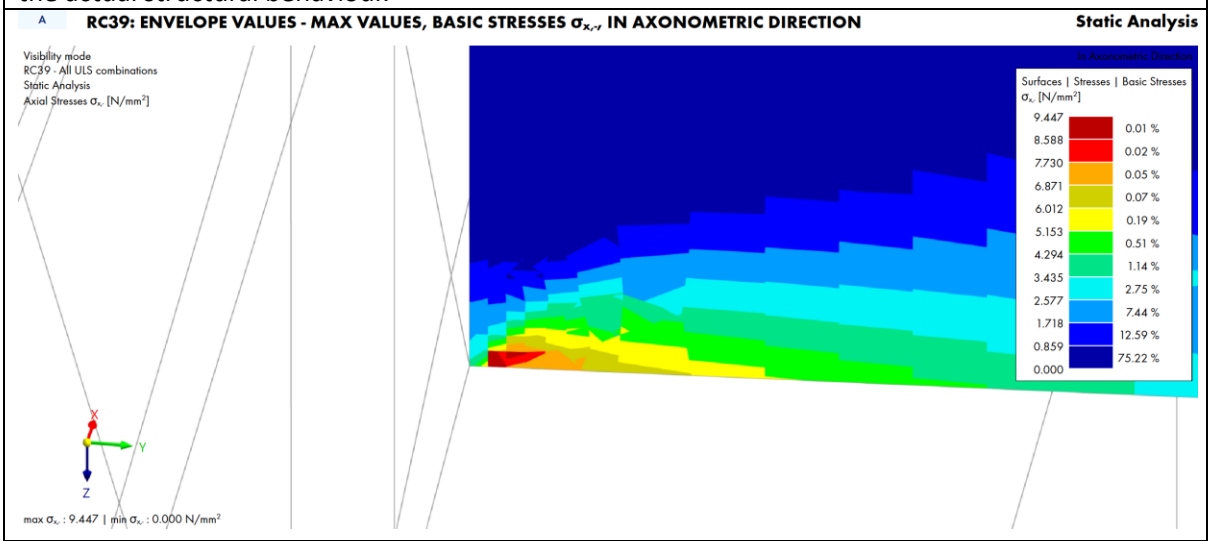

Stiffener plates set 3

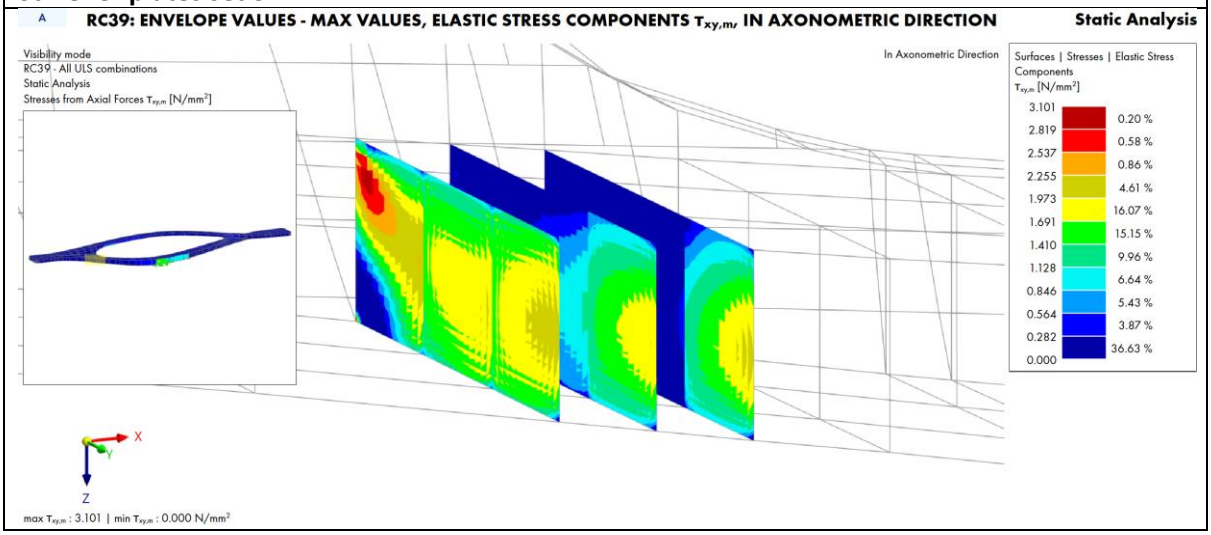

In the corner of the stiffener plate shown below, the stresses increase within a few mesh elements. This local stress peak is a numerical singularity and is therefore not representative of the actual structural behaviour.

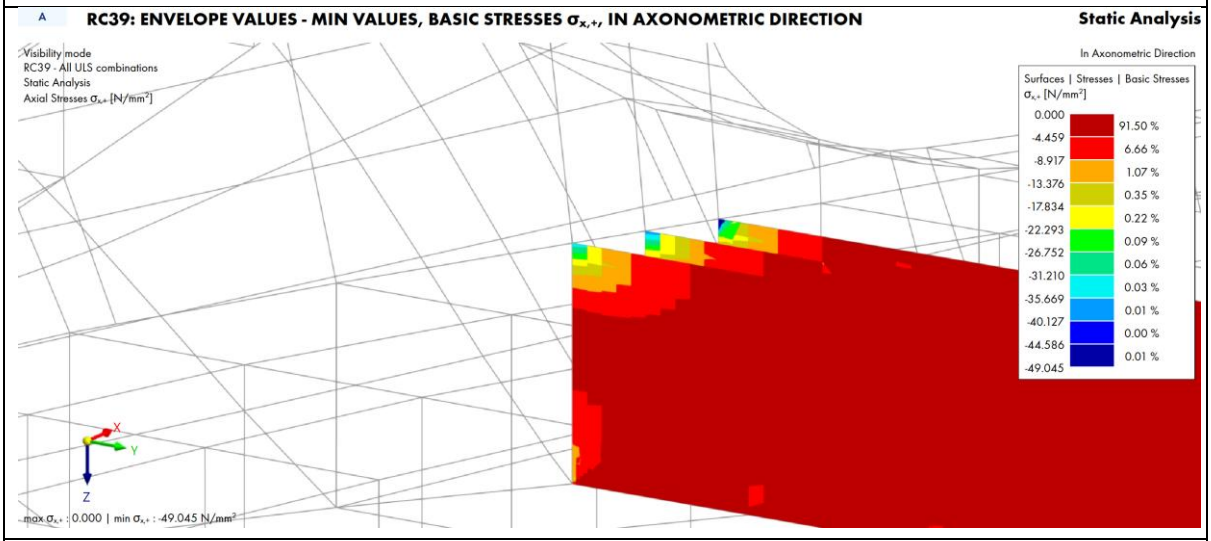

In the corner of the stiffener plate shown below, the stresses increase within a few mesh elements. This local stress peak is a numerical singularity and is therefore not representative of the actual structural behaviour.

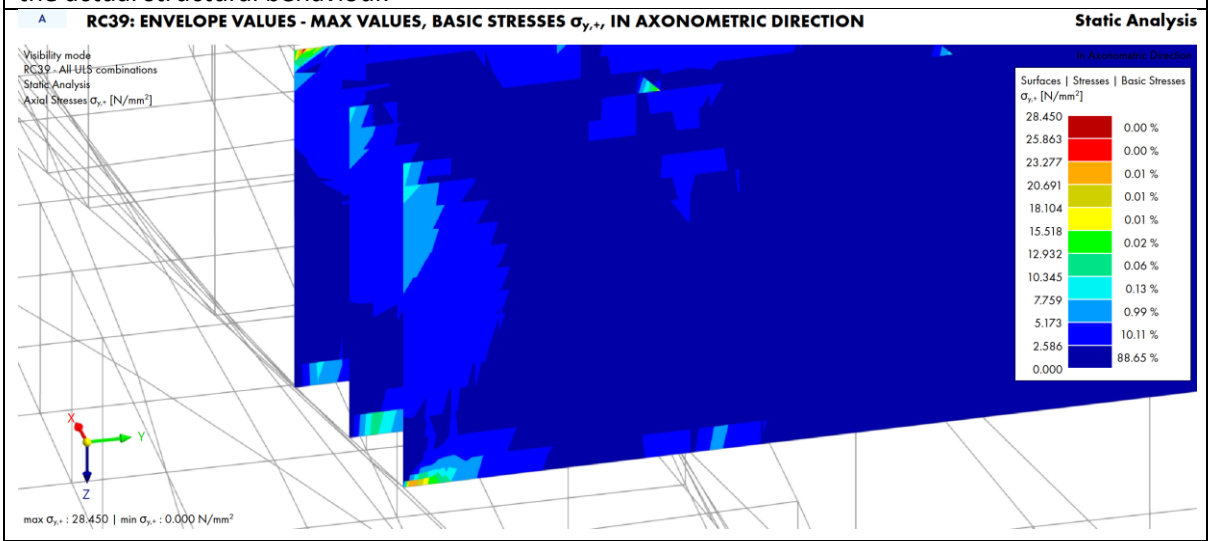

Stiffener plates set 4

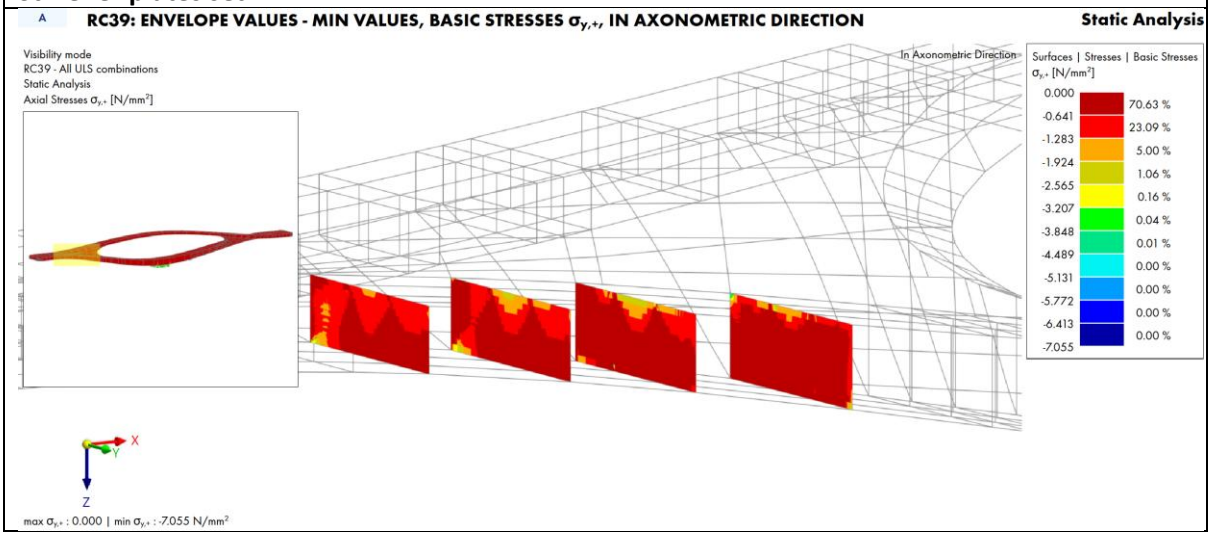

In the corner of the stiffener plate shown below, the stresses increase within a few mesh elements. This local stress peak is a numerical singularity and is therefore not representative of the actual structural behaviour.

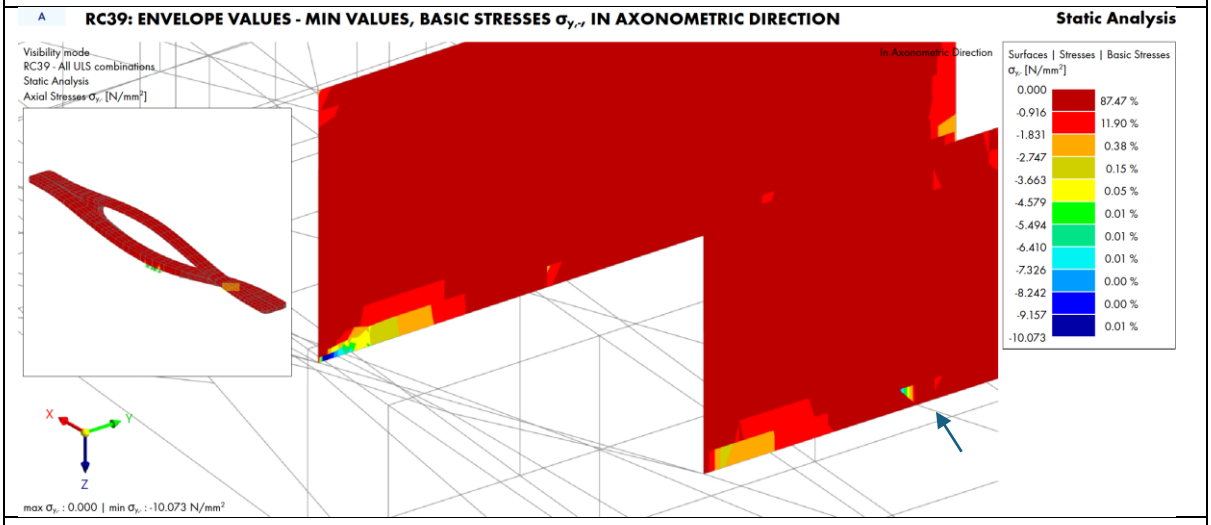

In the corner of the stiffener plate shown below, the stresses increase within a few mesh elements. This local stress peak is a numerical singularity and is therefore not representative of the actual structural behaviour.

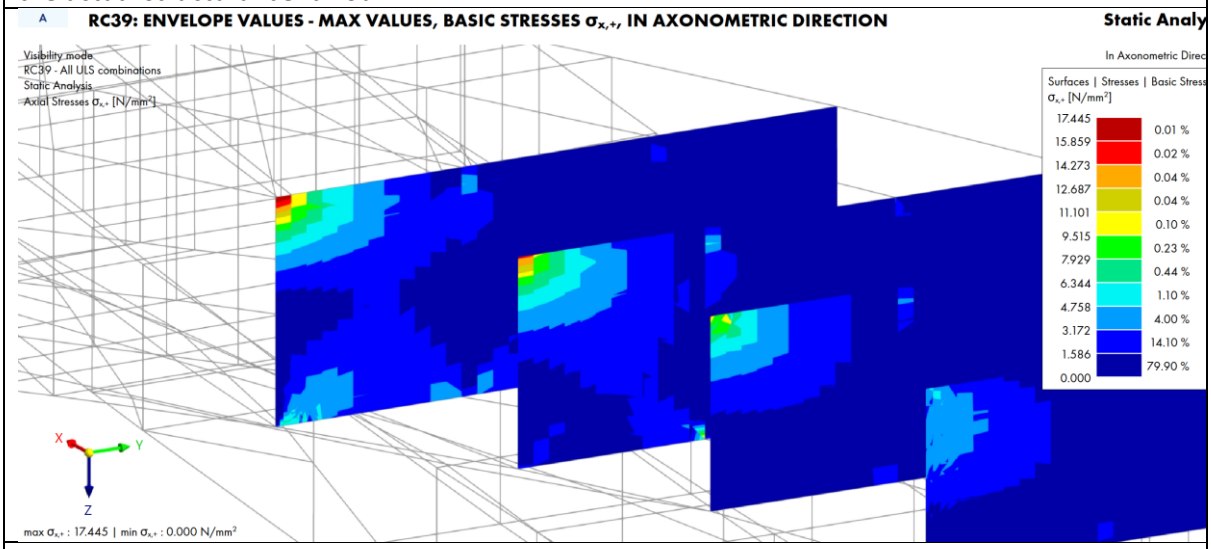

Stiffener plates set 5

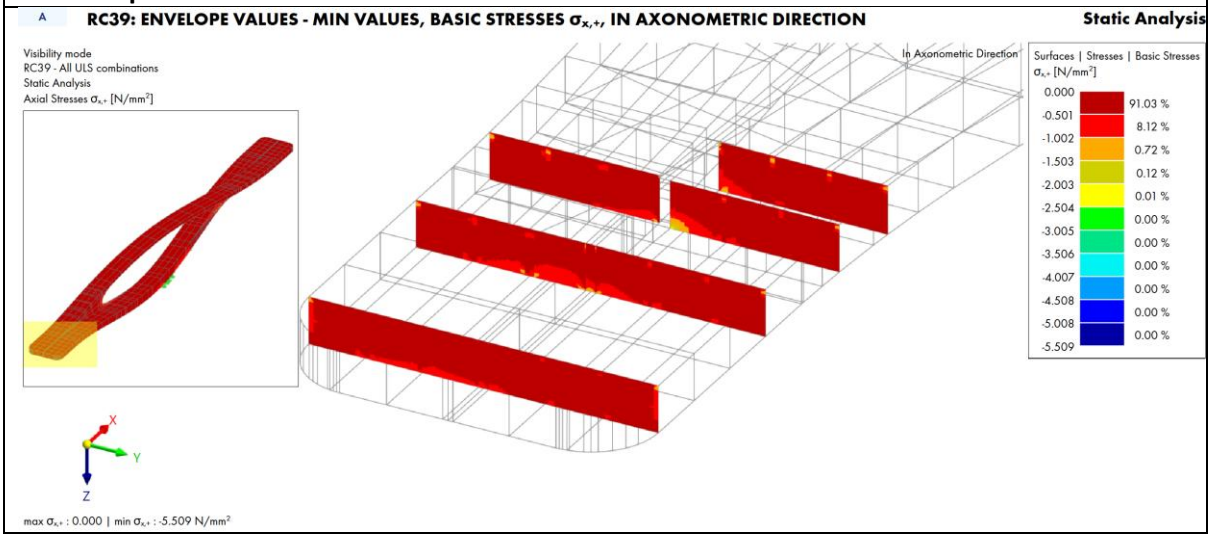

In the corner of the stiffener plate shown below, the stresses increase within a few mesh elements. This local stress peak is a numerical singularity and is therefore not representative of the actual structural behaviour.

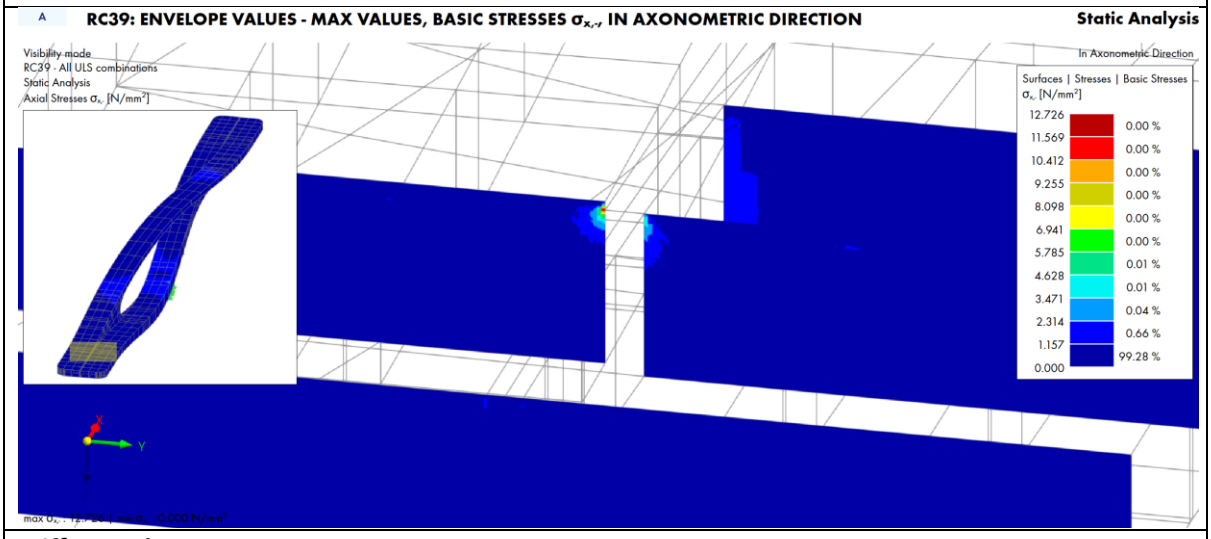

Stiffener plates set 6

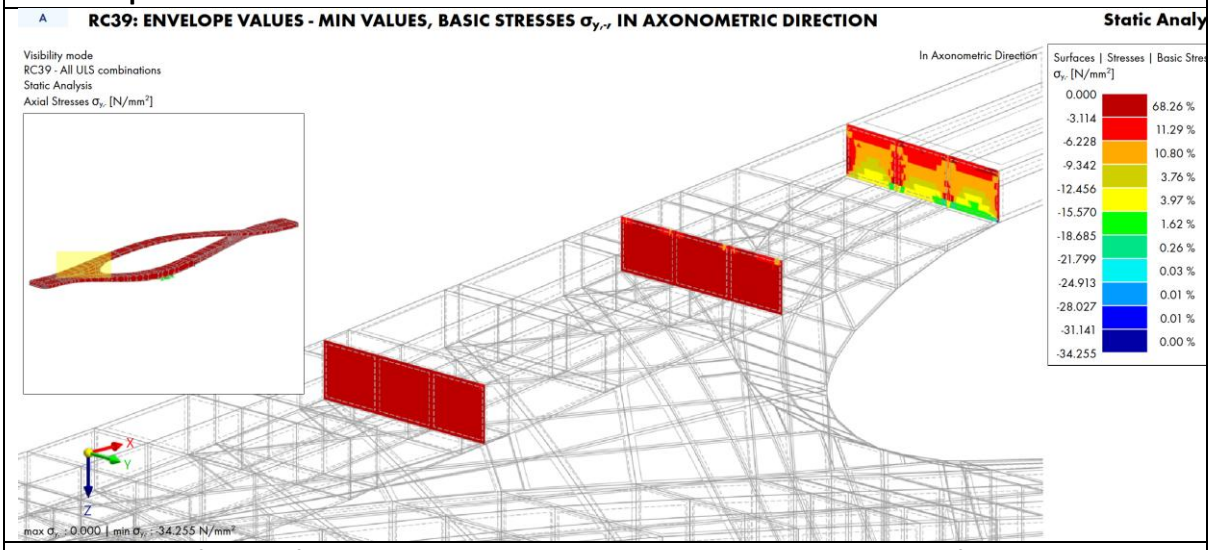

In the corner of the stiffener plate shown below, the stresses increase within a few mesh elements. This local stress peak is a numerical singularity and is therefore not representative of the actual structural behaviour.

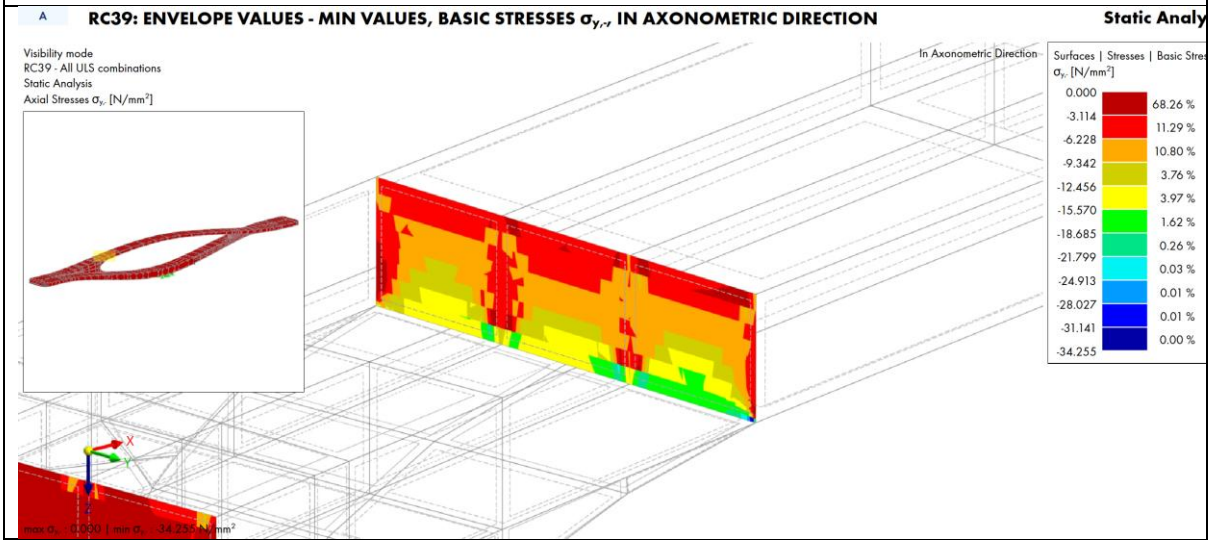

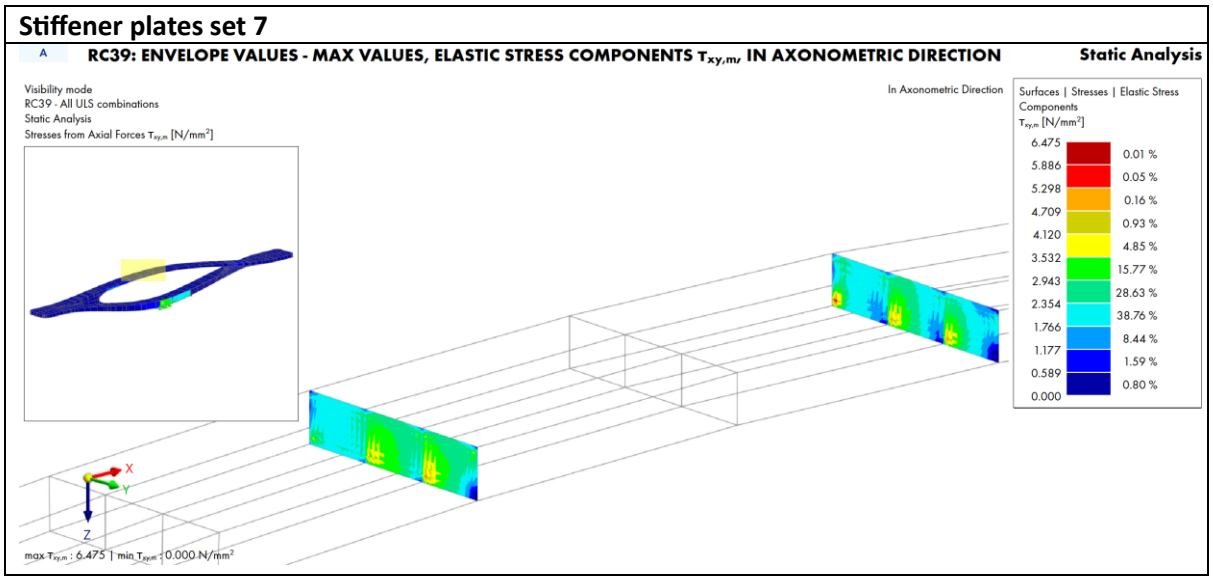

Table 122: Plate model singularities per component

Appendix T: Unity checks of the preliminary design

This appendix presents the unity check results and design stress limits for the preliminary design. The unity checks are provided for each structural component. The locations of the singularities in the finite element model are presented in Appendix S. Appendix S also contains overview figures of the different structural components.

Support plates

The material and design stress limits for the support plates are given in the table below.

		CUR 96 Strain limit [%]		**Material Stress limit** $[N/mm^2]$	**Design Material Stress limit** $[N/mm^2]$
Tension	$\varepsilon_{1t,Rk}$	1.2	$\sigma_{f1t} = \varepsilon_{1t,Rk} * E_1$	111.7	65.5
	$\varepsilon_{2t,Rk;low}$	1.2	$\sigma_{f2t} = \varepsilon_{2t,Rk;low} * E_2$	111.7	65.5
Compression	$\varepsilon_{1c,Rk}$	1.0	$\sigma_{f1c} = \varepsilon_{1c,Rk} * E_1$	93.1	54.6
	$\varepsilon_{2c,Rk;low}$	1.2	$\sigma_{f2c} = \varepsilon_{2c,Rk;low} * E_2$	111.7	65.5
Shear	$\gamma_{12,Rk}$	1.6	$\tau_{f12} = \gamma_{12,Rk} * G$	44.5	26.1

Table 123: Stress limits laminate support plates

The unity checks (UC) of different support plates sets are given in the tables below. The different sets are given in Appendix S including the locations where singularities appear.

Set 1	Max stress $[N/mm^2]$	UC	Side of the plate
σ_x tensile	16	0.24	Positive
σ_x compression	20	0.37	Negative
σ_y tensile	9	0.14	Negative
σ_y compression	9	0.14	Positive
τ_{xy}	5	0.19	Membrane

Table 124: UC of support plates set 1

Set 2	Max stress $[N/mm^2]$	UC	Side of the plate
σ_x tensile	12	0.18	Positive
σ_x compression	26	0.48	Positive
σ_y tensile	20	0.31	Positive
σ_y compression	25	0.38	Positive
τ_{xy}	10	0.38	Membrane

Table 125: UC of support plates set 2

Set 3 without plate next to arch	Max stress $[N/mm^2]$	UC	Side of the plate
σ_x tensile	18	0.27	Positive
σ_x compression	30	0.55	Positive
σ_y tensile	12	0.18	Positive
σ_y compression	20	0.31	Negative
τ_{xy}	9	0.34	Membrane

Table 126: UC of support plates set 3 without plate next to arch

Set 3 plate next to arch	Max stress $[N/mm^2]$	UC	Side of the plate
σ_x tensile	22	0.34	Negative
σ_x compression	89	1.63	Positive
σ_y tensile	31	0.47	Negative
σ_y compression	41	0.63	Negative
τ_{xy}	22	0.84	Membrane

Table 127: UC of support plates set 3 with plate next to arch

Set 4	Max stress $[N/mm^2]$	UC	Side of the plate
σ_x tensile	15	0.23	Positive
σ_x compression	12	0.22	Negative
σ_y tensile	15	0.23	Positive
σ_y compression	5	0.08	Positive
τ_{xy}	3	0.11	Membrane

Table 128: UC of support plates set 4

Side plates

The material and design stress limits for the side plates are given in the table below.

		CUR 96 Strain limit [%]		**Material Stress limit** $[N/mm^2]$	**Design Material Stress limit** $[N/mm^2]$
Tension	$\varepsilon_{1t,Rk}$	1.2	$\sigma_{f1t} = \varepsilon_{1t,Rk} * E_1$	189.9	111.4
	$\varepsilon_{2t,Rk;low}$	1.2	$\sigma_{f2t} = \varepsilon_{2t,Rk;low} * E_2$	62.9	36.9
Compression	$\varepsilon_{1c,Rk}$	1.0	$\sigma_{f1c} = \varepsilon_{1c,Rk} * E_1$	158.2	92.8
	$\varepsilon_{2c,Rk;low}$	1.2	$\sigma_{f2c} = \varepsilon_{2c,Rk;low} * E_2$	62.9	36.9
Shear	$\gamma_{12,Rk}$	1.6	$\tau_{f12} = \gamma_{12,Rk} * G$	29.6	15.3

Table 129: Stress limits laminate side plates

Arch plate

The unity checks of the arch plate is given in the table below. The locations where singularities occur are shown in Appendix S.

Arch plate	Max stress $[N/mm^2]$	UC	Side of the plate
σ_x tensile	47	0.42	Negative
σ_x compression	89	0.96	Negative
σ_y tensile	30	0.81	Positive
σ_y compression	30	0.81	Negative
τ_{xy}	27	1.76	Membrane

Table 130: UC of arch plate

Top side plate

The unity checks of the top side plate is given in the table below. The locations where singularities occur are shown in Appendix S.

Top side plate	Max stress $[N/mm^2]$	UC	Side of the plate
σ_x tensile	30	0.27	Positive
σ_x compression	92	0.99	Positive
σ_y tensile	27	0.73	Positive
σ_y compression	36	0.98	Positive
τ_{xy}	25	1.63	Membrane

Table 131: UC of top side plate

Bottom side plate

The unity checks of the bottom side plate is given in the table below. The locations where singularities occur are shown in Appendix S.

Bottom side plate	Max stress $[N/mm^2]$	UC	Side of the plate
σ_x tensile	36	0.32	Positive
σ_x compression	60	0.65	Negative
σ_y tensile	14	0.38	Positive
σ_y compression	19	0.51	Positive
τ_{xy}	18	1.18	Membrane

Table 132: UC of bottom side plate

Bottom plate

The material and design stress limits for the bottom plate are given in the table below.

		CUR 96 Strain limit [%]		**Material Stress limit** $[N/mm^2]$	**Design Material Stress limit** $[N/mm^2]$
Tension	$\varepsilon_{1t,Rk}$	1.2	$\sigma_{f1t} = \varepsilon_{1t,Rk} * E_1$	189.9	111.4
	$\varepsilon_{2t,Rk;low}$	1.2	$\sigma_{f2t} = \varepsilon_{2t,Rk;low} * E_2$	62.9	36.9
Compression	$\varepsilon_{1c,Rk}$	1.0	$\sigma_{f1c} = \varepsilon_{1c,Rk} * E_1$	158.2	92.8
	$\varepsilon_{2c,Rk;low}$	1.2	$\sigma_{f2c} = \varepsilon_{2c,Rk;low} * E_2$	62.9	36.9
Shear	$\gamma_{12,Rk}$	1.6	$\tau_{f12} = \gamma_{12,Rk} * G$	29.6	15.3

Table 133: Stress limits laminate bottom plate

The unity checks of the bottom plate is given in the table below. The locations where singularities occur are shown in Appendix S.

Bottom plate	Max stress $[N/mm^2]$	UC	Side of the plate
σ_x tensile	65	0.58	Positive
σ_x compression	120	1.29	Positive
σ_y tensile	20	0.54	Positive
σ_y compression	20	0.54	Negative
τ_{xy}	14	0.92	Membrane

Table 134: UC of bottom plate

C-shaped girders

The material and design stress limits for the C-shaped girders are given in the table below.

		CUR 96 Strain limit [%]		**Material Stress limit** $[N/mm^2]$	**Design Material Stress limit** $[N/mm^2]$
Tension	$\varepsilon_{1t,Rk}$	1.2	$\sigma_{f1t} = \varepsilon_{1t,Rk} * E_1$	111.7	65.5
	$\varepsilon_{2t,Rk;low}$	1.2	$\sigma_{f2t} = \varepsilon_{2t,Rk;low} * E_2$	111.7	65.5
Compression	$\varepsilon_{1c,Rk}$	1.0	$\sigma_{f1c} = \varepsilon_{1c,Rk} * E_1$	93.1	54.6
	$\varepsilon_{2c,Rk;low}$	1.2	$\sigma_{f2c} = \varepsilon_{2c,Rk;low} * E_2$	111.7	65.5
Shear	$\gamma_{12,Rk}$	1.6	$\tau_{f12} = \gamma_{12,Rk} * G$	44.5	26.1

Table 135: Stress limits laminate C-shaped girders

The unity checks of the C-shaped girders is given in the table below. The locations where singularities occur are shown in Appendix S.

C-shaped girders	Max stress $[N/mm^2]$	UC	Side of the plate
σ_x tensile	41	0.63	Positive
σ_x compression	42	0.77	Positive
σ_y tensile	36	0.55	Negative
σ_y compression	64	0.98	Positive
τ_{xy}	29	1.11	Membrane

Table 136: UC of C-shaped girders

Top plate

The material and design stress limits for the top plate are given in the table below.

		CUR 96 Strain limit [%]		**Material Stress limit** $[N/mm^2]$	**Design Material Stress limit** $[N/mm^2]$
Tension	$\varepsilon_{1t,Rk}$	1.2	$\sigma_{f1t} = \varepsilon_{1t,Rk} * E_1$	189.9	111.4
	$\varepsilon_{2t,Rk;low}$	1.2	$\sigma_{f2t} = \varepsilon_{2t,Rk;low} * E_2$	62.9	36.9
Compression	$\varepsilon_{1c,Rk}$	1.0	$\sigma_{f1c} = \varepsilon_{1c,Rk} * E_1$	158.2	92.8
	$\varepsilon_{2c,Rk;low}$	1.2	$\sigma_{f2c} = \varepsilon_{2c,Rk;low} * E_2$	62.9	36.9
Shear	$\gamma_{12,Rk}$	1.6	$\tau_{f12} = \gamma_{12,Rk} * G$	29.6	15.3

Table 137: Stress limits laminate top plate

The unity checks of the top plate is given in the table below. The locations where singularities occur are shown in Appendix S.

Top plate	Max stress $[N/mm^2]$	UC	Side of the plate
σ_x tensile	35	0.31	Negative
σ_x compression	24	0.26	Negative
σ_y tensile	11	0.30	Negative
σ_y compression	15	0.41	Negative
τ_{xy}	3	0.20	Membrane

Table 138: UC of top plate

Stiffener plates

The material and design stress limits for the stiffener plates are given in the table below.

		CUR 96 Strain limit [%]		**Material Stress limit** $[N/mm^2]$	**Design Material Stress limit** $[N/mm^2]$
Tension	$\varepsilon_{1t,Rk}$	1.2	$\sigma_{f1t} = \varepsilon_{1t,Rk} * E_1$	111.7	65.5
	$\varepsilon_{2t,Rk;low}$	1.2	$\sigma_{f2t} = \varepsilon_{2t,Rk;low} * E_2$	111.7	65.5
Compression	$\varepsilon_{1c,Rk}$	1.0	$\sigma_{f1c} = \varepsilon_{1c,Rk} * E_1$	93.08	54.6
	$\varepsilon_{2c,Rk;low}$	1.2	$\sigma_{f2c} = \varepsilon_{2c,Rk;low} * E_2$	111.7	65.5
Shear	$\gamma_{12,Rk}$	1.6	$\tau_{f12} = \gamma_{12,Rk} * G$	44.48	26.1

Table 139: Stress limits laminate stiffener plates

The unity checks of different stiffener plates sets are given in the tables below. The different sets are given in Appendix S including the locations where singularities appear.

Set 1	Max stress $[N/mm^2]$	UC	Side of the plate
σ_x tensile	14	0.21	Positive
σ_x compression	13	0.24	Positive
σ_y tensile	45	0.69	Positive
σ_y compression	60	0.92	Positive
τ_{xy}	37	1.42	Membrane

Table 140: UC of stiffener plates set 1

Set 2	Max stress $[N/mm^2]$	UC	Side of the plate
σ_x tensile	7	0.11	Positive
σ_x compression	6	0.11	Negative
σ_y tensile	7	0.11	Negative
σ_y compression	9	0.14	Positive
τ_{xy}	16	0.61	Membrane

Table 141: UC of stiffener plates set 2

Set 3	Max stress $[N/mm^2]$	UC	Side of the plate
σ_x tensile	21	0.32	Negative
σ_x compression	23	0.42	Positive
σ_y tensile	21	0.32	Negative
σ_y compression	17	0.26	Positive
τ_{xy}	37	1.42	Membrane

Table 142: UC of stiffener plates set 3

Set 4	Max stress $[N/mm^2]$	UC	Side of the plate
σ_x tensile	12	0.18	Negative
σ_x compression	10	0.18	Negative
σ_y tensile	11	0.17	Negative
σ_y compression	7	0.11	Positive
τ_{xy}	14	0.54	Membrane

Table 143: UC of stiffener plates set 4

Set 5	Max stress [N/mm^2]	UC	Side of the plate
σ_x tensile	6	0.09	Positive
σ_x compression	6	0.11	Positive
σ_y tensile	5	0.08	Negative
σ_y compression	6	0.09	Negative
τ_{xy}	6	0.23	Membrane

Table 144: UC of stiffener plates set 5

Set 6	Max stress [N/mm^2]	UC	Side of the plate
σ_x tensile	12	0.18	Positive
σ_x compression	12	0.22	Negative
σ_y tensile	16	0.24	Negative
σ_y compression	25	0.38	Negative
τ_{xy}	17	0.65	Membrane

Table 145: UC of stiffener plates set 6

Set 7	Max stress [N/mm^2]	UC	Side of the plate
σ_x tensile	5	0.08	Positive
σ_x compression	8	0.15	Negative
σ_y tensile	10	0.15	Positive
σ_y compression	6	0.09	Negative
τ_{xy}	7	0.27	Membrane

Table 146: UC of stiffener plates set 7

Appendix U: Deformation plots preliminary design

Characteristic

The characteristic deflection of w_2 without creep factor is given in the figure below.

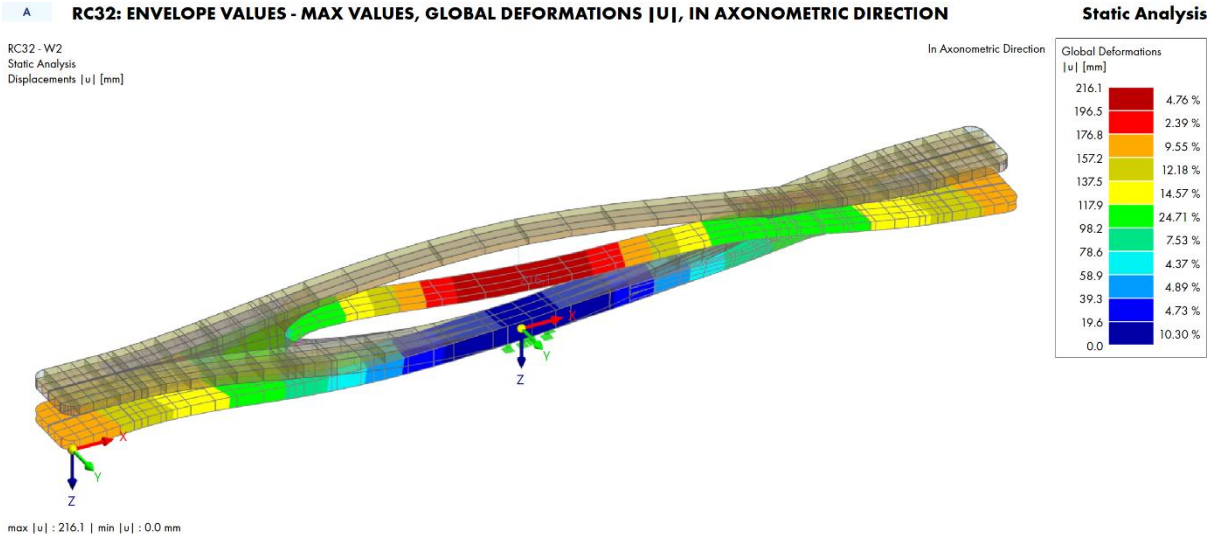

Figure 202: Characteristic deflection of w_2 without creep factor

The characteristic deflection of w_3 is given in the figure below.

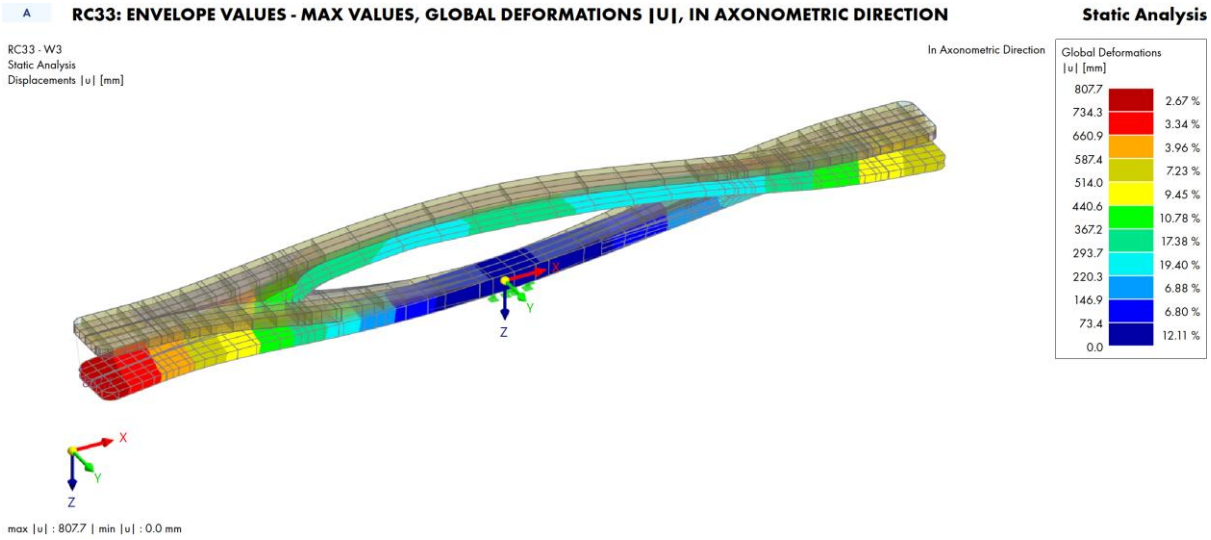

Figure 203: Characteristic deflection of w_3

Quasi-permanent

The quasi-permanent deflection of w_1 is given in the figure below.

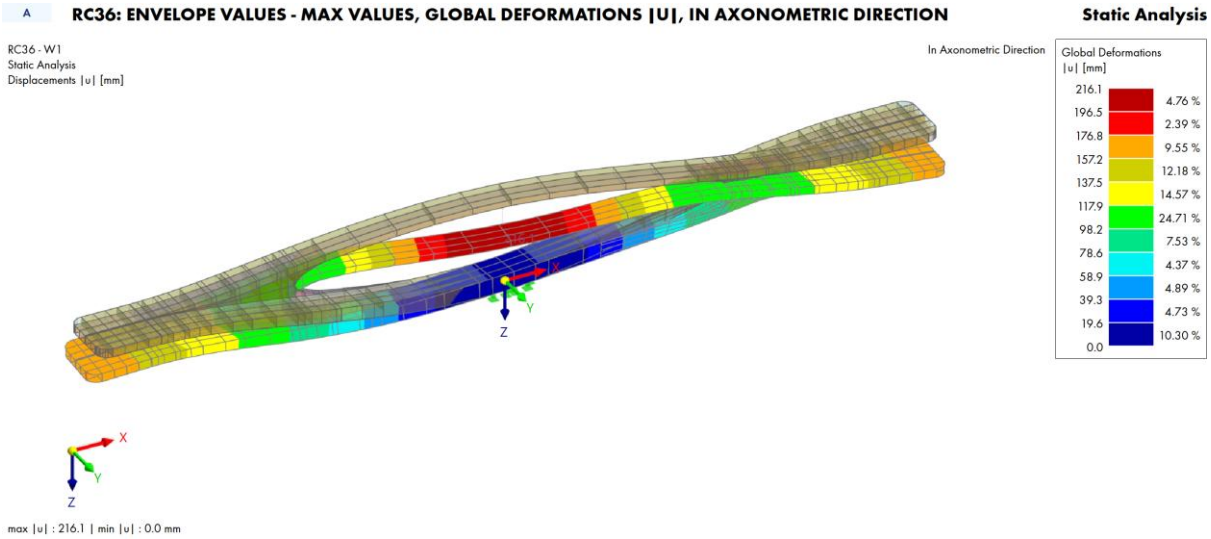

Figure 204: Quasi-permanent deflection of w_1

The quasi-permanent deflection of w_2 without creep factor is given in the figure below.

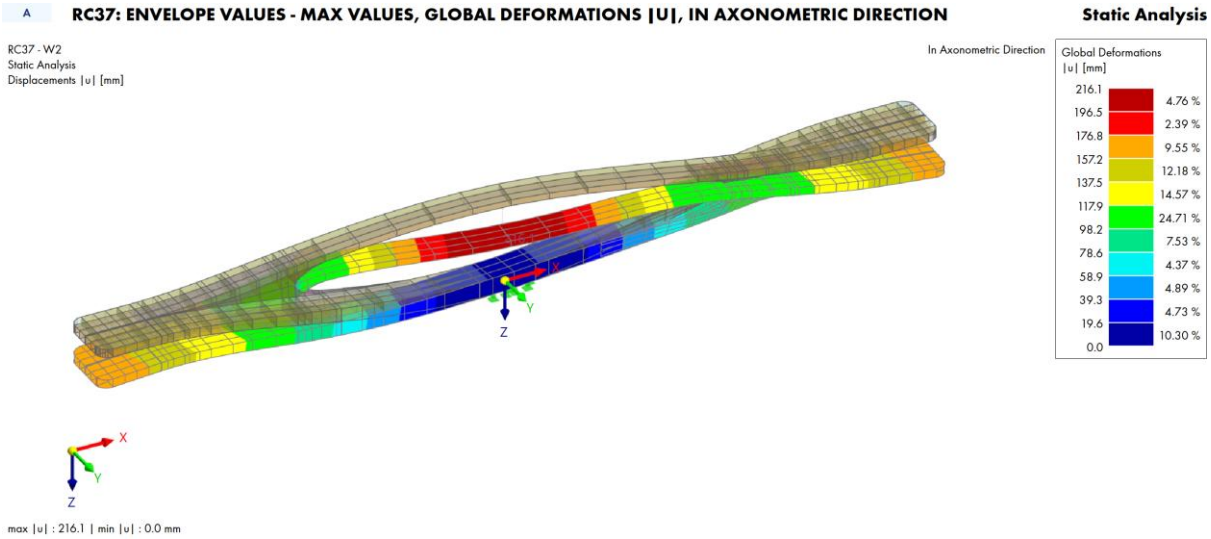

Figure 205: Quasi-permanent deflection of w_2 without creep factor

Appendix V: x-coordinates support and stiffener plates revised design

The support plates lie in the yz-plane; therefore, a single x-coordinate defines the position of each entire support plate. The x-coordinates given for the stiffener plates correspond to the points on the plates closest to $y = 0$, since the stiffener plates do not lie in the yz-plane.

Support plates x-coordinate [m]	Stiffener plates x-coordinate (for points closest to y = 0) [m]
	-24.288 (Side deck)
	-22.145 (Side deck)
-20.672	-20.672 (Lower deck) (Upper deck)
-19.718	-19.718 (Lower deck) (Upper deck)
-18.428	-18.428 (Lower deck) (Upper deck)
-17.143	-17.143 (Lower deck) (Upper deck)
-16.003	-16.003 (Lower deck) (Upper deck)
-14.584	-14.584 (Lower deck) (Upper deck)
-13.306	-13.306 (Lower deck)
-12.905	-12.905 (Lower deck) (Upper deck)
-12.499	-12.499 (Lower deck)
-11.926 (Below side arch)	-11.926 (Bottom side arch) (Lower deck)
-11.733 (On top side arch)	-11.733 (On top side arch) (Upper deck)
-10.751 (Below side arch)	-10.751 (Bottom side arch) (Lower deck)
	-10.706 (Upper deck)
-9.472 (Below side arch)	-9.472 (Bottom side arch) (Lower deck)
	-8.747 (Upper deck)
-8.191 (Below side arch)	-8.191 (Bottom side arch) (Lower deck)
-6.908 (Below side arch)	-6.908 (Bottom side arch) (Lower deck)
	-6.595 (Upper deck)
	-5.520 (Lower deck)
	-4.371 (Lower deck) (Upper deck)
	-2.204 (Lower deck)
	-2.202 (Upper deck)
	-1.373 (Lower deck)
	0.000 (Lower deck) (Upper deck)
	1.373 (Lower deck)
	2.202 (Lower deck)
	2.204 (Upper deck)
	4.371 (Lower deck) (Upper deck)
	5.520 (Lower deck)
	6.595 (Upper deck)
6.908 (Below side arch)	6.908 (Bottom side arch) (Lower deck)
8.191 (Below side arch)	8.191 (Bottom side arch) (Lower deck)
	8.747 (Upper deck)
9.472 (Below side arch)	9.472 (Bottom side arch) (Lower deck)
	10.706 (Upper deck)
10.751 (Below side arch)	10.751 (Bottom side arch) (Lower deck)
11.733 (On top side arch)	11.733 (On top side arch) (Upper deck)
11.926 (Below side arch)	11.926 (Bottom side arch) (Lower deck)
12.499	12.499 (Lower deck)
12.905	12.905 (Lower deck) (Upper deck)
13.306	13.306 (Lower deck)

14.584	14.584	(Lower deck) (Upper deck)
16.003	16.003	(Lower deck) (Upper deck)
17.143	17.143	(Lower deck) (Upper deck)
18.428	18.428	(Lower deck) (Upper deck)
19.718	19.718	(Lower deck) (Upper deck)
20.672	20.672	(Lower deck) (Upper deck)
	-22.145	(Side deck)
	-24.288	(Side deck)

Table 147: x-coordinates support and stiffener plates revised design

Appendix W: Thickness structures and input RFEM plates revised design

Support plates

Set 1 and set 2

The layering structure of the laminate is given in Figure 206 and the material properties are given in the table below.

Property	Membrane	Bending	Unit
E_1	9.308	11.037	GPa
E_2	9.308	9.006	GPa
G_{12}	2.780	2.273	GPa
υ_{12}	0.228650	0.186934	-
υ_{21}	0.228650	0.152534	-

Table 148: Material properties support plates set 1 and 2

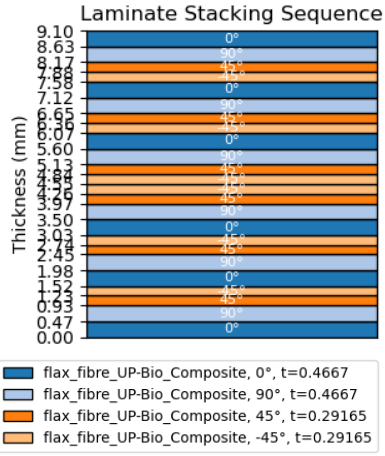

Figure 206: Layering structure support plates set 1 and 2

Input for RFEM plate model for support plates set 1 and 2:

- E_x = 9307.781 [N/mm^2]
- E_y = 9307.781 [N/mm^2]
- G_yz = 2779.664 [N/mm^2]
- G_xz = 2779.664 [N/mm^2]
- G_xy = 2779.664 [N/mm^2]
- nu_xy = 0.229 [-]
- nu_yx = 0.229 [-]
- Density of the side plate = 1320.0 [kg/m^3]
- Weight of the side plate = 13.20 [kN/m^3]
- Thickness = 9.10 [mm]

Set 3 without plate next to arch

The layering structure of the laminate is given in Figure 207 and the material properties are given in the table below.

Property	Membrane	Bending	Unit
E_1	9.308	9.811	GPa
E_2	9.308	9.260	GPa
G_{12}	2.780	2.625	GPa
υ_{12}	0.228650	0.215868	-
υ_{21}	0.228650	0.203725	-

Table 149: Material properties support plates set 3 without plate next to arch

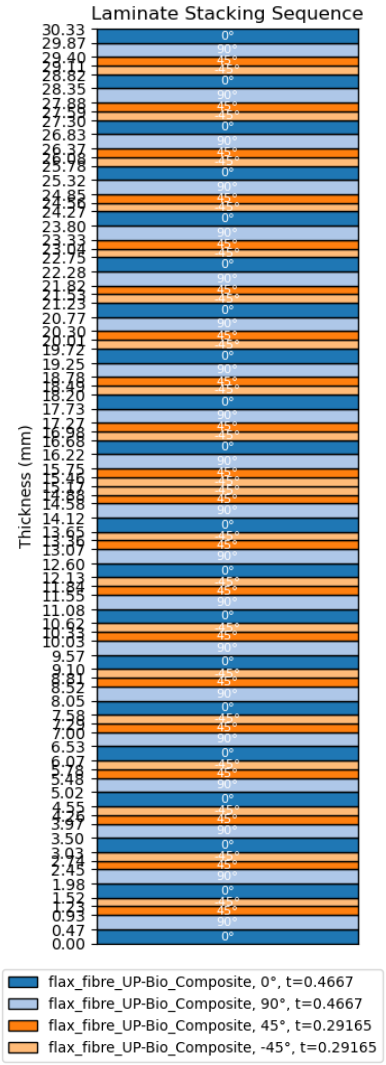

Figure 207: Layering structure support plates set 3 without plate next to arch

Input for RFEM plate model for support plates set 3 without plate next to arch:

- E_x = 9307.781 [N/mm^2]
- E_y = 9307.781 [N/mm^2]
- G_yz = 2779.664 [N/mm^2]
- G_xz = 2779.664 [N/mm^2]
- G_xy = 2779.664 [N/mm^2]
- nu_xy = 0.229 [-]
- nu_yx = 0.229 [-]
- Density of the side plate = 1320.0 [kg/m^3]
- Weight of the side plate = 13.20 [kN/m^3]
- Thickness = 30.33 [mm]

Set 3 with plate next to arch

The layering structure of the laminate is given in Figure 208 and the material properties are given in the table below.

Property	Membrane	Bending	Unit
E_1	9.308	9.603	GPa
E_2	9.308	9.284	GPa
G_{12}	2.780	2.689	GPa
υ_{12}	0.228650	0.221098	-
υ_{21}	0.228650	0.213762	-

Table 150: Material properties support plates set 3 with plate next to arch

Input for RFEM plate model for support plates set 3 with plate next to arch:

- E_x = 9307.781 [N/mm^2]
- E_y = 9307.781 [N/mm^2]
- G_yz = 2779.664 [N/mm^2]
- G_xz = 2779.664 [N/mm^2]
- G_xy = 2779.664 [N/mm^2]
- nu_xy = 0.229 [-]
- nu_yx = 0.229 [-]
- Density of the side plate = 1320.0 [kg/m^3]
- Weight of the side plate = 13.20 [kN/m^3]
- Thickness = 51.57 [mm]

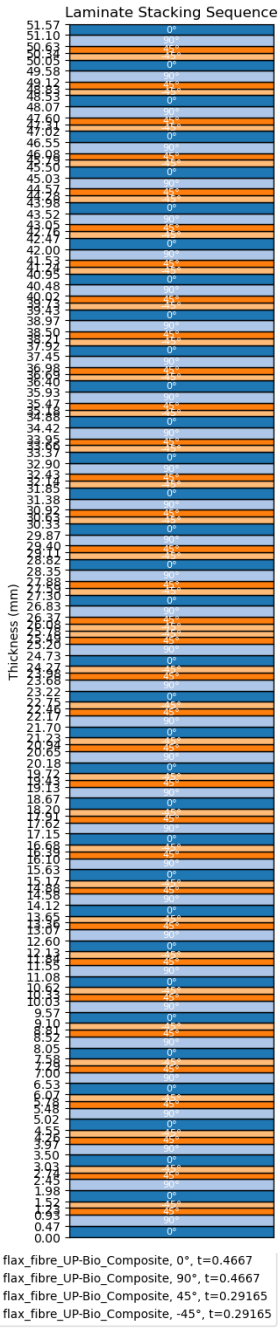

Figure 208: Layering structure support plates set 3 with plate next to arch

Set 4

The layering structure of the laminate is given in Figure 209 and the material properties are given in the table below.

Property	Membrane	Bending	Unit
E_1	9.308	10.328	GPa
E_2	9.308	9.174	GPa
G_{12}	2.780	2.473	GPa
υ_{12}	0.228650	0.203338	-
υ_{21}	0.228650	0.180629	-

Table 151: Material properties support plates set 4

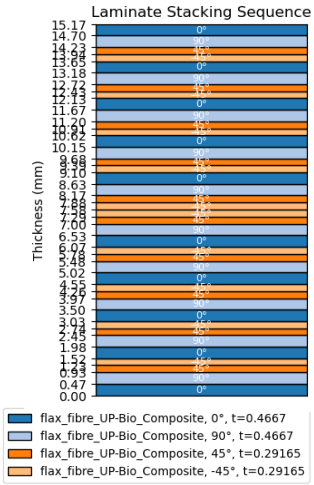

Figure 209: Layering structure support plates set 4

Input for RFEM plate model for support plates set 4:

- E_x = 9307.781 [N/mm^2]
- E_y = 9307.781 [N/mm^2]
- G_yz = 2779.664 [N/mm^2]
- G_xz = 2779.664 [N/mm^2]
- G_xy = 2779.664 [N/mm^2]
- nu_xy = 0.229 [-]
- nu_yx = 0.229 [-]
- Density of the side plate = 1320.0 [kg/m^3]
- Weight of the side plate = 13.20 [kN/m^3]
- Thickness = 15.17 [mm]

Side plates

The layering structure of the laminate is given in Figure 210 and the material properties are given in the table below.

Property	Membrane	Bending	Unit
E_1	14.000	14.082	GPa
E_2	6.427	6.713	GPa
G_{12}	2.112	1.978	GPa
υ_{12}	0.239115	0.210564	-
υ_{21}	0.109770	0.100387	-

Table 152: Material properties side plates

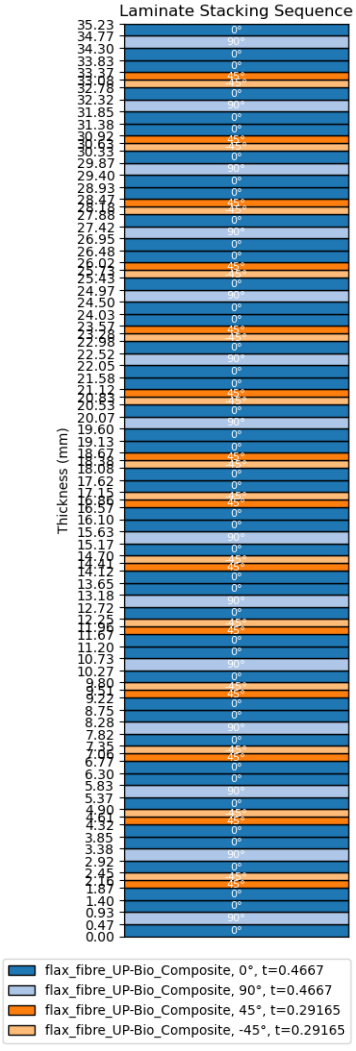

Figure 210: Layering structure side plates

Input for RFEM plate model for side plates:

- E_x = 14000 [N/mm^2]
- E_y = 6427 [N/mm^2]
- G_yz = 2112 [N/mm^2]
- G_xz = 2112 [N/mm^2]
- G_xy = 2112 [N/mm^2]
- nu_xy = 0.239 [-]
- nu_yx = 0.110 [-]
- Density of the side plate = 1320.0 [kg/m^3]
- Weight of the side plate = 13.20 [kN/m^3]
- Thickness = 35.23 [mm]

Bottom plate

The layering structure of the laminate is given in Figure 211 and the material properties are given in the table below.

Property	Membrane	Bending	Unit
E_1	15.822	15.990	GPa
E_2	5.241	5.475	GPa
G_{12}	1.853	1.703	GPa
υ_{12}	0.246580	0.210286	-
υ_{21}	0.081680	0.072008	-

Table 153: Material properties bottom plate

Input for RFEM plate model for bottom deck:

- E_x = 18471.805 [N/mm^2]
- E_y = 5241.034 [N/mm^2]
- G_yz = 1852.932 [N/mm^2]
- G_xz = 1852.932 [N/mm^2]
- G_xy = 1852.932 [N/mm^2]
- nu_xy = 0.247 [-]
- Density of the bottom deck = 1763.028 [kg/m^3]
- Weight of the bottom deck = 17.630 [kN/m^3]
- Thickness = 40.602 [mm]
- The width of the plate is 1800 [mm]
- The width of the plate from girder to girder is 1778.766 [mm]

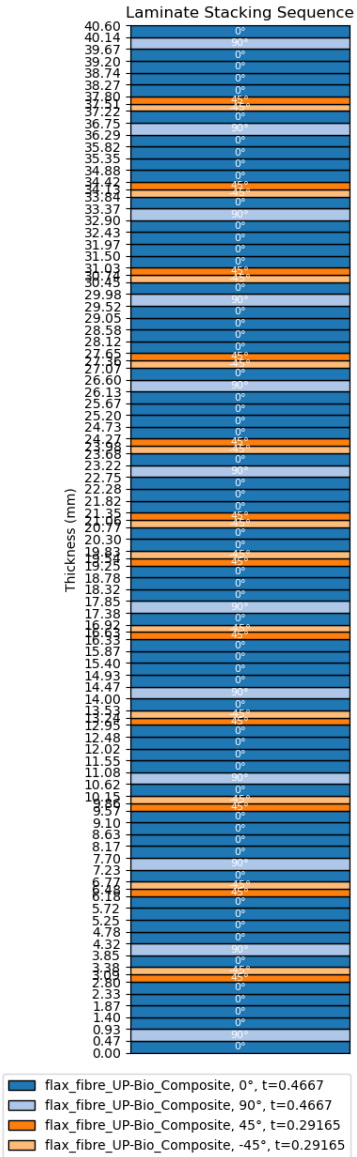

Figure 211: Layering structure bottom plate

C-shaped girders

The layering structure of the laminate is given in Figure 212 and the material properties are given in the table below.

Property	Membrane	Bending	Unit
E_1	9.308	10.031	GPa
E_2	9.308	9.227	GPa
G_{12}	2.780	2.560	GPa
υ_{12}	0.228650	0.210470	-
υ_{21}	0.228650	0.193607	-

Table 154: Material properties C-shaped girders

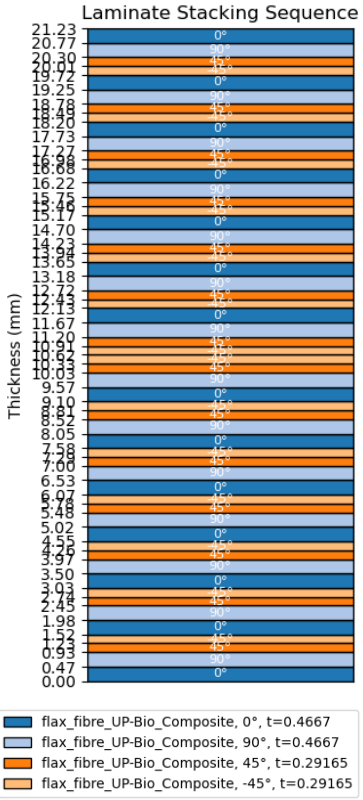

Figure 212: Layering structure C-shaped girders

Input for RFEM plate model for girders is:

- E_x = 9307.781 [N/mm^2]
- E_y = 9307.781 [N/mm^2]
- G_yz = 2779.664 [N/mm^2]
- G_xz = 2779.664 [N/mm^2]
- G_xy = 2779.664 [N/mm^2]
- nu_xy = 0.229 [-]
- Density of the girders = 1036.292 [kg/m^3]
- Weight of the girders = 10.363 [kN/m^3]
- Thickness = 21.234 [mm]
- The locations of the girders with respect to the left side of the cross-section is:
    - Girder 1 is located at 7.583 [mm]
    - Girder 2 is located at 602.338 [mm]
    - Girder 3 is located at 1212.662 [mm]
    - Girder 4 is located at 1807.417 [mm]
- The distance between the girders is:
    - Between girder 1 and girder 2 is 594.754 [mm]
    - Between girder 2 and girder 3 is 610.325 [mm]
    - Between girder 3 and girder 4 is 594.754 [mm]

Top plate

The layering structure of the laminate is given in Figure 213 and the material properties are given in the table below.

Property	Membrane	Bending	Unit
E_1	15.822	16.049	GPa
E_2	5.241	5.598	GPa
G_{12}	1.853	1.633	GPa
υ_{12}	0.246580	0.193800	-
υ_{21}	0.081680	0.067591	-

Table 155: Material properties top and bottom face

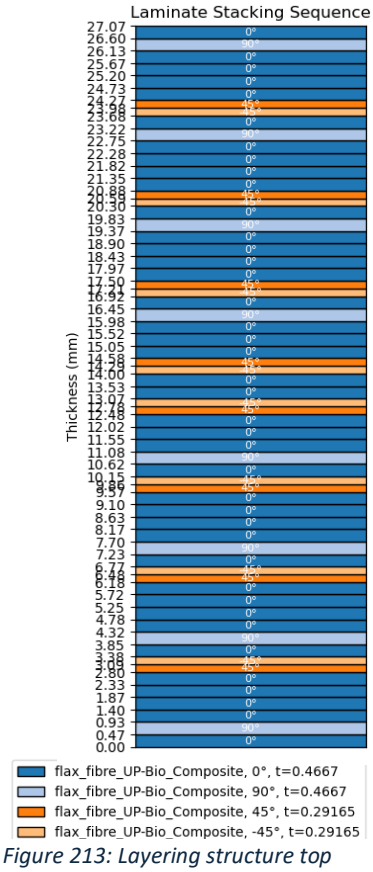

Figure 213: Layering structure top and bottom face

Input for RFEM plate model for top deck:

- E_x = 7471.672 [N/mm^2]
- E_y = 2202.821 [N/mm^2]
- G_yz = 779.684 [N/mm^2]
- G_xz = 779.684 [N/mm^2]
- G_xy = 779.684 [N/mm^2]
- nu_xy = 0.247 [-]
- nu_yx = 0.082 [-]
- Density of the top deck = 726.879 [kg/m^3]
- Weight of the top deck = 7.269 [kN/m^3]
- Thickness = 129.136 [mm]
- The width of the plate is 1800 [mm]
- The width of the plate from girder to girder is 1778.766 [mm]

Stiffener plates

The layering structure of the laminate is given in Figure 214 and the material properties are given in the table below.

Property	Membrane	Bending	Unit
E_1	9.308	11.037	GPa
E_2	9.308	9.006	GPa
G_{12}	2.780	2.273	GPa
υ_{12}	0.228650	0.186934	-
υ_{21}	0.228650	0.152534	-

Table 156: Material properties stiffener plates

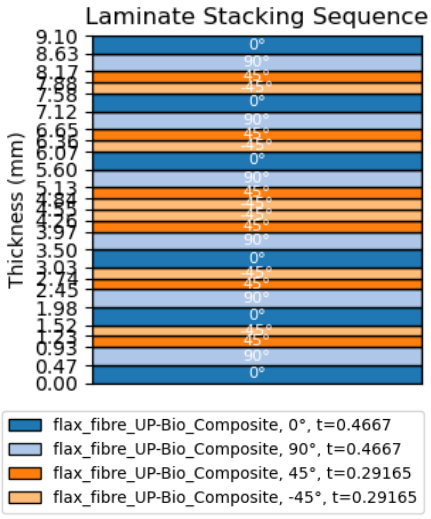

Figure 214: Layering structure stiffener plates

Input for RFEM plate model for stiffener plates:

- E_x = 9307.781 [N/mm^2]
- E_y = 9307.781 [N/mm^2]
- G_yz = 2779.664 [N/mm^2]
- G_xz = 2779.664 [N/mm^2]
- G_xy = 2779.664 [N/mm^2]
- nu_xy = 0.229 [-]
- nu_yx = 0.229 [-]
- Density of the side plate = 1320.0 [kg/m^3]
- Weight of the side plate = 13.20 [kN/m^3]
- Thickness = 9.10 [mm]

Appendix X: Stability analysis

Critical load factor	Buckling shape
0.562	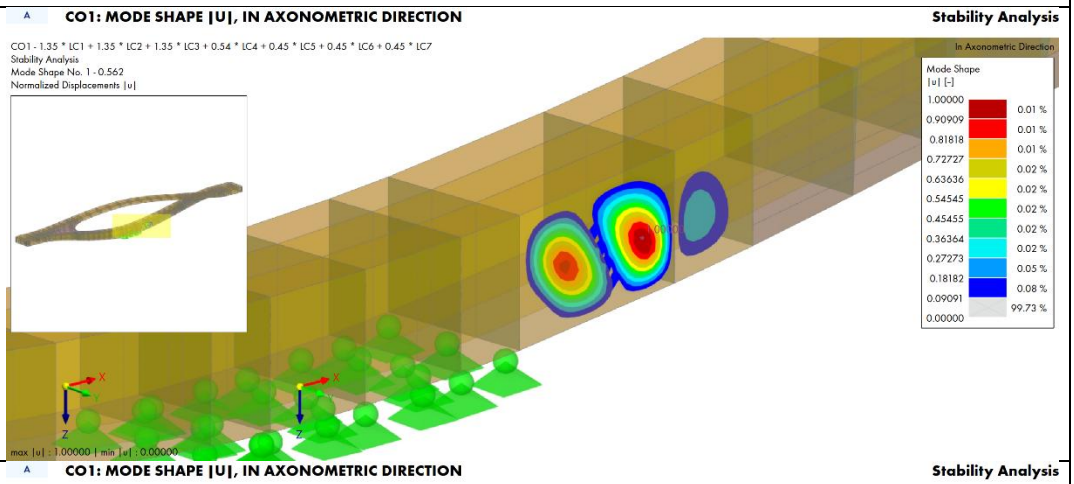
0.601	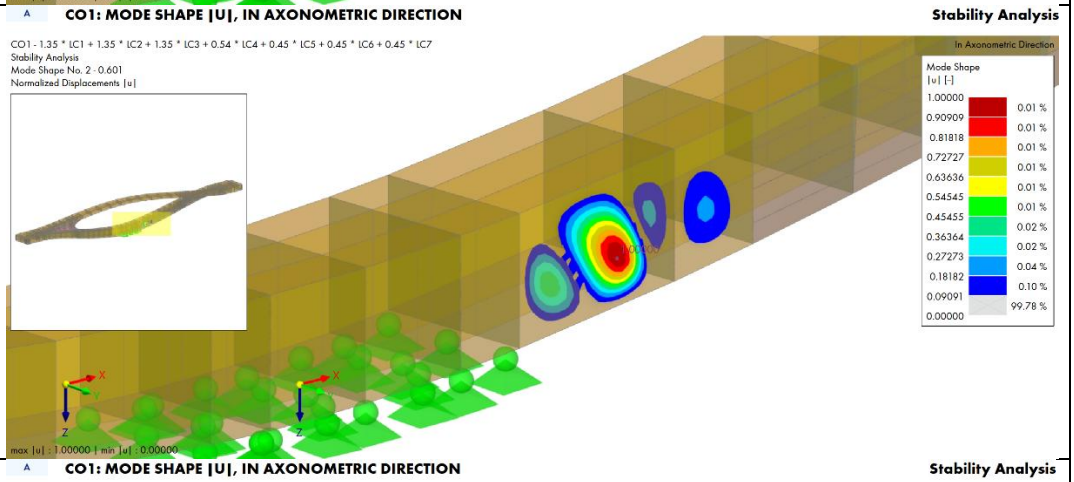
0.740	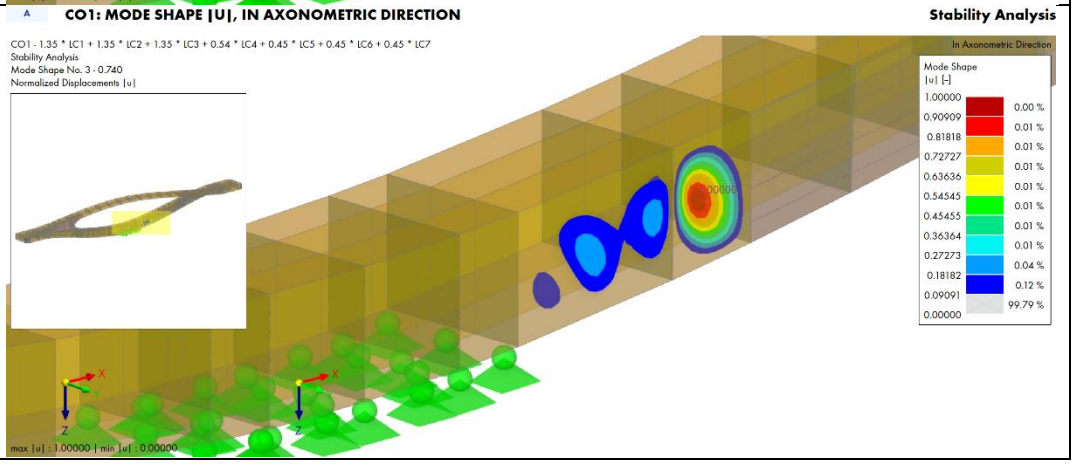

0.828	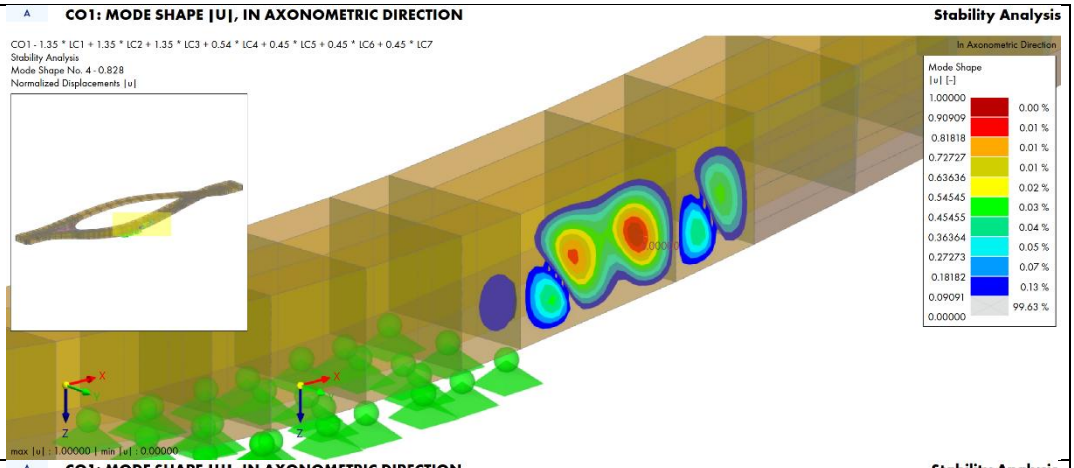
0.895	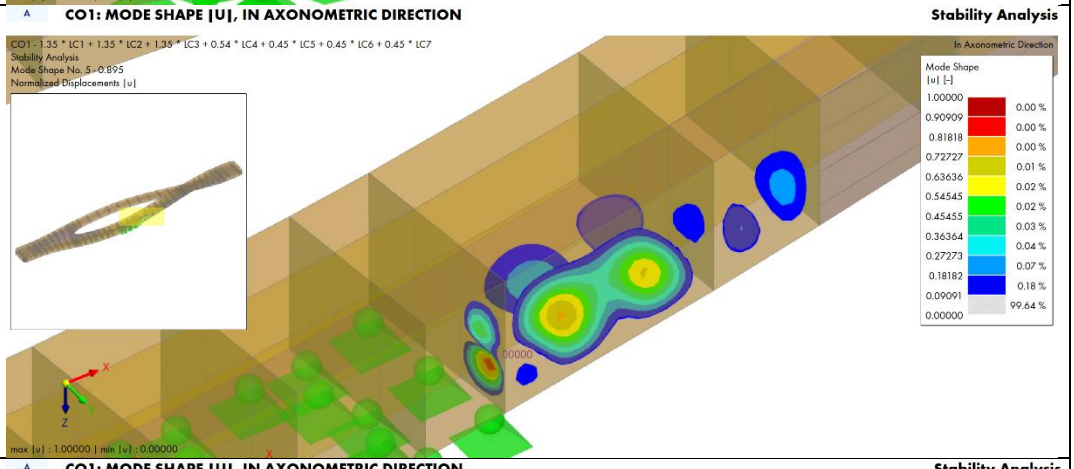
0.917	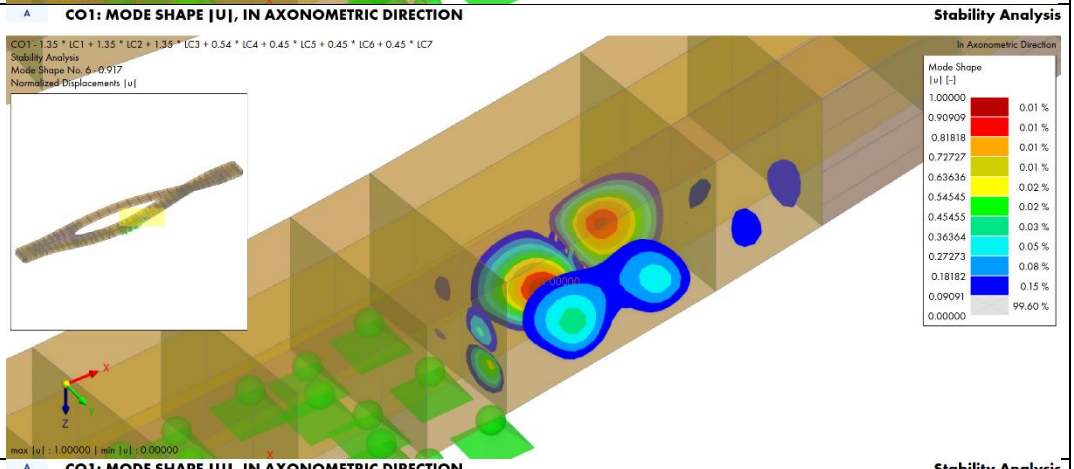
0.923	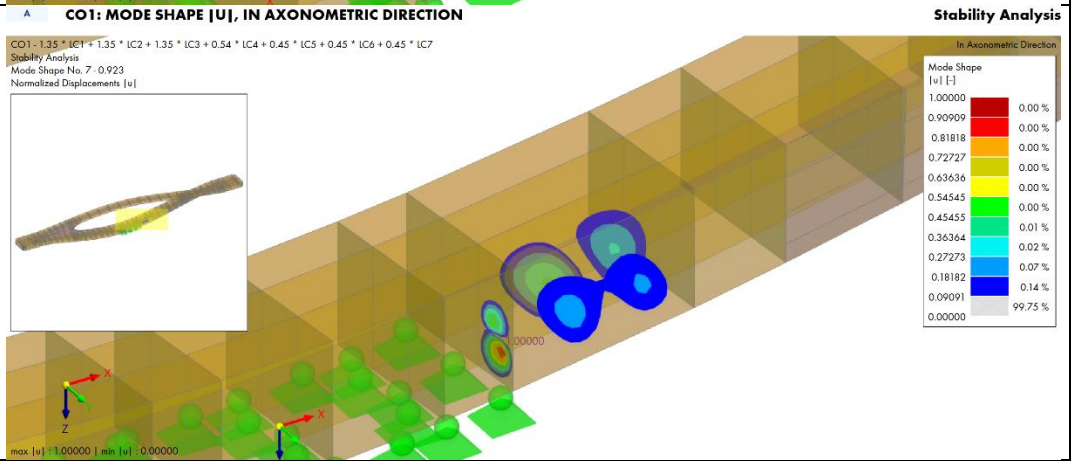

0.957	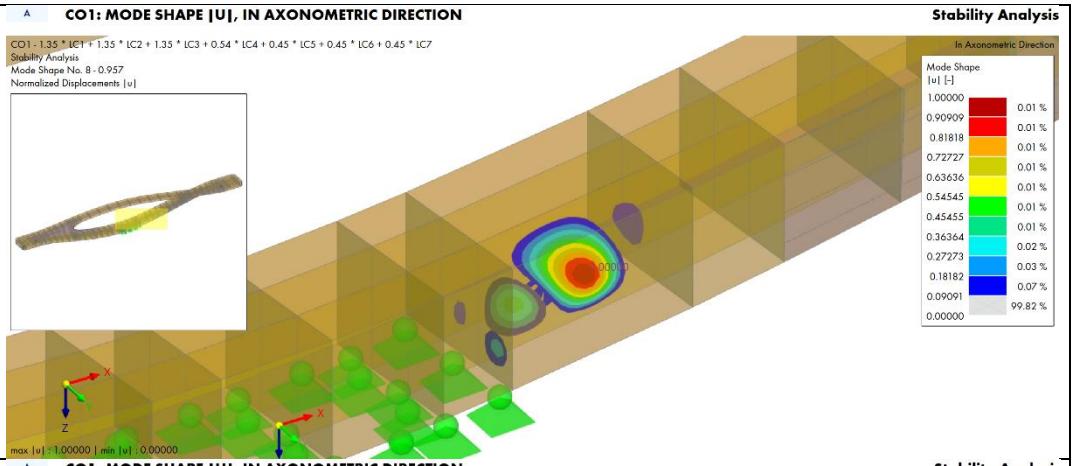
0.998	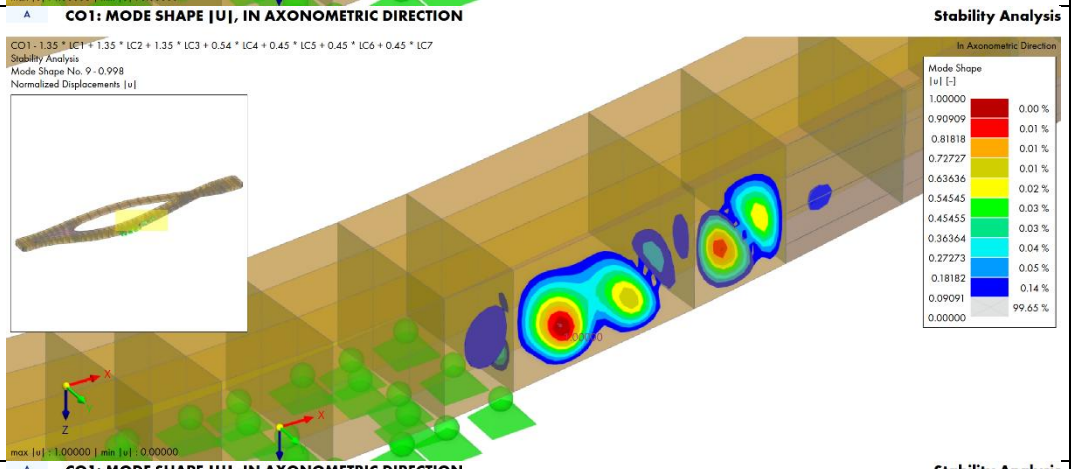
1.068	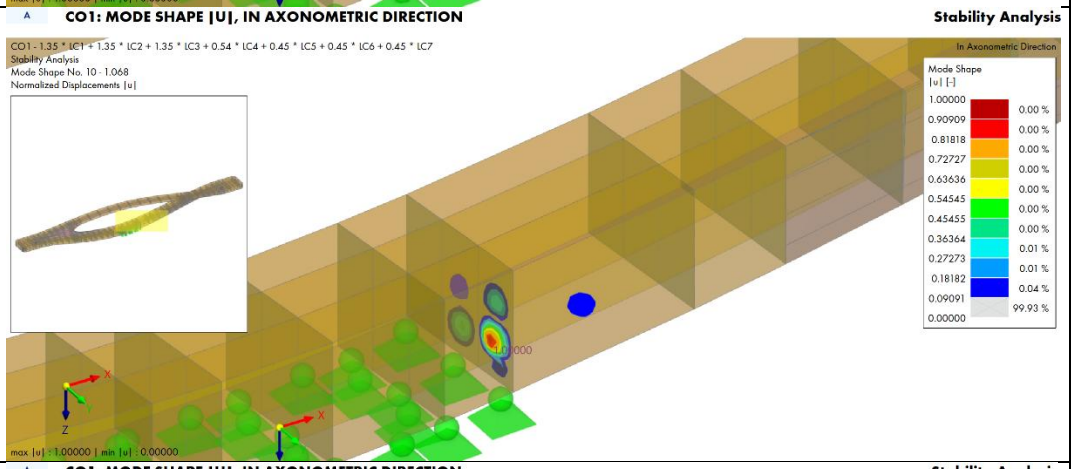
1.128	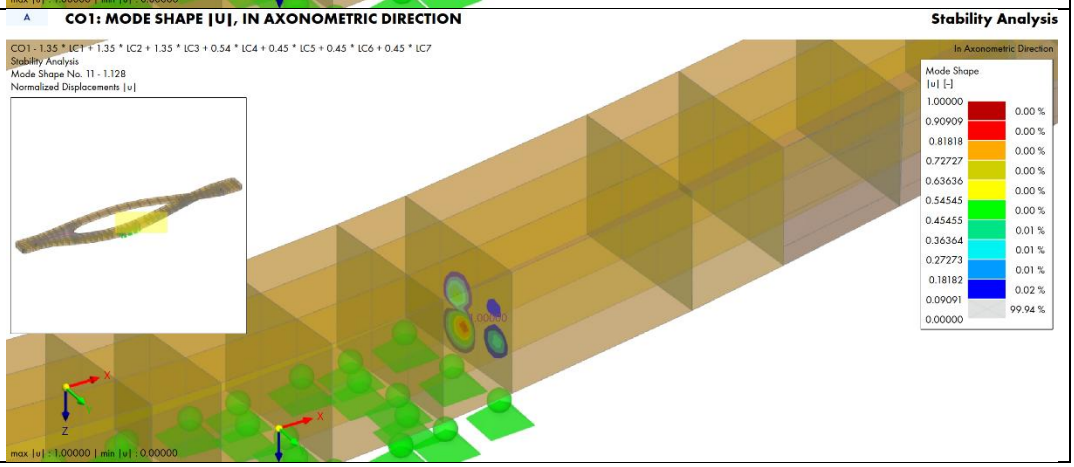

1.214	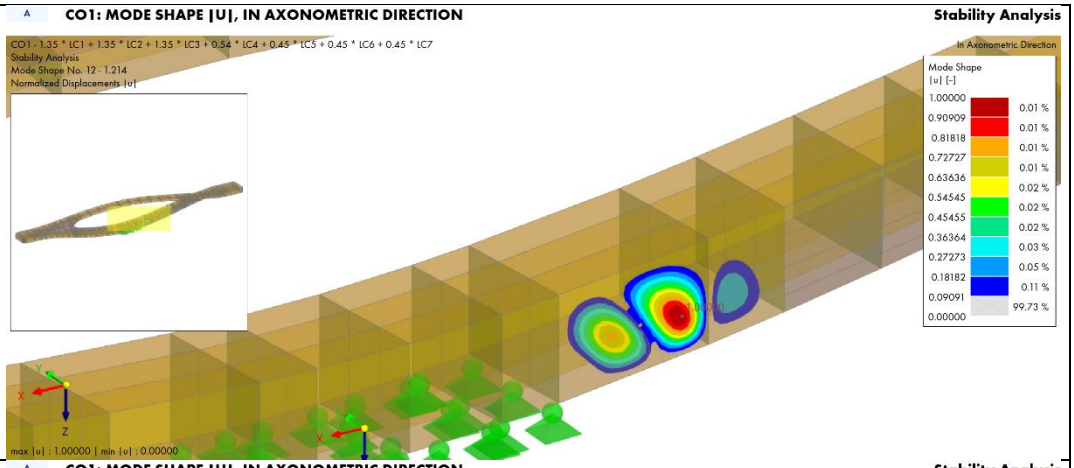
1.265	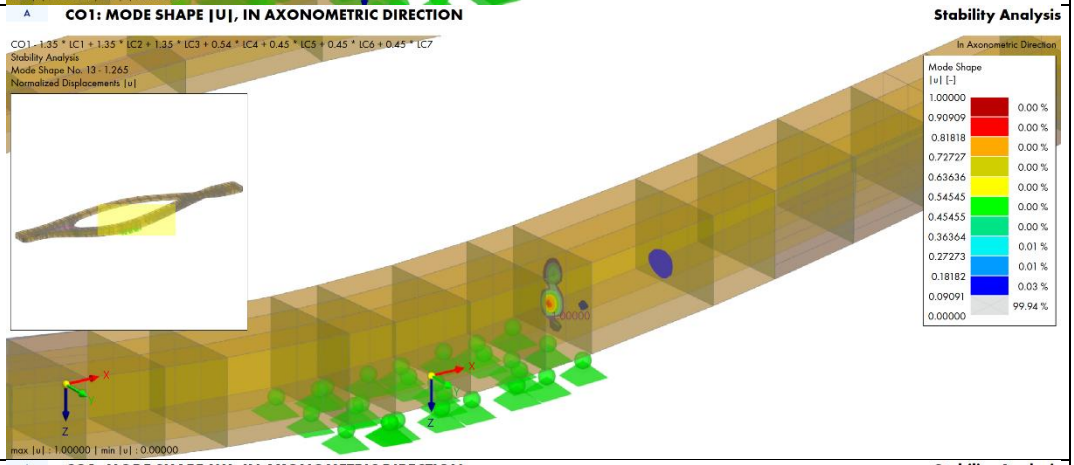
1.286	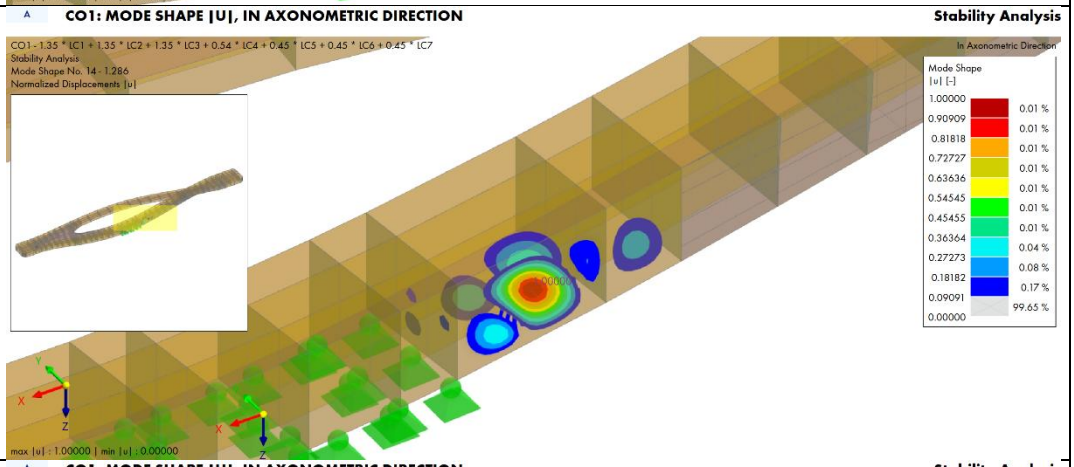
1.293	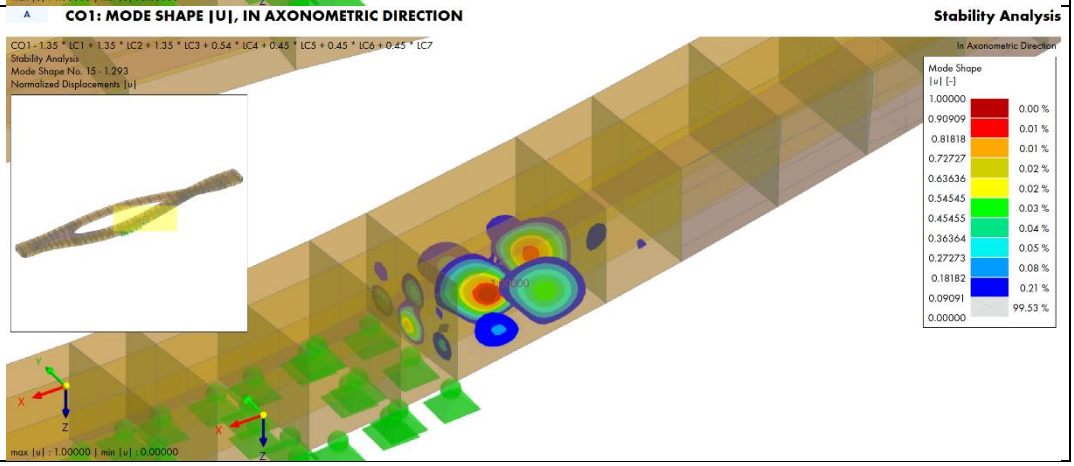

Table 157: Stability analysis first 15 critical buckling load factors and buckling shapes

Appendix Y: Modal shapes

Modal shapes

Mode number 1

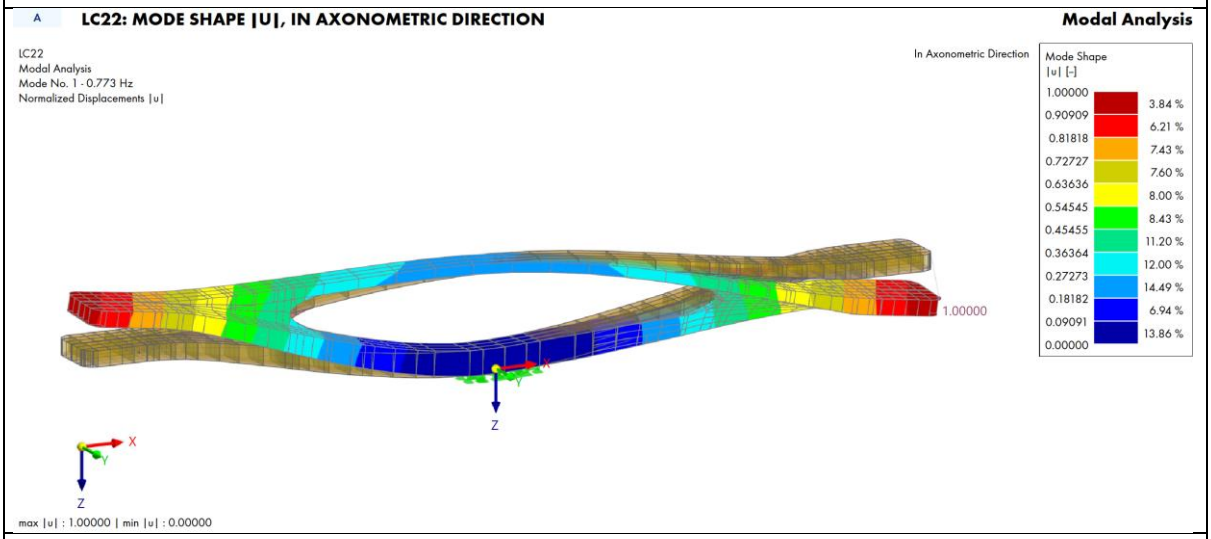

Mode number 2

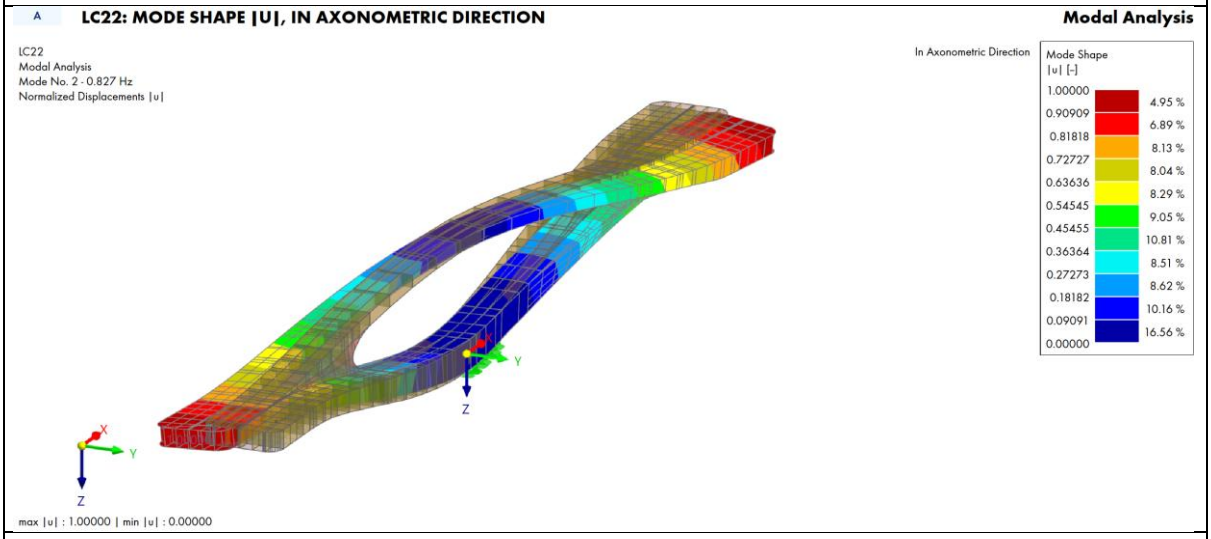

Mode number 3

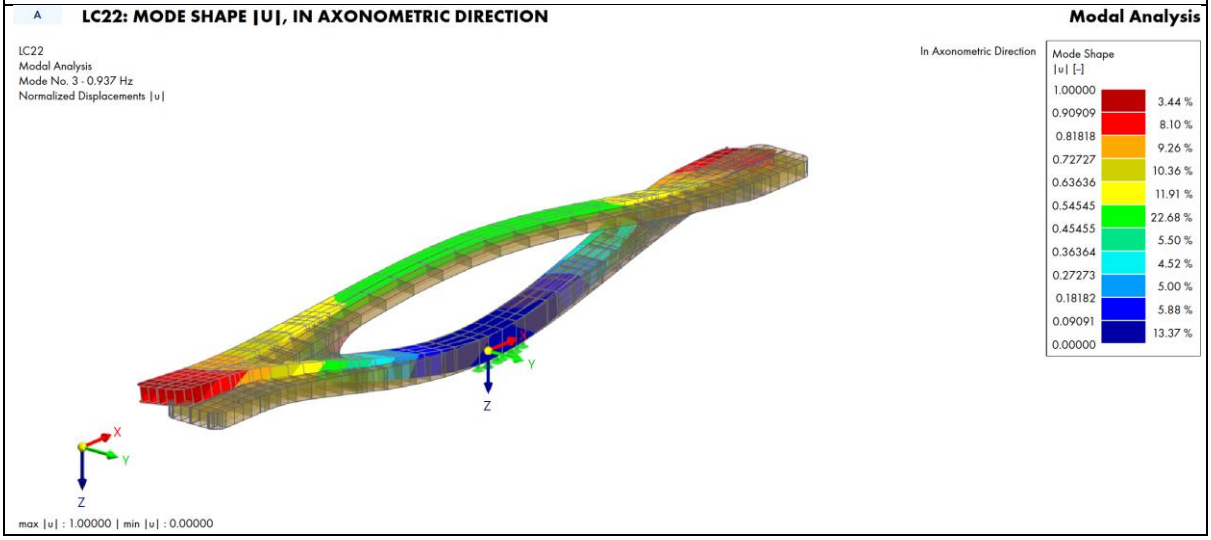

Mode number 4

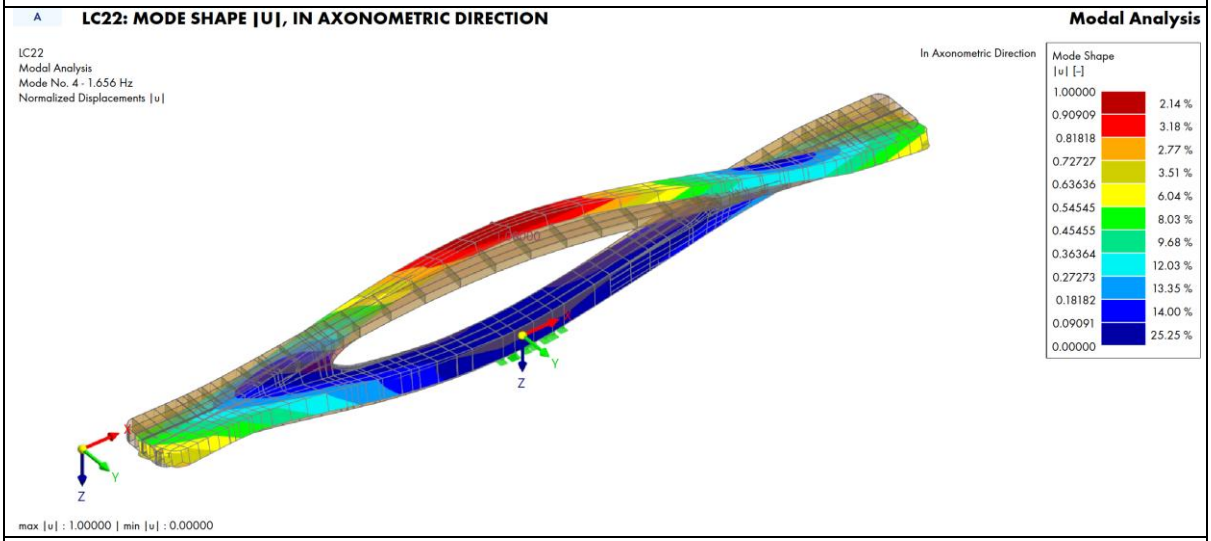

Mode number 5

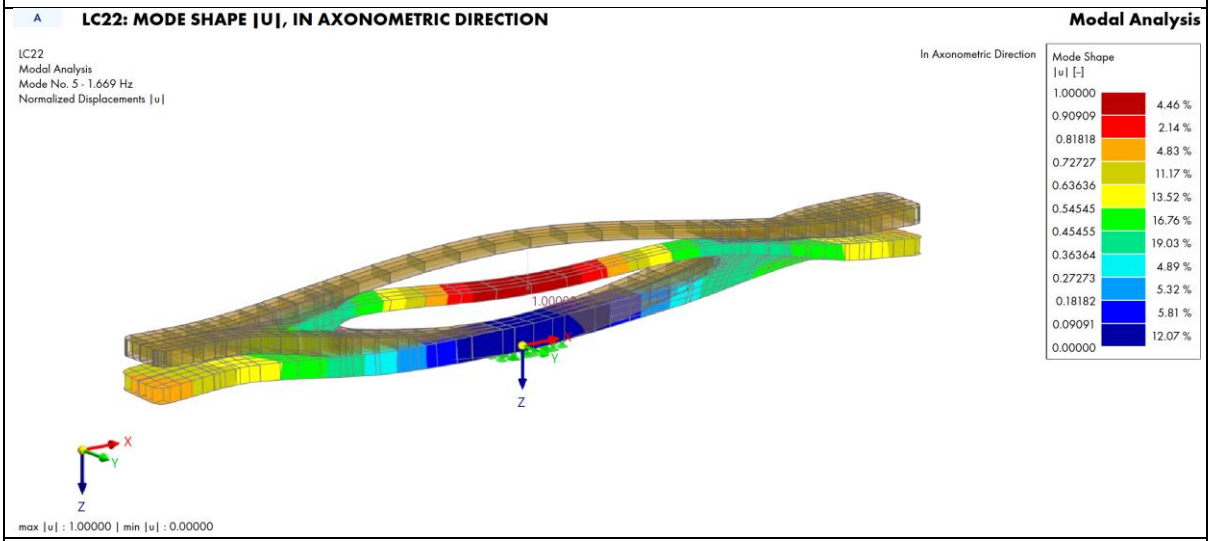

Mode number 6

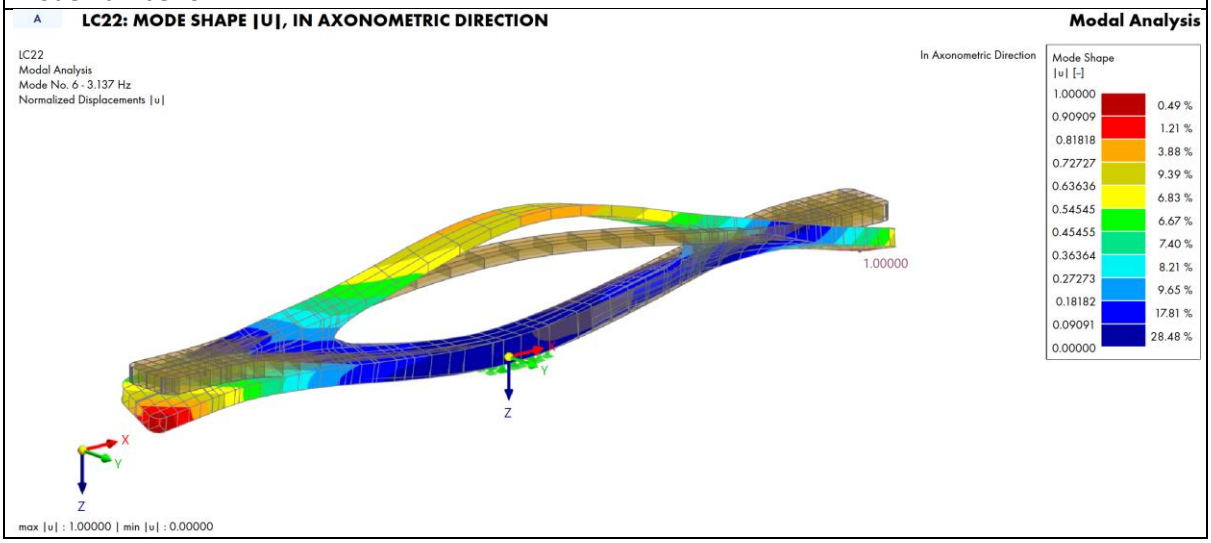

Mode number 7

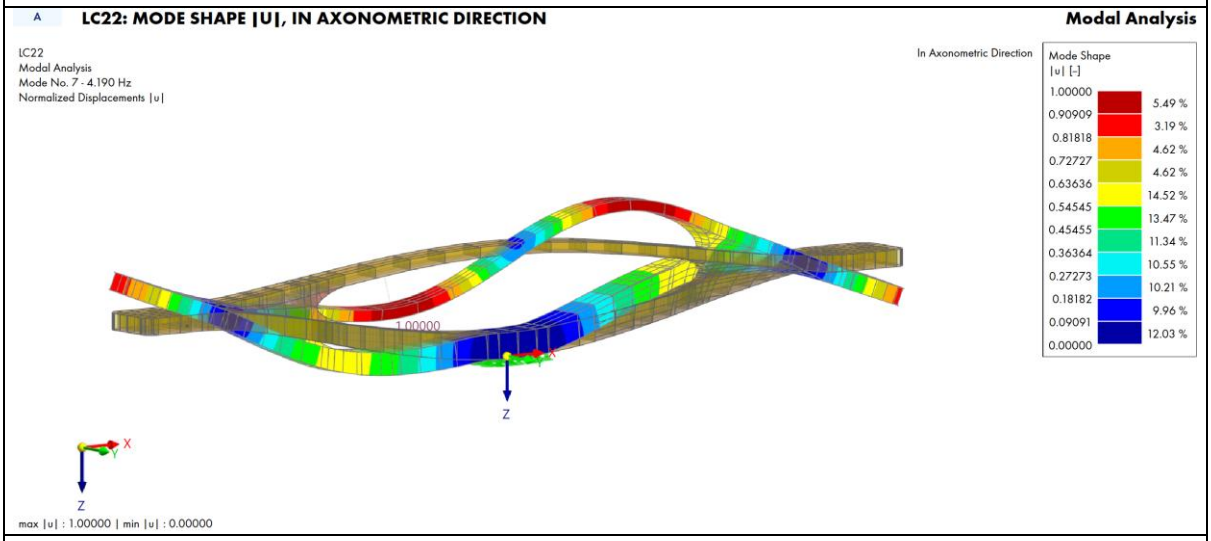

Mode number 8

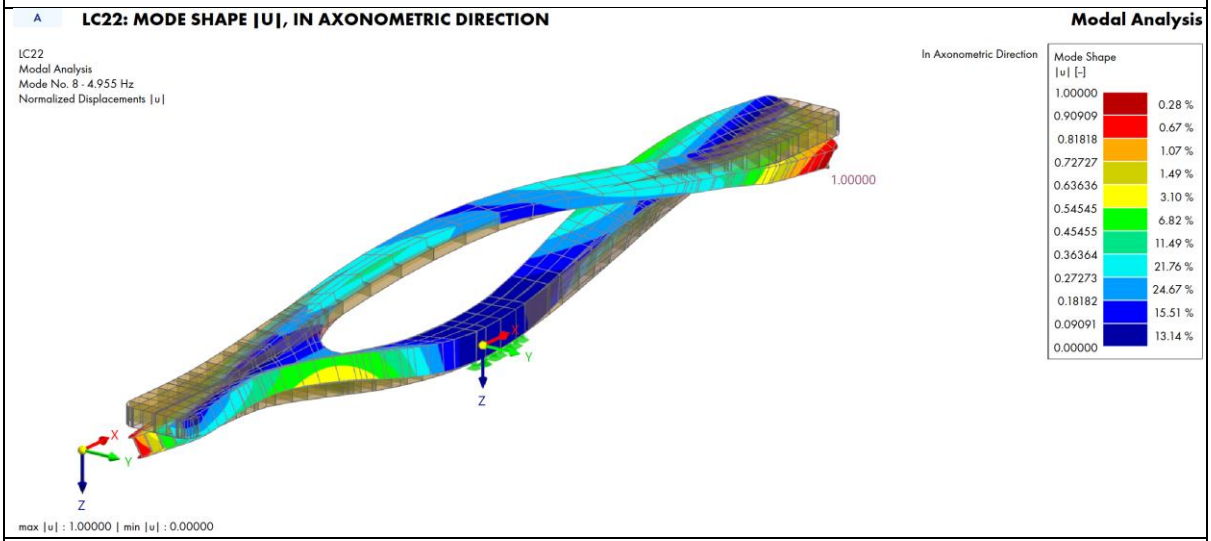

Mode number 9

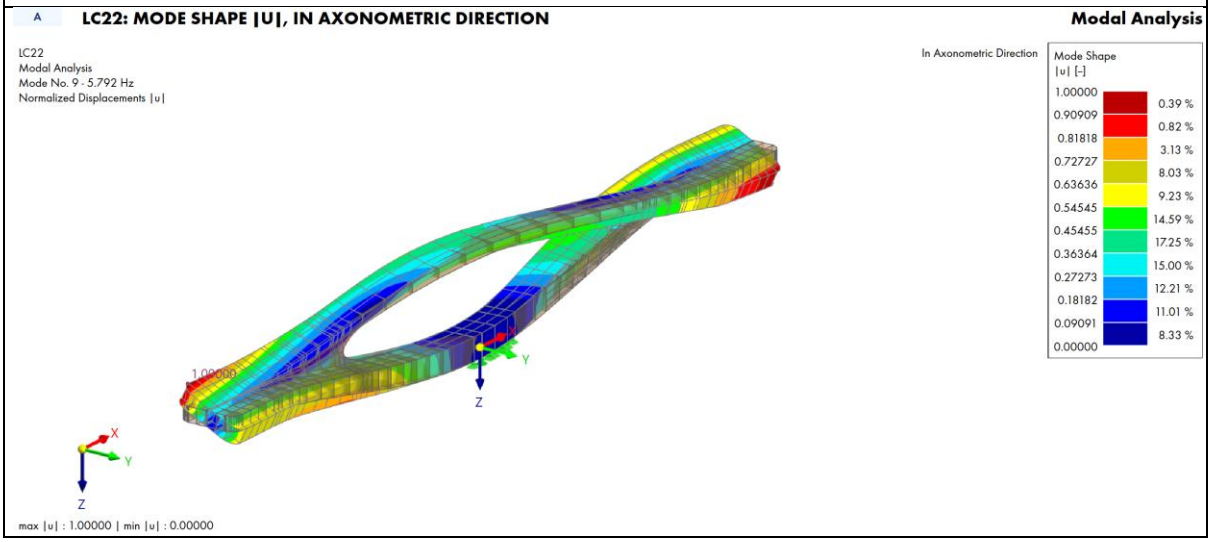

Mode number 10
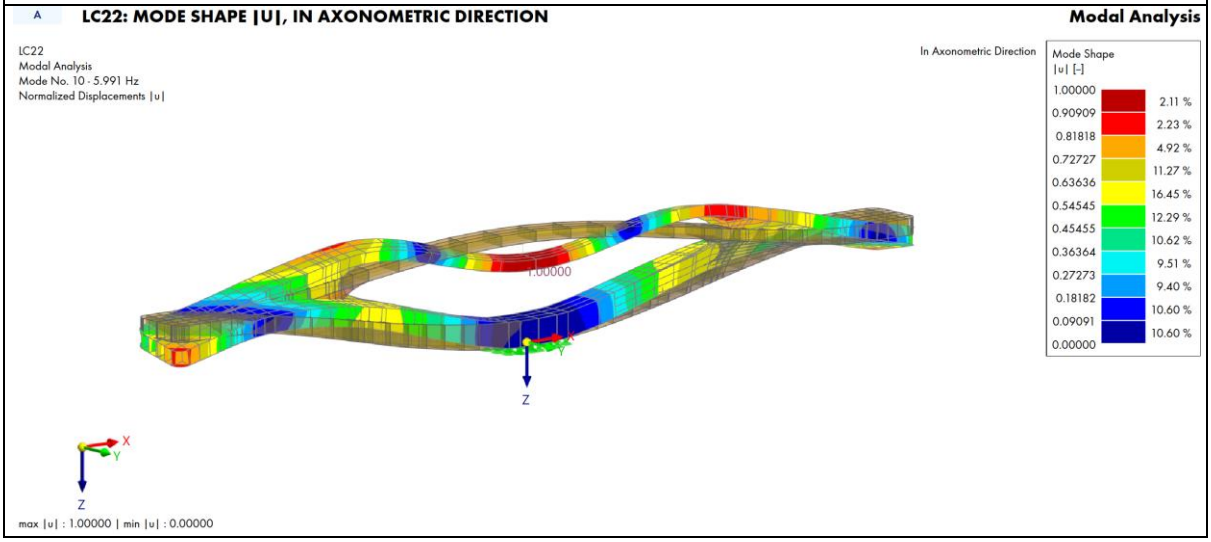

Table 158: Modal analysis first 10 mode shapes

Appendix Z: Thickness structures and input RFEM plates glass fibre design

Support plates

Set 1 and set 2

The layering structure of the laminate is given in Figure 215 and the material properties are given in the table below.

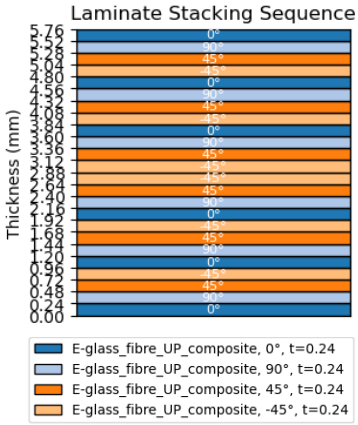

Figure 215:Layering structure support plates set 1 and 2

Property	Membrane	Bending	Unit
E_1	18.897	21.345	GPa
E_2	18.897	19.562	GPa
G_{12}	7.087	6.157	GPa
υ_{12}	0.333128	0.289710	-
υ_{21}	0.333128	0.265516	-

Table 159: Material properties support plates set 1 and 2

Input for RFEM plate model for support plates set 1 and 2:

- E_x = 18896.680 [N/mm^2]
- E_y = 18896.680 [N/mm^2]
- G_yz = 7087.346 [N/mm^2]
- G_xz = 7087.346 [N/mm^2]
- G_xy = 7087.346 [N/mm^2]
- nu_xy = 0.333 [-]
- nu_yx = 0.333 [-]
- Density of the side plate = 1875.0 [kg/m^3]
- Weight of the side plate = 18.75 [kN/m^3]
- Thickness = 5.76 [mm]

Set 3 without plate next to arch

The layering structure of the laminate is given in Figure 216 and the material properties are given in the table below.

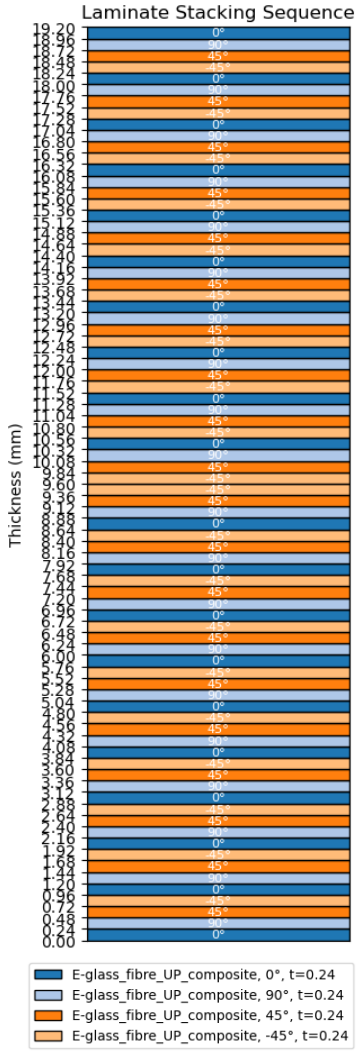

Figure 216: Layering structure support plates set 3 without plate next to arch

Property	Membrane	Bending	Unit
E_1	18.897	19.615	GPa
E_2	18.897	19.146	GPa
G_{12}	7.087	6.810	GPa
υ_{12}	0.333128	0.319813	-
υ_{21}	0.333128	0.312161	-

Table 160: Material properties support plates set 3 without plate next to arch

Input for RFEM plate model for support plates set 3 without plate next to arch:

- E_x = 18896.680 [N/mm^2]
- E_y = 18896.680 [N/mm^2]
- G_yz = 7087.346 [N/mm^2]
- G_xz = 7087.346 [N/mm^2]
- G_xy = 7087.346 [N/mm^2]
- nu_xy = 0.333 [-]
- nu_yx = 0.333 [-]
- Density of the side plate = 1875.0 [kg/m^3]
- Weight of the side plate = 18.75 [kN/m^3]
- Thickness = 19.20 [mm]

Set 3 with plate next to arch

The layering structure of the laminate is given in Figure 217 and the material properties are given in the table below.

Property	Membrane	Bending	Unit
E_1	18.897	19.344	GPa
E_2	18.897	19.057	GPa
G_{12}	7.087	6.914	GPa
υ_{12}	0.333128	0.324775	-
υ_{21}	0.333128	0.319960	-

Table 161: Material properties support plates set 3 with plate next to arch

Input for RFEM plate model for support plates set 3 with plate next to arch:

- E_x = 18896.680 [N/mm^2]
- E_y = 18896.680 [N/mm^2]
- G_yz = 7087.346 [N/mm^2]
- G_xz = 7087.346 [N/mm^2]
- G_xy = 7087.346 [N/mm^2]
- nu_xy = 0.333 [-]
- nu_yx = 0.333 [-]
- Density of the side plate = 1875.0 [kg/m^3]
- Weight of the side plate = 18.75 [kN/m^3]
- Thickness = 19.20 [mm]

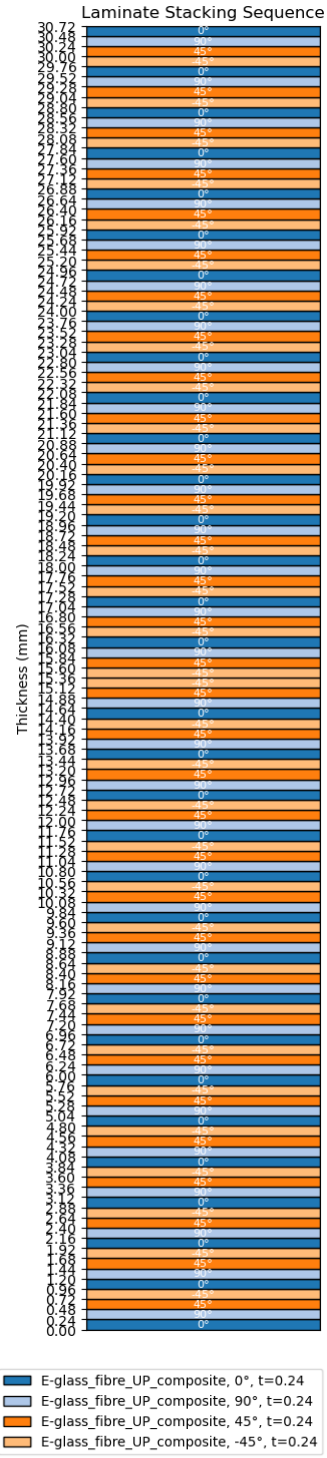

Figure 217: Layering structure support plates set 3 with plate next to arch

Set 4

The layering structure of the laminate is given in Figure 218 and the material properties are given in the table below.

Property	Membrane	Bending	Unit
E_1	18.897	20.347	GPa
E_2	18.897	19.352	GPa
G_{12}	7.087	6.531	GPa
υ_{12}	0.333128	0.306758	-
υ_{21}	0.333128	0.291762	-

Table 162: Material properties support plates set 4

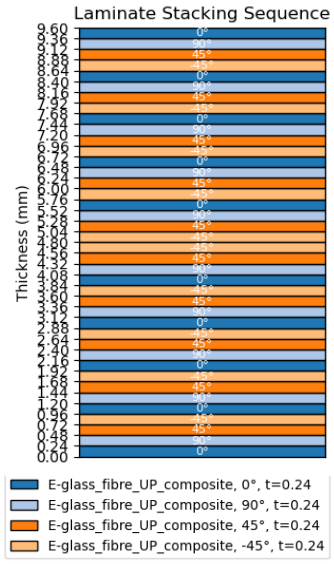

Figure 218: Layering structure support plates set 4

Input for RFEM plate model for support plates set 4:

- E_x = 18896.680 [N/mm^2]
- E_y = 18896.680 [N/mm^2]
- G_yz = 7087.346 [N/mm^2]
- G_xz = 7087.346 [N/mm^2]
- G_xy = 7087.346 [N/mm^2]
- nu_xy = 0.333 [-]
- nu_yx = 0.333 [-]
- Density of the side plate = 1875.0 [kg/m^3]
- Weight of the side plate = 18.75 [kN/m^3]
- Thickness = 9.60 [mm]

Side plates

The layering structure of the laminate is given in Figure 219 and the material properties are given in the table below.

Property	Membrane	Bending	Unit
E_1	25.253	20.347	GPa
E_2	16.700	19.352	GPa
G_{12}	5.808	6.531	GPa
υ_{12}	0.323369	0.306758	-
υ_{21}	0.213852	0.291762	-

Table 163: Material properties side plates

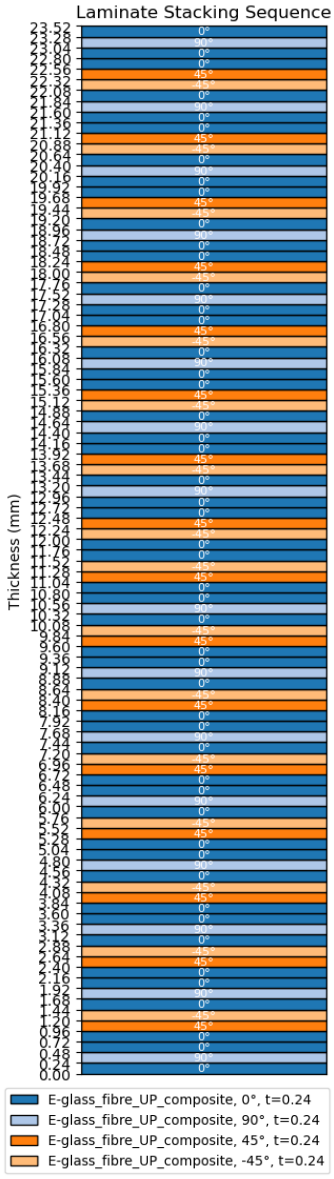

Figure 219: Layering structure side plates

Input for RFEM plate model for side plates:

- E_x = 25253 [N/mm^2]
- E_y = 16700 [N/mm^2]
- G_yz = 5808 [N/mm^2]
- G_xz = 5808 [N/mm^2]
- G_xy = 5808 [N/mm^2]
- nu_xy = 0.323 [-]
- nu_yx = 0.214 [-]
- Density of the side plate = 1875.0 [kg/m^3]
- Weight of the side plate = 18.75 [kN/m^3]
- Thickness = 23.52 [mm]

Bottom plate

The layering structure of the laminate is given in Figure 220 and the material properties are given in the table below.

Property	Membrane	Bending	Unit
E_1	28.055	28.613	GPa
E_2	15.556	15.881	GPa
G_{12}	5.244	4.955	GPa
υ_{12}	0.317815	0.296391	-
υ_{21}	0.176217	0.164508	-

Table 164: Material properties bottom plate

Input for RFEM plate model for bottom deck:

- E_x = 30037.401 [N/mm^2]
- E_y = 15555.667 [N/mm^2]
- G_yz = 5243.673 [N/mm^2]
- G_xz = 5243.673 [N/mm^2]
- G_xy = 5243.673 [N/mm^2]
- nu_xy = 0.318 [-]
- Density of the bottom deck = 2099.006 [kg/m^3]
- Weight of the bottom deck = 20.990 [kN/m^3]
- Thickness = 26.880 [mm]
- The width of the plate is 1800 [mm]
- The width of the plate from girder to girder is 1786.560 [mm]

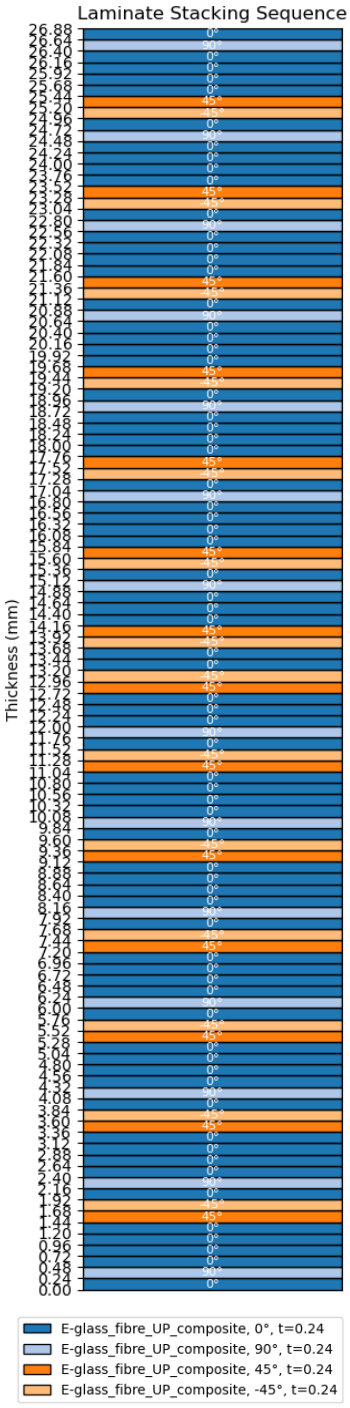

Figure 220: Layering structure bottom plate

C-shaped girders

The layering structure of the laminate is given in Figure 221 and the material properties are given in the table below.

Property	Membrane	Bending	Unit
E_1	18.897	19.927	GPa
E_2	18.897	19.240	GPa
G_{12}	7.087	6.690	GPa
υ_{12}	0.333128	0.314188	-
υ_{21}	0.333128	0.164508	-

Table 165: Material properties C-shaped girders

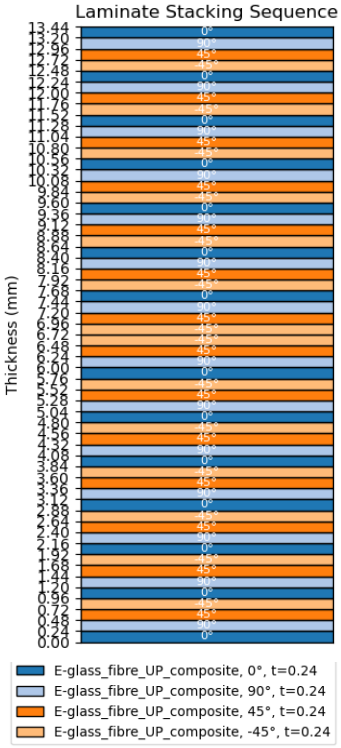

Figure 221: Layering structure C-shaped girders

Input for RFEM plate model for girders is:

- E_x = 18896.680 [N/mm^2]
- E_y = 18896.680 [N/mm^2]
- G_yz = 7087.346 [N/mm^2]
- G_xz = 7087.346 [N/mm^2]
- G_xy = 7087.346 [N/mm^2]
- nu_xy = 0.333 [-]
- Density of the girders = 1517.974 [kg/m^3]
- Weight of the girders = 15.180 [kN/m^3]
- Thickness = 13.440 [mm]
- The locations of the girders with respect to the left side of the cross-section is:
    - Girder 1 is located at 7.583 [mm]
    - Girder 2 is located at 602.338 [mm]
    - Girder 3 is located at 1212.662 [mm]
    - Girder 4 is located at 1807.417 [mm]
- The distance between the girders is:
    - Between girder 1 and girder 2 is 594.754 [mm]
    - Between girder 2 and girder 3 is 610.325 [mm]
    - Between girder 3 and girder 4 is 594.754 [mm]

Top plate

The layering structure of the laminate is given in Figure 222 and the material properties are given in the table below.

Property	Membrane	Bending	Unit
E_1	28.055	28.813	GPa
E_2	15.556	16.013	GPa
G_{12}	5.244	4.845	GPa
υ_{12}	0.317815	0.288168	-
υ_{21}	0.176217	0.160146	-

Table 166: Material properties top plate

Input for RFEM plate model for top deck:

- E_x = 9976.288 [N/mm^2]
- E_y = 5273.771 [N/mm^2]
- G_yz = 1778.942 [N/mm^2]
- G_xz = 1778.942 [N/mm^2]
- G_xy = 1778.942 [N/mm^2]
- nu_xy = 0.318 [-]
- nu_yx = 0.176 [-]
- Density of the top deck = 722.769 [kg/m^3]
- Weight of the top deck = 7.228 [kN/m^3]
- Thickness = 113.400 [mm]
- The width of the plate is 1800 [mm]
- The width of the plate from girder to girder is 1786.560 [mm]

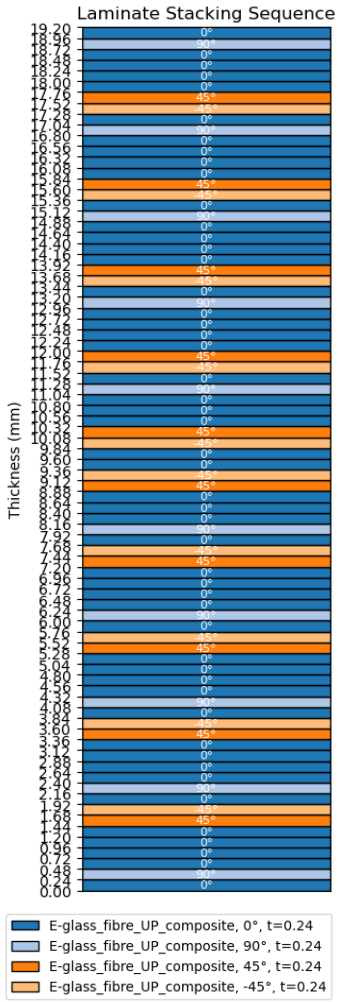

Figure 222: Layering structure top plate

Stiffener plates

The layering structure of the laminate is given in Figure 223 and the material properties are given in the table below.

Property	Membrane	Bending	Unit
E_1	18.897	21.345	GPa
E_2	18.897	19.562	GPa
G_{12}	7.087	6.157	GPa
υ_{12}	0.333128	0.289710	-
υ_{21}	0.333128	0.265516	-

Table 167: Material properties stiffener plates

Input for RFEM plate model for stiffener plates:

- E_x = 18896.680 [N/mm^2]
- E_y = 18896.680 [N/mm^2]
- G_yz = 7087.346 [N/mm^2]
- G_xz = 7087.346 [N/mm^2]
- G_xy = 7087.346 [N/mm^2]
- nu_xy = 0.333 [-]
- nu_yx = 0.333 [-]
- Density of the side plate = 1875.0 [kg/m^3]
- Weight of the side plate = 18.75 [kN/m^3]
- Thickness = 5.76 [mm]

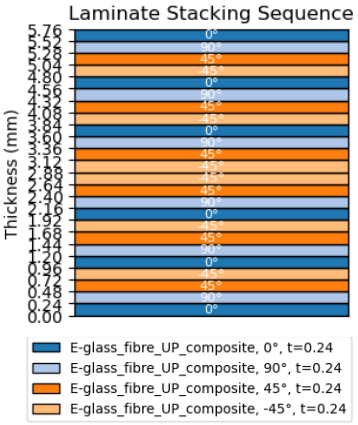

Figure 223: Layering structure stiffener plates

Appendix AA: Unity checks and flange design of the glass fibre design

This appendix presents the design stress limits, unity checks, and flange design of the glass fibre design. The unity checks are provided for each structural component. The locations of the singularities in the finite element model are presented in Appendix S. Appendix S also contains overview figures of the different structural components.

Support plates

The material and design stress limits for the support plates are given in the table below.

		CUR 96 Strain limit [%]		**Material Stress limit** $[N/mm^2]$	**Design Material Stress limit** $[N/mm^2]$
Tension	$\varepsilon_{1t,Rk}$	1.2	$\sigma_{f1t} = \varepsilon_{1t,Rk} * E_1$	226.7	133.1
	$\varepsilon_{2t,Rk;low}$	1.2	$\sigma_{f2t} = \varepsilon_{2t,Rk;low} * E_2$	226.7	133.1
Compression	$\varepsilon_{1c,Rk}$	1.0	$\sigma_{f1c} = \varepsilon_{1c,Rk} * E_1$	188.97	110.9
	$\varepsilon_{2c,Rk;low}$	1.2	$\sigma_{f2c} = \varepsilon_{2c,Rk;low} * E_2$	226.7	133.1
Shear	$\gamma_{12,Rk}$	1.6	$\tau_{f12} = \gamma_{12,Rk} * G$	113.4	66.5

Table 168: Stress limits laminate support plates

The unity checks (UC) of different support plates sets are given in the tables below. The different sets are given in Appendix S including the locations where singularities appear.

Set 1	Max stress $[N/mm^2]$	UC	Side of the plate
σ_x tensile	13	0.10	Positive
σ_x compression	21	0.19	Negative
σ_y tensile	15	0.11	Negative
σ_y compression	18	0.14	Positive
τ_{xy}	9	0.14	Membrane

Table 169: UC of support plates set 1

Set 2	Max stress $[N/mm^2]$	UC	Side of the plate
σ_x tensile	19	0.14	Positive
σ_x compression	43	0.39	Positive
σ_y tensile	45	0.34	Positive
σ_y compression	75	0.56	Positive
τ_{xy}	27	0.41	Membrane

Table 170: UC of support plates set 2

Set 3 without plate next to arch	Max stress $[N/mm^2]$	UC	Side of the plate
σ_x tensile	20	0.15	Positive
σ_x compression	28	0.25	Positive
σ_y tensile	36	0.27	Positive
σ_y compression	50	0.38	Positive
τ_{xy}	17	0.26	Membrane

Table 171: UC of support plates set 3 without plate next to arch plate

Set 3 plate next to arch	Max stress $[N/mm^2]$	UC	Side of the plate
σ_x tensile	26	0.20	Positive
σ_x compression	96	0.87	Positive
σ_y tensile	69	0.52	Positive
σ_y compression	67	0.50	Positive
τ_{xy}	25	0.38	Membrane

Table 172: UC of support plates set 3 with plate next to arch plate

Set 4	Max stress $[N/mm^2]$	UC	Side of the plate
σ_x tensile	37	0.28	Positive
σ_x compression	33	0.30	Negative
σ_y tensile	39	0.29	Positive
σ_y compression	24	0.18	Negative
τ_{xy}	9	0.14	Membrane

Table 173: UC of support plates set 4

To connect the support plates to the bottom half of the structure, the upper half of the structure, and the side plates, bonding flanges are provided along the plate edges. The required flange widths are determined from the internal force n_{xy}, the shear flow, obtained from the finite element analysis. The shear flow at the edges of the support plates is divided by the allowable adhesive shear stress of 1 MPa to determine the minimum flange width required for the bonded connection. The distributions of the maximum and minimum shear flow are presented in Figure 225 and Figure 224. The highest representative shear flow, excluding the local peaks, is 350 kN/m and occurs in the support plate adjacent to the arch plate. The required flange width is therefore:

$$\frac{350}{1} = 350\ mm$$

This flange is relatively wide, reflecting the high shear forces transferred through this connection. For the remaining support plates, the maximum representative shear flow is considerably lower, with a value of 150 kN/m. The required flange width for these plates is therefore:

$$\frac{150}{1} = 150\ mm$$

Based on these results, a flange width of 350 mm is adopted for the support plate adjacent to the arch plate, while a flange width of 150 mm is used for all other support plates. This provides sufficient bonding area to transfer the calculated shear forces without exceeding the allowable adhesive shear stress.

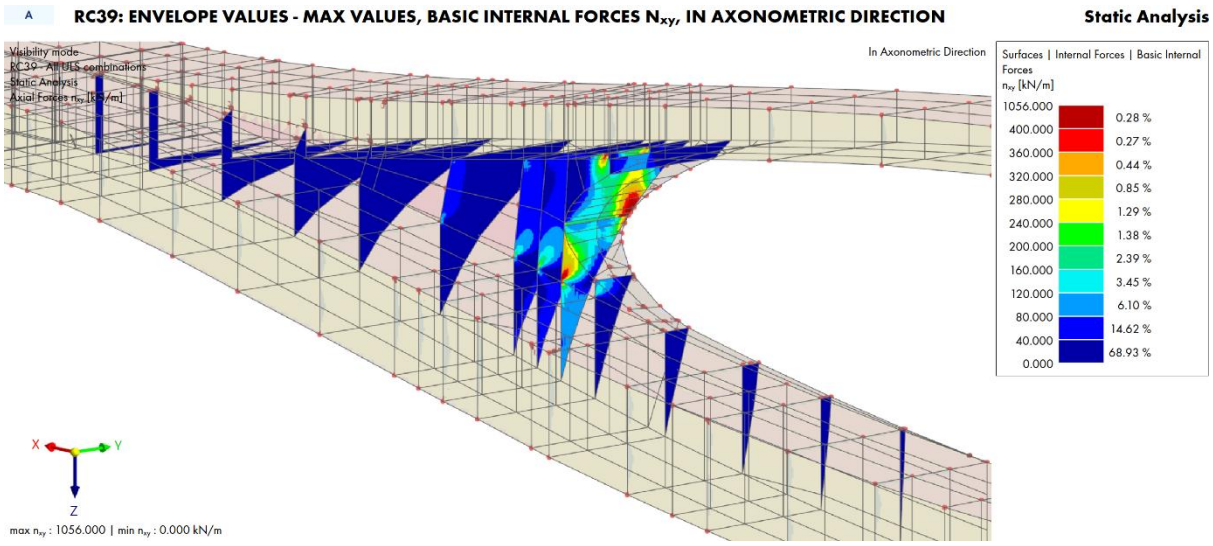

Figure 225: Max values of n_{xy} in support plates

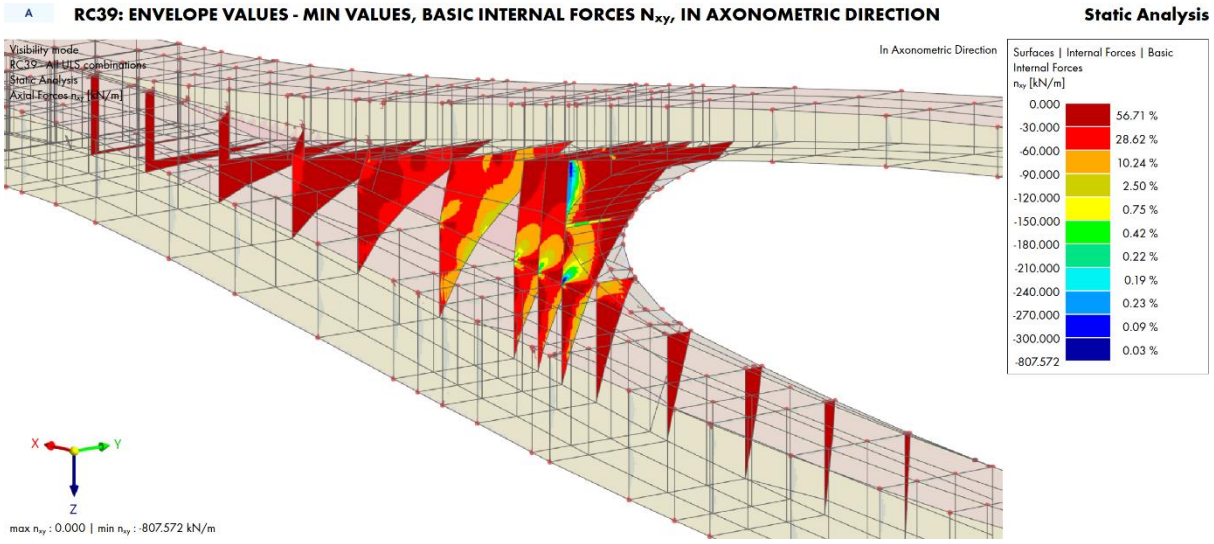

Figure 224: Min values of n_{xy} in support plates

Side plates

The material and design stress limits for the side plates are given in the table below.

		CUR 96 Strain limit [%]		Material Stress limit $[N/mm^2]$	Design Material Stress limit $[N/mm^2]$
Tension	$\varepsilon_{1t,Rk}$	1.2	$\sigma_{f1t} = \varepsilon_{1t,Rk} * E_1$	303.0	177.8
	$\varepsilon_{2t,Rk;low}$	1.2	$\sigma_{f2t} = \varepsilon_{2t,Rk;low} * E_2$	200.4	117.6
Compression	$\varepsilon_{1c,Rk}$	1.0	$\sigma_{f1c} = \varepsilon_{1c,Rk} * E_1$	252.5	148.2
	$\varepsilon_{2c,Rk;low}$	1.2	$\sigma_{f2c} = \varepsilon_{2c,Rk;low} * E_2$	200.4	117.6
Shear	$\gamma_{12,Rk}$	1.6	$\tau_{f12} = \gamma_{12,Rk} * G$	92.9	54.5

Table 174: Stress limits laminate side plates

Arch plate

The unity checks of the arch plate is given in the table below. The locations where singularities occur are shown in Appendix S.

Arch plate	Max stress $[N/mm^2]$	UC	Side of the plate
σ_x tensile	41	0.23	Positive
σ_x compression	110	0.74	Positive
σ_y tensile	87	0.74	Negative
σ_y compression	103	0.88	Positive
τ_{xy}	32	0.59	Membrane

Table 175: UC of arch plate

Top side plate

The unity checks of the top side plate is given in the table below. The locations where singularities occur are shown in Appendix S.

Top side plate	Max stress $[N/mm^2]$	UC	Side of the plate
σ_x tensile	40	0.22	Positive
σ_x compression	110	0.74	Positive
σ_y tensile	43	0.37	Positive
σ_y compression	70	0.60	Positive
τ_{xy}	32	0.59	Membrane

Table 176: UC of top side plate

Bottom side plate

The unity checks of the bottom side plate is given in the table below. The locations where singularities occur are shown in Appendix S.

Bottom side plate	Max stress $[N/mm^2]$	UC	Side of the plate
σ_x tensile	62	0.35	Positive
σ_x compression	126	0.85	Negative
σ_y tensile	30	0.26	Positive
σ_y compression	59	0.50	Negative
τ_{xy}	22	0.40	Membrane

Table 177: UC of bottom side plate

Bottom plate

The material and design stress limits for the bottom plate are given in the table below.

		CUR 96 Strain limit [%]		**Material Stress limit** $[N/mm^2]$	**Design Material Stress limit** $[N/mm^2]$
Tension	$\varepsilon_{1t,Rk}$	1.2	$\sigma_{f1t} = \varepsilon_{1t,Rk} * E_1$	336.6	197.6
	$\varepsilon_{2t,Rk;low}$	1.2	$\sigma_{f2t} = \varepsilon_{2t,Rk;low} * E_2$	186.7	109.5
Compression	$\varepsilon_{1c,Rk}$	1.0	$\sigma_{f1c} = \varepsilon_{1c,Rk} * E_1$	280.5	164.6
	$\varepsilon_{2c,Rk;low}$	1.2	$\sigma_{f2c} = \varepsilon_{2c,Rk;low} * E_2$	186.7	109.5
Shear	$\gamma_{12,Rk}$	1.6	$\tau_{f12} = \gamma_{12,Rk} * G$	83.9	49.2

Table 178: Stress limits laminate bottom plate

The unity checks of the bottom plate is given in the table below. The locations where singularities occur are shown in Appendix S.

Bottom plate	Max stress $[N/mm^2]$	UC	Side of the plate
σ_x tensile	62	0.31	Negative
σ_x compression	143	0.87	Positive
σ_y tensile	25	0.23	Positive
σ_y compression	20	0.18	Negative
τ_{xy}	15	0.30	Membrane

Table 179: UC of bottom plate

C-shaped girders

The material and design stress limits for the C-shaped girders are given in the table below.

		CUR 96 Strain limit [%]		**Material Stress limit** $[N/mm^2]$	**Design Material Stress limit** $[N/mm^2]$
Tension	$\varepsilon_{1t,Rk}$	1.2	$\sigma_{f1t} = \varepsilon_{1t,Rk} * E_1$	226.7	133.1
	$\varepsilon_{2t,Rk;low}$	1.2	$\sigma_{f2t} = \varepsilon_{2t,Rk;low} * E_2$	226.7	133.1
Compression	$\varepsilon_{1c,Rk}$	1.0	$\sigma_{f1c} = \varepsilon_{1c,Rk} * E_1$	188.97	110.9
	$\varepsilon_{2c,Rk;low}$	1.2	$\sigma_{f2c} = \varepsilon_{2c,Rk;low} * E_2$	226.7	133.1
Shear	$\gamma_{12,Rk}$	1.6	$\tau_{f12} = \gamma_{12,Rk} * G$	113.4	66.5

Table 180: Stress limits laminate C-shaped girders

The unity checks of the C-shaped girders is given in the table below. The locations where singularities occur are shown in Appendix S.

C-shaped girders	Max stress $[N/mm^2]$	UC	Side of the plate
σ_x tensile	47	0.35	Positive
σ_x compression	70	0.63	Positive
σ_y tensile	21	0.16	Negative
σ_y compression	88	0.66	Positive
τ_{xy}	38	0.57	Membrane

Table 181: UC of C-shaped girders

To verify the bonded connections between the C-shaped girders and the top and bottom decks, the shear stresses in the adhesive layer are evaluated. The verification is based on the internal force n_{xy}, the shear flow, obtained from the finite element analysis at the interface between the C-shaped girders and the deck panels. The corresponding shear flow distributions are shown in Figure 226 and Figure 227.

The maximum absolute shear flow at the edge of the girder is 300 kN/m. The peak values in the vicinity of the supports are disregarded, as these are influenced by local support effects and are not representative of the actual load transfer in the bonded connection.

Assuming that the shear flow is transferred uniformly through the adhesive joint, the average shear stress in the adhesive layer is determined by dividing the shear flow by the flange width. For the original flange width of 100 mm, the resulting shear stress is:

$$\frac{300}{100} = 3\ N/mm^2$$

This value exceeds the allowable adhesive shear stress of 1 MPa, indicating that the original flange width is insufficient.

To reduce the shear stress in the adhesive joint, the flange width of the C-shaped girders was increased to 300 mm. The resulting average shear stress becomes:

$$\frac{300}{300} = 1\ N/mm^2$$

This value is exactly equal to 1 N/mm^2. Therefore, a flange width of 300 mm is considered acceptable for the glass fibre design while providing a substantial reduction in the shear stress within the adhesive joint.

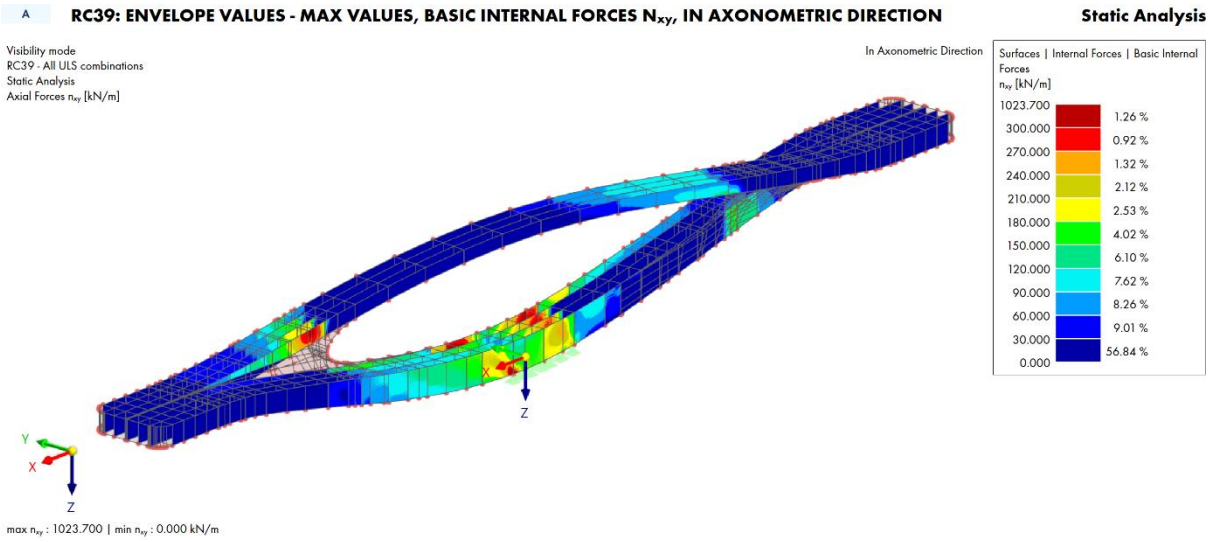

Figure 227: Max values of n_{xy} in C-shaped girders

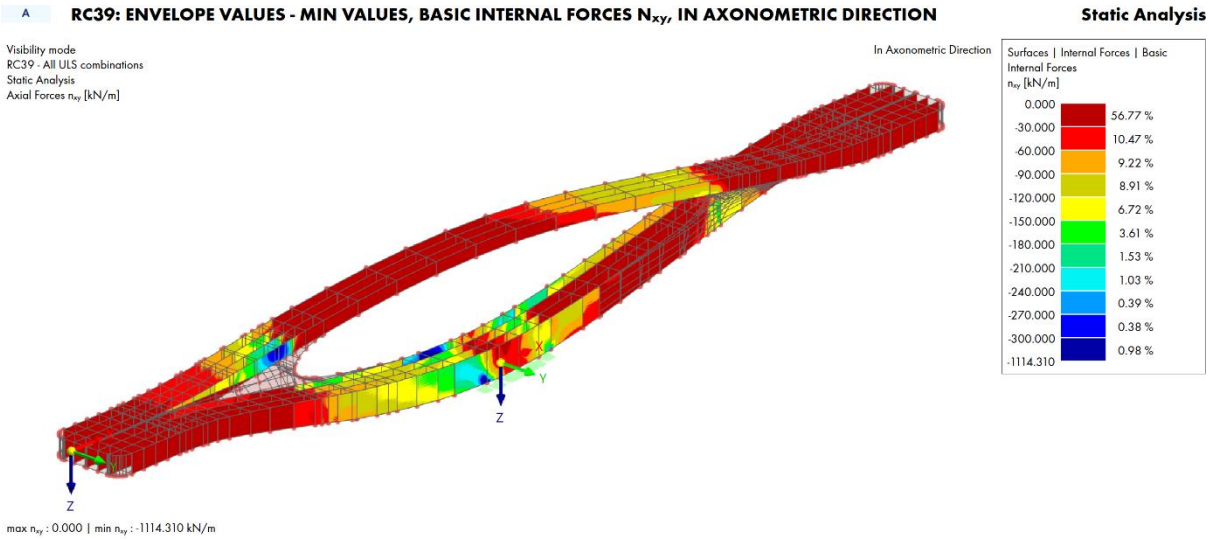

Figure 226: Min values of n_{xy} in C-shaped girders

Top plate

The material and design stress limits for the top plate are given in the table below.

		CUR 96 Strain limit [%]		**Material Stress limit** $[N/mm^2]$	**Design Material Stress limit** $[N/mm^2]$
Tension	$\varepsilon_{1t,Rk}$	1.2	$\sigma_{f1t} = \varepsilon_{1t,Rk} * E_1$	189.9	111.4
	$\varepsilon_{2t,Rk;low}$	1.2	$\sigma_{f2t} = \varepsilon_{2t,Rk;low} * E_2$	62.9	36.9
Compression	$\varepsilon_{1c,Rk}$	1.0	$\sigma_{f1c} = \varepsilon_{1c,Rk} * E_1$	158.2	92.8
	$\varepsilon_{2c,Rk;low}$	1.2	$\sigma_{f2c} = \varepsilon_{2c,Rk;low} * E_2$	62.9	36.9
Shear	$\gamma_{12,Rk}$	1.6	$\tau_{f12} = \gamma_{12,Rk} * G$	29.6	15.3

Table 182: Stress limits laminate top plate

The unity checks of the top plate is given in the table below. The locations where singularities occur are shown in Appendix S.

Top plate	Max stress $[N/mm^2]$	UC	Side of the plate
σ_x tensile	29	0.15	Negative
σ_x compression	20	0.12	Negative
σ_y tensile	15	0.14	Negative
σ_y compression	20	0.18	Negative
τ_{xy}	5	0.10	Membrane

Table 183: UC of top plate

Stiffener plates

The material and design stress limits for the stiffener plates are given in the table below.

		CUR 96 Strain limit [%]		**Material Stress limit** $[N/mm^2]$	**Design Material Stress limit** $[N/mm^2]$
Tension	$\varepsilon_{1t,Rk}$	1.2	$\sigma_{f1t} = \varepsilon_{1t,Rk} * E_1$	226.7	133.1
	$\varepsilon_{2t,Rk;low}$	1.2	$\sigma_{f2t} = \varepsilon_{2t,Rk;low} * E_2$	226.7	133.1
Compression	$\varepsilon_{1c,Rk}$	1.0	$\sigma_{f1c} = \varepsilon_{1c,Rk} * E_1$	188.97	110.9
	$\varepsilon_{2c,Rk;low}$	1.2	$\sigma_{f2c} = \varepsilon_{2c,Rk;low} * E_2$	226.7	133.1
Shear	$\gamma_{12,Rk}$	1.6	$\tau_{f12} = \gamma_{12,Rk} * G$	113.4	66.5

Table 184: Stress limits laminate stiffener plates

The unity checks of all the stiffener plates are given in the tables below. The different sets are given in Appendix S including the locations where singularities appear.

Stiffener plates	Max stress $[N/mm^2]$	UC	Side of the plate
σ_x tensile	45	0.34	Positive
σ_x compression	34	0.31	Negative
σ_y tensile	20	0.15	Positive
σ_y compression	39	0.29	Negative
τ_{xy}	26	0.39	Membrane

Table 185: UC of stiffener plates

To connect the stiffener plates to the girders, bonding flanges are provided along the plate edges next to the girders. The required flange widths are determined from the internal force n_{xy}, the shear flow, obtained from the finite element analysis. The shear flow at the edges of the stiffener plates is divided by the allowable adhesive shear stress of 1 MPa to determine the minimum flange width required for the bonded connection. The highest representative shear flow, excluding the local peaks and the peaks near the supports, is 120 kN/m. The required flange width is therefore:

$$\frac{120}{1} = 120\ mm$$

Appendix BB: Stability analysis glass fibre design

Critical load factor	Buckling shape or buckling location
0.447	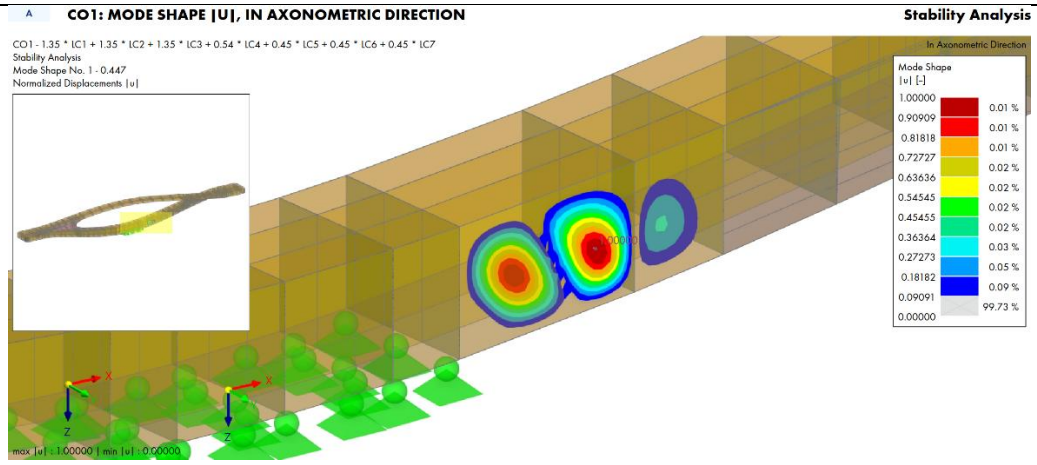 Similar buckling mode as the flax fibre design with critical load factor 0.562
0.478	Location: next to support Similar buckling mode as the flax fibre design with critical load factor 0.601
0.569	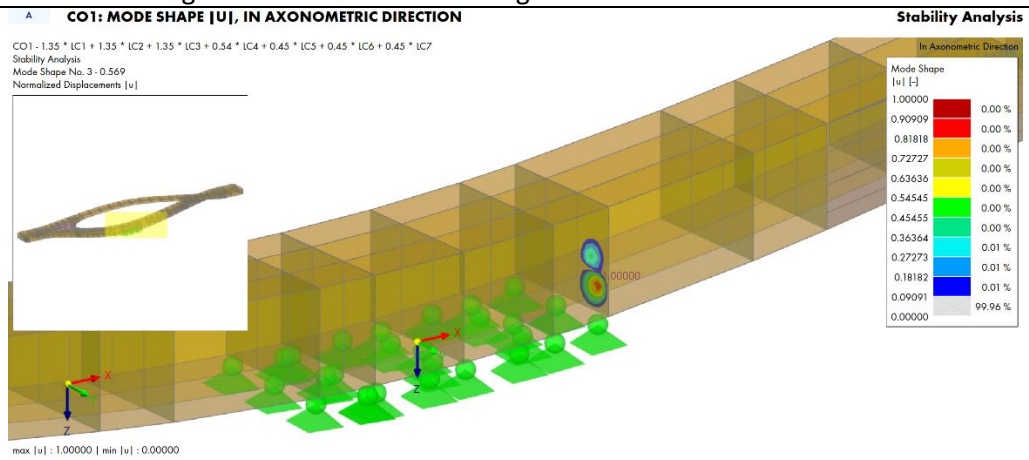
0.588	Location: next to support in C-shaped girder Similar buckling mode as the flax fibre design with critical load factor 0.740
0.634	Location: next to support in stiffener plates
0.653	Location: next to support in stiffener plates and C-shaped girder
0.686	Location: next to support in stiffener plates
0.712	Location: next to support in stiffener plates and C-shaped girder
0.717	Location: next to support in stiffener plates and C-shaped girder
0.727	Location: next to support in stiffener plates and C-shaped girder
0.747	Location: next to support in stiffener plates and C-shaped girder
0.752	Location: next to support in stiffener plates
0.791	Location: next to support in stiffener plates and C-shaped girder
0.822	Location: next to support in stiffener plates

0.846	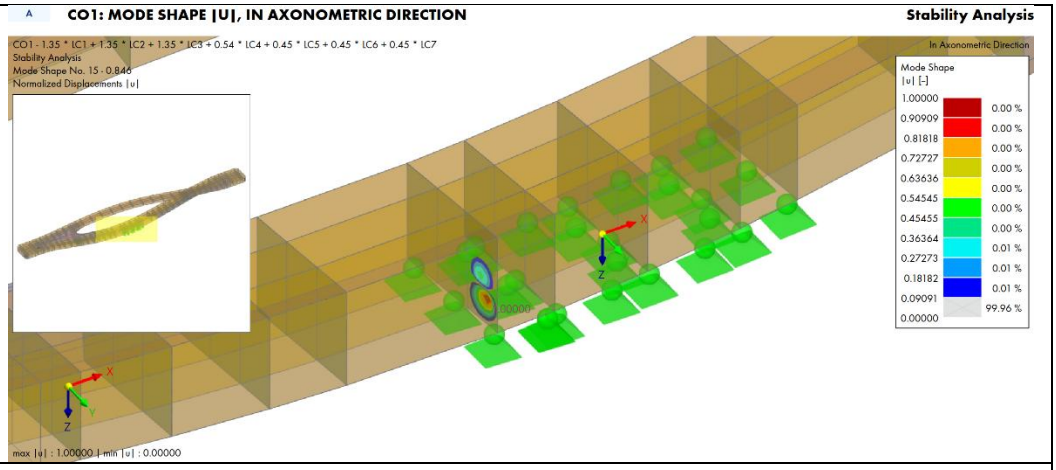
0.897	Location: next to support in stiffener plates
0.912	Location: next to support in stiffener plates
0.946	Location: next to support in stiffener plates and C-shaped girder
0.985	Location: next to support in stiffener plates and C-shaped girder
0.994	Location: next to support in stiffener plates and C-shaped girder
0.999	Location: next to support in stiffener plates and C-shaped girder
1.009	Location: next to support in stiffener plates and C-shaped girder
1.010	Location: next to support in stiffener plates and C-shaped girder
1.014	Location: next to support in stiffener plates and C-shaped girder
1.018	Location: next to support in stiffener plates and C-shaped girder
1.030	Location: next to support in stiffener plates and C-shaped girder
1.034	Location: next to support in stiffener plates and C-shaped girder
1.036	Location: next to support in stiffener plates and C-shaped girder
1.054	Location: next to support in stiffener plates and C-shaped girder
1.061	Location: next to support in stiffener plates and C-shaped girder
1.093	Location: next to support in C-shaped girder
1.096	Location: next to support in C-shaped girder
1.105	Location: next to support in stiffener plates and C-shaped girder
1.124	Location: next to support in stiffener plates and C-shaped girder
1.128	Location: next to support in stiffener plates and C-shaped girder
1.186	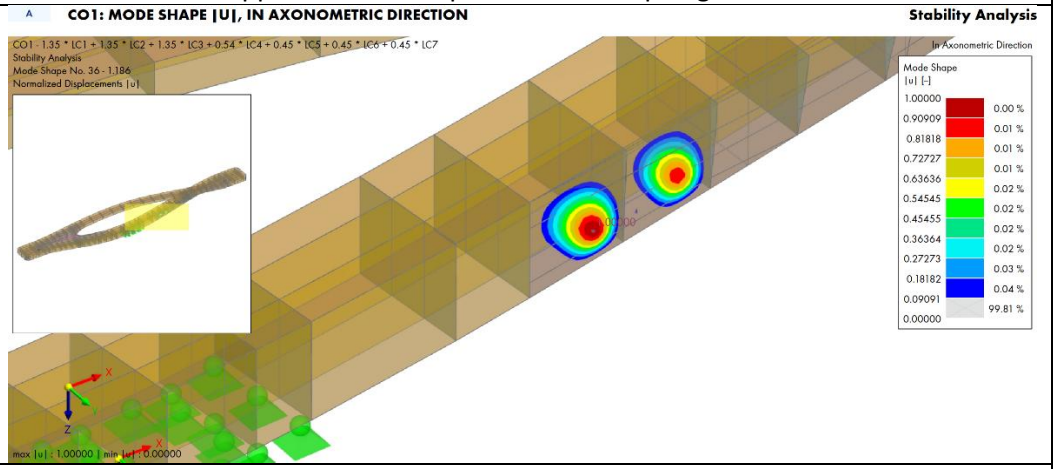
1.193	Location: next to support in stiffener plates
1.200	Location: In C-shaped girder around the same location as critical load factor 1.186

1.232	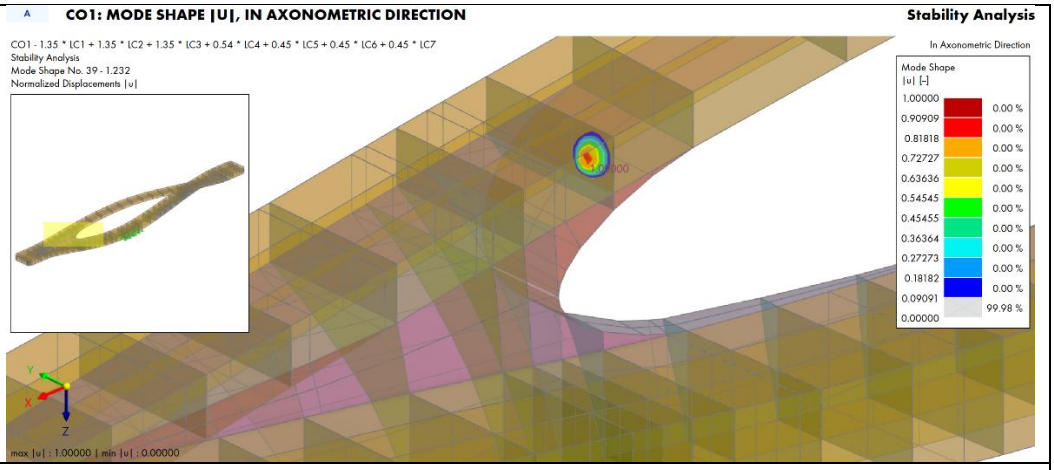
1.236	Location: next to support in stiffener plates and C-shaped girder

Table 186: Stability analysis first 40 critical buckling load factors and some buckling shapes of the glass fibre design

Appendix CC: Creep glass fibre composite

Creep shall be considered when verifying deformations and strength under long-term loading conditions. According to Article 2.4.5.4 of CUR 96:2019, the effect of creep can be taken into account by applying the following conversion factor:

$$\eta_{cv} = \frac{1}{r_v * t^n}$$

Where:

r_v is a factor representing the theoretical increase in strain in the considered lamella

t^n is the duration of the load in hours, where *n* is an exponent depending on the type of fibre reinforcement.

If the fibres are oriented in the direction of the long-term load, the following applies:

- $n = 0.01$ for a UD-lamella
- $n = 0.04$ for a woven lamella
- $n = 0.10$ for a mat lamella

For an axial load, the r_v can be calculated with:

$$r_v = \frac{E_i * t}{\sum E_{v,i} * t_{v,i}}$$

Where:

E_i is the stiffness of the laminate in the considered direction

t is the thickness of the laminate

$\sum E_{v,i} * t_{v,i}$ is the axial stiffness of the laminate in the considered direction adopted for creep analysis, whereby the stiffness of lamella whose fibres are not oriented in the direction of the long-term load is taken as 0.0 N/m²

For the glass fibre design, an overall creep factor is determined for a quasi-isotropic laminate to obtain a representative conversion factor. The laminate lay-up used for this calculation is shown in Figure 228. The E_x of this laminite is 18.897 GPa. The r_v for this laminate is:

$$r_v = \frac{18897 * 9.60}{10 * 37200 * 0.24} = 2.03$$

The mats are all UD lamella and a design life of 50 years is assumed. The factor is:

$$\eta_{cv} = \frac{1}{2.03 * (50 * 365.25 * 24)^{0.01}} = 0.43$$

This conversion factor is subsequently applied to account for the effects of creep in the long-term structural verifications. The maximum allowed stress under permanent load is:

$$\frac{18897 * 0.012 * 0.43}{1.38} = 70.6\ N/mm^2$$

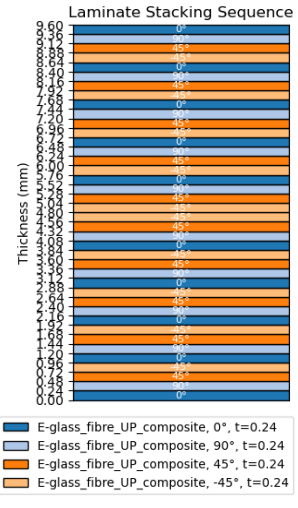

Figure 228: Layering composite creep factor glass fibre composite

The creep coefficient for 50 years is:

$$\frac{1}{\eta_{cv}} - 1 = \frac{1}{0.43} - 1 = 1.32$$

The values of $\eta_{cv}$and the corresponding creep coefficients for different time periods are presented in the table below.

Time [days]	η_{cv} [−]	Creep coefficient [-]
0	-	-
10	0.466	1.14
20	0.463	1.16
30	0.461	1.17
40	0.460	1.18

Table 187: Creep coefficients for different times for glass fibre

Appendix DD: Modal analysis glass fibre design

Modal shapes

Mode number 1

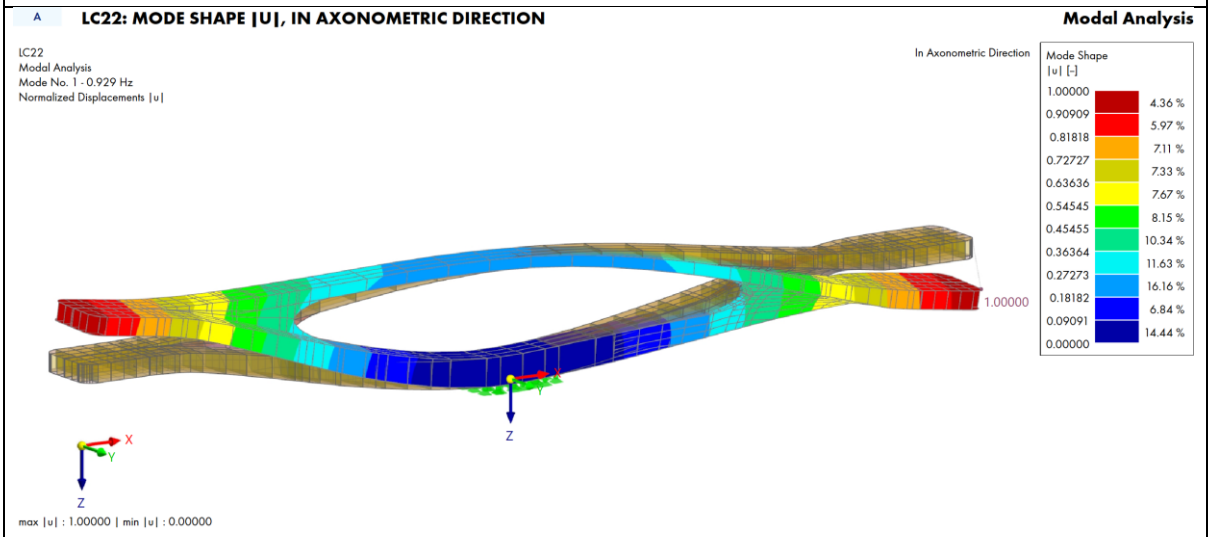

Mode number 2

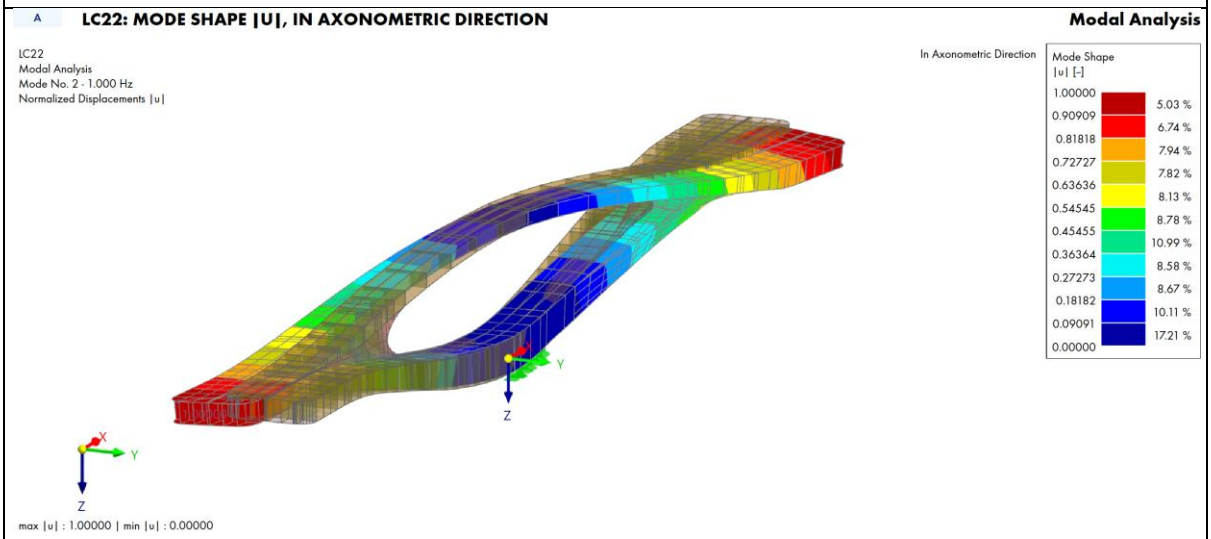

Mode number 3

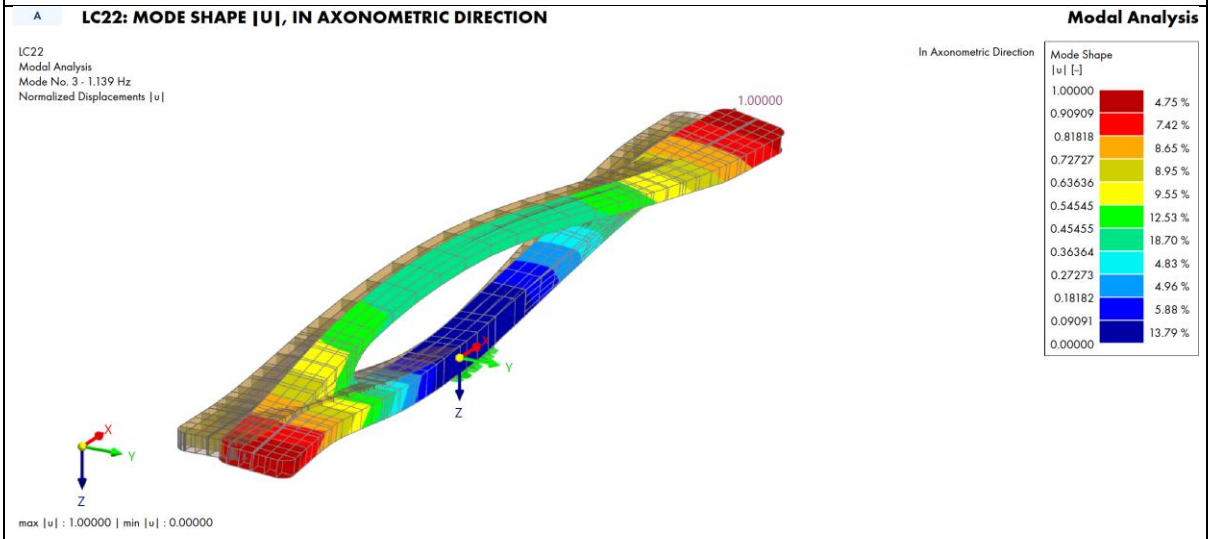

Mode number 4

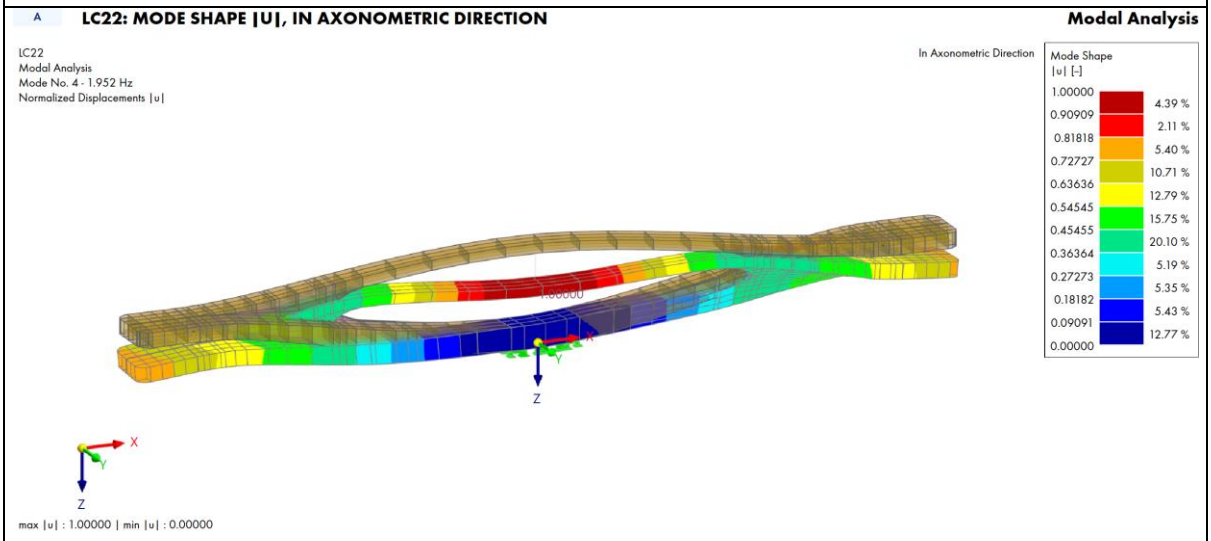

Mode number 5

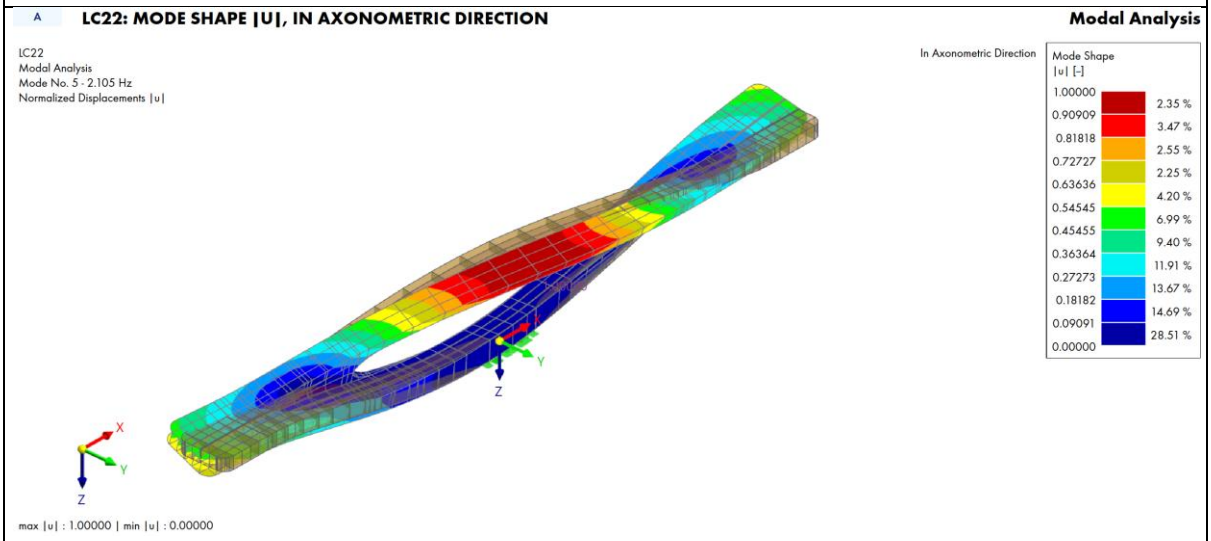

Mode number 6

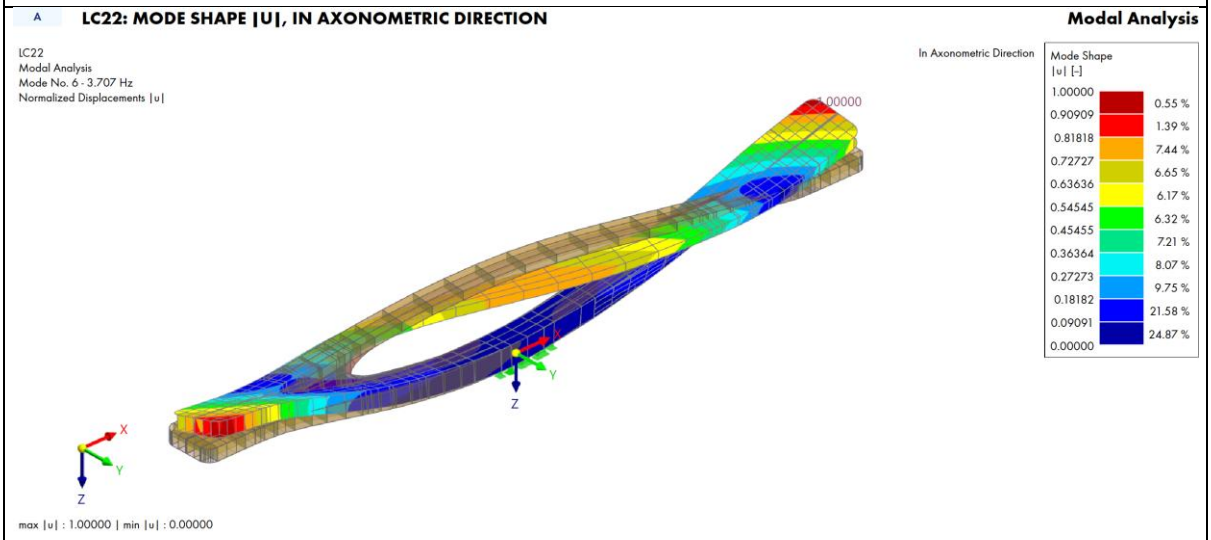

Mode number 7

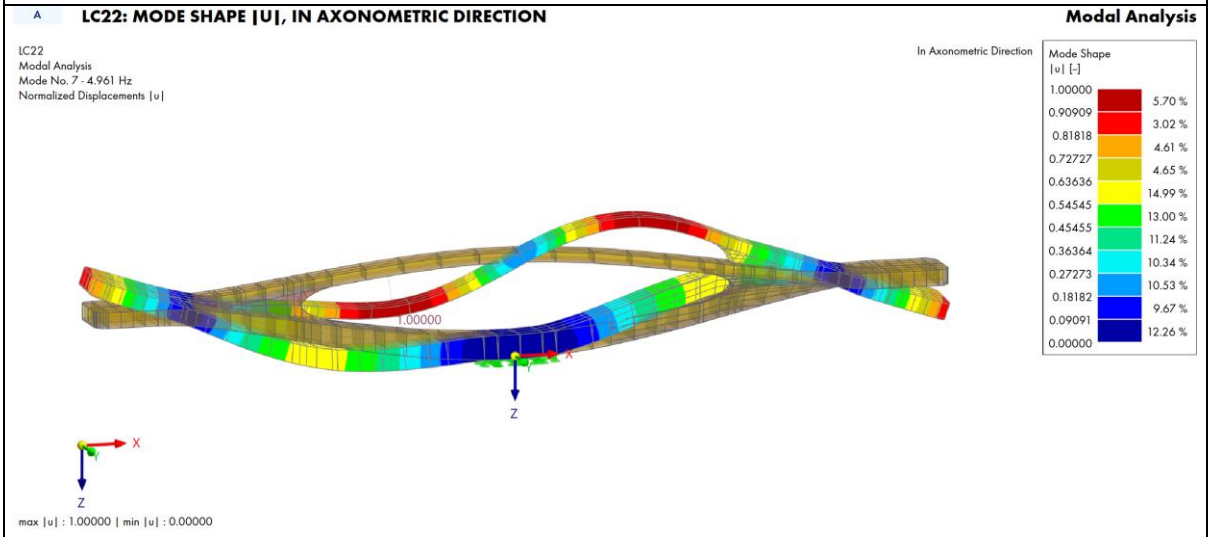

Mode number 8

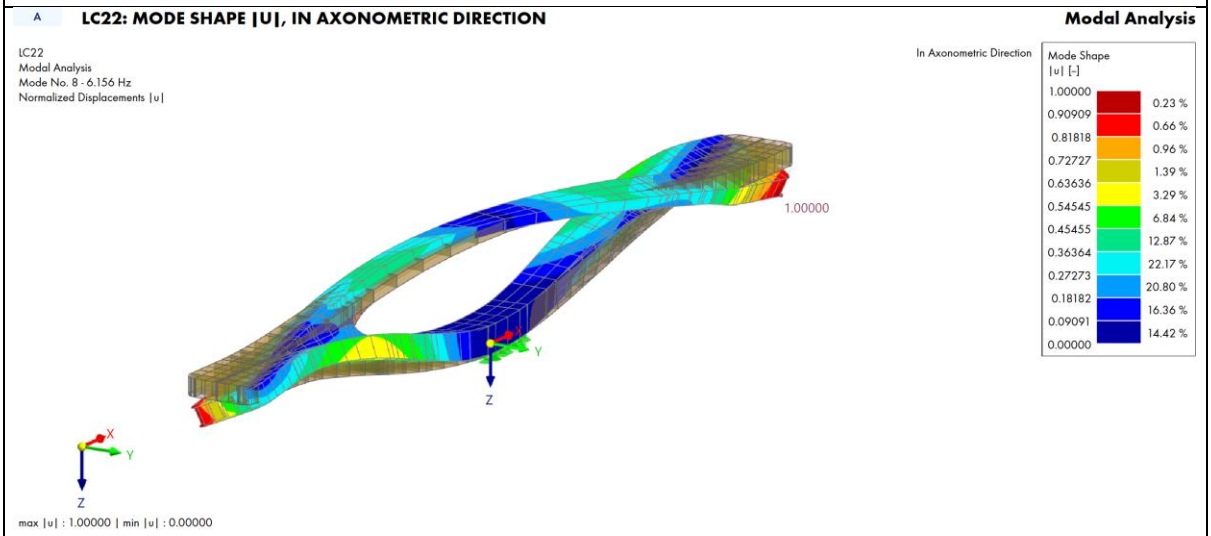

Mode number 9

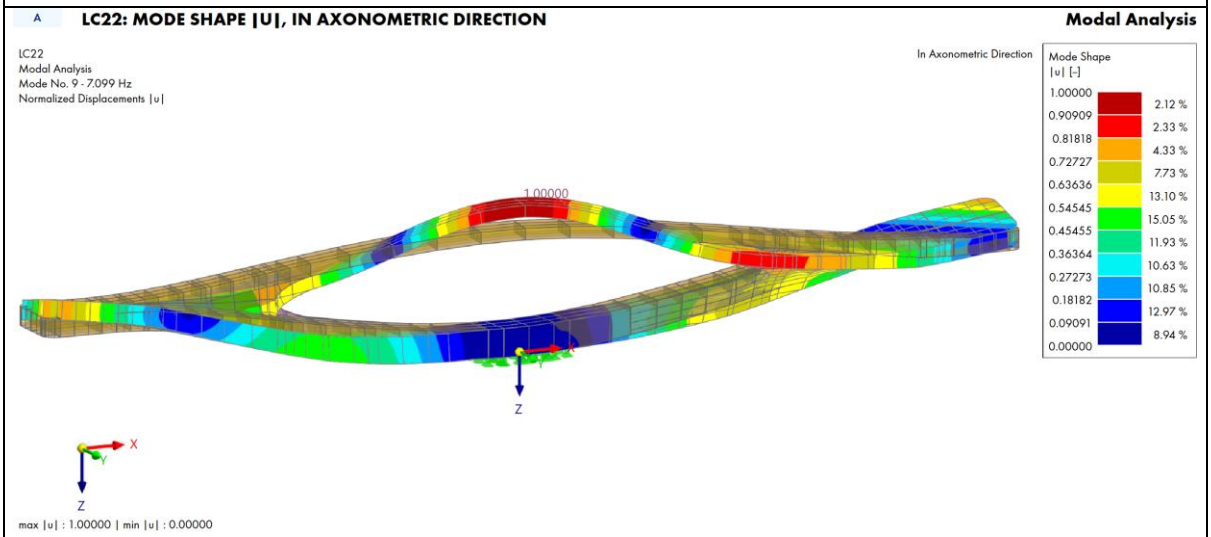

Mode number 10
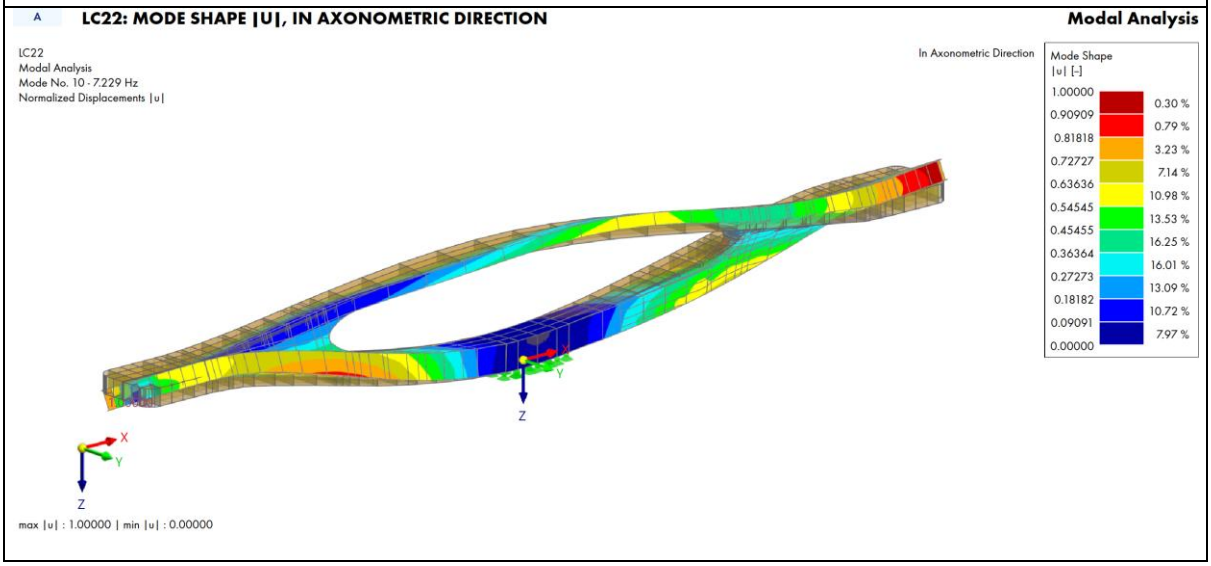

Table 188: Modal analysis first 10 mode shapes of the glass fibre design

Appendix EE: Testing of RWIND with simple structure

Before applying RWIND to the Seasaw, the modelling approach and selected RWIND settings were checked using a simple structure with a known geometry. The structure is 3 m high, 4 m wide, and 5 m long. The walls, top and bottom plates are made of 50 mm thick C30/45 concrete. The structure is fully clamped at the bottom plate and is shown in Figure 229. The structure is assumed to be located near the coast in Den Helder.

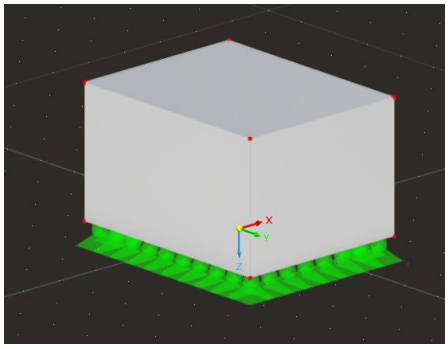

Figure 229: Test structure wind simulation

Wind loads according to Eurocode

The wind load can be calculated according to the Eurocode NEN-EN 1991-1-4 with:

$$F_w = C_s * C_d * C_f * q_p(z_e) * A_{ref}$$

Where:

$C_s * C_d$	is the structural factor which is equal to 1 for structures with a height lower as 15 meters according to the Eurocode
C_f	is the force coefficient for structure or structural component
$q_p(z_e)$	is the peak velocity pressure at reference height z_e
A_{ref}	is the reference area on structure or structural component

To get the wind pressure A_{ref} is left out:

$$p_w = C_s * C_d * C_f * q_p(z_e)$$

$q_p(z_e)$ is equal to 1.22 kN/m^2 for a reference height of 3 meters and zone I coastal, according to the Eurocode. The factor C_f is different for different parts of the structure, see Figure 230 for the different wind zones. The wind zones correspond to the values in Table 189 and Table 190.

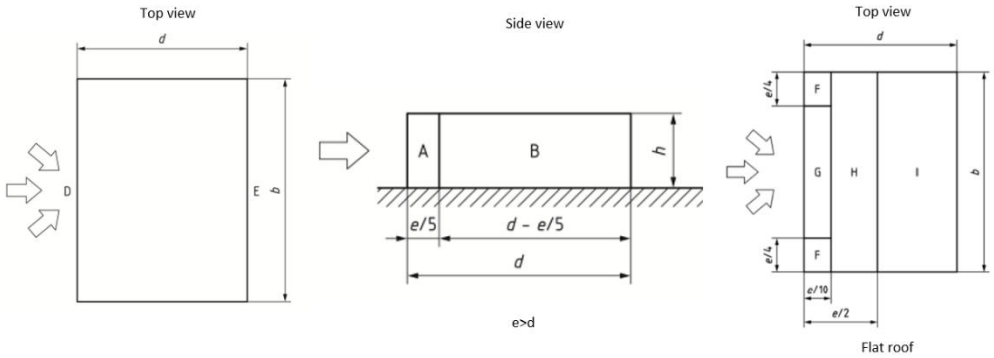

Figure 230: Wind zones Eurocode for e>d and flat roof, obtained from NEN-EN 1991-1-4

$\frac{h}{d}$	A	B	C	D	E
1	-1.2	-0.8	-0.5	+0.8	-0.5

Table 189: Force coefficients for zones A-E

	F	G	H	I
Sharp eaves	-1.8	-1.2	-0.7	+0.2/-0.2

Table 190: Force coefficients for zones F-I

For the simple structure is:

$$h = 3\ meters$$

$$b = 5\ meters$$

$$d = 4\ meters$$

$$e = 5\ meters$$

The lengths of the zones are shown in Figure 231.

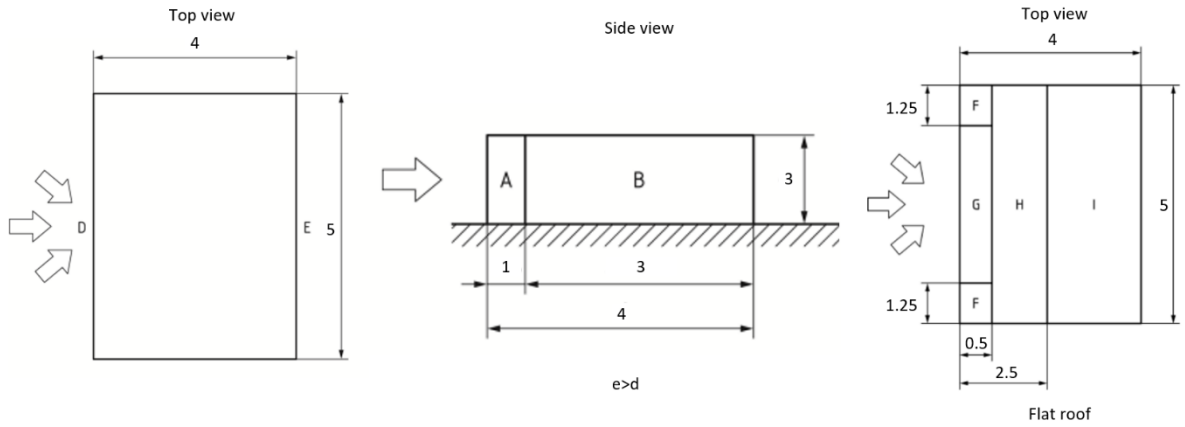

Figure 231: Wind zones Eurocode for e>d and flat roof with lengths in meters, obtained from NEN-EN 1991-1-4

The pressure loads of the different zones are shown in Table 191. If the pressure is positive it points to the surface and if the pressure is negative it points away from the surface.

Zone	$p_w = C_s * C_d * C_f * q_p(z_e)$	Pressure [kN/m²]	$A_{ref}\ [m^2]$	$F_w\ [kN]$
A	$p_w = 1 * -1.2 * 1.22$	-1.47	$1 * 3 = 3$	-4.41
B	$p_w = 1 * -0.8 * 1.22$	-0.98	$3 * 3 = 9$	-8.82
C	$p_w = 1 * -0.5 * 1.22$	-0.61	-	-
D	$p_w = 1 * +0.8 * 1.22$	$+0.98$	$5 * 3 = 15$	14.7
E	$p_w = 1 * -0.5 * 1.22$	-0.61	$5 * 3 = 15$	-9.15
F	$p_w = 1 * -1.8 * 1.22$	-2.20	$1.25 * 0.5 = 0.625$	-1.375
G	$p_w = 1 * -1.2 * 1.22$	-1.47	$2.5 * 0.5 = 1.25$	-1.84
H	$p_w = 1 * -0.7 * 1.22$	-0.854	$5 * 2 = 10$	-8.54
I	$p_w = 1 * +0.2 * 1.22$	$+0.25$	$5 * 1.5 = 7.5$	1.875
	$p_w = 1 * -0.2 * 1.22$	-0.25	$5 * 1.5 = 7.5$	-1.875

Table 191: Pressure in different zones

Wind loads according to RFEM

The structure was drawn in RFEM and a load case was made with calculation type wind simulation. The automatic wind tunnel size is used. The wind tunnel has the dimensions shown in Table 192.

	X	Y	Z
P_{min}	-25.300 [m]	-15.812 [m]	0.015 [m]
P_{max}	37.950 [m]	15.812 [m]	16.337 [m]

Table 192: Dimensions wind tunnel test structure

The wind is placed in x-direction. The simulation type is steady flow, turbulence is considered and use potential flow solver to calculate initial conditions is used. The other parameters are:

- Kinematic viscosity: $1.5 \times 10^{-5}\ \mathrm{m}^2/\mathrm{s}$, this value corresponds to standard atmospheric conditions at approximately 20 °C and is the default value in RWIND. Kinematic viscosity increases slightly with temperature, however, the resulting impact on the calculations is generally small. (Viscocity of air, Dynamic and Kinematic, sd)
- Numerical solver type: OpenFOAM
- Finite volume mesh density: 80%, the simulation was run with different mesh densities, 80% was chosen because the difference in total drag force between a mesh density of 75% and 80% was 3.4%. Higher mesh densities could not be evaluated due to the computational limitations of the laptop used for the simulations.
- Mesh refinement type: Distance from Surface
- Minimum number of iterations: 300
- Maximum number of iterations: 2500
- Turbulence model: RANS k-ε
- Residual type: Drag force
- Residual target value: 0.0001

For the advanced settings were the default parameters in RFEM used. The advanced settings are:

- Pressure field: $p = 0.200$
- Velocity field: $U = 0.500$
- Turbulent kinetic energy: $k = 0.500$
- Turbulent dissipation rate: $\varepsilon = 0.500$
- Specific turbulent dissipation rate (mean frequency of the turbulence): $\omega = 0.500$
- Modified turbulent kinetic viscosity: $\tilde{\nu} = 0.500$
- Turbulence intermittency: $\gamma_{int} = 0.500$
- Momentum thickness Reynolds number: $R_{e\theta} = 0.500$

Wind profile

The wind profile is obtained using RFEM. RFEM includes a wind simulation module that can be used to determine wind loads on structures.

The wind profile is determined according to standard - EN 1991 | NEN | 2023-03, using the following input parameters:

- Load zone: I
- Terrain category: Category 0
- Structure height: $h = 3\ m$
- Air density: $\rho = 1.25\ kg/m^3$
- Fundamental wind velocity: $v_{b,0} = 29.5\ m/s$
- Orography factor: $c_0 = 1.0$
- Directional factor: $c_{dir} = 1.0$
- Seasonal factor: $c_{season} = 1.0$
- Turbulence factor: $k_I = 1.0$
- Terrain factor: $k_r = 0.16$ (automatically determined by RFEM)
- Basic velocity factor: $q_b = 0.54\ kN/m^2$ (automatically determined by RFEM)

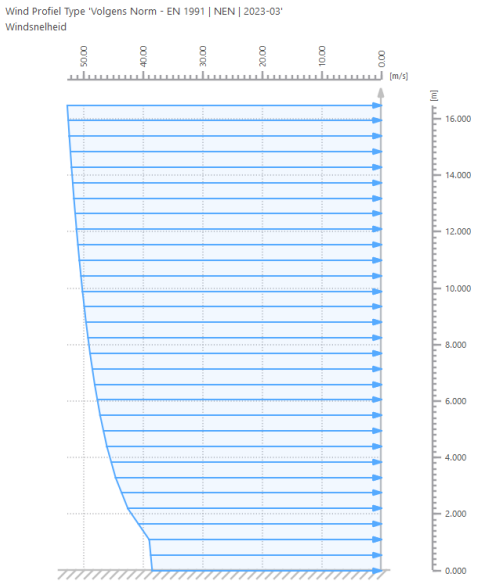

Figure 232: Wind profile test structure, obtained from RFEM

The resulting wind profile is presented in Figure 232 and Table 193.

Height z [m]	Wind velocity v [m/s]	Turbulence intensity I [%]
0.000	38.51	18.87
1.099	39.00	18.54
2.198	42.57	16.43
3.298	44.65	15.40
4.397	46.11	14.75
5.496	47.24	14.28
6.595	48.16	13.92
7.695	48.94	13.63
8.794	49.61	13.38
9.893	50.20	13.17
10.992	50.73	12.99
12.092	51.21	12.84
13.191	51.65	12.69
14.290	52.05	12.57
15.389	52.42	12.45
16.489	52.66	12.34

Table 193: Wind profile test structure

Results

The simulation results are presented in Figure 233 and Table 194. The simulation configuration is shown in Figure 234. According to the RWIND 3 online manual, a simulation is considered to have converged satisfactorily when either a minimum of 300 iterations has been completed or the pressure residual falls below 0.001. Both convergence criteria were satisfied in this simulation, indicating that the results are considered acceptably converged. (Online Manuals RWIND 3: Troubleshooting, sd)

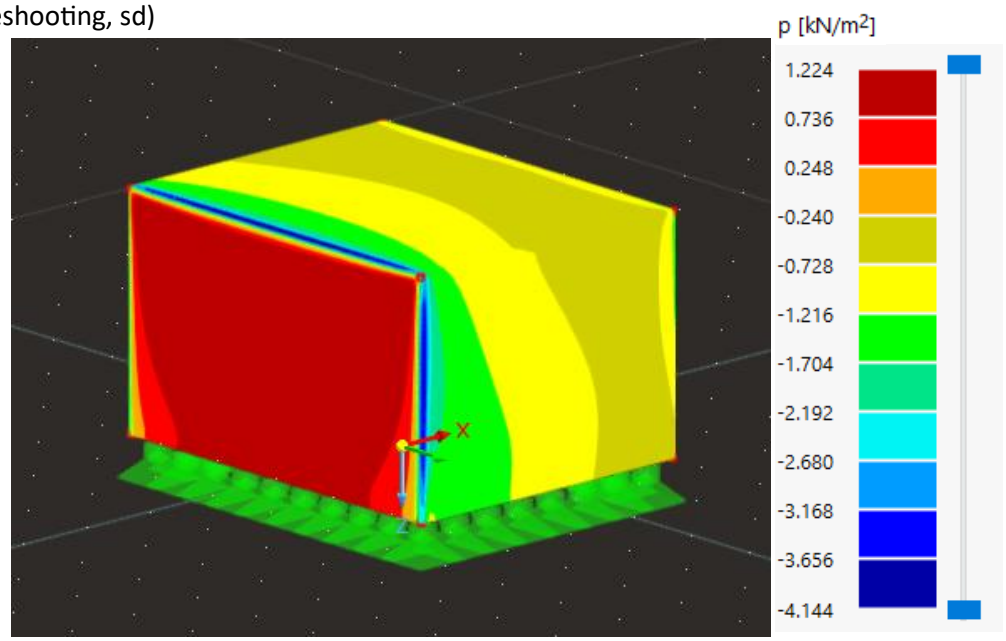

Figure 233: Result test wind simulation

Wind load component	Value [kN]
Drag force in x	24.048
Drag force in y	-0.001
Drag force in z	-19.797
Resultant drag force	31.128

Table 194: Results test structure

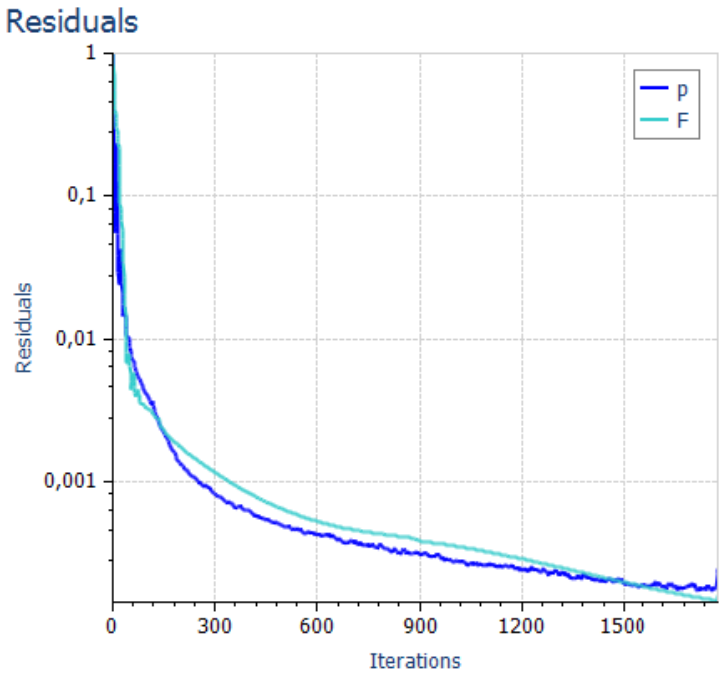

Figure 234: Residuals configurations wind simulation test structure

Conclusion

The results from the Eurocode and the RWIND simulation are compared in the table below.

RWIND simulation (p [kN/m²])	Eurocode	Comparison
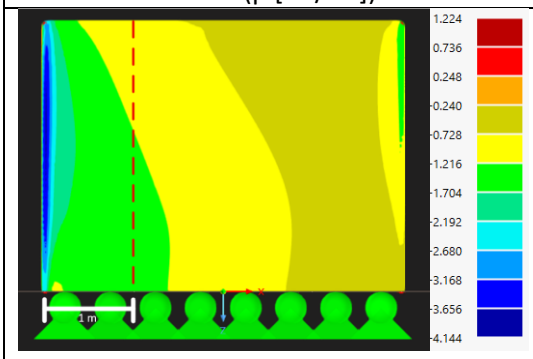	Zone A: -1.47 [kN/m²]	In the RWIND simulation, most of the pressures in zone A range from −1.216 to −1.704 [kN/m²], which is in good agreement with the Eurocode value.
	Zone B: -0.98 [kN/m²]	In the RWIND simulation, most of the pressures in zone B range from -0.240 and -1.216 [kN/m²], which is in good agreement with the Eurocode value.
Total in y: -0.001 [kN]	Total in y: 0.000 [kN]	The total load in the y-direction is approximately zero for both the Eurocode and the RWIND simulation, as the loads on opposite sides of the structure are equal in magnitude and opposite in direction.
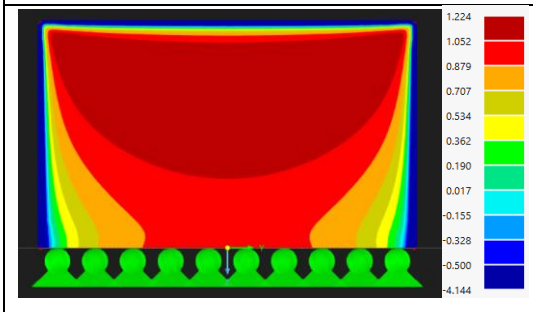	Zone D: $+0.98$ [kN/m²]	In the RWIND simulation, the pressure distribution is not uniform across the surface, whereas the Eurocode assumes a constant pressure within each wind zone. However, the average pressure obtained from the RWIND simulation is in good agreement with the corresponding Eurocode value.

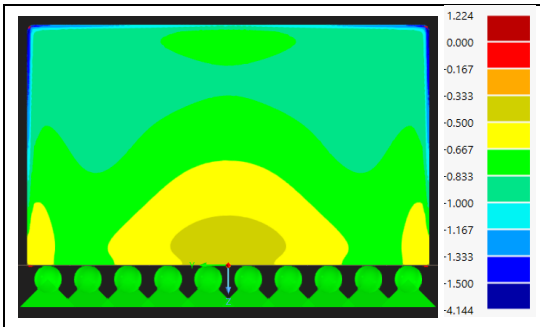	Zone E: -0.61 [kN/m^2]	The pressure distribution obtained from the RWIND simulation is not uniform across the surface, whereas the Eurocode assumes a uniform pressure within each wind zone. However, the average pressure predicted by the RWIND simulation is in good agreement with the corresponding Eurocode value.
Total in x: 24.048 [kN]	Total in x: 23.85 [kN]	The total force differs by only 0.198 kN, demonstrating that the results from the RWIND simulation and the Eurocode are in close agreement. The RWIND simulation predicts a slightly higher total force.
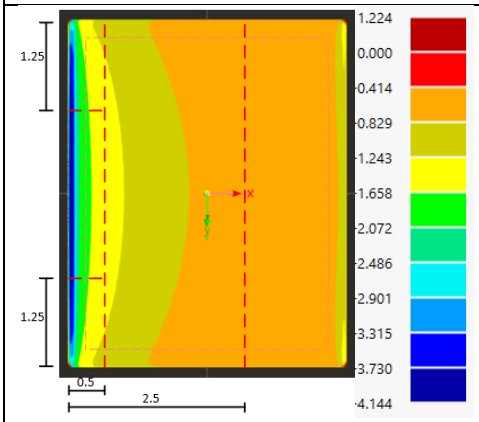	Zone F: -2.20 [kN/m^2]	The pressures predicted by the RWIND simulation in zone F are lower than the corresponding Eurocode value.
	Zone G: -1.47 [kN/m^2]	The average pressure predicted by the RWIND simulation for zone G is approximately equal to the corresponding Eurocode value.
	Zone H: -0.854 [kN/m^2]	The average pressure predicted by the RWIND simulation for zone H is approximately equal to the corresponding Eurocode value.
	Zone I: $+0.25$ [kN/m^2] -0.25 [kN/m^2]	The pressure in zone I predicted by the RWIND simulation is higher than the corresponding Eurocode value.
Total in z: -19.797 [kN]	Total in z: -15.005 [kN]	The total force in the z-direction predicted by the RWIND simulation is higher than the corresponding Eurocode value, with a difference of 4.792 kN. Furthermore, the pressure distribution across the different zones in the RWIND simulation differs from the simplified distribution assumed by the Eurocode.

Table 195: Zone comparison between RWIND and Eurocode

The Eurocode calculations were used as a reference to validate the results of the RWIND simulation. The comparison showed good agreement between the RWIND simulation and the Eurocode for most wind pressure zones. The RWIND simulation produces a more detailed and non-uniform pressure distribution than the simplified pressure distribution assumed by the Eurocode. Nevertheless, the average pressures in zones A, B, D, E, G, and H were close to the corresponding Eurocode values.

The total forces in the x- and y-directions also showed good agreement between the two methods. The total force in the y-direction was approximately zero for both methods, while the difference in the x-direction was only 0.198 kN. This indicates that, for the tested structure, the applied RWIND setup produces global wind forces of the same order of magnitude as the Eurocode calculation.

The largest difference was observed in the z-direction. The RWIND simulation predicted a higher total force than the Eurocode calculation. This difference is attributed primarily to the pressure distribution in zone I and the non-uniform pressure distribution obtained from the numerical simulation compared with the simplified Eurocode approach.

Overall, the comparison provided a check of the selected RWIND modelling approach and the interpretation of its results. The good agreement in the global forces and pressure values provides confidence in the selected RWIND setup as a basis for the subsequent wind-load analysis of the Seasaw.

Appendix FF: RWIND settings for the wind analysis of the Seasaw

This appendix presents the settings used for the wind simulations of the Seasaw. Three wind simulations were performed: a simulation without a modelled dike in the x-direction, a simulation without a modelled dike in the y-direction, and a simulation with a modelled dike in the x-direction.

The Seasaw geometry was modelled in RFEM before performing the wind simulations and has a height of approximately 5.5 m. Most RWIND settings were identical for the three simulations. These common settings are described first, followed by the parameters that differ between the simulations. The resulting wind profiles and computational domain dimensions are presented separately for each simulation. For the simulation including the dike, the dike was explicitly modelled in RWIND. The dike extends from x=-67.0 m to x=33.25 m, with horizontal terrain before and after these locations. The dike model has a maximum height of 14.1 m.

General RWIND settings

All three simulations were performed using steady flow with turbulence considered. The potential flow solver was used to calculate the initial conditions. The following RWIND settings were used for all three simulations unless stated otherwise:

- Kinematic viscosity: $1.5 * 10^{-5}\ \mathrm{m}^2/\mathrm{s}$, this value corresponds to standard atmospheric conditions at approximately 20 °C and is the default value in RWIND. Kinematic viscosity increases slightly with temperature, however, the resulting impact on the calculations is generally small. (Viscocity of air, Dynamic and Kinematic, sd)
- Numerical solver type: OpenFOAM
- Finite volume mesh density: 100%
- Mesh refinement type: Distance from Surface
- Boundary layers: Model NL: 5 and Tunnel BL: 5
- Minimum number of iterations: 300
- Turbulence model: RANS k-ε
- Residual type: Pressure
- Residual target value: 0.0001

The maximum number of iterations and the mesh sensitivity results differed between the simulations and are therefore given in Table 196.

Parameter	Without dike, x-direction	Without dike, y-direction	With dike, x-direction
Maximum number of iterations	3000	4000	5000
Difference in total drag force between 90% and 100% mesh density	2.0%	1.1%	7.7%

Table 196: RWIND settings that differ between the three simulations

The default RFEM values were used for the advanced settings. These settings were identical for all three simulations:

- Pressure field: $p = 0.200$
- Velocity field: $U = 0.500$
- Turbulent kinetic energy: $k = 0.500$
- Turbulent dissipation rate: $\varepsilon = 0.500$
- Specific turbulent dissipation rate (mean frequency of the turbulence): $\omega = 0.500$
- Modified turbulent kinetic viscosity: $\tilde{\nu} = 0.500$
- Turbulence intermittency: $\gamma_{int} = 0.500$
- Momentum thickness Reynolds number: $R_{e\theta} = 0.500$

Wind tunnel dimensions

The wind tunnel dimensions differed between the simulations because the wind direction and the presence of the dike affect the required computational domain. The wind tunnel for the simulation without dike in x-direction has the dimensions shown in Table 197.

	X	Y	Z
P_{min}	-70.179 [m]	-17.310 [m]	0.007 [m]
P_{max}	80.269 [m]	17.310 [m]	20.333 [m]

Table 197: Dimensions wind tunnel wind simulation in x-direction without dike

The wind tunnel for the simulation without dike in y-direction has the dimensions shown in Table 198.

	X	Y	Z
P_{min}	-87.033 [m]	-54.396 [m]	0.007 [m]
P_{max}	130.550 [m]	54.396 [m]	34.941 [m]

Table 198: Dimensions wind tunnel wind simulation in y-direction without dike

The wind tunnel for the simulation with dike in x-direction has the dimensions shown in Table 199. The resulting computational domain extends beyond the minimum recommended dimensions in all directions.

	X	Y	Z
P_{min}	-170.000 [m]	-50.000 [m]	0.000 [m]
P_{max}	335.000 [m]	50.000 [m]	120.000 [m]

Table 199: Dimensions wind tunnel wind simulation in x-direction with dike

For the simulations without a modelled dike, the automatically generated wind tunnel dimensions were used.

For the simulation including the dike, the automatically generated wind tunnel was not sufficiently large. The resulting blockage ratio was approximately 30.2%, which exceeds the recommended values for wind tunnel and CFD simulations. The computational domain was therefore increased manually. (Jörg Franke, Hellsten, Schlünzen, & Carissimo, 2007) The recommended minimum height of the computational domain is 5H above the structure, where H is the total height of the structure and dike. The total height is therefore:

$$5.5 + 14.1 = 19.6$$

The minimum height of the computational domain is therefore:

$$19.6 + 5 * 19.6 = 117.6\,m$$

In the y-direction, the computational domain should extend at least 2.3H from the structure. The required width on each side is therefore:

$$1.8 + 2.3 * 19.6 = 46.88\, m$$

A minimum distance of 5H is required between the inlet boundary and the dike. Therefore, the required domain length in the negative x-direction is:

$$67.0 + 5 * 19.6 = 165\, m$$

Similarly, a minimum distance of 15H is required between the dike and the outlet boundary. The required domain length in the positive x-direction is:

$$33.25 + 15 * 19.6 = 327.25\, m$$

Based on these requirements, the wind tunnel dimensions were selected as shown in Table 199. (Jörg Franke, Hellsten, Schlünzen, & Carissimo, 2007)

Model settings

For the Seasaw model, the Simplify model and Optimization options were enabled for all three simulations. A level of detail of 5 was used, and holes smaller than 0.05 m were closed.

For the simulation including the dike, the dike was modelled separately in RWIND and a mesh refinement level of 5 was applied to the dike.

Wind profiles

For all simulations, the wind profile was generated in RFEM according to EN 1991 | NEN | 2023-03. The following input parameters were used unless stated otherwise:

- Load zone: I
- Terrain category: Category 0
- Structure height: $h = 5.464\, m$
- Air density: $\rho = 1.25\, kg/m^3$
- Fundamental wind velocity: $v_{b,0} = 29.5\, m/s$
- Directional factor: $c_{dir} = 1.0$
- Seasonal factor: $c_{season} = 1.0$
- Turbulence factor: $k_I = 1.0$
- Terrain factor: $k_r = 0.16$
  (automatically determined by RFEM)
- Basic velocity factor: $q_b = 0.54\, kN/m^2$
  (automatically determined by RFEM)

The orography factor depend on the specific simulation. For the simulation without a modelled dike in x-direction was the orography factor equal to:

$$c_0 = 1.38$$

This value is determined in Appendix GG. The orography factor of the other simulations was 1.0.

Wind profile without dike in x-direction

The wind was applied in the x-direction. The wind profile used in the simulation is presented in Figure 235 and Table 200.

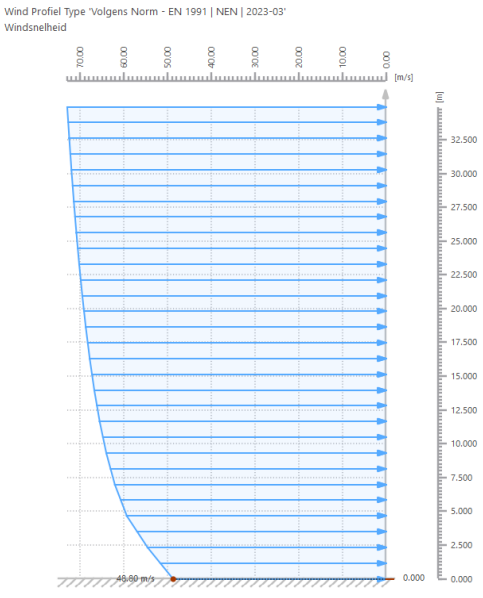

Figure 235: Wind profile wind simulation in x-direction without dike, obtained from RFEM

Height z [m]	Wind velocity v [m/s]	Turbulence intensity I [%]
0.000	48.80	13.68
2.329	54.65	11.79
4.658	59.41	10.60
6.987	62.17	10.01
9.316	64.13	9.62
11.645	65.65	9.35
13.974	66.89	9.13
16.303	67.93	8.96
18.631	68.84	8.81
20.960	69.64	8.69
23.289	70.35	8.58
25.618	70.99	8.48
27.947	71.58	8.40
30.276	72.12	8.32
32.605	72.62	8.25
34.934	73.09	8.19

Table 200: Wind profile wind simulation in x-direction without dike

Wind profile without dike in y-direction

The wind was applied in the y-direction. The wind profile used in the simulation is presented in Figure 237 and Table 201.

Height z [m]	Wind velocity v [m/s]	Turbulence intensity I [%]
0.00	38.51	18.87
2.33	42.87	16.28
4.66	46.40	14.63
6.99	48.45	13.81
9.32	49.90	13.28
11.65	51.02	12.90
13.97	51.94	12.60
16.30	52.71	12.36
18.63	53.38	12.16
20.96	53.96	11.99
23.29	54.49	11.84
25.62	54.97	11.71
27.95	55.40	11.59
30.28	55.80	11.48
32.61	56.17	11.39
34.93	56.51	11.30

Table 201: Wind profile wind simulation in y-direction without dike

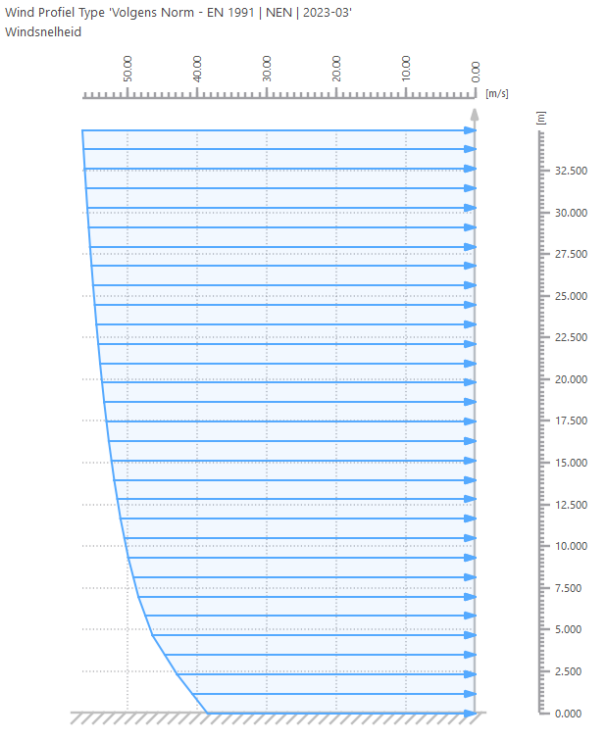

Figure 237: Wind profile wind simulation in y-direction without dike

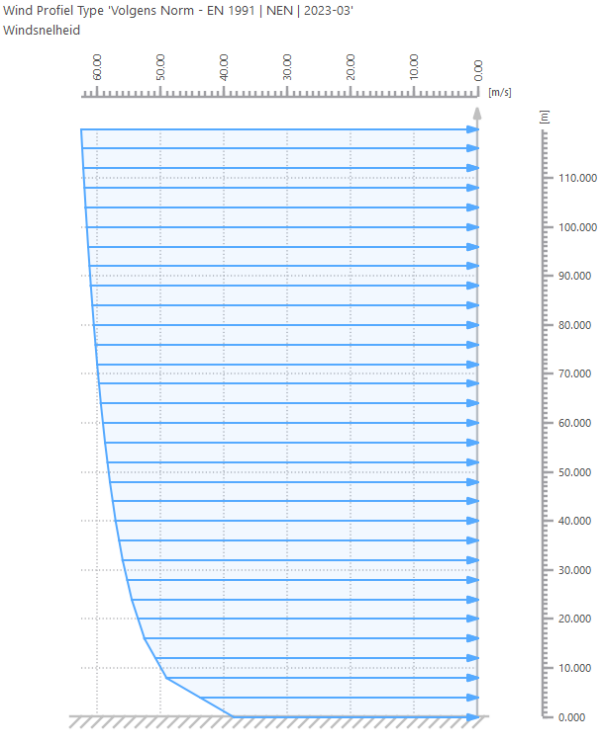

Figure 236: Wind profile wind simulation in x-direction with dike, obtained from RFEM

Wind profile with dike in x-direction

The wind was applied in the x-direction. The wind profile used in the simulation is presented in Figure 236 and Table 202.

Height z [m]	Wind velocity v [m/s]	Turbulence intensity I [%]
0.00	38.51	18.87
8.00	49.13	13.55
16.00	52.61	12.39
24.00	54.64	11.80
32.00	56.07	11.41
40.00	57.18	11.13
48.00	58.09	10.91
56.00	58.85	10.73
64.00	59.52	10.57
72.00	60.10	10.44
80.00	60.62	10.33
88.00	61.09	10.23
96.00	61.52	10.14
104.00	61.92	10.06
112.00	62.28	9.98
120.00	62.63	9.91

Table 202: Wind profile wind simulation in x-direction with dike

Appendix GG: Determining of orography factor

The orography factor is determined in accordance with NEN-EN 1991-1-4, Annex A. The geometry of the dike is shown in Figure 238.

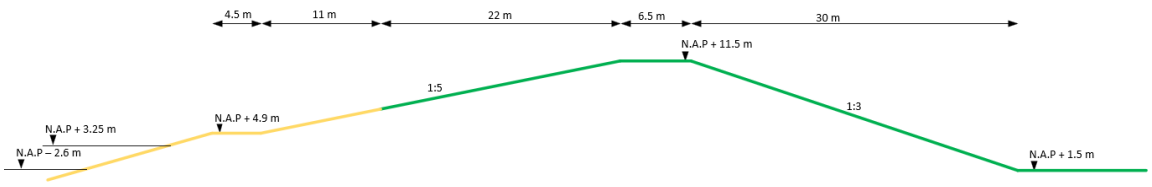

Figure 238: Estimation of the dike geometry

The geometric parameters of the dike are defined as follows:

- Wind ward slope length: $L_u = 63.8\ m$
- Effective height: $H = 14.1\ m$
- Windward slope: $\phi = \frac{14.1}{63.8} = 0.22$
- Since $0.05 < \phi < 0.3$, the effective slope length is: $L_e = 63.8$

According to NEN-EN 1991-1-4, the orography factor for a slope in the range $0.05 < \phi < 0.3$ given by:

$$c_o = 1 + 2 * s * \phi$$

Where:

s is the orography location factor

The location factor is determined from:

$$s = A * e^{(B * \frac{X}{L_u})}$$

With:

$$A = 0.1552 * \left(\frac{z}{L_e}\right)^4 - 0.08575 * \left(\frac{z}{L_e}\right)^3 + 1.8133 * \left(\frac{z}{L_e}\right)^2 - 1.9115 * \left(\frac{z}{L_e}\right) + 1.0124$$

$$B = 0.3542 * \left(\frac{z}{L_e}\right)^2 - 1.0577 * \left(\frac{z}{L_e}\right) + 2.6456$$

The Seasaw is located at the crest of the dike, therefore X = 0. The height of the structure above the crest is approximately 5.5 m. The factor $\frac{z}{L_e} = \frac{5.5}{63.8} = 0.08$. The orography location factor is:

$$s = A = 0.1552 * (0.08)^4 - 0.08575 * (0.08)^3 + 1.8133 * (0.08)^2 - 1.9115 * (0.08) + 1.0124$$

$$s = 0.87$$

The orography factor is:

$$c_o = 1 + 2 * 0.87 * 0.22 = 1.38$$

Appendix HH: Eurocode wind loads for comparison with RWIND simulations

This section presents the wind loads calculated according to NEN-EN 1991-1-4 for the Seasaw. These loads are used as reference values for comparison with the wind loads obtained from the RWIND simulations. The calculations are presented for wind acting in the x-direction and y-direction, using the coordinate system of the finite element model. This coordinate system differs from the coordinate system used in Chapter 5.2.3.

Eurocode wind loads for wind in the x-direction

According to the Eurocode, wind acting in the x-direction for a bridge results in both a horizontal load on the deck in the x-direction and a simultaneous horizontal load on the side of the deck in the y-direction. The wind load acting on the top of the deck in the x-direction is given by:

$$F_{w,x} = 0.4 * F_{w,y}$$

$$q_{w,x} = 0.4 * q_{w,y} = 0.4 * 2855.5 * d_{tot} = 1142.2 * d_{tot}\ [N/m]$$

The resulting wind loads acting on the structure in the x-direction are shown in Figure 240. The corresponding distributed loads acting on the top deck are presented in Figure 239. In addition, a distributed line load of 0.342 kN/m is applied in x-direction along the deck edges to account for the wind load acting on the balustrades.

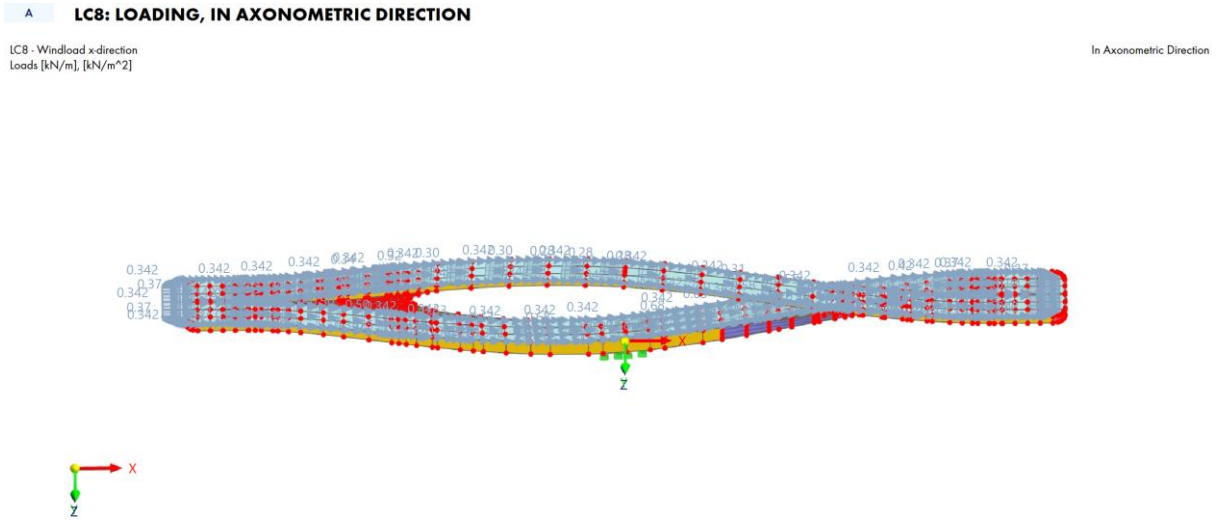

Figure 240: Applied load in the finite element model for the wind load in x-direction

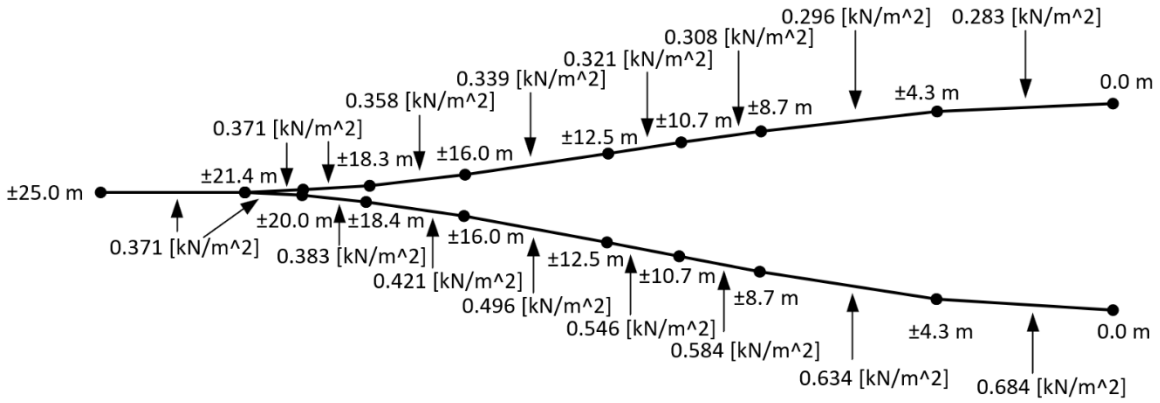

Figure 239: Distributed loads of half the structure which are applied on the finite element model for the wind load in x-direction

The simultaneous wind load acting in the y-direction is determined according to the Eurocode as:

$$F_{w,y\ acting\ simultaneous\ with\ x} = 0.4 * F_{w,y}$$

$$q_{w,y\ acting\ simultaneous\ with\ x} = 0.4 * q_{w,y} = 0.4 * 2855.5 * d_{tot} = 1142.2 * d_{tot}\ [N/m]$$

The wind loads acting in the y-direction are shown in Figure 241. The values presented in this figure correspond to the full Eurocode wind load, $q_{w,y}$, without the reduction factor of 0.4. This reduction factor is applied in the load combination representing wind acting in the x-direction. The applied loads on the side of the structure consist of a distributed pressure of $1.142\ kN/m^2$ and a line load of $0.686\ kN/m$ acting on the top of the girders to account for the wind load on the balustrades.

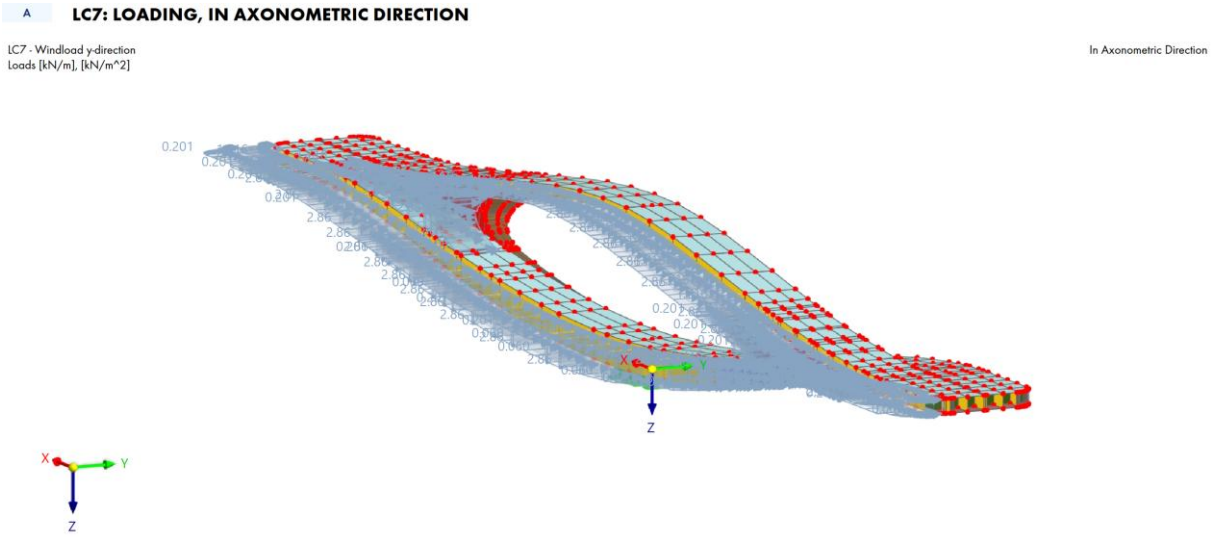

Figure 241: Applied load in the finite element model for the wind load in y-direction

The load combination representing wind in the x-direction is:

$$0.4 * LC7 + LC8$$

The sum of loads and resultant of reactions of the wind loads is given in the table below.

Sum of loads in:	[kN]
X	143.59
Y	136.19
Z	0.0
Resultant of reactions about:	[kNm]
X	-4.70
Y	-19.82
Z	114.50

Table 203: The sum of loads and resultant of reactions of the wind in x-direction

A global assessment of the stress distribution, excluding local singularities, resulted in the approximate stress ranges shown in Table 204.

Stress component	Stress range $[N/mm^2]$
σ_x, local x-direction	-7 to +7
σ_y, local y-direction	-3 to +3
τ_{xy}, shear stress	-4 to +4

Table 204: Approximate global stress ranges for the Eurocode wind load for wind in x-direction

The resulting deformation of the structure is shown in Figure 242.

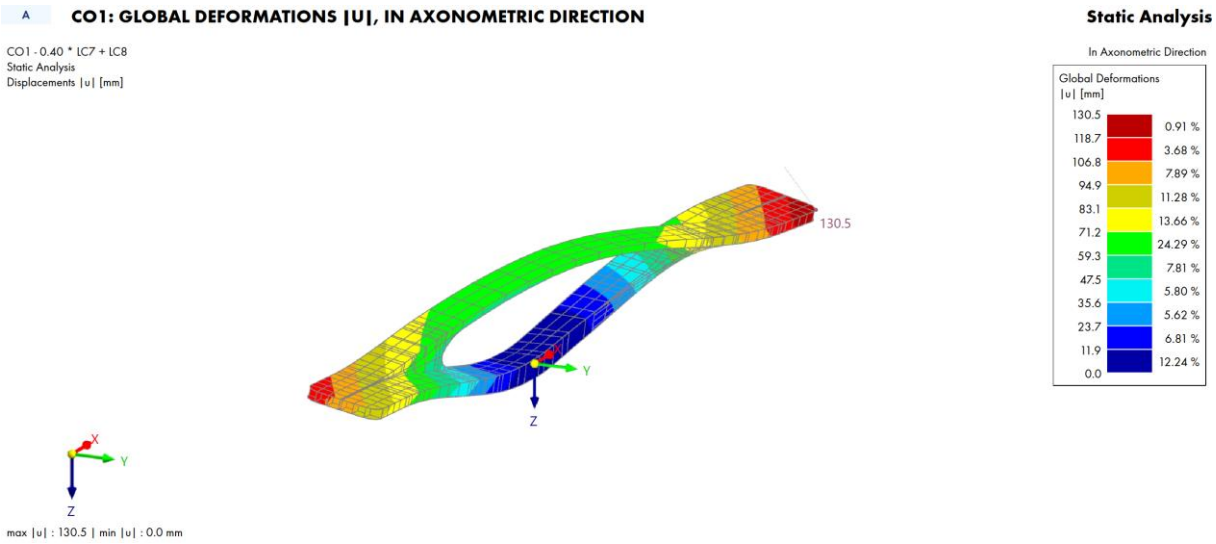

Figure 242: Deformations because of the wind in x-direction

Because of the inclined roof-like geometry of the Seasaw, the wind load provisions for canopies in NEN-EN 1991-1-4 may also be applicable for wind acting in the x-direction. The different load arrangements for duo-pitched canopies are shown in Figure 243.

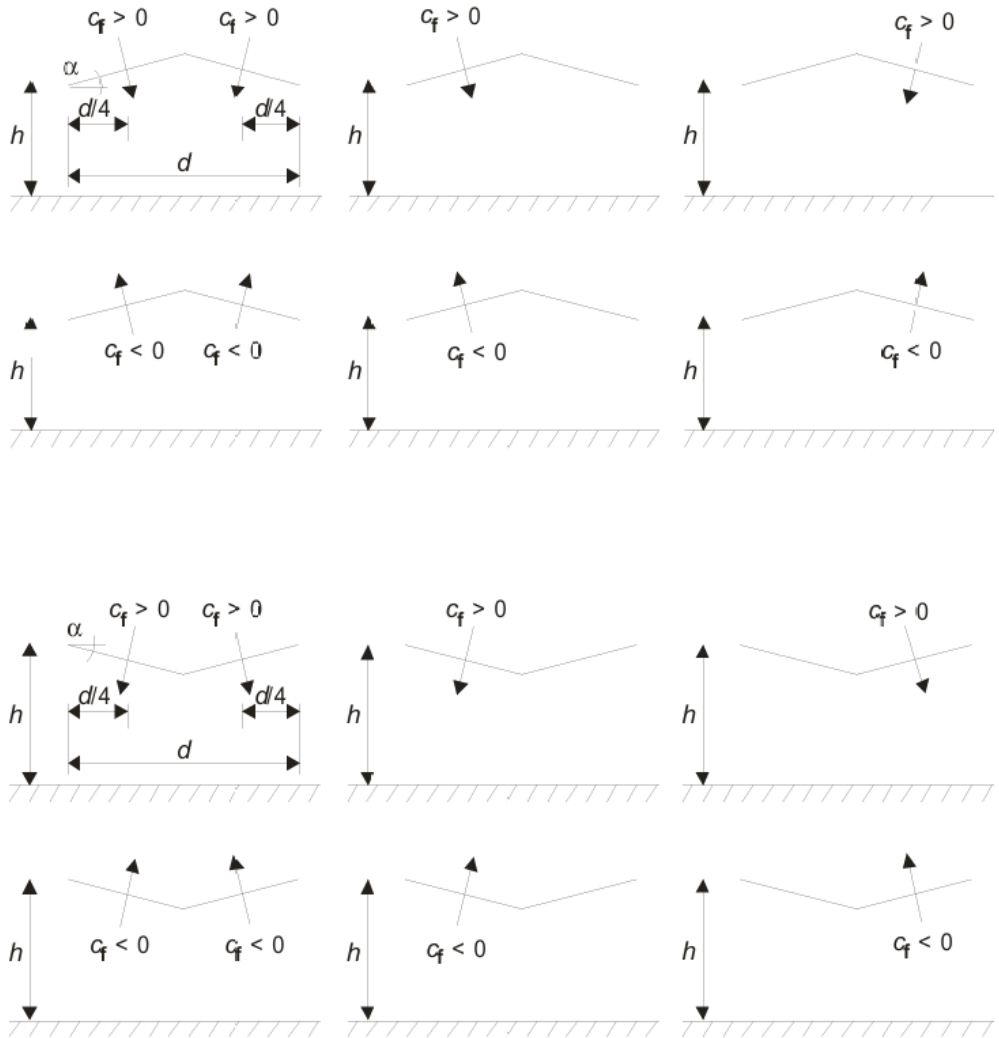

Figure 243: Load combinations derived from force coefficients for duo pitch canopies according to Eurocode NEN-EN 1991-1-4

The wind load can be calculated according to the Eurocode NEN-EN 1991-1-4 with:

$$F_w = C_s * C_d * C_f * q_p(z_e) * A_{ref}$$

Where:

$C_s * C_d$	is the structural factor which is equal to 1 for structures with a height lower as 15 meters according to the Eurocode
C_f	is the force coefficient for structure or structural component
$q_p(z_e)$	is the peak velocity pressure at reference height z_e
A_{ref}	is the reference area on structure or structural component

To get the wind pressure A_{ref} is left out:

$$p_w = C_s * C_d * C_f * q_p(z_e)$$

For the Seasaw, the structural height is 3.143 m, resulting in a peak velocity pressure of $q_p(z_e) = 1.22\ kN/m^2$ for a reference height of 3 meters and zone I coastal, according to the Eurocode. Since the average inclination of the structure is approximately 7°, the Eurocode values for slopes of 10° were adopted as a conservative approximation. The force coefficient depends on the degree of blocking, see Figure 244. A factor φ of 0 and 1 will both be taken into account for the structure. The force coefficients for a slope of +/-10° are given in Table 205. The resulting pressures are also given in the table.

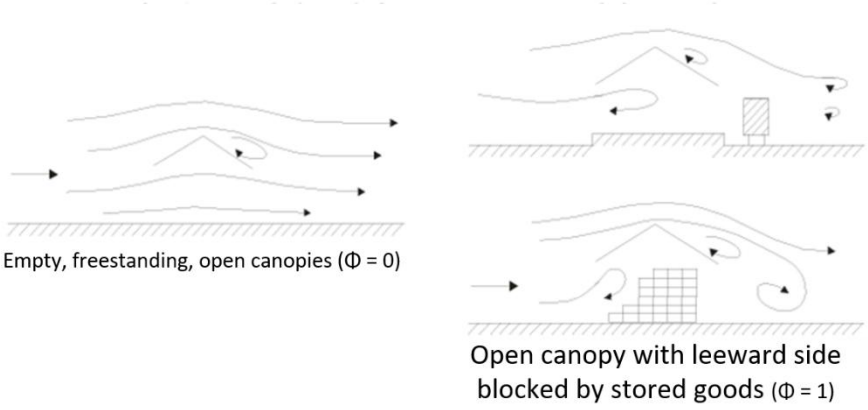

Figure 244: Airflow over canopies, obtained from NEN-EN 1991-1-4

Slope α [°]	Degree of blocking φ	Global force coefficient C_f	Wind pressure p_w $[kN/m^2]$
-10	Maximum for all φ	+0.4	+0.488
	Minimum for $\varphi = 0$	-0.6	-0.732
	Minimum for $\varphi = 1$	-1.4	-1.708
10	Maximum for all φ	+0.4	+0.488
	Minimum for $\varphi = 0$	-0.7	-0.854
	Minimum for $\varphi = 1$	-1.3	-1.586

Table 205: Force coefficients for canopies according to Eurocode 1991-1-4 with resulting pressures

The wind pressure for canopies can also be determined according to the Eurocode with:

$$p_w = q_p(z_e) * C_{p,net}$$

Where:

$q_p(z_e)$ is the peak velocity pressure at reference height z_e

$C_{p,net}$ is the net pressure coefficient

$q_p(z_e)$ is the same as before and is equal to $1.22\ kN/m^2$. The net pressure coefficients for a slope of +/-10° are given in the table below. The corresponding zoning is given in Figure 245. The resulting pressures for the different zones are given in Table 207.

Slope α [°]	Degree of blocking φ	Net pressure coefficient $C_{p,net}$			
		Zone A	Zone B	Zone C	Zone D
-10	Maximum for all φ	+0.6	+1.4	+0.8	+1.1
	Minimum for $\varphi = 0$	-0.8	-1.3	-1.5	-0.6
	Minimum for $\varphi = 1$	-1.6	-2.7	-2.6	-0.6
10	Maximum for all φ	+0.7	+1.8	+1.4	+0.4
	Minimum for $\varphi = 0$	-0.7	-1.5	-1.4	-1.4
	Minimum for $\varphi = 1$	-1.3	-2.0	-1.8	-1.8

Table 206: Net pressure coefficients for canopies according to Eurocode 1991-1-4

Slope α [°]	Degree of blocking φ	Wind pressure p_w $[kN/m^2]$			
		Zone A	Zone B	Zone C	Zone D
-10	Maximum for all φ	+0.732	+1.708	+0.976	+1.342
	Minimum for $\varphi = 0$	-0.976	-1.586	-1.830	-0.732
	Minimum for $\varphi = 1$	-1.952	-3.294	-3.172	-0.732
10	Maximum for all φ	+0.854	+2.196	+1.708	+0.488
	Minimum for $\varphi = 0$	-0.854	-1.830	-1.708	-1.708
	Minimum for $\varphi = 1$	-1.586	-2.440	-2.196	-2.196

Table 207: Resulting pressures

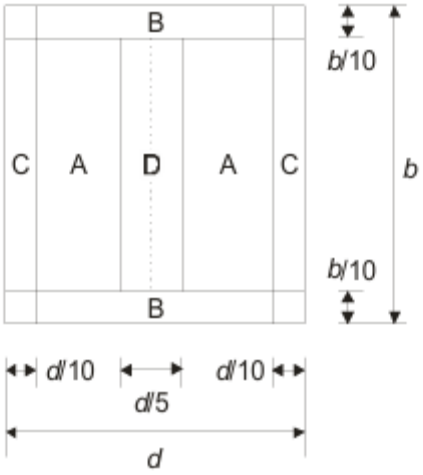

Figure 245: Zoning for net pressure coefficients for canopies according to Eurocode 1991-1-4

Eurocode wind loads for wind in the y-direction

According to the Eurocode is the wind load on a bridge for wind in y-direction equal to a load in y-direction on the side of the deck and a load in z-direction on the deck with a bending moment. The load in y-direction on the side of the deck is:

$$q_{w,y} = \frac{1}{2} * 1.25 * 29.5^2 * 5.25 * d_{tot} = 2855.5 * d_{tot}\ [N/m]$$

The wind loads acting in the y-direction are shown in Figure 246. The applied loads on the side of the structure consist of a distributed pressure of $2.856\ kN/m^2$ and a line load of $1.716\ kN/m$ acting on the top of the girders to account for the wind load on the balustrades.

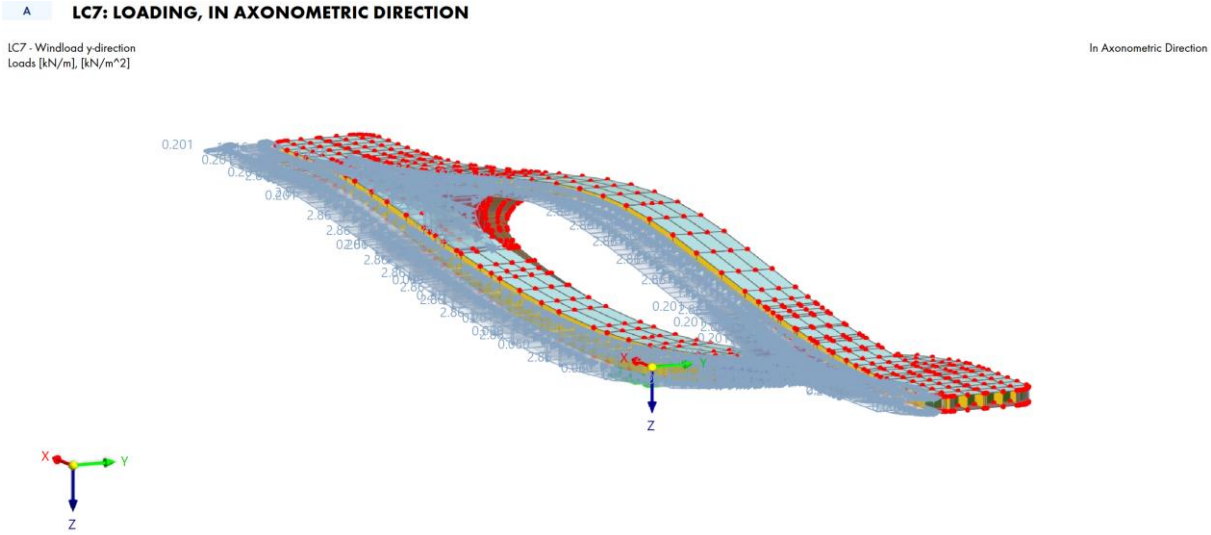

Figure 246: Applied load in the finite element model for the wind load in y-direction

The load in z-direction on the bridge is:

$$q_{w,z} = \frac{1}{2} * 1.25 * 29.5^2 * 0.9 * b = 489.5 * b = 489.5 * 1.8 = 881.1\ [N/m]$$

The distributed line load of the wind results in a distributed area load of:

$$q_{w,z} = \frac{0.881}{1.82} = 0.484\ [kN/m^2]$$

This load is applied on the top deck in z-direction.

The bending moment because of the eccentricity of the load in z-direction is:

$$m_{w,x} = 0.881 * 0.450 = 0.40\ kNm/m$$

The bending moment determined before is applied on the deck surface by a distributed load ranging from -0.24 to 0.24 in y-direction, see Figure 247.

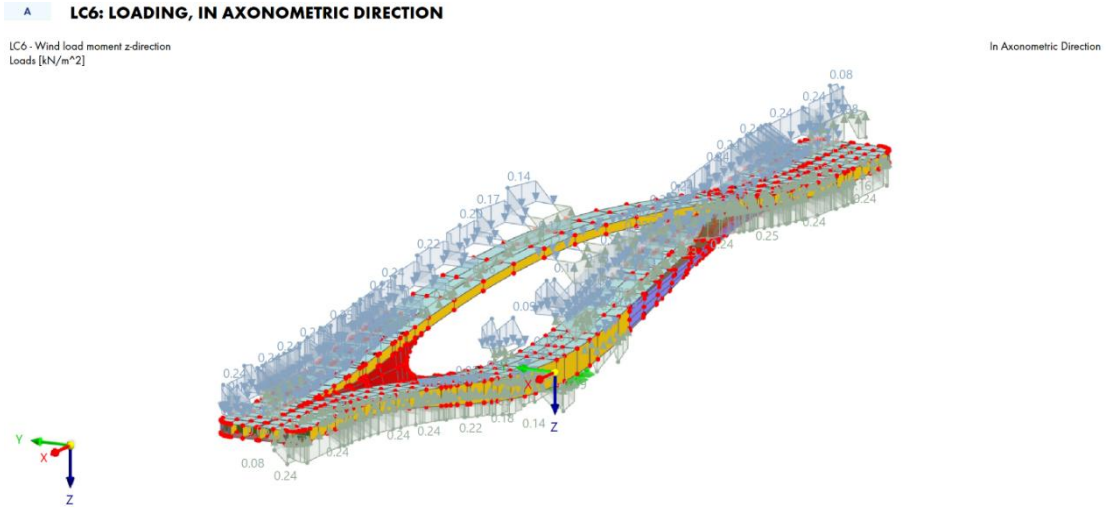

Figure 247: Bending moment wind load z-direction plate model

The load combination representing wind in the y-direction is:

$$LC5 + LC6 + LC7$$

The sum of loads and resultant of reactions of the wind loads is given in the table below.

Sum of loads in:	[kN]
X	0.0
Y	340.47
Z	89.25
Resultant of reactions about:	[kNm]
X	9.99
Y	0.33
Z	286.24

Table 208: The sum of loads and resultant of reactions of the wind in y-direction

The resulting deformation of the structure is shown in Figure 248.

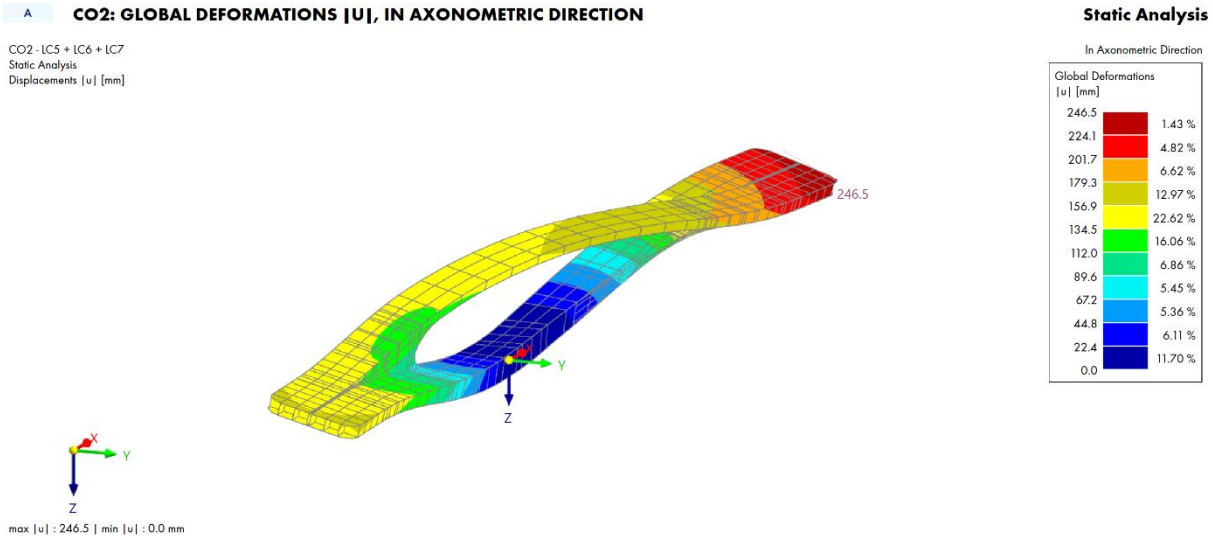

Figure 248: Deformations because of the wind in y-direction

A global assessment of the stress distribution, excluding local singularities, resulted in the approximate stress ranges shown in Table 209.

Stress component	Stress range $[N/mm^2]$
σ_x, local x-direction	-14 to +14
σ_y, local y-direction	-7 to +9
τ_{xy}, shear stress	-10 to +10

Table 209: Approximate global stress ranges for the Eurocode wind load for wind in y-direction